BEHAVIOR AND DESIGN OF METAL BUILDING FRAMES USING GENERAL PRISMATIC AND WEB-TAPERED STEEL I-SECTION MEMBERS

A Dissertation
Presented to
The Academic Faculty

by

Yoon Duk Kim

In Partial Fulfillment
of the Requirements for the Degree
Doctor of Philosophy in the
School of Civil and Environmental Engineering

Georgia Institute of Technology
May 2010

BEHAVIOR AND DESIGN OF METAL BUILDING FRAMES USING GENERAL PRISMATIC AND WEB-TAPERED STEEL I-SECTION MEMBERS

Approved by:

Dr. Donald W. White, Advisor
School of Civil and Environmental Engineering
Georgia Institute of Technology

Dr. Abdul-Hamid Zureick
School of Civil and Environmental Engineering
Georgia Institute of Technology

Dr. Rami M. Haj-Ali
School of Civil and Environmental Engineering
Georgia Institute of Technology

Dr. Sathya Hanagud
School of Aerospace Engineering
Georgia Institute of Technology

Dr. Kenneth M. Will
School of Civil and Environmental Engineering
Georgia Institute of Technology

Date Approved: March 31, 2010

To my parents, Yong Jin Kim and Young Hee Hahm and
my husband Hyun Seop Lee for their enormous support, patience, and love

ACKNOWLEDGEMENTS

It is a pleasure to express my gratitude to numerous people who helped me in many ways for the last six years to complete the journey of Ph.D candidacy. Without them, this dissertation would not have been possible.

First and foremost, I owe my deepest gratitude to my advisor Dr. Donald W. White for his encouragement, guidance and support for every step I took to complete this dissertation. His perpetual energy and enthusiasm in research and education has motivated me. He was always accessible and willing to help me with my research. It has been a privilege and an honor to work with and learn from Dr. White. I would also like to thank his wife, Mrs. Jane White, for sharing their precious family time on weekends with me so that I can meet Dr. White at his house to discuss my research. I appreciate the warm welcome she offered in her house and in our neighborhood.

My gratitude also goes to my thesis committee members, Dr. Kenneth M. Will, Dr. Abdul-Hamid Zureick, Dr. Rami M. Haj-ali, and Dr. Sathya Hanagud for their patience, encouragements and invaluable comments. Especially, Dr. Will and Dr. Zureick gave me great suggestions which I could improve my dissertation based on.

The generous support from Metal Building Manufacturers Association is greatly appreciated. The steering group for this research provided valuable feedbacks and suggestions regarding my research. I deeply owed Mr. Richard Kaehler for giving me the honor to be a co-author of AISC Design Guide 25. I thank Mr. Duane Becker, who provided the designs of two MBMA frames and answered all my questions about the

details of these frames. I would also like to thank Dr. W. Lee Shoemaker for his support and comments.

During my graduate study, I was fortunate to have many friends who offered their support in my research as well as a joy in daily life at GT. I would like to thank Cagri, Andres, Juan, Akhil and Yavuz for their friendship and senses of humor, which made our office a very cheerful work place. My special thanks go to Akhil Sharma who helped me setting up a refined finite element analysis of two MBMA frames using ABAQUS.

My deepest gratitude goes to my parents, Yong Jin Kim and Young Hee Hahm. My father, Yong Jin Kim, is a definition of a hardworking person. He taught me the work ethics and how to motivate myself to achieve my goals. At the same time, he is a loving father who dedicates his time to his family all the time. My mother, Young Hee Hahm, is the most loving and caring person I have ever known. It is truly amazing how she always knew what I needed before I realized. I cannot say how much love and support my parents gave me. I am so blessed to be their daughter.

Last but not least, words fail me to express my appreciation to my husband, Hyun Seop Lee. Ever since he came into my life, everyday has been a blessing. I didn't know how much love one can receive from the other before I met him. He dedicated so much of his time and effort to make it easier for me to concentrate doing my research and completing this dissertation. I can only hope that I will do the same when he needs it the most.

TABLE OF CONTENTS

LIST OF TABLES

LIST OF FIGURES

SUMMARY

Metal building frames are typically designed using welded prismatic and web-tapered members with doubly-symmetric and/or singly-symmetric cross sections. Until recently, the base U.S. provisions for design of frames with web-tapered members were provided in the AISC ASD (1989) and LRFD (1999) Specifications. Unfortunately, these previous AISC provisions address only a small range of practical designs. As a result, metal building manufacturers have tended to develop their own methods for design of the wide range of nonprismatic member geometries and configurations encountered in practice.

This research develops new design procedures for design of frames using general prismatic members and web-tapered members. An equivalent prismatic member concept utilized in prior research and the prior AISC provisions is generalized to accommodate the broad range of member types and configurations commonly used in metal building industry. Furthermore, the new design procedures incorporate many of the improvements achieved in the AISC (2005 & 2010) Specifications to metal building frame design. These improvements include a new stability design method, *the direct analysis method*, more complete considerations of different column buckling limit states (flexural, torsional and flexural-torsional buckling), and improved axial load and flexural resistance provisions. This research develops practical design-based procedures for simplified calculation of the elastic buckling resistances of prismatic and web-tapered members to facilitate the application of the proposed design methods. In addition, this research performs a relatively comprehensive assessment of beam lateral torsional buckling (LTB)

behavior and strength of prismatic and web-tapered members using refined virtual test simulation. It is demonstrated that web-tapered members behave in a comparable fashion to prismatic members. Based on the virtual simulation study, recommendations for potential improvement of the AISC LTB resistance equations are provided. Lastly, the strength behavior of several representative metal building frames is studied in detail using the same virtual test simulation capabilities developed and applied for the assessment of the beam LTB resistances.

CHAPTER I

INTRODUCTION

Metal building frames are commonly designed using web-tapered members with doubly-symmetric and/or singly-symmetric cross-sections. In addition, these frame types typically have a gable or single-slope roof and a single clear span, or multiple spans with the roof girder continuous over the interior columns. Web-tapered members have been utilized extensively in buildings and bridges for over 50 years due to the following advantages, which rolled I-section members cannot provide:

- Design Optimization: Web-tapered members can be shaped to provide the maximum strength and stiffness with the minimum weight. Web depths are made larger in areas with high moments and thicker webs are used in areas of high shear. Areas with less required moment and shear can be made with shallower and thinner webs respectively, saving significant amounts of material in comparison to rolled shapes.
- Fabrication Flexibility: Fabricators equipped to produce web-tapered members can create a wide range of optimized members from a minimal stock of different plates and coil. This can result in time and cost savings compared to the alternative of ordering or stocking an array of rolled shapes.

Web-tapered I-section members used in metal building systems typically have:

- Specified minimum yield strength $F_y \leq 55$ ksi,
- Homogeneous sections,
- Linear or piecewise linear web taper,
- Web taper angle between 0° and 15°,

- Flange thickness greater than or equal to the web thickness,
- Noncompact or slender flanges,
- Noncompact or slender webs (the webs are compact only at the bottom of web-tapered columns in most cases),
- Narrow flange widths compared to web depths particularly at deeper cross-sections,
- Unequal flange brace spacings on the inside and outside flanges with the outside flange braced at girts and purlins and the inside flanges braced by flange diagonals only where necessary to support the required loads, and
- Single-sided welding of the flanges to the web

In addition, metal building frames typically have

- Different column heights within the same story.
- Curved centroidal axes of the members due to single symmetry plus tapered geometry, and
- A centroidal axis that is inclined relative to the vertical direction in exterior columns, with the outside flanges usually being nominally vertical.

Up until the recent past, the base U.S. provisions for design of frames with web-tapered members were provided in the AISC ASD (1989) Specification. Unfortunately, the previous AISC (1989) provisions address only a small range of practical designs. In many situations in the design of the metal building frames, engineers have needed to exercise a great deal of judgment to accommodate specific manufacturing and construction needs (The limitations of the previous AISC (1989) provisions are addressed in detail in Section 1.1). As such, the stability design of these frame types has been conducted using various interpretations of the effective length method and the members

have been designed using various interpretations of the AISC AS (1989) resistance equations. Therefore, in the development of the AISC (2005) and (2010) Specifications, the previous provisions for design of web-tapered members have been excluded entirely. The objective of this research is to develop new design procedures for design of frames using web-tapered members. Key goals are: (1) to accommodate the broad range of member types and configurations commonly used in metal building construction and (2) to extend many of the improvements achieved in the 2005 and 2010 AISC Specifications to metal building frame design.

1.1. Background

Research on stability of members of varying cross-section can be traced back to the work of Euler (Ostwald, 1910), who derived the differential equation of the deflection curve and discussed columns of various shapes, including a truncated cone or pyramid. Lagrange (1770-1773) discussed the stability of bars bounded by a surface of revolution of the second degree. Timoshenko (1936) summarized various analytical and energy method solutions for the elastic buckling of nonprismatic columns and cited related work as early as Bairstow and Stedman (1914) and Dinnik (1914, 1916, 1929 & 1932). He also discussed a powerful procedure called the method of successive approximations, which makes it possible to estimate buckling loads along with upper and lower bounds for any variation of the geometry and/or axial loading along a member length.

Timoshenko (1936) demonstrated a graphical application of the method of successive approximations to a simply-supported column with a stepped cross-section subjected to a constant axial load. Bleich (1952) provided analytical solutions for the elastic buckling of simply-supported columns with linear and parabolically varying

depths between their "chords." Furthermore, he provided an overview of the method of successive approximations including a proof of its convergence. In addition, Bleich provided detailed discussions of numerical solution procedures utilized with the method of successive approximations for column flexural buckling and thin-walled open section beam lateral torsional buckling problems. These developments were based largely on the research by Newmark (1943) as well as by Salvadori (1951).

Timoshenko and Gere (1961) retained the solutions presented in (Timoshenko, 1936) and added a numerical solution for Timoshenko's original stepped column demonstration of the method of successive approximations. Timoshenko and Gere attributed the specific numerical implementation details they presented to Newmark (1943), and they referenced Newmark for more extensive discussions and additional applications. More recent discussions of the method of successive approximations are provided by Chen and Lui (1987) in their Section 6.7, and by Bazant and Cedolin (1991) in their Section 5.8. Timoshenko and Gere (1961) also discussed the calculation of inelastic strengths of bars with variable cross-section. They suggested that estimates of the inelastic strength of variable cross-section columns can be obtained using prismatic-section column curves along with the tangent modulus, E_t, at the cross-section having the maximum compressive stress.

In 1966, the Column Research Council (CRC) and the Welding Research Council (WRC) initiated the first concerted effort to address the complete strength behavior of metal building frames composed of tapered I-section members. Prior experimental studies by Butler and Anderson (1963) and Butler (1966) had addressed the elastic stability behavior of I-section beams tapered in both the flanges and webs and tested as

cantilever beam-columns. Starting in 1966, researchers at the State University of New York at Buffalo worked on numerous aspects of the problem. This research concluded with the development of the AISC (1978) Specification provisions as well as a synthesis of these provisions plus additional design procedures and recommendations by Lee et al. (1981). The SUNY Buffalo research was conducted under the joint sponsorship of the American Institute of Steel Construction, the American Iron and Steel Institute, the Metal Building Manufacturers Association and the Naval Facilities Engineering Command.

The first set of experimental tests aimed at understanding the inelastic stability behavior of tapered I-section beam-columns was conducted under the technical guidance of the CRC-WRC joint task committee and was documented by Prawel et al. (1974). These tests and other analytical studies provided the basis for an overall design approach summarized by Lee et al. (1972). These developments targeted members with linearly-tapered web depths. A key characteristic of the resulting design calculations was the use of *member length modification factors*. The modification factors mapped the physical linearly-tapered member to an equivalent prismatic member composed of the cross-section at its shallower end. The modified length for the equivalent prismatic member was selected such that this hypothetical member would buckle elastically at the same applied load as the physical linearly-tapered member. Length modification factors were developed by curve fitting to representative results from members with five different cross-sections. For in-plane flexural buckling under constant axial load, the corresponding modification factor was denoted by the symbol g. For out-of-plane lateral-torsional buckling (LTB) under approximately constant compression flange stress, two length modification factors were developed that paralleled the idealizations used in the

AISC (1969) ASD double-formula approach. One modification factor (h_s) was based on considering only the St. Venant torsional stiffness while the other (h_w) was based on considering only the warping torsion stiffness.

The equivalent column length (gL) only addressed the in-plane flexural buckling of columns with simply-supported end conditions. Therefore, a second length modification factor was applied to this length to account for the rotational restraint provided at the column ends by adjacent members. Idealized rectangular frame models similar to those employed in the development of the AISC alignment charts were used to derive design charts for the corresponding effective length factors K_γ. Two ideal rectangular frame alignment chart cases, sidesway prevented and sidesway uninhibited, were addressed. The total equivalent prismatic column length was therefore taken as the product of g and K_γ with the physical tapered member length, i.e., $K_\gamma\, gL$. Actually, the g parameter was absorbed into the charts provided for determination of K_γ, but the two factors are shown separately here to emphasize the concepts.

Once the equivalent prismatic column length $K_\gamma\, gL$ was determined, the AISC ASD equations were used to determine the column elastic or inelastic design strengths. It is important to note that all the above steps were simply a means of estimating the maximum axial stress along the length of the column *at incipient elastic buckling*. This was followed by the *mapping* of this *elastic buckling stress* to the *elastic or inelastic design stress*. This last step used the same mapping of the theoretical elastic buckling to the design buckling resistance employed for prismatic members.

The above calculations only addressed the in-plane flexural buckling column resistance of linearly-tapered web I-section members. The out-of-plane flexural buckling

resistance was addressed in exactly the same way as for prismatic members, since the weak-axis moment of inertia I_y is nearly constant along the length for members with prismatic flanges.

The calculation of the LTB design resistance involved the combination of the square root of the sum of the squares of the two elastic LTB contributions (one corresponding to the St. Venant torsional resistance and the other corresponding to the warping torsional resistance) to determine an estimate of the theoretical total elastic LTB stress under uniform bending and simply-supported end conditions. This stress was then multiplied by an additional parameter, labeled *B* in AISC (1978), which increased the calculated elastic buckling stress accounting for an estimate of: (1) end restraint from adjacent unbraced segments and/or (2) the effects of a flexural stress gradient along the tapered member length. The *B* parameter equations were developed in the research by Lee et al. (1972), Morrell and Lee (1974) and Lee and Morrell (1975). The base elastic LTB stress modified by *B* was taken as the estimated maximum flexural stress at incipient elastic LTB of the tapered section member. Similar to the column strength determination, this elastic stress was used with the AISC ASD prismatic member mapping from the theoretical elastic buckling resistance to the design LTB resistance.

Lee et al. (1972) recommended interaction equations for checking of linearly-tapered web I-section members for combined axial and flexural loadings. These equations paralleled the AISC ASD beam-column strength interaction equations for prismatic I-section members. The only change in the interaction equations implemented in AISC (1978) was a simplification in the C_m parameter, referred to as C'_m in the AISC tapered member provisions. Lee et al. (1972) developed a generalized C_m equation to

approximate the second-order elastic amplification of the maximum major-axis bending stress in linearly-tapered members at load levels corresponding to the nominal first-yield condition. This generalized equation accounts for the influence of linear web taper and a linear variation of the bending moment between the member ends. The AISC (1978) C'_m equations are identical to Lee's generalized C_m equation but correspond to the specific cases of: (1) single curvature bending with equal maximum flexural stress at both ends of the member and (2) single curvature bending with zero moment (or flexural stress) at the smaller end.

The above procedures have formed the primary basis for the AISC design provisions in Appendix D of the 8th Edition ASD Specification (AISC, 1978), Appendix F4 of the 1st Edition LRFD Specification (AISC, 1986), Appendix F7 of the 9th Edition ASD Specification (AISC, 1989), and Appendix F3 of the 2nd and 3rd Edition LRFD Specifications (AISC, 1993 and 1999).

The above approaches did not account for torsional or flexural-torsional buckling limit states in tapered columns and beam-columns. The flexural-torsional buckling limit state can be of particular importance for tapered members with unequal flange areas. Lee and Hsu (1981) addressed this design requirement by providing an alternate beam-column strength interaction equation that estimated the flexural-torsional buckling resistance of tapered members subjected to combined bending and axial compression. Lee and Hsu (1981) also developed charts that provided a coefficient required in the alternate beam-column strength interaction equation. These charts were included in Lee et al. (1981) but were never adopted within any of the AISC Specifications.

Furthermore, the above approaches did not address the in-plane stability design of I-section members consisting of two or more linearly tapered segments. These types of members are used commonly for roof girders or rafters in metal building frames. Lee et al. (1979) developed another extensive set of design charts that permitted the calculation of: (1) the equivalent pinned-end prismatic column length for doubly symmetric doubly tapered I-section members (analogous to the length gL), and (2) the *effective* equivalent prismatic column length accounting for the influence of end rotational end restraints for these members (analogous to the length $K_\gamma gL$). The second of these calculations was based again on idealized rectangular frame models similar to those associated with the AISC alignment charts. The authors provided charts and procedures for calculation of the equivalent rotational stiffness provided by adjacent tapered members again using the concept of the equivalent length of an alternate prismatic member composed of the shallowest cross-section along the tapered member length. These charts were included in Lee et al. (1981) but were never adopted within any of the AISC Specifications.

The provisions within the AISC Specifications from AISC (1978) through AISC (1999) were limited only to I-section members with equal-size flanges and linearly-varying web depths. This, combined with the unpopularity of design charts without underlying equations for calculation of the corresponding parameters, has led to limited acceptance of the AISC provisions. Metal building manufacturers have tended to develop their own specific mappings of the AISC prismatic member equations for design of the wide range of general nonprismatic member geometries and configurations encountered in practice. A number of the metal building manufacturers have made substantial investments of their own resources into research to validate their design

approaches. To complicate matters, the AISC provisions for design of prismatic I-section members have been greatly improved over the past forty years relative to the 1963 Specification procedures upon which the web-tapered member provisions of AISC (1978) were based. This has led to awkward differences in the design equations for prismatic and linearly-tapered I-section members in the AISC (1986, 1993 and 1999) provisions. As a result, the AISC Committee on Specification decided to drop the explicit consideration of nonprismatic I-section members entirely from the unified 2005 AISC provisions in favor of subsequent development of separate updated guidelines for these member types. It was anticipated that the subsequent developments could take significant advantage of the many advances that have been implemented for member and frame stability design in the time since the seminal work by Lee et al. (1981).

Since the culmination of the work by Lee et al. (1981), numerous other studies have been conducted to investigate various attributes of the behavior of nonprismatic I-section members and of frames composed of these member types. Salter et al. (1980), Shiomi et al. (1983) and Shiomi and Kurata (1984) have reported on additional experimental tests of isolated doubly symmetric beam-columns with linearly-tapered webs. However, these tests focused only on members with compact webs and flanges. As mentioned above, practical web-tapered members produced by American manufacturers often have noncompact or slender webs and flanges. Forest and Murray (1982) tested eight full-scale gable clear-span frames with proportions representative of American design practices under the sponsorship of Star Building Systems. They provided an assessment of the Star Building Systems design rules in place at that time as well as the procedures recommended by Lee et al. (1981). Forest and Murray concluded,

"No consistent set of design rules adequately predicted the frame strengths for all the loading combinations." However, the Star Building Systems design rules were judged to be safe. Jenner et al. (1985a & b) tested four clear-span frames. These tests demonstrated the importance of providing sufficient panel zone thickness to maintain the stiffness of the knee joint area. Davis (1996) conducted comparisons of AISC LRFD (1993) calculation procedures to the results from two other full-scale clear-span gable frame tests conducted at Virginia Tech. Local buckling of the rafter flanges governed the design resistances as well as the experimental failure modes. The predictions of the experimental resistances were consistently conservative by a small margin.

Watwood (1985) discussed the calculation of the appropriate effective length of the rafters in an example gable frame, accounting for the rafter axial compression and its influence on the sidesway stability of the overall structure. Watwood also investigated the sensitivity of his example frame design to the foundation boundary conditions and to unbalanced gravity loads. He suggested an approach for design of the rafters that in essence takes the buckling load of these members as their axial force at incipient sidesway buckling of the full structure. This typically results in an effective length factor for the rafters significantly larger than one.

Numerous other researchers have considered the influence of axial compression in the rafters of gable clear-span frames in the calculation of the overall sidesway buckling loads and in the design of the gable frame columns, e.g., Lu (1965), Davies (1990), and Silvestre and Camotim (2002). These results highlight an anomaly of the Effective Length Method (ELM) for structural stability design. Members that have small axial stress at incipient buckling of the frame generally have large effective length factors (K).

In some cases, these K factors are justified while in other cases they are not. If the member is indeed participating in the governing buckling mode, a large K value is justified. If the member is largely undergoing rigid-body motion in the governing buckling mode, or if it has a relatively light axial load and is predominantly serving to restrain the buckling of other members, a large K value is sometimes not justified. The distinction between these two situations requires significant engineering judgment. In any case, the ELM procedures recommended by Lee et al. (1981) rely on the *first-order elastic* stiffness of the adjacent members in determining the K_γ values. Unfortunately, if the adjacent members are also subjected to significant axial compression, their effective stiffnesses can be reduced substantially. In these cases, the Lee et al. (1981) K_γ procedures in essence rely on one member to restrain the buckling of its neighbor, then turn around and rely on the neighbor to restrain the buckling of the first member. Watwood (1985) shows a clear example illustrating the fallacy of this approach.

Cary and Murray (1997) developed a significant improvement upon the traditional calculation of alignment chart frame effective length factors for sway frames. Their approach built upon Lui's (1992) development of a story-stiffness based method for prismatic member frameworks. A common useful attribute of story-stiffness based methods is that they use the results of a first-order elastic drift analysis (typically one conducted for service design lateral loadings) to quantify the overall story buckling resistance. In addition, one of the most significant attributes of these methods is the fact that they account for the influence of gravity (leaning) columns on the frame sidesway buckling resistance. Conversely, the traditional AISC alignment chart and the Lee et al. (1981) effective length factor methods do not. This attribute can be a very important

factor in the proper stability design of wide modular frames having multiple bays and a large number of leaning (gravity) columns.

Cary and Murray (1997) did not address the potential significant degradation in the story buckling resistance due to axial compression in the beams or rafters of metal building structures. This axial compression is often negligible for modular building frames, but it can be quite significant in some gable clear-span frames such as the frame considered by Watwood (1985). Also, these investigators did not account for the influence of different height columns. This characteristic generally needs to be addressed in modular building frames as well as in single-slope roof clear-span frames. Eurocode 3 (CEN, 2005) provides guidance on when the common story-stiffness based approximations are appropriate for gable frames, although the origins and basis for the EuroCode3 guidelines are unknown.

Metal building frame members are usually proportioned such that they encounter some yielding prior to reaching their maximum resistance. Subsequent to the seminal work documented by Lee et al. (1981), a number of other research studies have focused on evaluation of inelastic beam and beam-column resistances and frame design. Jimenez (1998, 2005 and 2006) and Jimenez and Galambos (2001) conducted numerous inelastic stability studies of linearly tapered I-section members accounting for a nominal initial out-of-straightness, the Lehigh (Galambos and Ketter, 1959) residual stress pattern commonly used in the literature for rolled wide-flange members, and assuming compact cross-section behavior (i.e., no consideration of web or flange plate slenderness effects). Jimenez showed that the AISC (1999) provisions predicted the column inelastic buckling resistance with some minor conservatism for these types of members. Also, he observed

that the inelastic LTB curve for these types of members, predicted from inelastic buckling analyses, exhibited more of a pinched or concave up shape (rather than the linear transition curve assumed for the inelastic LTB range in AISC (1999)).

In addition, Jimenez observed that very short unbraced lengths were necessary for the compact I-section members considered in his study to reach their ultimate plastic moment capacity. It is important to note that this type of behavior has been observed as well in a number of inelastic buckling studies of prismatic I-section members (Narayanan 1983 and Nethercot 1974). White and Jung (2008) and White and Kim (2008) show that the linear transition curve for inelastic LTB in AISC (2005) is a reasonable fit to the mean resistances from experimental test data for all types of prismatic I-section members and provide a justification for the use of the AISC (2005) resistance factor $\phi_b = 0.9$ with these member types.

Other researchers have suggested simpler and more intuitive ways of determining the elastic buckling resistance of I-section members than the use of an equivalent prismatic member (with a modified length). Polyzois and Raftoyiannis (1998) reexamined the *B* factor equations from AISC (1978, 1986, 1989, 1993, 1999) and suggested changes that covered a wider range of geometry and loading cases. They questioned the use of the single modification factor (*B*) to account for both the stress gradient effects as well as the influence of LTB end restraint from adjacent segments. Consequently, they developed separate modification factors for each of these contributions to the elastic LTB resistance. In other developments, Yura and Helwig (1996) suggested a method of determining the elastic LTB resistance of linearly-tapered I-section members based on: (1) the use of the AISC (2005) C_b equations but written in

terms of the compression flange stresses rather than the member moments and (2) the use of the tapered member cross-section at the middle of the segment unbraced length.

Numerous researchers have worked on refined calculation of elastic LTB resistances for tapered I-section members in recent years. Andrade et al. (2005) and Boissonnade and Maquoi (2005) are two of the most recent papers in this area. Both of these papers show that the use of prismatic beam elements for the analysis of tapered beams (i.e., subdivision of the member into a number of small prismatic element lengths), can lead to significant errors when the behavior involves torsion.

Davies and Brown (1996), King (2001a & b) and Silvestre and Camotim (2002) have presented substantial information about the overall design of gable frame systems, including clear-span frames and multiple-span gable frames with moment continuity throughout and lightweight interior columns. Much of their discussions are oriented toward European practices and design standards, including plastic analysis and design of single-story gable frames using compact rolled I-section members with haunches at the frame knees. However, these studies also provide useful insights that are of value to American practice, although as noted previously American practice typically involves welded I-sections with thinner web and flange plates not permitted for traditional plastic design.

1.2. Objective and Scope of this Research

The objective of this research is to develop general design procedures for frames using web-tapered and other prismatic or nonprismatic members. The results from this research provide the basis for the AISC Design Guide 25, *Frame Design using Web-*

Tapered Members (Kaehler et al. 2010). A review of the Appendix F provisions of AISC (1989) establishes a number of the needs for this research:

1) The prior AISC (1989) provisions required the flanges to be of equal and constant area. More general cases such as singly symmetric members and unbraced segments having cross-section transitions should be addressed in the new design procedures.
2) The prior AISC (1989) provisions required the depth to vary linearly between the ends of the unbraced lengths. Cases including unbraced lengths having cross-section transitions and/or multiple tapered segments should be addressed in the new procedures.
3) The Appendix F provisions of AISC (1989) ASD define a mapping of the beam and column resistances from a theoretical elastic buckling value to an elastic or inelastic design resistance using the AISC (1989) beam and column equations. However, the AISC (2005 & 2010) resistance equations provide improved simplicity and accuracy for base prismatic member cases compared to the prior AISC ASD equations (White and Chang, 2007). It is desirable to use the AISC (2005 & 2010) resistance equations in new design procedures, while continuing to use a form of the concept of mapping the theoretical elastic buckling strengths to nominal buckling resistances.
4) The prior AISC (1989) column resistance equations for tapered members were based on the calculation of an equivalent elastic effective length factor, $K_\gamma g$. The effective length, $K_\gamma gL$, was the length at which an equivalent prismatic member composed of the smallest cross-section would buckle elastically at the same constant axial load as in the actual tapered column of length L. As noted in the previous section, the separate g parameter, which gives the equivalent length for simply-supported end

conditions, was actually absorbed into charts for determination of the rotational end restraint effects. Therefore, AISC (1989) shows just one factor, labeled as K_γ (i.e., K_γ in AISC (1989) is the same as $K_\gamma g$ in this discussion). The length $K_\gamma gL$ was used in the AISC (1989) equations to accomplish the above mapping from the theoretical elastic buckling stress to the column buckling resistance, expressed in terms of the axial stress. The AISC (1989) column buckling resistance corresponded specifically to the axial stress state at the smallest cross-section.

It is important to note that the calculation of the effective length $K_\gamma gL$ is only one way to obtain the axial stress of a web-tapered member at incipient buckling. The required use of the effective length factor $K_\gamma g$ in AISC (1989) combined with basing the approach of the smallest member cross-section limits the accuracy and generality of the previous provisions. If a design procedure can focus directly on the calculation of the elastic buckling load level for an unbraced length under consideration, it is possible to achieve better accuracy and generality.

5) The prior AISC (1989) column resistance equations for web-tapered members addressed only in-plane flexural buckling. The out-of-plane flexural buckling resistance was addressed in exactly the same way as for prismatic members, since the weak-axis moment of inertia I_y is nearly constant along the length for members with prismatic flanges. However, torsional or flexural-torsional buckling was not addressed in the AISC (1989) provisions for web-tapered members. It is desirable to address torsional or flexural-torsional buckling for web-tapered members in the new design procedures, to make the procedures more comprehensive.

6) In metal building frames, the outside flange is usually braced at the purlin or girt locations, and the inside flange is braced by diagonals from the girts or purlins but only at necessary locations to achieve the required strength. As a result, the unbraced length of the inside flange is often longer than that of the outside flange. In this case, the strength limit state is often governed by constrained-axis torsional buckling. Constrained-axis torsional buckling is not addressed in the prior AISC (1989) or current AISC (2010) Specifications. The new design procedures should address constrained-axis torsional buckling for prismatic and nonprismatic members.

7) The prior AISC (1989) flexural resistance equations also focused on a modification of the tapered member length, L. The basic concept was to replace the tapered beam by an "equivalent" prismatic beam with a different length, and with a cross-section identical to the one at the smaller end of the tapered beam. The equivalency condition was that both the actual tapered member and the equivalent prismatic member buckle elastically at the same flexural stress if the compression flange is subjected to uniform flexural compression. This led to two different length modifiers, labeled h_s and h_w, which were used with the ASD double-formula lateral-torsional buckling (LTB) resistance equations depending on whether the LTB resistance was dominated by the St. Venant torsional stiffness or the warping torsion stiffness. Rather than taking the elastic buckling stress as the larger of these two estimates, $F_{s\gamma}$ and $F_{w\gamma}$, as in the prismatic member AISC (1989) provisions, AISC (1989) Appendix F used the more refined estimate $(F_{s\gamma}^2 + F_{w\gamma}^2)^{0.5}$ to determine the base elastic LTB stress. A separate modifier, labeled B, was applied to this elastic buckling estimate to account for moment gradient effects and lateral restraint offered by adjacent unbraced

segments. Finally, for $B\,(F_{s\gamma}^2 + F_{w\gamma}^2)^{0.5} > F_y/3$, the AISC (1989) Appendix F flexural resistance equations mapped the above elastic buckling stress estimate, $B\,(F_{s\gamma}^2 + F_{w\gamma}^2)^{0.5}$, to an inelastic LTB design resistance using the prismatic member equations. For $B\,(F_{s\gamma}^2 + F_{w\gamma}^2)^{0.5} < F_y/3$, the design LTB resistance was taken the same as the theoretical elastic LTB resistance. The flexural stress at the larger end of the unbraced length was then compared to this design LTB resistance. As discussed in the previous item (4), the procedure for design of web-tapered members potentially can be more generalized if the method focuses directly on the calculation of the theoretical elastic buckling stress including moment gradient and lateral restraint effects. The use of the effective length factors h_s and h_w, and the tieing of these factors to the smallest cross section via limited calibration studies prevents the engineer from taking advantage of modern capabilities for determining accurate elastic buckling estimates for general members.

8) The prior AISC (1989) provisions address compression flange local buckling (FLB) on a cross-section by cross-section basis using the base prismatic member equations (AISC, 1989). The AISC (2005 and 2010) FLB equations give a simpler and more accurate characterization of the FLB resistance of I-section members (White and Chang, 2007) than the prior AISC (1989) provisions. The new design procedures should incorporate the AISC (2010) FLB equations.

9) The AISC (1989) provisions restrict both the tension and the compression flange to the same allowable LTB stress. A more rational tension flange yielding (TFY) limit should be considered for singly symmetric I-section members having a smaller

tension flange and a larger depth of the web in flexural tension than in flexural compression.

10) The AISC (1989) Appendix F provisions applied the base ASD prismatic beam-column strength interaction equations to assess the resistance of members subjected to combined flexure and axial force. A modified factor, labeled C'_m, was defined for two specific cases: (1) single curvature bending and approximately equal computed bending stresses at the ends and (2) computed bending stress at the smaller end equal to zero. The AISC (2010) beam-column strength interaction equations applyin an accurate to conservative fashion to estimate the resistance of all types of beam-column geometries including all combinations of column and beam resistance limit states. The new prismatic and nonprismatic member design procedures should consider the merit of utilizing the base AISC (2010) prismatic beam-column strength interaction equations.

11) The prior AISC (1989) Appendix F provisions required extensive use of charts for the calculation of the in-plane column buckling resistances (i.e., for the determination of $K_\gamma g$). It is desirable to have appropriate equations for design parameters rather than to use various charts for the resistance calculations.

12) The stability design provisions in the AISC (2010) Specifications are revised significantly relative to the previous Specifications. The 2010 Specification outlines three specific procedures for stability design. Of these three procedures, the direct analysis method typically provides an improved representation of the physical internal forces and moments in the structure. Furthermore, this method eliminates the

need for calculating the effective length factor *K*. The use of the direct analysis method should be investigated for the design of frames using nonprismatic members.

13) The stability design provisions in the AISC (2010) Specifications focus largely on the design of rectangular or tiered structures, although the base procedures are applicable to general geometries. Metal building frames typically have gable or single-slope roofs with a single span or multiple spans. As a result, the columns in metal building frames have different heights as well as inclined centroidal axes due to the tapered geometry. In addition, singly-symmetric tapered members have curved centroidal axes. These aspects should be addressed in the development of new design procedures.

All the aspects recognized above are addressed in this dissertation. The following are the major contributions of this research:

- Development of general framework for design of frames using web-tapered members and other nonprismatic members,
- Generalization of equivalent prismatic member approaches utilized in prior research and in prior AISC provisions, and the extension of the AISC (2010) column and flexural resistance provisions utilizing an equivalent prismatic member concept.
- Development of practical design-based procedures for simplified calculation of member elastic buckling resistances,
- Comprehensive assessment of beam lateral torsional buckling strength for prismatic and web-tapered members, and
- Development and application of general procedures for virtual test simulation.

1.3. Organization

First, Chapter 2 provides an overview of the stability design methods outlined in the AISC (2010) Specification. Then Chapter 3 addresses the development of prototype extensions of the AISC (2010) Specifications for design of frames using general member geometries and loadings. Chapter 4 outlines the development of practical design based elastic buckling solutions for prismatic and web-tapered members. Chapter 5 proposes general finite element analysis procedures for virtual test simulation. These simulation capabilities are utilized in the subsequent investigations presented in Chapters 6 through 8. Chapter 6 illustrates the results of virtual test simulation conducted for experimental tests using prismatic and web-tapered members. In addition, design check calculations are performed for the web-tapered member tests based on the prototype procedures outlined in Chapter 3. These design check calculations are compared with the experimental test results as well as the virtual test simulation results. Chapter 7 provides a comprehensive assessment of the lateral torsional buckling resistance of prismatic and web-tapered members using virtual test simulation. This chapter concludes with an assessment of reliability using the conventional 1^{st}-order 2^{nd}-moment method originally forwarded by Galambos and Ravindra (1976). Recommendations for potential improvement of the lateral torsional buckling resistance calculations in AISC (2010) are provided. Chapter 8 illustrates the design of two example metal building frames using the prototype procedures outlined in Chapter 3. In addition, this chapter discusses the results of virtual test simulation conducted for both the example frames. Lastly, Chapter 9 provides a summary and conclusions from this research. In addition, Chapter 9 discusses the impact of this research as well as suggestions for future work.

CHAPTER II

OVERVIEW OF STABILITY ANALYSIS AND DESIGN METHODS IN AISC (2010)

2.1 Background

Chapter C of AISC (2010), Design for Stability, states that *any* analysis and design procedure that addresses the following effects on the overall stability of the structure and its elements is permitted:

1. Flexural, axial and shear deformations (in members, connections and other components), and all other deformations that contribute to displacements of the structure,
2. Reduction in stiffness (and corresponding increases in deformations) due to residual stresses and material yielding,
3. *P*-Δ (*P*-large delta) effects, which are the effects of axial loads P acting through the relative transverse displacements of the member ends Δ (see Fig. 2.1),
4. *P*-δ (*P*-small delta) effects, which for initially straight members loaded by bending in a single plane, are due to the member axial load acting through the transverse bending displacements relative to the member chord (see Fig. 2.1),
5. *P*-Δ_o and *P*-δ_o effects, which are caused by the member axial loads acting through unavoidable initial Δ_o and δ_o geometric imperfections (within fabrication and erection tolerances) relative to the ideal configuration of the structure, and
6. Uncertainty in stiffness and strength.

The above statement gives the Engineer the freedom to select or devise methods that are best suited for the many different routine and nonroutine situations encountered in

practice. It allows for innovation within the constraints of the proper consideration of the physical effects that influence the structural response.

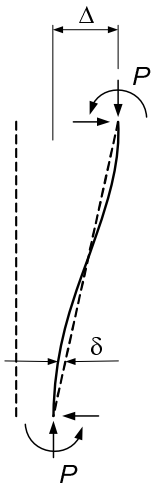

$P\Delta$ = Additional moment (couple) applied to the structure due to the member axial force acting through the relative transverse displacement of the member ends

$P\delta$ = Additional moment generated at a cross-section due to the member axial force acting through the transverse displacement relative to the member chord

Figure 2.1. Second-order P-Δ and P-δ effects.

Since the P-Δ and P-δ effects are central components of the frame stability behavior, it is useful to elaborate on their definitions. As illustrated in Figure 2.1, any relative transverse displacement Δ between a member's ends produces a couple of P times Δ, where P is the axial force transmitted by the member. This couple must be resisted by the structure. In typical tiered building systems, the predominant P-Δ effects come from the vertical columns. However, clear-span gable frames also have a P-Δ effect associated with the axial thrust in the rafters and the relative transverse displacement between the ends of the rafter segments, as shown in Figure 2.2. In certain types of structures, e.g., some types of modular frames, the predominant P-Δ effects come from simply-connected gravity columns (leaner columns), which depend on the lateral load resisting system for their lateral stability. Figure 2.3 gives a simple

illustration of this behavior. Under a sidesway displacement of the structure Δ, a lateral force equal to *P*Δ/L is required to maintain equilibrium of the leaner column in the deflected configuration. This lateral force must be resisted by the structure.

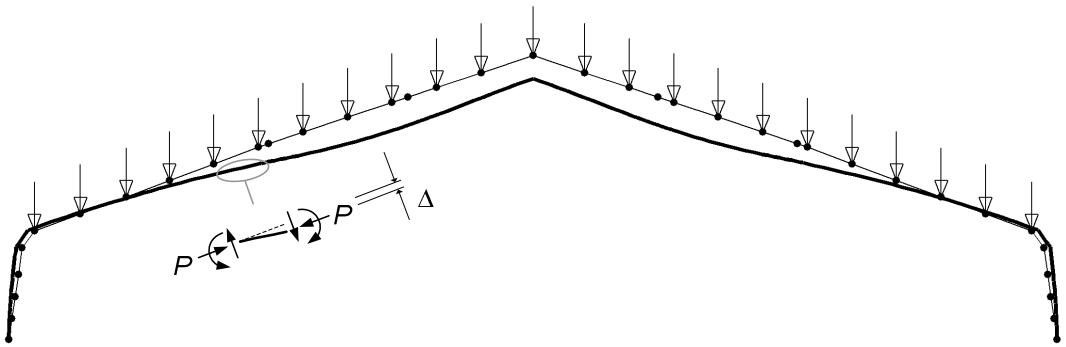

Figure 2.2. *P*-Δ effects in a rafter segment of a gable frame.

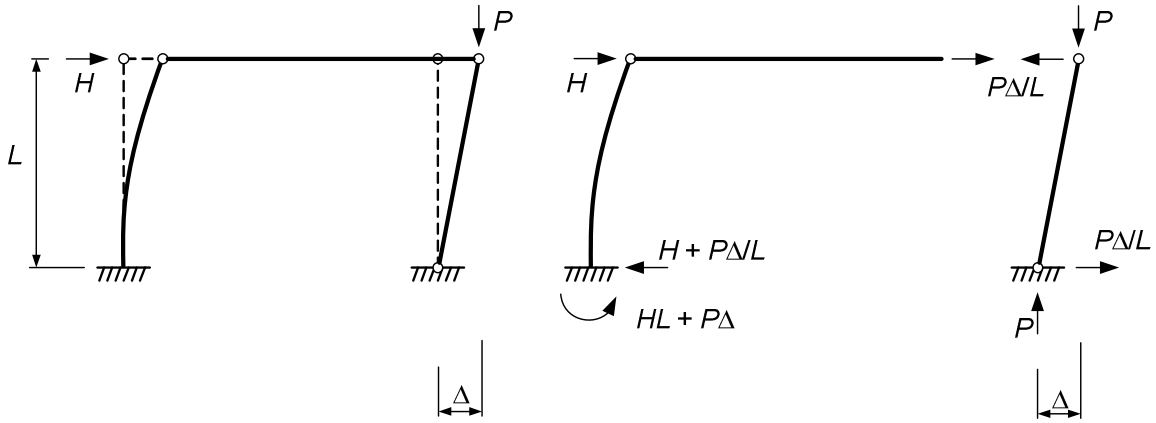

Figure 2.3. Illustration of *P*-Δ effects from a gravity (leaner) column.

Members that have small transverse displacements relative to their rotated chord and/or small axial forces have small *P*-δ effects. This includes leaner columns, which are commonly idealized as straight pin-ended struts and therefore have zero δ and zero *P*-δ effects, as well as stiff columns that deflect in sidesway mainly due to end rotation of the

adjacent beams (see Figure 2.4). However, members such as that shown in Figure 2.1 must resist additional moments of P times δ at the various cross-sections along their lengths. These P-δ moments increase the member deformations, and therefore they reduce the net member stiffnesses and increase the net sidesway displacements Δ. Interestingly, if the structure is subdivided into a large number of short-length elements, the representation of the P-Δ effect in each element is sufficient to capture both the overall member P-Δ and the internal member P-δ effects. Figure 2.2 is to some extent indicative of this attribute.

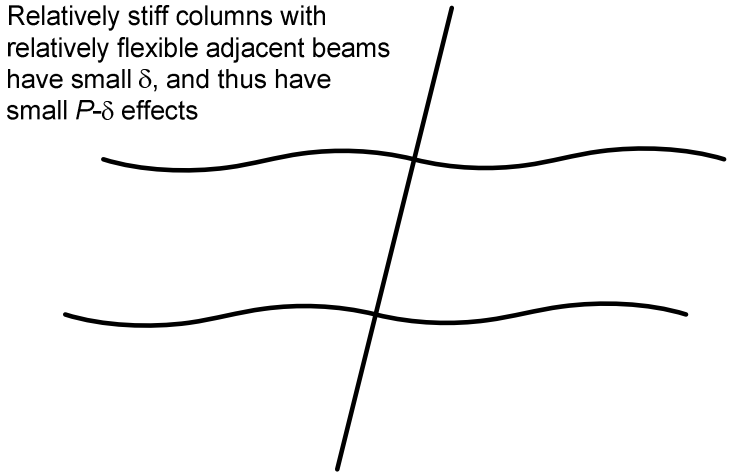

Figure 2.4. Illustration of deformed geometry resulting in small P-δ effects.

Guney and White (2007) study the number of elements required per member for P-large delta only analysis procedures to ensure less than 5 % error in the nodal displacements and less than 3 % error in the maximum internal moments for second-order elastic analysis of prismatic members with a wide range of loadings and end conditions. They also address the number of elements required to ensure less than 2 %

error in eigenvalue buckling analysis solutions. Based on the research by Guney and White (2007), the AISC Design Guide 25 provides tables showing the required number of elements to achieve the desired analysis accuracy for a given calculated $\alpha P_r / P_{eL}$ or $\alpha P_r / \overline{P}_{eL}$ value for sway columns with simply-supported bases, sway columns with top and bottom rotational restraints, and rafters and non-sway columns, where P_{eL} is the member elastic buckling load based on the idealized simply-supported end conditions and nominal elastic stiffness and $\overline{P}_{eL}$ is the member elastic buckling load based on the idealized simply-supported end conditions and reduced elastic stiffness specified by the direct analysis method. For example, at $\alpha P_r / P_{eL} = 0.15$, three elements are required for a sway column to ensure less than 5 % error in the nodal displacements and less than 3 % error in the maximum internal moments. In general, *P*-large delta only analysis procedures can adequately capture internal member *P*-δ effects when the subdivisions of members achieve $\alpha P_r \leq 0.02 P_{e\ell}$ or $\alpha P_r \leq 0.02 \overline{P}_{e\ell}$, where $P_{e\ell}$ is the element elastic buckling load based on idealized simply-supported end conditions and nominal stiffness and $\overline{P}_{e\ell}$ element elastic buckling load based on idealized simply-supported end conditions and reduced stiffness specified in the direct analysis method. Second-order analysis methods that directly include both *P*-Δ and *P*-δ effects at the element level generally provide better accuracy than *P*-large delta analysis procedures.

In tapered-web and general nonprismatic members, the centroidal axis is not straight, thus causing additional moments of *P* times *y*, where y is the shift in the centroidal axis relative to a straight chord between the cross-section centroids at the member ends (see Figure 2.5). This important effect is incorporated within a proper first-

order analysis, by virtue of the correct modeling of the geometry. Also, this is a member initial curvature effect rather than a P-δ effect. Additional P-δ moments are caused by the transverse bending displacements associated with the primary moments P times y. Typically, the initial curvature effect is incorporated in part by using multiple elements along the member length and locating the nodes of the analysis model along the curved cross-section centroidal axis. However, when one or both cross-sections are singly-symmetric, there is an abrupt shift in the centroidal axis at cross-section transitions. Also, it is convenient to use a straight reference axis that has a variable offset from the centroidal axis in some situations (e.g., placing the reference axis at a constant depth below the top of the steel in the rafters). In these cases, the first moment of the cross-sectional area is non-zero with respect to the reference axis.

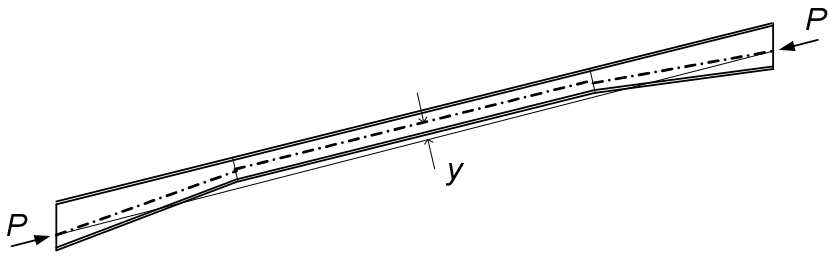

Figure 2.5. Member initial curvature effect of P times y.

Since the inception of the 1961 edition of the AISC Specification, when the concept of column effective length was first introduced by AISC, American design procedures generally have addressed all of the above effects in some fashion whenever they were deemed to have an important influence on the structural response. Member yielding, residual stress effects, and geometric imperfection effects traditionally have been addressed in the formulation of member design resistances, and have not been

considered in the analysis except the following case. Engineers have often included a nominal out-of-plumbness effect in the analysis of gravity load combinations, particularly if the geometry and loading are symmetric. Strictly, this is not necessary for the in-plane strength assessment of beam-columns in the prior AISC Specifications. However, this practice is necessary to determine P-Δ_o effects on bracing forces, beam moments, connection moments, and in-plane member moments for checking the out-of-plane resistance of beam-columns. There also has always been implicit recognition that the engineers can use their professional judgment to disregard specific effects (e.g., member shear deformations, connection deformations, etc.) whenever they are deemed to be negligible.

Furthermore, the 1961 AISC Specification, and other AISC Specifications up until 1986, relied strictly on the structural analysis *only* for calculation of linear elastic forces and moments within the idealized perfectly straight and plumb nominally elastic structural system. The influence of second-order (P-Δ and P-δ) effects was addressed solely by an amplifier applied discreetly to the flexural stresses from the linear elastic analysis, via the following beam-column strength interaction equation:

$$\frac{f_a}{F_a} + \frac{C_m f_b}{\left(1 - \frac{f_a}{F'_e}\right) F_b} \leq 1.0 \qquad \text{(Eq. 2.1)}$$

The expression

$$\frac{C_m}{\left(1 - \frac{f_a}{F'_e}\right)} = AF \qquad \text{(Eq. 2.2)}$$

in Eq. 2.1 is an approximate amplification factor (AF) for the member flexural stresses f_b, accounting for the second-order P-Δ and P-δ effects. LeMessurier (1977) and others later addressed the specifics of how to properly determine these amplified bending stresses in general cases, including multi-story structures and single-story structures with significant leaner column loads, all within the context of Allowable Stress Design. However, when the AISC (1989) ASD provisions are used, Engineers often apply Eq. 2.1 in ways that can significantly underestimate the physical second-order effects in certain types of structures. The accuracy of the calculations hinges largely on the proper determination of F_e, the member axial stress at incipient elastic buckling (considering the interaction of the member with the rest of the structure). The parameter F_e' is calculated by dividing this buckling stress by the column factor of safety, 23/12 = 1.92. The axial stress F_e' is determined typically using the equation

$$F_e' = \frac{12\pi^2 E}{23(KL_b / r_b)^2} \qquad \text{(Eq. 2.3)}$$

where KL_b/r_b is the column effective slenderness ratio in the plane of bending, and K is the effective length factor associated with the above buckling solution. Also, this K factor is used typically in the calculation of the column axial resistance F_a. If desired, $F_e' = F_e/1.92$ can be determined directly from the elastic buckling analysis model. Obviously if the "correct" F_e' is large relative to f_a, the second-order P-Δ and P-δ effects are small. The term C_m in Eqs. 2.1 and 2.2 is discussed subsequently.

AISC (1986) LRFD was the first American Specification to refer explicitly to the calculation of second-order moments from a structural analysis. This specification

introduced the following two-equation format for its primary beam-column strength interaction curve:

$$\frac{P_u}{2\phi_c P_n} + \frac{M_u}{\phi_b M_n} \le 1.0 \qquad \text{for } \frac{P_u}{\phi_c P_n} < 0.2 \qquad \text{(Eq. 2.4a)}$$

$$\frac{P_u}{\phi_c P_n} + \frac{8}{9}\frac{M_u}{\phi_b M_n} \le 1.0 \qquad \text{for } \frac{P_u}{\phi_c P_n} \ge 0.2 \qquad \text{(Eq. 2.4b)}$$

where M_u is defined as the maximum second-order elastic moment along the member length. AISC (1986) states that M_u may be determined from a second-order elastic analysis using factored loads. However it also provides an amplification factor procedure for calculation of the second-order elastic moments from a first-order elastic analysis. This procedure is in essence an approximate second-order analysis. The above moments M_u are the second-order elastic moments in the idealized initially plumb and straight, nominally elastic structure.

In all the AISC Specifications from AISC (1961) through AISC (1989) ASD and AISC (1999) LRFD, the influence of geometric imperfections and residual stresses was addressed solely within the calculation of the member resistances (F_a and F_b in ASD and P_n and M_n in LRFD). The *direct analysis* provisions that is first introduced in AISC (2005) and addressed in Chapter C of AISC (2010) recognize that specific advantages can be realized by moving an appropriate nominal consideration of these effects out of the resistance side and into the structural analysis side of the design equations. By incorporating an appropriate nominal consideration of these effects in the analysis, the resistance side of the design equations is greatly simplified and the accuracy of the design procedure is generally improved. These attributes are discussed further in the subsequent sections.

It is important to note that all of the above design procedures are based inherently on the use of second-order elastic analysis (first-order elastic analysis with amplifiers being considered as one type of second-order elastic analysis). Also, one must recognize that elastic analysis generally does not include the consideration of the member resistances in itself. Therefore, all of the above methods must include member resistance equations. However, the method of analysis and the equations for checking the member resistances are inextricably linked. Changes in the analysis calculation of the required strengths, e.g., f_a and $f_b C_m/(1\text{-}f_a/F'_e)$ in Eq. 2.1 or P_u and M_u in Eqs. 2.4, can lead to simplifications in the member resistances, typically F_a in Eq. 2.1 or P_n in Eqs. 2.4. Specifically, if the structural analysis can be configured to provide an appropriate representation of the internal member forces, the in-plane resistance of the structure can be checked entirely on a cross-section by cross-section basis. This is discussed in Section 2.2.

AISC (2005 and 2010) adopts the equations from AISC (1999) LRFD as a base representation of the beam-column resistances for all of its analysis and design procedures. However, the notation is generalized such that the equations apply to both ASD and LRFD:

$$\frac{P_r}{2P_c}+\frac{M_r}{M_c}\le 1.0 \qquad \text{for } \frac{P_r}{P_c}<0.2 \qquad \text{(Eq. 2.5a, AISC H1-1a)}$$

$$\frac{P_r}{P_c}+\frac{8}{9}\frac{M_r}{M_c}\le 1.0 \qquad \text{for } \frac{P_r}{P_c}\ge 0.2 \qquad \text{(Eq. 2.5b, AISC H1-1b)}$$

The terms in these equations are defined as follows:

P_r = the required compression strength, determined in ASD by analyzing the structure under 1.6 times the ASD load combinations and then dividing the results by 1.6, or

determined in LRFD by analyzing the structure under the LRFD load combinations.

M_r = the required flexural strength, determined in ASD by analyzing the structure under 1.6 times the ASD load combinations and then dividing the results by 1.6, or determined in LRFD by analyzing the structure under the LRFD load combinations.

P_c = the allowable or design compression resistance, given by P_n/Ω_c in ASD or by $\phi_c P_n$ in LRFD, where P_n is the nominal compression resistance determined in accordance with Chapter E.

M_c = the allowable or design flexural resistance, given by M_n/Ω_b in ASD or by $\phi_b M_n$ in LRFD, where M_n is the nominal flexural resistance determined in accordance with Chapter F.

ϕ_c and ϕ_b = resistance factors for axial compression and bending, both equal to 0.9.

Ω_c and Ω_b = factors of safety for axial compression and bending, both equal to 1.67.

For Equations 2.5a and b, another equation numbers are shown. In this dissertation, AISC (2010) equation numbers are denoted by "AISC" followed by the equation number. In many cases, Equations 2.5a and b provide a more liberal characterization of the beam-column resistances than the multiple beam-column strength curves in AISC ASD (1989).

It should be noted that the 1.6 factor applied to determine the required compression and flexural strengths under the ASD load combinations is smaller than the column safety factor of 1.92 within the AISC ASD (1989) amplification of the flexural stresses (see Eqs. 2.1 through 2.3). However, ASD-H1 also states that C_m shall be taken as 0.85 in Eqs. 2.1 and 2.2 for frames subject to joint translation. This C_m value typically underestimates the sidesway moment amplification effects (Salmon and Johnson 1996). Nevertheless, the ASD moment amplifier summarized in Eq. 2.2 is still conservative in

many practical cases. This is because the predominant second-order effects are often associated solely with the structure sidesway. Equation 2.1 applies a single amplifier indiscriminately to the total flexural stresses from both non-sway and sidesway displacements. The amplification factor procedure in AISC (1999) LRFD and AISC (2005 and 2010) is more accurate, but involves a cumbersome subdivision of the analysis into separate no-translation (*nt*) and lateral translation (*lt*) parts. Kuchenbecker et al. (2004) and White et al. (2007a & b) outline an amplified first-order elastic analysis approach that provides good accuracy for rectangular framing. This approach avoids the above cumbersome attributes of the AISC (1999, 2005 & 2010) amplification factor procedure

In the subsequent developments, it is useful to consider the characterization of separate in-plane and out-of-plane beam-column resistances using Eqs. 2.5. The in-plane beam-column resistance is addressed by neglecting out-of-plane flexural and/or flexural-torsional buckling in the calculation of P_c and by neglecting lateral-torsional buckling in the calculation of M_c. Correspondingly, the out-of-plane resistance is defined by considering solely the out-of-plane flexural and flexural-torsional buckling limit states in the determination of P_c (excluding the in-plane flexural buckling limit state), and by considering all the potential flexural limit states (lateral-torsional buckling, flange local buckling, tension flange yielding and general yielding) in the calculation of M_c. The interaction of general yielding and/or local buckling with column flexural buckling is included inherently within the calculation of both the in-plane and out-of-plane axial strengths P_{ci} and P_{co}. However, in the AISC (2005 and 2010) flexural resistance equations, lateral-torsional buckling, compression flange local buckling and tension

flange yielding are handled as separate and independent limit states. The smaller resistance from these separate limit states generally governs the flexural resistance. This research recommends that the compression flange local buckling and tension flange yielding limit states should be included in the calculation of the anchor point M_{co} for the beam-column out-of-plane strength using Eqs. 2.5. Otherwise, potential influences of compression flange local buckling or tension flange yielding on the out-of-plane beam-column resistance are neglected.

2.2 Direct Analysis Method

Table 2.1 summarizes three specific overriding stability design procedures defined in AISC (2010):

1. The *direct analysis method*, detailed in Sections C2 and C3,
2. The *effective length method*, detailed in Appendix 7, and
3. The *first-order analysis method*, detailed in Appendix 7.

Within the restrictions specified on their usage, and provided that effects such as connection rotations or member axial and shear deformations are properly considered in the analysis when these attributes are important, each of these methods is intended to comprehensively address all of the effects listed in the beginning of Section 2.1.

As seen in Table 2.1, the *direct analysis method* is the only one of the above three procedures that is generally applicable. In basic terms, this method involves the following simple modifications to the second-order elastic analysis: (1) the use of a reduced elastic stiffness and (2) for rectangular or tiered structures, the use of a notional lateral load equal to a fraction of the vertical load at each level of the structure. These two devices are adjustments to the second-order analysis that account for: (1) member

Table 2.1. Summary of AISC (2010) provisions for stability analysis and design.

	Direct Analysis (Sections C2 and C3)	**Effective Length (Appendix 7)**	**1st-Order Analysis (Appendix 7)**
Limitations on the Use of the Method	None	$\Delta_{2nd}/\Delta_{1st} \leq 1.5$	$\Delta_{2nd}/\Delta_{1st} \leq 1.5$, $\alpha P_r \leq 0.5\ P_y$ (See Note 6)
Type of Analysis	2nd-order (See Note 1)	2nd-order (See Note 1)	1st-order, B_1 is applied to the member total moment
Structure Geometry Used in the Analysis	Nominal (See Note 2)	Nominal	Nominal
Notional Load to be Applied in the Analysis	$0.002Y_i$ Minimum if $\Delta_{2nd}/\Delta_{1st} \leq 1.7$ Additive if $\Delta_{2nd}/\Delta_{1st} > 1.7$ (See Note 2)	$0.002Y_i$ minimum	$2.1(\Delta/L)Y_i \geq 0.0042Y_i$ additive
Effective Stiffness Used in the Analysis	0.8 * Nominal, except $EI_{eff} = 0.8\tau_b EI$ when $\alpha P_r > 0.5\ P_y$ (See Note 3)	Nominal	Nominal
	$\tau_b = 4[\alpha P_r/P_y(1-\alpha P_r/P_y)]$		
	Use of $\tau_b = 1$ is permitted in all cases if additional notional loads of $0.001Y_i$ are applied, additive to other lateral loads		
In-plane flexural buckling strength P_{ni}	P_{ni} is based on the unsupported length in the plane of bending, L_i (i.e., $K = 1$)	P_{ni} in moment-frame columns is based on a buckling analysis or the corresponding effective length KL; P_{ni} in all other cases is based on $KL_i = L_i$ (i.e., $K = 1$).	P_{ni} is based on the unsupported length in the plane of bending, L_i
	If $\alpha P_r \leq 0.10\ P_{eL}$, or if a member out-of-straightness of 0.001L or the equivalent notional loading is included in the analysis, P_{ni} may be taken equal to QP_y (See Notes 4 & 5)	If $\Delta_{2nd}/\Delta_{1st} \leq 1.1$, K may be taken equal to one in all cases.	
Out-of-plane flexural buckling strength P_{no}	P_{no} is based on the unsupported length in the out-of-plane direction, L_o		
	Alternatively, P_{no} may be based on an out-of-plane buckling analysis or the corresponding effective length KL_o (see Note 4)		

Notes on Table 2.1:

General Note. $\Delta_{2nd}/\Delta_{1st}$ is the ratio of the 2nd-order drift to the 1st-order drift (for rectangular frames, $\Delta_{2nd}/\Delta_{1st}$ may be taken as B_2 calculated by Section 8.2.2). Δ/L is the largest 1st-order drift from all the stories in the structure. In structures that have flexible diaphragms, the Δ/L in each story is taken as the average drift weighted in proportion to the vertical load, or alternatively, the maximum drift. All $\Delta_{2nd}/\Delta_{1st}$ and Δ/L ratios shall be calculated using the LRFD load combinations or using a factor of $\alpha = 1.6$ applied to the gravity loads in ASD. The factor α is 1.0 for LRFD and 1.6 for ASD. The term Y_i is the total gravity load applied at a given level of the structure. P_{eL} is the member elastic buckling resistance based on the actual unsupported length in the plane of bending, $\pi^2 EI/L^2$ for prismatic members.

Note 1. Any legitimate method of second-order analysis that includes both $P\Delta$ and $P\delta$ effects is permitted, including 1st-order analysis with amplifiers. Section C2.1 in AISC (2010) addresses the conditions when the $P\delta$ effects can be neglected. In the Commentary of Section C2.1, more detailed guidelines are provided the limits when a $P\Delta$ analysis can adequately capture the $P\delta$ effects using one element per member with less than 5 and 3 % errors in the sidesway displacements and the corresponding internal moments respectively. The cases addressed are sway columns with simply-supported based conditions, sway columns with rotational restraints at both ends, and members subjected to predominantly non-sway end conditions. If the specified limits are exceeded, either multiple elements must be used per member to obtain accurate second-order internal moments in general from a *P*-large delta analysis, or a *P*-small delta amplifier must be applied to the element internal moments. Kaehler et al. (2010) provide further guidelines for the appropriate number of $P\Delta$ analysis elements to adequately capture the *P*-δ effects. Accurate general *P*-Δ analysis solutions may be obtained by maintaining $\alpha P_r \leq 0.02\, P_{e\ell}$, where $P_{e\ell}$ is the elastic buckling load based on the idealized simply-supported end conditions, an element length ℓ, and E if the analysis uses the nominal stiffness and $0.8\tau_b E$ if the direct analysis method is used.

Note 2. A nominal initial out-of-plumbness of $\Delta_o/L = 0.002$ may be used directly in lieu of applying $0.002Y_i$ minimum or additive notional loads. $\Delta_{2nd}/\Delta_{1st}$ specified in the direct analysis method is determined using the reduced effective stiffness specified in the first column of Table 2.1.

Note 3. The nominal stiffness and geometry should be employed for checking serviceability limit states. The reduced effective stiffness and the notional loads or nominal initial out-of-plumbness are required only in considering strength limit states.

Note 4. AISC (2010) does not explicitly state this provision in the context of the direct analysis method. This provision is encompassed within the Chapter C requirements for general stability analysis and design, which allow any method of analysis and design that addresses the effects listed at the beginning of Section 2.1.

Note 5. The largest unconservative error associated with the limit $\alpha P_r \leq 0.10\, P_{eL}$ is approximately five percent and occurs for a simply-supported, concentrically loaded column with zero moment, $Q = 1$, and $\alpha P_r = 0.10\, P_{eL} = \phi_c P_y$. The target of five percent maximum unconservative error is based on the original development of the AISC LRFD beam-column strength equations (ASCE 1997; Surovek-Maleck and White 2004a).

Note 6. The 1st-order analysis method does not account for the influence of significant axial compression in the rafters of clear-span frames. Therefore, this method strictly should not be applied for the analysis and design of the primary moment frames in these types of structures.

inelasticity and reliability considerations at the strength limit of the most critical member or members, as well as (2) the effects of a nominal initial out-of-plumbness Δ_o, within fabrication and erection tolerances, on the internal forces and moments at the above strength limit. The direct analysis method provides an improved representation of the *actual* second-order inelastic forces and moments in the structure at the strength limit of the most critical member or members. Due to this improvement in the calculation of the internal forces and moments, AISC (2010) bases its calculation of P_{ni}, the column nominal strength for checking the in-plane resistance in Eqs. 2.5, on the actual unsupported length in the plane of bending.

Interestingly, the use of the stub-column strength for P_{ni} (QP_y for columns with slender compression elements) was actively considered in the development of the direct analysis approach (Surovek-Maleck and White 2004a). Although this is a viable option, it requires the modeling of out-of-straightness in the analysis for members subjected to large axial compression (to properly capture in-plane limit states dominated by non-sway column flexural-buckling). The modeling of member out-of-straightness adds an additional level of complexity to the analysis, and in many steel structures, P_{ni} based on the actual unsupported length is only slightly smaller than QP_y. Therefore, AISC (2010) recommends the use of P_{ni} based on the actual unsupported length. However, in many metal building structural systems, the member axial loads are small enough such that the beam-column resistance is represented accurately using $P_{ni} = QP_y$, without the inclusion of any member out-of-straightness in the analysis. In other cases the modeling of member out-of-straightness may be needed to accurately capture the strength limit.

2.3 Effective Length Method

The *effective length method* is in essence the traditional AISC method of design since 1961, but with the addition of a notional minimum lateral load for gravity-load only combinations. This minimum lateral load accounts for the influence of nominal geometric imperfections on the brace forces, beam moments, connection moments and in-plane member moments used for out-of-plane strength design of beam-columns. In actuality, the effects of any physical out-of-plumbness exist for all load combinations. However, these effects tend to be small and are overwhelmed by the effects of the primary lateral loads in all the ASCE 7 lateral load combinations, as long as the structure's sidesway amplification is not excessive. Therefore, in the AISC (2005) effective length method, the notional lateral loads are specified solely as minimum lateral loads in the gravity load only combinations.

AISC (2010) disallows the use of the effective length method when the second-order amplification of the sidesway displacements is larger than 1.7, i.e., $\Delta_{2nd}/\Delta_{1st} > 1.7$ (based on the nominal elastic stiffness of the structure). This is due to the fact that the effective length method significantly underestimates the internal forces and moments in certain cases when this limit is exceeded (Deierlein 2003 & 2004; Kuchenbecker et al. 2004; White et al. 2006). For structures with $\Delta_{2nd}/\Delta_{1st} > 1.7$, AISC (2010) requires the use of the direct analysis method. Correspondingly, when using the direct analysis approach with structures having $\Delta_{2nd}/\Delta_{1st} \leq 1.7$, AISC (2005) allows the Engineer to apply the notional lateral loads (or the corresponding nominal out-of-plumbness) as minimum values used solely with the gravity load only combinations.

For column and beam-column in-plane strength assessment in moment frames, the effective length approach generally focuses on the calculation of the member axial stresses F_{ei} at incipient buckling of an appropriately selected model (the subscript "*i*" is used to denote in-plane flexural buckling). This buckling model is usually some type of subassembly that is isolated from the rest of the structural system (ASCE 1997). Engineers often handle the elastic buckling stresses (F_{ei}) implicitly, via the corresponding column effective lengths KL_i. The effective length is related to the underlying elastic buckling stress via the relationship

$$F_{ei} = \frac{\pi^2 E}{(KL_i / r_i)^2} \qquad \text{(Eq. 2.6a)}$$

or

$$K_i = \sqrt{\frac{\pi^2 E / (L_i / r_i)^2}{F_{ei}}} \qquad \text{(Eq. 2.6b)}$$

In the effective length method, the influences of residual stresses, P-Δ_o effects and P-δ_o effects are addressed implicitly in the calculation of P_{ni} from the column strength equations. These equations can be written either in terms of KL_i or F_{ei} (AISC 2010). Unfortunately, the selection of an appropriate subassembly buckling model generally requires considerable skill and engineering judgment. As a result, there is a plethora of different buckling models and K factor calculations. In certain cases the different models can produce radically different results. A few examples are provided below

In particular, one should note that a rigorous buckling analysis of the complete structure does not in general provide an appropriate F_{ei} or K_i. Members that have small axial stress F_{ei} at the buckling limit (relative to $\pi^2E/(L_i/r_i)^2$) tend to have high values for

K_i in Eq. 2.6b. In some cases, these large K_i values are justified while in other cases they are not. If the member is indeed participating in the governing buckling mode, a large K_i is justified. If the member is largely undergoing rigid-body motion in the governing buckling mode, or if it has a relatively light axial load and is predominantly serving to restrain the buckling of other members, a large K_i value is sometimes not justified. The distinction between these two situations requires engineering judgment. Furthermore, the concept of effective length is more obscure and less useful for general nonprismatic members subjected to nonuniform axial compression.

Some of the situations requiring the greatest exercise of judgment to avoid excessively large K values include: (1) columns in the upper stories of tall buildings, (2) columns with highly flexible and/or weak connections and (3) beams or rafters in portal frames, which may have significant axial compression due to the horizontal thrust at the base of the frame. There is no simple way of quantifying the relative participation of a given member in the overall buckling of the structure or subassembly under consideration. Quantifying the participation requires an analysis of the sensitivity of the buckling load to variations in the member sizes. Even if one conducted such an analysis, there is no established metric for judging when Eq. 2.6b should or should not be used. Engineers typically base their effective length calculations on story-by-story models to avoid the first of the above situations. They idealize columns with weak and/or flexible connections as pin-ended leaner columns with $K = 1$ to avoid the second situation. Lastly, they often use $K = 1$, or $K < 1$ (counting on rotational restraint from the sidesway columns), for design of the beams or rafters in portal frames, although the F_{ei} of these

members obtained from an eigenvalue buckling analysis of the full structure may suggest $K > 1$ via Eq. 2.6b.

The direct analysis method provides a simpler more accurate way of addressing frame in-plane stability considerations. By including an appropriately reduced nominal elastic stiffness, an appropriate nominal out-of-plumbness of the structure, and an appropriate out-of-straightness (for members subjected to high axial loads) in the analysis, the member length considerations can be completely removed from the resistance side of the design equations. The member in-plane column strength term P_{ni} is simply taken equal to QP_y. In-plane stability is addressed by estimating the required internal cross-section strengths P_r and M_r directly from the analysis, and by comparing these required strengths against appropriate cross-section resistances.

2.4 First-Order Analysis Method

The *first-order analysis method*, summarized in Table 2.1, is in essence a simplified conservative application of the direct analysis approach, targeted at rectangular or tiered building frames. This method involves:

- The implicit application of a conservative sidesway amplification factor of 1.5 (conservative as long as $\Delta_{2nd}/\Delta_{1st} < 1.5$) to the 1st-order story drift Δ/L or a nominal initial out-of-plumbness of $\Delta_o/L = 0.002$, whichever is larger. The 1st-order story drift Δ/L is taken as the largest drift from all the stories in the structure, calculated under the LRFD load combinations or with a factor of 1.6 applied to the gravity loads in ASD. In structures that have flexible diaphragms, the Δ/L in each story is taken as the average drift weighted in proportion to the vertical load, or alternatively, the maximum drift

- The inclusion of the direct analysis stiffness reduction factor of 0.8 implicitly in the second-order amplification of the above Δ/L or Δ_o/L, resulting in an amplification of the sidesway displacements by a factor of 2.1 rather than 1.5.
- The assumption that all the stories of the structure have a sidesway deflection equal to the above maximum amplified value.
- Inclusion of the corresponding P-Δ effects in the 1st-order analysis, by applying the P-Δ shear forces corresponding to the above sidesway displacement at each level of the structure (these P-Δ shears are applied in addition to any other lateral loads).
- Amplification of the corresponding total member moments obtained from the analysis by the non-sway amplification factor B_1 calculated as specified in Appendix 8 in AISC (2010).

The first-order analysis method is restricted to frames with $\Delta_{2nd\text{-}order}/\Delta_{1st\text{-}order} \leq 1.5$ as well as to cases where $\alpha P_r \leq 0.5P_y$ in all of the members whose flexural stiffnesses contribute to the lateral stability of the structure. The limit $\alpha P_r \leq 0.5P_y$ prevents the application of the method to structures where the sidesway stiffnesses are reduced significantly by combined residual stress effects and large column axial compression.

Although the first-order analysis method can be useful for simplified analysis and design of metal buildings in their longitudinal braced direction, this method does not include the effects of rafter axial compression on the flexural response of the primary moment frames. Also, this method is really just a direct analysis with a number of simplifying assumptions. There are numerous other ways to apply direct analysis using an approximate second-order analysis, many of which are less conservative than the

above approach. Therefore, the first-order analysis method is not considered further in this research.

It should be noted that both the direct analysis method and effective length method require a second-order elastic analysis. However, any legitimate method of second-order elastic analysis is allowed, including first-order analysis with amplifiers, when the amplifiers are sufficiently accurate. The stiffnesses and notional lateral loads (or nominal geometric imperfections) used in the analysis are different in each of the methods (see Table 2.1).

The beam-column out-of-plane resistance check is the same in both of the above methods, albeit with different values of P_r and M_r. In AISC (2010), the simplest out-of-plane beam-column resistance check is given by Eqs. 2.5 but with $P_n = P_{no}$, where P_{no} is the out-of-plane flexural or flexural-torsional buckling strength of the member as a concentrically-loaded column. Other enhanced beam-column out-of-plane strength checks are provided in AISC (2010) and are discussed in Sections 2.6.2 and 3.4.1.

2.5 Fundamental Comparison of The Direct Analysis and Effective Length Methods

The differences between the direct analysis and the effective length methods are predominantly in the way that they handle the beam-column in-plane strength check. Figures 2.6a and 2.6b, adapted from Deierlein (2004), illustrate the fundamental differences. Figure 2.6a shows a representative beam-column in-plane check using the traditional effective length approach, i.e., the effective length method as outlined in Table 2.1 but with no limitations on the use of the method and with zero notional load. The dashed curve in the figure is the AISC (2010) beam-column strength envelope, given by Eqs. 2.5. The anchor point for this curve on the vertical axis, $P_{n(KLi)}$, is the member

nominal axial strength determined using the effective length KL_i (or equivalently, using the member elastic buckling stress F_{ei} as illustrated by Eqs. 2.6). The anchor point on the horizontal axis is the member in-plane flexural resistance M_{ni}, which is based in AISC (2010) either on flange local buckling or general flexural yielding considerations. The other two curves in the plot indicate the member internal axial force and moment under increasing applied loads on the structure. The curve labeled "actual response" is determined from an experiment or from a rigorous second-order distributed plasticity analysis that accounts for all the significant stability effects, whereas the second curve is from a second-order elastic analysis of the idealized straight and plumb, nominally elastic structure. The actual response curve indicates larger moment than the second-order elastic analysis curve due to the combined effects of partial yielding and geometric imperfections, which are not included in the elastic second-order analysis. The maximum value of P on the actual response curve (P_{max}) is the largest value of the axial force that the member can sustain at its stability limit. Correspondingly, the nominal design strength is defined by the intersection of the force-point trace from the second-order elastic analysis with the $P_{n(KLi)}$ based envelope. The effective length provisions have been calibrated such that this intersection point gives an accurate to conservative estimate of the actual maximum strength.

The reduced stiffness and the notional load (or the corresponding nominal out-of-plumbness) in the direct analysis method are calibrated to estimate the actual response using a second-order elastic analysis. This is illustrated by Figure 2.6b, where the force-point trace of the member internal axial force and moment from the second-order elastic

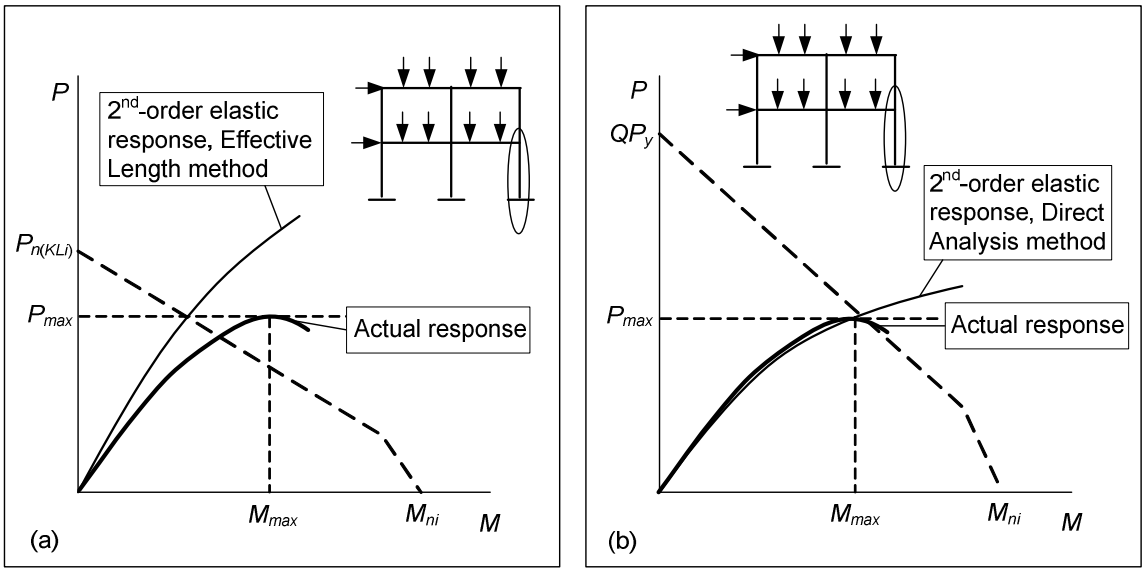

Figure 2.6. Comparison of beam-column strength interaction checks for (a) the effective length method (with zero notional load) and (b) the direct analysis method.

analysis (conducted using the reduced stiffness and notional lateral loads) is close to the actual response plot. The calibration is done to achieve parity between the actual compressive strength (indicated by P_{max} on the actual response curve) and the nominal design strength. By accounting for residual stress, partial member yielding and geometric imperfection effects in the second-order elastic analysis, the resistance can be checked on a member cross-section basis. That is, the anchor point on the vertical axis for the beam-column strength envelope can be taken as QP_y. As noted in Section 2.1, the use of $P_{ni} = QP_y$ requires that the member axial force must be smaller than $0.10P_{eL}$, or the use of a member out-of-straightness of $0.001L$ in the analysis (to capture in-plane limit states dominated by non-sway column flexural-buckling). AISC (2010) bases P_{ni} on the actual unsupported length in the plane of bending to avoid the need for consideration of member out-of-straightness in a general frame analysis. The anchor point on the horizontal axis (M_{ni}) is the same in both the direct analysis and the effective length methods. In the

direct analysis method, the internal force and moment (P and M) and the strength envelope (with the anchor points QP_y and M_{ni}) are an improved representation of the actual response. Conversely, in the traditional effective length approach (i.e., the effective length method with no notional load included), smaller idealized values of P and M are checked against a correspondingly reduced beam-column strength interaction curve. The direct analysis method accounts for the in-plane system stability effects directly within the second-order analysis. Conversely, the effective length method accounts for the in-plane system stability effects by reducing the member axial strength P_{ni} via an effective length KL_i or the elastic buckling stress F_{ei} obtained (implicitly or explicitly) from an appropriately configured buckling analysis.

2.6 Illustrative Examples

The concepts discussed in Section 2.5 are best understood by considering a few simple examples. The following subsections highlight two basic case studies, one taken from the AISC (2005) TC10 and Specification Committee developments and the other created by modifying an example design problem considered by the Specification Committee. Other more detailed examples are presented by Maleck (2001), Maritinez-Garcia (2002), Deierlein (2003), Surovek-Maleck and White (2004a & b), Kuchenbecker et al. (2004), and White et al. (2006 and 2007a and b).

2.6.1 Cantilever Beam-Column

One of the simplest illustrations of the direct analysis and effective length methods is the solution for the design strength of a fixed-base cantilever composed of a rolled wide-flange section. Figure 2.7a shows a W10x60 cantilever subjected to a vertical load P and a proportional horizontal load of $H = 0.01P$, adapted from Deierlein

(2004). The bending is about the major axis and the member is braced out-of-plane such that its in-plane resistance governs. In this problem, the member in-plane strength governs in both the direct analysis and the effective length methods if the member is braced at its top and bottom in the out-of-plane direction, the enhanced AISC (2005) beam-column strength interaction equations are employed, and $K = 0.7$ is used for the calculation of P_{no}, the column strength in the out-of-plane direction. The column slenderness in the plane of bending is $L/r = 40$ based on the member's actual length and $KL/r = 80$ based on the effective length (with $K = 2$).

Figure 2.7b shows plots of the axial load versus the moment at the column base, determined using three approaches: (1) the traditional effective length method (no minimum notional lateral load included), (2) the direct analysis method, and (3) a rigorous second-order distributed plasticity analysis. Load and Resistance Factor Design (LRFD) is used with a resistance factor of $\phi_c = \phi_b = 0.9$ in each of these solutions. The rigorous distributed plasticity analysis is based on a factored stiffness and strength of $0.9E$ and $0.9F_y$, an out-of-plumbness and out-of-straightness on the geometry of $0.002L$ and $0.001L$ respectively (oriented in the same direction as the bending due to the applied loads), the Lehigh residual stress pattern (Galambos and Ketter 1959) with a maximum compressive nominal residual stress at the flange tips of $0.3(0.9F_y) = 0.27F_y$, and an assumed elastic-perfectly plastic material stress-strain response. A small post-yield stiffness of $0.001E$ is used for numerical stability purposes. These are established parameters for calculation of benchmark design strengths in LRFD using a distributed plasticity analysis (ASCE 1997; Martinez-Garcia 2002; Deierlein 2003; Maleck and White 2003; Surovek-Maleck and White 2004b; White et al. 2006). AISC (2010)

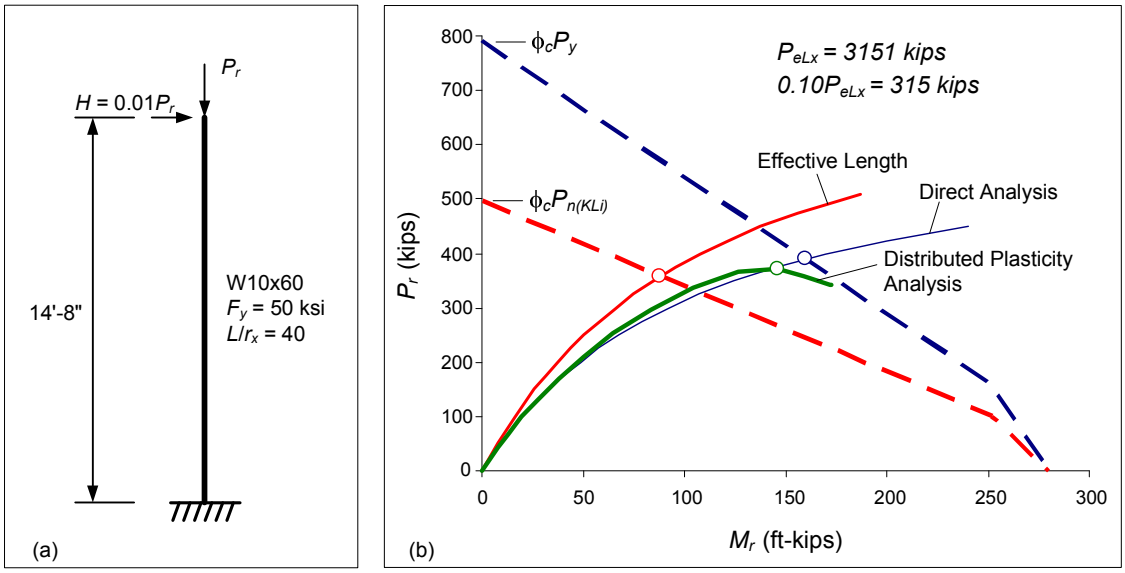

Figure 2.7. Cantilever beam-column example.

specified these analysis requirements in Appendix 1, Design by Inelastic Analysis.

One should note that the internal moment from the direct analysis is larger than that obtained from the traditional effective length method. This is due to the use of a reduced stiffness of $0.8EI_x$, as well as a notional lateral load of $0.002P$, which is added to the applied lateral load. Although the axial load at the intersection of the force-point trace with the strength envelope is slightly larger than $0.10P_{eLx} = 0.10(\pi^2 EI_x/L^2) = 315$ kips in this problem, the member out-of-straightness effects are not considered in the second-order elastic analysis by the direct analysis method and the axial load anchor point for the direct analysis strength curve is taken as $\phi_c P_y = 796$ kips. The plot in Figure 2.7b shows that the direct analysis internal moments are very similar to the internal moments calculated by the rigorous inelastic analysis. Overlaid on the above force-point traces are the beam-column strength envelopes, where the $\phi_c P_n$ anchor points are $\phi_c P_{n(KLi)}$ = 496 kips for the effective length method and $\phi_c P_y = 796$ kips for the direct analysis

method.

The design strengths, determined as the combined P and M at the intersections with the in-plane beam-column strength curves (Eqs. 2.5), are summarized in Table 2.2. The ratios of the maximum base moments $M_{max} = HL + P(\Delta + \Delta_o)$ to the primary moment HL indicate the magnitude of the second-order effects. The axial load at the direct analysis strength limit, which is representative of the strength in terms of the total applied load, is five percent higher than that obtained from the distributed plasticity analysis. Conversely, the axial load at the effective length method beam-column strength limit is four percent smaller than that obtained from the distributed plasticity solution. Both of these estimates are within the targeted upper bound of five percent unconservative error relative to the refined analysis established in the original development of the AISC LRFD beam-column strength equations (ASCE 1997; Surovek-Maleck and White 2004a).

Table 2.2. Summary of calculated design strengths, cantilever beam-column example.

Design Method	P_{max} (kips)	M_{max} (ft-kips)	M_{max}/HL	$P_{max}/P_{max\,(Distributed\ Plasticity)}$
Traditional Effective Length (no notional load)	357	88	1.68	0.96
Direct Analysis	390	160	2.79	1.05
Distributed Plasticity Analysis	371	146	2.68	

The difference in the calculated internal moments is much larger. This difference is expected since the effective length approach compensates for the underestimation of the actual moments by reducing the value of the axial resistance term P_{ni}, whereas the direct analysis method imposes additional requirements on the analysis to obtain an

improved estimate of the actual internal moments. This more accurate calculation of the internal moments also influences the design of the restraining members and their connections. For instance, in this example, the column base moments from the direct analysis method are more representative of the actual moments required at this position to support the applied loads associated with the calculated member resistance. In this regard, the direct analysis method provides a direct calculation of the required strengths for all of the structural components. Conversely, the traditional effective length approach generally necessitates supplementary requirements for calculation of the required component strengths. AISC (2010) implements these supplementary requirements as (1) a minimum notional lateral load to be applied with gravity-only load combinations and (2) a limit on the use of the effective length method to frames having $\Delta_{2nd}/\Delta_{1st} \leq 1.5$, as summarized in Table 2.1.

2.6.2 Single Story Rectangular Frame

Figure 2.8 shows a slightly modified version of one of the design problems posed during the process of validating and checking the final AISC (2005) provisions by the Specification Committee (DP-13). This problem is a single-story rectangular frame. It provides a somewhat more realistic illustration of the potential of AISC (2005 and 2010) for certain types of metal building frames, although it uses rolled I-section members. The interior columns in the structure are all leaning columns. All the beam-to-column connections are simple except for the connections to the exterior columns, which are assumed to be fully-restrained. The beams are made continuous over the interior columns in the modified example, whereas the frame studied by the AISC Specification Committee used simple connections at the ends of the beams for all the interior joints.

This modification is performed to simulate typical conditions at the interior columns in modular metal building frames. Due to the continuity of the beams, the exterior columns are reduced from W12x72 sections in the AISC frame to W12x65 sections in the modified example. Also, the beams are reduced from W24x68 sections in the exterior spans and W27x84 sections in the interior spans of the AISC frame to W24x62 sections in this example. The resulting modified frame has similar drift characteristics under lateral loads; both the AISC example and the modified example satisfy a maximum drift criterion of $L/100$ for the nominal (unfactored) wind load based on a first-order elastic analysis. The strength behavior of the lateral load resisting beams and columns is similar in both frames, with of course the exception of the beam continuity effects over the interior columns in the modified design. The reader is referred to White et al. (2006) for a detailed discussion of the behavior of the AISC frame.

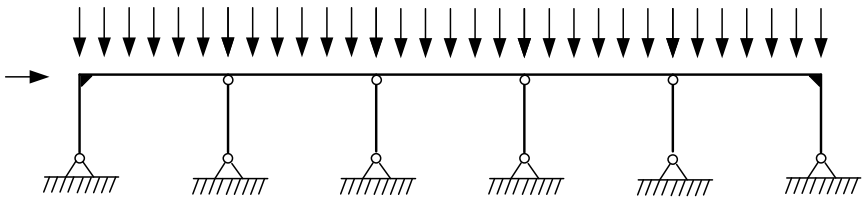

Exterior columns:	W12x65	F_y = 50 ksi
Interior columns:	W8x31	E = 29,000 ksi
Beams:	W24x62	
Beam span lengths:	40 ft	
Story height:	20 ft	
Unfactored Loads:	D = 1.0 kip/ft	LRFD Load Combinations:
	S = 1.2 kip/ft	LC1: 1.2D + 1.6S
	W = 10 kips	LC2: 1.2D + 0.5S + 1.6W

Figure 2.8. Modified version of AISC single-story rectangular frame example DP-13.

The exterior columns in both examples are subjected to relatively light axial loads, whereas they experience substantial gravity load moments as well as significant wind load moments. Also, the frames have significant second-order effects, i.e., amplification of the member internal bending moments. The columns are braced in the out-of-plane direction at their base and at the roof height. Simple base conditions are assumed in both the in-plane and out-of-plane directions, and simple connections are assumed in the out-of-plane direction at the column tops. The beams are assumed to be braced sufficiently such that their flexural resistance is equal to M_p. This problem is considered for the following LRFD load combinations:

1. Load Case 1 (LC1): 1.2 Dead + 1.6 Snow
2. Load Case 2 (LC2): 1.2 Dead + 0.5 Snow + 1.6 Wind

Figure 2.9 shows the applied fraction of the design loads versus the story drift for these two load combinations on the modified single-story frame, obtained from a rigorous second-order distributed plasticity analysis having the same attributes as described above for the cantilever beam-column. The distributed plasticity analysis gives a maximum in-plane capacity of 1.19 times the factored design load level for LC1 and 1.03 of the factored design load level for LC2. Table 2.3 compares the fractions of the design loads giving a unity check of 1.0 for the in-plane strength from Eqs. 2.5 for each of the design methods to the above load capacities from the distributed plasticity analysis. In this frame, the right-hand side exterior column is the most critical member in the effective length check for both load cases and in the direct analysis check for LC2. In the direct analysis check for LC1, the negative beam moment over the left-most interior column gives the most critical strength check. One can observe that the direct analysis

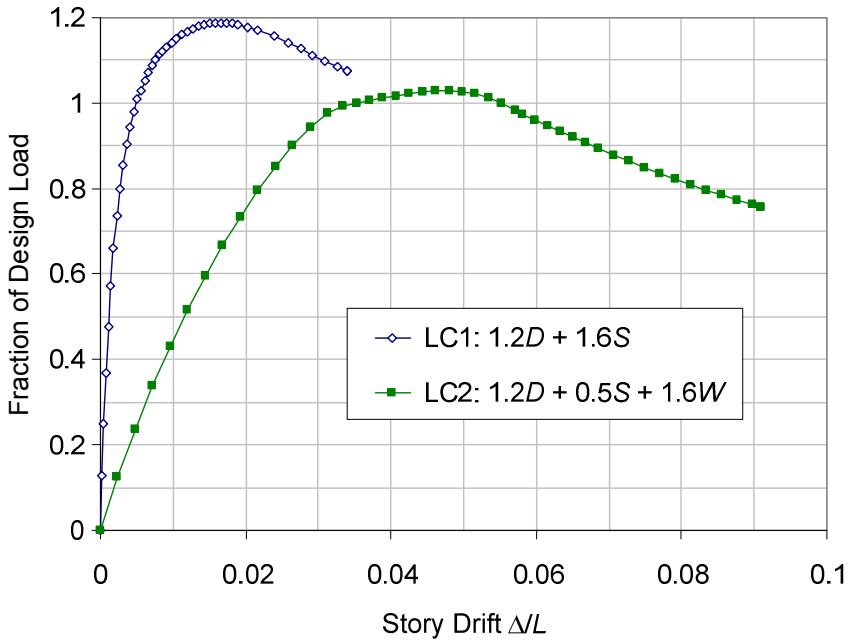

Figure 2.9. Load versus story drift from distributed plasticity analysis for load cases 1 and 2, modified DP-13 example.

Table 2.3. Fraction of design loads corresponding to a unity check of 1.0 for the right-hand beam-column, and maximum capacities predicted by distributed plasticity analysis, modified DP-13 example.

Design Method	LC1	LC2
Traditional Effective Length (no notional load)	1.05	0.81
Direct Analysis	1.18	0.95
Distributed Plasticity Analysis	1.19	1.03

method closely captures the resistances from the refined distributed plasticity solution, predicting that 1.18 of LC1 and 0.95 of LC2 can be applied prior to reaching the maximum strength of the critical leeward column. That is, the strength for the gravity load combination is underestimated by 0.8 percent, while the strength for the wind load combination is underestimated by 7.8 percent. The larger underestimation for the wind load case is largely due to inelastic redistribution in the structure after a plastic hinge

forms at the top of the leeward column. However, there is little redundancy in the structural system as the column strength limit is approached for the gravity load combination. Nevertheless, the most critical member check for LC1 by direct analysis is the beam negative moment check over the left-most interior column. The large elastic negative bending moment at this location reaches the factored plastic moment resistance of the beam $\phi_b M_p$ at 1.10 of the design load. The distributed plasticity solution for LC1 indicates substantial inelastic redistribution from a beam plastic hinge at this location prior to the structure reaching its strength limit at 1.19 of the design load. The right-most exterior column is critical for all the other design checks by either the direct analysis or the effective length methods.

The traditional effective length method (with zero notional lateral load) dramatically underestimates the resistance of the modified DP-13 frame, satisfying the unity check of Eqs. 2.5 at 1.05 and 0.81 of the design load levels for LC1 and LC2 respectively. That is, the effective length method gives a capacity of only 1.05/1.19 = 0.88 and 0.81/1.03 = 0.79 of the in-plane capacity from the distributed plasticity analysis for LC1 and LC2. A key reason for these underestimations is illustrated in Figures 2.10 and 2.11, which show the force-point traces for the axial load and moment in the leeward beam-column by each of the solutions versus the in-plane beam-column resistance envelopes for LC1 and LC2 respectively. The significant in-plane stability effects in this example result in a $P_{n(KLi)}$ of only $0.11P_y$ for LC1 and $0.09P_y$ for LC2. The corresponding effective length factors for the leeward column are 5.11 and 4.75 using a rigorous sidesway buckling analysis for each of the load combinations. The direct analysis method gives a substantially larger estimate of the in-plane resistance because it

focuses on a more realistic estimate of the internal moments and the corresponding member resistances. In determining the anchor point $P_{n(KLi)}$ for its beam-column strength envelope, the effective length method overemphasizes the response of the structure to unrealistic loads causing uniform axial compression in all of its columns. The physical strength of this frame is dominated by the amplified internal moments (a large fraction of which are not related to the sidesway of the structure) reaching the flexural resistance of the leeward beam-column, not by a column failure under concentrically-applied member axial loads.

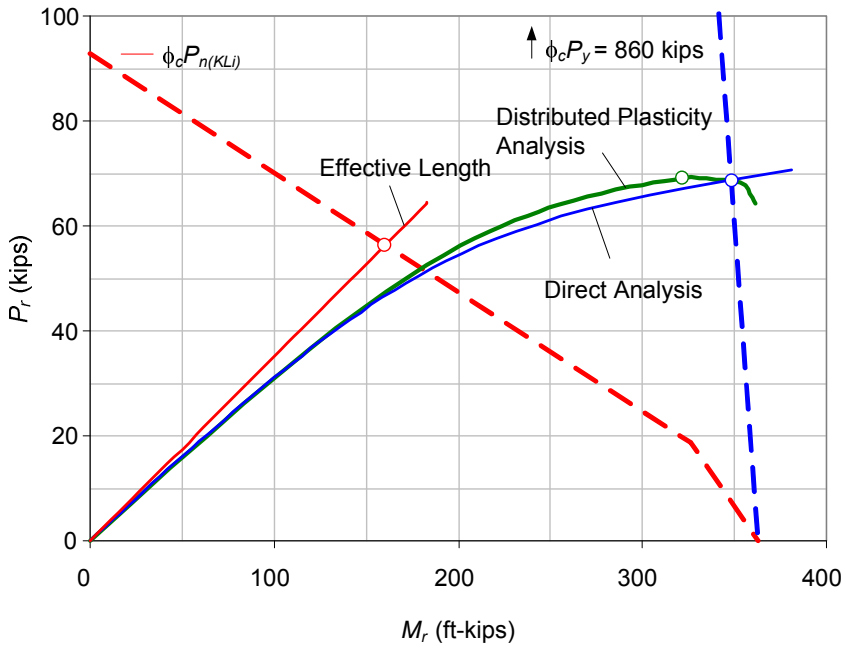

Figure 2.10. Force-point trace for the leeward beam-column by the effective length method, the direct analysis method and distributed plasticity analysis, LC1, modified DP-13 example.

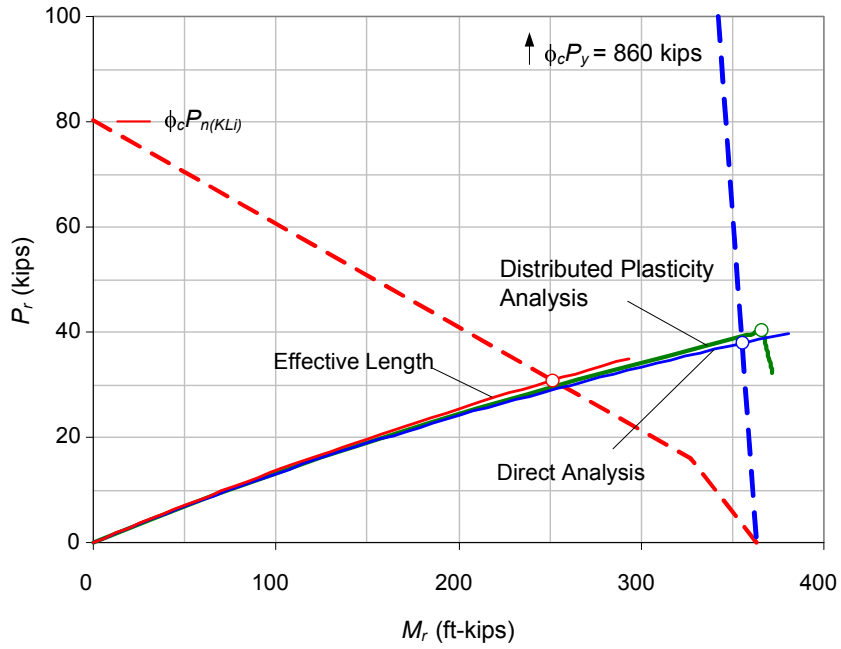

Figure 2.11. Force-point trace for the leeward beam-column by the effective length method, the direct analysis method and distributed plasticity analysis, LC2, modified DP-13 example.

AISC (2010) provides the following enhanced beam-column strength interaction equation for checking the out-of-plane resistance of doubly-symmetric rolled I-section members subjected to single axis flexure and compression:

$$\frac{P_r}{P_{co}}\left(1.5-0.5\frac{P_r}{P_{co}}\right)+\left(\frac{M_r}{C_b M_{cx(Cb=1)}}\right)^2 \le 1.0 \qquad \text{(Eq. 2.7, AISC H1-2)}$$

where P_{co} is the out-of-plane column strength, M_{cx} is the governing major-axis flexural resistance of the member determined in accordance with Chapter F using C_b = 1, and C_b is lateral-torsional buckling modification factor specified in Section F1. It should be emphasized that the value of $C_b M_{cx(Cb=1)}$ may be larger than $\phi_b M_{px}$ in LRFD or M_{px}/Ω_b in ASD. Equation 2.7 is derived from the fundamental form for the out-of-plane lateral-torsional buckling strength of doubly-symmetric I-section members in LRFD,

$$\left(\frac{M_r}{C_b\phi_b M_{nx(Cb=1)}}\right)^2 \le \left(1-\frac{P_r}{\phi_c P_{no}}\right)\left(1-\frac{P_r}{\phi_c P_{ez}}\right) \qquad \text{(Eq. 2.8, AISC C-H1-6)}$$

where P_{ez} is the elastic torsional buckling strength. Equation 2.7 is developed by substituting a lower bound of 2.0 for the ratio of P_{ez}/P_{no} for W section members with $KL_o = KL_z$. This enhanced out-of-plane beam-column strength interaction equation in AISC (2010) is improved from the one in AISC (2005), which assumes the upper bound of $P_{ez}/P_{no} = \infty$. In addition, in the prior AISC (2005) provisions, the fact that $C_b M_{nx(Cb=1)}$ may be larger than M_p was not apparent. Based on Eq. 2.7, the out-of-plane resistance does not govern for both LC1 and LC2 for the above example frame.

CHAPTER III

RECOMMENDED EXTENSIONS OF THE AISC (2010) PROVISIONS FOR FRAMES WITH GENERAL MEMBER GEOMETRIES AND LOADINGS

This chapter develops new design procedures for frames using web-tapered and other prismatic and nonprismatic members. The procedures developed in this chapter provide the basis of the AISC Design Guide 25, *Frame Design using Web-Tapered Members* (Kaehler et al. 2010). In this dissertation, this design guide is referred to as MBMA/AISC (2010). The new design procedures are based on the fundamental concept of using Specification nominal strength curves as a "mapping" from the theoretical elastic buckling resistance to the nominal resistance at the cross-section having the largest value of $f_r/F_{y.eq}$, taken equal to f_r/F_y in most cases. The detailed procedures of mapping are explained in Section 3.2 and Appendix A for column resistance calculations and in Section 3.3 for flexural resistance calculations.

The validity of this fundamental concept is based on the AISC (2005 & 2010) column strength curve mapping being appropriate for any column member buckling limit state (in-plane and out-of-plane flexural buckling, torsional buckling, flexural-torsional buckling, or constrained-axis torsional buckling of prismatic or nonprismatic column unbraced lengths), and for the beam LTB strength curve mapping being appropriate for any beam member LTB limit state (prismatic or non-prismatic beam member unbraced lengths). Conceptually, the use of the above mappings should always be conservative for web-tapered or nonprismatic members, barring the existence of any other attributes specific to web-tapered or nonprismatic members as a group. Such attributes might be:

- Use of single-sided welding for a given group,
- Larger geometric imperfection for a given group, and
- Etc.

There do not appear to be any such attributes that are particularly unique to web-tapered or other nonprismatic members. The fact that the above mappings are always conservative, given the above caveat, is due to the fact that the web-tapered and general nonprismatic members will in the worst case be loaded in a true uniform stress condition. Usually, they are not subjected to uniform stress.

This research proposes the above fundamental concept, and then proceeds to investigate the broader problem of the stability design behavior and strength of members and frames using both prismatic and nonprismatic cross-section members over a relatively wide range of cross-section and member slenderness attributes.

This chapter first outlines a recommended application of the direct analysis and effective length methods of AISC (2010) to structures with general nonrectangular configurations, nonprismatic member geometries and nonuniform member axial loadings. The proposed approach is based on the generalization of the fundamental concepts and findings established in the above seminal research studies, while also taking advantage of subsequent improvements in the state of knowledge with respect to stability design embodied in AISC (2010). In addition, this chapter gives the detailed procedures for calculating the axial and flexural capacity ratios for general nonprismatic members subjected to nonuniform axial compression.

3.1 Stability Design

The recommended effective length approach is in essence the like named method

outlined in Table 2.1, but with a modified calculation of the nominal resistances P_n and M_n, reflecting the behavior for general member geometries and loadings. Also, as discussed in the subsequent sections, it is useful to consider the resistances in the context of the complete calculation of the governing member axial and flexural capacity ratios P_r/P_c and M_r/M_c, rather than focusing separately on the required strengths and the design resistances. It is assumed that the internal axial forces and moments are determined by an accurate second-order elastic analysis accounting for the influence of the nonprismatic geometry on the stiffness and P-Δ and P-δ effects. Vandepitte (1982), Gaiotti and Smith (1989), White and Hajjar (1991), White et al. (2007a & b) and Kuchenbecker et al. (2004) discuss various approaches for conducting such an analysis, mostly in the context of rectangular frames. Many of these approaches can be applied or adapted to general non-rectangular frames composed of nonprismatic members. Galambos (1988) gives analytical slope-deflection equations for second-order analysis of frames composed of members with linearly-tapered web depths.

The recommended direct analysis method focuses on the following specific options from Table 2.1, combined with a similar but simpler calculation of the member capacity ratios (relative to the calculations by the effective length approach):

1. Use of a reduced elastic stiffness equal to 80 percent of the nominal elastic stiffness of the structure for the structural analysis, and in the rare cases where the cross-section axial force αP_r is larger than $0.5P_y$, use of an effective member flexural rigidity equal to $0.8\tau_b EI$ at the corresponding cross-section locations.
2. Explicit application of a nominal sidesway offset (out-of-plumbness) of $0.002H$ at all the nodes in the second-order elastic analysis model relative to the ideal geometry,

where H is the node height measured from the lowest base elevation of the structure. For frames with unequal height columns and nonuniform member axial loads, this explicit definition of the out-of-plumb geometry is more straightforward and less error prone than the use of notional lateral loads. Also, the above definition includes an out-of-plumbness effect in gable frame rafters that is difficult to specify in any other way. The specified out-of-plumbness of $0.002H$ is consistent with a tolerance on the out-of-plumb geometry of 1/500 specified in the MBMA (2006) Standard. The above nodal offsets are applied in the direction of the sidesway in each of the load combinations. In cases where the applied loads and the geometry are symmetric, the out-of-plumbness can be applied in either direction. One should note that, for gable or single-slope roof frames with a shallow roof pitch, the above approach and the use of notional loads of $N_i = 0.002P_i$ at each of the columns are equivalent for all practical purposes, as illustrated by Figure 3.1. One may use either of these approaches as a matter of preference or convenience.

3. For unsupported member lengths in the plane of bending where αP_r is larger than 10 percent of the member elastic Euler buckling load, based on the in-plane unsupported length, explicit application of an additional member out-of-straightness of $0.001L$ in the elastic analysis. In many frames, none of the member axial loads will exceed the above limit and therefore member out-of-straightness need not be included in the structural analysis. The above limit can be checked using a conservative estimate of the member elastic buckling load in many cases. Where needed, the above out-of-straightness is applied in the direction of the largest member transverse displacement relative to a straight chord between the cross-section centroids at the member ends.

Either a parabolic or a kinked curve with the maximum out-of-straightness at the mid-length of the member is acceptable.

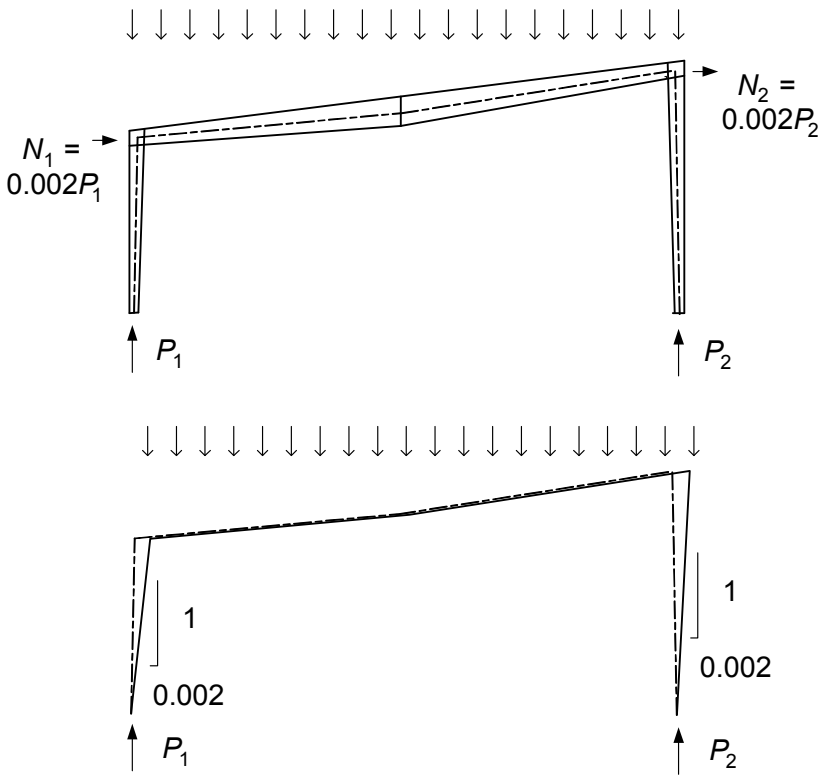

Figure 3.1. Equivalency of explicit nominal out-of-plumb geometry of $0.002H$ and applied notional loads $N_i = 0.002P_i$ at each column.

4. Given the satisfaction of the above requirements in the structural analysis, the member in-plane capacity ratios are determined on a cross-section by cross-section basis using Eqs. 2.5 along with $P_{ni} = QP_y$ and the member in-plane flexural resistance M_{ni} (excluding the consideration of lateral-torsional buckling). The member out-of-plane capacity ratios are calculated using the out-of-plane axial resistance P_{no} and the governing member flexural resistance M_n (including consideration of the LTB limit

state). The calculation of the flexural resistances is the same for both the effective length and the direct analysis methods.

3.2 Axial Capacity Ratio

3.2.1 Base Equations

The base AISC (2010) nominal column strength equations are expressed in terms of the axial stress as

$$F_n = \left(0.658^{QF_y/F_e}\right)QF_y \qquad \text{for } F_e/QF_y \geq 0.44 \qquad \text{(Eq. 3.1a, AISC E7-2)}$$

$$F_n = 0.877F_e \qquad \text{for } F_e/QF_y < 0.44 \qquad \text{(Eq. 3.1b, AISC E7-3)}$$

where F_y is the minimum specified yield strength, F_e is the axial stress at elastic column buckling, based on beam theory, and Q is the AISC column strength reduction factor accounting for the effect of slender cross-section elements under uniform axial compression. The nominal column strength in terms of load is given by

$$P_n = F_n A_g \qquad \text{(Eq. 3.2, AISC E7-1)}$$

Correspondingly, the column design strength is

$$F_c = F_n/\Omega \quad \text{or} \quad P_c = P_n/\Omega \quad \text{for ASD} \qquad \text{(Eq. 3.3a)}$$

and

$$F_c = \phi F_n \quad \text{or} \quad P_c = \phi P_n \quad \text{for LRFD} \qquad \text{(Eq. 3.3b)}$$

The required axial load capacity (i.e., the member internal axial force determined from the structural analysis) is denoted by

$$P_r = f_r A_g \qquad \text{(Eq. 3.4)}$$

where f_r is the corresponding applied (or required) axial stress and A_g is the cross-section gross area. The quantities P_r and f_r are obtained from the structural analysis for the load

combination under consideration, e.g., D + L for ASD or 1.2D + 1.6L for LRFD.

In the following developments, it is useful to express the column elastic buckling stress F_e as the required design axial stress f_r times the applied load ratio γ_e, i.e.,

$$F_e = \gamma_e f_r \qquad \text{(Eq. 3.5)}$$

In addition, an equivalent yield strength $F_{y.eq}$ is introduced. For members without slender elements, $F_{y.eq} = F_y$. Otherwise, $F_{y.eq} = QF_y$.

By making this substitution, the nominal column strength may be written in the form

$$F_n = \left(0.658^{\frac{1}{\gamma_e (f_r / F_{y.eq})}} \right) F_{y.eq} \qquad \text{for } \gamma_e \left(\frac{f_r}{F_{y.eq}} \right) \geq 0.44 \qquad \text{(Eq. 3.6a)}$$

$$F_n = 0.877 \gamma_e f_r \qquad \text{for } \gamma_e \left(\frac{f_r}{F_{y.eq}} \right) < 0.44 \qquad \text{(Eq. 3.6b)}$$

and the axial capacity ratio, $P_r/P_c = f_r/F_c$, may be written for ASD as

$$\frac{f_r}{F_c} = \frac{P_r}{P_c} = \frac{f_r}{F_{y.eq}} \Omega \left(0.658^{\frac{-1}{\gamma_e (f_r / F_{y.eq})}} \right) \qquad \text{for } \gamma_e \left(\frac{f_r}{F_{y.eq}} \right) \geq 0.44 \qquad \text{(Eq. 3.7a)}$$

$$\frac{f_r}{F_c} = \frac{P_r}{P_c} = \frac{\Omega}{0.877} \left(\frac{1}{\gamma_e} \right) \qquad \text{for } \gamma_e \left(\frac{f_r}{F_{y.eq}} \right) < 0.44 \qquad \text{(Eq. 3.7b)}$$

The above as well as other traditional column resistance equations have been developed predominantly from tests and analytical studies of uniformly loaded prismatic columns. However, these types of equations also have been applied to assess the axial load resistance of tapered web I-section members. The seminal research in this area is documented in Lee et al. (1981) and in Galambos (1988) among other references. The common practice for calculating the column axial capacity ratio for general members is:

1) Determine the elastic buckling load level, denoted by γ_e in the above, and then

2) Where the column axial stress level at incipient buckling necessitates the consideration of inelastic buckling, "map" the elastic buckling capacity to the inelastic buckling resistance by focusing on the behavior at the most highly stressed cross-section along the member length.

This is the approach taken in the research by Lee et al. (1981) for various specific member geometries. However, the procedure can be generalized to other geometries including multiple tapers, cross-section plate transitions, and/or nonuniform axial loading. Equations 3.7a and b for the axial capacity ratio are particularly useful in this context. One can show that the ratio $f_r/F_c = P_r/P_c$ is always largest at the cross-section along the member length where $f_r/F_{y.eq}$ is the largest. This f_r/F_c may be taken generally as an accurate to conservative estimate of the axial capacity ratio for I-section members of arbitrary geometry subjected to concentric axial compression.

Figure 3.2 illustrates the fundamental concept of the above procedure, which is explained in detail in the next section. One can envision that the general nonuniformly-loaded nonprismatic member is replaced by an equivalent prismatic member that has the same γ_e as well as a uniform cross-section stress ratio $f_r/F_{y.eq}$ equal to the maximum $f_r/F_{y.eq}$ along the length of the general member. It is important to note that for nonprismatic members subjected to nonuniform axial compression, f_r, $F_{y.eq}$ and $f_r/F_{y.eq}$ vary along the length of the member; however, there is only one load level corresponding to each of the potential member elastic buckling modes. This load level is represented by the load ratio γ_e, via Eq. 3.5. The complete procedure is explained in the next section.

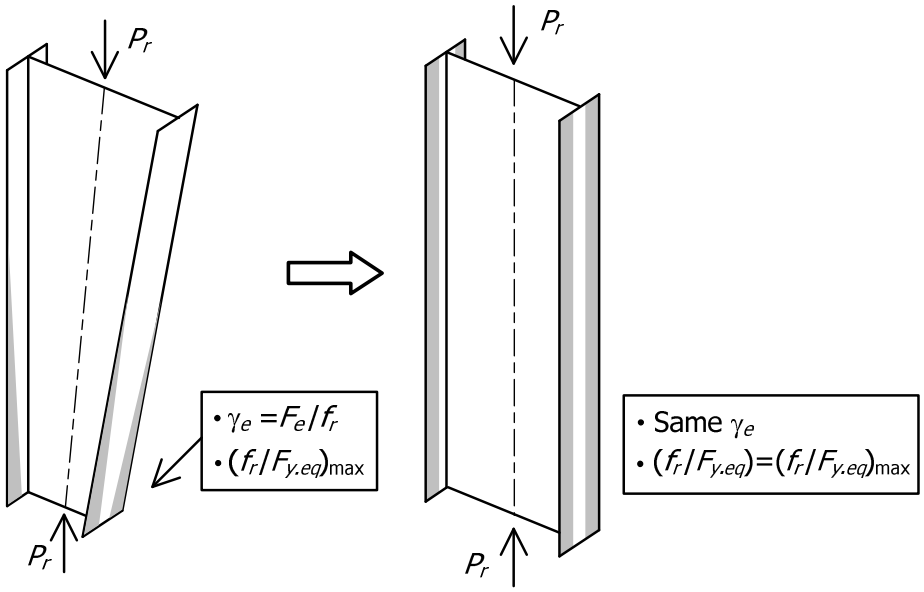

Figure 3.2. Mapping from a general nonprismatic member to an equivalent prismatic member.

3.2.2 General Procedure

Given the above equations, a procedure to determine the governing member axial capacity ratio $f_r/F_c = P_r/P_c$ for a general I-section member is developed. Each step of this general procedure is explained below and shown in Figure 3.3:

1) Calculate $f_r = P_r/A_g$ at various sections along the member length as shown in Figures 3.3a and b.
2) For checking the in-plane resistance by the direct analysis method, the corresponding member axial resistance is simply $F_{y.eq}$, assuming that the caveats discussed below are satisfied. For members with slender elements, Q is determined based on the flange and web slenderness values at each cross-section using $f = F_y$ (this step is not shown in Figure 3.3.) Then, $f_r/F_c = P_r/P_c = f_r/(F_{y.eq}/\Omega_c)$ in ASD or $(f_r/(\phi_c F_{y.eq})$ in LRFD and the calculations are complete at this step. The governing P_r/P_c is the largest value

obtained for all the cross-sections along the member unsupported length in the plane of bending.

It is important to note that this simplified calculation is valid only when $\alpha P_r \leq 0.10P_{eL}$. For $\alpha P_r > 0.10P_{eL}$, one must include a nominal member out-of-straightness within the analysis as explained in Section 3.1, or alternately, P_{ni} may be calculated as detailed in the subsequent steps using the member γ_{ex} based on idealized simply-supported end conditions. In many metal building frames, $\alpha P_r \leq 0.10P_{eL}$.

For checking the member out-of-plane strength in the direct analysis method, or for checking the in-plane or out-of-plane strength using the effective length approach, continue to the next step.

3) Determine the minimum load ratio for elastic buckling of the member

$$\gamma_{e,min} = \min(\gamma_{ex}, \gamma_{ey}, \gamma_{eTF}) \qquad \text{(Eq. 3.8)}$$

as appropriate, where γ_{ex} is the critical load ratio for elastic flexural buckling about the major axis, γ_{ey} is the critical load ratio for elastic flexural buckling about the minor axis, and γ_{eTF} is the critical load ratio for elastic torsional or flexural-torsional buckling. The critical load ratio γ_e can be determined using cross-sections at mid-span and simplified methods developed in Chapter 4 for linearly-tapered web members. For general members, γ_e can be calculated analytically based on open-section thin-walled beam theory. The term $\gamma_{e,min}$ is simply the multiple of f_r (and P_r) required to reach incipient elastic buckling of the member as a column subjected to concentric axial load (see Figure 3.3c). It is important to recognize that only one $\gamma_{e,min}$ exists for a member under consideration.

4) Calculate the axial resistance based on the assumption of $Q = 1$, by substituting $Q = 1$, the maximum value of f_r/F_y along the column length and $\gamma_{e,min}$ into Eqs. 3.6. This axial capacity is represented by the symbol F_{n1} (see Figure 3.3c). The cross-section with the largest value of f_r/F_y, denoted by $(f_r/F_y)_{max}$, always has the largest axial capacity ratio f_r/F_{n1} based on the assumption of $Q = 1$. Note that if all the cross-section elements are nonslender and Q is indeed equal to 1.0, one simply calculates the capacity ratio as $f_r/F_c = f_r/(F_{n1}/\Omega)$ in ASD, or $f_r/F_c = f_r/\phi F_{n1}$ in LRFD, at this stage to complete the calculations. If Q is less than 1.0 at any cross-sections along the member length, continue to the next step.

5) Based on the above axial resistance F_{n1}, determined assuming $Q = 1$, calculate $\gamma_{n1} = F_{n1}/f_r$ at the cross-section corresponding to $\left(f_r/F_y\right)_{max}$ as shown in Figure 3.3c. The load ratio γ_{n1} is simply the multiple of the design load required to reach the nominal axial resistance based on $Q = 1$.

6) Calculate $f = \gamma_{n1} f_r$ at various sections along the member length as shown in Figure 3.3d. These are the axial stresses corresponding to the nominal column axial resistance for $Q = 1$. This term is needed below to determine the local buckling effects on the axial resistance, via the Q factor.

7) Calculate $Q = Q(f)$ (i.e., Q as a function of f ($= \gamma_{n1} f_r$) obtained in Step 6) at the various sections along the member length using the Q factor equations from AISC (2010). This step is shown in Figure 3.3e.

8) Calculate the member axial capacity at the cross-section corresponding to $(f_r/QF_y)_{max}$, accounting for local buckling effects, by substituting $\gamma_{e,min}$, $(f_r/QF_y)_{max}$ and Q into Eqs.

3.6, where Q is determined at the cross-section corresponding to $\left(f_r / QF_y\right)_{\max}$. This is shown in Figure 3.3f.

9) Calculate the axial capacity ratio $P_r/P_c = f_r/F_c$, where F_c is related to F_n by Eqs. 3.3. Alternately, the axial capacity ratio may be calculated directly from Eqs. 3.7 using $\left(f_r / QF_y\right)_{\max}$, $\gamma_{e,min}$, and the value of Q at the section corresponding to $\left(f_r / QF_y\right)_{\max}$. As noted in the previous section, this is always the largest value of P_r/P_c from all the cross-sections along the member length (see Figure 3.3g).

The above procedure for calculation of $f_r/F_y = P_r/P_y$ can be simplified by calculating Q factors based on $f = F_y$ instead of $f = \gamma_{n1} f_r$. By doing this, steps (4) to (7) are not necessary. However, it should be noted that using the Q factor values based on $f = F_y$ are slightly to moderately smaller than those based on $f = \gamma_{n1} f_r$. For example, the Q factors calculated with $f = F_y$ are 2 to 11 % smaller than those calculated with $f = \gamma_{n1} f_r$ for members in the exterior rafter span of a modular frame shown in Chapter 8 as an example frame.

The above calculation of the axial capacity ratio f_r/F_c or P_r/P_c is generally an accurate to conservative estimate for nonprismatic geometries and/or members subjected to nonuniform axial compression. This is because the inelastic column strength equation (Eq. 3.1a) is based on the case of nominally uniform axial stress along the entire member length. However, f_r is typically not uniform along the length of nonprismatic nonuniformly-loaded I-section members (see Figure 3.3b). As a result, the overall inelastic member flexural or flexural-torsional buckling tends to be less critical in these types of members compared to prismatic uniformly-loaded I-section columns. This has been demonstrated by Jiminez and Galambos (2001). It should be noted that the

influence of bending due to the non-straight centroidal axis of these general types of members is captured by including the moment P_r times y in the calculation of M_r (see Figure 2.5) and via the use of the beam-column strength interaction equations.

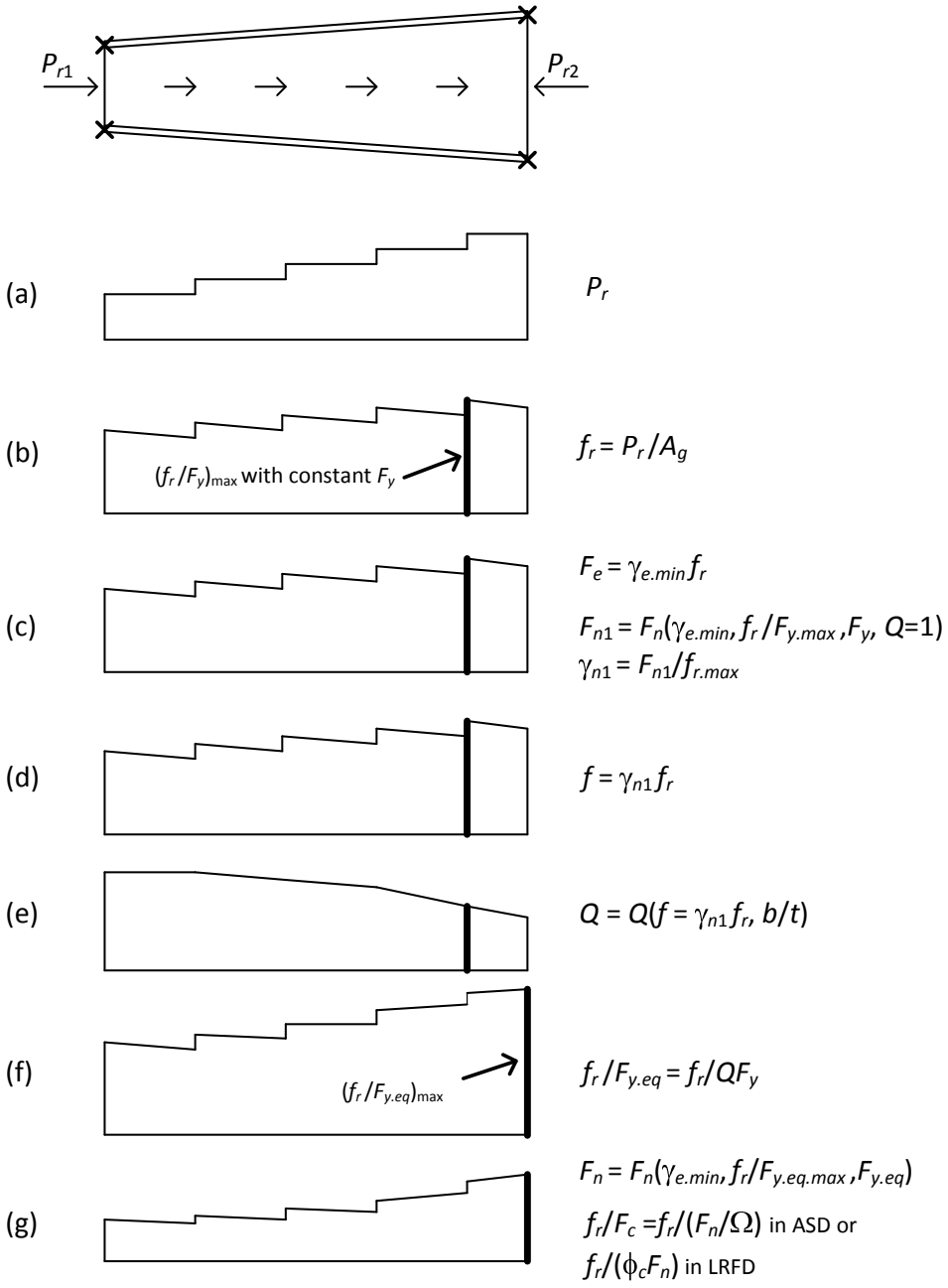

Figure 3.3. Axial capacity calculations using AISC (2010) resistance equations.

Any additional capacity beyond that obtained using the above procedure is dependent on the degree of taper and other changes in the member cross-section as well as the variation of the axial load P_r along the member length. Potential enhancements in the calculated axial capacity ratio, relative to that obtained by the above approach, appear to be on the same order of magnitude as potential enhancements associated with the use of multiple column strength curves. Furthermore, in many cases, the axial capacity ratio is rather small compared to the flexural capacity ratio for these member types. Therefore, it is suggested that the benefits associated with potential refinement of the above approach (e.g., multiple column curves) would be minor for most metal building frames. The above approach is closely related to the approaches forwarded by Lee et al. (1981) and Watwood (1985), yet it is general for any type of nonprismatic-section nonuniformly-loaded member.

As an alternate, the AISI (2001) unified effective width equations can be used to calculate axial resistances of nonprismatic members subjected to nonuniform axial loads. The AISI (2001) approach provides more accurate solutions typically for box sections with slender elements and large KL/r. A general procedure developed using the AISI (2001) unified effective width equations is outlined in Appendix A.

3.3 Flexural Capacity Ratio

The flexural resistance equations in both AISC (2005 & 2010) and AASHTO (2004 & 2007) have been updated relative to previous Specifications to simplify their logic, organization and application, while also improving their accuracy and generality. The base flexural resistance equations of these Specifications are, with minor exceptions, fundamentally the same. AASHTO (2004 & 2007) provides some limited guidance for

application of the equations to members with tapered webs and/or cross-section transitions. AISC (2005 & 2010) does not address these extensions at all. Nevertheless, the equations can be readily extended to address general nonprismatic geometries by employing concepts similar to those discussed above for assessment of the axial load resistance. Lee et al. (1981) have employed similar concepts in their recommended procedures.

In the following section, the basic format of the AISC (2010) and AASHTO (2007) flexural resistance equations is presented first. Then the "mapping" of these flexural resistance equations to a general form applicable to nonprismatic members is explained. White and Chang (2007) give a number of examples illustrating the improvements in the flexural resistance calculations in AISC (2005) relative to AISC ASD (1989) for prismatic I-section members. White (2008) provides complete flowcharts and a detailed discussion of the background to the AISC (2005) and AASHTO (2004) flexural resistance equations. White and Jung (2008) and White and Kim (2008) provide an extensive analysis of the above flexural resistance equations versus a comprehensive collection of experimental test results for prismatic I-section members. The flexural resistance equations in AISC (2010) and AASHTO (2007) are the same as those in AISC (2005) and AASHTO (2004).

3.3.1 Basic Format of the AISC (2010) and AASHTO (2007) Flexural Resistance Equations

The flexural stability resistance equations in AASHTO (2007) and AISC (2010) are closest in form and function to those of AISC (1999). All the flange local buckling (FLB) and lateral torsional buckling (LTB) resistance equations in both Specifications are

based consistently on the logic of identifying the two anchor points shown in Figure 3.4 for the case of uniform major-axis bending. Anchor Point 1 is located at the effective length $KL_b = L_p$ for LTB, or the flange slenderness $[\lambda_{fc} = b_{fc}/2t_{fc}] = \lambda_{pf}$ for FLB, corresponding to development of the maximum potential flexural resistance. This resistance is labeled in the figure as M_{max} (in terms of the bending moment) or F_{max} (in terms of the corresponding compression flange flexural stress), where $M_{max} = M_p$ for

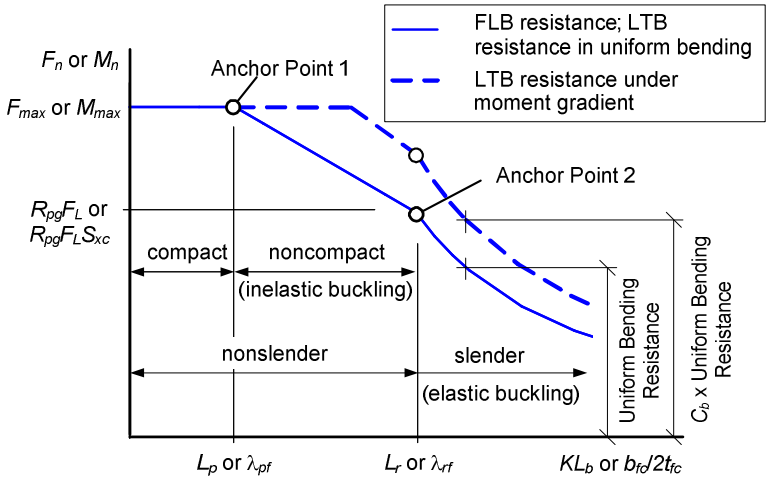

Figure 3.4. Basic form of FLB and LTB resistance equations.

members with a compact web and compact compression flanges. However, it is generally less than M_p for other cross-section types. Anchor Point 2 is located at the effective length $KL_b = L_r$, or flange slenderness $b_{fc}/2t_{fc} = \lambda_{rf}$, for which the LTB or FLB resistances are governed by elastic buckling. The ordinate of Anchor Point 2 is taken (in terms of the bending moment) as $R_{pg}F_LS_{xc} = 0.7R_{pg}F_{yc}S_{xc}$ (or $0.7R_{pg}M_{yc}$) for most I-shapes, where M_{yc} is the nominal yield moment associated with the compression flange and R_{pg} is the web bend buckling strength reduction factor, equal to 1.0 for sections with compact or noncompact webs. The inelastic buckling resistance is expressed simply as a

line between these two anchor points. For $KL_b > L_r$ or $b_{fc}/2t_{fc} > \lambda_{rf}$, the nominal resistance is defined explicitly as the theoretical elastic buckling moment or flange stress. The basic format shown in Figure 3.4, adopted from AISC (1999), greatly facilitates the definition of simple yet comprehensive flexural resistance equations. AISC (2010) categorizes the limit state associated with the plateau in Figure 3.3 as flexural yielding. AASHTO (2007) simply states that the LTB or FLB resistance is M_{max} or F_{max} when the corresponding compactness limits are satisfied. The flange resistance calculations are addressed in the same way as AASHTO (2007) in this dissertation.

For unbraced lengths subjected to moment gradient, the calculated LTB resistance is modified by the moment gradient factor, C_b, as illustrated in Figure 3.4. In these cases, the uniform bending elastic and inelastic LTB strengths are scaled by C_b, with the exception that the resistance is capped by F_{max} or M_{max}. The calculated FLB resistance for moment gradient cases is the same as that for uniform bending, neglecting the relatively minor influence of moment gradient effects.

For doubly-symmetric I-section members, only the LTB and FLB limit states need to be considered. However, for members having a larger compression flange such that $S_{xc} > S_{xt}$, the tension flange yielding (TFY) limit state also must be checked. For slender web members, the TFY limit state is essentially the same as the tension flange yielding checks in AISC LRFD (1999) and ASD (1989). However, for noncompact-web members, the TFY resistance varies smoothly from the yield moment resistance M_{yt} for members having a web proportioned at the noncompact-web limit to the plastic moment resistance M_p for members having a web proportioned at the compact-web limit.

3.3.2 Generalization of the AISC (2010) Flexural Resistance Equations to Members with Nonprismatic Cross-Section Geometry

The AISC (2010) FLB and TFY flexural resistance equations are effectively member cross-section checks. Hence, these equations can be applied directly to a general nonprismatic member on a cross-section by cross-section basis. One determines the required moment M_r or the required flange flexural stress f_r at all the cross-sections along a member's length. Then, the flexural capacity ratio is determined for each cross-section by dividing the above required values by the cross-section design resistance M_c or F_c. The largest flexural capacity ratio is the governing ratio for the member. Obviously, when performing manual calculations, engineers can often identify by inspection one or only a few sections that need to be checked to determine the governing flexural capacity ratio. However, for automated design assessment, one would typically check the cross-section flexural resistances at a specified small interval along the member lengths.

In contrast to the FLB and TFY limit state equations, the LTB resistance cannot be checked solely on a cross-section by cross-section basis. The LTB resistance depends generally on the member properties along the entire unbraced length under consideration, as well as the loading configuration (e.g., the moment gradient and the position of any applied loads through the member depth) and the boundary conditions at the ends of the member (e.g., the continuity with adjacent unbraced lengths). This is similar in many respects to the determination of the out-of-plane column axial resistance.

Consider the AISC (2010) inelastic LTB flexural resistance for a general prismatic I-section member with $C_b = 1$. This resistance may be expressed by the following single equation:

$$M_n = R_{pg} R_{pc} M_{yc} \left[1 - \left(1 - \frac{F_L S_{xc}}{R_{pc} M_{yc}} \right) \left(\frac{KL_b - L_p}{L_r - L_p} \right) \right] \leq R_{pg} R_{pc} M_{yc}$$

for $L_p < KL_b \leq L_r$ (Eq. 3.9, AISC F4-2 & F5-3)

where:

R_{pg} is the web bend-buckling strength reduction factor for a slender-web I-section member, which accounts for shedding of web stresses to the compression flange from the post-buckled web plate. This term is equal to 1.0 for I-sections with a noncompact or compact web.

R_{pc} is the web plastification factor, which is in essence the effective shape factor for a noncompact- or compact-web cross-section. This term is equal to 1.0 for slender-web members, but varies from 1.0 at the web noncompact limit to the shape factor M_p/M_{yc} for compact-web members.

M_{yc} is the cross-section yield moment corresponding to the compression flange.

F_L is the compression flange flexural stress at incipient nominal yielding on the cross-section, including compression flange residual stress effects as well as tension flange yielding effects (residual stress effects are not included for the tension flange, since the tension flange residual stresses only have a minor effect on the stability behavior of the compression flange). This stress is specified by AISC (2010) as

$F_L = 0.7F_y$ (Eq. 3.10a, AISC F4-6a)

for general noncompact and compact-web section members with $S_{xt}/S_{xc} \geq 0.7$ and implicitly for slender-web section members in the resistance equations of AISC (2010) Section F5, and

$F_L = F_y S_{xt}/S_{xc} \geq 0.5F_y$ (Eq. 3.10b, AISC F4-6b)

for general noncompact and compact-web section members with $S_{xt}/S_{xc} < 0.7$.

S_{xc} is the elastic section modulus to the compression flange.

S_{xt} is the elastic section modulus to the tension flange.

KL_b is the member effective length under consideration, often taken equal to the actual length L_b.

L_p is the compact bracing limit for uniform bending, shown previously in Figure 3.3.

L_r is the noncompact bracing limit for uniform bending, shown previously in Figure 3.3.

To "map" or "transform" Eq. 3.8 to a form that is useful and applicable for the assessment of nonprismatic members, consider the AISC (2010) expression for the elastic LTB resistance in uniform bending obtained by taking $J = 0$,

$$F_{eLTB(J=0)} = \frac{\pi^2 E}{(KL_b / r_t)^2} \qquad \text{(Eq. 3.11, AISC F5-4)}$$

where

$$r_t = \frac{b_{fc}}{\sqrt{12\left(\frac{h_o}{d} + \frac{1}{6}\frac{h_c t_w}{b_{fc} t_{fc}}\frac{h^2}{h_o d}\right)}} \qquad \text{(Eq. 3.12a, AISC F4-10)}$$

is the effective LTB radius of gyration for a general I-section. By taking $h \cong h_o \cong d$, Eq. 3.12a is approximated accurately and conservatively as the radius of gyration of the compression flange plus one-third of the compressed portion of the web, i.e.,

$$r_t = \frac{b_{fc}}{\sqrt{12\left(1 + \frac{1}{6}\frac{h_c t_w}{b_{fc} t_{fc}}\right)}} \qquad \text{(Eq. 3.12b)}$$

The use of Eq. 3.11 greatly simplifies the following developments, but as discussed subsequently, the accuracy of the final general LTB resistance expression is not affected

by this simplification. This equation may be re-written in the following form for the KL_b corresponding to a given cross-section r_t and a given critical LTB stress $F_{eLTB(J=0)}$:

$$KL_b = \pi r_t \sqrt{E / F_{eLTB(J=0)}} \qquad \text{(Eq. 3.13)}$$

Also, consider the AISC (2010) and AASHTO (2007) expression for the compact unbraced length

$$L_p = 1.1 r_t \sqrt{E / F_{yc}} \qquad \text{(Eq. 3.14, AISC F4-7)}$$

as well as the simplified expression for the noncompact unbraced length obtained by taking J equal to zero:

$$L_r = \pi r_t \sqrt{E / F_L} \qquad \text{(Eq. 3.15, AISC F5-5)}$$

If Eqs. 3.13 through 3.15 are substituted into Eq. 3.8, this equation takes the form

$$M_n = R_{pg} R_{pc} M_{yc} \left[1 - \left(1 - \frac{F_L S_{xc}}{R_{pc} M_{yc}} \right) \left(\frac{\pi \sqrt{\frac{F_{yc}}{F_{eLTB}}} - 1.1}{\pi \sqrt{\frac{F_{yc}}{F_L}} - 1.1} \right) \right] \leq R_{pg} R_{pc} M_{yc} \text{ for}$$

$$\frac{1.1}{\pi} \leq \sqrt{\frac{F_{yc}}{F_{eLTB}}} < \sqrt{\frac{F_{yc}}{F_L}} \qquad \text{(Eq. 3.16)}$$

Although the above developments utilize the simplifying assumption of $J = 0$ in Eqs. 3.11 and 3.15, the final form given by Eq. 3.16 provides the same results, for all practical purposes, as the initial form given by Eq. 3.9 when the "exact" elastic LTB critical stress is used for F_{eLTB}. Equation 3.16 is particularly useful for LTB assessment of unbraced lengths where the geometry is nonprismatic. This equation provides a "mapping" from the elastic LTB strength to an appropriate inelastic LTB resistance. Similar to the

previous development of the column resistance equations, the ratio F_{yc}/F_{eLTB} in Eq. 3.16 may be expressed as

$$\frac{F_{yc}}{F_{eLTB}} = \frac{1}{\gamma_{eLTB}(f_r / F_{yc})} = \frac{1}{\gamma_{eLTB}(M_r / M_{yc})} \qquad \text{(Eq. 3.17)}$$

at the cross-section with the largest f_r/F_{yc} or M_r/M_{yc}, where γ_{eLTB} is the multiple of the design loads at which elastic LTB of the member unbraced length occurs, i.e.,

$$\gamma_{eLTB} = F_{eLTB}/f_r = M_{eLTB}/M_r \qquad \text{(Eq. 3.18)}$$

and f_r is the required compression flange elastic stress for a given design load combination. It is important to recognize that the term $\gamma_{eLTB}f_r/F_{yc}$ in Eq. 3.17 is the same as $\gamma_e f_r/F_{y.eq}$ developed in the member axial resistance with $\gamma_e = \gamma_{eLTB}$, $F_{y.eq} = F_{yc}$. Also, similar to the discussions pertaining to the member axial resistance, M_r, M_{yc} and M_r/M_{yc} can all vary in general along the member length. However, there is only one elastic LTB load level for a given unbraced length. This level is quantified by the load ratio γ_{eLTB}. The elastic LTB load level γ_{eLTB} can be determined using the simplified procedure developed in Chapter 4 for linearly-tapered web members. For general members, γ_{eLTB} can be calculated analytically based on open-section thin-walled beam theory.

Equation 3.16 is applicable not only for uniform bending of prismatic members; it may be employed also for moment gradient and stress gradient cases in prismatic and nonprismatic members. For stress gradient cases in nonprismatic members, two approaches are proposed in this research. In the first approach, the stress gradient resistance is obtained in the essentially same way as the AISC (2010) approach for the moment gradient cases in prismatic members. One calculates the uniform stress LTB resistance $M_{n(Cb=1)}$ using Eq. 3.16 with the elastic LTB critical stress F_{eLTB} based on C_b =

1.0, and a stress-gradient factor C_b separately. The stress gradient LTB resistance M_n is determined by $C_b M_{n(Cb=1)}$. This procedure requires the appropriate estimate of C_b for a member under consideration. The recommendations on calculation of C_b factors for linearly-tapered web members are outlined in Section 4.4. This approach is adopted in the AISC (2010) Design Guide 25 for tapered members with a single linear taper and no section transition with the unbraced length. In this dissertation, this approach is referred to *MBMA/AISC-1 procedure*. For general nonprismatic members, one calculates the elastic LTB critical stress F_{eLTB} for the given member loading and end restraint conditions. If F_{yc}/F_{eLTB} falls within the limits stated in Eq. 3.16, F_{yc}/F_{eLTB} is substituted to determine the inelastic LTB strength. This approach parallels the usage of C_b in the LTB equations of AISC ASD (1989). The AISC (2010) Design Guide 25 suggests this approach for all the members within the scope of the Design Guide 25. In this dissertation, this approach is referred to *MBMA/AISC-2 procedure*.

In the limit that a web-tapered member is proportioned such that the flange stress is approximately constant, the effective C_b is essentially equal to 1.0 and Eqs. 3.9 and 3.16 give nearly identical results. For moment gradient cases, the use of Eq. 3.16 in MBMA/AISC-2 procedure is conservative relative to the calculations in AISC (2010) based on Eq. 3.9 with $C_b > 1$ or in MBMA/AISC-1 procedure, especially within the inelastic LTB range. The AISC (2010) and MBMA/AISC-1 procedures give essentially the same inelastic LTB resistances with $C_b > 1$.

Using the MBMA/AISC-1 procedure, if $(F_{yc}/F_{eLTB(Cb=1)})^{0.5}$ is less than $1.1/\pi = 0.35$, then the LTB resistance is simply

$$M_n = M_{max} = R_{pg} R_{pc} M_{yc} \qquad \text{(Eq. 3.19a)}$$

as represented by the plateau in Figure 3.3. Furthermore, if $F_{eLTB(Cb=1)} < F_L$, elastic LTB governs and the LTB resistance is

$$M_n = C_b R_{pg} F_{eLTB} S_{xc} \leq R_{pg} F_{eLTB} S_{xc} \quad \text{(Eq. 3.19b)}$$

Similarly using the MBMA/AISC-2 procedure, the plateau strength is

$$M_n = M_{max} = R_{pg} R_{pc} M_{yc} \quad \text{for } (F_{yc}/F_{eLTB})^{0.5} \leq 1.1/\pi \quad \text{(Eq. 3.20a)}$$

and the elastic LTB resistance is

$$M_n = R_{pg} F_{eLTB} S_{xc} \quad \text{for } F_{eLTB} < F_L \quad \text{(Eq. 3.20a)}$$

3.3.3 General Procedure

The above equations may be applied for calculation of the LTB resistance of nonprismatic I-section members in a similar fashion to the application of the axial load resistance equations discussed previously. However, the procedure is not as involved for the flexural resistance check, since the AISC (2010) and AASHTO (2007) flexural resistance provisions handle FLB and LTB as separate and independent limit states. Also, for slender web members, the effects of web local bend buckling and the subsequent postbuckling response are handled via the R_{pg} parameter. For compact or noncompact web members, the web plastification factor R_{pc} should be considered. A general procedure for calculation of the governing M_r/M_c for a given unbraced length is developed in this section. Each step of this general procedure is explained below and shown in Figure 3.5:

1) Determine the diagrams for M_r and $f_r/F_{yc} = M_r/M_{yc}$ along the length of the unbraced segment under consideration (see Figures 3.5a and b). Note that for members subjected to axial load, the additional moment associated with the axial force P_r times

the y distance from the reference axis to the cross-section neutral axis needs to be included in the calculation of M_r.

2) Calculate the elastic LTB resistance of the member unbraced length, using beam theory, and determine the ratio of $\gamma_{eLTB} = F_{eLTB}/f_r$ at the cross-section with the largest value of M_r/M_{yc}. As mentioned above, γ_{eLTB} can be calculated using the simplified method developed in Chapter 4 for linearly-tapered web members. For general members, γ_{eLTB} can be calculated analytically based on open-section thin-walled beam theory. If the web is slender at any position along the length of the segment under consideration, the above elastic LTB resistance must be determined using $J = 0$. This is because the AISC (2010) resistance equations are based on $J = 0$ for slender-web members. The reason for taking $J = 0$ is that these types of members tend to exhibit either a minor difference between the F_{eLTB} values obtained using the actual J or using $J = 0$, or particularly in cases with heavy flanges, the LTB resistance tends to be reduced significantly due to web distortion effects (Bradford 1992; White and Jung 2008).

3) Calculate $\gamma_{eLTB}(f_r/F_{yc})$ as well as $R_{pc}R_{pg}$ at various locations throughout the unbraced segment length (see Figures 3.5c and d). To simplify the calculation, one can substitute the minimum $R_{pc}R_{pg}$ and $\gamma_{eLTB}(f_r/F_{yc})_{\max}$ into Eqs. 3.16, 3.19 and 3.20 as appropriate to determine the nominal flexural resistance M_n (Figure 3.5e). One should note that the flexural capacity ratio M_r/M_c is always the largest at the cross-section with the largest f_r/F_{yc} if the minimum $R_{pc}R_{pg}$ is used in the calculation of M_n.

4) Figure 3.5d shows the calculation of R_{pg} based on the yield strength F_{yc}. However, the use of M_n/S_{xc} rather than F_{yc} provides more optimistic estimates for R_{pg}, which

results in larger flexural capacity M_n for a given member. If more optimistic estimates of R_{pg} and M_n are desirable, one can use the M_n values obtained in step (3) or in Figure 3.5(e) to update R_{pg} values (see Figure 3.5f). Using the new $R_{pc}R_{pg.min}$, the flexural capacity M_n is also updated. One should iterate this process until the solution converges

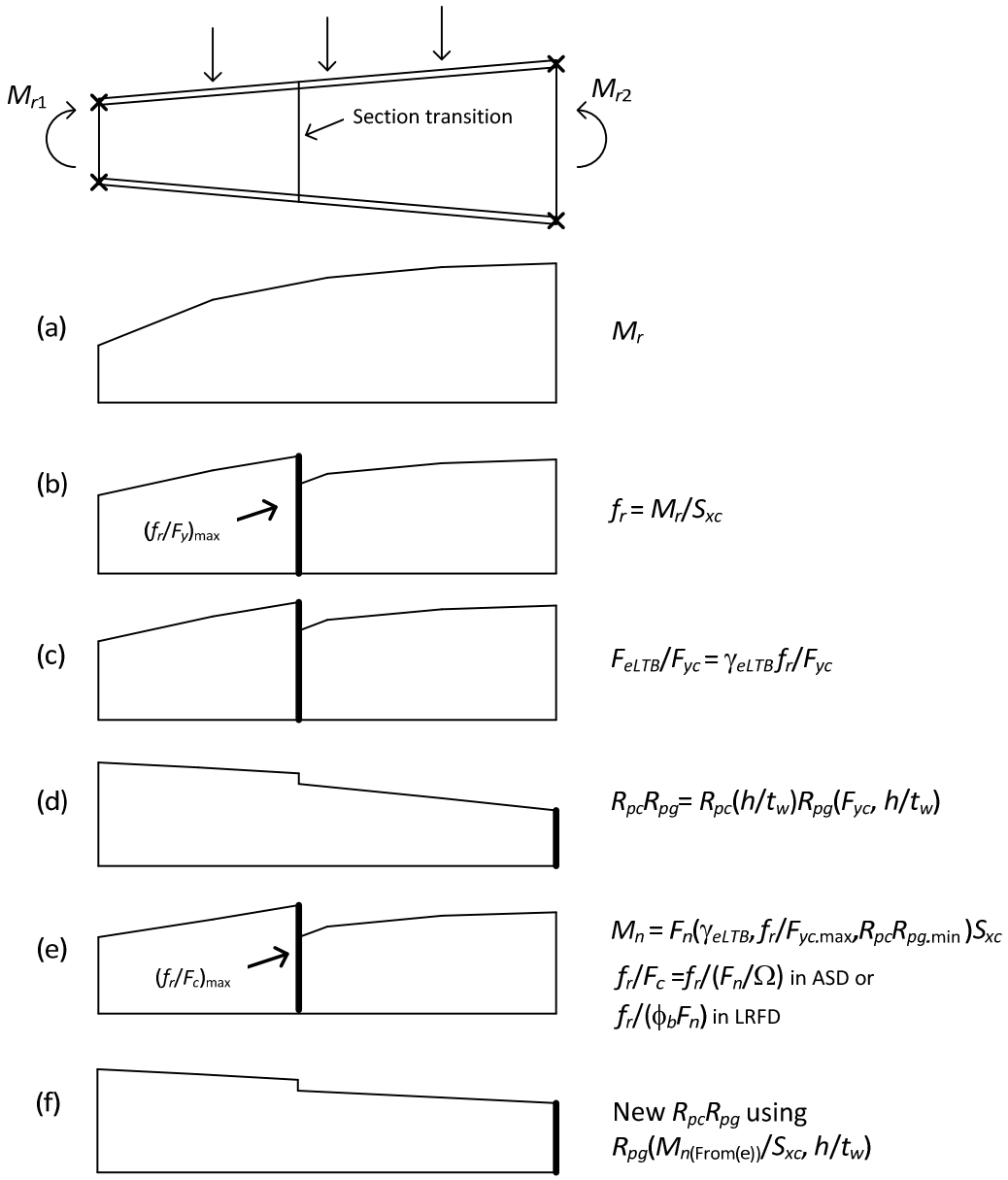

Figure 3.5. Flexural capacity calculations using AISC (2010) resistance equations.

Alternately, one can calculate the flexural capacity M_n at various locations using $R_{pc}R_{pg}$ at the same location where M_n is calculated. The estimates of the flexural capacity ratio obtained with $R_{pc}R_{pg}$ calculated via cross-section by cross-section basis can be more accurate. However, for most flexural members in metal building frames, the use of the minimum $R_{pc}R_{pg}$ provides accurate to slightly conservative estimates compared to the above alternate calculations.

3.4 Interaction between the Flexural and Axial Resistances

Figure 3.6 shows representative first-yield and fully-plastic axial force-moment strength envelopes for a short compact singly-symmetric I-section member. Interestingly, these envelopes are not symmetric. The strength interaction curves have a bulge in the quadrants where the axial and flexural stresses are additive either in compression or in tension on the larger flange. One should note that the fully-plastic strength is only an upper-bound theoretical limit. The actual resistance for a singly-symmetric beam-column member is influenced in general by combined local and overall member stability effects.

The dark solid curve in Figure 3.7 shows a representative strength envelope for a hypothetical simply-supported finite-length beam-column with noncompact and/or slender cross-section elements and a singly-symmetric cross-section profile. Also shown as dashed lines in the figure are the base AISC (2010) beam-column strength interaction curves given by Eqs. 2.5. White and Kim (2003) discuss the behavior of various strength interaction equations and review the limited experimental test results for prismatic doubly- and singly-symmetric I-section beam-columns with noncompact and/or slender webs and compact, noncompact and slender flanges. They conclude that the bilinear

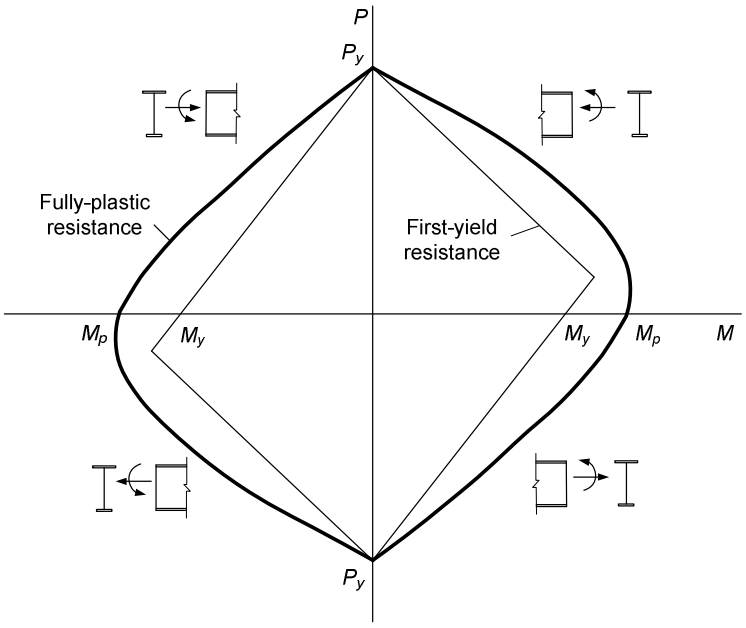

Figure 3.6. Representative first-yield and fully-plastic axial force-moment strength envelopes for a short compact singly-symmetric I-section member.

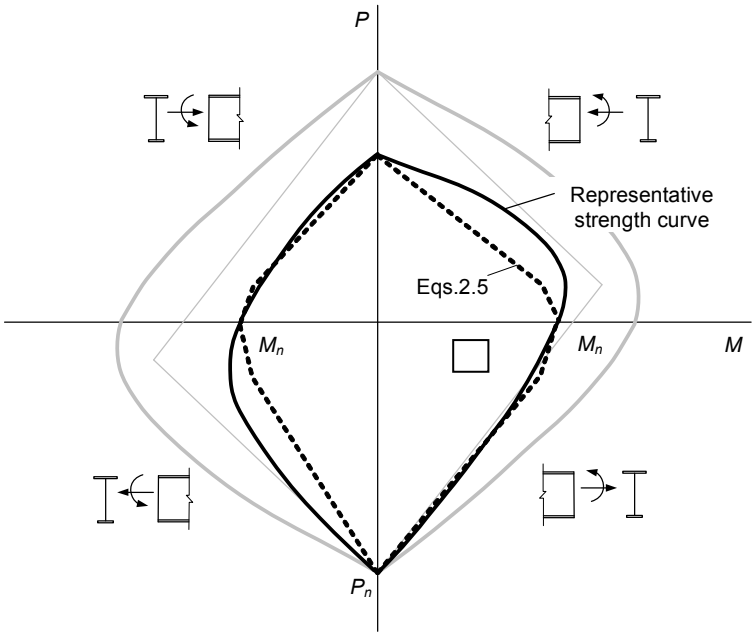

Figure 3.7. Representative strength envelope for a hypothetical simply-supported finite-length beam-column with noncompact and/or slender cross-section elements and AISC (2010) strength interaction curves (Eqs. 2.5) superposed on the strength curves from Figure 3.6.

strength curves given by Eqs. 2.5 provide an accurate to conservative characterization of the in-plane and out-of-plane beam-column resistances from the available tests. Galambos (2001a & b) proposes a refined procedure for determining the resistance of prismatic singly-symmetric compact I-section members, and makes similar observations pertaining to Eqs. 2.5. Generally, Eqs. 2.5 provide an accurate to slightly conservative characterization of the in-plane resistance for doubly-symmetric I-section members and for singly-symmetric I-section members with the smaller flange subjected to additive flexural and axial stresses. They appear to be somewhat conservative relative to the physical beam-column in-plane and out-of-plane resistance in many cases involving singly-symmetric I-section members when the larger flange is subjected to additive axial and flexural compression or tension. The studies by Lee and Hsu (1981) provide evidence of this conclusion for tapered-web singly-symmetric members. Equations 2.5 provide a significantly conservative assessment of the out-of-plane stability limit state for typical rolled doubly-symmetric column-type I-section beam-columns subjected to large axial compression. However, they appear to give an accurate to slightly conservative assessment of the out-of-plane resistance for other I-section geometries and loadings.

3.4.1 Enhanced Beam-Column Out-of-Plane Resistance Equations

As noted previously, AISC (2010) specifies Eq. 2.7 as an enhanced description of the out-of-plane resistance of doubly-symmetric rolled I-section beam-columns. The analytical basis for this equation comes from the solution of the differential equations of equilibrium for a simply-supported elastic member subjected to axial compression and unequal end moments (McGuire 1968). This solution yields the equation

$$\frac{M^2}{C_b^2 r_o^2 P_{ey} P_{ez}} = \left(1 - \frac{P}{P_{ey}}\right)\left(1 - \frac{P}{P_{ey}}\frac{P_{ey}}{P_{ez}}\right) \qquad \text{(Eq. 3.21a)}$$

where

$$P_{ey} = \frac{\pi^2 E I_y}{L^2} \qquad \text{(Eq. 3.21b)}$$

is the out-of-plane column flexural buckling load,

$$P_{ez} = \frac{1}{r_o^2}\left(\frac{\pi^2 E C_w}{L^2} + GJ\right) \qquad \text{(Eq. 3.21c)}$$

is the column torsional buckling load, and

$$r_o^2 = \frac{1}{A}\left(I_x + I_y\right) \qquad \text{(Eq. 3.21d)}$$

is the polar radius of gyration of the cross-section. The term in the denominator on the left side of Eq. 3.21a is the square of the elastic lateral-torsional buckling resistance of the member, i.e.,

$$M_e = \sqrt{C_b^2 r_o^2 P_{ey} P_{ez}} = C_b \frac{\pi}{L}\sqrt{\left(\frac{\pi E}{L}\right)^2 I_y C_w + E I_y G J} \qquad \text{(Eq. 3.21e)}$$

where C_b is the moment gradient modifier, of which the AISC (2010) formula is an accurate approximation. Equation 2.7 is obtained by assuming $P_{ez} / P_{ey} = 2.0$, by replacing P and M by the required strengths P_r and M_r, and by replacing M_e and P_{ey} by the design resistances $\phi_c P_{no}$ and $C_b \phi_b M_{nx(Cb=1)}$. The resulting Eq. 2.7 provides a much improved assessment of the out-of-plane resistance of typical rolled column-type I-sections, particularly in cases where the design resistances are governed by inelastic buckling and/or yielding limit states. However, for general doubly-symmetric I-section members with longer member lengths where the resistances are governed by elastic

buckling, it would be prudent to retain the term P_{ey}/P_{ez} from Eq. 3.21a. This gives the following expanded form of Eq. 2.7:

$$\left(\frac{M_r}{\phi_b M_{nx}}\right)^2 \le \left(1-\frac{P_r}{\phi_c P_{no}}\right)\left(1-\frac{P_r}{\phi_c P_{ez}}\right) \qquad \text{(Eq. 3.22a)}$$

or equivalently

$$\frac{P_r}{\phi_c P_{no}}+\frac{P_r}{\phi_c P_{ez}}-\frac{P_r^2}{\phi_c{}^2 P_{no} P_{ez}}+\left(\frac{M_r}{C_b\phi_b M_{nx}}\right)^2 \le 1.0 \qquad \text{(Eq. 3.22b)}$$

Figure 3.8 shows the shape of Eq. 3.21a for several values of P_{ez}/P_{ey}. For prismatic or nearly prismatic doubly-symmetric members with unbraced lengths typical of metal building construction, P_{ez}/P_{ey} is generally greater than 1.0. However, it is not uncommon for this parameter to be only slightly larger than 1.0. In this case, one can observe that Eqs. 2.5, with P_r and M_r replaced by P and M and with P_{co} and M_c replaced by P_{ey} and M_e, provides a slightly liberal characterization of the theoretical beam-column elastic buckling resistance for small values of P/P_{ey}. Interestingly, Eqs. 2.5 nearly match Eq. 3.22a for $P/P_{ey} \le 0.2$ when Eq. 3.22a is used with $P_{ez}/P_{ey} = \infty$. The base AISC (2010) beam-column strength curve defined by Eqs. 2.5 tends to be slightly unconservative for large P/P_{ey} when P_{ez}/P_{ey} is close to 1.0, whereas it is significantly conservative relative to Eq. 3.21a for large P_{ez}/P_{ey}.

There is no precedent for applying Eq. 2.7 or Eqs. 3.22 to beam-columns having noncompact or slender cross-section elements, or to any type of tapered-web or generally nonprismatic beam-column members. AISC (2010) permits the application of Eq. 2.7 only to doubly-symmetric rolled I-section members. Some enhancement relative to Eqs. 2.5 is possible in certain situations. However, the precise shape of the beam-column strength envelope depends on the mode of failure (FLB, LTB or TFY in the limit of zero

axial force, weak- or strong-axis flexural buckling or flexural-torsional buckling in the limit of zero moment, and variations between these limits for combined axial loading and flexure). Stated alternately, the precise shape of the beam-column strength envelope depends on the member parameters that influence the resistance in the various above axial and flexural modes of failure as well as potentially different interactions between the different failure modes. Further research is needed to determine how to best characterize these additional resistances. In the absence of further refinements, the general use of Eqs. 2.5 is recommended in this research. The member beam-column strength checks are handled in this fashion for the example frames presented in Chapter 8.

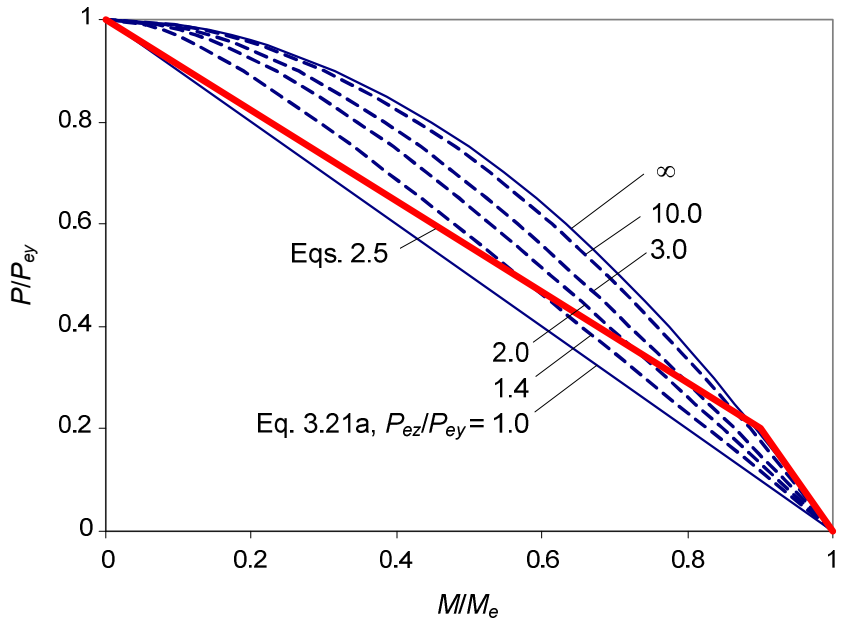

Figure 3.8. Theoretical elastic out-of-plane strength envelope for simply-supported doubly-symmetric I-section beam-columns versus the base AISC (2010) beam-column strength interaction curve.

CHAPTER IV

PRACTICAL DESIGN-BASED ELASTIC BUCKLING CALCULATIONS AND LIMITS

This chapter addresses the recommended procedures to calculate elastic buckling loads for in-plane and out-of-plane flexural buckling, torsional or flexural-torsional buckling, constrained-axis torsional buckling, and lateral torsional buckling. The recommended procedures are evaluated by a number of parametric study conducted using a finite element analysis software, GT-Sabre (Chang 2006). All the recommended procedures discussed in this chapter are adopted in the design guide, *Frame Design using Web-Tapered Members* (MBMA/AISC 2010).

4.1 In-Plane and Out-of-Plane Flexural Buckling

There are a number of useful design-oriented methods for calculation of the elastic flexural buckling resistance of general tapered and stepped cross-section members. However, the direct analysis method eliminates the calculation of γ_{ex}, since the in-plane column resistance P_{ni} is taken simply as QP_y. The consideration of in-plane stability effects is moved entirely into the calculation of the required component forces and moments. Obviously, this greatly simplifies the in-plane stability design.

In the effective length method, one needs to determine γ_{ex}. Various procedures have been developed for determining γ_{ex} for in-plane sidesway buckling of general moment frames. For portal frames with significant axial thrust in the roof girder, or gable frames with significant axial compression in the rafters, the influence of the axial compression in the roof girder or rafters must be considered. Lu (1965) and Davies

(1990) outline simplified procedures that account for this effect in gable frames composed of prismatic I-section members. Also, rigorous eigenvalue buckling analysis using a proper second-order analysis model of the structure is an increasingly viable option. In Chapter 8, several methods to determine γ_{ex} for in-plane sidesway buckling in the effective length method are discussed with the example frame designs.

For calculating the elastic flexural buckling strength of a member with ideal pinned-pinned end conditions ($K = 1$), the method of successive approximations (Timoshenko and Gere 1961) is very useful for nonprismatic, nonuniformly loaded members. This method uses an iterative beam analysis to find the axial load $\gamma_{ex(K=1)}$. The design guide, *Frame Design using Web-Tapered Members* (MBMA/AISC 2010) provides the details of the suggested implementations of this approach based on Timoshenko and Gere (1961) and Newmark (1943).

For out-of-plane buckling of unbraced lengths with prismatic flanges (no flange plate transitions) and minor variation of the axial load along the length, the column elastic flexural buckling resistance can be estimated simply as

$$P_{ey} = \pi^2 EI_y / (KL_y)^2 \qquad \text{(Eq. 4.1)}$$

(Lee et al. 1981; Galambos 1988) using the minor-axis moment of inertia at the cross-section at mid-span. It is generally accepted that the effective length for out-of-plane flexural buckling can be taken as the actual unbraced length in Eq. 4.1, i.e., $KL_y = L_y$ or $K = 1$. However, if desired, an out-of-plane column effective length may be determined by considering the buckling interaction between adjacent unbraced lengths. This generally gives $K < 1$ for the most critical unbraced lengths and $K > 1$ for the adjacent unbraced lengths, which restrain the buckling of the critical segment. Given the above out-of-plane

flexural buckling load P_{ey}, the load ratio corresponding to out-of-plane elastic flexural buckling can be estimated as

$$\gamma_{ey} = \frac{P_{ey}}{P_{r,\max}} \qquad \text{(Eq. 4.2)}$$

where $P_{r,max}$ is the maximum required internal axial force for the unbraced segment and design load combination under consideration.

4.2 Torsional or Torsional-Flexural Buckling

4.2.1 Recommended Procedures for Prismatic Members

AISC (2005 & 2010) requires that the torsional or flexural-torsional buckling (TB or TFB) limit state must be checked in addition to the in-plane and out-of-plane flexural buckling. In general, members having:

- relatively thin cross-section elements, and/or
- large differences in the flange sizes (significant monosymmetry), and/or
- little restraint against member twisting

can buckle in a torsional or flexural-torsional mode at a load level γ_{eTF} that is smaller than the load level γ_{ey}. AISC (2010) gives the following equations for checking torsional and flexural-torsional buckling of prismatic I-section members:

(a) For doubly-symmetric members:

$$F_{eTF} = F_{ez} = \left[\frac{\pi^2 EC_w}{(KL_z)^2} + GJ\right]\frac{1}{I_x + I_y} \qquad \text{(Eq. 4.3, AISC E4-4)}$$

(b) For singly-symmetric members, where the y axis is the axis of symmetry:

$$F_{eTF} = \left(\frac{F_{ey} + F_{ez}}{2H}\right)\left[1 - \sqrt{1 - \frac{4F_{ey}F_{ez}H}{(F_{ey} + F_{ez})^2}}\right] \qquad \text{(Eq. 4.4a, AISC E4-5)}$$

where:

$$C_w = \frac{h_o^2 I_{y1}}{I_{y1}/I_{y2} + 1} \qquad \text{(Eq. 4.4b)}$$

= cross-section warping constant

$$J = \frac{ht_w^3}{3} + \frac{b_{f1}t_{f1}^3}{3}\left(1 - 0.63\frac{t_{f1}}{b_{f1}}\right) + \frac{b_{f2}t_{f2}^3}{3}\left(1 - 0.63\frac{t_{f2}}{b_{f2}}\right) \qquad \text{(Eq. 4.4c)}$$

= cross-section St. Venant torsional constant

G = shear modulus of elasticity

KL_z = effective length for torsional buckling, typically taken as the unsupported length between locations where the member is prevented from twisting, either by lateral bracing of both flanges or by torsional bracing including stiffening to prevent cross-section web distortion

$$F_{ey} = \frac{\pi^2 E}{(KL_y/r_y)^2} \qquad \text{(Eq. 4.4d, AISC E4-8)}$$

$$F_{ez} = \left[\frac{\pi^2 EC_w}{(KL_z)^2} + GJ\right]\frac{1}{A\bar{r}_o^2} \qquad \text{(Eq. 4.4e, AISC E4-9)}$$

= elastic torsional buckling load for a general singly-symmetric member

$$H = 1 - \frac{y_o^2}{\bar{r}_o^2} \qquad \text{(Eq. 4.4f, AISC E4-10)}$$

$$\bar{r}_o^2 = y_o^2 + \frac{I_x + I_y}{A} \qquad \text{(Eq. 4.4g, AISC E4-11)}$$

= square of the polar radius of gyration about the shear center

$$y_o = -h_1 + \frac{h_o}{I_{y1}/I_{y2} + 1} \qquad \text{(Eq. 4.4h)}$$

= y coordinate of the shear center with respect to the cross-section centroid

h_1 = absolute value of the distance from the centroid of the flange on the negative y side of the cross-section centroid to the cross-section centroid

h_o = distance between the centroids of the flanges

$$I_{y1} = t_{f1} b_{f1}^3/12 \quad \text{(Eq. 4.4i)}$$

= moment of inertia of the flange on the negative y side of the cross-section centroid about the minor-axis of the cross-section

$$I_{y2} = t_{f2} b_{f2}^3/12 \quad \text{(Eq. 4.4j)}$$

= moment of inertia of the flange on the positive y side of the cross-section centroid about the minor-axis of the cross-section

Given the above prismatic column buckling stresses F_{eTFB}, the elastic buckling load ratio is obtained simply as

$$\gamma_{eTF} = F_{eTFB}/f_r \quad \text{(Eq. 4.5)}$$

4.2.2 Evaluation of Recommended Procedures for Prismatic Members

Equation 4.3 defines the member axial stress corresponding to pure torsional buckling of a doubly-symmetric member. Torsional buckling and flexural buckling are always uncoupled in simply-supported doubly-symmetric shapes, whereas they are always coupled in singly-symmetric members. One can show that torsional buckling never leads to any significant reduction in the axial resistance for all practical prismatic doubly-symmetric I-section members with $KL_z \leq KL_y$. Generally, P_{nTF}/P_{ny} (the ratio of the nominal column strengths using Eq. 4.3 versus Eq. 4.4d for calculation of F_e) is smaller for smaller h/b_f, larger b_f/t_f, larger h/t_w and larger QF_y. If one combines $h/b_f = 1$, $b_f/t_f = 38$, $h/t_w = 270$ and $QF_y = 65$ ksi as the worst-case limits, the smallest value of P_{nTF}/P_{ny} is obtained as 0.96 at $KL_y/r_y = 58.9$, assuming $KL_z = KL_y$. That is, torsional buckling leads to

a maximum reduction of only four percent in the nominal column resistance for all practical doubly-symmetric I-shapes. The accounting for end-restraint effects (if they are accounted for at all) in the calculation of the elastic buckling loads is not anywhere near this precise. Also, the ratio P_{nTF}/P_{ny} increases rapidly with increases in h/b_f. Therefore, torsional buckling of doubly-symmetric I-section members never needs to be considered, unless $KL_z > KL_y$.

For prismatic singly-symmetric members with $KL_z = KL_y$, γ_{eTF} is generally smaller than γ_{ey}. However, in metal building construction, the flanges of singly-symmetric I-sections often have equal widths and only the flange thicknesses differ. In this case, y_o tends to be relatively small and the influence of the smaller γ_{eTF} is always less than five percent as long as $0.67 \leq t_{f1}/t_{f2} \leq 1.5$.

For members with equal-width flanges, the largest reduction in the calculated strengths due to smaller γ_{eTF} occurs for $b_f/t_f = 31$, $h/b_f = 9$, $h/t_w = 270$, $QF_y = 65$ ksi, $KL_y/r_y = 136$ and $KL_z = KL_y$ ($b_f/t_f = 38$ gives $t_f/t_w < 1$ for the smaller flange given the above parameters). Therefore, if the above limit is satisfied, flexural-torsional buckling never needs to be considered for practical prismatic I-section members with equal-width flanges and $KL_z \leq KL_y$.

Interestingly, the reductions in the flexural-torsional buckling resistance for prismatic I-section members with unequal width flanges are significant in many practical cases even when there are rather small differences in the flange widths. This is because the lateral moment of inertia of the flanges varies with $(b_f)^3$, and hence only minor changes in the relative flange widths result in a significant shift in the cross-section shear center relative to its centroid. The shift in the cross-section centroid is somewhat similar

to the shift in the shear center due to changes in the flange thickness; however, the shift in the shear center is typically significantly different than the shift in the centroid due to changes in the flange width. Therefore, there does not appear to be any simple way to exclude the need to consider flexural-torsional buckling for all I-section members with unequal flange widths.

4.2.3 Recommended Procedures for Web-Tapered Members

For web-tapered I-section members with prismatic flanges, the essentially same guidelines described above are suggested for calculating torsional or flexural-torsional buckling loads. The recommended guidelines are as follows:

(1) Members with $K_zL \leq K_yL$ and doubly symmetric cross-sections: There is no need to consider torsional buckling in this case. The weak axis flexural buckling load of the member governs relative to the torsional buckling load for all practical member geometries. The weak axis flexural buckling load is calculated by the following equation.

$$P_{ey} = \frac{\pi^2 EI_y}{(K_y L)^2} \qquad \text{(Eq. 4.6)}$$

where I_y is the weak axis moment of inertia of the cross-section at the mid-span. The lengths K_yL and K_zL are defined as follows:

K_yL = effective length for flexural buckling about y-axis, typically taken in practice simply as the length between brace points that prevent lateral translation in the out-of-plane direction (K_y = 1.0).

K_zL = effective length for torsional buckling, typically taken simply as the length between the brace points where twisting of the cross-section is prevented.

(2) Members with $K_zL \leq K_yL$ and singly symmetric cross-sections with equal flange width and the ratio of flange thicknesses $0.67 \leq t_{f1}/t_{f2} \leq 1.5$: There is no need to consider

flexural-torsional buckling. The elastic flexural-torsional buckling resistance can be estimated by the weak axis flexural buckling equation (Eq. 4.6) without significant error.

(3) Members with $K_zL \leq K_yL$ and singly symmetric cross-sections with the flange thickness ratio violating the limit in (2) or with unequal flange width: The elastic TFB resistance can be calculated using Eqs 4.4 through 4.5 shown above.

It should be emphasized that for linearly tapered web-members, all the above recommended equations are used with the cross-section at the middle of the member unbraced length under consideration.

To evaluate the accuracy of the suggested guidelines, a total of 60 linearly-tapered simply-supported members are studied in this study. The details of the parametric study are discussed in Section 4.2.4 below. The parametric study shows that the errors in the suggested procedures are insignificant compared to the buckling solutions obtained from elastic eigenvalue buckling analysis using the open-section beam theory. Therefore, it can be concluded that the elastic TB and TFB estimates by the recommended procedures described above are sufficiently accurate for design application.

For more general nonprismatic members, the guidelines for calculating torsional or flexural-torsional buckling loads are unknown. For these members, it appears the use of advanced 3D buckling analysis software is inevitable for determining $\gamma_{eTF.}$

4.2.4 Evaluation of Recommended Procedures for Web-Tapered Members

4.2.4.1 Test Configuration and Parameter Selection

Table 4.1 shows the eight groups and the corresponding member dimensions for the selected test members. These test cases are originally selected for the parametric study conducted to investigate the elastic lateral torsional buckling of linearly-tapered

web members. For a detailed discussion of the targeted parameters and the selection of the groups, the reader is referred to Section 4.4.2.

The reasons why the members from the elastic LTB study are considered in the elastic torsional or flexural-torsional buckling study are as follows: (a) the selected test cases represent a wide range of the targeted design parameters and (b) they contain three types of cross-section geometries that need to be considered in assessing the elastic torsional and flexural-torsional buckling estimates. The three type of cross-section geometries are doubly-symmetric sections, singly-symmetric sections with $b_{fb}/b_{ft} = 1.0$ and $t_{fb}/t_{ft} = 1.5$, and singly-symmetric sections with $b_{fb}/b_{ft} = 1.5$ and $t_{fb}/t_{ft} = 1.0$ (the subscript t and b denote the top and bottom flange respectively). It should be noted that the top flange is always taken as the smaller flange in this study.

The groups shown in Table 4.1 are selected such that (a) the full ranges of all the targeted design parameters are considered, (b) the design parameter limits derived from consultation with MBMA research committee are satisfied, and (c) the test cases are representative of approximately 250 cases that are possible from a comprehensive variation of all the selected parameters. The limits on the design parameters are specified in Kaehler (2005) and are adopted in MBMA/AISC (2010) in most parts. These design parameter limits are as follows.

(1) $F_y \leq 55$ ksi.

(2) Homogeneous members only: $F_{yf} = F_{yw}$.

(3) Web taper angle $\beta \leq 15$ degrees.

(4) Thickness of each flange greater than or equal to the web thickness: $t_f \geq t_w$.

(5) Flange slenderness ration of $b_f/2t_f \leq 18$.

(6) Flange width $b_f \leq h/7$ throughout each unbraced length L_b. If $L_b \leq 1.1 r_t (E/F_y)^{0.5}$, where r_t is calculated using the largest section depth within the unbraced length, $b_f \leq h/9$ throughout the unbraced length. In Kaehler (2005), the flange width limit of $b_f \leq h/9$ throughout the unbraced length is allowed for all cases. In Chapter 7 of this dissertation, it is shown that the h/b_f values affect the lateral torsional buckling resistances of beams significantly. With $h/b_{fc} = 7$ at the deep end of linearly-tapered web members, the LTB resistances are reduced significantly.

(7) Web slenderness (without transverse stiffeners), $h/t_w \leq 0.42(E/F_y) \leq 260$.

It can be seen in Table 4.1 that each group (except groups II and V) has three cases varying the symmetry of the cross section: (a) a doubly-symmetric cross section, (b) a singly-symmetric cross section with equal flange width and $t_{fb}/t_{ft} = 1.5$, and (c) a singly-symmetric cross section case with $b_{fb}/b_{ft} = 1.5$ and equal flange thickness. In group II, there is no singly-symmetric cross-section case with $b_{fb}/b_{ft} = 1.0$ and $t_{fb}/t_{ft} = 1.5$ and in group V, a singly-symmetric cross-section case with $b_{fb}/b_{ft} = 1.5$ and $t_{fb}/t_{ft} = 1.0$ is not considered. This is because these cases violate the design parameter limits listed above.

Several additional cases are considered to study the accuracy of the estimates for critical elastic TB and TFB cases (i.e., cases where the TB and TFB estimates are smallest relative to the out-of-plane flexural buckling estimate). These additional cases are discussed subsequently.

Table 4.1. The cross-section dimensions at the mid-span of test members.

Group	Case	h (in)	t_w (in)	b_{fb} (in)	t_{fb} (in)	b_{ft} (in)	t_{ft} (in)	L_b (ft)	β (°)
I	1	30	0.30	15	1.25	15	1.25	14	10
	2	30	0.30	15	1.25	10	1.25	14	10
	3	30	0.30	15	1.25	15	0.83	14	10
II	4	30	0.23	7.5	0.31	7.5	0.31	9	15
	5	30	0.23	7.5	0.31	5	0.31	9	15
III	6	30	0.23	15	0.42	15	0.42	13	10
	7	30	0.23	15	0.42	10	0.42	14	10
	8	30	0.23	15	0.42	15	0.28	13	10
IV	9	30	0.23	7.5	0.31	7.5	0.31	18	5
	10	30	0.23	7.5	0.31	5	0.31	18	5
	11	30	0.23	15	0.63	15	0.42	35	5
V	12	30	0.23	5	0.42	5	0.42	8	15
	13	30	0.23	5	0.42	5	0.28	8	15
VI	14	30	0.23	5	0.42	5	0.42	6	10
	15	30	0.23	7.5	0.63	5	0.63	10	10
	16	30	0.23	5	0.42	5	0.28	6	10
VII	17	30	0.23	5	0.42	5	0.42	6	15
	18	30	0.23	7.5	0.63	5	0.63	10	15
	19	30	0.23	5	0.42	5	0.28	6	15
VIII	20	30	0.30	15	0.42	10	0.42	13	10
	21	30	0.23	7.5	0.31	5	0.31	6	10
	22	30	0.23	15	0.63	10	0.63	14	10

Figure 4.1 shows a typical configuration of a linearly tapered I-section member. It should be noted that when the cross-section is singly-symmetric the member centroidal axis is slightly curved. In the current study, the end displacements v and w and the cross-section twist ϕ are constrained at the cross-section centroid at each of the member ends. The degree of freedom u is taken along a straight axis through the cross-section centroids at the member ends. The degree of freedom w is in the direction perpendicular to the plane of the page. The direction of the degree of freedom v is defined using the right hand rule given the directions for u and w. Each member is subject to a constant axial load along their length.

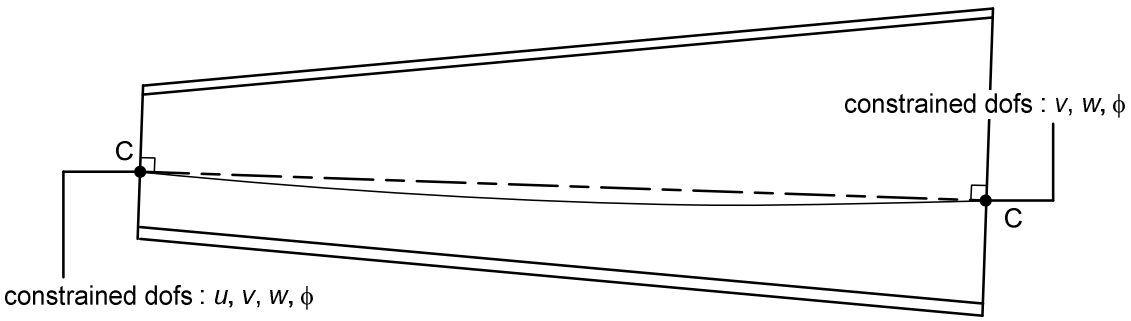

Figure 4.1. Configuration of a typical test member

4.2.4.2. Comparisons between Elastic Eigenvalue Analysis Results and the Recommended Procedures

For the buckling analysis of the selected test cases, the finite element analysis program GT-Sabre (Chang 2006) is used with an open-section thin-walled beam element having 14 degrees of freedom. Each member is modeled with eight elements and the end boundary conditions are applied at the locations illustrated in Figure 4.1. An eigenvalue buckling analysis is performed to determine the buckling load of each member. In this section, the results from the eigenvalue buckling analysis are compared with the elastic torsional and flexural-torsional buckling estimates are obtained as described in the Section 4.2.3.

4.2.4.2.1. $K_zL = K_yL$: Doubly-symmetric cross-section cases

As discussed above, the reduction due to the consideration of torsional buckling (TB) is not significant for all practical prismatic doubly-symmetric I-section members with $K_zL \leq K_yL$. The maximum reduction is 4 % when $h/b_f = 1$, $h/t_w = 270$, $b_f/2t_f = 19$ and $F_y = 65$ ksi. The value of K_yL/r_y is 58.9 assuming $K_zL = K_yL$ for this critical case. It should be noted that a case with $K_zL = K_yL$ is the most critical case of $K_zL \leq K_yL$. Based on the limits for the cross-section geometry in MBMA/AISC (2010) this worst case

becomes a prismatic member with $h/b_f = 1$, $h/t_w = 260$, $b_f/2t_f = 18$ and $QF_y = 55$ ksi. For these combined parameters, P_{nTF}/P_{ny} is 0.96 when $K_yL/r_y = 60.0$ where P_{nTF} is the nominal axial strength based on the torsional or flexural-torsional buckling of the member and P_{ny} is the nominal axial strength based on the weak axis flexural buckling.

Three linearly tapered members are developed based on the above prismatic case ($h/b_f = 1$, $h/t_w = 260$, $b_f/2t_f = 18$, $QF_y = 55$ ksi and $K_yL/r_y = 60.0$). The cross-section dimensions at the mid-span of these members are shown in Table 4.2. Table 4.3 shows values of P_{nTF}/P_{ny} calculated for three linearly tapered members developed based on the above prismatic case. It should be noted that the maximum limit of $h/t_w = 260$ from Kaehler (2005) is applied at the largest end and the smallest value of h/b_f equal to 1.0 from Kaehler (2005) is applied at the smallest end in defining the most critical practical member dimensions. With a slight taper angle ($\beta = 1°$), the ratio of P_{nTF}/P_{ny} is 0.98, which is larger than the corresponding prismatic case. Larger taper angles result in larger P_{nTF}/P_{ny} such that the weak axis flexural buckling load closely predicts the TB resistance of the member (see Table 4.3). Based on these results, one can conclude that the torsional buckling resistance does not need to be considered at all for either constant depth or linearly-tapered doubly-symmetric I-section members.

Table 4.2. The cross-section dimensions at the mid-span for test cases A through C

Case	h (in)	t_w (in)	b_{fb} (in)	t_{fb} (in)	b_{ft} (in)	t_{ft} (in)	L_b (ft)	β (°)
A	30	0.13	27	0.74	27	0.74	33	1
B	30	0.16	18	0.50	18	0.50	23	5
C	30	0.21	14	0.38	14	0.38	16	10

Table 4.3. The ratio of P_{nTF}/P_{ny} for the worst cases of linearly-tapered doubly-symmetric I-section members

Case	β (°)	h/t_w	$b_{fb}/2t_{fb}$	h/b_{fb}	b_{fb}/b_{ft}	t_{fb}/t_{ft}	$K_y L/r_y$	P_{nTF}/P_{ny}
A	1	233	18	1.1	1	1	54	0.98
B	5	185	18	1.7	1	1	60	1.03
C	10	145	18	2.2	1	1	60	1.07

Table 4.4 shows the elastic out-of-plane flexural buckling estimates based on the suggestion (1) in Section 4.2.3 (i.e, torsional buckling is assumed to never govern) and the solutions from the finite element analysis done by GT-Sabre. The results are shown in terms of the ratio of the elastic buckling strength to the applied load. The last four columns of Table 4.4 are: (1) the elastic weak axis flexural strength from Eqs. 4.1 and 4.2 (shown as $\gamma_{ey\text{-}mid}$), (2) the buckling analysis results using GT-Sabre (shown as γ_{eFEA}), (3) the ratio of the buckling analysis results from GT-Sabre to the weak axis flexural strength of the member ($\gamma_{eFEA}/\gamma_{ey\text{-}mid}$), and (4) the error in the elastic weak axis flexural buckling estimates versus the FEA results. For the calculation of the γ_{eFEA} values, a reference axial force equal to the yield load of the cross-section at the shallow end of the members, P_{yo}, is applied (this approach is applied also for all the subsequent γ_e calculations) in the GT-Sabre analysis. This yield load P_{yo} is calculated based on the yield strength F_y = 55 ksi.

In Table 4.4, the maximum values of the error are highlighted. Positive error means that the test member has less capacity than the elastic weak axis flexural strength obtained from Eq. 4.1. The maximum unconservative error in the elastic weak-axis flexural buckling resistance is 7.8 % (see case A in Table 4.4). However as seen in Table 4.3, P_{nTF}/P_{ny} is 0.98 in case A so the error of neglecting the elastic TB strength does not affect the nominal axial strength of the member significantly. That is, the unconservative

error of 7.8 % reported for case A in Table 4.4 corresponds to the *elastic* buckling solutions, while the actual member design strength is based on *inelastic* buckling. Therefore, the maximum unconservative error in the design resistance is actually only about 2 %. The maximum conservative error is obtained for case 12 in Table 4.4. In this case $\gamma_{ey\text{-}mid}$ is 0.9 % smaller than the elastic buckling strength obtained by finite element analysis. In most cases the error is not significant. The mean value of $\gamma_{eFEA}/\gamma_{ey\text{-}mid}$ is 0.99. The value of the standard deviation is 0.02 and the coefficient of variation is 2 %.

Table 4.4. Results from FEA and the elastic weak axis flexural buckling estimates $P_{ey\text{-}mid}$ for linearly-tapered doubly-symmetric I-section members.

Case	β (°)	h/t_w	$b_{fb}/2t_{fb}$	h/b_{fb}	b_{fb}/b_{ft}	t_{fb}/t_{ft}	(1)$\gamma_{ey\text{-}mid}$	(2)γ_{eFEA}	(3)$\gamma_{eFEA}/\gamma_{ey\text{-}mid}$	(4) Error
A	1	233	18	1.1	1	1	1.78	1.65	0.93	7.8%
B	5	185	18	1.7	1	1	1.82	1.83	1.00	-0.4%
C	10	145	18	2.2	1	1	1.58	1.58	1.00	0.1%
1	10	100	6	2	1	1	3.00	2.98	0.99	0.5%
4	15	130	12	4	1	1	1.20	1.19	0.99	0.9%
6	10	130	18	2	1	1	2.93	2.94	1.00	-0.3%
9	5	130	12	4	1	1	0.26	0.26	0.99	1.0%
12	15	130	6	6	1	1	0.63	0.64	1.01	-0.9%
14	10	130	6	6	1	1	0.95	0.96	1.01	-0.7%
17	15	130	6	6	1	1	1.03	1.04	1.01	-0.7%

4.2.4.2.2. $K_zL = K_yL$: Singly symmetric cases with equal flange width and $t_{fb}/t_{ft} = 1.5$

It is discussed above that the reduction in the nominal axial strength of prismatic singly-symmetric members due to the consideration of torsional flexural buckling is not significant if the members satisfy certain limits. The limits are (a) the flange widths of the singly-symmetric cross-section are equal and (b) the value of the ratio of the larger flange thickness to the smaller flange thickness, t_{f1}/t_{f2} is less than or equal to 1.5. In the current study, cases with $t_{fb}/t_{ft} = 1.5$ are considered since this is the worst case that satisfies the limit (b). For prismatic singly-symmetric I-section members with equal

flange width and $t_{fb}/t_{ft} = 1.5$, the worst case is a member with $h/b_f = 9$, $h/t_w = 270$, $b_f/2t_f = 15.5$, $QF_y = 65$ ksi and $K_yL/r_y = 136$. Table 4.5 shows the cross-section dimensions for several linearly-tapered singly-symmetric members developed based on the above prismatic singly-symmetric case (cases D through F). The ratio of P_{nTF}/P_{ny} for each case is shown in Table 4.6. In cases D through F, the web slenderness h/t_w of the cross-section

Table 4.5. The cross-section dimensions at the mid-span for test cases D through F

Case	h (in)	t_w (in)	b_{fb} (in)	t_{fb} (in)	b_{ft} (in)	t_{ft} (in)	L_b (ft)	β (°)
D	30	0.13	4.3	0.27	4.3	0.18	7	5
E	30	0.14	4.3	0.27	4.3	0.18	6	10
F	30	0.16	4.6	0.29	4.6	0.19	7	15

Table 4.6. The ratio of P_{nTF}/P_{ny} for the worst cases of linearly-tapered singly-symmetric I-section members with $b_{fb}/b_{ft} = 1.0$ and $t_{fb}/t_{ft} = 1.5$

Case	β (°)	h/t_w	$b_{fb}/2t_{fb}$	h/b_{fb}	b_{fb}/b_{ft}	t_{fb}/t_{ft}	$K_y L/r_y$	P_{nTF}/P_{ny}
D	5	233	8	7	1	1.5	113	0.96
E	10	214	8	7	1	1.5	107	0.96
F	15	188	8	6.5	1	1.5	114	0.96

at the mid-length is determined such that h/t_w at the largest end is equal to 260, the maximum limit for h/t_w in Kaehler (2005). The values of h/b_{fb} in cases D and E equal to 7 at mid-span are based on the maximum limit specified by Kaehler (2005). In case F, the value of h/b_{fb} at the mid-span of 6.53 gives $h/b_{fb} = 9.0$ at the largest end (the maximum limit for h/b_{fb} at the largest end based on Kaehler (2005)). At the time of this parametric study, the limits on the cross-section parameters are based on Kaehler (2005). In MBMA/AISC (2010), the maximum limit of $h/b_f = 7$ is recommended at the largest end in general. The larger limit of $h/b_f = 9$ is permitted only for beams with $L_b \leq$

$1.1r_t(E/F_y)^{0.5}$ where r_t is calculated using the largest section depth of the given members. Chapter 7 shows that the value of h/b_f affects the lateral torsional buckling resistances significantly, especially if $h/b_{fc} > 4$.

For all three cases shown in Table 4.6, the value of P_{nTF}/P_{ny} is obtained as 0.96. This indicates that the elastic torsional flexural buckling does not need to be considered for linearly-tapered singly-symmetric I-section members with equal flange width and $t_{fb}/t_{ft} = 1.5$. The maximum unconservative error in the strength prediction is limited to approximately 4 %.

The comparisons of the elastic weak axis flexural buckling estimates $\gamma_{ey\text{-}mid}$ to the buckling solutions from finite element analysis are shown in Table 4.7. Generally the weak axis flexural buckling load ratio $\gamma_{ey\text{-}mid}$ is a few percent larger than the buckling solution from the finite element analysis. The maximum unconservative error is 3.7 % (see case F). The mean of $\gamma_{eFEA}/\gamma_{ey\text{-}mid}$ is 0.97 and the standard deviation is 0.01. The coefficient of variation is 1 %.

Table 4.7. Results from FEA and the elastic weak axis flexural buckling estimates $P_{ey\text{-}mid}$ for linearly-tapered singly-symmetric I-section members with $b_{fb}/b_{ft} = 1.0$ and $t_{fb}/t_{ft} = 1.5$.

Case	β (°)	h/t_w	$b_{fb}/2t_{fb}$	h/b_{fb}	b_{fb}/b_{ft}	t_{fb}/t_{ft}	(1)$\gamma_{ey\text{-}mid}$	(2)γ_{eFEA}	(3)$\gamma_{eFEA}/\gamma_{ey\text{-}mid}$	(4) Error
D	5	233	8	7	1	1.5	0.45	0.43	0.97	3.3%
E	10	214	8	7	1	1.5	0.54	0.52	0.97	3.2%
F	15	188	8	6.5	1	1.5	0.54	0.52	0.96	3.7%
3	10	100	6	2	1	1.5	2.92	2.87	0.98	2.0%
8	10	130	18	2	1	1.5	2.76	2.69	0.97	2.9%
11	5	130	12	2	1	1.5	0.48	0.48	0.99	0.8%
13	15	130	6	6	1	1.5	0.56	0.55	0.97	3.3%
16	10	130	6	6	1	1.5	0.84	0.81	0.97	3.3%
19	15	130	6	6	1	1.5	0.91	0.88	0.97	3.4%

4.2.4.2.3.. $K_zL = K_yL$: Singly symmetric cases with equal flange thickness and b_{fb}/b_{ft} = 1.5

For prismatic singly-symmetric members that have equal flange thickness and different flange width, the reduction in the axial strength due to flexural-torsional buckling is significant even the difference in the flange width is small. This is because the shear center location is moved significantly relative to the change of the centroid location when a cross-section has different flange widths. In this section, the ratio of the flange widths is taken equal to 1.5 since b_{fb}/b_{ft} = 1.5 is a practical maximum limit for this ratio. One can show that when h/b_f = 4, h/t_w = 260, $b_f/2t_f$ = 18, QF_y = 55 ksi and K_yL/r_y = 121, a prismatic singly-symmetric member with equal flange thickness and b_{fb}/b_{ft} = 1.5 has a value of P_{nTF}/P_{ny} equal to 0.62. Cases G and H are generated based on this prismatic member (Table 4.8). If one combines h/t_w = 260, $b_{fb}/2t_{fb}$ = 18, b_{fb}/b_{ft} = 1.5 and β = 15°, then the value of h/b_{ft} at the largest end exceeds the maximum limit of h/b_f = 9. Therefore this case is not considered. In cases G and H, the values of P_{nTF}/P_{ny} equal to 0.62 and 0.65 are obtained respectively (see Table 4.9).

Table 4.8. The cross-section dimensions at mid-span of test cases G and H

Case	h (in)	t_w (in)	b_{fb} (in)	t_{fb} (in)	b_{ft} (in)	t_{ft} (in)	L_b (ft)	β (°)
G	30	0.15	10	0.28	6.7	0.28	16	5
H	30	0.18	7.5	0.21	5.0	0.21	16	10

Table 4.9. The ratio of P_{nTF}/P_{ny} for the worst cases of linearly-tapered singly-symmetric I-section members with b_{fb}/b_{ft} = 1.5 and t_{fb}/t_{ft} = 1.0

Case	β (°)	h/t_w	$b_{fb}/2t_{fb}$	h/b_{fb}	b_{fb}/b_{ft}	t_{fb}/t_{ft}	K_yL/r_y	P_{nTF}/P_{ny}
G	5	202	18	3	1.5	1	108	0.62
H	10	165	18	4	1.5	1	181	0.65

In this case, it is suggested that the elastic flexural-torsional buckling strength of linearly tapered members can be estimated using the AISC (2010) TFB equations with the cross-section at mid-span. Table 4.10 shows the results from the elastic TFB calculated using the AISC (2010) TFB equations and the cross-section at mid-span and the results from the buckling analysis using GT-Sabre. The last four columns of Table 4.10 are: (1) the elastic flexural-torsional buckling strength from Eqs. 4.4 and 4.5 (shown as γ_{eAISC}), (2) the buckling analysis results using GT-Sabre (shown as γ_{eFEA}), (3) the ratio of the buckling analysis results from GT-Sabre to the elastic flexural-torsional buckling strength of the member based on AISC (2010) ($\gamma_{eFEA}/\gamma_{eAISC}$), and (4) the error in the elastic flexural-torsional buckling estimates using AISC (2010) versus the FEA results. The maximum conservative error of the elastic TFB estimates based on the AISC (2010) equation is 1.5 % (see case 18). Cases 10 and 21 give a maximum unconservative error of 1.3 %. The mean value of $\gamma_{eFEA}/\gamma_{eAISC}$ is 1.00. The standard deviation is 0.01 and the coefficient of variation is 1 %.

Table 4.10. Results from FEA and the elastic TFB estimates using the AISC (2010) TFB equation for linearly-tapered singly-symmetric I-section members with b_{fb}/b_{ft} = 1.5 and t_{fb}/t_{ft} = 1.0.

Case	β (°)	h/t_w	$b_{fb}/2t_{fb}$	h/b_{fb}	b_{fb}/b_{ft}	t_{fb}/t_{ft}	(1) γ_{eAISC}	(2) γ_{eFEA}	(3)$\gamma_{eFEA}/\gamma_{eAISC}$	(4) Error
G	5	202	18	3	1.5	1	0.32	0.33	1.01	-0.8%
H	10	165	18	4	1.5	1	0.17	0.17	1.00	-0.3%
2	10	100	6	2	1.5	1	1.49	1.51	1.01	-1.1%
5	15	130	12	4	1.5	1	0.53	0.53	0.99	1.0%
7	10	130	18	2	1.5	1	1.29	1.29	1.00	0.1%
10	5	130	12	4	1.5	1	0.12	0.12	0.99	1.3%
15	10	130	6	4	1.5	1	0.55	0.56	1.01	-0.8%
18	15	130	6	4	1.5	1	0.61	0.62	1.02	-1.5%
20	10	100	18	2	1.5	1	1.26	1.26	1.00	0.1%
21	10	130	12	4	1.5	1	0.94	0.93	0.99	1.3%
22	10	130	12	2	1.5	1	1.35	1.36	1.00	-0.4%

4.3 Constrained-Axis Torsional Buckling

4.3.1 Recommended Procedures

A common practice in metal building frames is that the outside flange is braced at each girt or purlin; however, the inside flange may be braced at a wider spacing, by extending a diagonal brace only from certain girts or purlins to the flange. In this situation, it is generally unconservative and unsafe to assume that the member can develop an axial resistance based on weak-axis flexural buckling assuming that the purlins or girts are braced points. Rather, the member axial resistance may be calculated based on torsional buckling about an effective axis located at the centroidal depth of the girts or purlins using a torsional buckling unbraced length KL_z equal to the distance between the locations where diagonal braces are provided to the inside flange and the cross-section is effectively prevented from twisting. The calculations for this case are summarized below. Equations 4.3 and 4.4 are not applicable for this problem since the twisting of the member is effectively constrained to occur about an axis other than the shear center.

For the cases where the outside flange is braced out-of-plane by the purlins or girts at a shorter length, $L_{b.outside}$ while the inside flange is braced out-of-plane at a longer length, $L_{b.inside}$, the following equation (Eq. 4.7) is suggested to calculate the constrained-axis torsional buckling of the member under the consideration. This equation is provided by Timoshenko and Gere (1961) for singly-symmetric prismatic member configurations such as that illustrated in Figure 4.2:

$$P_{eTF} = \frac{\left(EC_w + EI_y a_s^{\,2}\right)\left(\pi / L_{b.inside}\right)^2 + GJ}{r_x^{\,2} + r_y^{\,2} + a_c^{\,2}} \qquad \text{(Eq. 4.7)}$$

where a_s and a_c are the distances from the cross-section shear center and the cross-section centroid to the brace point respectively. The length $L_{b.inside}$ in Eq. 4.7 is the distance between the points at which the cross-section is prevented from twisting, i.e., $L_{b.inside} = K_z L$. It is suggested that Eq. 4.7 should be used with the cross-section properties at the middle of the length $L_{b.inside}$ under consideration for calculating the constrained axis torsional buckling load. The evaluation of this recommendation is discussed in the next section. The parametric study shows that the constrained-axis torsional buckling estimates by the recommended procedure are sufficiently accurate for design application.

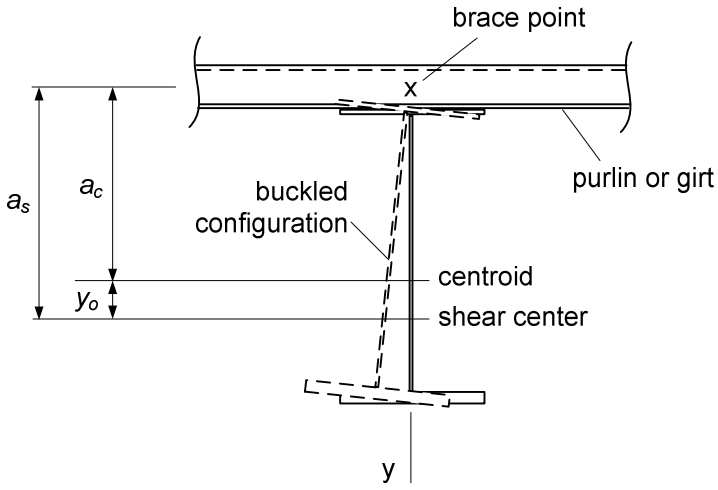

Figure 4.2. Dimensions for calculation of flexural-torsional buckling about the axis of the purlins or girts.

4.3.2 Evaluation of Recommended Procedures

4.3.2.1 Test Configutation

To evaluate the use of the recommended equations for the elastic constrained-axis torsional buckling load of the linearly-tapered web members, a parametric study is conducted. The same test members selected for the study of the elastic torsional or

flexural-torsional buckling are used for this study as well (see Table 4.1). For all the test members, the total length of the members is set to $L_{b.inside} = K_z L$ in this study. That is, twisting is prevented at the test member ends. Also, the test member out-of-plane displacements are assumed to be prevented by a purlin (or a girt) attached to the top (outside) flange at the member mid-length. That is, $L_{b.outside} = K_y L = L_{b.inside}/2$. These boundary conditions cause the out-of-plane buckling mode to be a torsional buckling about the constrained axis at the centerline of the purlin depth.

Figure 4.3 shows a typical configuration of a linearly tapered I-section member. The boundary conditions at the ends of the test configuration are the same as discussed in Section 4.2.4.1. To consider constrained axis elastic TB, an 8 inch deep purlin (or girt) is assumed to be attached to the top flange at the mid-length of the member, i.e., the degrees of freedom v and w are constrained at the centroidal depth of the purlin located at the member mid-length. In these cases, the reported length L_b in Table 4.1 is the length $L_{b.inside}$. Each member is subject to a constant axial load along their length.

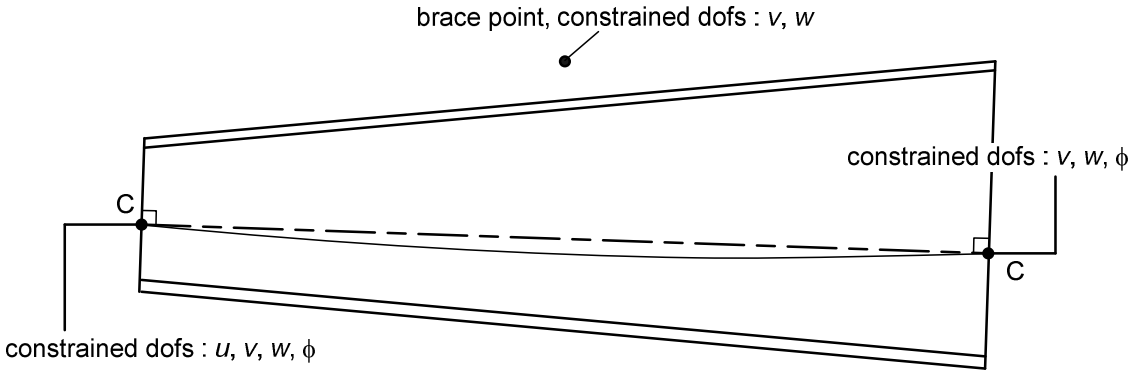

Figure 4.3. Configuration of a typical test member

4.3.2.2. Comparisons between Elastic Eigenvalue Analysis Results and the Recommended Procedures

The eigenvalue buckling analysis of the selected test members is conducted using GT-Sabre as described in Sectoin 2.3. Table 4.11 shows the results from the calculation based on Eq. 4.7 and the GT-Sabre buckling solutions (the results from Eq. 4.7 are denoted by γ_{eCAB}). Group "DS" denotes the prior doubly-symmetric cross-section cases, "SS-1" denotes the singly-symmetric cross-section cases with equal flange width, and "SS-2" indicates the singly-symmetric cross-section cases with equal flange thickness. The maximum unconservative error is 4.0 % in case B. Case 11 gives the maximum conservative error of 2.8 %. Case 11 has a singly-symmetric case with equal flange width and $t_{fb}/t_{ft} = 1.5$. The mean value of $\gamma_{eCAB}/\gamma_{eFEA}$ is 1.00 and the standard deviation is 0.01. The coefficient of variation is 1 %. Figure 4.4 shows the typical buckling mode shape of a linearly-tapered member with the out-of-plane displacements constrained at the purlin mid-depth location.

4.4 Lateral Torsional Buckling

4.4.1 Recommended Procedures

For calculation of the elastic lateral torsional buckling resistance of linearly tapered I-section members, the following procedures are recommended.

(1) Determine the moment diagram for the unbraced length under consideration.

(2) Calculate the compression flange stresses along the unbraced length given the above moments and the elastic section modulus at each cross-section, i.e., $f = M/S_{xc}$.

(3) Calculate C_b using the equations in AASHTO (2007). For tapered members, the factor C_b accounts for the nonuniform distribution of the flange stresses rather than the moments along the unbraced length. Therefore, the factor C_b is called a *stress-gradient*

Table 4.11. Results from finite element analysis and the elastic torsional and flexural-torsional buckling estimates based on the Timoshenko and Gere (1961) TB equation.

Group	Case	β (°)	h/t_w	$b_{fb}/2t_{fb}$	h/b_{fb}	b_{fb}/b_{ft}	t_{fb}/t_{ft}	(1) γ_{eCAB}	(2) γ_{eFEA}	(3)$\gamma_{eFEA}/\gamma_{eCAB}$	(4) Error
DS	A	1	233	18	1.1	1	1	1.73	1.73	1.00	-0.2%
	B	5	185	18	1.7	1	1	1.64	1.58	0.96	4.0%
	C	10	145	18	2.2	1	1	2.00	2.00	1.00	-0.2%
SS-1	D	5	233	8	7	1	1.5	0.60	0.61	1.01	-0.8%
	E	10	214	8	7	1	1.5	0.73	0.74	1.01	-0.9%
	F	15	188	8	6.5	1	1.5	0.74	0.74	1.01	-0.8%
SS-2	G	5	202	18	3	1.5	1	0.82	0.83	1.01	-0.7%
	H	10	165	18	4	1.5	1	0.46	0.46	1.01	-0.9%
I	1	10	100	6	2	1	1	3.22	3.20	0.99	0.9%
	2	10	100	6	2	1.5	1	3.23	3.25	1.01	-0.7%
	3	10	100	6	2	1	1.5	3.23	3.24	1.00	-0.3%
II	4	15	130	12	4	1	1	1.42	1.41	0.99	0.9%
	5	15	130	12	4	1.5	1	1.43	1.42	0.99	0.8%
III	6	10	130	18	2	1	1	3.17	3.18	1.00	-0.2%
	7	10	130	18	2	1.5	1	3.20	3.22	1.01	-0.7%
	8	10	130	18	2	1	1.5	3.21	3.23	1.00	-0.5%
IV	9	5	130	12	4	1	1	0.32	0.32	0.99	0.8%
	10	5	130	12	4	1.5	1	0.32	0.31	0.99	1.1%
	11	5	130	12	2	1	1.5	0.56	0.58	1.03	-2.8%
V	12	15	130	6	6	1	1	0.77	0.77	1.01	-0.8%
	13	15	130	6	6	1	1.5	0.77	0.77	1.01	-0.9%
VI	14	10	130	6	6	1	1	1.14	1.15	1.01	-0.6%
	15	10	130	6	4	1.5	1	1.34	1.35	1.01	-0.9%
	16	10	130	6	6	1	1.5	1.13	1.14	1.01	-0.5%
VII	17	15	130	6	6	1	1	1.24	1.25	1.01	-0.6%
	18	15	130	6	4	1.5	1	1.50	1.52	1.02	-1.7%
	19	15	130	6	6	1	1.5	1.23	1.24	1.01	-0.5%
VIII	20	10	100	18	2	1.5	1	3.18	3.19	1.01	-0.5%
	21	10	130	12	4	1.5	1	2.56	2.53	0.99	1.3%
	22	10	130	12	2	1.5	1	3.21	3.24	1.01	-0.9%

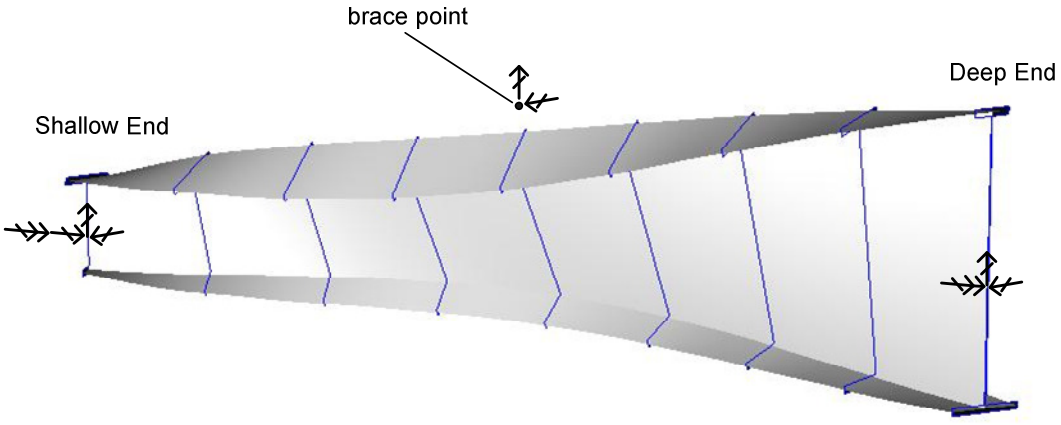

Figure 4.4. Representative torsional buckling mode shape for a linearly tapered member with a constrained axis on the top flange (snapshot from GT-Sabre (Chang 2006)).

factor in this study. AASHTO (2007) specifies the calculation of C_b as follows:

$$C_b = 1.0 \qquad \text{(Eq. 4.8, AASHTO 6.10.8.2.3-6)}$$

for members where $f_{mid}/f_2 \geq 1$ or $f_2 = 0$, and

$$C_b = 1.75 - 1.05\frac{f_1}{f_2} + 0.3\left(\frac{f_1}{f_2}\right)^2 \leq 2.3 \qquad \text{(Eq. 4.9, AASHTO 6.10.8.2.3-7)}$$

for all other common situations, where:

f_2 = absolute value of the largest compressive flange stress at either end of the unbraced length of the flange under consideration. If the stress is zero or tensile in the flange under consideration at both ends of the unbraced length, f_2 is taken equal to zero.

f_{mid} = flange stress at the middle of the unbraced length of the flange under consideration, taken as positive in compression and negative in tension.

$$f_1 = f_0 \qquad \text{(Eq. 4.10, AASHTO 6.10.8.2.3-10)}$$

when the variation in the flange stress between the brace points is concave in shape, and otherwise

$$f_1 = 2f_{mid} - f_2 \geq f_0 \qquad \text{(Eq. 4.11, AASHTO 6.10.8.2.3-11)}$$

f_0 = flange stress at the brace point opposite to the one corresponding to f_2, taken as positive in compression and negative in tension.

Figure 4.5 from Chapter 6 of the NSBA Steel Bridge Design Handbook (White 2006) shows several sample cases of the application of the AASHTO C_b equations. The first two cases have a "concave" flange stress envelope (i.e., the absolute value of f_{mid} is less than the absolute value of the average of f_2 and f_0). In these cases, f_1 is simply taken equal to f_0 as shown by Eq. 4.10. In the other two cases, the flange stress envelope is "convex" and f_1 is calculated from Eq. 4.11.

(4) Determine the elastic buckling stress corresponding to the cross-section having the largest applied flange stress (or the largest ratio of the applied moment to the yield moment) along the unbraced length as

$$F_{eLTB} = C_b M_{e.mid} / S_{xc.mid} \qquad \text{(Eq. 4.12)}$$

where $M_{e.mid}$ is calculated from the AISC (2010) elastic LTB equation for a prismatic member using the properties at the mid-span of the unbraced length, and $S_{xc.mid}$ is the elastic section modulus at the mid-span.

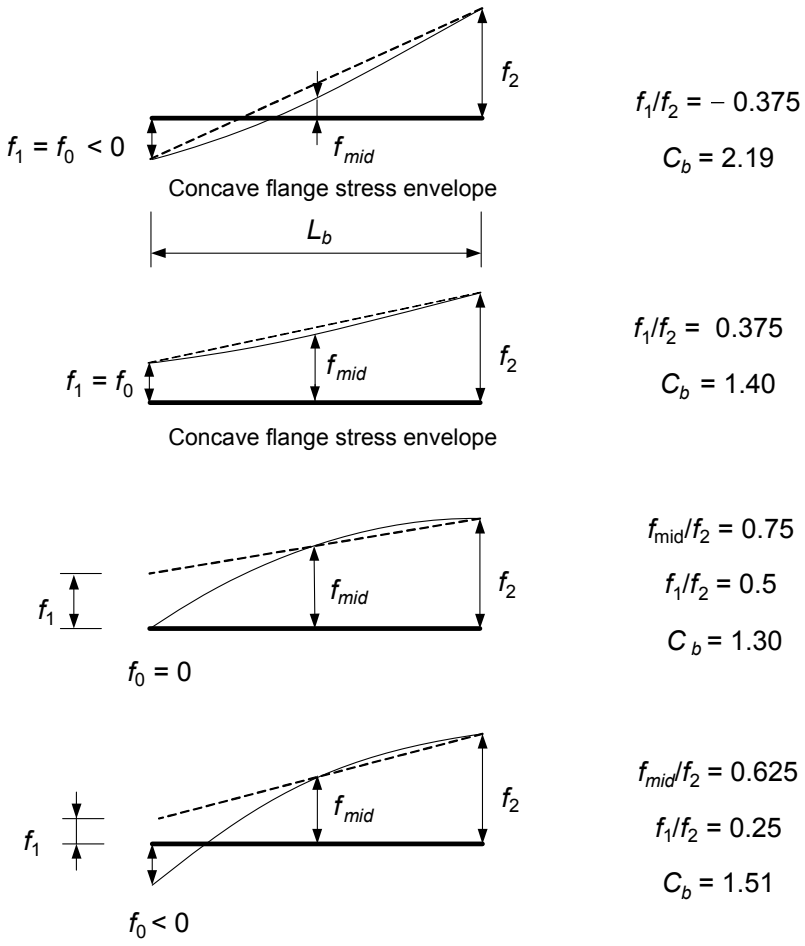

Figure 4.5. Sample cases for calculation of the AASHTO (2007) moment gradient modifier (Ch.6, Steel Bridge Design Handbook)

For reverse curvature bending cases, it is necessary to consider both flanges separately. For example, the buckling stress of the top flange is calculated using the cross-section at the mid-span and taking the top flange as the compression flange. The stress-gradient factor, C_b of the top flange is calculated using the flange stresses $f_{a(top)}$, $f_{b(top)}$, $f_{c(top)}$ and $f_{max(top)}$ in this flange. The elastic LTB estimate of the top flange buckling load ratio, $\gamma_{eLTB(top)}$ is

$$\gamma_{eYH(top)} = C_{b(top)} F_{e(top)} / f_{max(top)} \quad \text{(Eq. 4.13)}$$

where $f_{max(top)}$ is the maximum compressive stress in the top flange. The same procedure is repeated for the bottom flange to obtain $\gamma_{eLTB(bottom)}$. Given these two γ_{eLTB} values, the elastic LTB load ratio of the linearly-tapered web members under consideration is

$$\gamma_{eLTB} = \min(\gamma_{eLTB(top)}, \gamma_{eLTB(bottom)}) \quad \text{(Eq. 4.14)}$$

The recommended procedures for the elastic LTB load ratio of linearly-tapered web members are based on the procedures suggested by Yura and Helwig (1996). The main difference between these two procedures is the calculation of the C_b factor. Yura and Helwig (1996) suggest to use AISC (2005) equation, which is the same as the AISC (2010) equation, but with the compression flange stresses in place of the corresponding moment values. This modified equation is

$$C_b = \frac{12.5 f_{\max}}{3f_a + 4f_b + 3f_c + 2.5 f_{\max}} \leq 3.0 \quad \text{(Eq. 4.15)}$$

where f_{max} is the absolute value of the maximum flange stress, f_a and f_c are the absolute values of the flange stress at quarter point and three-quarter point of the unbraced length, and f_b is the absolute value of the flange stress at the mid-span of the unbraced length. The parametric study conducted in this research shows that the recommended procedures

using the AASHTO (2007) equations (Eqs. 4.8 to 4.11) provide better estimates for the elastic LTB load ratio than the Yura and Helwig (1996) procedures. The details of the test configurations and parameters and the results from the parametric study are discussed in the next sections. The first part of the parametric study focuses on evaluating the accuracy of the Yura and Helwig (1996) approach. The second part of the parametric study shows the better accuracy of the recommended procedures for calculating the elastic LTB load ratios for the linearly-tapered web members.

4.4.2 Evaluation of Recommended Procedures

4.4.2.1 Test Configuration and Parameter Selection

The test members for the parametric study are selected by varying several key nondimensional design parameters. The key nondimensional design parameters are based on the cross-section at the mid-span of members. A clear web depth, h equal to 30 inches is selected at the mid-span to establish the physical dimensions for all the members. The nondimensional design parameters are as follows:

(1) Taper angle β. Values of β equal to 5, 10 and 15 degrees are selected. The value β = 15 degrees is the suggested maximum taper angle for linearly tapered members as shown in Section 4.2.4.1. According to Lee et al. (1972), beam theory is applicable as long as the taper angle is less than 15 degrees.

(2) Web slenderness ratio h/t_w. Values of the web slenderness ratio equal to 100 and 130 are selected such that the cross-section at mid-span is noncompact (in the first case) and slender (in the second case). In all cases, the web slenderness ratio h/t_w at the larger end is restricted to be less than the maximum limit of $h/t_w = 260$ (see Section 4.2.4.1).

(3) Compression flange slenderness ratio $b_{fc}/2t_{fc}$. Values of $b_{fc}/2t_{fc}$ equal to 6, 12 and 18 are selected as representative values. The ratio $b_f/2t_f = 18$ is the maximum limit of the flange slenderness in MBMA/AISC (2010).

(4) Section aspect ratio h/b_{fc}. Values of h/b_{fc} from 2 to 6 are selected. These values satisfy the maximum limit of $h/b_{fc} = 7$ at mid-span suggested by Kaehler (2005). The members considered in the initial variation of the design parameters and the selection of the first five test groups satisfy the limit $h/b_f \leq 9$ at their deeper end suggested by Kaehler (2005). This limit is violated in one of the subsequent additional member groups. As mentioned in Section 4.2.4.1, the limit of h/b_{fc} at the largest end of the web-tapered members is $h/b_{fc} \leq 7$ based on MBMA/AISC (2010).

(5) Flange width ratio b_{fc}/b_{ft}, where b_{ft} is the width of the tension flange. Values of b_{fc}/b_{ft} equal to 1.0 and 1.5 are selected.

(6) Flange thickness ratio t_{fc}/t_{ft}, where t_{ft} is the flange thickness of the tension flange. Similar to the flange width ratios, values of t_{fc}/t_{ft} equal to 1.0 and 1.5 are selected in the current study. Values of t_{fc}/t_{ft} less than 1.0 are not considered as a practical option in metal building frames.

(7) Lateral torsional buckling slenderness, L_b/r_t. The values of L_b/r_t are varied from 40 to 120 in increments of 20.

It should be noted that the top flange is taken as the primary flange in compression in all the cases shown in this section. That is, $M = M_y$ is applied at the deeper end of the member, causing compression in the top flange, in all cases. Therefore all the selected compression flange parameters in the above are based on the top flange. For example, the parameter (3) is applied for the top flange and the parameter (5) is the ratio of the top

flange width to the bottom flange width. After generating all possible test configurations from the cross-section nondimensional parameters listed above, cases that violate the parameter limits discussed above are eliminated. The reasons for the elimination of these cases are: 1) the web slenderness ratio, h/t_w at the smallest section is less than 40, 2) the flange thickness is smaller than the web thickness or 3) the maximum limit of the section aspect ratio, h/b_{fc} at the larger end is exceeded. Approximately 250 cases remain after this process is complete. Rather than study all 250 of these cases in a brute force fashion, five groups of test configurations are selected from this larger number of tests. For each group, three cases are considered: 1) A doubly-symmetric section, 2) A singly-symmetric section with $b_{fc}/b_{ft} = 1.5$ and $t_{fc}/t_{ft} = 1.0$ and 3) A singly-symmetric section with $b_{fc}/b_{ft} = 1.0$ and $t_{fc}/t_{ft} = 1.5$. The five groups of test configurations selected are as follows:

- Group I – cases with small $X^2 = S_{xc}h_o/J$: Members with small X^2 have a relatively large contribution from the St. Venant torsional stiffness to their LTB resistance. By selecting members having the smallest X^2, any potential influence of this attribute on the accuracy of the Yura and Helwig estimate should be highlighted. It is found that when $h/t_w = 100$, $b_{fc}/2t_{fc} = 6$ and $h/b_{fc} = 2$ are combined, the cross-section has relatively small X^2 compared to other cases. For this combination of parameters, certain limits of the cross-section properties discussed above are violated in all cases if β is taken equal to 15^o. Therefore, $\beta = 10°$ is selected. An LTB slenderness $L_b/r_t = 40$ is selected since for larger values of L_b/r_t the web slenderness ratio h/t_w at the smaller end would be less than 40. Also, for smaller values of L_b/r_t, the effect of LTB on the member design resistance is reduced (i.e., the design LTB resistance tends toward the plateau associated with the maximum potential flexural strength).

- Group II – cases with large $X^2 = S_{xc}h_o/J$: Members with large X^2 have a relatively large contribution from the warping torsion stiffness to their LTB resistance. By selecting members having the largest X^2, any potential influence of this attribute on the accuracy of the Yura and Helwig estimate should be highlighted. It is found that a cross-section with $h/t_w = 130$, $b_{fc}/2t_{fc} = 12$ and $h/b_{fc} = 4$ has a relatively large X^2. In this case, $\beta = 15°$ and $L_b/r_t = 60$ are selected. The LTB slenderness $L_b/r_t = 60$ is selected to avoid violating the h/t_w limits while maximizing the influence of LTB on the member design resistance. With this combination, the case with $b_{fc}/b_{ft} = 1.0$ and $t_{fc}/t_{ft} = 1.5$ is not studied since the tension flange thickness is smaller than the web thickness in this case. Therefore, test members with 1) a doubly-symmetric section and 2) a singly-symmetric section with $b_{fc}/b_{ft} = 1.5$ and $t_{fc}/t_{ft} = 1.0$ are studied in this group.
- Group III – cases with $b_{fc}/2t_{fc} = 18$: Test beams with the largest targeted flange slenderness are selected for this group. These types of members tend to have relatively large X^2, but not as large as the cases selected for Group II. The results from the Group I and Group II studies indicate that members with large X^2 tend to exhibit larger errors in the Yura and Helwig estimates. Group III provides another set of cases with relatively large X^2. For a cross-section with $b_{fc}/2t_{fc} = 18$, h/b_{fc} needs to be 2. With other values of h/b_{fc} the tension flange thickness would be smaller than the web thickness, which is not allowed by Kaehler (2005) and MBMA/AISC (2010). $\beta = 10°$ and $h/t_w = 130$ are the largest values for the taper angle and the web slenderness that can be combined with $b_{fc}/2t_{fc} = 18$ respectively without violating limits specified above. The value of L_b/r_t equal to 40 is the only value of L_b/r_t that

can be used with the above parameters. Otherwise, the web slenderness at the smaller end h/t_w is less than 40.

- Group IV – cases with longer unbraced length: Members with a long unbraced length such that the design resistance is governed by elastic LTB are certainly more sensitive to errors in the elastic LTB estimates than cases where the design resistance is governed by inelastic LTB. Group IV targets these types of members. To select few cases with a longer unbraced length, an intermediate value for the flange slenderness of $b_{fc}/2t_{fc} = 12$ and a small taper angle $\beta = 5°$ are selected. For the doubly-symmetric section case and the singly-symmetric section case with $b_{fc}/b_{ft} = 1.5$ and $t_{fc}/t_{ft} = 1.0$, $h/b_{fc} = 4$ and $L_b/r_t = 120$ are selected. However, for the singly-symmetric section case with $b_{fc}/b_{ft} = 1.0$ and $t_{fc}/t_{ft} = 1.5$, $h/b_{fc} = 2$ and $L_b/r_t = 100$ are used to satisfy the dimensional requirements specified by Kaehler (2005) and MBMA/AISC (2010) and to have h/t_w larger than 40 at the shallow end.
- Group V – cases with $h/b_{fc} = 6$: The design resistances for members with large h/b_{fc} are typically more sensitive to the LTB limit state. Group V explores whether the errors in the Yura and Helwig estimates are different for these types of members. The flange slenderness $b_{fc}/2t_{fc} = 6$ is the only value that can be combined with $h/b_{fc} = 6$. The maximum values of the web slenderness ratio and the taper angle that can be used in combination of $h/b_{fc} = 6$ and $b_{fc}/2t_{fc} = 6$ are $h/t_w = 130$ and $\beta = 15°$ respectively. $L_b/r_t = 80$ is the maximum value of the LTB slenderness that can be used in these cases. However, when the cross-section is singly-symmetric with $b_{fc}/b_{ft} = 1.5$ and $t_{fc}/t_{ft} = 1.0$, the tension flange width becomes smaller than the minimum limit of 5 inches with above parameters. Therefore 1) a doubly-symmetric case and

2) a singly-symmetric with b_{fc}/b_{ft} = 1.0 and t_{fc}/t_{ft} = 1.5 case are studied. If a deeper web is used (e.g. h = 48 in), the minimum limit of the flange width from Kaehler (2005) can be satisfied with the selected parameters above. When the member is scaled up to have h = 48 inches at the mid-span, the tension flange width b_{ft} becomes 5.33 inches. However, h at the larger end becomes 68 inches and the section aspect ratio h/b_{ft} at the larger end (h/b_{ft} = 12.8) exceeds the maximum limit of 9 (Kaehler 2005). Therefore, the member with h = 48 inches is not considered.

Table 4.12 shows the specific member dimensions for the 13 cases studied within the above five groups. In all cases, the web is slender at the deeper end. Thus all the test members are considered as slender web members and the elastic LTB loads must be calculated with J = 0 as described in Chapter 3.

Table 4.12. The cross-section dimensions at the mid-span of test members (Groups I through V)

Group	Case	h (in)	t_w (in)	b_{fb} (in)	t_{fb} (in)	b_{ft} (in)	t_{ft} (in)	L_b (ft)	β (°)
I	1	30	0.30	15	1.25	15	1.25	14	10
	2	30	0.30	15	1.25	10	1.25	14	10
	3	30	0.30	15	1.25	15	0.83	14	10
II	4	30	0.23	7.5	0.31	7.5	0.31	9	15
	5	30	0.23	7.5	0.31	5	0.31	9	15
III	6	30	0.23	15	0.42	15	0.42	13	10
	7	30	0.23	15	0.42	10	0.42	14	10
	8	30	0.23	15	0.42	15	0.28	13	10
IV	9	30	0.23	7.5	0.31	7.5	0.31	18	5
	10	30	0.23	7.5	0.31	5	0.31	18	5
	11	30	0.23	15	0.63	15	0.42	35	5
V	12	30	0.23	5	0.42	5	0.42	8	15
	13	30	0.23	5	0.42	5	0.28	8	15

For each test member, five loading conditions are applied. In all cases, the yield moment based on the largest cross-section (M_{yL}) is applied at the larger end such that the top flange is in compression. As noted above, all the cross-section parameters reported in

this document are based on taking the top flange as the compression flange and the bottom flange as the tension flange. The yield strength, F_y of the members is taken as 55 ksi (F_{yc}=F_{yt} =F_y). In every singly-symmetric cross-section case, the bottom flange is smaller than the top flange so if the yield moment based on the top flange is applied to the cross-section, then the bottom flange stress becomes larger than the yield strength. For this reason the yield moment of each singly-symmetric cross-section case is calculated based on the bottom flange. For each of the cases shown in Table 4.12, five loading conditions are considered by applying different fractions of the yield moment based on the smallest cross-section (M_{ys}) at the smaller end. Similar to the way that M_{yL} is calculated, M_{ys} is obtained based on the bottom flange for singly-symmetric cross-section cases. The five loading cases are as follows:

(1) $M_L = M_{yL}$ and $M_s = M_{ys}$: Both moments are applied such that the top flange is in compression. M_L denotes the applied moment at the larger end and M_s denotes the applied moment at the smaller end. This applied load produces a moment gradient factor, C_b approximately equal to 1.0 (the maximum value of C_b is 1.01 based on Eq. 4.15).

(2) $M_L = M_{yL}$ and $M_s = 0.5M_{ys}$: This case gives values of C_b (from Eq. 4.15) that vary from 1.07 to 1.18 depending on the test beam geometry.

(3) $M_L = M_{yL}$ and $M_s = 0$: In this case, C_b varies from 1.17 to 1.43.

(4) $M_L = M_{yL}$ and $M_s = -0.5M_{ys}$: This loading condition creates reverse curvature bending in the test beams. In this case, the bottom flange is in compression at the smaller end and the top flange is in compression at the larger end. This is true for the loading condition (5) as well. The values of C_b vary from 1.30 to 1.83.

(5) $M_L = M_{yL}$ and $M_s = -1.0M_{ys}$: The values of C_b in this loading condition range from 1.45 to 1.93.

It should be noted that in cases where a singly-symmetric member is subjected to reverse curvature bending and the smaller flange of the member is in compression for only small part of a given unbraced length, C_b obtained by Eq. 4.15 can be significantly conservative since this equation does not consider the sign of flange stresses. In addition, AISC (2010) requires the use of the cross-section monosymmetry parameter, R_m, for calculating C_b in the case of reverse curvature bending of singly-symmetric I-sections. However, R_m is not included in the calculation of C_b in this study, since accurate to conservative results are obtained for the cases considered without the use of this parameter. Also, this modification is not suggested by Yura and Helwig (1996).

4.4.2.2 Comparisons between Elastic Eigenvalue Analysis Results and the Yura and Helwig (1996) Procedures

For the buckling analysis of the selected test cases, the GT-Sabre (Chang 2006) FEA program is used with an open section beam element having 14 degrees of freedom. Each beam member is modeled with 10 elements and the boundary conditions are applied at the shear center location. An eigenvalue buckling analysis is performed to determine the buckling load of each member. The elastic lateral torsional buckling estimates are obtained using the Yura and Helwig (1996) procedures.

Table 4.13 shows the Yura and Helwig (1996) estimates and the solutions from the GT-Sabre finite element analysis. The results are shown in terms of the ratio of the elastic LTB strength to the applied load. The last four columns of Table 4.13 are: (1) the elastic LTB estimates from Yura and Helwig (1996) (shown as γ_{eYH}), (2) the buckling analysis results using GT-Sabre (shown as γ_{eFEA}), (3) the ratio of the buckling analysis

results from GT-Sabre to the Yura and Helwig (1996) estimates ($\gamma_{eFEA}/\gamma_{eYH}$), and (4) the error in the Yura and Helwig (1996) estimates versus the FEA results. Positive error means that the Yura and Helwig (1996) approach gives an unconservative estimate for the elastic LTB of the test member compared to the FEA result. For each test case, the results for the five loading conditions are shown in the order: (1) $M_s/M_{ys} = 1.0$, (2) $M_s/M_{ys} = 0.5$, (3) $M_s/M_{ys} = 0$, (4) $M_s/M_{ys} = -0.5$, and (5) $M_s/M_{ys} = -1.0$.

The following conclusions can be reached by an inspection of Table 4.13:

- The maximum unconservative error in the Yura and Helwig (1996) estimate is 8.8 %. This error is obtained for case 4 of group II (for $M_s/M_{ys} = 1.0$). The maximum conservative error is obtained for case 2 of group I (for $M_s/M_{ys} = -1.0$). This Yura and Helwig estimate is 66.4 % smaller than the GT-Sabre result. The maximum errors are highlighted in Table 2. The mean value of $\gamma_{eFEA}/\gamma_{eYH}$ is 1.18. The value of the standard deviation is 0.48 and the coefficient of variation is 40.6 %.
- For single curvature bending, the Yura and Helwig approach shows unconservative errors in the beams with C_{b1} approximately equal to 1.0 in most cases. Cases 4 and 5 are the only cases where γ_{eYH} are unconservative compared to FEA solutions for $C_b > 1.0$. With larger β, larger h/t_w, larger b_{fc}/t_{fc} and larger h/b_{fc}, the unconservative errors in the Yura and Helwig estimates are in all cases larger.
- By comparisons between cases 4 and 5 and cases 12 and 13 under single curvature bending, it can be observed that $b_{fc}/2t_{fc}$ has a larger effect on the unconservative errors in the Yura and Helwig estimates than h/b_{fc} and L_b/r_t. Even though cases 12 and 13 have larger h/b_{fc} and L_b/r_t, the values of γ_{eYH} from these cases are 5.7 % and 3.9 % unconservative while the γ_{eYH} values from cases 4 and 5 are 8.8 % and 7.6 % unconservative compared to γ_{eFEA}.

Table 4.13. Results from finite element analysis and the Yura and Helwig (1996) estimate (Groups I through V).

Group	Case	β (°)	h/t_w	$b_{fb}/2t_{fb}$	h/b_{fb}	b_{fb}/b_{ft}	t_{fb}/t_{ft}	L_b/r_t	M_s/M_{ys}	C_b	(1) γ_{eYH}	(2) γ_{eFEA}	(3)$\gamma_{eFEA}/\gamma_{eYH}$	(4) Error
I	1	10	100	6	2	1	1	40	1.0	1.00	3.26	3.19	0.98	2.3%
									0.5	1.11	3.60	3.65	1.01	-1.4%
									0	1.26	4.09	4.21	1.03	-2.8%
									-0.5	1.46	4.74	4.87	1.03	-2.7%
									-1.0	1.73	5.64	5.58	0.99	0.9%
	2	10	100	6	2	1.5	1	40	1.0	1.00	4.29	4.23	0.99	1.5%
									0.5	1.11	4.77	4.81	1.01	-0.8%
									0	1.26	5.39	5.49	1.02	-1.9%
									-0.5	1.42	3.87	6.22	1.61	-37.8%
									-1.0	1.68	2.28	6.79	2.97	-66.4%
	3	10	100	6	2	1	1.5	40	1.0	1.00	4.24	4.26	1.00	-0.3%
									0.5	1.11	4.71	4.84	1.03	-2.8%
									0	1.26	5.32	5.55	1.04	-4.0%
									-0.5	1.45	6.13	6.35	1.04	-3.5%
									-1.0	1.69	5.15	7.18	1.39	-28.3%
II	4	15	130	12	4	1	1	60	1.0	1.01	1.45	1.34	0.92	8.8%
									0.5	1.05	1.52	1.50	0.99	1.4%
									0	1.17	1.70	1.68	0.99	0.8%
									-0.5	1.33	1.93	1.90	0.99	1.5%
									-1.0	1.54	2.23	2.13	0.96	4.4%
	5	15	130	12	4	1.5	1	60	1.0	1.01	1.63	1.51	0.93	7.6%
									0.5	1.05	1.70	1.67	0.98	1.7%
									0	1.17	1.88	1.85	0.98	1.7%
									-0.5	1.28	1.34	2.04	1.53	-34.5%
									-1.0	1.45	0.76	2.21	2.91	-65.6%
III	6	10	130	18	2	1	1	40	1.0	1.00	3.26	3.17	0.97	3.0%
									0.5	1.09	3.56	3.62	1.02	-1.7%
									0	1.24	4.05	4.17	1.03	-2.9%
									-0.5	1.44	4.69	4.82	1.03	-2.6%
									-1.0	1.72	5.58	5.52	0.99	1.2%
	7	10	130	18	2	1.5	1	40	1.0	1.01	4.00	3.91	0.98	2.2%
									0.5	1.11	4.40	4.42	1.01	-0.6%
									0	1.25	4.95	5.02	1.01	-1.4%
									-0.5	1.39	3.58	5.66	1.58	-36.9%
									-1.0	1.63	2.10	6.19	2.95	-66.1%
	8	10	130	18	2	1	1.5	40	1.0	1.01	3.98	3.95	0.99	0.7%
									0.5	1.11	4.38	4.47	1.02	-2.1%
									0	1.25	4.93	5.09	1.03	-3.1%
									-0.5	1.42	5.64	5.79	1.03	-2.6%
									-1.0	1.64	4.72	6.52	1.38	-27.5%
IV	9	5	130	12	4	1	1	120	1.0	1.00	0.36	0.35	0.96	4.5%
									0.5	1.13	0.41	0.41	1.00	-0.4%
									0	1.32	0.48	0.49	1.02	-1.8%
									-0.5	1.61	0.58	0.58	1.01	-0.5%
									-1.0	1.83	0.66	0.69	1.04	-4.0%
	10	5	130	12	4	1.5	1	120	1.0	1.00	0.41	0.40	0.97	3.2%
									0.5	1.13	0.46	0.46	1.00	-0.1%
									0	1.32	0.54	0.54	1.01	-0.6%
									-0.5	1.56	0.41	0.63	1.53	-34.7%
									-1.0	1.80	0.24	0.67	2.83	-64.7%
	11	5	130	12	2	1	1.5	100	1.0	1.01	0.66	0.65	0.99	1.0%
									0.5	1.07	0.70	0.71	1.02	-2.0%
									0	1.17	0.77	0.79	1.03	-2.8%
									-0.5	1.30	0.84	0.87	1.03	-2.7%
									-1.0	1.41	0.67	0.95	1.42	-29.5%
V	12	15	130	6	6	1	1	80	1.0	1.01	0.82	0.77	0.95	5.7%
									0.5	1.07	0.87	0.88	1.01	-0.7%
									0	1.22	0.99	1.00	1.01	-1.4%
									-0.5	1.41	1.15	1.15	1.01	-0.5%
									-1.0	1.67	1.36	1.31	0.97	3.6%
	13	15	130	6	6	1	1.5	80	1.0	1.01	0.90	0.87	0.96	3.9%
									0.5	1.08	0.97	0.98	1.01	-1.3%
									0	1.21	1.09	1.11	1.02	-1.7%
									-0.5	1.38	1.24	1.25	1.01	-0.7%
									-1.0	1.59	1.04	1.40	1.34	-25.6%

- In cases 9 and 10, the taper angle, β is smaller and the lateral torsional buckling slenderness, L_b/r_t is larger than in cases 4 and 5. Table 4.13 shows that cases 9 and 10 have smaller unconservative error than cases 4 and 5 for single curvature bending. From this observation, it can be concluded that the taper angle has a larger effect on the unconservative error of the γ_{eYH} estimates than L_b/r_t.
- For single curvature bending, the use of singly-symmetric sections does not have a significant effect on the accuracy of the recommended procedure with C_{b1}. The maximum increase in the error of the Yura and Helwig estimates due to the use of a singly-symmetric section is obtained in case 3 (group I) with $M_s/M_{ys} = 0.5$. The error using this singly-symmetric section with $t_{fc}/t_{ft} = 1.5$ is 2.8 % conservative while the error for case 1 is 1.4 % conservative. The maximum decrease in the error is obtained in case 11 with $M_s/M_{ys} = 1.0$ in group IV. The error using the singly-symmetric section with $t_{fc}/t_{ft} = 1.5$ (case 11) is 1.0 % unconservative while the error using the doubly symmetric section (case 9) is 4.5 % unconservative.
- For reverse curvature bending, the use of singly-symmetric sections has a significant effect on the accuracy of the Yura and Helwig procedure under the loading $M_s/M_{ys} = -1.0$. Furthermore the singly-symmetric cross-section cases with $b_{fc}/b_{ft} = 1.5$ show large conservative errors under the loading $M_s/M_{ys} = -0.5$ as well. For example, for cases 2 and 3 (group I) with $M_s/M_{ys} = -1.0$ the Yura and Helwig estimates are 66.4 % and 28.3 % conservative compared to γ_{eFEA}. For case 2 with $M_s/M_{ys} = -0.5$ γ_{eYH} is 37.8 % conservative compared to γ_{eFEA} while γ_{eYH} in case 3 with the same loading condition is 3.5 % conservative compared to γ_{eFEA}. With the doubly-symmetric cross-section (case 1 in group I), the Yura and Helwig estimates are only 2.7 %

conservative for M_s/M_{ys} = -0.5 and 0.9 % unconservative for M_s/M_{ys} = -1.0. It appears that the large conservative errors due to the singly-symmetric cross-sections in reverse curvature bending are caused by the conservatism of applying the AISC (2010) C_b equation in an adhoc fashion to tapered web members (Eq. 4.13). The AISC C_b equation was originally derived only for doubly-symmetric prismatic members. This equation does not consider the actual sign of any of its flange stress terms.

Based on the conclusions explained above, three additional groups of test members are selected to explore the effects of the taper angle and the web slenderness on the elastic LTB estimates of linearly-tapered web members. The specific cross-section dimensions at the mid-span of each member are shown in Table 4.14. The additional groups are arrived at by the following logic:

Table 4.14. The cross-section dimensions of test members (Groups VI through VIII)

Group	Case	h (in)	t_w (in)	b_{fb} (in)	t_{fb} (in)	b_{ft} (in)	t_{ft} (in)	L_b (ft)	β (°)
VI	14	30	0.23	5	0.42	5	0.42	6	10
	15	30	0.23	7.5	0.63	5	0.63	10	10
	16	30	0.23	5	0.42	5	0.28	6	10
VII	17	30	0.23	5	0.42	5	0.42	6	15
	18	30	0.23	7.5	0.63	5	0.63	10	15
	19	30	0.23	5	0.42	5	0.28	6	15
VIII	20	30	0.30	15	0.42	10	0.42	13	10
	21	30	0.23	7.5	0.31	5	0.31	6	10
	22	30	0.23	15	0.63	10	0.63	14	10

- Group VI – modified cases of group II using β = 10° : To study the effect of the taper angle, three cases are selected from the combination of β = 10°, h/t_w = 130, $b_{fc}/2t_{fc}$ = 6, and L_b/r_t = 60. These cases are derived from the group II cases since group II shows the maximum unconservative errors in Table 4.13. For the doubly-symmetric case

and the singly-symmetric case with $t_{fc}/t_{ft} = 1.5$, the value of h/b_{fc} equal to 6 is selected (see cases 14 and 16). However, for the singly-symmetric case with $b_{fc}/b_{ft} = 1.5$, $h/b_{fc} = 4$ is selected since otherwise the tension flange width would violate the minimum limit of 5 inches (see case 15). As discussed in the description of group V, if a larger value of h at mid-span is used, b_{ft} would satisfy the minimum limit. However, the value of h/b_{ft} at the larger end would exceed the maximum limit of $h/b_{fc} \leq 9$. The values of the flange slenderness ratio and the section aspect ratio are selected such that the limits specified in Kaehler (2005) are not violated for $\beta = 10°$.

- Group VII – modified cases of group VI using $\beta = 15°$: Three cases in this group are selected as described above except using $\beta = 15°$. In case 18, the section aspect ratio h/b_{ft} at the larger end (9.2) is slightly larger than the maximum limit of h/b_f (9.0). This is because the tension flange width is 0.67 times smaller than the compression flange in case 18. This case is still considered in this study for demonstration purposes, although the above maximum limit is slightly violated.
- Group VIII – modified cases of case 7 in group III : The purpose of this group is to study the effect of the web slenderness, the flange slenderness, and the section aspect ratio on the accuracy of the recommended approach with C_{b1}. From the results shown in Table 4.13, it is expected that the flange slenderness $b_{fc}/2t_{fc}$ has a larger effect on the accuracy of the Yura and Helwig estimates than the web slenderness h/t_w or the section aspect ratio h/b_{fc}. The group VIII cases are selected based on the cases in group III since these cases have the largest value of the flange slenderness. In case 20, the web slenderness, h/t_w is changed to 100 from 130. Then the flange slenderness, $b_{fc}/2t_{fc}$ and the section aspect ratio are changed to 12 and 4 (case 21). Lastly in case

22, only the flange slenderness $b_{fc}/2t_{fc}$ is changed to 12.

The finite element analysis results and the Yura and Helwig (1996) estimates are shown in Table 4.15. The following conclusions can be reached by an inspection of Table 4.15:

Table 4.15. Results from finite element analysis and the Yura and Helwig (1996) estimate (Groups VI through VIII)

Group	Case	β (°)	h/t_w	$b_{fb}/2t_{fb}$	h/b_{fb}	b_{fb}/b_{ft}	t_{fb}/t_{ft}	L_b/r_t	M_s/M_{ys}	C_b	(1) γ_{eYH}	(2) γ_{eFEA}	(3)$\gamma_{eFEA}/\gamma_{eYH}$	(4) Error
VI	14	10	130	6	6	1	1	60	1.0	1.00	1.45	1.43	0.99	1.1%
									0.5	1.17	1.69	1.75	1.03	-3.2%
									0	1.43	2.06	2.18	1.06	-5.3%
									-0.5	1.83	2.64	2.74	1.03	-3.4%
									-1.0	1.93	2.79	3.28	1.18	-14.9%
	15	10	130	6	4	1.5	1	60	1.0	1.00	1.74	1.73	1.00	0.2%
									0.5	1.14	1.98	2.02	1.02	-2.3%
									0	1.33	2.30	2.37	1.03	-3.1%
									-0.5	1.56	1.75	2.75	1.57	-36.4%
									-1.0	1.81	1.01	2.92	2.89	-65.4%
	16	10	130	6	6	1	1.5	60	1.0	1.00	1.62	1.63	1.01	-0.6%
									0.5	1.17	1.89	1.97	1.04	-3.8%
									0	1.42	2.29	2.43	1.06	-5.6%
									-0.5	1.80	2.91	3.00	1.03	-3.0%
									-1.0	1.91	2.22	3.47	1.56	-35.8%
VII	17	15	130	6	6	1	1	60	1.0	1.00	1.45	1.41	0.97	3.1%
									0.5	1.12	1.62	1.65	1.02	-1.9%
									0	1.32	1.90	1.97	1.03	-3.2%
									-0.5	1.59	2.31	2.35	1.02	-1.9%
									-1.0	1.82	2.63	2.76	1.05	-4.6%
	18	15	130	6	4	1.5	1	60	1.0	1.01	1.72	1.67	0.97	3.1%
									0.5	1.07	1.83	1.85	1.01	-0.8%
									0	1.18	2.02	2.04	1.01	-0.9%
									-0.5	1.29	1.44	2.26	1.57	-36.4%
									-1.0	1.46	0.82	2.45	3.00	-66.7%
	19	15	130	6	6	1	1.5	60	1.0	1.01	1.61	1.59	0.99	1.2%
									0.5	1.13	1.81	1.85	1.03	-2.5%
									0	1.31	2.10	2.18	1.04	-3.4%
									-0.5	1.57	2.51	2.56	1.02	-1.9%
									-1.0	1.80	2.09	2.94	1.41	-28.8%
VIII	20	10	100	18	2	1.5	1	40	1.0	1.01	3.90	3.79	0.97	2.8%
									0.5	1.10	4.26	4.28	1.00	-0.4%
									0	1.24	4.79	4.85	1.01	-1.1%
									-0.5	1.38	3.47	5.46	1.57	-36.4%
									-1.0	1.62	2.03	5.97	2.93	-65.9%
	21	10	130	12	4	1.5	1	40	1.0	1.00	3.70	3.63	0.98	1.8%
									0.5	1.18	4.34	4.39	1.01	-1.2%
									0	1.42	5.25	5.38	1.02	-2.3%
									-0.5	1.79	4.21	6.42	1.52	-34.4%
									-1.0	1.91	2.25	6.19	2.75	-63.7%
	22	10	130	12	2	1.5	1	40	1.0	1.00	4.15	4.09	0.99	1.4%
									0.5	1.11	4.60	4.64	1.01	-1.0%
									0	1.25	5.18	5.29	1.02	-2.0%
									-0.5	1.41	3.73	5.98	1.60	-37.6%
									-1.0	1.66	2.19	6.53	2.98	-66.4%

- Among the additional study cases, the maximum unconservative error is obtained from cases 17 and 18 with M_s/M_{ys} = 1.0. In both cases, γ_{eYH} shows 3.1 % unconservative error compared to γ_{eFEA}. The maximum value of the conservative

error is 66.7 % from case 18 with M_s/M_{ys} = -1.0. These maximum values of error are highlighted in the table. The mean value of the ratio of the finite element analysis result to the Yura and Helwig estimate ($\gamma_{eFEA}/\gamma_{eYH}$) in groups VI to VIII is 1.31 and the standard deviation is 0.61. The coefficient of variation is 46.1 %. The statistics for the ratio $\gamma_{eFEA}/\gamma_{eYH}$ are summarized in Table 4.16 for all of the groups considered in this study.

Table 4.16. Summary of statistics from the parametric study

Group	Case	$\gamma_{eFEA}/\gamma_{eYH}$		
		Mean	Std. Dev.	COV (%)
I - V	1 - 13	1.18	0.48	40.6
VI - VIII	14 - 22	1.31	0.61	46.1
I - VIII	1 - 22	1.23	0.53	43.4

- For single curvature bending in the group VI and group VII cases, it can be observed that when the taper angle is larger, the unconservative error becomes larger when the members are loaded with M_s/M_{ys} = 1.0. However, the conservative errors are smaller with larger β when M_s/M_{ys} = 0.5 or 0.
- For reverse curvature bending, smaller β gives larger conservative errors in some cases with M_s/M_{ys} = -0.5 and -1.0 (e.g. case 14 vs. case 17). However, in case 18 with M_s/M_{ys} = -1.0 γ_{eYH} is 66.7 % smaller than γ_{eFEA} while in case 15 with the same loading condition, γ_{eYH} is 65.4 % smaller than γ_{eFEA}.
- By comparing case 7 in Table 4.13 and case 20 in Table 4.15, it can be seen that smaller h/t_w gives slightly smaller error in both single curvature bending and reverse curvature bending except for the loading condition of M_s/M_{ys} = 1.0. For M_s/M_{ys} = 1.0,

the value of h/t_w equal to 100 gives 2.8 % unconservative error (case 20) while h/t_w equal to 130 gives 2.2 % unconservative error (case 7).

- From cases 7, 21 and 22 one can observe the effects of the changes in the flange slenderness and the section aspect ratio. Case 7 has the largest unconservative error of 2.2 % in uniform bending and case 21 has the largest conservative error of 2.3 % in single curvature bending with zero moment at the smaller end. For reverse curvature bending, case 22 has the largest conservative errors of 37.6 % and 66.4 % for M_s/M_{ys} = -0.5 and M_s/M_{ys} = -1.0 respectively.

4.4.2.3 Comparisons between Elastic Eigenvalue Analysis Results and the Recommended Procedures

In this section, the accuracy of the recommended procedures for calculating the elastic LTB estimates is evaluated. The recommended procedures calculate the elastic LTB estimates based on the cross-section at mid-span as suggested by Yura and Helwig (1996) but using C_b calculated by AASHTO (2007) equations. Tables 4.17 and 4.18 show the comparisons between the virtual test simulations results and the elastic LTB estimates obtained by the recommended procedures (shown as γ_{eLTB}) . The maximum unconservative error from the study of groups I to V is 8.1 % in case 4 and the maximum conservative error is 54.9 % in case 10. The mean value of the ratio of $\gamma_{eFEA}/\gamma_{eLTB}$ is 1.07 and the standard deviation is 0.26. The coefficient of variation of the errors in Table 4.19 is 24.5 %. From the study of groups VI to VIII, the maximum unconservative error is 2.7 % in case 17 and the maximum conservative error is 56.3 % in case 21. The mean value of the ratio of $\gamma_{eFEA}/\gamma_{eLTB}$ is 1.15 and the standard deviation is 0.36. The coefficient of variation is 31.3 %. The maximum errors are highlighted in Tables 4.17 and 4.18. The maximum unconservative and conservative errors for the recommended procedures

(γ_{eLTB}) are slightly smaller than the corresponding values for the Yura and Helwig (1996) procedures (γ_{eYH}). However the values of the coefficient of variation are significantly better for γ_{eLTB} than the corresponding values for γ_{eYH} (See Table 4.19).

It should be noted that the conservative errors in the singly-symmetric cross-section cases with b_{fc}/b_{ft} = 1.5 subjected to M_s/M_{ys} = -0.5 are reduced significantly by using the recommended procedures with AASHTO (2004 & 20007) equations for C_b. For example, the conservative error of 37.8 % for γ_{eYH} from Case 2 is reduced to 0.8 % for γ_{eLTB}. This is the largest reduction in the conservative error due to the use of $C_{b(\text{AASHTO})}$.

Furthermore, the use of $C_{b(\text{AASHTO})}$ reduces the conservative errors in the singly-symmetric cross-section cases with t_{fc}/t_{ft} = 1.5 subjected to M_s/M_{ys} = -1.0 significantly. The largest reduction in these cases is obtained from Case 3. The conservative error of γ_{eYH} is 28.3 %, while the error of γ_{eLTB} is 2.4 %. It appears that for the beams with singly-symmetric cross-section with b_{fc}/b_{ft} = 1.5 and M_s/M_{ys} = -1.0, the recommended procedures with AASHTO (2007) equations for C_b still show relatively large conservative error. However, it is important to note that it is not common to design linearly-tapered web members subject to double curvature bending. Since the AASHTO (2007) equations are simpler to apply (they require the calculation of only three values for the flange stresses rather than four), and also they are more intuitive for reversed curvature bending cases (since Eq. 4.15 is blind to the sign of the stresses), Engineers may prefer the AASHTO (2007) equations.

4.4.3 End Restraint Consideration

To consider the end restraint effects in linearly-tapered web members for the elastic LTB estimates, Ozgur et al. (2007) suggest the use of the design-based procedure developed

Table 4.17. Results from finite element analysis and the LTB estimate based on the recommended procedures (Groups I through V)

Group	Case	β (°)	h/t_w	$b_{fb}/2t_{fb}$	h/b_{fb}	b_{fb}/b_{ft}	t_{fb}/t_{ft}	L_b/r_t	M_s/M_{ys}	C_b	(1) γ_{eLTB}	(2) γ_{eFEA}	(3)$\gamma_{eFEA}/\gamma_{eLTB}$	(4) Error
I	1	10	100	6	2	1	1	40	1.0	1.00	3.25	3.19	0.98	2.1%
									0.5	1.10	3.59	3.65	1.02	-1.5%
									0	1.26	4.10	4.21	1.03	-2.6%
									-0.5	1.45	4.72	4.87	1.03	-3.1%
									-1.0	1.68	5.45	5.58	1.02	-2.4%
	2	10	100	6	2	1.5	1	40	1.0	1.00	4.28	4.23	0.99	1.2%
									0.5	1.11	4.76	4.81	1.01	-0.9%
									0	1.26	5.40	5.49	1.02	-1.6%
									-0.5	1.44	6.17	6.22	1.01	-0.8%
									-1.0	2.30	3.13	6.79	2.17	-53.9%
	3	10	100	6	2	1	1.5	40	1.0	1.00	4.23	4.26	1.01	-0.6%
									0.5	1.11	4.70	4.84	1.03	-2.9%
									0	1.26	5.34	5.55	1.04	-3.8%
									-0.5	1.44	6.11	6.35	1.04	-3.9%
									-1.0	2.30	7.01	7.18	1.02	-2.4%
II	4	15	130	12	4	1	1	60	1.0	1.00	1.45	1.34	0.92	8.1%
									0.5	1.03	1.49	1.50	1.00	-0.4%
									0	1.15	1.67	1.68	1.01	-1.0%
									-0.5	1.30	1.88	1.90	1.01	-0.7%
									-1.0	1.48	2.14	2.13	0.99	0.6%
	5	15	130	12	4	1.5	1	60	1.0	1.00	1.61	1.51	0.94	6.6%
									0.5	1.04	1.67	1.67	1.00	-0.2%
									0	1.14	1.85	1.85	1.00	-0.3%
									-0.5	1.28	2.06	2.04	0.99	0.9%
									-1.0	2.30	1.20	2.21	1.84	-45.6%
III	6	10	130	18	2	1	1	40	1.0	1.00	3.25	3.17	0.97	2.7%
									0.5	1.09	3.54	3.62	1.02	-2.2%
									0	1.24	4.04	4.17	1.03	-3.1%
									-0.5	1.43	4.66	4.82	1.03	-3.3%
									-1.0	1.66	5.39	5.52	1.02	-2.3%
	7	10	130	18	2	1.5	1	40	1.0	1.00	3.98	3.91	0.98	1.7%
									0.5	1.10	4.38	4.42	1.01	-1.1%
									0	1.24	4.94	5.02	1.02	-1.6%
									-0.5	1.42	5.63	5.66	1.01	-0.7%
									-1.0	2.30	2.96	6.19	2.09	-52.3%
	8	10	130	18	2	1	1.5	40	1.0	1.00	3.96	3.95	1.00	0.2%
									0.5	1.10	4.35	4.47	1.03	-2.6%
									0	1.24	4.92	5.09	1.03	-3.3%
									-0.5	1.42	5.60	5.79	1.03	-3.2%
									-1.0	1.62	6.41	6.52	1.02	-1.7%
IV	9	5	130	12	4	1	1	120	1.0	1.00	0.36	0.35	0.96	4.1%
									0.5	1.13	0.41	0.41	1.00	-0.3%
									0	1.34	0.48	0.49	1.01	-0.7%
									-0.5	1.61	0.58	0.58	1.01	-0.6%
									-1.0	1.93	0.70	0.69	0.98	1.5%
	10	5	130	12	4	1.5	1	120	1.0	1.00	0.41	0.40	0.97	2.7%
									0.5	1.13	0.46	0.46	1.00	0.0%
									0	1.33	0.54	0.54	1.00	0.4%
									-0.5	2.30	0.60	0.63	1.04	-3.7%
									-1.0	2.30	0.30	0.67	2.22	-54.9%
	11	5	130	12	2	1	1.5	100	1.0	1.00	0.65	0.65	0.99	0.5%
									0.5	1.06	0.69	0.71	1.03	-3.0%
									0	1.16	0.76	0.79	1.04	-3.9%
									-0.5	1.28	0.83	0.87	1.04	-4.2%
									-1.0	1.41	0.92	0.95	1.04	-3.7%
V	12	15	130	6	6	1	1	80	1.0	1.00	0.81	0.77	0.95	5.1%
									0.5	1.06	0.86	0.88	1.02	-2.0%
									0	1.21	0.98	1.00	1.02	-2.4%
									-0.5	1.39	1.13	1.15	1.02	-1.9%
									-1.0	1.61	1.31	1.31	1.00	-0.3%
	13	15	130	6	6	1	1.5	80	1.0	1.00	0.90	0.87	0.97	3.0%
									0.5	1.06	0.95	0.98	1.03	-2.6%
									0	1.20	1.07	1.11	1.03	-2.9%
									-0.5	1.36	1.22	1.25	1.02	-2.2%
									-1.0	1.56	1.40	1.40	1.00	-0.2%

Table 4.18. Results from finite element analysis and the Yura and Helwig (1996) estimate with C_b based on AASHTO (2007) equations (Groups VI through VIII)

Group	Case	β (°)	h/t_w	$b_{fb}/2t_{fb}$	h/b_{fb}	b_{fb}/b_{ft}	t_{fb}/t_{ft}	L_b/r_t	M_s/M_{ys}	C_b	(1) γ_{eLTB}	(2) γ_{eFEA}	(3)$\gamma_{eFEA}/\gamma_{eLTB}$	(4) Error
VI	14	10	130	6	6	1	1	60	1.0	1.00	1.45	1.43	0.99	0.9%
									0.5	1.19	1.71	1.75	1.02	-1.8%
									0	1.47	2.12	2.18	1.03	-2.7%
									-0.5	1.83	2.64	2.74	1.04	-3.5%
									-1.0	2.27	3.28	3.28	1.00	0.0%
	15	10	130	6	4	1.5	1	60	1.0	1.00	1.73	1.73	1.00	-0.2%
									0.5	1.15	1.98	2.02	1.02	-1.9%
									0	1.35	2.33	2.37	1.02	-1.9%
									-0.5	2.30	2.57	2.75	1.07	-6.5%
									-1.0	2.30	1.28	2.92	2.28	-56.1%
	16	10	130	6	6	1	1.5	60	1.0	1.00	1.61	1.63	1.01	-0.9%
									0.5	1.19	1.92	1.97	1.02	-2.4%
									0	1.46	2.36	2.43	1.03	-3.0%
									-0.5	1.80	2.91	3.00	1.03	-3.0%
									-1.0	2.30	2.68	3.47	1.29	-22.7%
VIII	17	15	130	6	6	1	1	60	1.0	1.00	1.45	1.41	0.97	2.7%
									0.5	1.12	1.62	1.65	1.02	-1.9%
									0	1.33	1.92	1.97	1.02	-2.3%
									-0.5	1.59	2.30	2.35	1.02	-2.1%
									-1.0	1.91	2.76	2.76	1.00	0.1%
	18	15	130	6	4	1.5	1	60	1.0	1.00	1.71	1.67	0.98	2.3%
									0.5	1.06	1.81	1.85	1.02	-2.1%
									0	1.17	2.00	2.04	1.02	-2.2%
									-0.5	1.30	2.22	2.26	1.02	-1.6%
									-1.0	2.30	1.28	2.45	1.91	-47.6%
	19	15	130	6	6	1	1.5	60	1.0	1.00	1.60	1.59	0.99	0.7%
									0.5	1.13	1.81	1.85	1.03	-2.5%
									0	1.32	2.12	2.18	1.03	-2.7%
									-0.5	1.57	2.51	2.56	1.02	-2.0%
									-1.0	2.30	2.68	2.94	1.10	-9.0%
IX	20	10	100	18	2	1.5	1	40	1.0	1.00	3.88	3.79	0.98	2.2%
									0.5	1.09	4.23	4.28	1.01	-1.1%
									0	1.23	4.78	4.85	1.02	-1.5%
									-0.5	1.40	5.43	5.46	1.00	-0.5%
									-1.0	2.30	2.89	5.97	2.06	-51.5%
	21	10	130	12	4	1.5	1	40	1.0	1.00	3.69	3.63	0.98	1.6%
									0.5	1.19	4.40	4.39	1.00	0.3%
									0	1.46	5.40	5.38	1.00	0.3%
									-0.5	2.30	5.42	6.42	1.19	-15.6%
									-1.0	2.30	2.71	6.19	2.29	-56.3%
	22	10	130	12	2	1.5	1	40	1.0	1.00	4.13	4.09	0.99	1.0%
									0.5	1.11	4.58	4.64	1.01	-1.2%
									0	1.26	5.19	5.29	1.02	-1.9%
									-0.5	1.43	5.91	5.98	1.01	-1.1%
									-1.0	2.30	3.05	6.53	2.14	-53.4%

Table 4.19. Summary of the statistics from the study using the Yura and Helwig procedures with AISC C_b vs. the recommended procedures with AASHTO C_b.

Group	Case	γ_e calculation	$\gamma_{eFEA}/\gamma_{e.calculated}$		
			Mean	Std. Dev.	COV (%)
I - V	1 - 13	γ_{eYH}	1.18	0.48	40.6
		γ_{eLTB}	1.07	0.26	24.5
VI - VIII	14 - 22	γ_{eYH}	1.31	0.61	46.1
		γ_{eLTB}	1.15	0.36	31.3
I - VIII	1 - 22	γ_{eYH}	1.23	0.53	43.4
		γ_{eLTB}	1.10	0.31	27.8

by Nethercot and Trahair (1976). This procedure accounts for the end warping restraints from the adjacent less critical unbraced lengths. The consideration of the end restraint effects combined with the recommended procedures described in Section 4.4.1, more refined inelastic LTB resistances can be obtained for linearly-tapered web members. It is noted in Ozgur et al. (2007) that the consideration of the end restraint effects increases the demands on the out-of-plane beam bracing system in general. The specific demands on the out-of-plane bracing systems in the linearly-tapered web members and the frames with web-tapered members are not in the scope of this research. Therefore, the approach suggested by Ozgur et al. (2007) is not considered in this research except a few example calculations shown in Chapter 8.

CHAPTER V

PROCEDURES FOR FINITE ELEMENT VIRTUAL TEST SIMULATION

This chapter discusses the general procedures used for finite element virtual test simulation conducted in this study. The procedures described in this chapter are the same for all the virtual test simulations unless otherwise noted. The details in the modeling (e.g., loading and boundary conditions) that are different from the general procedures are addressed where the specific test cases are discussed.

5.1 Test Configurations

Figure 5.1 shows a typical test configuration for a tapered beam. All the test members used in the parametric study are torsionally simply-supported beams subjected to the end moments. For the full nonlinear finite element simulations, a commercial software package ABAQUS (Simulia 2009) is used. The test members are modeled with a four-node shell element (S4R) for all the cross-section components. The finite element models have a relatively dense mesh with 20 elements through the web depth and 12 elements through the flange width in general. For the singly-symmetric members with different flange widths (b_{fc}/b_{ft} = 0.67 or 1.5) shown in Chapter 7, the larger flange is modeled with 12 elements through the width, while the smaller flange is modeled with eight elements through the width. The number of elements used for each cross-section component is decided such that the selected nominal residual stress pattern is well applied while the reasonable analysis time is maintained. The selected nominal residual stress pattern is discussed subsequently.

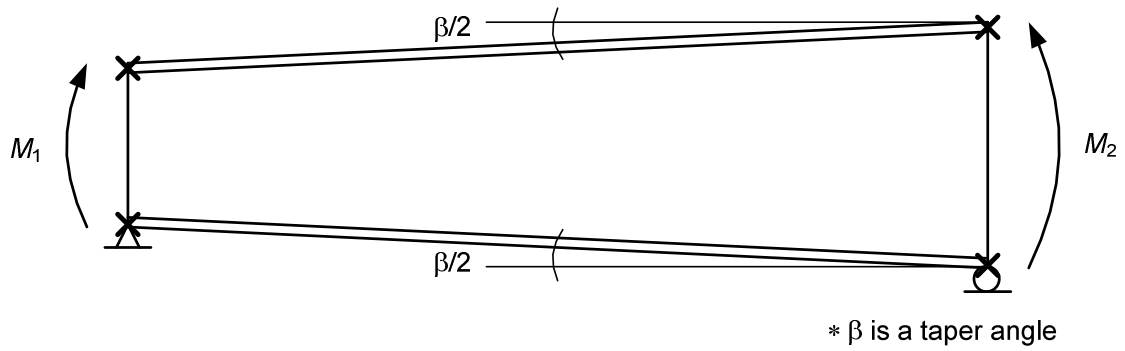

Figure 5.1. Typical test configuration for a tapered beam test.

5.2 Geometry and Boundary Conditions

All the parametric study cases, both prismatic and tapered members are torsionally simply-supported beams subjected to the end moments as shown in Figure 5.1. To achieve the beam kinematics at the ends of the beams modeled using S4R, the additional geometric restraints are required. Figure 5.2 shows the geometric restraints used to enforce the beam kinematics at the ends of the beams as well as the boundary conditions used to achieve the torsionally simply-supported conditions. In Figure 5.2, Points *a* and *e* denote any nodes on top and bottom flanges respectively except the nodes at the web-flange juncture. Similarly, Point *c* denotes any nodes on web except the nodes at the web-flange juncture. Points *b* and *d* are the nodes at the top and bottom web-flange junctures respectively. In addition, Axis 1 is the longitudinal axis of the members and Axes 2 and 3 are the major and minor bending axes of I sections respectively.

With the geometric restraints shown in Figure 5.2, the followings are enforced at the both ends.

- The web remains straight while it is allowed to rotate about the bottom web-flange juncture node, Point *d*.

- The flanges remain straight while they are free to rotate about the web-flange junctures, Points *b* and *d*.

Therefore, the beams kinematics are enforced at both ends without restraining the warping. It should noted that these geometric restraints satisfy an equilibrium at both ends if θ_2 of a deformed geometry shown in Figure 5.2 is less than 0.04 radians. Otherwise results from virtual test simulation are not accurate.

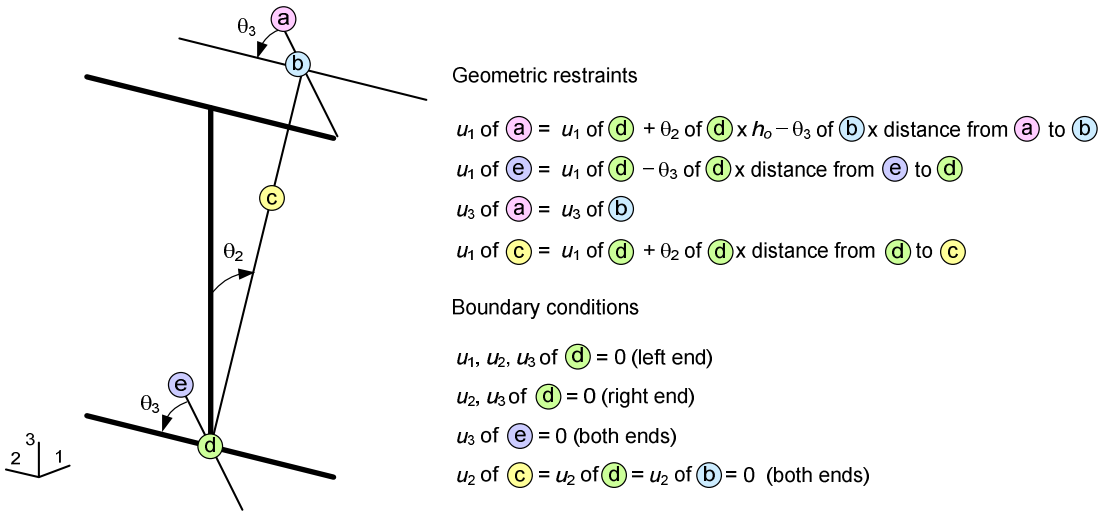

Figure 5.2. Geometric restraints and boundary conditions of test members

In addition to the geometric restraints, Figure 5.2 shows the boundary conditions that are applied to the finite element models. For the pin support at the left end, all the displacement degrees of freedom are restrained at Point *d* the vertical displacements u_3 of all the bottom flange nodes are restrained. For the roller support at the right end, the lateral displacements u_2 are restrained for all the nodes in the bottom flange including Point *d* and u_3 are restrained only at Point *d*. Lastly, the lateral displacements of all the nodes in the web including the web-flange juncture nodes are restrained at both ends.

5.3 Nominal Residual Stress Pattern

Figure 5.3 shows the nominal residual stress pattern selected in this study. The selected residual stress pattern is self-equilibrating for each cross-section component. Because of the tapered geometry of the web panels, it is important to use the self-equilibrating residual stress pattern for the tapered members. Otherwise, the residual stress patterns need to be varied for each cross-section throughout the beam unbraced lengths.

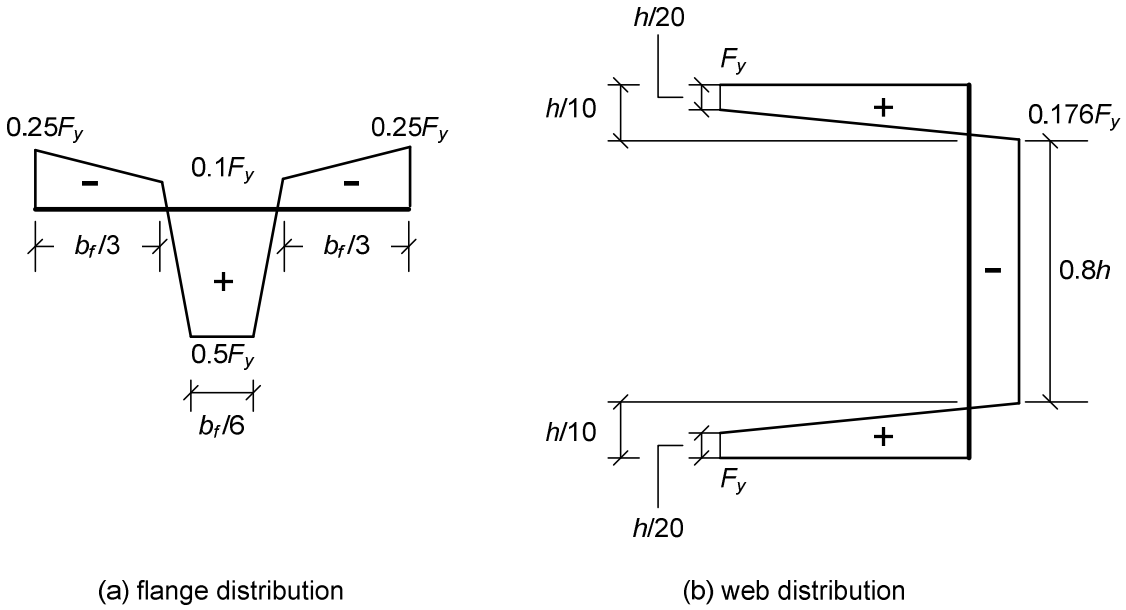

Figure 5.3. Nominal residual stress pattern

In the nominal residual stress pattern, the maximum compressive residual stress in the flanges is $0.25F_y$ at the tip of the flanges. The maximum compressive stress decreases linearly within the one-third of the flange width $b_f/3$ from the tips. In the vicinity of the web-flange juncture, the maximum tensile residual stress is $0.5F_y$. In the web, the maximum tensile residual stress is F_y within the length of $h/20$ from the web-

flange juncture, where h is the clear web depth. In the middle of the web, there is a constant compressive residual stress of $0.176F_y$. This residual stress pattern is selected as a representative pattern for welded I-section members. It should be noted that for members with a slender web, the compressive residual stress of $0.176F_y$ is larger than a web plate buckling stress assuming singly-supported boundary conditions. For these cases, the residual stresses in the web panel are scaled down such that the compressive residual stress in the middle of the web is same as the web plate buckling stress.

The residual stress pattern shown in Figure 5.3 is determined based on fit to residual stress measurements provided by Prawel et al. (1974). In this dissertation, the residual stress pattern shown in Figure 5.3 is referred to as "*best-fit Prawel residual stress pattern*." A number of virtual test simulations, which are conducted for experimental tests performed by Prawel et al. (1974), show that the best-fit Prawel residual stress pattern provides reasonable lower bound compared to the experimental test results. The details about the analysis results of experimental tests in Prawel et al. (1974) and the justifications of using the best-fit Prawel residual stress pattern for virtual test simulation are discussed in Chapter 6.

5.4 Imperfection Shape and Amplitude

Figure 5.4 shows the selected geometric imperfection shape and the amplitude of $L_b/1000$ that are used in the virtual test simulations conducted in this study. The selected geometric imperfection shape involves with the sweep in the compression flange. The parametric study conducted in this study focuses on the lateral torsional buckling (LTB) resistances of the prismatic and tapered members. The flange sweep imperfection has a

significant effect on the beam lateral torsional buckling failures than the eigenvalue buckling shapes, which typically involve with the local buckling in the web.

An imperfection shape with the flange sweep is obtained as follows. A linear analysis is performed with the test beams subject to a line load along the web-flange juncture nodes of the compression flange. Based on the lateral deformation obtained from this analysis, a scale factor is calculated such that the scaled deformed shape of the test beam has a maximum lateral deformation of $L_b/1000$, where L_b is the unbraced length. This scaled deformed shape is then imposed as an imperfect geometry of the test beam without any residual strain. The amplitude of $L_b/1000$ is selected based on the election tolerances of the code of standard practice (AISC 2005).

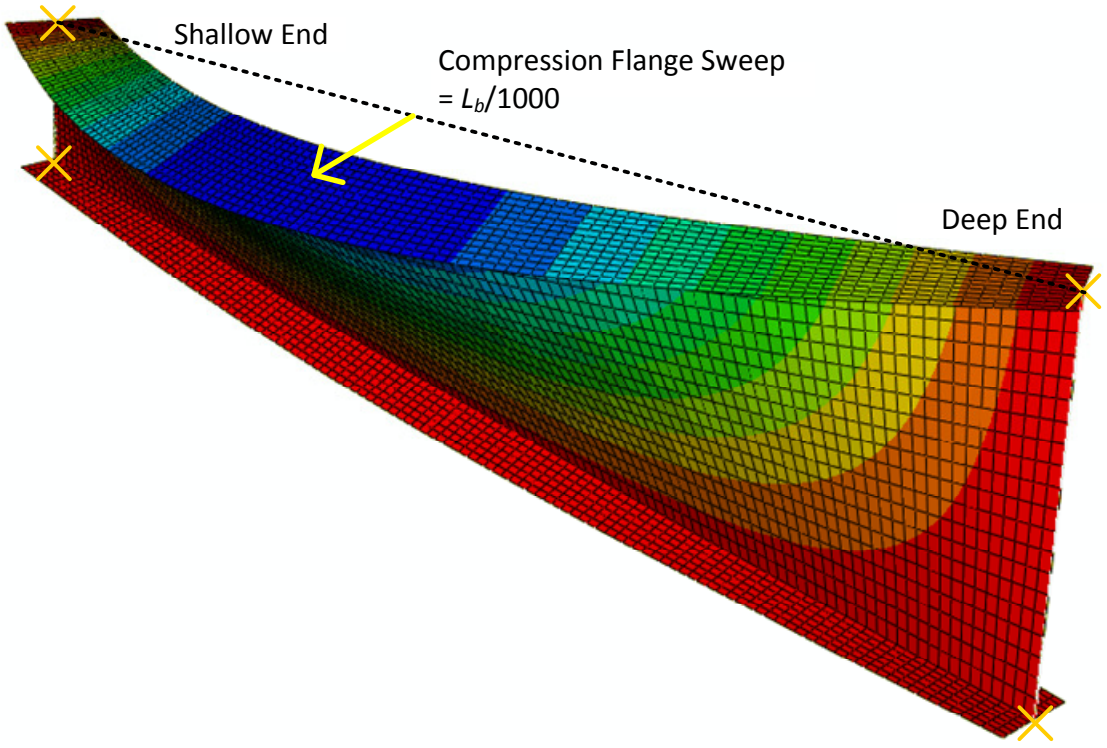

Figure 5.4. Typical geometric imperfection shape

5.5 Material Properties

Figure 5.5 shows a typical stress-strain curve for a yield strength F_y of 55 ksi, which is used in the virtual test simulations. For the material with F_y = 55 ksi, a ultimate strength F_u of 70 ksi is assumed based on the minimum ultimate strength for the A572 Grade 55 material. In addition, it is assumed that the strain hardening strain ε_{st} is ten times the yield strain and the strain hardening modulus E_{st} is 700 ksi. The strain hardening strength F_{st} is calculated as

$$F_{st} = F_y + 2/3(F_u - F_y) = 55 + 2/3(70\text{-}55) = 65 \text{ ksi} \quad \text{(Eq. 5. 1)}$$

The engineering strain at the ultimate strength ε_u is calculated as

$$\varepsilon_u = 70\varepsilon_y = 70 \times (55/29000) = 0.133 \text{ in/in} \quad \text{(Eq. 5. 2)}$$

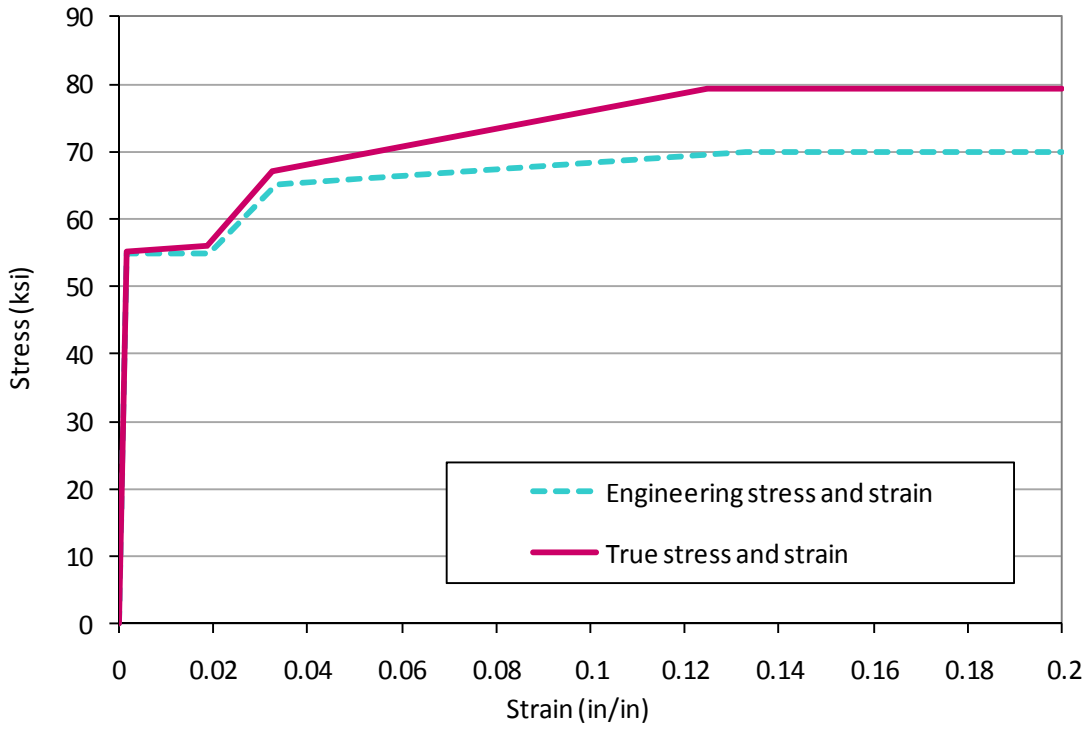

Figure 5.5. Typical stress-strain curve (F_y = 55 ksi).

Because the four-node shell element used in this study (S4R) is a general large strain formulation, the material properties in the finite element models should be based on the true stress-strain curve. From the engineering stress-strain curve generated as discussed above, the true stress-strain curve is obtained using Eq. 5.3 and 5.4.

$$\sigma_{true} = \sigma_{eng} \times (1 + \varepsilon_{eng}) \quad \text{(Eq. 5. 3)}$$

$$\varepsilon_{true} = \ln(1 + \varepsilon_{eng}) \quad \text{(Eq. 5. 4)}$$

At the ultimate strength, the values of σ_{true} and ε_{true} are 79.3 ksi and 0.125 in/in. It is assumed that the ultimate stress of 79.3 ksi remains constant for $\varepsilon_{true} > 0.125$ in/in as shown in Figure 5.5.

CHAPTER VI

EVALUATION OF MEMBER RESISTANCE EQUATIONS USING EXPERIMENTAL TEST DATA

In this chapter, the recommended extensions of AISC (2010) developed in Chapter 3 are evaluated using experimental test data. Furthermore, the virtual test simulation procedures developed in Chapter 5 are evaluated by conducting virtual test simulations of prismatic and tapered members used in physical tests. The first part of the chapter discusses the virtual test simulation results of the prismatic member tests. The effect of the residual stress patterns and geometric imperfections is addressed. The second part of the chapter discusses the virtual test simulation results of the tapered member tests. For the selected tapered tests, the member resistances are calculated based on the procedures developed in Chapter 3. These resistance calculations are then compared with the experimental test and virtual test simulation results.

6.1 Prismatic Member Tests

6.1.1 Test Configurations for Selected Experiments

6.1.1.1 Dux and Kitipornchai (1983) and Wong-Chung and Kitipornchai (1987)

Dux and Kitipornchai (1983) tested nine simply-supported prismatic beams with three different configurations. Figure 6.1 shows the test configurations of nine specimens. For each configuration, three beams with different lengths are tested. Case (a) is three-point bending test generates a moment-gradient factor C_b = 1.75 for both unbraced lengths A-B and B-C. Cases (b) and (c) are four point bending tests with the middle unbraced lengths B-C in the uniform-bending or moment-gradient condition respectively. For the middle segment of Case (c), the value of C_b is 1.16. It should noted that these C_b

values are calculated using the C_b equation in the commentary for Chapter F in AISC (2010). Table 6.1 shows the dimensions of the test specimens. It should be noted that all the test members have compact flanges and compact webs in flexure. In this study, one specimen of each test configuration is analyzed by the virtual test simulations. The selected test cases are highlighted in Table 6.1 (Tests 3, 6, and 9).

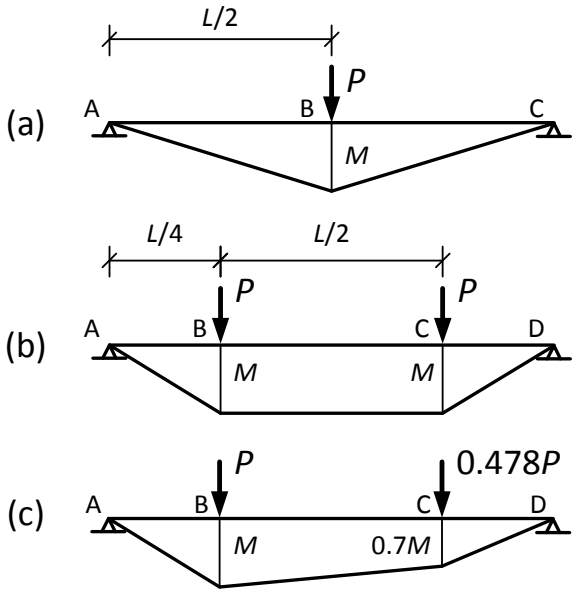

Figure 6.1. Test configurations (Dux and Kitipornchai 1983).

Table 6.1. Section dimensions (Dux and Kitipornchai 1983).

Test Configuration	Test No.	h (in)	t_w (in)	b_{fc} (in)	t_{fc} (in)	b_{ft} (in)	t_{ft} (in)	L (in)	L_b (in)
(a)	1	9.67	0.26	5.80	0.42	5.86	0.42	433	217
	2	9.67	0.27	5.80	0.42	5.86	0.42	354	177
	3	9.67	0.26	5.86	0.42	5.84	0.41	315	157
(b)	4	9.67	0.26	5.86	0.42	5.84	0.41	236	118
	5	9.67	0.27	5.81	0.43	5.82	0.41	197	98
	6	9.67	0.27	5.82	0.41	5.81	0.43	276	138
(c)	7	9.67	0.27	5.82	0.41	5.81	0.43	276	138
	8	9.67	0.27	5.81	0.42	5.82	0.41	315	157
	9	9.67	0.27	5.81	0.43	5.82	0.41	354	177

Wong-Chung and Kitipornchai (1987) conducted four-point bending tests using eleven prismatic beams. Figure 6.2 and Table 6.2 show the typical configuration and the dimensions of the tests. As shown in Table 6.2, there are three groups of tests which have the same nominal geometry but different bracing conditions for the partial brace at the middle of the segment B-D: no brace, lateral brace on the tension flange, lateral braced at the shear center, and rotational brace. It should be noted that the support and loading points are fully braced by restraining the lateral displacement as well as the twisting. Wong-Chung and Kitipornchai (1987) concluded that the lateral brace placed at the shear center and the rotational brace are fully effective while the lateral brace placed at the tension flange has practically no effect so the inelastic LTB strength of the middle segment is essentially same as the test specimen without any intermediate bracing. In this study, two test specimens from each group are selected for the virtual test simulations: the test specimens with no intermediate brace and with a lateral brace at the tension flange. The selected tests are highlighted in Table 6.2 (Tests 1, 2, 5, 6, 9, and 10). It should be noted that the lateral braces at the tension flange are not modeled in the virtual test simulations of Tests 2, 6, and 10 based on the conclusion of Wong-Chung and Kitipornchai (1987). In this way, the complexity of modeling the intermediate partial braces in the virtual test simulations is removed. Therefore, the evaluation of the general procedures of the virtual test simulations becomes more straightforward.

6.1.1.2 Richter (1998)

Richter (1998) conducted the four-point bending tests using a total of 29 beams. Figure 6.3 shows the typical configuration of these tests. With this test set-up,

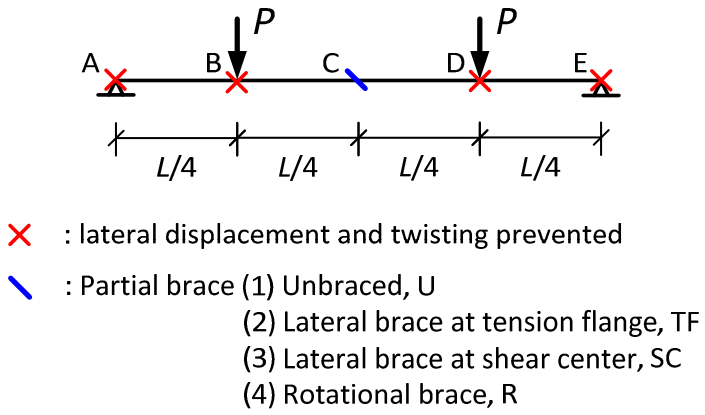

Figure 6.2. Test configuration (Wong-Chung and Kitipornchai 1987).

Table 6.2. Section dimensions (Wong-Chung and Kitipornchai 1987).

Test No.	Test Configuration	h (in)	t_w (in)	b_{fc} (in)	t_{fc} (in)	b_{ft} (in)	t_{ft} (in)	L (in)	L_b (in)
1	U	9.23	0.26	5.73	0.43	5.72	0.43	441	220
2	TF	9.23	0.27	5.70	0.43	5.76	0.43	441	220
3	SC	9.23	0.26	5.76	0.43	5.72	0.43	441	110
4	R	9.23	0.26	5.76	0.43	5.70	0.43	441	110
5	U	9.23	0.26	5.69	0.43	5.76	0.43	354	177
6	TF	9.29	0.26	5.77	0.43	5.76	0.43	354	177
7	SC	9.23	0.25	5.74	0.42	5.72	0.43	354	89
8	R	9.23	0.25	5.74	0.42	5.74	0.43	354	89
9	U	9.23	0.26	5.74	0.43	5.75	0.42	276	138
10	TF	9.22	0.26	5.69	0.43	5.74	0.43	276	138
11	SC	9.23	0.26	5.72	0.43	5.74	0.43	276	69

the middle segment B-C is always under uniform bending. In the base test set-up, the middle segment B-C is 300 inch long so that the elastic LTB governs the segment. Once the base test set-up is installed, the unbraced lengths within the segment B-C are varied by adding equally-spaced intermediate bracings on the compression flange (see Figure 6.3). The unbraced length of 37.5 inches is less than the plastic limit of the unbraced length L_p. With longer unbraced lengths, the segment B-C is governed by inelastic LTB.

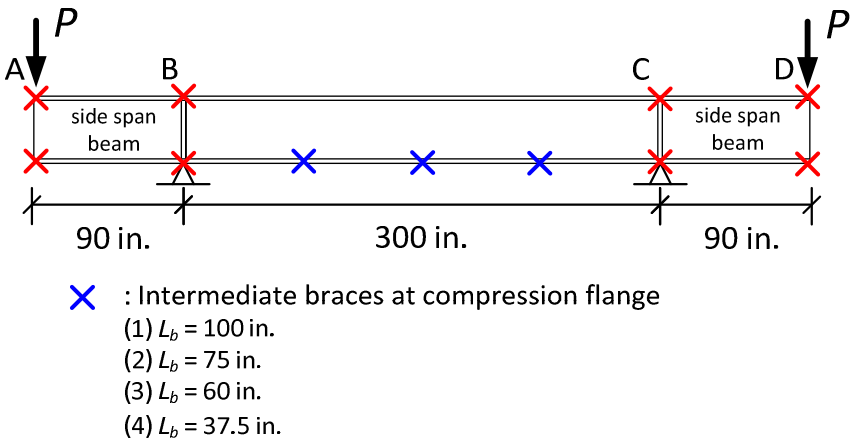

Figure 6.3. Test configuration (Richter 1988).

Table 6.3. Section dimensions (Richter 1988).

Test No.	h (in)	t_w (in)	b_{fc} (in)	t_{fc} (in)	b_{ft} (in)	t_{ft} (in)	L (in)	L_b (in)	Web slenderness
5	18.0	0.16	4.99	0.31	4.96	0.31	300	38	noncompact
6	18.0	0.16	4.98	0.31	4.99	0.32	300	60	
7	18.0	0.16	4.98	0.31	4.96	0.31	300	60	
8	17.9	0.16	4.98	0.31	4.98	0.31	300	75	
9	18.0	0.16	4.98	0.31	4.99	0.31	300	100	
10	17.9	0.16	4.95	0.31	4.97	0.31	300	100	
11	24.0	0.16	4.98	0.31	4.98	0.31	300	38	slender
12	24.0	0.16	4.99	0.31	5.00	0.31	300	60	
13	24.0	0.16	4.98	0.31	4.98	0.31	300	60	
14	23.9	0.16	4.97	0.31	4.96	0.32	300	75	
15	24.0	0.16	4.96	0.31	4.96	0.31	300	75	
16	24.0	0.16	4.98	0.31	4.98	0.31	300	100	

Richter (1998) tested a wide range of flange and web slenderness: compact and noncompact flanges, and compact, noncompact, and slender webs. In this study, the test cases with compact flanges and noncompact and slender webs are considered. These test cases are selected because members with noncompact and slender webs are more common in the metal building frames than compact-section members. Table 6.3 shows

the dimensions of the selected test beams. The test cases selected for full nonlinear virtual test simulations are highlighted in Table 6.3.

6.1.1.3 Schilling (1985) and Schilling and Morcos (1988)

Schilling (1985) and Schilling and Morcos (1988) conducted three-point bending tests using three beams each. Figure 6.4 shows the typical test configuration. All three beams in Schilling (1985) have noncompact flanges and slender webs. The test beams in Schilling and Morcos (1988), Tests S, M, and D have compact flanges and compact, noncompact, and slender webs respectively. Table 6.4 shows the section dimensions and the yield strengths for all the test beams. It should be noted that the inelastic LTB governs for all the cases and the value of the moment gradient factor C_b is 1.75 based on the C_b equation in the commentary in AISC (2010). Because of the large C_b value, the AISC (2010) resistances for all the test beams from Schilling (1985) and Schilling and Morcos (1988) are the plateau strengths. In this study, the virtual test simulations are conducted for all the test beams shown in Table 6.4. .

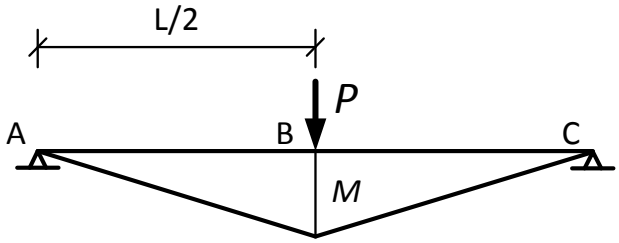

Figure 6.4. Test configuration (Schilling 1985 and Schilling and Morcos 1988).

Table 6.4. Section dimensions and properties
(Schilling 1985 and Schilling and Morcos 1988).

	Test No.	h (in)	t_w (in)	b_{fc} (in)	t_{fc} (in)	b_{ft} (in)	t_{ft} (in)	L (in)	L_b (in)	F_{yc} (ksi)	F_{yt} (ksi)	F_{yw} (ksi)
Schilling (1985)	US	17.0	0.21	6.97	0.52	6.97	0.52	144	72	58.8	58.8	56.2
	UL	24.0	0.20	6.96	0.53	6.96	0.53	156	78	58.8	58.8	56.2
	SL	30.4	0.20	6.92	0.53	6.92	0.53	168	84	58.8	58.8	56.2
Schilling and Morcos (1988)	S	23.5	0.21	5.00	0.28	13.31	0.28	144	72	59.4	59.4	65.2
	M	23.5	0.21	9.00	0.49	13.66	0.49	156	78	58.2	58.2	65.2
	D	36.0	0.21	12.25	0.62	12.25	0.62	168	84	49.6	49.6	65.2

6.1.2 Virtual Simulation of the Tests

6.1.2.1 Load and Displacement Boundary Conditions

The basic procedures to model the experimental tests considered in this chapter are the same as described in Chapter 5. All the cross-section components are modeled with four-node shell elements. For these test cases, it is not necessary to enforce the beam kinematics at the ends in the virtual test models since the test beams are not subject to the end moment loadings. At all the locations where the test beams are fully braced, the lateral displacement at the top and bottom web-flange juncture nodes is restrained. For the intermediate braces in the tests by Richter (1988), only the web-flange juncture nodes of the compression flange are laterally restrained.

6.1.2.2 Residual Stress Patterns

Dux and Kitipornchai (1983) and Wong-Chung and Kitipornchai (1987) provide the detailed information about the measured residual stresses of their test beams. In the virtual test simulations of these tests, the measured residual stresses are applied. Because the measured residual stresses are known, the tests by Dux and Kitipornchai (1983) and Wong-Chung and Kitipornchai (1987) are the best cases to study the effect of the different residual stress pattern by comparing the experimental test and the virtual test

simulation results. Therefore in this study, a several residual stress pattern is applied to Test 6 from Dux and Kitipornchai (1983) and all the selected test cases from Wong-Chung and Kitipornchai (1987) to evaluate the virtual test simulation procedures as well as the effect of the different residual stress patterns. Only the tests with the middle segments under uniform bending are selected. This is because otherwise, it can be difficult to distinguish the moment-gradient effect and the residual stress effect from the virtual test simulations. The selected residual stress patterns are as follows:

(a) The measured residual stresses reported by Dux and Kitipornchai (1983) and Wong-Chung and Kitipornchai (1987),

(b) The Lehigh residual stress pattern (Galambos and Ketter 1959),

(c) The residual stress pattern suggested by Essa and Kennedy (2000),

(d) The best-fit Prawel residual stress pattern shown in Chapter 5.

Each residual stress pattern is discussed subsequently.

Measured residual stresses (Dux and Kitipornchai 1983 and Wong-Chung and Kitipornchai 1987). Dux and Kitipornchai (1983) and Wong-Chung and Kitipornchai (1987) reported the mean values of the residual stresses at each point where the residual stresses are measured within a cross section. Based on the mean values, a residual stress pattern for each test case is developed such that the sum of the forces is zero and the residual stress pattern is symmetric about the center of each cross-section component. Figure 6.5 shows the residual stress pattern for Test 6 in Dux and Kitipornchai (1983). The residual stress patterns for other test cases are very similar to the one shown in

Figure 6.5. The measured residual stresses show that the flanges are mostly in tension whereas the web is mostly in compression.

Lehigh residual stress (Galambos and Ketter 1959). Galambos and Ketter (1959) recommend the residual stress pattern shown in Figure 6.6 for the rolled sections. This pattern has the compressive stress of $0.3F_y$ at the tips of the flanges and a small tensile stress at the web-flange juncture. In this residual stress pattern, the web is entirely in tension with the same tensile stress as the web-flange junctures of the flanges.

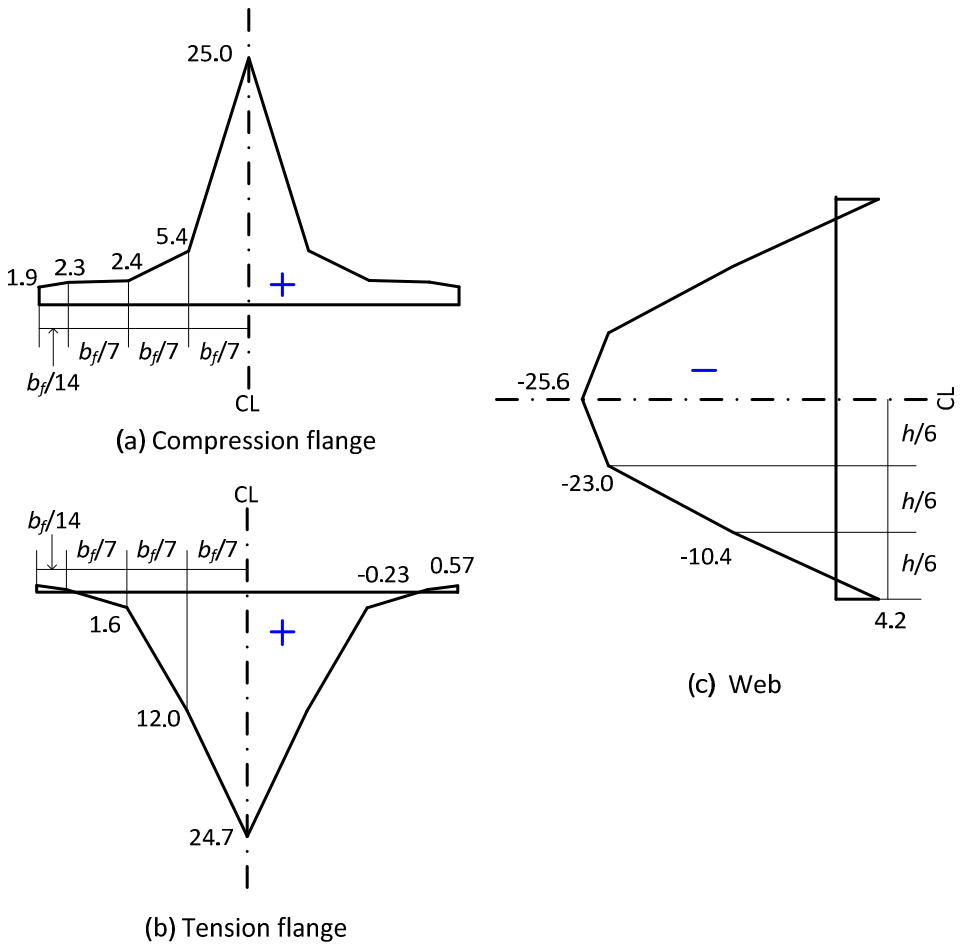

Figure 6.5. Residual stress pattern for Test 6 (Dux and Kitipornchai 1983).

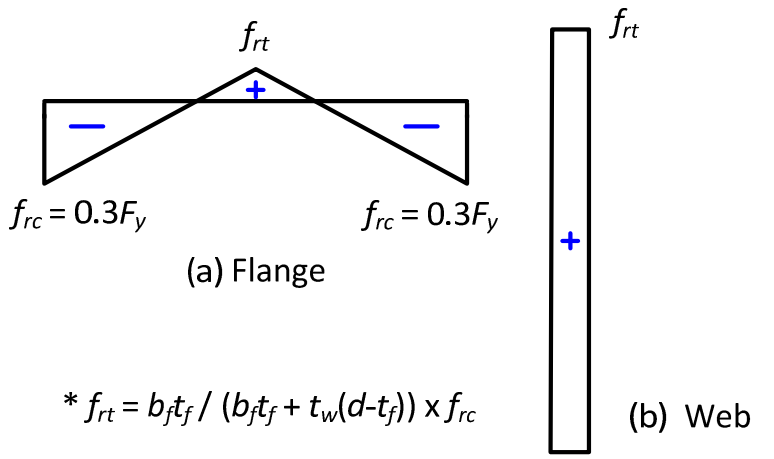

Figure 6.6. Lehigh residual stress pattern (Galambos and Ketter 1959).

Essa and Kennedy (2000) residual stress. Figure 6.7 shows the residual stress pattern suggested by Essa and Kennedy (2000) for hot-rolled I-section columns. One can see that this residual stress pattern cannot be applied to the I-sections with $t_w(d - t_f)/(b_f t_f) > 1.33$. Otherwise, the tensile stress at the quarter points of the flanges becomes larger than the tensile stress at the flange tips ($0.3F_y$). The tests by Dux and Kitipornchai (1983) and Wong-Chung and Kitipornchai (1987) satisfy the limit of $t_w(d - t_f)/(b_f t_f) \leq 1.33$. Even though this residual stress pattern is recommended for columns, it is useful to study how much the LTB strength is affected if more optimistic residual stress pattern is used.

Best-fit Prawel residual stress. The best-fit Prawel residual stress pattern shown in Section 5.3 is developed in this research for welded I-section members. The reader is referred to Section 6. 2.3. By applying this pattern to the tests from Dux and Kitipornchai (1983) and Wong-Chung and Kitipornchai (1987), the different effect from the residual stress patterns for rolled and welded-sections can be studied. The AISC (2010) provisions provide one LTB design curve for both rolled and welded I-section members. Conversely, the CEN (2005) provisions suggest four different design curves

for rolled and welded I-section members with $h/b_{fc} \leq 2$ and $h/b_{fc} > 2$. This is discussed in the subsequent section. For the tests by Richter (1998), Schilling (1985), and Schilling and Morcos (1988), the information about the measured residual stress is unknown. Therefore, the best-fit Prawel residual stress pattern is applied for these tests.

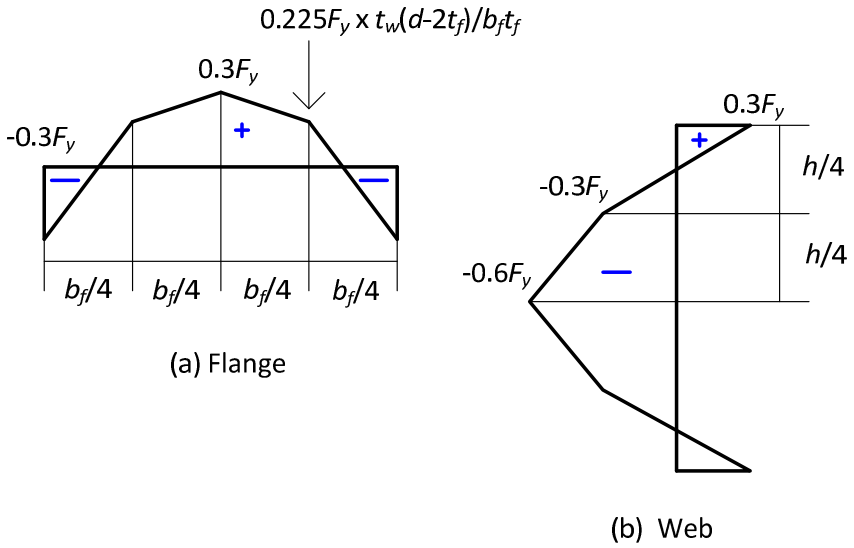

Figure 6.7. Essa and Kennedy (2000) residual stress pattern.

6.1.2.3 Imperfection Shape and Amplitude

For all the selected tests, the imperfection shapes are generated based on the procedures described in Chapter 5. In all the cases, the maximum imperfection is applied in the most critical segments with the maximum magnitude of $L_b/1000$. For the tests from Richter (1998) with several unbraced lengths, the one of the middle unbraced length has the maximum imperfection. Figure 6.8 shows the imperfection shape of Test 14 from Richter (1998). Dux and Kitipornchai (1983) and Wong-Chung and Kitipornchai (1987) provide the measured values of the initial out-of-straightness of the beams as well as the

initial twist in the cross section. For the sake of the simplicity in the modeling, all the imperfection shapes of these tests are generated as described above. Figure 6.9 shows the imperfection shape of Test 6 from Wong-Chung and Kitipornchai (1987). For the virtual test simulations conducted with the measured residual stresses, the maximum imperfection magnitude of the measured out-of-straightness of the test beams is applied. The results of these simulations are compared with the virtual test simulations conducted with the maximum imperfection magnitude of $L_b/1000$. For all the simulations conducted using residual stresses other than the measured residual stresses, the maximum imperfection magnitude of $L_b/1000$ is used.

6.1.2.4 Material Properties

Dux and Kitipornchai (1983) and Wong-Chung and Kitipornchai (1987) provide the mean values for the yield stress of flanges F_{yf} and the web F_{yw} and the young's modulus from a total of 25 tension coupons, 17 from the flanges and 8 from the webs. Richter (1998) also provides a set of the yield strength of the web and flanges for each shipment of the test beams. All the selected test beams shown in Table 6.3 are from one shipment. Table 6.5 shows the yield strengths for the flanges and the web of the selected test members of Dux and Kitipornchai (1983), Wong-Chung and Kitipornchai (1987), and Richter (1998). For these selected tests, the yield strengths shown in Table 6.5 are used in the virtual test simulations. Schilling (1985) and Schilling and Morcos (1988) reported the yield strengths of the flanges and the webs for each test case (see Table 6.4). In the virtual test simulations, the measured yield strength of each test case is applied for the tests conducted by Schilling (1985) and Schilling and Morcos (1988). The measurement of the young's modulus is provided only by Dux and Kitipornchai (1983)

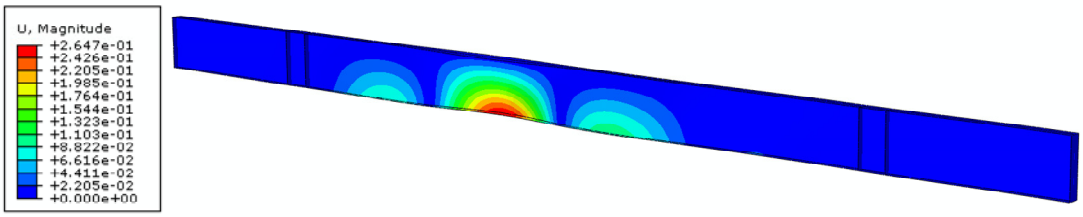

Figure 6.8. Imperfection shape of Test 14 (Richter 1998, deformation scale factor = 20).

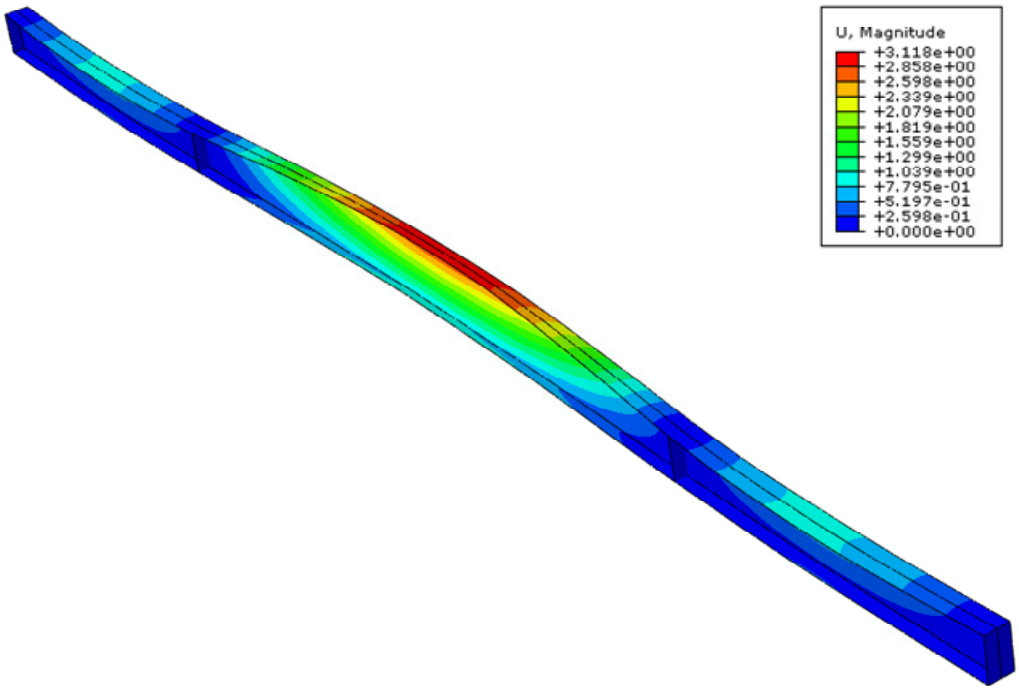

Figure 6.9. Imperfection shape of Test 6 (Wong-Chung and Kitipornchai 1987, deformation scale factor = 2).

Table 6.5. Summary of yield strengths.

Test	F_{yc} *(ksi)*	F_{yt} *(ksi)*	F_{yw} *(ksi)*
Dux and Kitipornchai (1983)	41.3	41.3	46.6
Wong-Chung and Kitipornchai (1987)	42.5	42.5	47.4
Richter (1998)	48.4	48.7	52.5

and Wong-Chung and Kitipornchai (1987). This information is unknown for all the other selected test members. Therefore, all the virtual test simulations are conducted assuming the young's modulus of 29000 ksi.

The true stress-strain curves used in the virtual test simulations are generated in the way described in Section 5.5. The ABAQUS S4R shell element is a large strain formulation, capable of handling large strain effects to whatever extent is required by the physical structure being analyzed. Therefore, the true stress-strain response is the appropriate material description to be input to ABAQUS. Figure 6.10 shows the stress-strain curves for F_y = 41.3 ksi for the tests by Dux and Kitipornchai (1983).

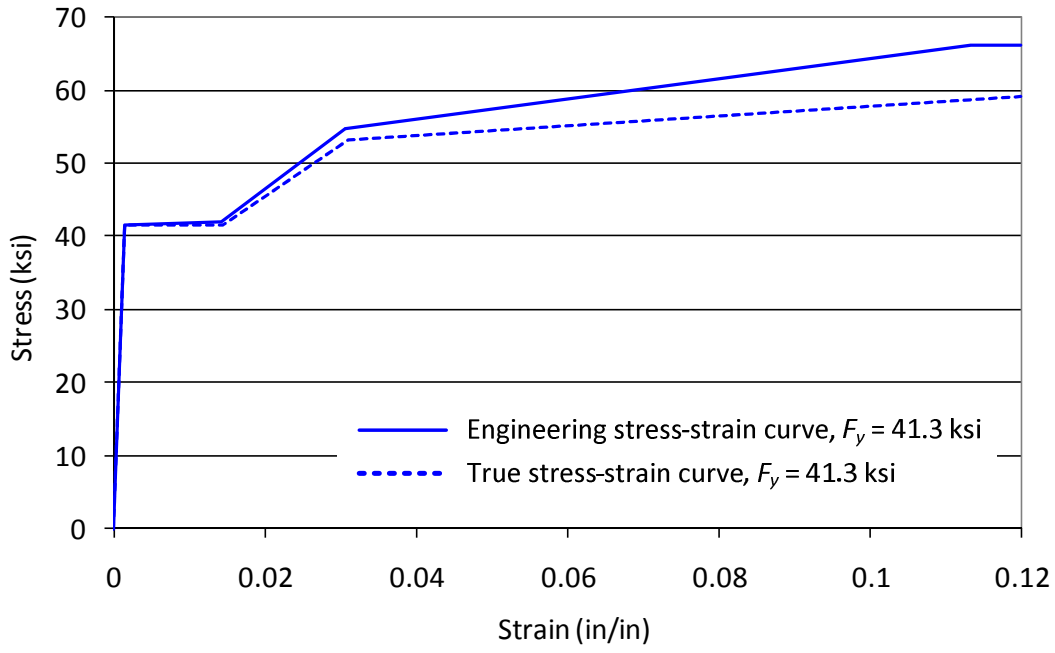

Figure 6.10. Stress-strain curve for F_y = 41.33 ksi (Dux and Kitipornchai 1983).

6.1.3 Assessment of Results

6.1.3.1 Dux and Kitipornchai (1983) and Wong-Chung and Kitipornchai (1987)

Figure 6.11 shows the experimental results of the four-point bending tests where the middle segment B-C is under uniform bending: Tests 4 to 6 in Dux and Kitipornchai (1983) and all the selected test cases in Wong-Chung and Kitipornchai (1987). In the same plot, the virtual test simulation results of the selected tests as well as the LTB resistance curves based on AISC (2010) and CEN (2005) are shown. As mentioned above, the virtual test simulations are conducted for Test 6 in Dux and Kitipornchai (1983) and Tests 1, 2, 5, 6, 9, and 10 in Wong-Chung and Kitipornchai (1987). In this plot, the ordinate is a normalized flexural strength M/M_{yc} and the abscissa is a normalized flange stress term, $(F_y/F_e)^{0.5}$.

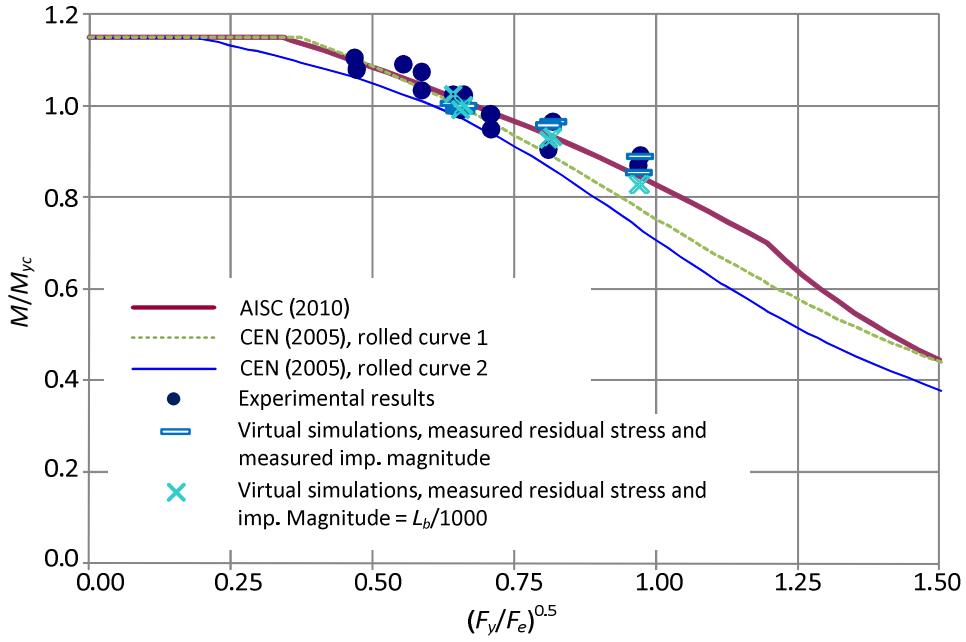

Figure 6.11. The virtual simulation results with measured residual stresses and different imperfection magnitude
(Dux and Kitipornchai 1983 and Wong-Chung and Kitipornchai 1987).

It should be noted that the AISC (2010) curve is slightly convex within the inelastic LTB range. This occurs when a linear inelastic LTB curve based on unbraced lengths is converted to an inelastic LTB curve based on a normalized flange stress term $(F_y/F_e)^{0.5}$ for members with $J \neq 0$. For members with $J = 0$, an inelastic LTB curve remains linear either with L_b or $(F_y/F_e)^{0.5}$.

The CEN (2005) provisions suggest four different design curves for "general rolled and welded I-sections" with $h/b_{fc} \leq 2$ and $h/b_{fc} > 2$. The most optimistic curve is used for rolled I-sections with $h/b_{fc} \leq 2$ and the most conservative curve is used for welded I-sections with $h/b_{fc} > 2$. The CEN (2005) rolled curve 2 shown in Figure 6.12 is the LTB curve for general rolled I-section with $h/b_{fc} \leq 2$. In addition, the CEN (2005) provisions provide a second set of resistance curves for "rolled and equivalent welded I-sections" with $h/b_{fc} \leq 2$ and $h/b_{fc} > 2$. This second set of the LTB resistance curves is more optimistic by providing a longer plateau length and larger LTB resistances for the beams under consideration. The CEN (2005) rolled curve 1 in Figure 6.12 is the LTB curve for rolled I-section with $h/b_{fc} \leq 2$. It can be seen that the plateau length of the CEN (2005) rolled curve 1 is essentially same as the one of the AISC (2010) resistance curve. The range of the rolled I-sections for which the CEN (2005) rolled curve 1 cannot be applied is not clearly defined in CEN (2005). In this study, it is assumed that both CEN (2005) resistance curves for rolled I-section can be applied for all the rolled I-sections specified in AISC (2010). For welded I-sections, however, only the CEN (2005) resistance curve for "general welded I-sections" is considered in this study.

In Figure 6.11, all the virtual test results are obtained using the measured residual stresses but the maximum imperfection magnitude is varied. One set of the virtual test

simulations is conducted using the measured maximum imperfection magnitude reported for each test beam (see Table 6.1 and 6.2). The other set of virtual test simulation is conducted using a magnitude of L_b/1000. It is observed that using the "actual" information about the residual stresses and the geometric imperfections, the virtual test simulations can estimate the experimental test results very well. The maximum difference between the virtual test simulation and the experimental result is 5.8 % for Test 6. However, for all the other tests, the virtual test simulations can predict the experimental result within 1.0 % in average. This confirms that the general procedures for the virtual test simulations described in Chapter 5 are appropriate.

Figure 6.11 also shows that the different magnitude of the imperfection has small effect on the LTB strengths of the test beams. The smallest imperfection magnitude is measured for Test 2 in Wong-Chung and Kitipornchai (1987): L_b/5000. For this test, the LTB strengths using L_b/1000 is 6.8 % smaller than the LTB strengths using the measured imperfection magnitude (L_b/5000). Therefore, it is decided to use the imperfection magnitude of L_b/1000 for all the virtual test simulations conducted in this study.

Figure 6.12 shows the LTB strengths of the virtual test simulations conducted using an imperfection magnitude of L_b/1000 and different residual stress patterns described above. The experimental results and the LTB resistance curves based on AISC (2010) and CEN (2005) are shown as well. As seen in Figure 6.5, the measured residual stresses show the flanges are mostly in tension and the web is mostly in compression for the rolled-section beams tested by Dux and Kitipornchai (1983) and Wong-Chung and Kitipornchai (1987). The residual stress pattern suggested by Essa and Kennedy (2000) is the closest to the measured residual stress pattern. Therefore it is expected that the

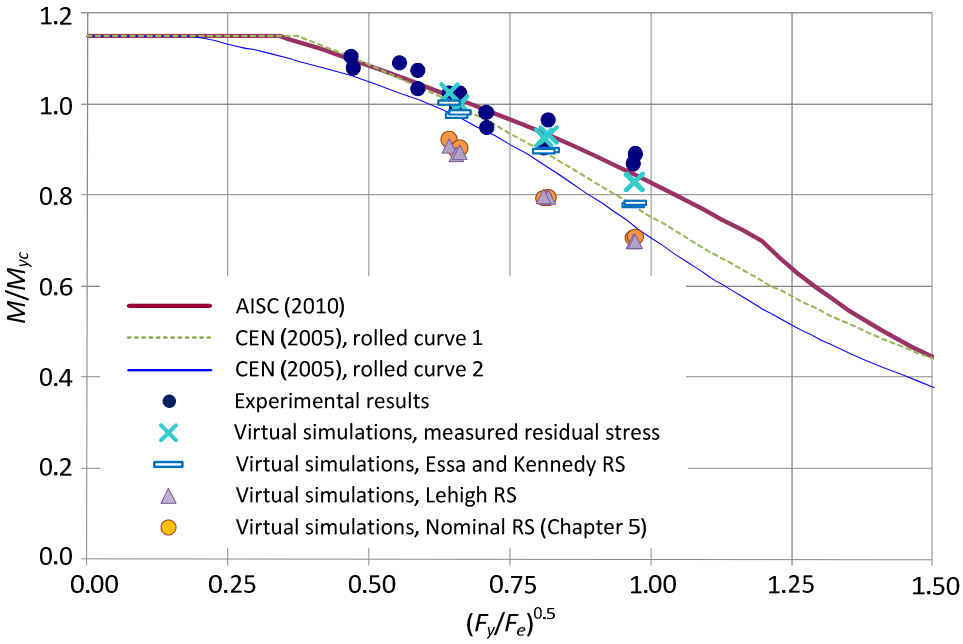

Figure 6.12. The virtual simulation results with imperfection magnitude of $L_b/1000$ and different residual stress patterns (Dux and Kitipornchai 1983 and Wong-Chung and Kitipornchai 1987).

virtual test simulation results obtained using the Essa and Kennedy residual stresses are the closest to the results from the experiments and the virtual simulations using the measured residual stresses. When the Lehigh residual stress pattern (Galambos and Ketter 1959) is used, the LTB strengths from the virtual test simulations are decreased further. The reductions of the LTB strengths due to the use of the Lehigh residual stress pattern are 13.2 % from the results obtained with the measured residual stresses and 10.2 % from the results obtained with the Essa and Kennedy residual stresses.

As mentioned above, the best-fit Prawel residual stress pattern for welded I-sections is also applied to the selected test beams in Dux and Kitipornchai (1983) and Wong-Chung and Kitipornchai (1987). It is important to note that when the best-fit Prawel residual stress pattern for welded I-sections is applied in the virtual test

simulations, the LTB strengths are essentially the same as the ones obtained using the Lehigh residual stress pattern for rolled I-sections. This supports the use of one LTB design curve for both rolled and welded I-sections, as specified in AISC (2010). This is observed in the parametric study discussed in Chapter 7 as well.

Figures 6.13 and 6.14 show the virtual test results of Tests 3 and 9 in Dux and Kitipornchai (1983) respectively. For these tests, the virtual test simulations are conducted using the measured residual stresses and the measured imperfection magnitude. In Figure 6.13, the experimental test results of Tests 1 to 3 are shown. For these tests, the moment gradient factor C_b is 1.75 in AISC (2010). Due to the large moment gradient factor, the inelastic LTB strengths of the test beams 1 and 2 are the plateau strength. In CEN (2005), the moment gradient factor C_1 is applied to the calculation of the elastic LTB stress F_e. This procedure is essentially same as the approach recommended for the calculation of the LTB strengths of the tapered members described in Chapter 3.

In addition to the moment gradient factor C_1, CEN (2005) suggests another factor f, which accounts for nonuniform yielding within the unbraced length. This factor f applies only to the "rolled and equivalent welded I-section" curves. The LTB strengths based on the CEN (2005) rolled curve 1 shown in Figures 6.13 and 6.14 are obtained including the f factor. In Figure 6.14, the experimental results of Tests 7 to 9 in Dux and Kitipornchai (1983) are shown. The moment gradient factor C_b of these tests is 1.16 in AISC (2010) and C_1 is 1.15 in CEN (2005). As seen in Figure 6.11, the virtual simulations provide good estimates of the experimental results for Tests 3 and 9 when the measured residual stresses and imperfection magnitudes are applied.

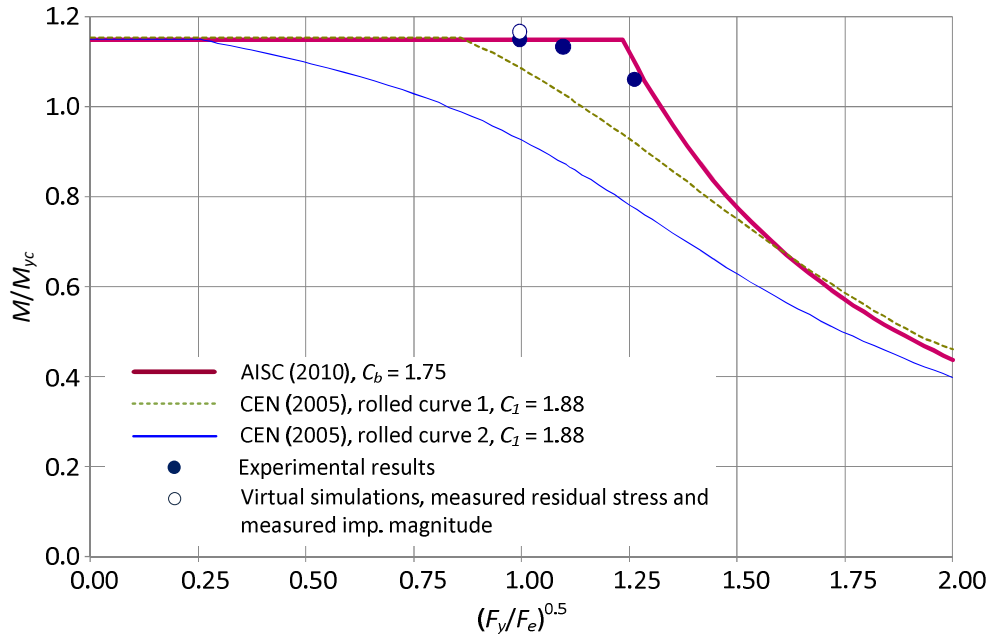

Figure 6.13. The virtual simulation results with measured residual stress and imperfection magnitude (Test 3 in Dux and Kitipornchai 1983).

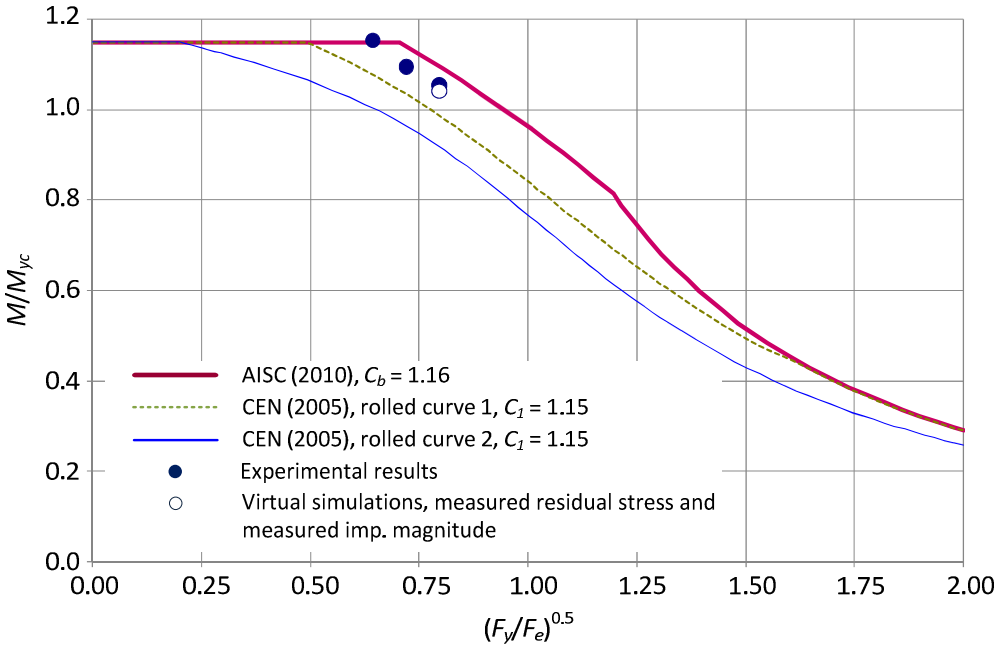

Figure 6.14. The virtual simulation results with measured residual stress and imperfection magnitude (Test 9 in Dux and Kitipornchai 1983).

6.1.3.2 Richter (1998)

Figure 6.15 illustrates the virtual test simulation results of the tests with compact flanges and a noncompact web in Richter (1998). The experimental test results of Tests 5 to 10 as well as the LTB resistance curves based on AISC (2010) and CEN (2005) are also shown. It should be note that Tests 7 and 10 are replicates of Tests 6 and 9 respectively. As discussed above, the virtual test simulations of Tests 5, 6, 8, and 9 are conducted using the best-fit Prawel residual stress pattern and the flange sweep imperfection with a maximum magnitude of $L_b/1000$. For Test 5 with the shortest unbraced length, the virtual test simulation strength is only 2.8 % smaller than the experimental test result.

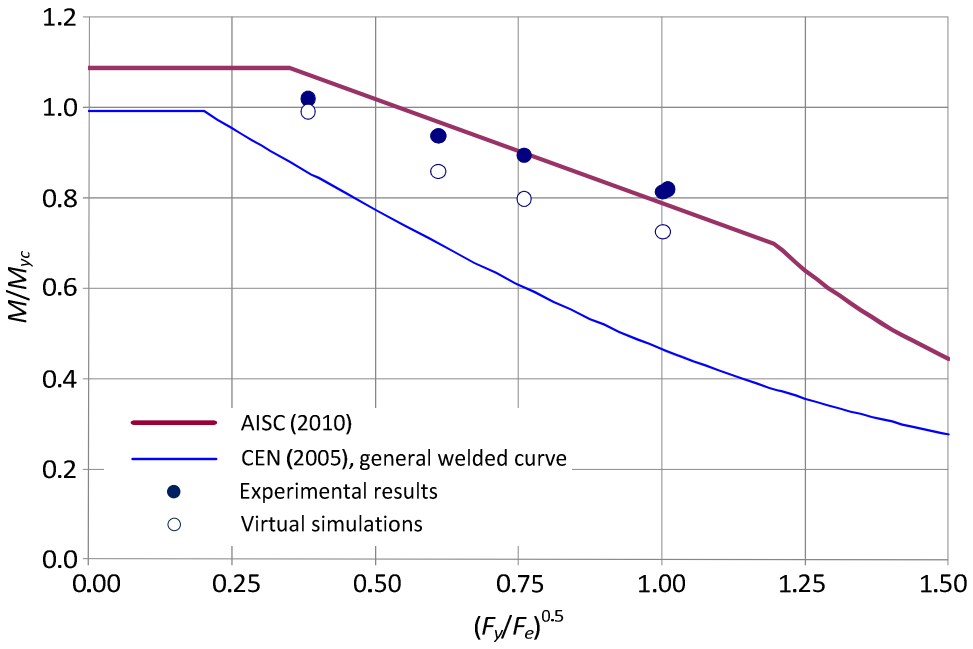

Figure 6.15. The virtual simulation results with best-fit Prawel residual stress and imperfection magnitude of $L_b/1000$, compact-flange and noncompact-web tests (Richter 1998).

The LTB resistance based in AISC (2010) is slightly higher than both the experimental and virtual test strengths for Test 5. For all the other cases shown in Figure 6.15, the experimental test results are very close to the LTB resistances based on AISC (2010). The virtual test simulations of these cases are 10 % smaller than the experimental results in average. In Figure 6.15, the CEN (2005) LTB resistance curve for general welded I-sections is shown. For all the cases with noncompact or slender webs considered in this study, the LTB resistances based on CEN (2005) are most conservative. Most the beams with a noncompact web based on AISC (2010) are categorized as "Class 4" cross-sections in CEN (2005), for which an "effective section modulus" should be determined to get the plateau strength $S_{eff} F_{yc}$. For Tests 5 to 10 in Richter (1998), the effective section modulus is practically same as the section modulus based on the compression flange S_{xc}, which results in the plateau strength of CEN (2005) is close to M_{yc}.

Figure 6.16 shows the virtual test simulation and the experimental test results of compact-flange and slender-web tests in Richter (1998): Tests 11 to 16. It should be noted that Tests 13 and 15 are replicates of Tests 12 and 14 respectively. Similar to the test cases discussed above, the experimental results of Tests 11 to 16 are close to or slightly smaller than the AISC (2010) LTB resistances. It can be seen in Figure 6.16 that the virtual test simulation result of Test 11 ($(F_y/F_e)^{0.5} = 0.4$) is essentially the same as the experimental test result. For Tests 12 to 15 shown in the middle of the inelastic LTB region ($0.6 \leq (F_y/F_e)^{0.5} < 0.8$), the virtual test simulations of Tests 12 and 14 estimate the LTB strengths 8.9 % and 5.8 % smaller than the experimental test results. For Test 16

with the longest unbraced length L_b = 100 in., the virtual test result is 6.8 % smaller than the experimental results.

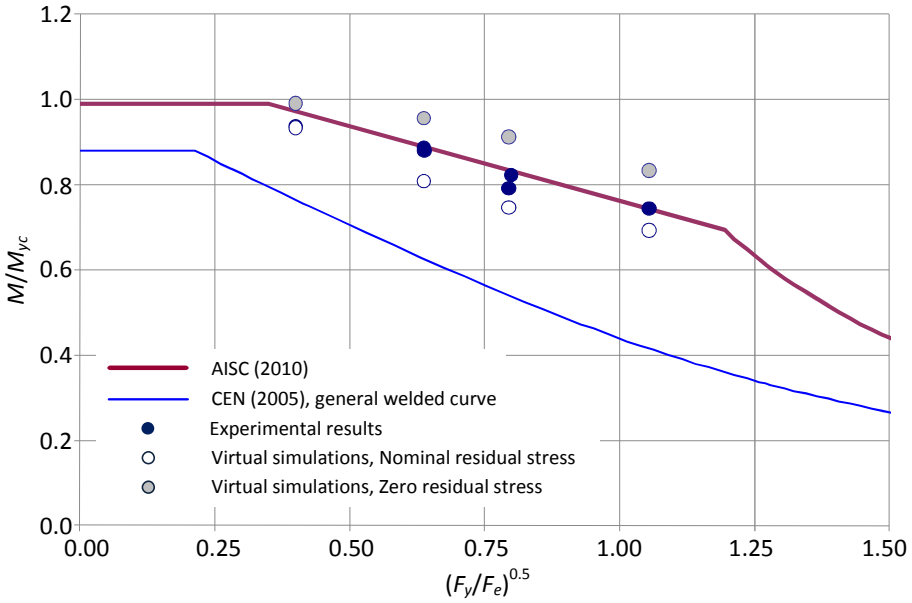

Figure 6.16. The virtual simulation results, compact-flange and slender-web tests (Richter 1998).

Using the test cases considered in Figure 6.16, the effect of the residual stress pattern is examined. Since the measured residual stress information is unknown in Richter (1998), another set of virtual test simulations is conducted with zero residual stresses in the finite element models. The virtual test simulation result with zero residual stress is 10 % larger than the experimental test results in average. It should be noted that the tests conducted by Richter (1998) are one-side welded (determined by personal communication). Therefore, the "actual" residual stresses in the specimens tested in Richter (1998) are somewhat smaller than the best-fit Prawel residual stresses. However, the virtual test simulations with the best-fit Prawel residual stresses provide reasonable estimates of the experimental test results in general.

6.1.3.3 Schilling (1985) and Schilling and Morcos (1988)

As mentioned above, Schilling (1985) conducted three-point bending tests on three noncompact-flange and slender-web beams. Also, Schilling and Morcos (1988) tested three beams with compact flanges and a compact, noncompact, and slender web by three-point bending loading conditions. Figure 6.17 shows the virtual test simulation result of Test D, a doubly-symmetric beam with compact flanges and a slender web considered by Schilling and Morcos (1988). Because the moment gradient factor C_b is large, the AISC (2010) LTB resistances of all the test beams considered in this section are the plateau strengths. Figure 6.17 shows that the virtual test simulation result of Test D is essentially same as the experimental test result. Also the LTB strengths of Test D based on the experimental and virtual tests are slightly higher than the plateau strength of AISC (2010). The plateau strength of CEN (2005) is in essence the same as the one of AISC (2010). However, the plateau length is significantly shorter than AISC (2010), which results in the conservative estimate of the LTB strength for Test D. Table 6.6 shows a summary of M_{exp}/M_{FEA} values for all the tests considered in this section. The average of M_{exp}/M_{FEA} is 0.99. The maximum and minimum values of M_{exp}/M_{FEA} are obtained for Tests S and UL respectively. Test S is a doubly-symmetric beam with compact flanges and a compact web. Test UL is a singly-symmetric beam with noncompact flanges and a slender web.

6.2 Web-Tapered Member Tests

6.2.1 Test Configurations for Selected Experiments

6.2.1.1 Prawel, Morrell, and Lee (1974)

Prawel, Morrell and Lee (1974) tested three beams and 12 beam-columns, each

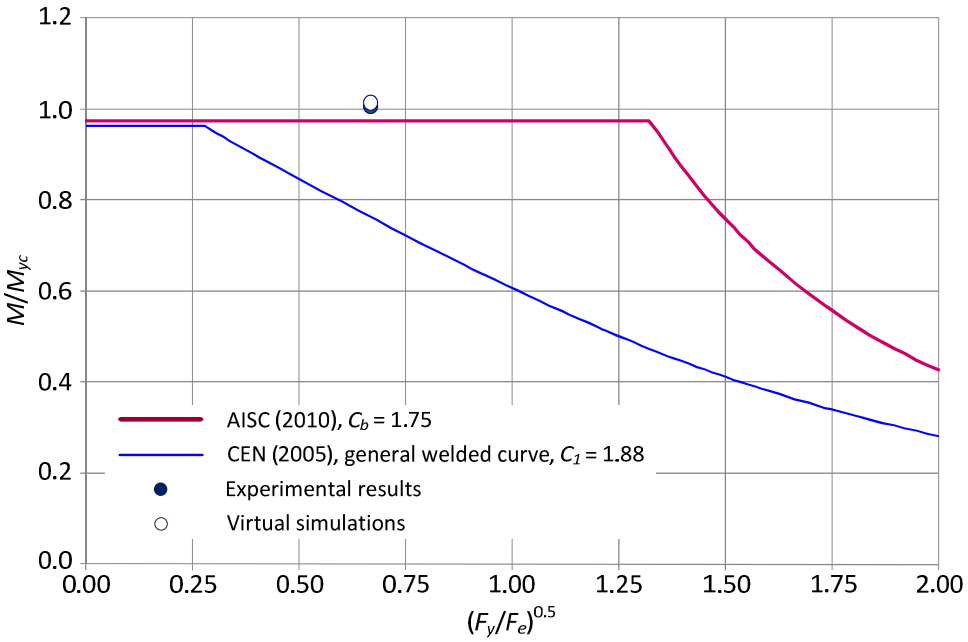

Figure 6.17. The virtual simulation results, Test D (Schilling and Morcos 1988).

Table 6.6. Summary of M_{exp}/M_{FEA} for all the tests in Schilling (1985) an Schilling and Morcos (1988).

Tests		$(F_y/F_{e\,(Cb=1)})^{0.5}$	M_{exp}/M_{yc}	M_{FEA}/M_{yc}	M_{exp}/M_{FEA}
Schilling (1985)	US	0.54	0.95	1.00	0.95
	UL	0.46	0.98	1.07	0.92
	SL	0.45	0.97	1.02	0.95
Schilling and Morcos (1988)	S	0.53	1.21	1.14	1.07
	M	0.60	1.13	1.08	1.05
	D	0.67	1.01	1.01	0.99

having a linearly-tapered web and prismatic flanges. The configuration for the beam tests is shown in Figure 6.18. All these tests are simply-supported doubly-symmetric I-section members. For tests LB-3 and LB-5, the top and bottom flanges are laterally braced at the supports A and D and at the load points B and C. Two vertical loads are applied using $\xi = 0.28$, where ξ is the ratio of the applied load at C to the applied load at B. This ratio of

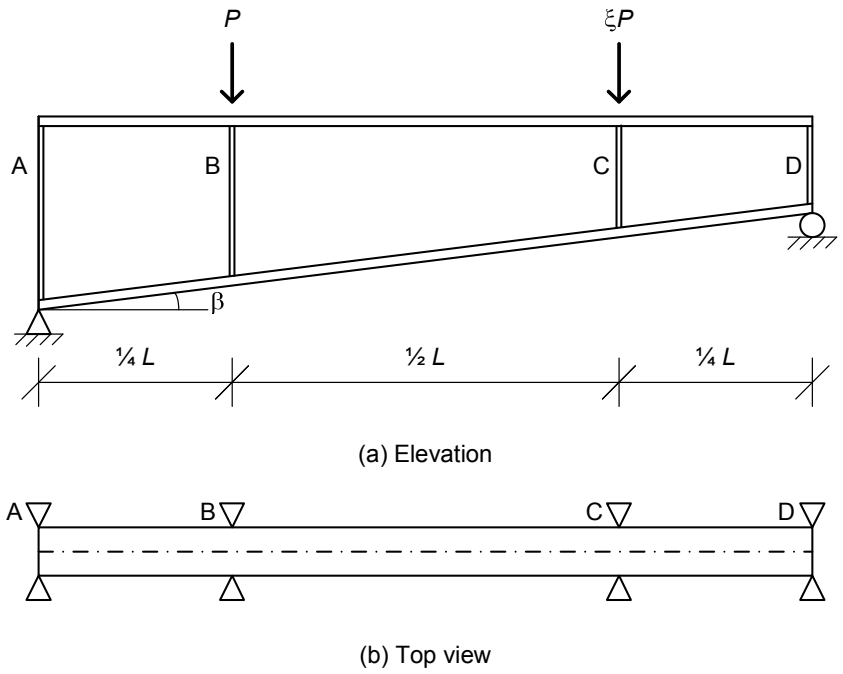

Figure 6.18. Configuration of the beam tests from Prawel et al. (1974)

Table 6.7. Description of the beam tests from Prawel et al. (1974)

Group	Member	Edge Prep.	d_s (in)	d_L (in)	t_w (in)	b_f (in)	t_f (in)	L (in)	β (°)	ξ	h_L/t_w	slenderness
(1)	LB-3	SC	6.0	16.0	0.105	4.0	0.25	144.0	3.97	0.28	147.6	slender
	LB-5	SC	6.0	16.0	0.105	4.0	0.25	96.0	5.95	0.28	147.6	slender
	LB-6	SC	6.0	16.0	0.105	4.0	0.25	96.0	5.95	0.0	147.6	slender

the two loads produces approximately a uniform flange stress in the middle segment B-C. The LB-6 beam is similar to LB-5 except that it has only a single load applied at B (i.e., ξ = 0) and no lateral bracing at C. As a result, the segment B-D of LB-6 has a significant flange stress gradient.

The dimensions of the above test beams are shown along with other pertinent information in Table 6.7. The format of the presentation in this table is repeated subsequently for all the other tests. Also, for the subsequent discussions, these beam tests are categorized as Group (1). The 1st column of Table 6.7 shows whether the plates are

shear cut or oxygen cut. The abbreviation SC denotes shear cut edges for the cross-section plates. All of the beam tests in Group 1 have shear cut edges. Subsequent tables show that some of the plate edges are oxygen cut (denoted by the abbreviation OC).

The terms d_L and d_s in Table 6.7 are the total section depth at the deep and shallow ends of the member, points A and D respectively in Figure 6.18, t_w is the web thickness, b_f and t_f are the flange width and thickness, L is the total beam length, β is the taper angle between the flanges and ξ is the applied load ratio as explained above. The slenderness ratio of the web at the deep end is also shown in the next to last column of the table and the classification of the web in flexure (slender, noncompact or compact) is shown in the last column.

The flanges of the above test beams are compact in flexure, that is, $(b_f/2t_f = 8) < (0.38\sqrt{E/F_y} = 8.97)$ based on $F_y = 52$ ksi, the yield stress indicated by Prawel et al. (1974) for both the flange and the web plates in all of the tests. The web is noncompact in flexure at B $[(h/t_w = 124) < (5.70\sqrt{E/F_y} = 135)]$ and compact in flexure at C $[(h/t_w = 76.2) < (3.76\sqrt{E/F_y} = 88.8)]$ in each of these tests.

Figure 6.19 illustrates the configuration of the beam-column tests from Prawel et al. (1974). All these tests are cantilevers with linearly tapered webs and prismatic flanges. The beam-columns are oriented such that their top flange is inclined at an angle α relative to the horizontal. Both flanges of the beam-columns are laterally braced at the free end of the cantilever (point B) and a single vertical load is applied at the free end. The warping boundary conditions are free and the flanges are free to rotate about a vertical axis at the free end of the cantilever. However, the warping and out-of-plane bending rotations of the flanges are taken as fixed at the fixed end of the cantilever. These tests are

categorized into three groups based on the slenderness classification of the web at the deep end of the member: Group (2) - slender, Group (3) - noncompact and Group (4) - compact.

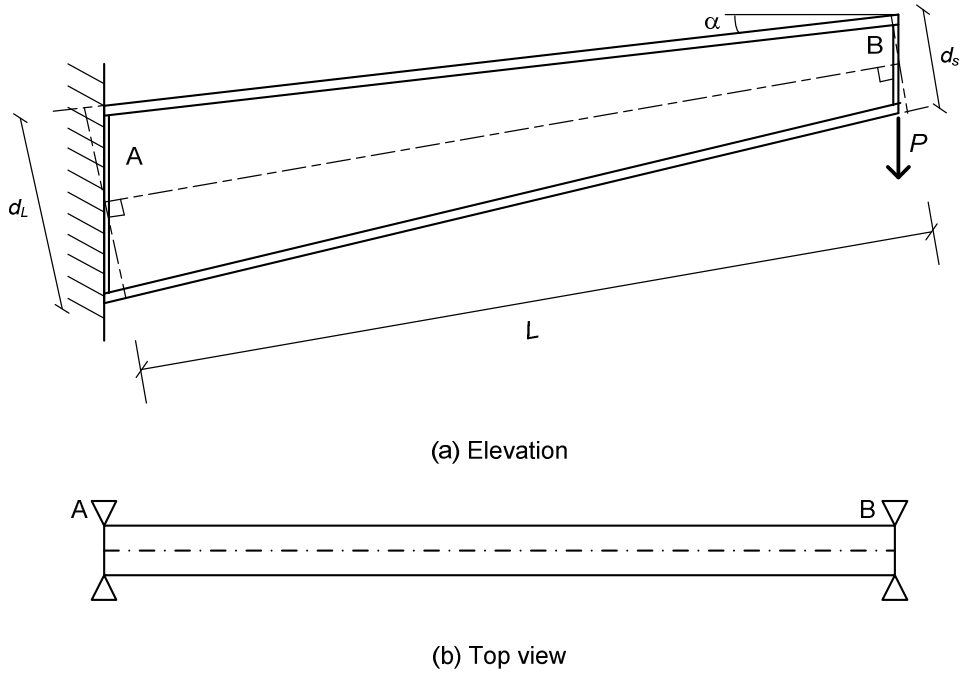

Figure 6.19. Configuration of the beam-column tests from Prawel et al. (1974)

Table 6.8 shows the dimensions and other pertinent information for each of the Prawel et al. (1974) beam-column tests. The section depths and the member lengths are taken perpendicular and parallel to the centroidal axis (see Figure 6.19). Since all the beam-columns are doubly-symmetric, the location of shear center is identical to the centroid and the centroidal axis is straight. There are four different members in each group. In Groups (2) and (4), the tests are collected into two pairs having a different angle of orientation of the top flange $\alpha = 30^o$ and 20^o. Within each of these pairs, the tests differ only in the type of edge preparation for the plates (SC or OC). The four

members in Group (3) each have different values for the inclination angle α varying from 0° to 30°. Also, the cross-section plates are shear cut in two tests and oxygen cut in the other two tests in this group. The flanges are noncompact in flexure [$(0.38\sqrt{E/F_y} = 8.97) < (b_f/2t_f = 12) < (0.95\sqrt{k_cE/F_L})$] based on $F_L = 0.7$ (52 ksi) = 36.4 ksi and given k_c values in all of these beam-column tests. The values of noncompact limit ($0.95\sqrt{k_cE/F_L}$) varies from 15.86 to 20.93 based on k_c = 0.35, 0.39 and 0.55 for Groups (2), (3), and (4) respectively. The slenderness of the web at the deep end of these specimens (point A) is shown in the next to last column of Table 6.8. The noncompact limit of the web in flexure is $h/t_w < 5.70\sqrt{E/F_y} = 134.6$ based on F_y = 52 ksi.

Table 6.8. Description of the beam-column tests from Prawel et al. (1974)

Group	Member	Edge Prep.	α (°)	d_s (in)	d_L (in)	t_w (in)	b_f (in)	t_f (in)	L (in)	β (°)	h_L/t_w	slenderness
(2)	LBC-5	SC	30	6.2	17.5	0.105	6.0	0.25	112.8	5.72	161.9	slender
	LBC-6	OC	30	6.2	17.5	0.105	6.0	0.25	112.8	5.72		
	LBC-10	SC	20	6.1	17.5	0.105	6.0	0.25	114.0	5.71		
	LBC-11	OC	20	6.1	17.5	0.105	6.0	0.25	114.0	5.71		
(3)	LBC-1	SC	0	6.0	11.8	0.105	6.0	0.25	120.0	2.77	107.6	noncompact
	LBC-12	OC	10	6.0	11.8	0.105	6.0	0.25	115.9	2.86		
	LBC-9	SC	20	6.1	11.8	0.105	6.0	0.25	115.4	2.83		
	LBC-4	OC	30	6.1	11.8	0.105	6.0	0.25	114.7	2.84		
(4)	LBC-2	OC	30	6.0	6.0	0.105	6.0	0.25	116.5	0.0	52.4	compact
	LBC-3	SC	30	6.0	6.0	0.105	6.0	0.25	116.5	0.0		
	LBC-7	SC	20	6.0	6.0	0.105	6.0	0.25	116.5	0.0		
	LBC-8	OC	20	6.0	6.0	0.105	6.0	0.25	116.5	0.0		

6.2.1.2 Salter, Anderson, and May (1980)

Eight beam-column tests (C1 through C8) were conducted by Salter et al. (1980). Figure 6.20 shows the configuration of these tests. All the test members are flexurally simply-supported doubly-symmetric I-section members with linearly-tapered webs and prismatic flanges. Also, the flanges are free to rotate about a vertical axis at the ends of

the members. However, the attachments to end fixtures effectively prevent warping of the flanges and torsional rotation of the cross-section at the member ends. The test members are oriented such that their centroidal line is horizontal.

It should be noted that the displacement boundary conditions are applied at 5.51 inches away from the actual ends of the beam in the physical test. An axial force is applied first at the shallow end and then an end moment is applied at the deep end of the members such that the top flange is in flexural compression. Four parameters were varied in these tests: (1) the taper angle β, (2) the ratio of the axial load to the Euler buckling load based on the actual member length P/P_{eL}, (3) the member length L, and (4) intermediate or lack of intermediate lateral bracing.

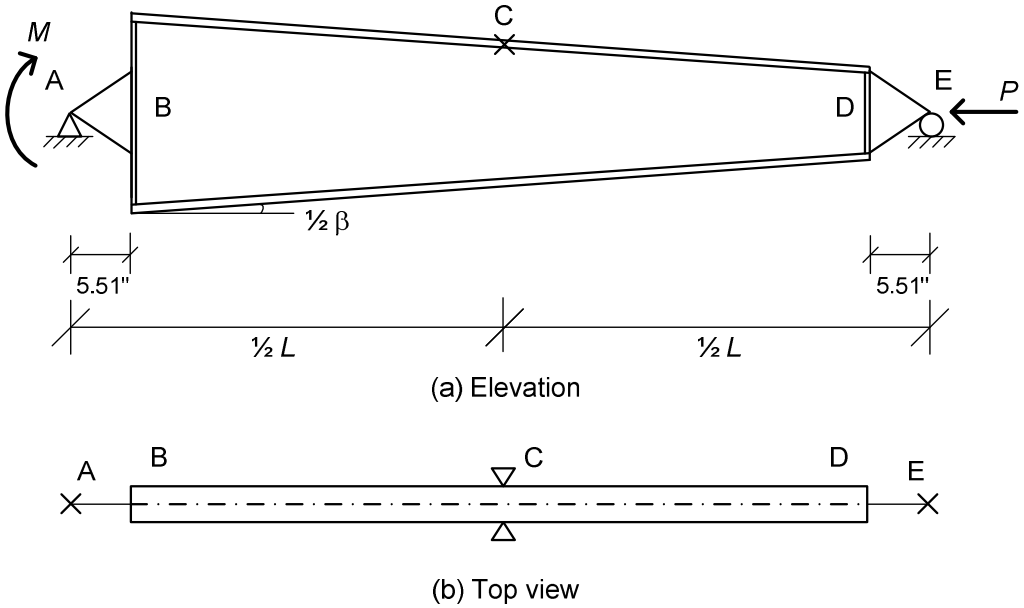

Figure 6.20. Configuration of the beam-column tests from Salter et al. (1980)

Table 6.9 shows the details of the eight beam-columns from Salter et al. (1980). These tests are subdivided into three groups. In each group, the values of β and P/P_{eL} are varied as shown in the table. The Euler buckling load P_{eL} of each member is calculated as

$$P_{eL} = \frac{\pi^2 EI'}{L^2} \qquad \text{(Eq.6.1)}$$

where I' is the moment of inertia of a cross-section located at $0.5L(I_{small}/I_{large})^{0.0732}$ from the smaller end and L is the actual member length. This simplified equation is provided in MBMA/AISC (2010) for the calculation of the Euler buckling load based on the actual member length for linearly-tapered web members. In Table 6.3, the values of P/P_{ys} are also shown, where P_{ys} is the yield strength calculated based on the smallest cross-section and the values of F_y provided by Salter et al. (1980). The members in Groups (1) and (3) have similar longer lengths while the members in the Group (2) have shorter lengths. Members C6 and C7 are similar to members C2 and C3; however, C6 and C7 have an intermediate brace at their tension flange at mid-span. Member C8 is similar to C1 but also has a lateral brace at its compression flange at mid-span. The flanges and the webs are compact in flexure for all the tests in Salter et al. (1980). Salter et al. (1980) provide a single measured value for the initial sweep imperfection in each of these tests, denoted by the symbol δ_o/L in Table 6.9. These values are used subsequently as the amplitude of an overall out-of-plane bow imperfection for the full nonlinear virtual test studies of several of these tests.

6.2.1.3 Shiomi and Kurata (1984)

Shiomi and Kurata (1984) tested 24 doubly-symmetric I-section beam-columns.

Table 6.9. Description of the beam-column tests from Salter et al. (1980).

Group	Member	d_s (in)	d_L (in)	t_w (in)	b_f (in)	t_f (in)	L (in)	β (°)	F_y (ksi)	P/P_{eL}	P/P_{ys}	δ_o/L	h_L/t_w	slenderness
(1)	C1	5.04	11.77	0.19	4.00	0.25	103.23	4.18	47.14	0.022	0.17	1/564	60.52	compact
	C2	4.96	10.89	0.19	4.02	0.25	103.15	3.68	47.14	0.050	0.34	1/718	55.65	compact
	C3	4.90	9.86	0.18	4.02	0.25	103.11	3.08	47.14	0.057	0.34	1/494	50.90	compact
(2)	C4	4.02	9.92	0.19	3.50	0.19	74.92	5.28	45.69	0.026	0.25	1/297	51.62	compact
	C5	4.04	8.03	0.19	3.50	0.18	74.92	3.58	45.69	0.067	0.50	1/2537	41.32	compact
(3)	C6	4.96	10.93	0.18	4.04	0.25	103.11	3.71	48.59	0.050	0.33	1/689	56.70	compact
	C7	4.88	9.82	0.19	4.04	0.25	103.11	3.07	48.59	0.058	0.33	1/426	50.38	compact
	C8	4.92	11.81	0.19	4.00	0.25	103.11	4.28	48.59	0.045	0.33	1/624	60.85	compact

Figure 6.21 illustrates the configuration of these tests and Table 6.10 provides pertinent information about each test. The OT test series (Group (1) in Table 6.10) contains simply-supported beam-columns without any lateral brace within the member length. Also, for these tests, bending about the major- and minor-axis is unrestrained at both ends. Information about the twisting and warping boundary conditions at the member ends is not provided specifically by Shiomi and Kurata (1984). It is assumed in this study that both twisting and warping are restrained at the member ends. This is decided based on the description of the test set up in Shiomi and Kurata (1984). The IT test series (Group (2) in Table 6.10) have two lateral braces, each at 1/3L from the member ends (points B and C). For the IT series tests, Shiomi and Kurata indicate that bending about the weak axis is restrained at point D. Twisting and warping are fully restrained at both ends for these tests as well. It can be observed in Figure 6.21 that the test members are oriented such that the centroidal axis is horizontal (as same as in the tests by Salter et al. 1980). An axial force and an end moment are applied at the deep end of these members such that the bottom flange is in flexural compression. In the tests by Shiomi and Kurata (1984), the taper angle β, the member length L and the flange size are varied. The measured amplitudes of initial imperfections are also shown in Table 6.10. These values are used

subsequently for the full nonlinear virtual test simulations of the selected Shiomi tests. The webs and the flanges are compact in flexure for all the test members in Shiomi and Kurata (1984).

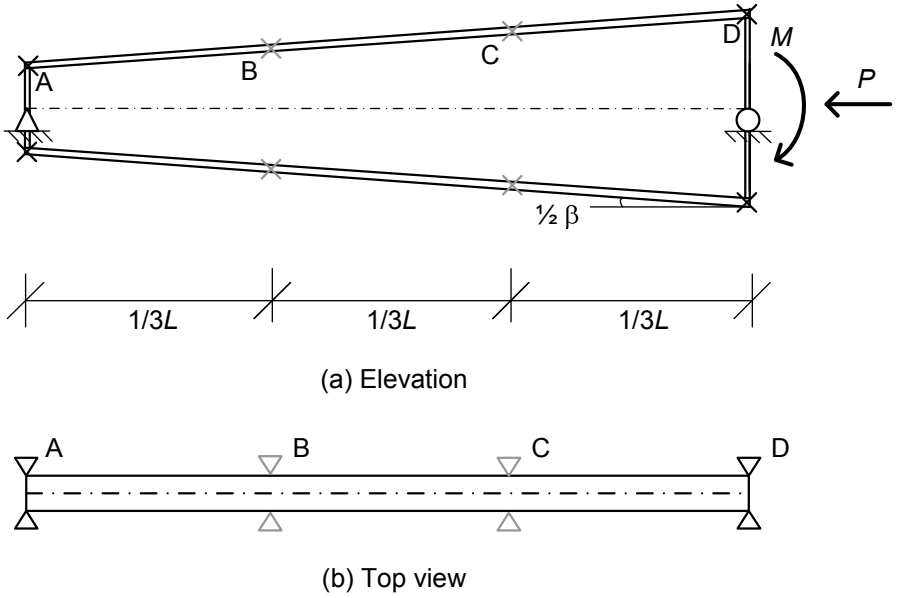

Figure 6.21. Configuration of the beam-column tests from Shiomi and Kurata (1984).

Table 6.10. Description of the beam-column tests from Shiomi and Kurata (1984).

Group	Member	d_s (in)	d_L (in)	t_w (in)	b_f (in)	t_f (in)	L (in)	β (°)	F_{yf} (ksi)	F_{yw} (ksi)	P/P_{eL}	P/P_{ys}	M/M_{yL}	δ_o/L	h_L/t_w	slenderness
(1)	OT-1.4-2	5.4	7.24	0.24	4.75	0.31	78.74	1.34	41.72	43.88	0.060	0.48	0.69	1/5000	27.77	compact
	OT-1.4-4	5.39	7.27	0.24	5.11	0.31	98.43	1.09	38.39	44.95	0.060	0.33	0.70	1/800	27.88	compact
	OT-1.6-1	6.57	10.13	0.24	3.20	0.32	118.11	1.72	40.43	41.22	0.021	0.13	0.78	1/2000	39.80	compact
	OT-1.6-2	5.42	8.19	0.24	4.35	0.32	78.74	2.02	41.50	42.13	0.053	0.49	0.41	1/2200	31.72	compact
	OT-1.6-4	5.55	8.41	0.24	5.01	0.32	98.43	1.67	41.53	42.63	0.070	0.45	0.54	1/2800	32.64	compact
	OT-1.6-5	5.61	8.49	0.24	4.94	0.31	118.11	1.40	41.70	44.30	0.069	0.31	0.60	1/1600	33.02	compact
	OT-1.8-1	4.98	8.45	0.24	4.39	0.32	78.74	2.53	40.75	42.33	0.063	0.58	0.46	1/3800	32.78	compact
	OT-1.8-3	5.40	9.09	0.24	4.75	0.32	98.43	2.14	41.77	41.64	0.068	0.46	0.54	1/2000	35.47	compact
	OT-1.8-4	5.70	9.81	0.24	4.76	0.31	98.43	2.39	42.58	43.32	0.044	0.33	0.66	1/1900	38.60	compact
	OT-1.8-5	5.60	9.49	0.24	4.96	0.32	118.11	1.89	41.14	42.71	0.062	0.32	0.59	1/2000	37.12	compact
	OT-2.0-1	4.58	8.50	0.24	3.94	0.32	78.74	2.85	42.12	41.13	0.066	0.56	0.38	1/1700	33.02	compact
	OT-2.0-3	5.88	10.87	0.24	3.95	0.31	98.43	2.90	42.56	40.13	0.037	0.33	0.56	1/5000	42.99	compact
	OT-2.0-4	5.70	10.54	0.24	4.94	0.36	118.11	2.35	41.22	42.72	0.056	0.33	0.63	1/1500	41.24	compact
	OT-2.0-5	5.71	10.57	0.24	4.93	0.36	118.11	2.36	41.10	43.49	0.076	0.46	0.53	1/3000	41.36	compact
	OT-2.2-3	5.54	11.03	0.24	4.76	0.32	98.43	3.19	42.05	39.91	0.051	0.45	0.50	1/1600	43.64	compact
	OT-2.2-5	5.59	11.43	0.24	4.94	0.32	118.11	2.83	42.34	41.23	0.054	0.35	0.64	1/1300	45.32	compact
	OT-2.4-1	4.58	10.07	0.24	3.96	0.31	78.74	3.98	42.85	40.07	0.061	0.64	0.40	1/3300	39.64	compact
	OT-2.4-3	4.57	10.02	0.24	3.97	0.31	98.43	3.17	42.66	40.18	0.067	0.45	0.42	1/3800	39.44	compact
	OT-2.4-4	5.74	12.48	0.24	4.94	0.36	118.11	3.27	42.00	40.72	0.047	0.35	0.62	1/1500	49.39	compact
(2)	IT-1.4-1	5.41	7.14	0.24	4.34	0.32	78.74	1.26	41.85	41.79	0.071	0.56	0.65	1/4000	27.32	compact
	IT-1.6-2	5.55	8.04	0.24	4.37	0.32	78.74	1.81	42.67	38.63	0.061	0.57	0.68	1/2900	31.09	compact
	IT-1.8-3	4.98	8.31	0.24	4.34	0.31	78.74	2.42	43.01	40.29	0.044	0.39	0.95	1/6400	32.26	compact
	IT-2.2-5	4.63	9.22	0.24	3.96	0.31	78.74	3.34	42.91	38.85	0.030	0.28	0.96	1/1700	36.10	compact
	IT-2.4-6	4.68	9.93	0.24	3.95	0.32	78.74	3.82	40.80	43.25	0.017	0.18	1.10	1/3100	39.01	compact

6.2.2 Nominal Resistance Calculations

6.2.2.1 Calculation Procedures

The nominal resistances for all the test members from Prawel et al. (1974), Salter et al. (1980) and Shiomi and Kurata (1984) are calculated using the prototype AISC (2010) procedures outlined in Chapter 3. The elastic lateral torsional buckling (LTB) load ratio γ_{eLTB} is determined by rigorous eigenvalue buckling analyses using GT-Sabre (Chang 2006). These analyses account for the specific warping and lateral bending boundary conditions of the different tests. These boundary conditions are usually addressed in simplified ways in design practice. However, when testing the validity of design procedures, it is important to investigate their accuracy considering all the displacement constraints. Otherwise, the displacement constraints can artificially inflate the test resistances relative to the calculated design resistances. Once the above "exact" γ_{eLTB} values are calculated, these ratios are used in the calculation of the elastic or inelastic buckling nominal resistance M_n. For members subjected to axial loads, the governing column buckling load ratio γ_e is determined using the recommended procedures described in Chapter 4 assuming torsionally simply-supported boundary conditions except the test C8 in Salter et al. (1980) and the IT test series in Shiomi and Kurata (1984). For these tests, the exact γ_e values are obtained by rigorous eigenvalue buckling analysis using the boundary conditions of the physical tests.

It is found in this study that in all but one case the results from the nominal resistance calculations are closest to the experimental and the refined inelastic virtual test strengths when the flexural resistance M_n is calculated by scaling the nominal lateral-torsional buckling (LTB) resistance for the case of uniform flange stress by the flange

stress gradient factor, C_b. In this study, this procedure is referred to as "MBMA/AISC-1 procedure" in the subsequent discussions.

To obtain the C_b factor in the context of the above rigorous buckling analysis procedures, the following steps are used:

(1) An eigenvalue buckling analysis is conducted using the specific load and displacement boundary conditions for a given test, but with zero axial force. From this result, the value of the maximum LTB flange stress $F_{e.max}$ along the unbraced length is obtained. The cross-section where the flange stress is maximum is also identified.

(2) The end moment values are determined such that the compression flange of the given member is stressed uniformly throughout the unbraced length. Based on this applied loading, the elastic LTB compression flange stress under the uniform-stress condition $F_{e.uniform}$ is determined from a new eigenvalue buckling analysis.

(3) The flange stress gradient factor C_b is calculated as

$$C_b = F_{e.\max} / F_{e.uniform} \qquad \text{(Eq. 6.2)}$$

It should be noted that the above "exact" procedure is applicable only for members that do not have any intermediate bracing, i.e., it applies only to members with a single unbraced length. This is because it is difficult to separate the effects of moment gradient from the end restraint effects obtained from adjacent unbraced segments in a rigorous eigenvalue buckling analysis. In this study, LB-3, LB-5 and LB-6 in Prawel et al. (1974), C6 through C8 in Salter et al. (1980), and the IT test series in Shiomi and Kurata (1980) have multiple unbraced lengths.

In the interest of simplicity, the design strengths for the members having multiple

unbraced lengths are calculated by using the LTB design equations (Eqs. 3.16 and 3.20) and the elastic LTB load ratio γ_{eLTB} obtained directly from an eigenvalue buckling analysis as described in Step (1) above. In the subsequent sections, this procedure is referred "MBMA/AISC-2 procedure". In this procedure, the stress gradient is implemented in essence as a square root of C_b effect in terms of the length F_{eLTB}. One can observe that the AISC (1989) ASD Specification uses this approach in its Eqs. (F1-6) and (F1-7). The MBMA/AISC -2 procedure tends to give somewhat more conservative inelastic LTB results for cases with large flange stress gradients. Both MBMA/AISC-1 and MBMA/AISC-2 procedures give the same LTB resistances for the beams with C_b close to 1.0 or for elastic LTB.

In Appendix B, all the flexural design strengths are calculated by the MBMA/AISC-2 procedure with γ_{eLTB} determined from an eigenvalue analysis using the actual loading conditions. The unity check results using these flexural design strengths are also shown in Appendix B. In addition, the flexural resistances calculated by the MBMA/AISC-1 procedure with the γ_{eLTB} determined by the recommended design-based procedures (see Section 4.4.1) are presented in Appendix C with the corresponding unity checks. In the subsequent discussion, this approach is referred as "the MBMA/AISC-$1_{(\gamma_{eLTB\text{-}Ch4})}$ procedure." The unity check results from the three different procedures discussed above are compared in the subsequent section.

6.2.2.2 Nominal Resistances of Selected Experiments

Tables 6.11 through 6.13 show the resistance calculations for the Prawel et al. (1974) tests. These resistances are calculated and the strength ratios are determined using the maximum axial load and moment obtained from the physical tests as the applied

loadings. Since the objective here is to compare nominal resistances to the test strengths, and since the member axial loads are small relative to $0.5P_y$, the elastic second-order analysis is conducted using a stiffness reduction of $0.9\tau_b = 0.9(1.0) = 0.9$. However, there is little second-order amplification of the flexural stresses in these tests. For all the Prawel tests, out-of-plane flexural buckling governs the calculation of the axial strength P_n. In the beam tests, the axial force is essentially zero. For the beam-column tests where the members are inclined at a larger angle α, some axial forces exist but the axial resistance ratios are quite small.

The flexural strengths for the Prawel et al. (1974) beam-column tests are calculated using the MBMA/AISC-1 procedure. Since the beam tests have two or three unbraced lengths within their length (see Figure 6.18), the flexural resistances are estimated by the MBMA/AISC-2 procedure. The cell with the values of M_r/M_c for the governing limit state of each test is highlighted in Table 6.12.

For the cases in Group (1), lateral torsional buckling (LTB) governs while for all the cases in Groups (2) to (4), flange local buckling (FLB) governs. These failure modes are observed by Prawel et al. (1974) in their physical tests as well. It should be noted that by using the MBMA/AISC-1 procedure, the LTB limit state for the beam-columns reaches the maximum flexural strength, $R_{pg}R_{pc}M_{yc}$ (where R_{pg} is the web bend-buckling strength reduction factor, R_{pc} is web plastification factor and M_{yc} is the yield moment corresponding to the compression flange).

All of the Prawel et al.(1974) tests fail either in inelastic LTB or inelastic FLB based on the above calculations. In most cases, the nominal resistance calculations predict the experimental results conservatively. The test LB-5 in group (1) is the only

case where the resistance calculation is unconservative compared to the experimental test result. The maximum conservative difference is obtained for LB-C-6. The unity check value for this case is 1.20.

As discussed above, all the beams in Prawel et al. (1974) (i.e., LB-3 through LB-6 in Group (1)) have slender webs at the deep end and compact flanges. The test beam-columns have compact, noncompact or slender webs and noncompact flanges. These members represent proportions commonly used in metal building frames. Therefore a study of the test members in Prawel et al. (1974) can give useful information to understand the behavior of web-tapered members used by the metal building industry. Also as mentioned above, the flexural resistances of these members are in the inelastic LTB or FLB ranges. In the middle of these regions, the member strength is sensitive to the effect of residual stress and initial imperfections. In this study, all the beam members in Prawel et al. (1974) are studied by full nonlinear virtual test simulations. Also, from each group of beam-columns, two members are selected for the virtual test simulation: from Group (2), LBC-5 and LBC-10, from Group (3), LBC-1 and LBC-9, and from Group (4), LBC-3 and LBC-7. All these selected members have cross-section plates with shear cut edges. The virtual test models of the selected experiments are created based on the general procedures explained in Chapter 5.

The design checks for the test members in Salter et al. (1980) and Shiomi and Kurata (1984) are shown in Tables 6.14 through 6.19. All the members tested by these researchers are subject to relatively large axial forces compared to the tests by Prawel et al. (1974) (see Tables 6.14 and 6.19).

All the test members in Salter et al. (1980) do not have slender elements. Therefore $Q = 1.0$ for all cases and $(f_r/F_y)_{\max}$ can be used in the calculation of the nominal axial stress F_n (see Chapter 3). Out-of-plane flexural buckling governs the axial resistance for all the members tested by Salter et al. (1980) except C8. The members C6 and C7 have an intermediate lateral brace on the tension flange at mid-span. However, Salter et al. (1980) observed that these braces do not have any significant effect on the flexural strength of the members. Therefore, the intermediate lateral brace in C6 and C7 are not considered in this study for calculating the design strengths. The test C8 has an intermediate brace on its compression flange at mid-span. Salter et al. (1980) observes the compression-flange brace in C8 has a substantial effect on the member capacity. Therefore, the axial strength of C8 is calculated considering the constrained-axis torsional buckling limit state. The constrained axis torsional buckling strength of this member is slightly larger than the out-of-plane flexural buckling strength calculated using the entire member length as the unbraced length. The flexural resistance of C8 is obtained by considering the two unbraced segments separately. The left segment, denoted by C8L, governs the flexural resistance of the member so the flexural resistance and the unity check value are shown for C8L. For all the cases except C8L, the flexural strength M_n is equal to $M_{max} = R_{pg}R_{pc}M_{yc} = M_p$ for both LTB and FLB. This is because these members have compact webs and compact flanges combined with sufficiently short unbraced lengths and sufficiently high C_b values. The flexural resistance of C8L is governed by inelastic LTB and is calculated in this Section using the MBMA/AISC-2 procedure and a rigorous buckling analysis for the given loading. For all the members in Salter et al.

(1980), the unity checks are conservative relative to the experimental results. C8L shows the maximum conservative result of 1.23.

Of the Salter tests, C1 and C8 are selected for further virtual test simulation study. This is because: (1) C1 and C8 are subject to relatively large flexural loads compared to the other cases, (2) the flexural strengths of these members are in the inelastic LTB range when the MBMA/AISC-2 procedure is employed (C1 : $(F_y/F_{eLTB})^{0.5} = (F_y/F_{e.max})^{0.5} =$ 0.66 and C8L : $(F_y/F_{eLTB})^{0.5} = (F_y/F_{e.max})^{0.5} = 0.39$), and (3) these two members have similar geometry but C8 has one intermediate lateral brace. So these members can give information about the behavior involving the constrained axis flexural buckling and the benefit from the lateral bracing on the compression flange.

The test members in Shiomi and Kurata (1984) behave in a similar fashion to the Salter et al. (1980) test members. All the members are subject to relatively large axial force. For the OT series tests, out-of-plane flexural buckling governs the axial resistance while for the IT series tests, in-plane flexural buckling governs. Also, for the IT tests, $1/\gamma_{ex}$ is less than 0.10 in all cases. Therefore, P_n is taken equal to QP_y for these tests based on the direct analysis method as discussed in Chapter 3. For all the test members in Shiomi and Kurata (1984), $Q = 1.0$ and $(f_r/F_y)_{\max}$ is used in the calculation of F_n. Since the web and the flanges are compact, and since the unbraced lengths are sufficiently small and the C_b values are sufficiently large for all the members, the flexural strength is equal to $M_{max} = R_{pg}R_{pc}M_{yc} = M_p$ for both LTB and FLB. The design checks for all the Shiomi tests are conservative relative to the experimental tests. The maximum conservative result is observed for the test OT 2.4-1.

Table 6.11. Axial resistance calculations (Prawel et al. 1974)

Group	Member	γ_e	x_1 (in)	P_r (kips)	$(f_r/F_y)_{max}$	F_{n1} (ksi)	γ_{n1}	x_{max} (ft)	f (ksi)	Q_s	Q_a	Q	$(f_r/QF_y)_{max}$	F_n (ksi)	P_r/P_c
(1)	LB-3	663	108	0.2	0.0015	34.2	437	108	34.2	1.000	0.893	0.893	0.0017	31.9	0.002
	LB-5	850	72	0.4	0.0026	43.1	315	72	43.1	1.000	0.875	0.875	0.0030	38.6	0.004
	LB-6	516	72	0.6	0.0043	43.1	191	72	43.1	1.000	0.875	0.875	0.0050	38.6	0.006
(2)	LB-C-5	25	95	7.8	0.0419	34.9	16	24	28.9	0.857	0.805	0.69	0.0503	25.7	0.070
	LB-C-6	23	95	8.5	0.0457	34.8	15	24	28.9	0.857	0.805	0.69	0.0550	25.7	0.077
	LB-C-10	36	105	5.2	0.0281	34.4	24	26	28.9	0.857	0.806	0.691	0.0342	25.6	0.048
	LB-C-11	37	105	5.1	0.0275	34.4	24	26	28.9	0.857	0.806	0.691	0.0335	25.6	0.047
(3)	LB-C-1	1091	30	0.2	0.0008	31.8	783	0.0	30.7	0.883	0.857	0.757	0.0010	26.8	0.001
	LB-C-12	119	28	1.6	0.0077	32.9	83	0.0	31.7	0.883	0.855	0.755	0.0098	27.4	0.014
	LB-C-9	61	110	2.9	0.0156	33.4	41	0.0	30.8	0.883	0.857	0.757	0.0190	27.4	0.027
	LB-C-4	38	98	5.0	0.0266	34.3	25	0.0	30.6	0.883	0.857	0.757	0.0314	27.7	0.045
(4)	LB-C-2	79	0.0	2.4	0.0129	34.5	51	0.0	34.5	0.971	0.978	0.949	0.0136	33.4	0.020
	LB-C-3	90	0.0	2.1	0.0114	34.5	58	0.0	34.5	0.971	0.978	0.949	0.0120	33.4	0.018
	LB-C-7	139	0.0	1.4	0.0074	34.5	90	0.0	34.5	0.971	0.978	0.949	0.0077	33.4	0.011
	LB-C-8	146	0.0	1.3	0.0070	34.5	95	0.0	34.5	0.971	0.978	0.949	0.0074	33.4	0.011

Table 6.12. Flexural resistance calculations (Prawel et al. 1974)

Group	Member	γ_{eLTB}	$x_{max(LTB)}$ (in)	$(M_r/M_{yc})_{max}$	$R_{pg(LTB)}$	R_{pc}	$M_{n(LTB)}$ (ft-kips)	$M_r/M_{c(LTB)}$	$x_{max(FLB)}$ (in)	$R_{pg(FLB)}$	$M_{n(FLB)}$ (ft-kips)	$M_r/M_{c(FLB)}$	Gov. M_r (ft-kips)	Governing M_r/M_c
(1)	LB-3	2.54	62	1.094	1.000	1.027	53	1.176	36	1.000	71	1.062	63	1.176
	LB-5	6.60	42	0.935	1.000	1.027	58	0.929	24	1.000	71	0.907	54	0.929
	LB-6	3.94	24	1.005	1.000	1.028	67	1.037	24	1.000	71	0.977	69	1.037
(2)	LB-C-5	4.28	0.0	0.906	0.982	1.000	122	0.977	0.0	0.987	113	1.057	119	1.057
	LB-C-6	3.91	0.0	0.991	0.982	1.000	122	1.069	0.0	0.987	113	1.157	131	1.157
	LB-C-10	3.91	0.0	0.955	0.982	1.000	122	1.033	0.0	0.987	113	1.115	126	1.115
	LB-C-11	3.95	0.0	0.935	0.982	1.000	122	1.013	0.0	0.987	113	1.091	123	1.091
(3)	LB-C-1	3.91	0.0	1.051	1.000	1.059	83	1.053	0.0	1.000	76	1.146	87	1.146
	LB-C-12	4.64	0.0	0.952	1.000	1.059	83	0.947	0.0	1.000	76	1.038	79	1.038
	LB-C-9	4.36	0.0	1.032	1.000	1.059	83	1.024	0.0	1.000	76	1.125	85	1.125
	LB-C-4	4.66	0.0	0.996	1.000	1.059	84	0.986	0.0	1.000	76	1.086	82	1.086
(4)	LB-C-2	6.34	0.0	1.103	1.000	1.076	40	1.037	0.0	1.000	37	1.135	42	1.135
	LB-C-3	7.20	0.0	0.966	1.000	1.076	40	0.909	0.0	1.000	37	0.994	37	0.994
	LB-C-7	6.96	0.0	0.995	1.000	1.076	40	0.936	0.0	1.000	37	1.023	38	1.023
	LB-C-8	7.38	0.0	0.946	1.000	1.076	40	0.889	0.0	1.000	37	0.973	36	0.973

Table 6.13. Unity check calculations (Prawel et al. 1974)

Group	Member	Governing P_r/P_c	Governing M_r/M_c	U.C.
(1)	LB-3	0.002	1.176	1.18
	LB-5	0.004	0.929	0.93
	LB-6	0.006	1.037	1.04
(2)	LB-C-5	0.070	1.057	1.09
	LB-C-6	0.077	1.157	1.20
	LB-C-10	0.048	1.115	1.14
	LB-C-11	0.047	1.091	1.11
(3)	LB-C-1	0.001	1.146	1.15
	LB-C-12	0.014	1.038	1.05
	LB-C-9	0.027	1.125	1.14
	LB-C-4	0.045	1.086	1.11
(4)	LB-C-2	0.020	1.135	1.15
	LB-C-3	0.018	0.994	1.00
	LB-C-7	0.011	1.023	1.03
	LB-C-8	0.011	0.973	0.98

Table 6.14. Axial resistance calculations (Salter et al. 1980)

Group	Member	γ_e	x_1 (in)	P_r (kips)	$(f_r/F_y)_{max}$	F_{n1} (ksi)	γ_{n1}	x_{max} (ft)	f (ksi)	Q_s	Q_a	Q	$(f_r/QF_y)_{max}$	F_n (ksi)	P_r/P_c
(1)	C1	3.99	98	22.4	0.1660									25.0	0.312
	C2	2.03	98	44.9	0.3335									25.4	0.619
	C3	2.03	98	44.9	0.3401									25.7	0.623
(2)	C4	4.24	69	22.4	0.2429									30.4	0.365
	C5	2.01	69	44.9	0.5021									30.2	0.760
(3)	C6	2.06	98	44.9	0.3275									26.2	0.608
	C7	2.06	98	44.9	0.3241									26.0	0.606
	C8	2.13	98	44.9	0.3254									26.6	0.595

Table 6.15. Flexural resistance calculations (Salter et al. 1980)

Group	Member	$\gamma_{eLTB.uniform}$	C_b	γ_{eLTB}	$x_{max(LTB)}$ (in)	$(M_r/M_{yc})_{max}$	$R_{pg(LTB)}$	R_{pc}	$M_{n(LTB)}$ (ft-kips)	$M_r/M_{c(LTB)}$	$x_{max(FLB)}$ (in)	$R_{pg(FLB)}$	$M_{n(FLB)}$ (ft-kips)	$M_r/M_{c(FLB)}$	Gov. M_r (ft-kips)	Governing M_r/M_c
(1)	C1	1.83	1.27	2.32	5.5	0.975	1.000	1.160	69	0.840	5.5	1.000	69	0.840	58	0.840
	C2	2.68	1.29	3.46	5.5	0.691	1.000	1.154	62	0.599	5.5	1.000	62	0.599	37	0.599
	C3	2.81	1.33	3.74	5.5	0.685	1.000	1.142	53	0.600	5.5	1.000	53	0.600	32	0.600
(2)	C4	3.04	1.21	3.68	5.5	0.881	1.000	1.184	41	0.744	5.5	1.000	41	0.744	31	0.744
	C5	4.62	1.30	6.01	5.5	0.612	1.000	1.170	29	0.523	5.5	1.000	29	0.523	15	0.523
(3)	C6	2.68	1.29	3.46	5.5	0.685	1.000	1.148	63	0.596	5.5	1.000	63	0.596	38	0.596
	C7	2.74	1.33	3.64	5.5	0.684	1.000	1.146	56	0.597	5.5	1.000	56	0.597	33	0.597
	C8L	N/A	N/A	8.09	5.5	0.817	1.000	1.161	70	0.717	5.5	1.000	71	0.704	50	0.717

Table 6.16. Unity check calculations (Salter et al. 1980)

Group	Member	Governing P_r/P_c	Governing M_r/M_c	U.C.
(1)	C1	0.312	0.840	1.06
	C2	0.619	0.599	1.15
	C3	0.623	0.600	1.16
(2)	C4	0.365	0.744	1.03
	C5	0.760	0.523	1.22
(3)	C6	0.608	0.596	1.14
	C7	0.606	0.597	1.14
	C8L	0.595	0.717	1.23

Table 6.17. Axial resistance calculations (Shiomi and Kurata 1984)

Group	Member	γ_e	x_1 (in)	P_r (kips)	$(f_r/F_y)_{max}$	F_{n1} (ksi)	γ_{n1}	x_{max} (ft)	f (ksi)	Q_s	Q_a	Q	$(f_r/QF_y)_{max}$	F_n (ksi)	P_r/P_c
(1)	OT1.4-2	3.08	0.0	83.1	0.4870									31.6	0.644
	OT1.4-4	3.60	0.0	56.6	0.3419									27.3	0.480
	OT1.6-1	2.00	0.0	17.9	0.1278									9.1	0.569
	OT1.6-2	2.52	0.0	80.5	0.4933									29.6	0.691
	OT1.6-4	2.44	0.0	81.1	0.4455									28.3	0.654
	OT1.6-5	2.30	0.0	55.5	0.3123									23.3	0.559
	OT1.8-1	2.25	0.0	92.6	0.5902									29.7	0.809
	OT1.8-3	2.11	0.0	80.2	0.4606									27.1	0.709
	OT1.8-4	2.77	0.0	59.5	0.3352									27.1	0.526
	OT1.8-5	2.30	0.0	58.2	0.3240									23.4	0.569
	OT2.0-1	1.89	0.0	80.0	0.5612									27.7	0.834
	OT2.0-3	1.86	0.0	50.5	0.3394									20.7	0.657
	OT2.0-4	2.26	0.0	65.8	0.3359									23.7	0.584
	OT2.0-5	1.63	0.0	90.3	0.4629									23.6	0.805
	OT2.2-3	2.16	0.0	78.9	0.4681									26.4	0.709
	OT2.2-5	2.11	0.0	62.7	0.3494									23.3	0.617
	OT2.4-1	1.63	0.0	91.3	0.6688									27.3	0.983
	OT2.4-3	1.48	0.0	64.5	0.4708									22.1	0.857
	OT2.4-4	2.14	0.0	69.4	0.3579									23.6	0.618
(2)	IT1.4-1	14.1	0.0	90.8	0.5539									41.8	0.554
	IT1.6-2	16.4	0.0	92.8	0.6044									38.6	0.604
	IT1.8-3	22.4	0.0	61.3	0.4070									40.3	0.407
	IT2.2-5	33.0	0.0	40.6	0.3057									38.8	0.306
	IT2.4-6	60.1	0.0	25.3	0.1771									40.8	0.177

Table 6.18. Flexural resistance calculations (Shiomi and Kurata 1984)

Group	Member	$\gamma_{eLTB.uniform}$	C_b	γ_{eLTB}	$x_{max(LTB)}$ (in)	$(M_r/M_{yc})_{max}$	$R_{pg(LTB)}$	R_{pc}	$M_{n(LTB)}$ (ft-kips)	$M_r/M_{c(LTB)}$	$x_{max(FLB)}$ (in)	$R_{pg(FLB)}$	$M_{n(FLB)}$ (ft-kips)	$M_r/M_{c(FLB)}$	Gov. M_r (ft-kips)	Governing M_r/M_c
(1)	OT1.4-2	6.71	1.63	10.9	79	0.688	1.000	1.140	45	0.603	79	1.000	45	0.603	27	0.603
	OT1.4-4	5.39	1.63	8.77	98	0.708	1.000	1.160	45	0.610	98	1.000	45	0.610	28	0.610
	OT1.6-1	1.22	1.51	1.84	118	0.785	1.000	1.187	52	0.661	118	1.000	52	0.661	35	0.661
	OT1.6-2	9.33	1.55	14.4	79	0.410	1.000	1.142	50	0.359	79	1.000	50	0.359	18	0.359
	OT1.6-4	6.17	1.54	9.51	98	0.539	1.000	1.134	58	0.475	98	1.000	58	0.475	27	0.475
	OT1.6-5	3.76	1.55	5.81	118	0.602	1.000	1.146	57	0.526	118	1.000	57	0.526	30	0.526
	OT1.8-1	8.53	1.48	12.6	79	0.466	1.000	1.149	52	0.405	79	1.000	52	0.405	21	0.405
	OT1.8-3	5.49	1.48	8.13	98	0.532	1.000	1.134	61	0.469	98	1.000	61	0.469	29	0.469
	OT1.8-4	4.24	1.47	6.22	98	0.657	1.000	1.145	68	0.573	98	1.000	68	0.573	39	0.573
	OT1.8-5	3.87	1.48	5.73	118	0.586	1.000	1.144	67	0.513	118	1.000	67	0.513	34	0.513
	OT2.0-1	8.42	1.42	12.0	79	0.372	1.000	1.141	49	0.326	79	1.000	49	0.326	16	0.326
	OT2.0-3	3.25	1.42	4.62	98	0.567	1.000	1.142	67	0.497	98	1.000	67	0.497	33	0.497
	OT2.0-4	3.60	1.44	5.17	118	0.629	1.000	1.143	83	0.550	118	1.000	83	0.550	46	0.550
	OT2.0-5	4.27	1.43	6.12	118	0.53	1.000	1.149	83	0.461	118	1.000	83	0.461	38	0.461
	OT2.2-3	5.56	1.40	7.76	98	0.497	1.000	1.128	79	0.440	98	1.000	79	0.440	35	0.440
	OT2.2-5	3.28	1.39	4.54	118	0.634	1.000	1.135	86	0.558	118	1.000	86	0.558	48	0.558
	OT2.4-1	7.26	1.35	9.80	79	0.400	1.000	1.135	61	0.352	79	1.000	61	0.352	21	0.352
	OT2.4-3	4.62	1.35	6.23	98	0.422	1.000	1.137	60	0.371	98	1.000	60	0.371	22	0.371
	OT2.4-4	3.42	1.36	4.65	118	0.619	1.000	1.132	104	0.547	118	1.000	104	0.547	57	0.547
(2)	IT1.4-1	N/A	N/A	52.1	79	0.645	1.000	1.133	42	0.569	79	1.000	42	0.569	24	0.569
	IT1.6-2	N/A	N/A	47.1	79	0.670	1.000	1.112	49	0.602	79	1.000	49	0.602	29	0.602
	IT1.8-3	N/A	N/A	30.5	79	0.957	1.000	1.122	50	0.853	79	1.000	50	0.853	43	0.853
	IT2.2-5	N/A	N/A	23.1	79	0.964	1.000	1.122	53	0.859	79	1.000	53	0.859	46	0.859
	IT2.4-6	N/A	N/A	20.7	79	1.091	1.000	1.177	60	0.927	79	1.000	60	0.927	56	0.927

Table 6.19. Unity check calculations (Shiomi and Kurata 1984)

Group	Member	Governing P_r/P_c	Governing M_r/M_c	U.C.
(1)	OT1.4-2	0.644	0.603	1.18
	OT1.4-4	0.480	0.610	1.02
	OT1.6-1	0.569	0.661	1.16
	OT1.6-2	0.691	0.359	1.01
	OT1.6-4	0.654	0.475	1.08
	OT1.6-5	0.559	0.526	1.03
	OT1.8-1	0.809	0.405	1.17
	OT1.8-3	0.709	0.469	1.13
	OT1.8-4	0.526	0.573	1.04
	OT1.8-5	0.569	0.513	1.03
	OT2.0-1	0.834	0.326	1.12
	OT2.0-3	0.657	0.497	1.10
	OT2.0-4	0.584	0.550	1.07
	OT2.0-5	0.805	0.461	1.21
	OT2.2-3	0.709	0.440	1.10
	OT2.2-5	0.617	0.558	1.11
	OT2.4-1	0.983	0.352	1.30
	OT2.4-3	0.857	0.371	1.19
	OT2.4-4	0.618	0.547	1.10
(2)	IT1.4-1	0.554	0.569	1.06
	IT1.6-2	0.604	0.602	1.14
	IT1.8-3	0.407	0.853	1.17
	IT2.2-5	0.306	0.859	1.07
	IT2.4-6	0.177	0.927	1.02

For the Shiomi tests, OT 1.6-1 and OT 2.0-3 are selected for full nonlinear virtual tests. This is because: (1) the flexural strength ratios for these members are relatively large compared to those for many of the other members in Shiomi and Kurata (1984) and (2) the flexural strengths of these members are in the inelastic LTB range when MBMA/AISC-2 procedure is employed (OT 1.6-1 : $(F_y/F_{eLTB})^{0.5} = (F_y/F_{e.max})^{0.5} = 0.83$ and OT 2.0-3 : $(F_y/F_{eLTB})^{0.5} = (F_y/F_{e.max})^{0.5} = 0.62$). It should be emphasized, however, the large C_b values of these tests produce the LTB resistances equal to M_p.

6.2.2.3 Comparisons between the Unity Checks Determined by Different Procedures

Tables 6.20 through 6.22 compare the unity check calculations based on the MBMA/AISC-1 and the MBMA/AISC-2 procedures for all the experimental tests studied here. Also, the design strengths calculated based on γ_{eLTB} determined by the Chapter 4 procedure and the MBMA/AISC-1 procedure are shown in the last column of Tables 6.20 to 6.22 (MBMA/AISC-1$_{(\gamma_{eLTB\text{-}Ch4})}$). For these unity check calculations, the end restraint effect from the adjacent segments is neglected in the γ_{eLTB} calculations based on the Chapter 4 procedure. As mentioned above, all the unity checks are calculated based on the maximum axial load and moment measured in the physical tests.

The MBMA/AISC-2 procedure gives equal or slightly higher unity check values compared to the MBMA/AISC-1 procedure in all cases. The three beam tests in Prawel et al. (1974) have two intermediate braces. Therefore the design strengths are not calculated using the MBMA/AISC-1 procedure for these tests as explained in the previous section. All the beam-column tests in Prawel et al. (1974) are governed by the flange local buckling (FLB) resistance. This is why the design strengths using the MBMA/AISC-1 and the MBMA/AISC-2 procedures are identical for these tests. For

C8L in Salter et al. (1980) and IT series in Shiomi and Kurata (1984), which have intermediate braces, the design strengths using the MBMA/AISC-1 procedure are not determined in this study.

Table 6.20. Summary of unity check calculations for Prawel et al. (1974)

Group	Member	U.C.		
		MBMA/AISC-1	MBMA/AISC-2	MBMA/AISC-1$_{(\gamma_{eLTB\text{-}Ch4})}$
(1)	LB-3	N/A	1.18	1.33
	LB-5	N/A	0.93	1.00
	LB-6	N/A	1.04	0.98
(2)	LB-C-5	1.09	1.09	1.09
	LB-C-6	1.20	1.20	1.20
	LB-C-10	1.14	1.14	1.14
	LB-C-11	1.11	1.11	1.11
(3)	LB-C-1	1.15	1.15	1.15
	LB-C-12	1.05	1.05	1.05
	LB-C-9	1.14	1.14	1.14
	LB-C-4	1.11	1.11	1.11
(4)	LB-C-2	1.15	1.15	1.15
	LB-C-3	1.00	1.00	1.00
	LB-C-7	1.03	1.03	1.03
	LB-C-8	0.98	0.98	0.98

Table 6.21. Summary of unity check calculations for Salter et al. (1980)

Group	Member	U.C.		
		MBMA/AISC-1	MBMA/AISC-2	MBMA/AISC-1$_{(\gamma_{eLTB\text{-}Ch4})}$
(1)	C1	1.06	1.19	1.24
	C2	1.15	1.24	1.27
	C3	1.16	1.23	1.24
(2)	C4	1.03	1.10	1.14
	C5	1.22	1.27	1.27
(3)	C6	1.14	1.22	1.26
	C7	1.14	1.22	1.23
	C8L	N/A	1.26	1.29

It should be emphasized that the elastic LTB load ratios $\gamma_{eLTB\text{-}Ch4}$ are determined based on the assumption that the critical segment is torsionally simply-supported. In other words, any lateral bending or warping end restraint is neglected in the calculation of

γ_{eLTB} based on the Chapter 4 procedure. The unity checks by the MBMA/AISC-1$_{(\gamma_{eLTB\text{-}Ch4})}$ procedure are larger for the Prawel et al. (1974) LB-3 and LB-5 tests whereas they are smaller for the LB-6 test than the design checks based on the other two approaches.

Table 6.22. Summary of unity check calculations for Shiomi and Kurata (1984).

Group	Member	U.C.		
		MBMA/AISC-1	MBMA/AISC-2	MBMA/AISC-1$_{(\gamma_{eLTB\text{-}Ch4})}$
(1)	OT1.4-2	1.18	1.18	1.18
	OT1.4-4	1.02	1.04	1.02
	OT1.6-1	1.16	1.34	1.37
	OT1.6-2	1.01	1.02	1.01
	OT1.6-4	1.08	1.09	1.08
	OT1.6-5	1.03	1.07	1.03
	OT1.8-1	1.17	1.18	1.17
	OT1.8-3	1.13	1.15	1.13
	OT1.8-4	1.04	1.07	1.04
	OT1.8-5	1.03	1.07	1.03
	OT2.0-1	1.12	1.14	1.12
	OT2.0-3	1.10	1.16	1.13
	OT2.0-4	1.07	1.12	1.08
	OT2.0-5	1.21	1.26	1.23
	OT2.2-3	1.10	1.13	1.10
	OT2.2-5	1.11	1.17	1.15
	OT2.4-1	1.30	1.32	1.31
	OT2.4-3	1.19	1.23	1.23
	OT2.4-4	1.10	1.16	1.15
(2)	IT1.4-1	N/A	1.06	1.04
	IT1.6-2	N/A	1.14	1.11
	IT1.8-3	N/A	1.17	1.13
	IT2.2-5	N/A	1.07	1.03
	IT2.4-6	N/A	1.02	1.00

These positive or negative differences are a function of the actual end restraint conditions, which are neglected in the $\gamma_{eLTB\text{-}Ch4}$ calculation, as well as differences between the AASHTO C_b equations and the "exact" moment gradient effect captured by the eigenvalue buckling analyses. The unity checks for all the Prawel et al. (1974) beam-column tests are identical for all the calculation procedures. This is because all of these tests are governed by the FLB limit state. The results using the MBMA/AISC-1$_{(\gamma_{eLTB\text{-}Ch4})}$ approach are similar to those obtained by the MBMA/AISC-2 procedure with the "exact"

γ_{eLTB}. Both of these results tend to be accurate to conservative relative to the U.C. values obtained from the MBMA/AISC-1 procedure. In the case of the MBMA/AISC-2 procedure, the conservatism is due to the way that the mapping between the elastic and inelastic LTB resistances is handled within the inelastic LTB range. In the case of the MBMA/AISC-1$_{(\gamma_{eLTB\text{-}Ch4})}$ procedure, the conservatism is due to the neglect of all end restraint effects and due to the conservatism of the AASHTO C_b equations in certain cases (note that in some cases, the AASHTO C_b equations can be slightly liberal compared to the analytical elastic LTB results as shown in Chapter 4).

Among the tests studied also by virtual test simulations, the cases that are most appropriate for the investigation of the accuracy of the MBMA/AISC-1 and the MBMA/AISC-2 procedures are C1 in Salter et al. (1980) and OT.1.6-1 and OT.2.0-3 in Shiomi and Kurata (1984). It should be noted that these tests have compact webs and compact flanges. The comparisons between the unity check values and the virtual test simulation results are discussed subsequently.

6.2.3 Virtual Simulation of the Tests

6.2.3.1 Load and Displacement Boundary Conditions

The basic procedures to generate the virtual test models of the experiments are the same as the general procedures shown in Chapter 5. The details of the load and displacement boundary conditions for the selected experimental tests are described subsequently. For the beam tests of Prawel et al. (1974), the lateral bracing is represented by point lateral restraints at the top and bottom web-flange junctures at points A through D (see Figure 6.18). The vertical displacements are restrained across the full bottom flange width at the support points A and D, and the longitudinal displacement is

restrained at the bottom web-flange juncture at point A. The concentrated loads are modeled as a uniformly distributed line load across the flange width. The transverse stiffeners are assumed to be the same total width and thickness as the flanges, for the sake of simplicity of the finite element models. The dimensions of the actual transverse stiffeners were not specified in the original research report. This attribute of the members is not expected to have any significant influence on the results. Transverse stiffeners are modeled at points A through D in Figure 6.18. For the beam-column tests of Prawel et al. (1974), all the displacements and rotations are restrained for all the cross-section nodes at point A (see Figure 6.2). The lateral bracing is modeled by point lateral restraints at the top and bottom web-flange junctures at point B. The concentrated load is modeled as described above and applied at point B. Transverse stiffeners are modeled at the end points A and B for the beam-column members.

To model the fixtures in the physical Salter et al. (1980) tests, a beam-type multiple point constraint is used in ABAQUS at points A and E (see Figure 6.20). All the displacements are restrained at point A and the vertical and lateral displacements are restrained at point E. Twisting is restrained for both points A and E but the lateral bending is unrestrained. The beam-type multiple point constraint prevents warping at both ends. For C8, the lateral displacement is restrained at the web-flange juncture at point C. In the virtual test simulations, the axial force is applied first then the end moment is subsequently applied as in the physical tests.

Shiomi and Kurata (1984) do not provide any detailed description of their end fixtures. It is assumed that the support conditions are applied at the ends of the actual members. At point A, all the displacements are restrained and at point B, the vertical and

lateral displacements are restrained (see Figure 6.21). Twisting is restrained at both end points but the lateral bending is unrestrained. A beam-type multiple point constraint is used at the end cross-sections to model the warping restraints. For these tests, the axial force and the end moment are applied simultaneously.

6.2.3.2 Residual Stress Patterns

In this study, the effect of the residual stress patterns in the web-tapered members is study by considering four different residual stress patterns. These four different residual stress patterns are as follows:

(1) The residual stress pattern recommended by ECCS (1983) for inelastic analysis modeling for rolled I-section members with $d/b_f > 1.2$.

(2) A residual stress pattern based on Prawel et al. (1974) but with all the residual stress values multiplied by 0.8.

(3) The residual stress pattern specified in the original experimental investigation, whenever this information is provided. In this section, the development of the nominal selected residual stress pattern shown in Chapter 5 is discussed. This residual stress pattern is developed by using average values of the measured residual stresses presented by Prawel et al. (1974) for a representative specimen. The best-fit Prawel residual stresses are applied to the tests by Prawel et al. (1974) and Shiomi and Kurata (1984)[1]. Salter et al. (1984) suggest using a residual stress pattern based on the studies by Young and Robinson (1975). Therefore this residual stress pattern is used for the tests by Salter et al. (1984).

[1] Shiomi and Kurata (1984) provide the residual stress measurements for one member. This member has a linearly tapered web and linearly tapered flanges. Three residual stress measurements are shown along the member length for this case. However, a suggestion for the nominal residual stress pattern is not provided. Therefore a residual stress pattern based on Prawel et al. (1974) is used for virtual test simulations of the test members from Shiomi and Kurata (1984).

Each of the above best-fit Prawel residual stress patterns is explained in more detail below:

ECCS (1983) residual stress pattern. A residual stress pattern suggested by ECCS (1983) for inelastic analysis of rolled I-section members with $d/b_f > 1.2$ is shown in Figure 6.22. ECCS (1983) specifies equal values of $0.3F_y$ in tension and compression for these beam-type I-sections. As a result, this residual stress pattern is self-equilibrating in each of the cross-section plates. It is recognized that the use of the ECCS (1983) rolled I-section stress patterns for detailed study of the behavior of welded I-section members is hard to justify. However it is useful to understand the effect of this residual stress pattern on the flexural resistance of the linearly-tapered welded I-section members. This is because by studying the results with this residual stress, one can understand the relative effect of other residual stress patterns suggested for web-tapered welded I-section members better. It should be noted that many researchers have not considered the initial residual stress pattern at all in their finite element analysis simulations, e.g., (Richter 1998; Miller and Earls 2003, 2004, 2005, & Hong and Uang 2006). Jimenez (1998, 2001, 2005 & 2006) used a rolled I-section residual stress pattern for his virtual test studies with web-tapered members. The virtual test simulation results using this residual stress pattern are labeled as "*ECCS*."

0.8 of the Prawel et al. (1974) residual stress pattern. Prawel et al. (1974) suggest a residual stress pattern based on the residual stress measurements of members with shear cut edges. Figure 6.23 shows the self-equilibrating residual stress pattern obtained by applying a slight modification to the residual stress pattern provided by Prawel et al. (1974). It is found, however, that the virtual test simulation results for LB-3 using this

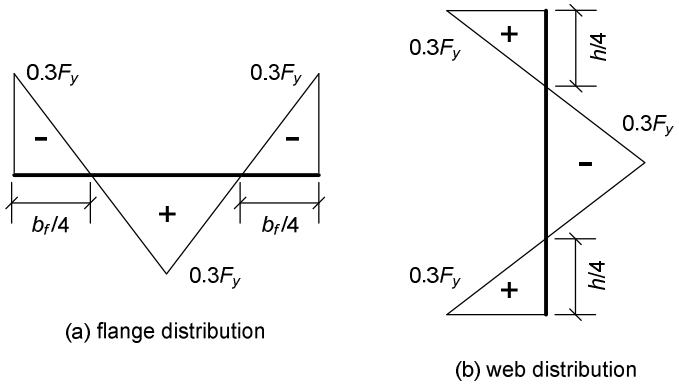

Figure 6.22. Residual stress pattern similar to that suggested by ECCS (1983)

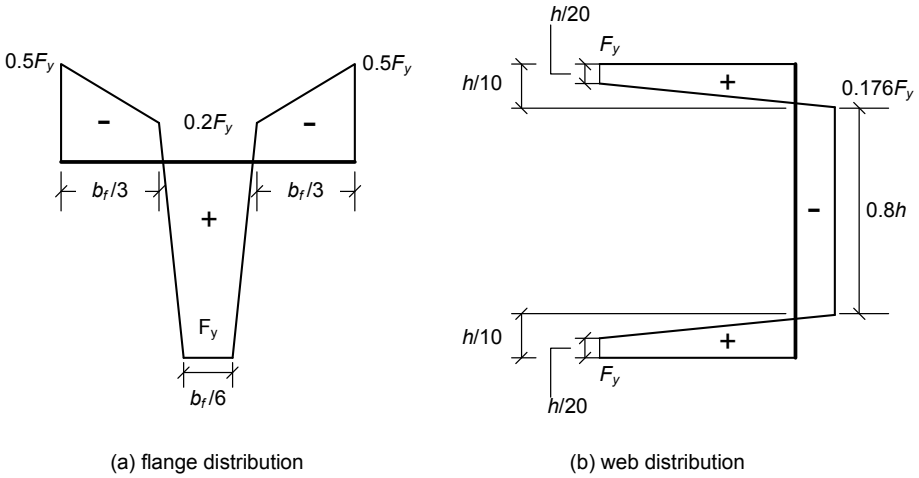

Figure 6.23. Residual stress pattern with self-equilibrating stresses in the flanges and webs, based on the residual stress distribution suggested by Prawel et al. (1974).

residual stress pattern are significantly conservative compared to the experimental test results and the design check calculations. This is discussed in the subsequent section. Furthermore the one residual stress measurement provided in Prawel et al. (1974) (see Figure 6.24) does not show residual stress values that are as severe as the residual stress pattern in Figure 6.23. Therefore it is suggested the use of 0.8 of the Prawel et al. (1974) based pattern in the virtual test simulations as one potential option to obtain more realistic

predictions. The virtual test results using this residual stress pattern are labeled as "*0.8 Prawel*."

Best-fit Prawel residual stress pattern. Figure 6.24 shows representative residual stress measurements for a member with shear cut plates from Prawel et al. (1974). It should be emphasized that the maximum compression in the flanges with shear cut edges is only 19.4 ksi whereas in the residual stress pattern suggested by Prawel et al. (1974), the maximum compression in the flanges with shear cut edges is $0.5F_y$ = 26 ksi. Similarly the maximum measured tension in the flanges with shear cut edges is 38.9 ksi whereas the nominal Prawel et al. (1974) residual stress pattern shows F_y=52 ksi for the maximum tension in the flanges. Table 6.23 shows the mean values of the maximum measured residual stresses in compression and tension in each of the cross-section plates.

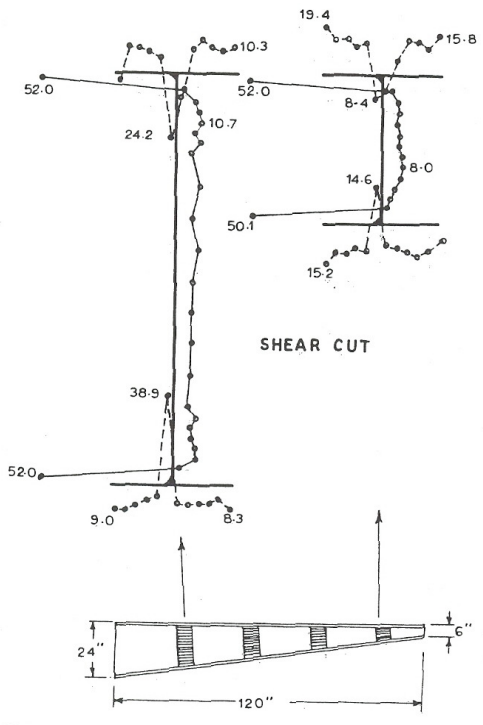

Figure 6.24. Representative measured residual stress patterns from Prawel et al. (1974).

Table 6.23. Mean values of the maximum measured residual stress

	residual stress (ksi)		f/F_y	
	tension	compression	tension	compression
flange	21.5	13.0	0.41	0.25
web	51.5	9.4	0.99	0.18

Based on this observation, the best-fit Prawel residual stress pattern shown in Section 5.3 is developed by reducing the flange residual stresses shown in Figure 6.23 by 1/2. The web residual stresses of the best-fit Prawel residual stress pattern are the same as the ones shown in Figure 6.23. The virtual test results using this residual stress pattern are labeled as "*Best-fit Prawel Residual Stress*" in this Chapter.

Young and Robinson (1975) residual stress pattern. Young and Robinson (1975) suggest a form of residual stress pattern for axially-loaded welded steel columns as shown in Figure 6.25. To define the shape of the tension blocks, the following equation is provided with non-dimensional parameters *a* and *b*:

$$F_r = \frac{(a+b)}{2-(a+b)} F_y \qquad \text{(Eq. 6.3)}$$

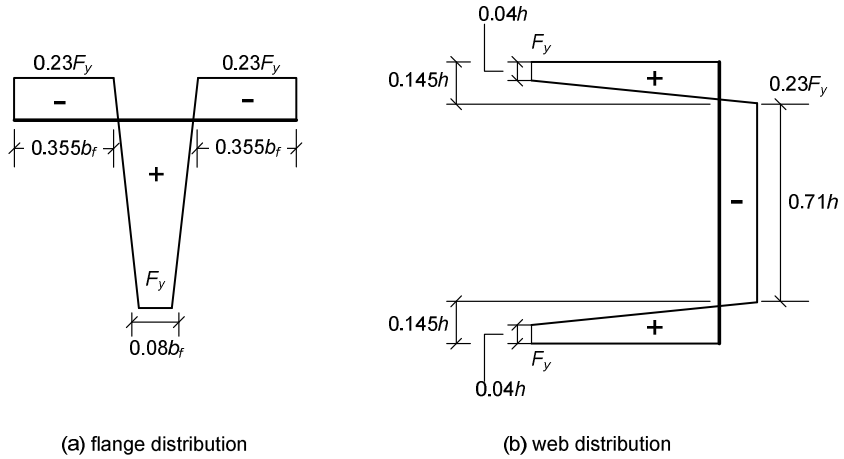

Figure 6.25. The residual stress pattern suggested by Salter et al. (1980) based on Young and Robinson (1975).

Salter et al. (1980) find the values of a and b to be approximately equal to 0.08 and 0.29 in the flanges. These values give a residual compressive stress of 0.23 F_y. The same values of a and b are suggested for the web by Salter et al. (1980). As discussed above, this residual stress pattern is used for the virtual test simulations of the Salter tests instead of the best-fit Prawel residual stress pattern. The virtual test simulation results using this residual stress pattern are labeled as "*Young & Robinson*."

6.2.3.3 Imperfection Shape and Amplitude

As discussed in Chapter 5, an imperfection shape with a compression flange sweep is used in the virtual test simulations. For the tests by Prawel et al. (1974), an amplitude of L_b/1000 is used. For the tests by Salter et al. (1980) and Shiomi and Kurata (1984), the amplitude of the geometric imperfection measured by the authors is used for each test. Figures 6.26 and 6.27 show the imperfection shape used in the study for the beam tests and the beam-column tests in Prawel et al. (1974) respectively.

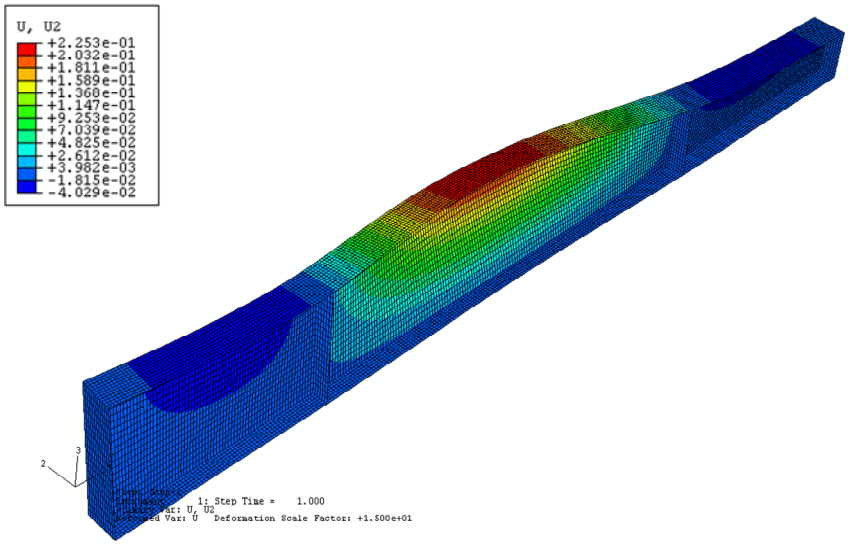

Figure 6.26. The imperfection shape with a compression flange sweep for the beam tests in Prawel et al. (1974) (scale factor = 15.0)

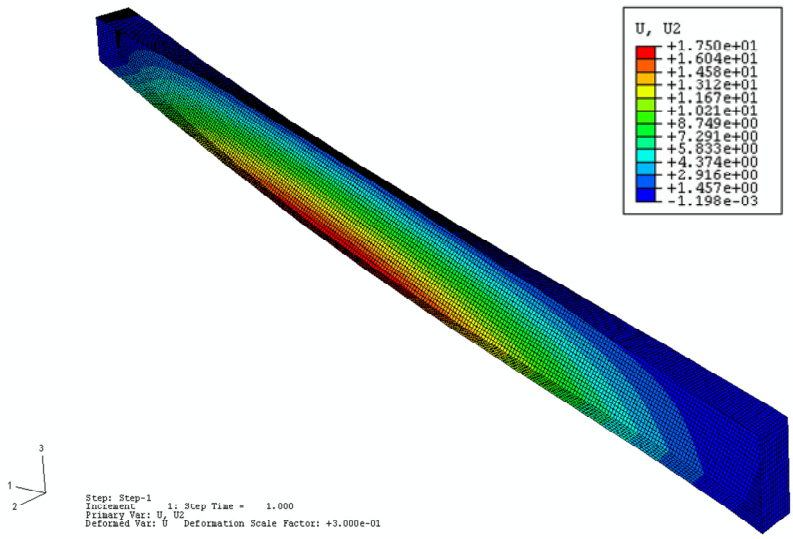

Figure 6.27. The imperfection shape with a compression flange sweep for the beam-column tests in Prawel et al. (1974) (scale factor = 0.3)

6.2.3.4 Material Properties

All the test members in Prawel et al. (1974) are fabricated from ASTM A242 steel with a nominal yield strength of 42 ksi. The measured yield strength of 52 ksi is reported by Prawel et al. (1974). This value is close to the specified minimum yield stress of 50 ksi for A242 steel plates and bars with thickness up to 0.75 in. (AISC 2005b). The corresponding specified minimum ultimate tensile strength is 70 ksi. Information about the stress-strain relationship is not provided in Prawel et al. (1974). It is expected that the thinner web plates should have a larger yield strength than that of the flanges. Also, it is observed that shear tension field action of the segment A-B is relatively dominant at the failure load of all the beam tests in Prawel et al. (1974), especially for LB-5 and LB-6. In this study, it is assumed that the yield strength of the web panel is 65 ksi for the beam tests LB-5 and LB-6. This eliminates a predominant shear failure mechanism in the end

panels in the virtual test simulations. For LB-3 and the beam-column tests, however, a yield strength of 52 ksi is used for all the cross-section plates.

Salter et al. (1980) reported the values of the yield strength F_y for each test (see Table 6.3). These values are the mean values from three measured yield strengths, one from each flange plate and one from the web for each member. A value of the elastic modulus equal to 29877 ksi is provided by Salter et al. (1980). For C1, the value of F_y equal to 47.14 ksi is reported and for C8, F_y is equal to 48.59 ksi.

All the test members in Shiomi and Kurata (1984) are fabricated from SS-41 grade steel with a minimum yield strength of 34.1 ksi. Shiomi and Kurata (1984) provide the values of the ratio of the applied axial force to the yield force based on the smallest cross-section and the ratio of the applied end moment to the yield moment based on the largest cross-section for each test member. From these values, the actual yield strengths for the web and the flange can be deduced (see Table 6.10). The calculated yield strengths for the selected tests are shown in Table 6.18. It should be noted that the yield strength of the flange plates is slightly larger than the yield strength of the web in OT-2.0-3. Nevertheless the AASHTO (2007) hybrid factor R_h is approximately 1.00 for this test. It should be noted that the AASHTO (2007) equations are essentially the same as the AISC (2010) equations, and include the consideration of hybrid girders.

Table 6.24 Yield strength values for OT-1.6-1 and OT-2.0-3

Member	Yield strength (ksi)	
	flange	web
OT-1.6-1	40.4	41.2
OT-2.0-3	42.6	40.1

The true stress-strain curves used in the virtual test simulations are generated in the way described in Section 5.5. The ABAQUS S4R shell element is a large strain formulation, capable of handling large strain effects to whatever extent is required by the physical structure being analyzed. Therefore, the true stress-strain response is the appropriate material description to be input to ABAQUS. Figure 6.28 shows the stress-strain curves for F_y = 52 ksi used in the Prawel test simulations. The values of the true stress and the corresponding plastic strain used in the ABAQUS input are shown in Tables 6.25 and 6.26. The stress values for the first data points are the results of the conversion to the true stress from the nominal yield strength values in the 1st raw of Tables 6.25 and 6.26. The true-stress true-strain curves are assumed to vary linearly between the specified data points as shown in Figure 6.28.

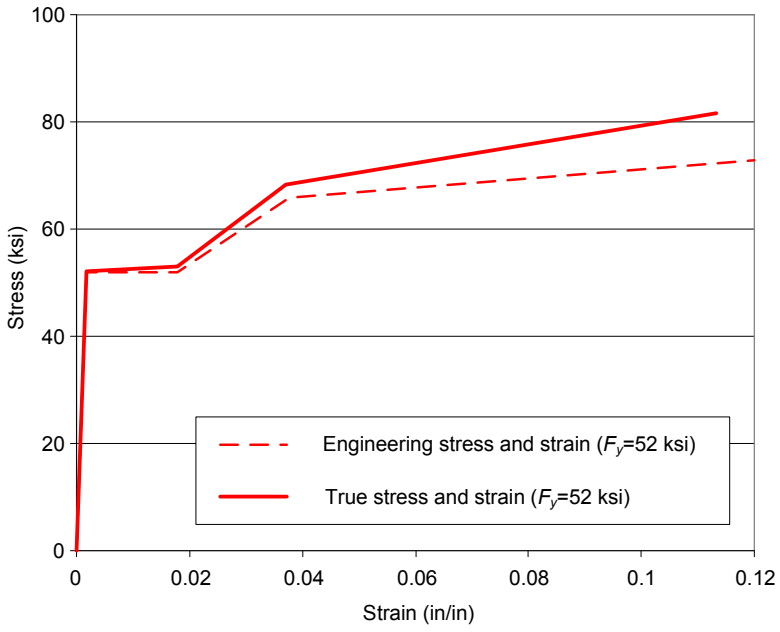

Figure 6.28. Stress-strain curve for F_y = 52 ksi.

Table 6.25. Values of stress and strain used in ABAQUS for the Prawel et al (1974) and the Salter et al. (1980) tests.

Prawel et al. (1974)				Salter et al. (1980)			
F_y = 52 ksi		F_y = 65 ksi		F_y = 47.14 ksi		F_y = 48.59 ksi	
Stress (ksi)	Plastic Strain (in/in)	Stress (ksi)	Plastic Strain (in/in)	Stress (ksi)	Plastic Strain (in/in)	Stress (ksi)	Plastic Strain (in/in)
52.09	0.000	65.15	0.000	47.21	0.000	48.67	0.000
52.93	0.016	66.46	0.020	47.88	0.014	49.38	0.014
68.35	0.035	77.75	0.033	61.73	0.031	63.69	0.032
81.94	0.115	92.55	0.143	73.29	0.102	75.77	0.105

Table 6.26. Values of stress and strain used in ABAQUS for the Shiomi and Kurata (1984) tests.

Shiomi and Kurata (1984)							
OT-1.6-1				OT-2.0-3			
F_{yf} = 40.4 ksi		F_{yw} = 41.2 ksi		F_{yf} = 42.6 ksi		F_{yw} = 40.1 ksi	
Stress (ksi)	Plastic Strain (in/in)	Stress (ksi)	Plastic Strain (in/in)	Stress (ksi)	Plastic Strain (in/in)	Stress (ksi)	Plastic Strain (in/in)
40.49	0.000	41.27	0.000	42.63	0.000	40.19	0.000
40.99	0.012	41.80	0.013	43.19	0.013	40.69	0.012
52.71	0.027	53.77	0.028	55.58	0.029	52.31	0.027
62.12	0.091	63.44	0.093	65.71	0.096	61.63	0.090

6.2.4 Assessment of Results

6.2.4.1 Prawel et al. (1974) Tests

***Prawel et al. 1974 - Beam test LB-3*.** The virtual test and experimental results for LB-3 are summarized in Figure 6.29. For LB-3, lateral torsional buckling governs the flexural resistance. Therefore, the nominal LTB resistance curve obtained using the MBMA/AISC-2 procedure is also shown in Figure 6.29. The elastic lateral torsional buckling stress $F_{e.max}$ is obtained from a rigorous eigenvalue buckling analysis using GT-Sabre (Chang 2006). The ratios of the virtual test simulation results and the experimental results to the nominal flexural resistances obtained by the MBMA/AISC procedures are shown in Table 6.27.

For LB-3, the experimental result is 18 % larger than the nominal resistance based on the MBMA/AISC-2 procedure. The virtual test result using the ECCS residual stress pattern (Case 1) is not obtained due to finite element analysis solution difficulties. It is expected that the result for Case 1 is larger than Case 2. For this beam, using the residual stress pattern suggested by Prawel et al. (1974) shown as "Prawel", the virtual test simulation result is 16 % smaller than the MBMA/AISC-2 strength and 29 % smaller than the experimental results. It should be noted that the experimental result of LB-3 is even higher than the plateau strength of the LTB curve. Therefore, it is believed that the experimental test results for LB-3 are larger than should be expected for members having its characteristics. Using the best-fit Prawel residual stress pattern, the virtual test result is 94 % of the design strength.

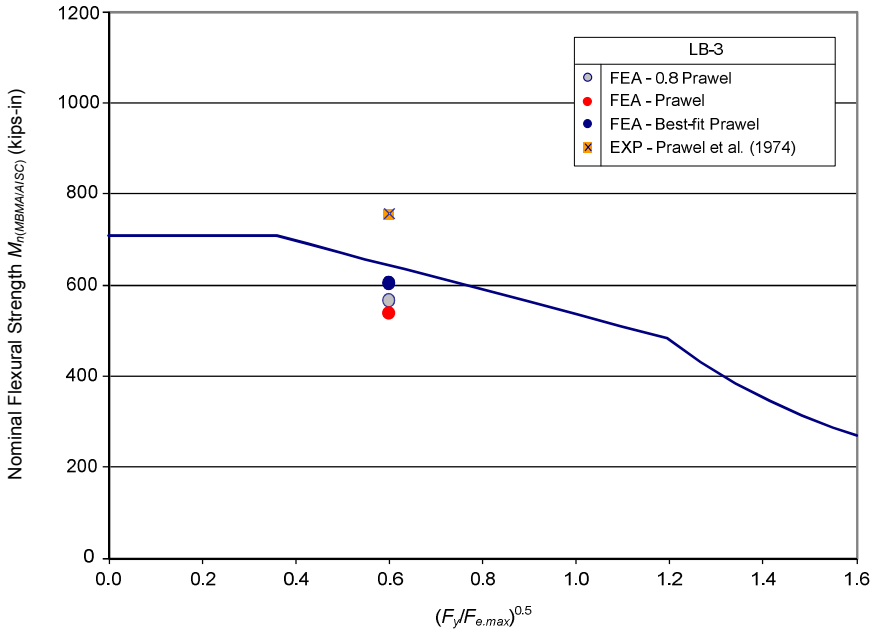

Figure 6.29. Flexural strength versus $(F_y/F_{e.max})^{0.5}$, LB-3 test from Prawel et al. (1974).

Table 6.27. Summary of $M_{max}/M_{n(MBMA/AISC)}$ for tests LB-3.

Member	Case	Residual Stress	M_{max} (kips-in)	$M_{n\,(MBMA/AISC)}$ (kips-in)	$M_{max}/M_{n\,(MBMA/AISC)}$
LB-3	Prawel et al. (1974)		756	643	1.18
	1	ECCS	N/A		N/A
	2	0.8 Prawel	567		0.88
	3	Prawel	539		0.84
	4	Best-fit Prawel	604		0.94

Prawel et al. 1974 - Beam tests LB-5 and LB-6. Figure 6.30 and Table 6.28 show the virtual test and experimental results for LB-5 and LB-6. Similar to LB-3, LTB governs the flexural resistance of these two tests. Therefore, the LTB resistance curve is shown in Figure 6.30. This design strength is obtained from the MBMA/AISC-2 procedure. It can be seen from Figure 6.30 and Table 6.28 that the virtual test solutions using the ECCS (1983) residual stress pattern give a larger flexural strength than the strength obtained using the other residual stress patterns. Using the best-fit Prawel stress pattern, the virtual test results are 88 % and 91 % of the nominal strength for LB-5 and LB-6 respectively. For LB-6, the result for Case 3 is not obtained due to virtual test solution difficulties. It is expected that the solution for this case would be slightly smaller than the result for Case 2. If F_y = 52 ksi is assumed for web plate in LB-5, the resistance is reduced to 75 % of the design strength while the result using F_y = 65 ksi is 87 % of $M_{n(MBMA/AISC)}$. Figures 6.31 and 6.32 show the mid-thickness von Mises stresses and the mid-thickness equivalent plastic strain of LB-5 at the maximum load respectively. It is obvious that the shear tension field action is dominant at the maximum load of LB-5.

For LB-5, the experimental result is 7 % smaller than the nominal flexural strength while for LB-6 the experimental result is 4 % larger than $M_{n(MBMA/AISC)}$. As noted above the middle segment B-C of LB-5 has uniform flange stress whereas the critical

segment B-D of LB-6 has a stress gradient. Using the AASHTO C_b equation as suggested in Chapter 4, the moment gradient factor C_b of LB-6 is 1.16. It is shown in Table 6.21 that the experimental result of LB-3 is 18 % larger than $M_{n(MBMA/AISC)}$. The LB-3 test result by Prawel et al. (1974) is significantly larger than $M_{n(MBMA/AISC)}$ relative to the test results of LB-5 and LB-6.

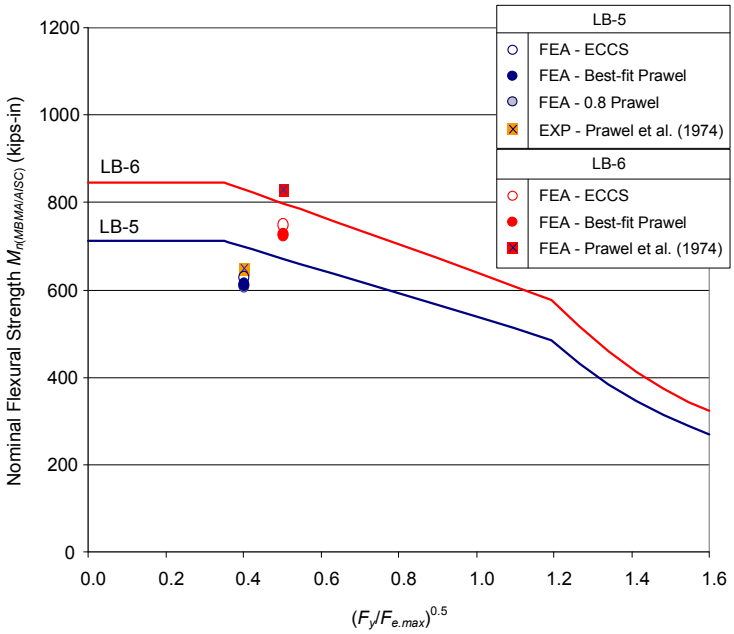

Figure 6.30. Flexural strength versus $(F_y/F_{e.max})^{0.5}$, LB-5 and LB-6 tests from Prawel et al. (1974).

Table 6.28. Summary of $M_{max}/M_{n(MBMA/AISC)}$ for tests LB-5 and LB-6.

Member	Case	Residual Stress	M_{max} (kips-in)	$M_{n\,(MBMA/AISC)}$ (kips-in)	$M_{max}/M_{n\,(MBMA/AISC)}$
LB-5	Prawel et al. (1974)		648	698	0.93
	1	ECCS	628		0.90
	2	0.8 Prawel	607		0.87
	3	Best-fit Prawel	611		0.88
LB-6	Prawel et al. (1974)		828	798	1.04
	1	ECCS	747		0.94
	2	0.8 Prawel	N/A		N/A
	3	Best-fit Prawel	726		0.91

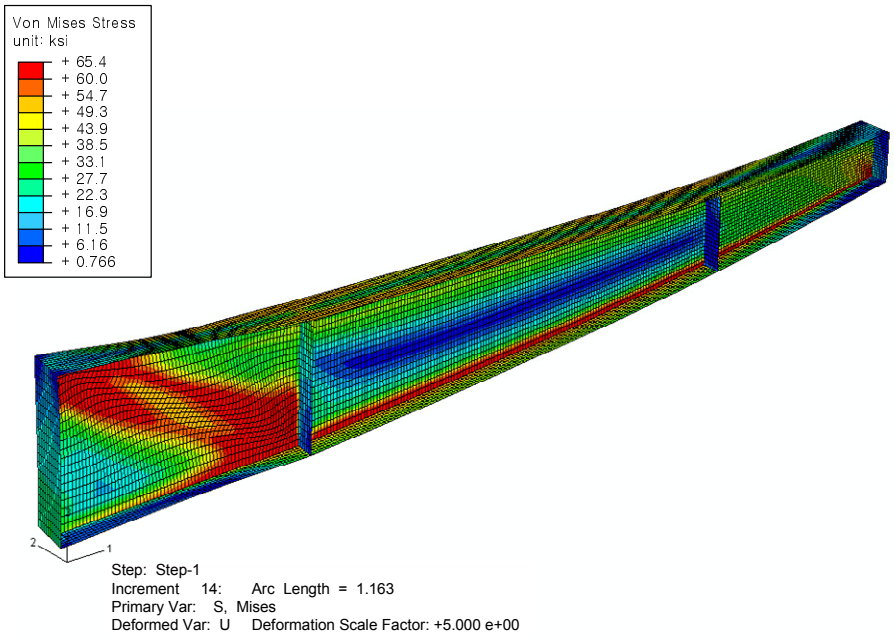

Figure 6.31. Mid-thickness von Mises stresses and deflected shape at the maximum load of LB-5 (displacement scale factor = 5).

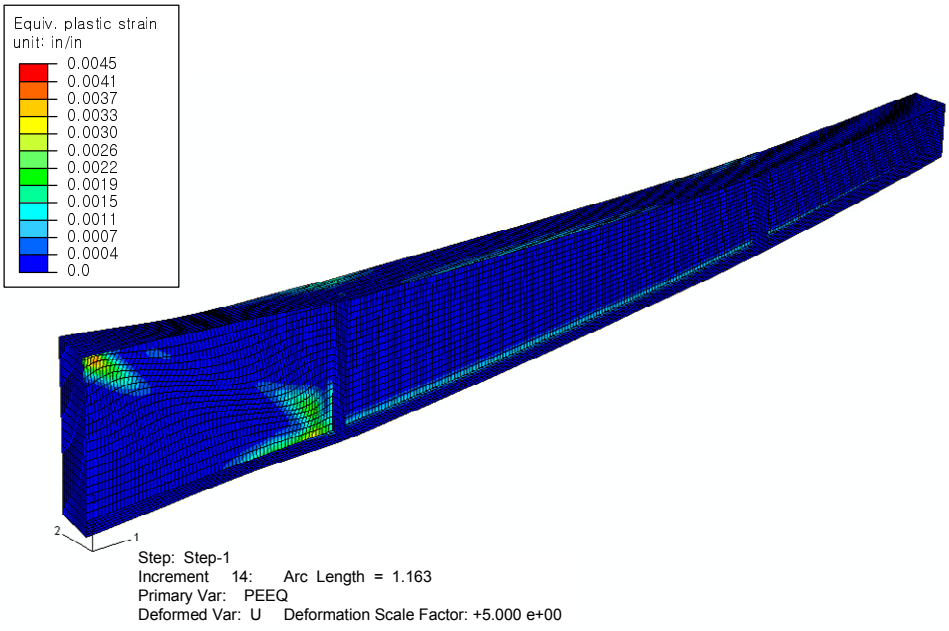

Figure 6.32. Mid-thickness equivalent plastic strains and deflected shape at the maximum load of LB-5 (displacement scale factor = 5).

Prawel et al. 1974 - Beam-column tests LBC-5 and LBC-10. For the Prawel et al. (1974) beam-column tests, the influence of the axial force must be considered in the assessment of resistance of the members. Nevertheless, all the beam-columns in Prawel et al. (1974) have relatively small axial forces. The maximum value of P/P_n is 0.077, which is obtained for LBC-5. Therefore it is expected that the reduction in the flexural resistance due to the axial force is small. For all the beam-columns from Prawel et al. (1974) studied below, the virtual test and experimental results are expressed in terms of the 1st-order moment at the member fixed end. The flexural resistance based on the MBMA/AISC procedures is expressed in terms of the 1st-order moment including the reduction in strength due to the axial force. This resistance is denoted by "$M_{n1}{}^{*}{}_{(MBMA/AISC)}$". The procedure for including the axial force effect in the calculation of the design resistance $M_{n1}{}^{*}{}_{(MBMA/AISC)}$ is explained below.

The 1st-order moment at the fixed support, M_{1max}, is equal to HL, where H is the applied shear force obtained as Pcos(α') and L is the length of the member along its centroidal axis (see Figure 6.33). One can generate the *P-M* strength interaction curve by determining the anchor points (P_n, 0) and (0, M_n). Figure 6.34 shows the *P-M* interaction curve and a force-point trace curve for LBC-5. The abscissa of the plot is the moment at the fixed end obtained from the 2nd-order elastic analysis using the Direct Analysis approach in GT-Sabre (Chang 2006). $M_n{}^{*}{}_{(MBMA/AISC)}$ is obtained from the intersection of the interaction curve and the force-point trace. Next, the amplification factor AF is calculated as $M_n{}^{*}{}_{(MBMA/AISC)}/M_{1max}$ for the corresponding applied loading, since $M_n{}^{*}{}_{(MBMA/AISC)}$ is a 2nd-order moment. When the amplification factor AF is known, the 1st-order flexural resistance including the beam-column effect, $M_{n1}{}^{*}{}_{(MBMA/AISC)}$, is calculated as:

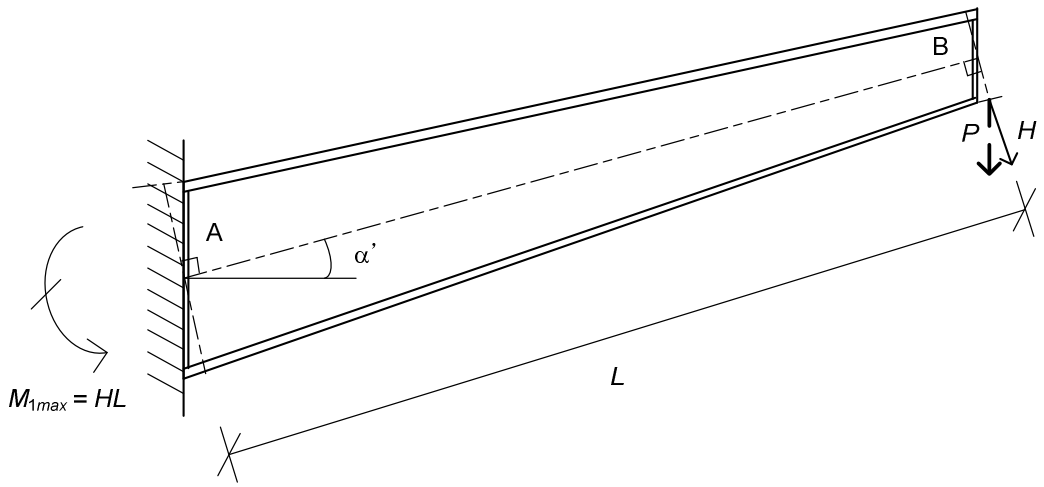

Figure 6.33. Calculation of the 1st-order moment of beam-column.

$$M_{n1}^{*}{}_{(MBMA/AISC)} = M_n \left[\frac{1}{\frac{P/2P_n}{M_{1\max}/M_n} + AF} \right] \qquad \text{for } P/P_n < 0.2 \qquad \text{(Eq. 6.4)}$$

$$M_{n1}^{*}{}_{(MBMA/AISC)} = M_n \left[\frac{1}{\frac{P/P_n}{M_{1\max}/M_n} + \frac{8}{9}AF} \right] \qquad \text{for } P/P_n \geq 0.2 \qquad \text{(Eq. 6.5)}$$

With $M_n^{*}{}_{(MBMA/AISC)}$ obtained from Figure 6.36 and $M_{1max} = HL$, the amplification factor AF for LBC-5 is calculated as 1.01. The corresponding 1st-order AISC (2010) flexural resistance including the beam-column effect is $M_{n1}^{*}{}_{(MBMA/AISC)}$ = 1299 kips-in. Since the maximum value of AF for all the beam-column tests is 1.01, the amplification factor AF is assumed equal to 1.01 for all the other Prawel et al. (1974) beam-column tests.

Figures 6.35 and 6.36 and Table 6.29 show the virtual test results and the

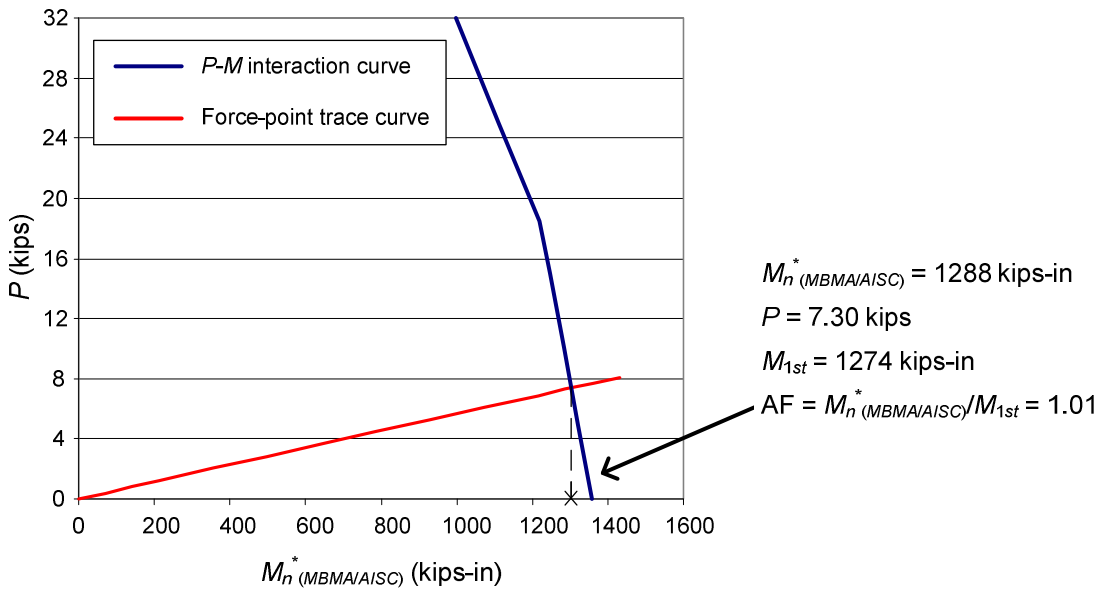

Figure 6.34. *P-M* interaction curve and response curve for LBC-5.

experimental results of LBC-5 and LBC-10 versus the nominal flexural strength including the beam-column effect. The nominal resistance curve without consideration of axial load is also shown for a reference in Figure 6.35 and 6.36. For all the beam-column members from Prawel et al. (1974) analyzed in this study, the flange local buckling (FLB) resistance governs. Therefore the design resistance is shown in terms of the flange slenderness $b_f/2t_f$. When the 0.8 Prawel residual stress pattern is used, the virtual test results are 2 % and 3 % larger than $M_{n1}^{*}{}_{(MBMA/AISC)}$ for LBC-5 and LBC-10 respectively. While the virtual test results with the same residual stress pattern for both beam-columns are similar, the experimental result of LBC-5 is slightly smaller than the experimental result of LBC-10. The experimental results are 9 % and 14 % larger than $M_{n1}^{*}{}_{(MBMA/AISC)}$ for LBC-5 and LBC-10 respectively. The use of the best-fit Prawel residual stress gives 8 % and 9 % larger strengths than $M_{n1}^{*}{}_{(MBMA/AISC)}$ for LBC-5 and LBC-10 respectively.

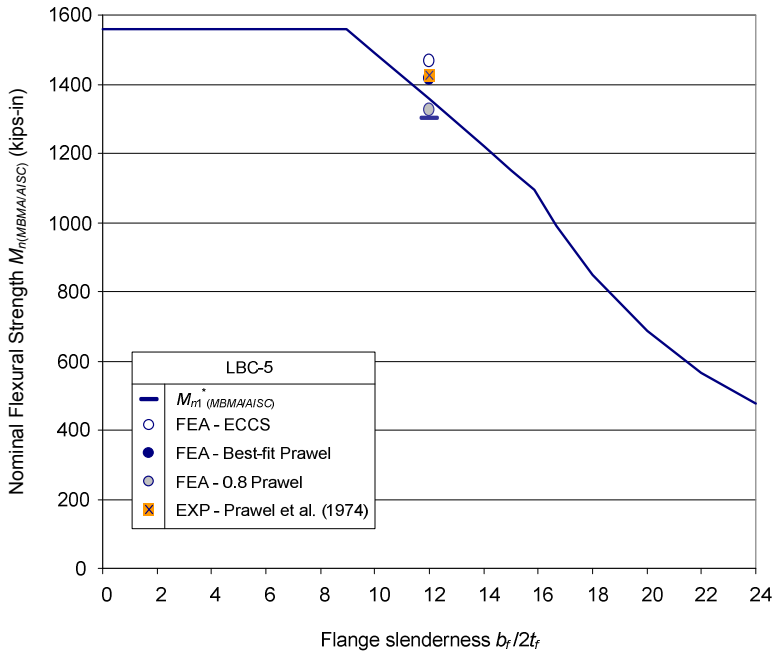

Figure 6.35. Flange local buckling resistance and virtual test strengths versus $b_f/2t_f$, LBC-5 test from Prawel et al. (1974) (slender webs at deep end).

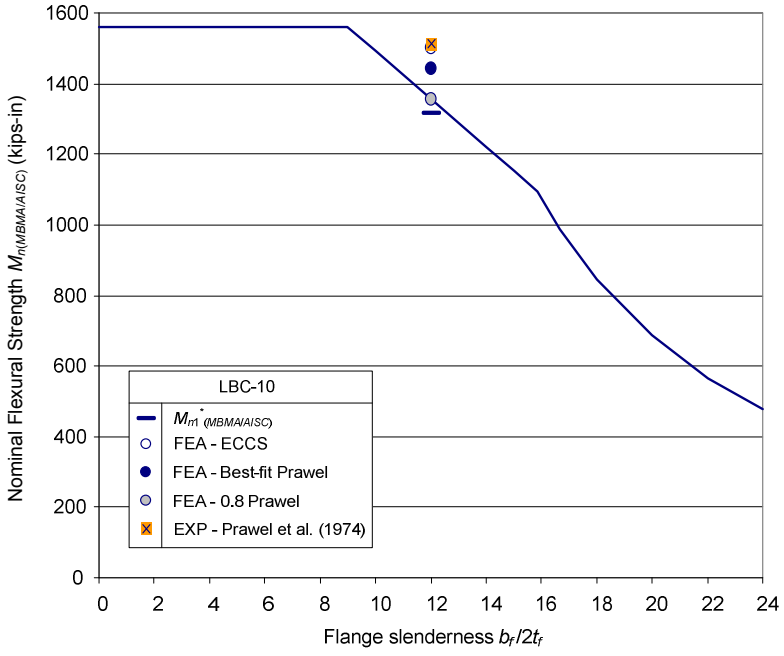

Figure 6.36. Flange local buckling resistance and virtual test strengths versus $b_f/2t_f$, LBC-10 test from Prawel et al. (1974) (slender web at deep end).

Table 6.29. Summary of $M_{1max}/M_{n1}^{*}{}_{(MBMA/AISC)}$ for tests LBC-5 and LBC-10

Member	Case	Residual Stress	M_{max} (kips-in)	$M_{n1}^{*}{}_{(MBMA/AISC)}$ (kips-in)	$M_{max}/M_{n1}^{*}{}_{(MBMA/AISC)}$
LBC-5	Prawel et al. (1974)		1421	1299	1.09
	1	ECCS	1461		1.12
	2	0.8 Prawel	1320		1.02
	3	Best-fit Prawel	1409		1.08
LBC-10	Prawel et al. (1974)		1502	1314	1.14
	1	ECCS	1490		1.13
	2	0.8 Prawel	1348		1.03
	3	Best-fit Prawel	1432		1.09

Prawel et al. 1974 - Beam-column tests LBC-1 and LBC-9. The cantilevered beam-column tests LBC-1 and LBC-9 have the same geometry but a different angle of inclination α (see Table 2). The virtual test and experimental results are compared to the nominal strength in Figures 6.37 and 6.38 and Table 6.30. It can be seen in Figures 6.37 and 6.38 that the ultimate strength of LBC-1 and LBC-9 are practically same even though LBC-9 is inclined by 20° at the top flange while LBC-1 has $\alpha = 0^{o}$. The reason for this behavior is that even though LBC-9 is inclined by 20°, the axial force in the member is small as noted above. For both members, the experimental results are larger than $M_{n1}^{*}{}_{(MBMA/AISC)}$ (16 % for LBC-1 and 12 % for LBC-9). When the best-fit Prawel residual stress pattern with the initial geometric imperfection described above is used, the virtual test results are very close to the experimental test results. In LBC-1, the virtual test result with the modified Prawel residual stress is 17 % larger than $M_{n1}^{*}{}_{(MBMA/AISC)}$. In LBC-9, $M_{(FEA)}$ using the best-fit Prawel residual stress is 13 % larger than $M_{n1}^{*}{}_{(MBMA/AISC)}$. For these cases, the use of the 0.8 Prawel residual stress does not affect the resistance obtained from the finite element analysis significantly.

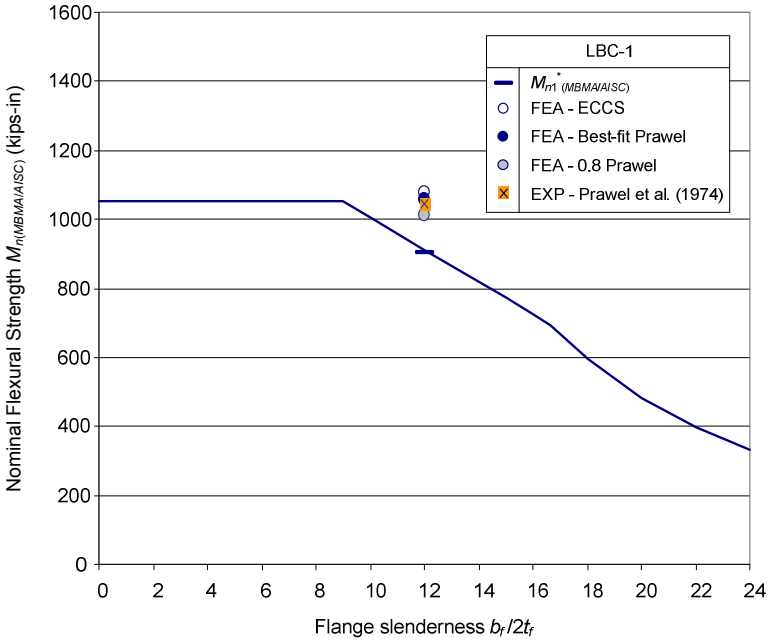

Figure 6.37. Flange local buckling resistance and virtual test strengths versus $b_f/2t_f$, LBC-1 test from Prawel et al. (1974) (noncompact webs at deep end).

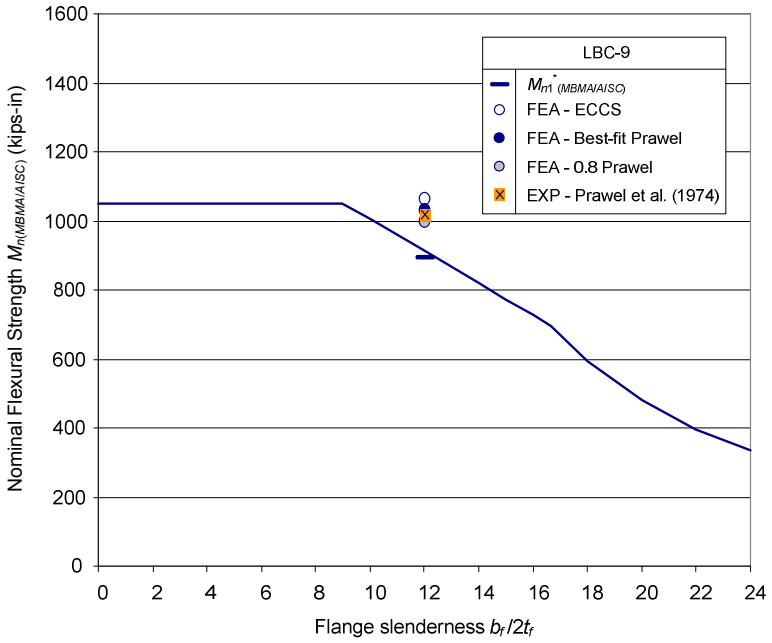

Figure 6.38. Flange local buckling resistance and virtual test strengths versus $b_f/2t_f$, LBC-9 test from Prawel et al. (1974) (noncompact webs at deep end).

Table 6.30. Summary of $M_{1max}/M_{n1}^{*}{}_{(MBMA/AISC)}$ for tests LBC-1 and LBC-9.

Member	Case	Residual Stress	M_{max} (kips-in)	$M_{n1}^{*}{}_{(MBMA/AISC)}$ (kips-in)	$M_{max}/M_{n1}^{*}{}_{(MBMA/AISC)}$
LBC-1	Prawel et al. (1974)		1044	902	1.16
	1	ECCS	1076		1.19
	2	0.8 Prawel	1012		1.12
	3	Best-fit Prawel	1055		1.17
LBC-9	Prawel et al. (1974)		999	892	1.12
	1	ECCS	1043		1.17
	2	0.8 Prawel	976		1.09
	3	Best-fit Prawel	1011		1.13

Prawel et al. 1974 - Beam-column tests LBC-3 and LBC-7. The beam-columns LBC-3 and LBC-7 are prismatic members with an inclination of 30° and 20° respectively (see Table 6.2). In Table 6.31 and Figures 6.39 and 6.40, it can be seen that the strengths of both beam-columns are practically the same. For LBC-3, the experimental result is approximately the same as $M_{n1}^{*}{}_{(MBMA/AISC)}$ while for LBC-7, the experimental result is 3 % larger than $M_{n1}^{*}{}_{(MBMA/AISC)}$. The virtual test solutions for both members give 14 to 16 % larger strength than $M_{n1}^{*}{}_{(MBMA/AISC)}$.

Table 6.31. Summary of $M_{1max}/M_{n1}^{*}{}_{(MBMA/AISC)}$ for tests LBC-3 and LBC-7

Member	Case	Residual Stress	M_{max} (kips-in)	$M_{n1}^{*}{}_{(MBMA/AISC)}$ (kips-in)	$M_{max}/M_{n1}^{*}{}_{(MBMA/AISC)}$
LBC-3	Prawel et al. (1974)		434	434	1.00
	1	ECCS	502		1.16
	2	0.8 Prawel	497		1.14
	3	Best-fit Prawel	501		1.15
LBC-7	Prawel et al. (1974)		449	436	1.03
	1	ECCS	504		1.16
	2	0.8 Prawel	500		1.15
	3	Best-fit Prawel	503		1.15

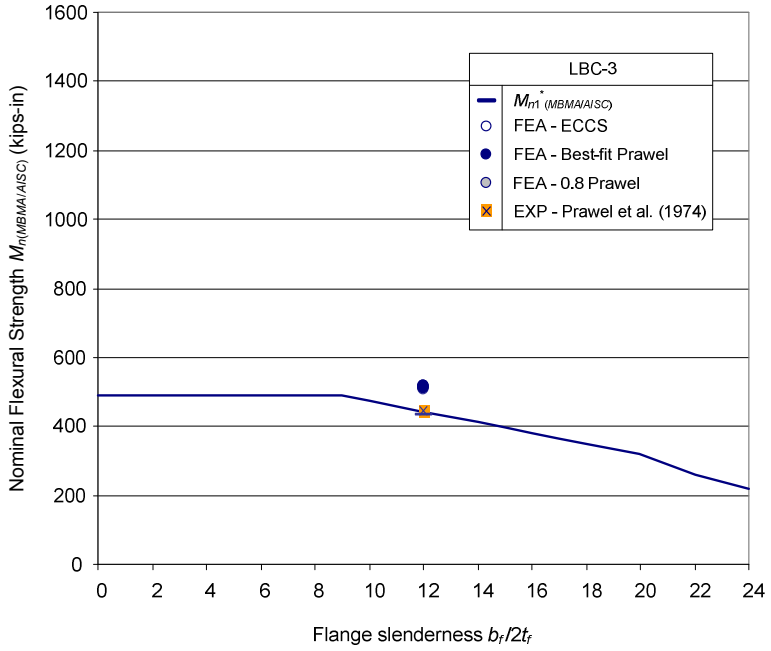

Figure 6.39. Flange local buckling resistance and virtual test strengths versus $b_f/2t_f$, LBC-3 test from Prawel et al. (1974) (prismatic and compact web).

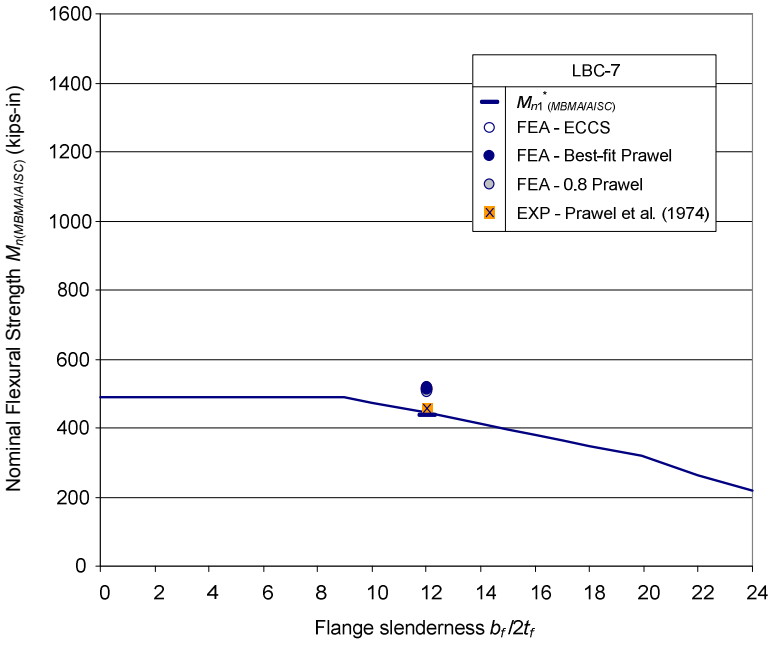

Figure 6.40. Flange local buckling resistance and virtual test strengths versus $b_f/2t_f$, LBC-7 test from Prawel et al. (1974) (prismatic and compact web)

6.2.4.2 Salter et al. (1980) Tests, C1 and C8

The two tests C1 and C8 are selected from Salter et al. (1980) for virtual test study. For these tests, the applied axial forces are relatively large compared to the axial forces considered by Prawel et al. (1974). The ratios of the applied axial force to the yield force at the smaller end are 0.17 and 0.33 for C1 and C8 respectively (see Table 6.9). Therefore, it is useful to compare the virtual test results and the experimental results to the MBMA/AISC strengths using the *P-M* strength interaction curves. Figures 6.41 and 6.42 show the P-M interaction curves versus the virtual test and experimental results for C1 and C8 respectively.

The abscissa in Figures 6.41 and 6.42 is the moment at the deep end obtained from the 2nd order analysis using GT-Sabre (Chang 2006). It should be noted that even though a relatively large axial force exists in the member, the values of the moment at the deep end are the values of the applied moment. For all the tests from Salter et al. (1980) the flexural strengths as well as the unity checks are governed by the cross-section at the deep end. This is because there is no *P*-Δ effect at the support in these cases. Therefore the amplification factor for these moments is 1.0.

Table 6.32 shows the experimental results and the virtual test results in terms of the 1st order moment. These results are compared to $M_{n1}{}^{*}{}_{(MBMA/AISC)}$ using Eqs. 6.4 and 6.5 with AF=1.0. For C1, the experimental result is 6 % larger than $M_{n1}{}^{*}{}_{(MBMA/AISC)}$. The ECCS residual stress gives the largest resistance in this case. The use of Young and Robinson residual stress gives a flexural resistance close to the result using 0.8 Prawel residual stress. When the Young and Robinson and 0.8 Prawel residual stress patterns are used, the virtual test results are 85 % and 84 % of $M_{n1}{}^{*}{}_{(MBMA/AISC)}$ respectively.

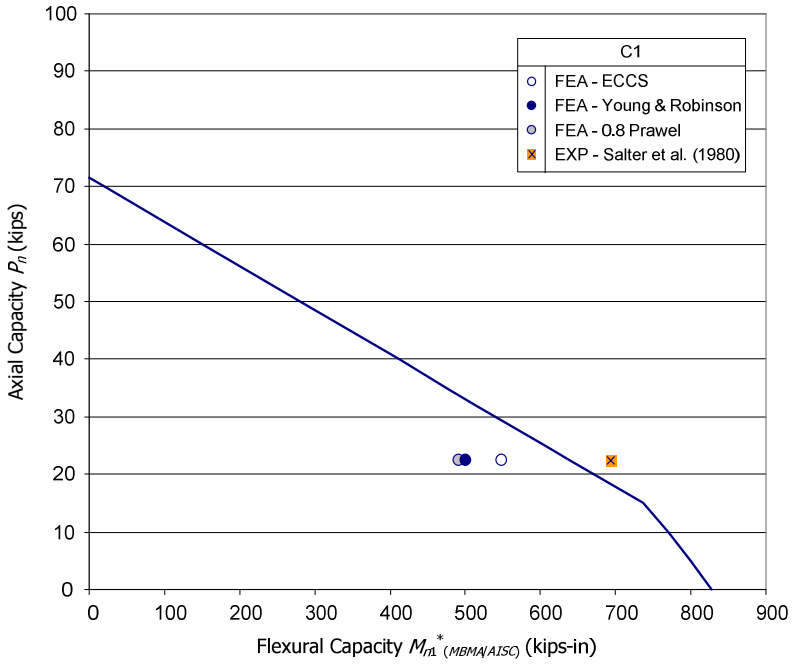

Figure 6.41. *P-M* interaction curve and virtual test strengths, C1 test from Salter et al. (1980).

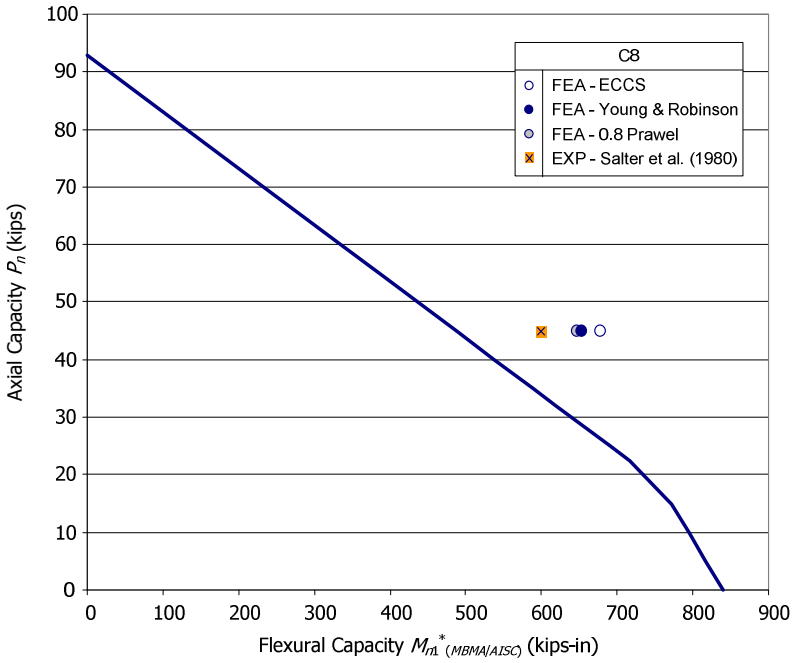

Figure 6.42. *P-M* interaction curve and virtual test strengths, C8 test from Salter et al. (1980)

As mentioned above, the design strengths compared with the experimental and the virtual test results are calculated using the MBMA/AISC-1 procedure for C1. In this test, the MBMA/AISC-2 procedure gives more conservative results relative to the experimental result but closer results to the virtual test strength. This is not the case for C8.

Table 6.32. Summary of $M_{1max}/M_{n1}^{*}{}_{(MBMA/AISC)}$ for tests C1 and C8.

Member	Case	Residual Stress	M_{max} (kips-in)	$M_{n1}^{*}{}_{(MBMA/AISC)}$ (kips-in)	$M_{max}/M_{n1}^{*}{}_{(MBMA/AISC)}$
C1	Salter et al. (1980)		694	655	1.06
	1	ECCS	548	607	0.90
	2	0.8 Prawel	491	588	0.84
	3	Young & Robinson	501	587	0.85
C8	Salter et al. (1980)		600	537	1.12
	1	ECCS	678	565	1.20
	2	0.8 Prawel	647	556	1.16
	3	Young & Robinson	653	554	1.18

The test member C8 has an intermediate lateral brace on its compression flange at mid-span. The segment B-C has larger unity check value in this case (see Figure 6.9). Therefore in Figure 6.42, the nominal flexural resistance calculated based on the segment B-C (see Figure 6.9) is shown. The nominal axial strength P_n for the segment B-C is calculated based on the cross-section at C. The result from Salter et al. (1980) is 12 % larger than $M_{n1}^{*}{}_{(MBMA/AISC)}$. As expected, ECCS gives the largest flexural resistance – 20 % larger than $M_{n1}^{*}{}_{(MBMA/AISC)}$. Using Young and Robinson residual stress and 0.8 Prawel residual stress, the virtual test results are 17 % larger than $M_{n1}^{*}{}_{(MBMA/AISC)}$. Due to the intermediate lateral bracing on the compression flange the flexural resistance obtained from the experimental test of C8 is only 16 % smaller than that of C1 even though the applied axial force in C8 is twice of the axial force in C1. Also the design strength based

on the assumption that the intermediate bracing is effective for the flexural resistance is close to the experimental result.

6.2.4.3 Shiomi and Kurata (1984) Tests, OT-1.6-1 and OT-2.0-3

The OT-1.6-1 and OT-2.0-3 tests are selected for virtual test from the 24 beam-column tests conducted by Shiomi and Kurata (1984). Similar to the tests C1 and C8, relatively large axial forces are applied in OT-1.6-1 and OT-2.0-3. For OT-1.6-1, the ratio of the applied force to the yield strength based on the smallest cross-section P/P_{ys} is equal to 0.13. For OT-2.0-3, the value of P/P_{ys} is equal to 0.33. Figures 6.43 and 6.44 show the virtual test and experimental results versus the P-M strength interaction curve for OT-1.6-1 and OT-2.0-3 respectively. For the same reason explained in the previous section for the tests conducted by Salter et al. (1980), the amplification factor of the moment at the deep end is 1.0.

The virtual test results and the experimental results are compared to the nominal flexural resistance $M_{n1}{}^{*}{}_{(MBMA/AISC)}$ in Table 6.33. It can be seen in Table 6.33 that the experimental results for OT-1.6-1 and OT-2.0-3 are 17 % and 10 % larger than $M_{n1}{}^{*}{}_{(MBMA/AISC)}$. For OT-1.6-1, the ECCS residual stress pattern gives 6 % larger strength than the nominal resistance. The best-fit Prawel residual stress gives 4 % larger M_{1max} than $M_{n1}{}^{*}{}_{(MBMA/AISC)}$ while the 0.8 Prawel gives 10 % smaller resistance than $M_{n1}{}^{*}{}_{(MBMA/AISC)}$. For OT-2.0-3, Case 1 has 20 % larger strength than the nominal resistance. Case 2 and 3 have 16 % and 4 % larger strength than $M_{n1}{}^{*}{}_{(MBMA/AISC)}$.

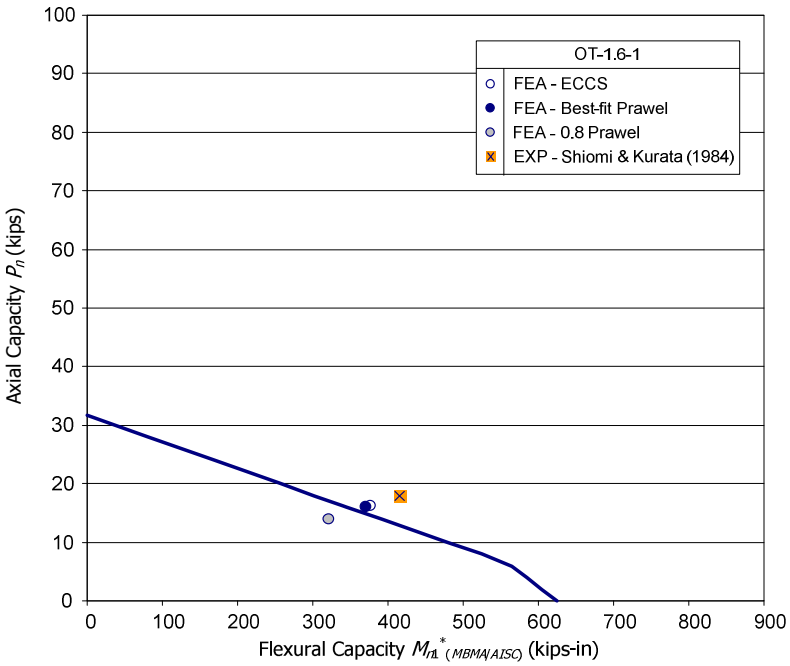

Figure 6.43. P-M interaction curve and virtual test strengths, OT-1.6-1 test from Shiomi and Kurata (1984).

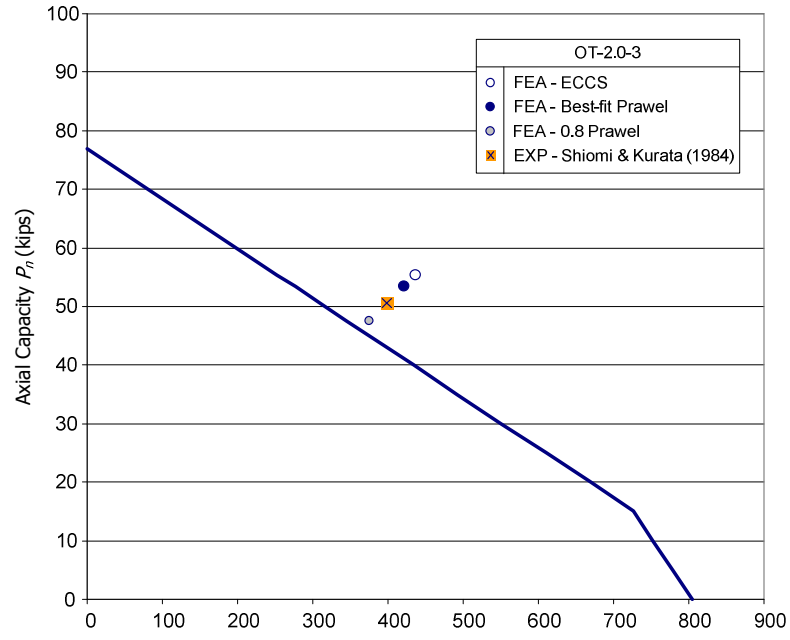

Figure 6.44. P-M interaction curve and virtual test strengths, OT-2.0-3 test from Shiomi and Kurata (1984).

Table 6.33. Summary of $M_{1max}/M_{n1}^{*}{}_{(MBMA/AISC)}$ for tests OT-1.6-1 and OT-2.0-3.

Member	Case	Residual Stress	M_{max} (kips-in)	$M_{n1}^{*}{}_{(MBMA/AISC)}$ (kips-in)	$M_{max}/M_{n1}^{*}{}_{(MBMA/AISC)}$
OT-1.6-1	Shiomi & Kurata (1984)		416	357	1.17
	1	ECCS	377		1.06
	2	0.8 Prawel	321		0.90
	3	Best-fit Prawel	371		1.04
OT-2.0-3	Shiomi & Kurata (1984)		399	363	1.10
	1	ECCS	437		1.20
	2	0.8 Prawel	376		1.04
	3	Best-fit Prawel	421		1.16

6.2.4.4 Summary

From virtual test simulation, it is observed that using the best-fit Prawel residual stress pattern developed in this study, the finite element analysis results are reasonably close to the design checks based on the MBMA/AISC procedures in most cases. Therefore, it is decided to use the best-fit Prawel residual stress pattern for all the virtual test simulations conducted in Chapter 7. The most conservative case is LB-5 where the virtual test result with the best-fit Prawel residual stress pattern is 12 % smaller than the nominal resistance. In the case of LBC-1, the use of the best-fit Prawel residual stress gives 17 % larger strength than $M_{n1}^{*}{}_{(MBMA/AISC)}$. For the members where the values of $(F_y/F_e)^{0.5}$ are close to the limit of the plateau strength in the LTB curves (e.g., LB-5 and LB-6), the residual stress pattern does not affect the finite element analysis solutions significantly. The maximum differences associated with the different residual stress patterns are obtained for OT-1.6-1 and OT-2.0-3. For these members, the virtual test strengths using the ECCS (1983) pattern are 6 % and 20 % larger than the nominal resistance, $M_{n1}^{*}{}_{(MBMA/AISC)}$ in each member, while the virtual test strengths using the 0.8 Prawel residual stress pattern are 10 % smaller and 4 % larger than $M_{n1}^{*}{}_{(MBMA/AISC)}$.

The difference between the LTB resistance calculations using the MBMA/AISC-1 and MBMA-AISC-2 procedures is studied by the virtual test simulations for C1, OT-1.6-1 and OT-2.0-3. For OT-1.6-1 and OT-2.0-3, the flexural resistance using the MBMA/AISC-1 procedure is close to the experimental results and the virtual test results. except for the test C1 from Salter et al. (1980). For C1, the LTB resistance using the MBMA/AISC-1 procedure is close to the experimental result but somewhat unconservative compared to the virtual test results. It should be emphasized that all the test members obtained from Salter et al. (1980) and Shiomi and Kurata (1984) are the compact-section members. The different resistances from the MBMA/AISC-1 and MBMA/AISC-2 procedures are studied with a large number of parametric study in Chapter 7.

CHAPTER VII

ASSESSMENT OF BEAM LATERAL TORSIONAL BUCKLING RESISTANCE CALCULATIONS BY FINITE ELEMENT VIRTUAL TEST SIMULATION

In this chapter, a large number of parametric studies are conducted to understand the lateral torsional buckling (LTB) behavior of prismatic and tapered beams. Virtual test simulation is performed as described in Chapter 5 using a full nonlinear finite element analysis (FEA). The results of virtual test simulation are discussed and compared with the lateral torsional buckling capacity calculated based on the different design provisions. The design provisions considered in this study are AISC (2010) and CEN (2005) for prismatic members and MBMA/AISC (2010) for tapered members. Based on the virtual test simulation results and the experimental test data including those shown in Chapter 6 and the load model statistics for ASCE 7, the reliability index for beam lateral torsional buckling is estimated using AISC (2010) for prismatic members and using MBMA/AISC (2010) for tapered members.

7.1 Test Configurations and Variables

The test members for parametric study are selected by varying several key design parameters. Both prismatic and tapered members are generated using these design parameters. For tapered members, the selected parameters are based on the cross-section at the deep end of members. A clear web depth, h equal to 40 inches is selected to establish the physical dimensions for all the members and a yield strength of 55 ksi is used. The design parameters are as follows:

(1) Section aspect ratio h/b_{fc}. Values of h/b_{fc} from 1 to 7 are selected (h/b_{fc} = 1, 1.5, 2, 4, 5.5, and 7). In MBMA/AISC (2010), it is suggested to limit the value of this ratio to 7 at the deep end in general. Previous research by Kim and White (2008) suggests that the section aspect ratio has significant effect on the LTB strength of steel I-beams. This is also observed by White and Barth (1998) and Rebelo et al. (2009). Therefore, it is decided to focus on the effect of h/b_{fc} in the current study.

(2) Web slenderness ratio h/t_w. Values of the web slenderness ratio from 40 to 180 are selected (h/t_w = 40, 85, 100, 115, 130 and 180). The web slenderness values of 40 and 85 are within the compact limit, $\lambda_{pw} = 3.76(E/F_y)^{0.5} = 86.34$ with F_y = 55 ksi. The web is noncompact with h/t_w = 100, 115, and 130 and the web is slender with h/t_w = 180 (the web noncompact limit is $\lambda_{rw} = 5.7(E/F_y)^{0.5} = 130.89$). In a few extreme cases with singly-symmetric sections and larger compression flanges, the web is compact even though h/t_w = 130.. These cases are the beams with h/b_{fc} = 1, $b_{fc}/2t_{fc}$ = 12, h/t_w = 130, and b_{fc}/b_{ft} = 1.5 or t_{fc}/t_{ft} = 1.5.

(3) Compression flange slenderness ratio $b_{fc}/2t_{fc}$. Values of $b_{fc}/2t_{fc}$ equal to 6 and 12 are selected as representative values. The flanges are compact with $b_{fc}/2t_{fc}$ = 6 ($\lambda_{pf} = 0.38(E/F_y)^{0.5} = 8.73$) and flanges are noncompact with $b_{fc}/2t_{fc}$ = 12 ($\lambda_{rf} = 0.95(k_cE/F_L)^{0.5} = 16.3$).

(4) In this research, the lateral torsional buckling limits are expressed in terms of flange stress, $(F_y/F_{e(Cb=1)})^{0.5}$. The values of $(F_y/F_{e(Cb=1)})^{0.5}$ are varied from 0.2 to 1.75. The selected values of $(F_y/F_{e(Cb=1)})^{0.5}$ are 0.2, 0.35, 0.775, 1.2, 1.4, 1.7, and 1.75. In this research, the flexural strength at the plateau of the LTB resistance curves is defined as

plateau strength. At the limit of plateau strength, $(F_y/F_{e(Cb=1)})^{0.5}$ equals 0.35 and at the limit of inelastic lateral torsional buckling, $(F_y/F_{e(Cb=1)})^{0.5}$ equals 1.2.

(5) Taper angle β. A target value of β equal to 10 is used in general for tapered members. For the cases where β of 10 degrees combined with other design parameters makes the resulting h/t_w at the shallow end less than 40, β of 5 degrees is used.

(6) Flange thickness ratio t_{fc}/t_{ft}. The value of t_{fc}/t_{ft} is varied to generate singly-symmetric as well as doubly-symmetric members. MBMA/AISC (2010) suggests that one need not consider flexural-torsional buckling in the evaluation of the axial strength P_n when the value of t_{fc}/t_{ft} satisfies the following limit:

$$0.67 \leq t_{fc}/t_{ft} \leq 1.5 \qquad \text{(Eq. 7.1)}$$

and the flange widths are the same. The basis of this limit is provided in Section 4.2. When a member cross section satisfies this limit, the reduction in P_n due to the smaller flexural-torsional buckling strength than the out-of-plane flexural buckling strength is less than five percent. Therefore the values of t_{fc}/t_{ft} equal to 0.67, 1.0, and 1.5 are selected in this study.

(7) Flange width ratio b_{fc}/b_{ft}. The value of b_{fc}/b_{ft} equal to 0.67, 1.0 and 1.5 are selected to generate singly-symmetric as well as doubly-symmetric members. It should be noted that for the cases where $b_{fc} \neq b_{ft}$, the flange thickness ratios are kept at 1.0. Similarly, for the cases where $t_{fc} \neq t_{ft}$, the flange width ratios are kept at 1.0.

After generating all possible test configurations from the cross-section parameters listed above, cases that violate certain parameter limits are eliminated. The reasons for the elimination of these cases are: 1) the web slenderness ratio h/t_w at the shallow end is less than 40 even with β = 5 degrees, 2) the flange thickness is smaller than the web

thickness, 3) the flange thickness is larger than six times the web thickness, or 4) the flange width is larger than the web depth at the shallow end. After this process is complete, four groups of test configurations are selected with the different combinations of the flange slenderness and web slenderness ratios. For each of these groups, the aspect ratio h/b_{fc} is varied. Table 7.1 summarizes the geometric parameters of the selected test members. In the last column of this table, the values of taper angle β are listed. For the cases where only prismatic members are considered, the values of β are indicated as 0, and for the cases where both prismatic and tapered members are considered, the values of β are denoted by "0 to 10".

Table 7.1. Geometric parameters of selected members.

h/b_{fc}	$b_{fc}/2t_{fc}$	h/t_w	b_{fc}/b_{ft}	t_{fc}/t_{ft}	β degrees
1	6	40	1	1	0
1.5	6	40	1	1	
2	6	40	1	1	
4	6	100	1	1	0 to 10
			1.5	1	
			1	1.5	
5.5	6	100	1	1	
7	6	100	1	1	
			1.5	1	
			0.67	1	
			1	0.67	
1	12	130	1	1	0
			1.5	1	
			1	1.5	
2	12	130	1	1	
4	12	130	1	1	
4	6	180	1	1	0 to 10
			1.5	1	
			1	1.5	
5.5	6	180	1	1	
7	6	180	1	1	
			1.5	1	
			1	1.5	
			0.67	1	
			1	0.67	

Figure 7.1 shows typical test configurations of tapered and equivalent prismatic members. All the members are torsionally simply-supported. In Figure 7.1, M_{yL} and M_{ys} denote the yield moment of the cross section at the deep end and the shallow end of tapered members respectively. The loading configuration shown in Figure 7.1 provides approximate uniform stress conditions for tapered members (i.e., $C_b \approx 1.0$) and uniform bending conditions for prismatic members.

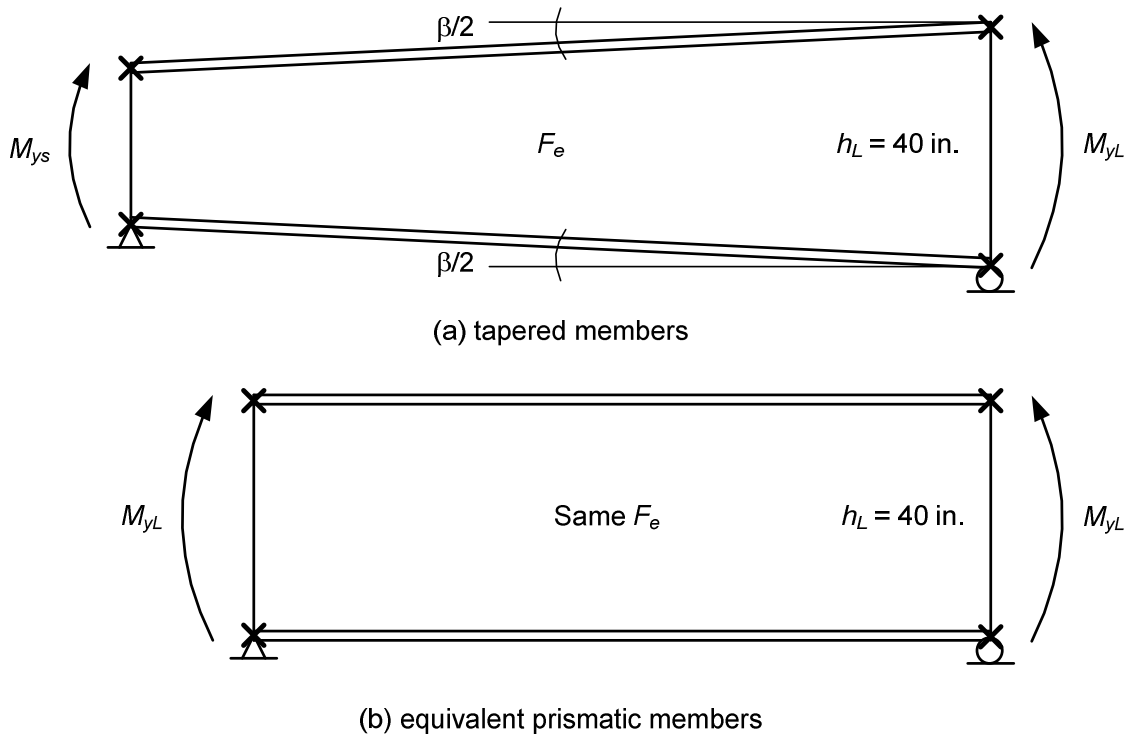

Figure 7.1. Typical test configurations of tapered and equivalent prismatic members.

7.2 Virtual Simulation of the Tests

In this section, the virtual test simulation results are discussed. For all the cases generated as discussed above, uniform-stress loading conditions (or uniform-bending loading conditions for prismatic members) are considered. From virtual test simulation

of members with uniform-stress loading conditions, a number of key observations are made on the LTB resistance of prismatic and web-tapered members. The cases that illustrate these important aspects are selected for virtual test simulation with stress-gradient loading conditions (or moment-gradient loading conditions for prismatic members). Sections 7.2.1 and 7.2.2 discuss the analysis results of doubly-symmetric and singly-symmetric test cases with uniform-stress conditions (or uniform-bending conditions). Similarly, Sections 7.2.3 and 7.2.4 discuss the analysis results for the doubly-symmetric and singly-symmetric test cases with stress-gradient conditions (or moment-gradient conditions).

7.2.1 Doubly-Symmetric Tests with Uniform-Stress Conditions

7.2.1.1 Members with compact flanges and a compact web ($b_{fc}/2t_{fc} = 6$ and $h/t_w = 40$)

Figures 7.2 through 7.4 show the analysis results for compact-section members with h/b_{fc} values of 1.0, 1.5 and 2.0. In all the figures shown in this chapter, the LTB strengths of test members are shown in terms of a normalized ratio M/M_{yc}, where M_{yc} is the yield moment of the compression flange and $(F_y/\gamma_e f_r)^{0.5}$. For prismatic members, the values of $(F_y/\gamma_e f_r)^{0.5}$are same as the values of $(F_y/F_{e(Cb=1)})^{0.5}$ selected for generating test members. In Figures 7.2 to 7.4, the data points for the virtual test simulation solutions are shown at $(F_y/\gamma_e f_r)^{0.5}$ = 0.2, 0.35, 0.775, 1.2, 1.4, and 1.75 except the case with h/b_{fc} = 1.0. For the prismatic members with h/b_{fc} = 1.0 and $(F_y/\gamma_e f_r)^{0.5}$ = 1.75, the end rotations are larger then 0.04 radians at the strength limit, which invalidates the linear multi-point constraint enforcing beam kinematics at the member ends (see Section 5.2). Therefore, the analysis results from these beams are not shown in Figure 7.2. For the tapered

members, the values of $(F_y/\gamma_e f_r)^{0.5}$ are not necessarily the same as the values of $(F_y/F_{e(Cb=1)})^{0.5}$. The reason for this is explained in Section 7.2.1.2.

In these figures, four resistance curves are shown. One resistance curve is based on the AISC (2010) provisions and three resistance curves based on the CEN (2005) provisions are shown. The AISC (2010) Specifications provide one curve for both rolled and welded sections. Conversely, in CEN (2005), there are different curves for rolled and welded sections as discussed in Section 6.1. It can be seen in Figures 7.2 to 7.4 that the AISC (2010) curves are slightly convex within the inelastic LTB range. This happens because for the members with stockier cross sections, the St. Venant torsional constant J makes the inelastic LTB curve convex when the conversion of the AISC (2010) curves based on the unbraced lengths to the flange stress term $(F_y/\gamma_e f_r)^{0.5}$ is performed. In Figures 7.2 to 7.4, two resistance curves for special and general rolled I-section members (CEN (2005), rolled curves 1 and 2) and one curve for general welded I-section members are shown. The rolled-section curves from CEN (2005) are very close to the AISC (2010) LTB curve in general. The CEN (2005) rolled-section curves give slightly smaller strengths within the inelastic LTB region. The general welded-section curve in CEN (2005), however, gives significantly conservative LTB strengths compared to the AISC (2010) curve and the CEN (2005) rolled-section curves.

In Figures 7.2 to 7.4, two sets of virtual test simulation results are shown. One set of virtual test simulation results is obtained using the best-fit Prawel residual stress pattern selected for this study. As discussed in Chapter 5, the best-fit Prawel residual stress pattern is for the welded I-sections. Since the cross section dimensions of these members are similar to those of the rolled I-sections, a separate set of analyses are

conducted using Lehigh residual stress pattern for rolled I-sections (Galambos and Ketter 1959, see Figure 6.6).

It can be seen in Figures 7.2 to 7.4, the LTB strengths obtained from virtual test simulation are in between the LTB nominal capacities based on AISC (2010) and CEN (2005). This is true for all the cases considered in this study. It should be also noted that the differences in the residual stress patterns for the welded and rolled I-sections do not significantly affect the virtual test simulation results. In Figures 7.2 to 7.4, the virtual test simulation results using the two residual stress patterns are practically the same. This observation supports that one LTB resistance curve works for both rolled and welded sections as specified in AISC (2010).

It is shown in Figures 7.2 to 7.4 that the virtual simulation develops the plateau strength of AISC (2010) and CEN (2005) at $(F_y/\gamma_e f_r)^{0.5} = 0.2$. The virtual test simulation results at $(F_y/\gamma_e f_r)^{0.5} = 0.35$ are close to the nominal strengths of the CEN (2005) rolled 2 and general welded-section curves, which are slightly smaller than the nominal strengths of AISC (2010) and CEN (2005) rolled curve 1. The virtual test simulation results become somewhat smaller than the AISC (2010) strengths when $(F_y/\gamma_e f_r)^{0.5} = 0.775$ and 1.2. For longer-length beams with $(F_y/\gamma_e f_r)^{0.5} = 1.4$ and 1.75, the virtual test simulation results are close to or slightly smaller than the elastic LTB strengths based on AISC (2010). For all the cases shown above, the virtual test simulation strengths are slightly to moderately larger than the CEN (2005) curve for general welded-section curve.

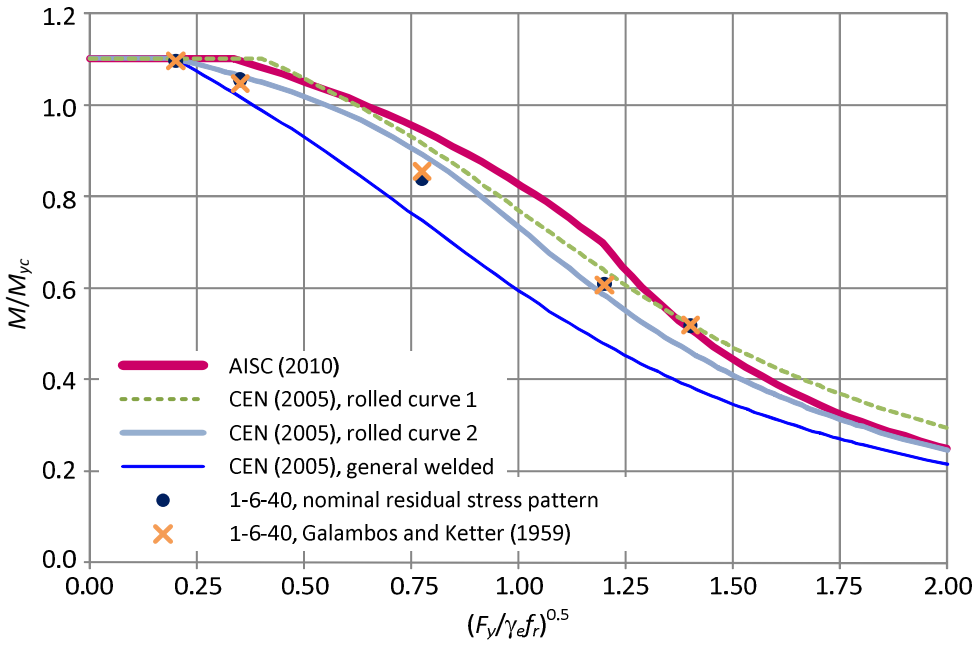

Figure 7.2. Analysis results for $h/b_{fc} = 1.0$, $b_{fc}/2t_{fc} = 6$, and $h/t_w = 40$.

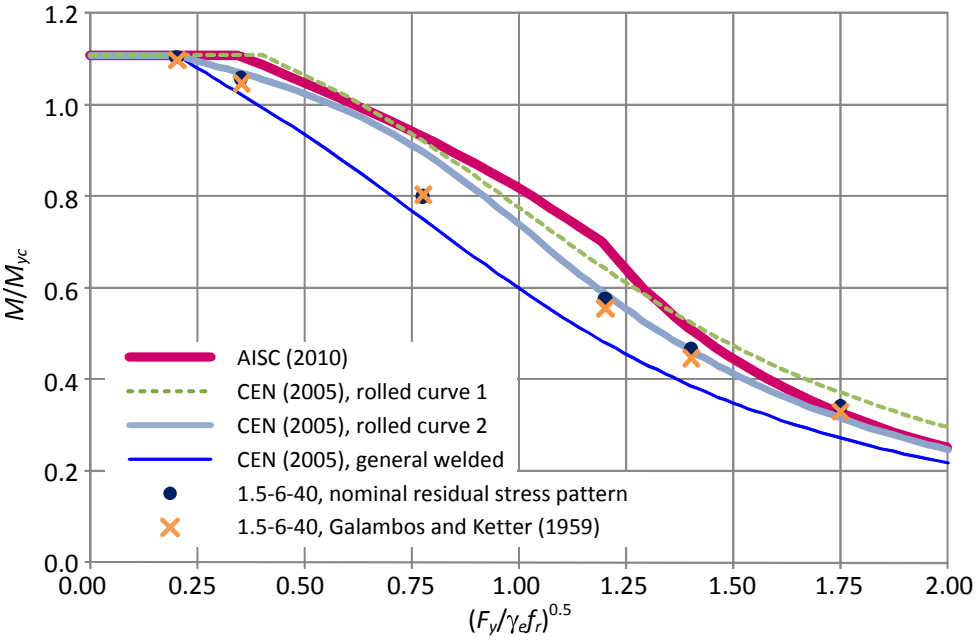

Figure 7.3. Analysis results for $h/b_{fc} = 1.5$, $b_{fc}/2t_{fc} = 6$, and $h/t_w = 40$.

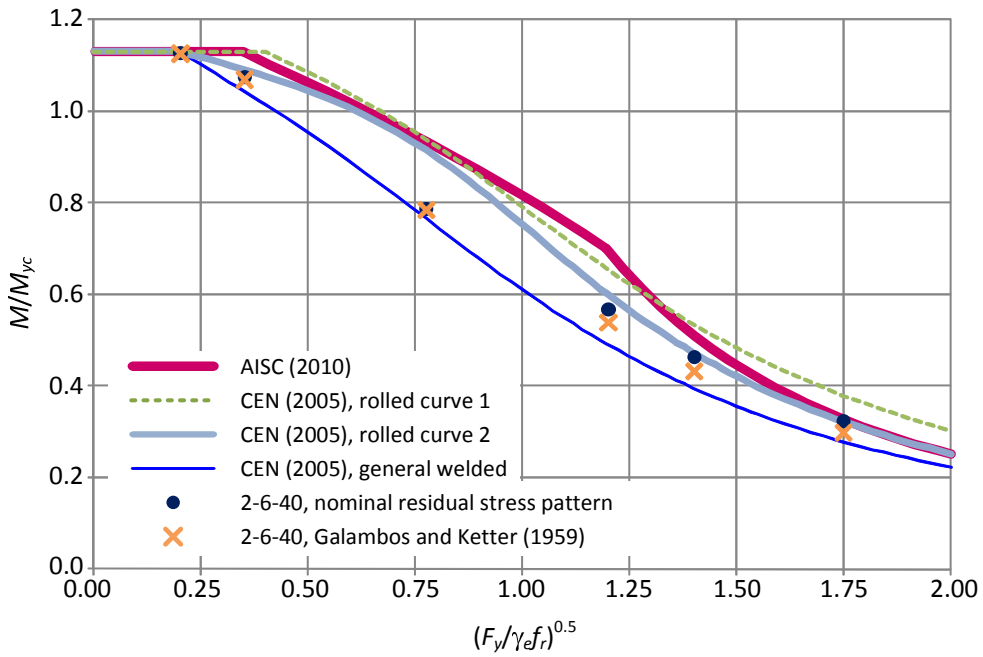

Figure 7.4. Analysis results for $h/b_{fc} = 2.0$, $b_{fc}/2t_{fc} = 6$, and $h/t_w = 40$.

Table 7.2 summarizes the M_{FEA}/M_{AISC} values of the test beams shown above. It is seen in Figures 7.2 to 7.4 that there is practically no difference between the virtual test simulation results using two different residual stress patterns. Therefore, only the values of M_{FEA} obtained using the selected nominal welded residual stress pattern are shown in Table 7.2. It should be noted that the ratio of M_{FEA} to M_{AISC} is smaller with higher h/b_{fc} values. In addition, the values of M_{FEA}/M_{AISC} are smaller for the beams with $(F_y/\gamma_e f_r)^{0.5} =$ 0.775 and 1.2. The smallest value of M_{FEA}/M_{AISC} is 0.81, which occurs for the case with $h/b_{fc} = 2.0$ and $(F_y/\gamma_e f_r)^{0.5} = 1.2$.

Figures 7.5 and 7.6 illustrate the von Mises and the equivalent plastic strain contour plots at the peak load for the test member with $h/b_{fc} = 2.0$, $(F_y/\gamma_e f_r)^{0.5} = 0.775$, and the selected best-fit Prawel residual stresses. All the response contour plots shown in this chapter are obtained at the mid-surface of the elements unless otherwise noted. It is

shown in Figures 7.5 and 7.6 that about half of compression flange is yielded at the peak load for this case. Figure 7.7 shows the equivalent plastic strain contour for the test member with h/b_{fc} = 2.0, $(F_y/\gamma_e f_r)^{0.5}$ = 1.2, and the best-fit Prawel residual stresses at the peak load. It can be seen that approximately one-quarter of the compression flange in the center of the beam has been yielded.

Table 7.2. Summary of M_{FEA}/M_{AISC} for the cases with compact sections and h/b_{fc} = 1.0, 1.5, and 2.0 (best-fit Prawel residual stress pattern).

M_{FEA}/M_{AISC}	$(F_y/F_e)^{0.5}$					
Case	0.2	0.35	0.775	1.2	1.4	1.75
1-6-40	1.00	0.96	0.93	0.87	1.02	n/a
1.5-6-40	1.00	0.95	0.89	0.82	0.92	1.04
2-6-40	1.00	0.95	0.86	0.81	0.90	0.99

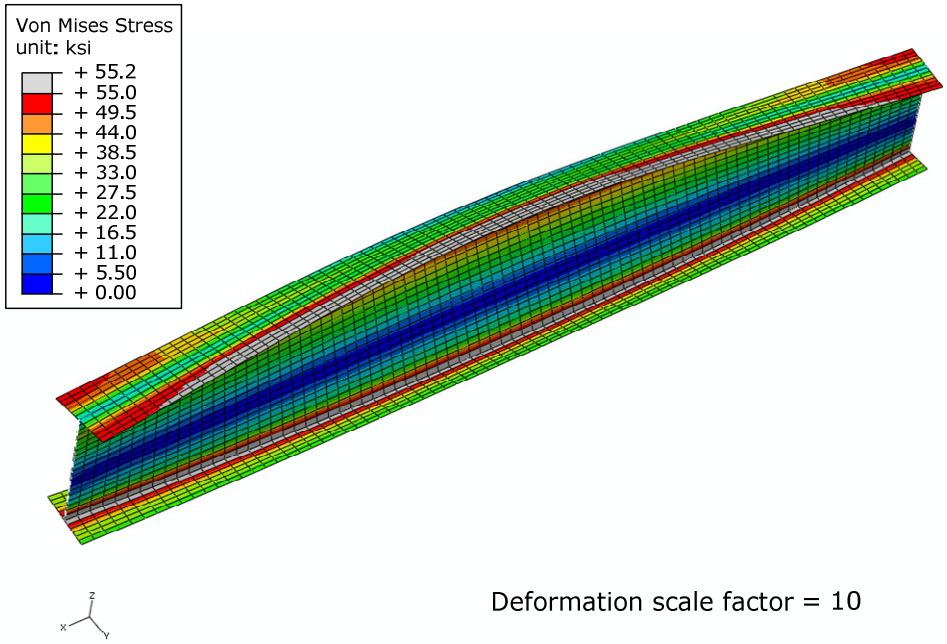

Figure 7.5. von Mises contour plot at peak load
(prismatic beam with h/b_{fc} = 2, $b_{fc}/2t_{fc}$ = 6, h/t_w = 40, and $(F_y/\gamma_e f_r)^{0.5}$ = 0.775).

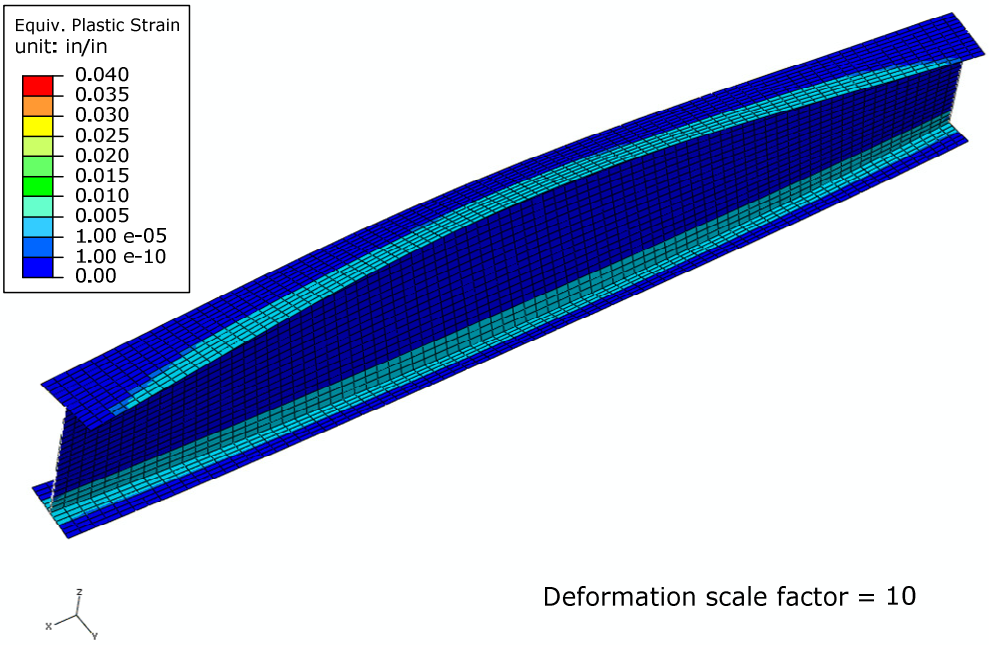

Figure 7.6. Equivalent plastic strain contour plot at peak load (prismatic beam with $h/b_{fc} = 2$, $b_{fc}/2t_{fc} = 6$, $h/t_w = 40$, and $(F_y/\gamma_e f_r)^{0.5} = 0.775$).

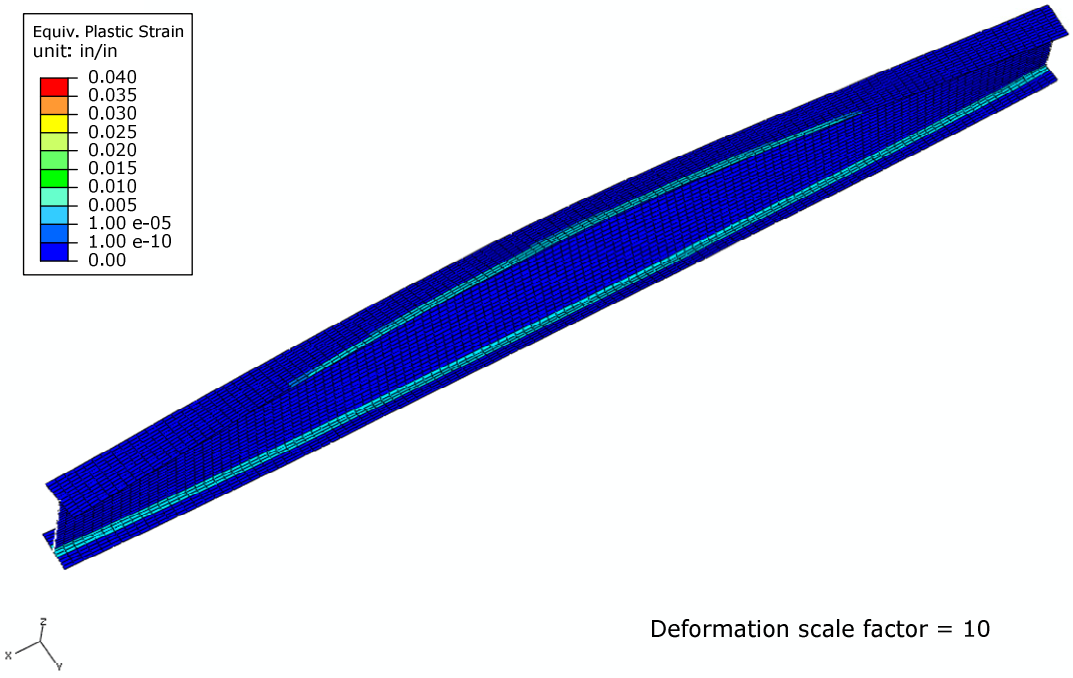

Figure 7.7. Equivalent plastic strain contour plot at peak load (prismatic beam with $h/b_{fc} = 2$, $b_{fc}/2t_{fc} = 6$, $h/t_w = 40$, and $(F_y/\gamma_e f_r)^{0.5} = 1.2$).

7.2.1.2 Members with compact flanges and a noncompact web ($b_{fc}/2t_{fc}$ = 6 and h/t_w = 100)

Figures 7.8 through 7.10 show the virtual test simulation results of prismatic and tapered members with compact flanges and a noncompact web with h/b_{fc} values of 4.0, 5.5 and 7.0. In these figures, two LTB resistance curves based on AISC (2010) and CEN (2005) are shown for prismatic members and one LTB curve based on the design guide, *Frame Design using Web-Tapered Members* (MBMA/AISC 2010) is shown for tapered members. The members considered in this section are categorized as Class 4 in CEN (2005). Therefore CEN (2005) requires that they are designed based on the general welded-section curve shown in Figures 7.8 to 7.10. It should be noted that in Figures 7.8 to 7.10, the AISC (2010) and MBMA/AISC (2010) curves are essentially the same. Because the LTB resistance calculations in MBMA/AISC (2010) are developed based on the use of $J = 0$ (see Section 3.3.2), the differences between the AISC (2010) and MBMA/AISC (2010) curves are larger for members with large St. Venant torsional effect. For the cases presented in this dissertation, there is no big differences between the AISC (2010) and MBMA/AISC (2010) curves as seen in Figures 7.8 to 7.10.

As described above, the test members are generated in six different lengths: $(F_y/F_e)^{0.5}$ = 0.2, 0.35, 0.775, 1.2, 1.4, and 1.7. Since the flange stresses f_r are constant throughout the unbraced lengths in prismatic members, the value of $(F_y/F_e)^{0.5}$ is always same as the value of $(F_y/\gamma_e f_r)^{0.5}$. In tapered members, however, the flange stresses f_r vary throughout the unbraced length under the given loadings because of the variation in the cross section. To calculate γ_e for LTB of tapered members, the cross section where the flange stress is the maximum is identified. At this location, the elastic LTB load level γ_e

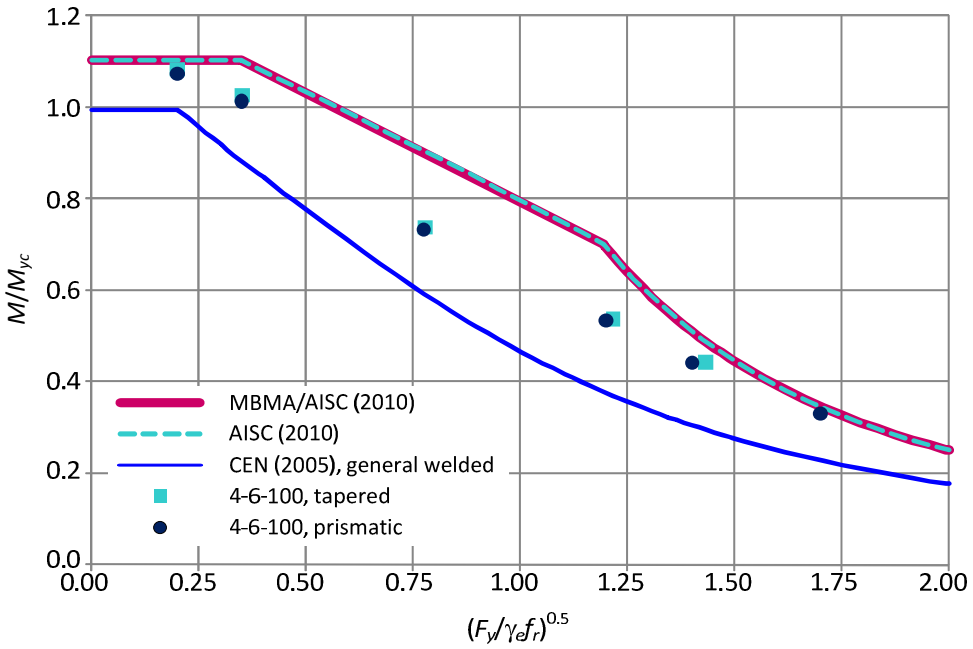

Figure 7.8. Analysis results for $h/b_{fc} = 4.0$, $b_{fc}/2t_{fc} = 6$, and $h/t_w = 100$.

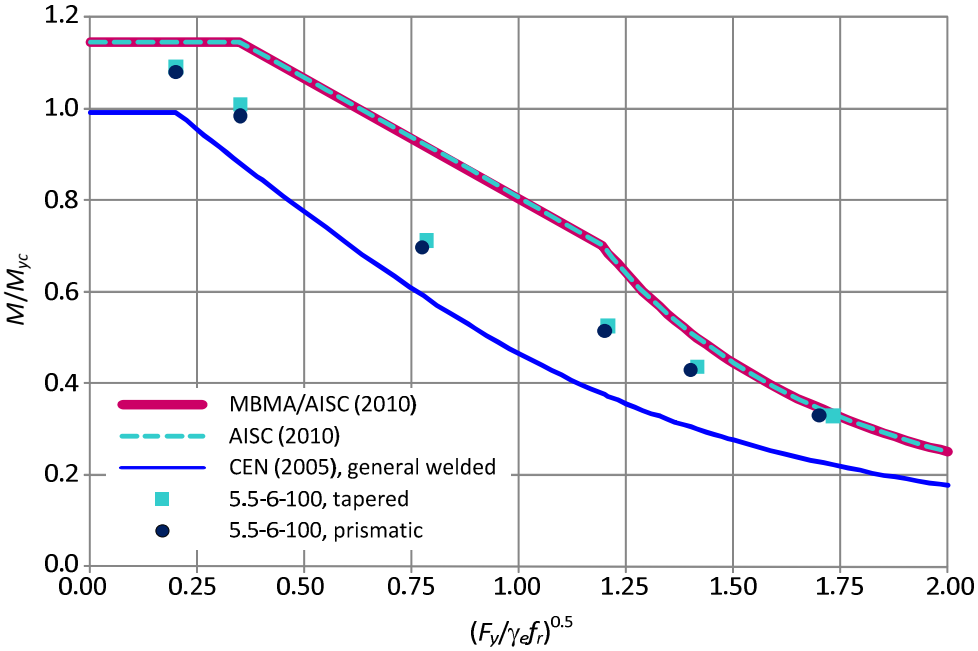

Figure 7.9. Analysis results for $h/b_{fc} = 5.5$, $b_{fc}/2t_{fc} = 6$, and $h/t_w = 100$.

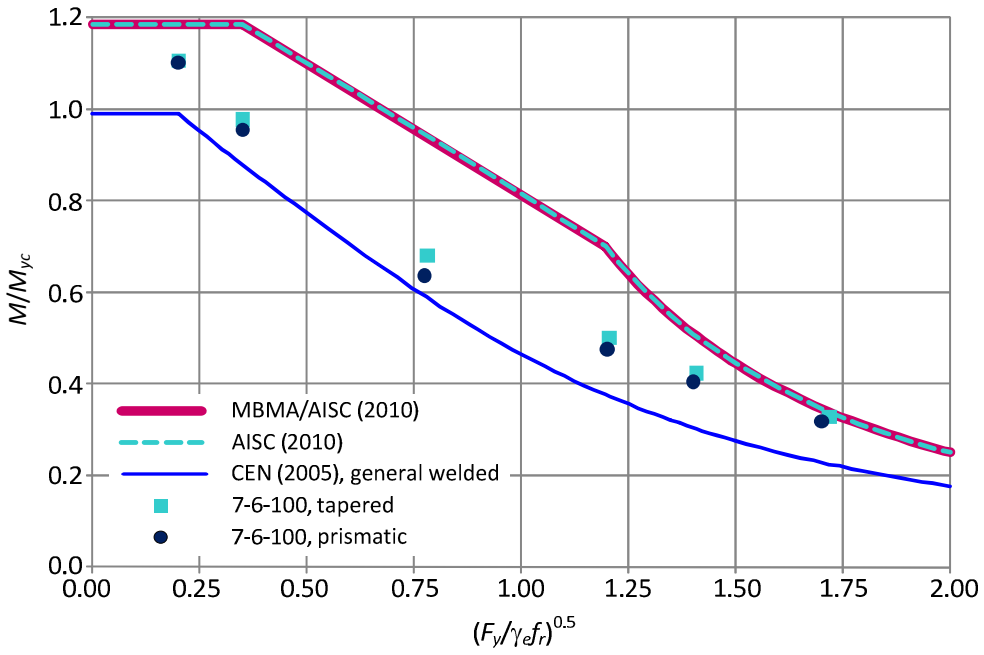

Figure 7.10. Analysis results for $h/b_{fc} = 7.0$, $b_{fc}/2t_{fc} = 6$, and $h/t_w = 100$.

is calculated by $F_e/f_{r.max}$. It is important to note that for a given tapered beam, one γ_e exists. Furthermore, the influence of the web slenderness varies along the web for web-tapered members. As a result, the controlling design check for LTB can occur at the location other than $f_{r.max}$. The LTB resistances of tapered beams are shown based on $(F_y/\gamma_e f_r)^{0.5}$, where f_r is determined at the location where the controlling LTB design check occurs. Therefore, the $(F_y/F_e)^{0.5}$ value is not necessarily the same as the $(F_y/\gamma_e f_r)^{0.5}$ value for tapered members. For all the cases considered in this study, the governing flexural capacity of tapered members is obtained at the deep end. However, the maximum flange stress $f_{r.max}$ is obtained another location within the unbraced length for the longer length beams in general. This is the reason why the virtual test simulation data points for the tapered members are not exactly at the selected $(F_y/F_e)^{0.5}$ values that are used for design of test beams (see Figures 7.8 to 7.10).

It should be noted that the virtual test simulation results for tapered beams are practically the same or slightly higher than the virtual simulation results of equivalent prismatic beams. This shows that the equivalent prismatic member concept, which is developed in this study and employed in MBMA/AISC (2010), works well. Table 7.3 compares the values of M_{FEA}/M_{yc} for the tapered and prismatic beams with h/b_{fc} = 7.0, $b_{fc}/2t_{fc}$ = 6.0, and h/t_w = 100. The maximum difference between M_{FEA}/M_{yc} of tapered and prismatic beams is 6.9 % for the beams with $(F_y/\gamma_e f_r)^{0.5}$ = 0.775. Figure 7.11 shows the normalized applied moment M_{FEA}/M_{yc} versus the plastic rotation plots for the tapered and prismatic beams with h/b_{fc} = 7.0, $b_{fc}/2t_{fc}$ = 6.0, and h/t_w = 100, and $(F_y/\gamma_e f_r)^{0.5}$ = 0.775. Except the fact that the maximum M_{FEA}/M_{yc} of the tapered beam is slightly larger than the one of the prismatic beam, the plots for tapered and prismatic members are very similar. In Figure 7.12, the plots of the normalized applied moment versus the out-of-plane displacements at mid-length are shown. It can be seen that the response of the tapered beam is very similar to that of the prismatic beam.

Table 7.3. Summary of M_{FEA}/M_{AISC} for tapered and prismatic members with h/b_{fc} = 7, $b_{fc}/2t_{fc}$ = 6, and h/t_w = 100.

M_{FEA}/M_{yc}	$(F_y/F_e)^{0.5}$					
Case	0.2	0.35	0.775	1.2	1.4	1.7
Tapered	1.11	0.98	0.68	0.50	0.42	0.33
Prismatic	1.10	0.95	0.64	0.48	0.40	0.32

Table 7.4 provides a summary of $M_{FEA}/M_{MBMA\text{-}AISC}$ for the tapered members considered in this section. As seen in the previous section, the $M_{FEA}/M_{MBMA\text{-}AISC}$ values are significantly reduced with increasing h/b_{fc} values. The cases considered in this

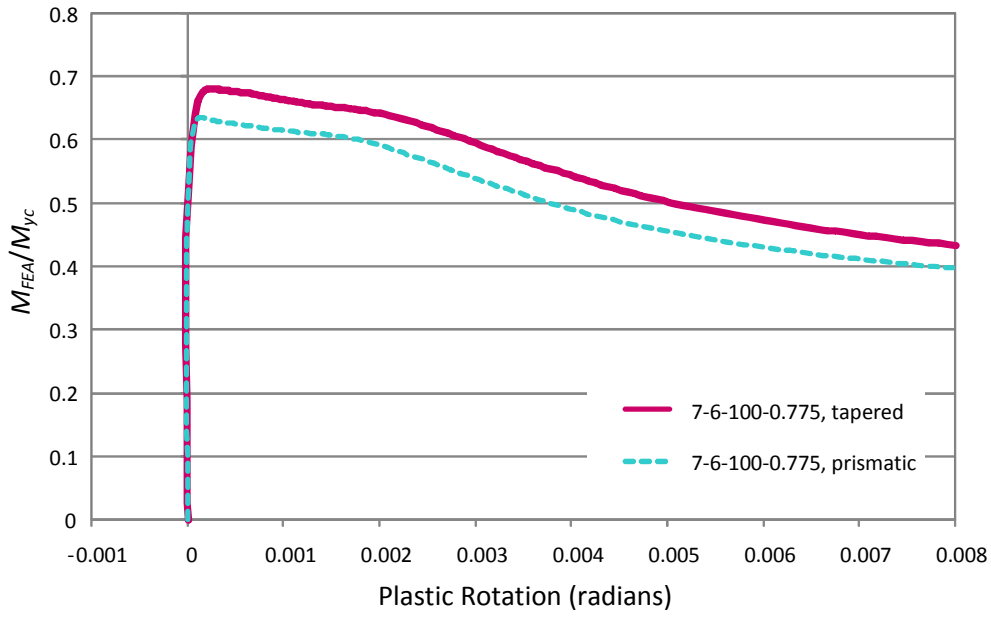

Figure 7.11. Applied moments versus plastic rotation ($h/b_{fc} = 7$, $b_{fc}/2t_{fc} = 6$, and $h/t_w = 100$).

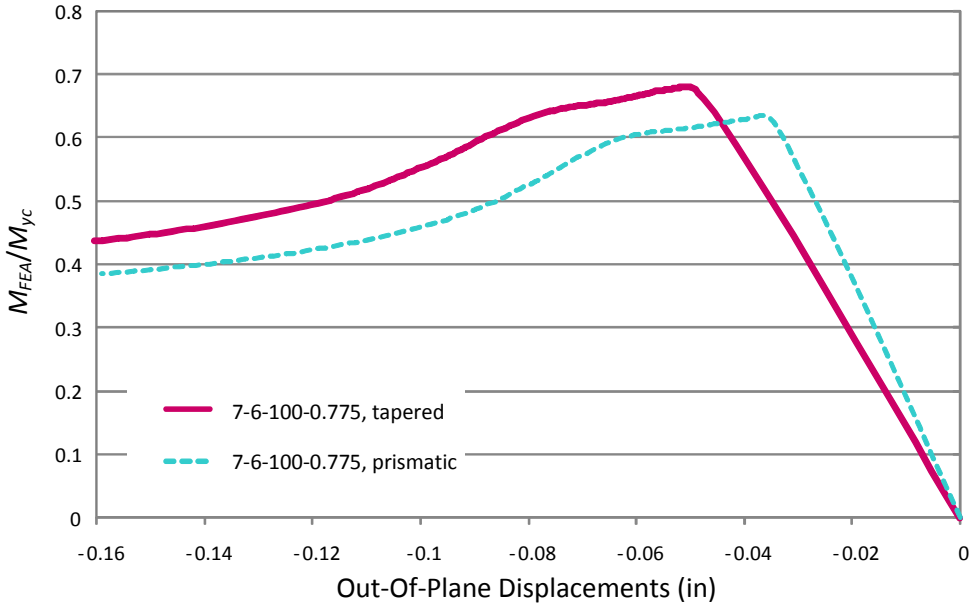

Figure 7.12. Applied moments versus out-of-plane displacements ($h/b_{fc} = 7$, $b_{fc}/2t_{fc} = 6$, and $h/t_w = 100$).

section are the worst cases where the virtual test simulation strengths are significantly lower than the AISC (2010) LTB estimates. The maximum decrease in $M_{FEA}/M_{MBMA\text{-}AISC}$ occurs for the case with $h/b_{fc} = 7$, $b_{fc}/2t_{fc} = 6$, $h/t_w = 100$, and $(F_y/\gamma_e f_r)^{0.5} = 0.775$. The $M_{FEA}/M_{MBMA\text{-}AISC}$ value for this case is 11.6 % smaller than the corresponding case with $h/b_{fc} = 4$. Figures 7.13 and 7.14 show the von Mises stress and the equivalent plastic strain contours for the case with $h/b_{fc} = 7$, $b_{fc}/2t_{fc} = 6$, $h/t_w = 100$, and $(F_y/\gamma_e f_r)^{0.5} = 0.775$. As seen in Figure 7.6, approximate half of compression flange is yielded at the peak load. Also the web-flange juncture at the tension flange is yielded due to the high residual stress in this region.

Table 7.4. Summary of $M_{FEA}/M_{MBMA\text{-}AISC}$ for tapered members with $b_{fc}/2t_{fc} = 6$, $h/t_w = 100$, and $h/b_{fc} = 4$, 5.5, and 7

$M_{FEA}/M_{MBMA\text{-}AISC}$	$(F_y/F_e)^{0.5}$					
Case	0.2	0.35	0.775	1.2	1.4	1.7
4-6-100	0.98	0.93	0.82	0.79	0.91	n/a
5.5-6-100	0.95	0.88	0.78	0.77	0.87	0.99
7-6-100	0.93	0.82	0.73	0.73	0.84	0.97

Figures 7.9 and 7.10 show that with $h/b_{fc} = 5.5$ and 7, the finite element models can not develop the plateau strengths at the short lengths correspond to $(F_y/F_e)^{0.5} = 0.2$ and 0.35. It is important to recognize that the lengths of these beams are less than or approximately equal to the web depths. Figures 7.15 shows the von Mises stress and the equivalent plastic strain contours at peak load for the case with $h/b_{fc} = 7$, $b_{fc}/2t_{fc} = 6$, $h/t_w = 100$, and $(F_y/F_e)^{0.5} = 0.2$. The ratio of the unbraced length to the web depth at the deep end L_b/h for this case is 0.43. At the peak load, the compression and tension flanges of this member are nearly fully yielded and approximately one-half of the web is yielded as well.

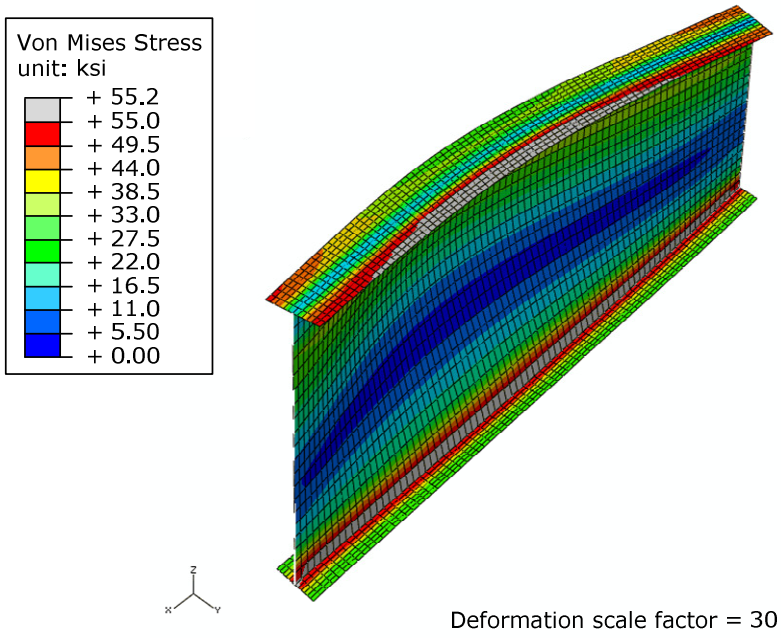

Figure 7.13. von Mises contour plot at peak load
(tapered beam with $h/b_{fc} = 7$, $b_{fc}/2t_{fc} = 6$, $h/t_w = 100$, and $(F_y/\gamma_e f_r)^{0.5} = 0.775$).

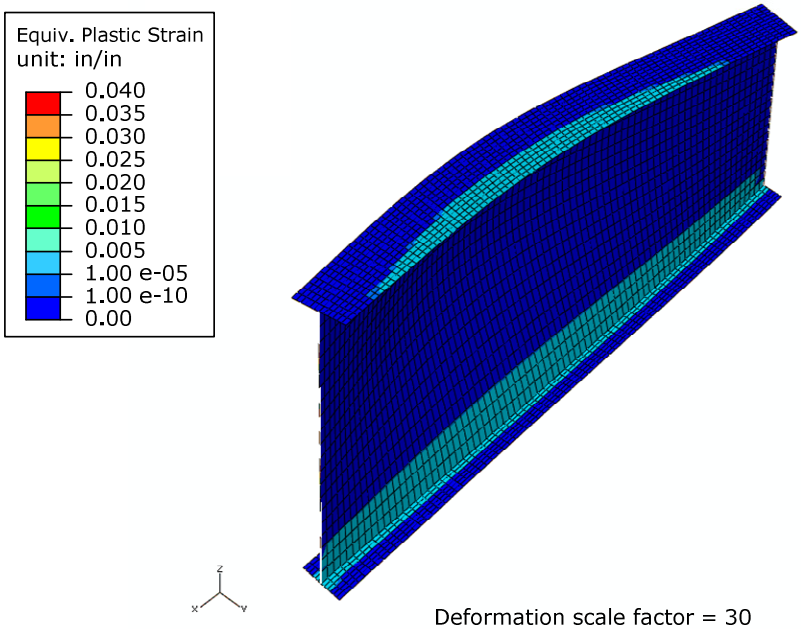

Figure 7.14. Equivalent plastic strain contour plot at peak load
(tapered beam with $h/b_{fc} = 7$, $b_{fc}/2t_{fc} = 6$, $h/t_w = 100$, and $(F_y/\gamma_e f_r)^{0.5} = 0.775$).

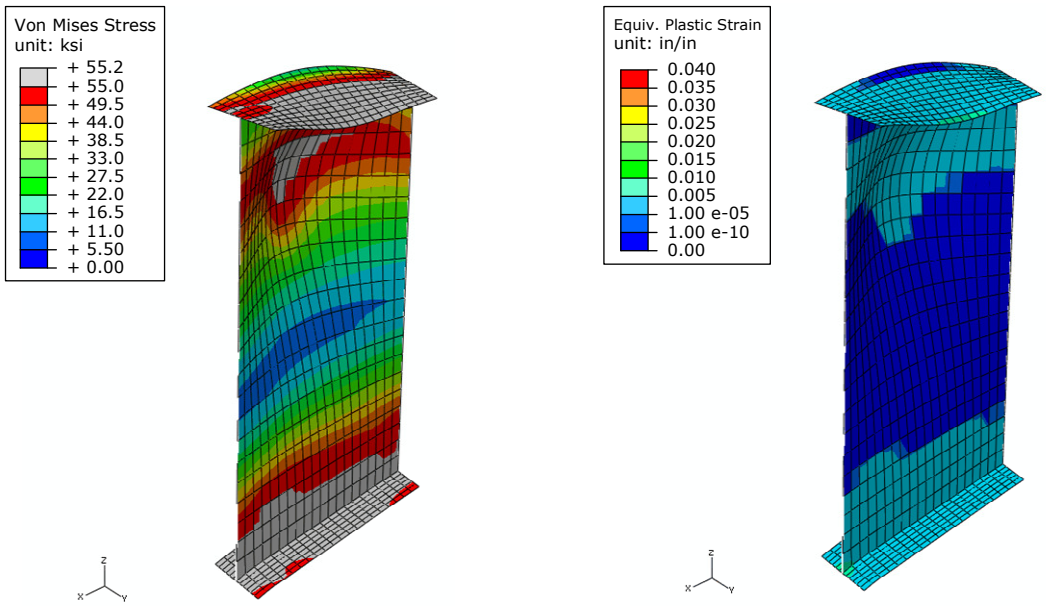

(a) von Mises stress contour

(b) Equivalent plastic strain contour

Deformation scale factor = 20

Figure 7.15. von Mises stress and equivalent plastic strain contour plots at peak load (tapered beam with $h/b_{fc} = 7$, $b_{fc}/2t_{fc} = 6$, $h/t_w = 100$, and $(F_y/F_e)^{0.5} = 0.2$).

Table 7.4 shows the significant reductions of the $M_{FEA}/M_{MBMA\text{-}AISC}$ values with increasing h/b_{fc} values. However, Figures 7.8 to 7.10 show that the reductions of the M_{FEA}/M_{yc} values are actually smaller than the reductions of the M_{FEA}/M_{AISC} or $M_{FEA}/M_{MBMA\text{-}AISC}$ values with increasing h/b_{fc} values. Table 7.5 shows a summary of the M_{FEA}/M_{yc} values for tapered members with $h/b_{fc} = 4$, 5.5, and 7. The values of M_{yc} are calculated at the deep end of tapered members. For most cases, the M_{FEA}/M_{yc} values are close for the beams with the same $(F_y/F_e)^{0.5}$ values. The maximum difference in M_{FEA}/M_{yc} is found in the cases with $(F_y/F_e)^{0.5} = 0.775$. The M_{FEA}/M_{yc} value for the beam with $h/b_{fc} = 7$ and $(F_y/F_e)^{0.5} = 0.775$ is 7.7 % smaller than the corresponding case with $h/b_{fc} = 4$.

Table 7.5. Summary of M_{FEA}/M_{yc} for tapered members with $b_{fc}/2t_{fc} = 6$, $h/t_w = 100$, and $h/b_{fc} = 4$, 5.5, and 7

M_{FEA}/M_{yc}	$(F_y/F_e)^{0.5}$					
Case	0.2	0.35	0.775	1.2	1.4	1.7
4-6-100	1.08	1.03	0.74	0.54	0.44	n/a
5.5-6-100	1.09	1.01	0.71	0.53	0.44	0.33
7-6-100	1.11	0.98	0.68	0.50	0.42	0.33

Based on the analysis results shown in Figures 7.8 to 7.10, a number of important observations can be made to explain why the AISC (2010) curves for the cases considered above are significantly optimistic compared to the virtual test simulation results. First of all, Figures 7.8 to 7.10 show that the plateau lengths of the AISC (2010) curves are longer than implied by the virtual test simulation results, which results in the unconservative predictions of the LTB capacity at $(F_y/F_e)^{0.5} = 0.35$ for all the cases studied in this section. The plateau length of $(F_y/F_e)^{0.5} = 0.2$ in CEN (2005) seems more reasonable compared to the virtual test simulation results. It also should be noted that the maximum moment capacity of beams with a noncompact web in AISC (2010) is overly optimistic compared to the virtual test simulation results throughout the inelastic LTB range. As discussed above, with large h/b_{fc} values, the maximum moment capacity of AISC (2010) cannot be reached even with very short beams. The AISC (2010) capacity at the inelastic LTB limit seems somewhat optimistic as well compared to the virtual test simulation results. At the inelastic LTB limit, $(F_y/F_e)^{0.5} = 1.2$, the values of M_{FEA}/M_{yc} are from 0.50 to 0.54 for the cases studied in this section (see Table 7.5). These values are 23 % to 28 % smaller than $M_{AISC}/M_{yc} = 0.7$ at this limit. Finally, it is observed from the virtual test simulation results that the LTB strengths are reduced with large h/b_{fc} values especially within the inelastic LTB region. This supports the concave shape of the curves

of CEN (2005) for general welded I-section members. On the contrary, AISC (2010) suggests a straight-line transition for inelastic LTB from the maximum capacity to the elastic LTB strength. The combined effect of all the above factors generates the significant differences between the LTB strengths based on the virtual test simulation and the AISC (2010) Specifications for the cases considered in this section.

As mentioned above, the cross sections of the test members studied in this section are categorized as Class 4 in CEN (2005). The maximum moment capacity of beams with Class 4 cross sections is calculated by

$$M_{CEN,max} = S_{eff} F_y \quad \text{(Eq. 7.2)}$$

where S_{eff} is an effective section modulus. For the doubly-symmetric test cases with a noncompact web, the values of S_{eff} are only slightly less than S_{xc} (see Figures 7.8 to 7.10). It is observed that the finite element models can develop the yield moment capacity of beams with $(F_y/\gamma_\epsilon f_r)^{0.5} \leq 0.35$.

7.2.1.3 Members with noncompact flanges and a noncompact web ($b_{fc}/2t_{fc} = 12$ and $h/t_w = 130$)

Figures 7.16 through 7.18 show the virtual test simulation results of members with noncompact flanges and a noncompact web with h/b_{fc} values of 1, 2 and 4. For the cases with $h/b_{fc} = 1$ and 2, only prismatic members are generated. On the other hand, for the cases with $h/b_{fc} = 4$, both prismatic and tapered members are studied. Because of the noncompact flanges, the maximum moment capacities in AISC (2010) are governed by flange local buckling (FLB). In Figures 7.16 to 7.18, the FLB limit of AISC (2010) is shown by the horizontal line. It should be noted that for the flange local buckling checks, the MBMA/AISC (2010) design guide suggests using the FLB equations of AISC (2010).

Therefore, the FLB limit of AISC (2010) shown in Figures 7.21 applies also to the tapered members.

Based on CEN (2005), the web and flanges of the above sections are Class 4. Therefore, the resistance curve for general welded sections is applied. It should be noted that in CEN (2005), different curves are suggested for members with $h/b_{fc} \leq 2$ and $h/b_{fc} > 2$. For the cases with $h/b_{fc} = 1$ and 2, the CEN (2005) curves are slightly convex from the plateau to the middle of inelastic LTB region and slightly concave from the middle of inelastic LTB region to the elastic LTB region. This can be seen more clearly in the CEN (2005) rolled curve 2, which is shown in Figures 7.2 to 7.4. Conversely, for cases with $h/b_{fc} = 4$, the CEN (2005) curves are entirely concave except for the plateau.

Figures 7.16 to 7.18 illustrate that at short unbraced lengths, the test beams can develop larger moments than the FLB limits. It should be noted, however, the imperfection shape employed in this study is developed focusing on the LTB failures not on the FLB failures. At $(F_y/F_e)^{0.5} = 0.775$, the virtual test simulation strengths are smaller than the AISC (2010) estimates and larger than the CEN (2005) estimates as seen in the previous sections. It should be noted in Figure 7.18 that the virtual test simulation results of tapered beams are practically same as the results of prismatic beams with noncompact flanges. This is consistent with the results of compact-flange cases in Sections 7.2.1.1 and 7.2.1.2. Table 7.6 shows a summary of M_{FEA}/M_{AISC} for the prismatic members governed by LTB. The trend that the ratio of M_{FEA}/M_{AISC} becomes smaller with large h/b_{fc} values is again exhibited in this summary.

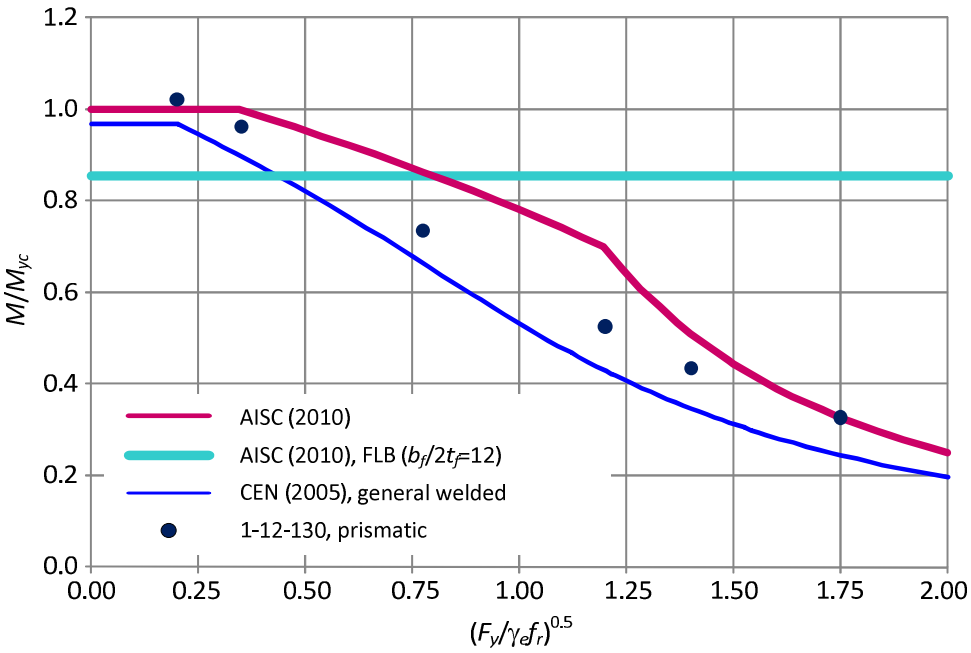

Figure 7.16. Analysis results for h/b_{fc} = 1.0, $b_{fc}/2t_{fc}$ = 12, and h/t_w = 130.

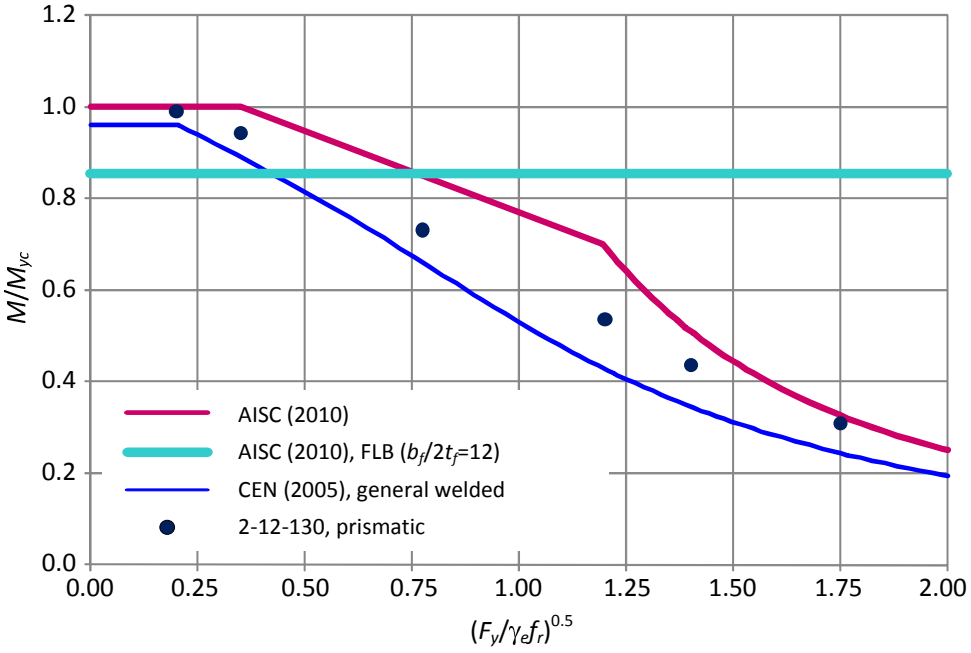

Figure 7.17. Analysis results for h/b_{fc} = 2.0, $b_{fc}/2t_{fc}$ = 12, and h/t_w =130.

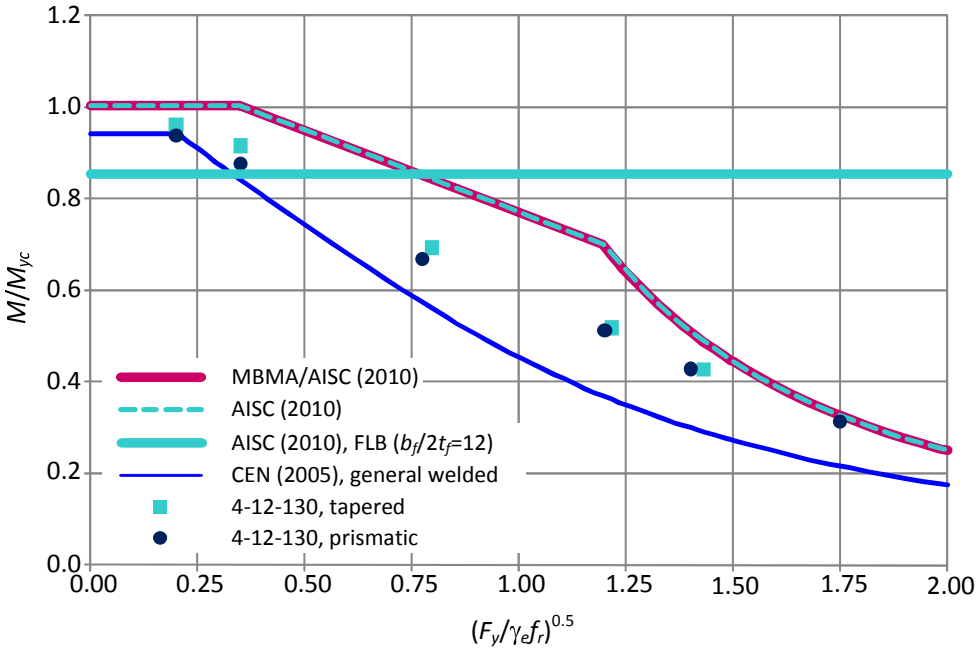

Figure 7.18. Analysis results for h/b_{fc} = 4.0, $b_{fc}/2t_{fc}$ = 12, and h/t_w =130.

Table 7.6. Summary of M_{FEA}/M_{AISC} for prismatic members with $b_{fc}/2t_{fc}$ = 12, h/t_w = 130, and h/b_{fc} = 1, 2, and 4

M_{FEA}/M_{AISC}	$(F_y/F_e)^{0.5}$			
Case	0.775	1.2	1.4	1.75
1-12-130	0.85	0.75	0.85	1.00
2-12-130	0.86	0.77	0.86	0.95
4-12-130	0.79	0.73	0.84	0.96

7.2.1.4 Members with compact flanges and a slender web ($b_{fc}/2t_{fc}$ = 6 and h/t_w = 180)

Figures 7.19 through 7.21 show the virtual test simulation results for members with compact flanges and a slender web with h/b_{fc} values of 4, 5.5 and 7. For these cases, both tapered and prismatic members are considered. In Figures 7.19 to 7.21, a range of resistance curves is shown for CEN (2005). This is because the calculations of the elastic LTB moment for members with a slender web in AISC (2010) and MBMA/AISC (2010)

are different from the calculations in CEN (2005). In AISC (2010) and MBMA/AISC (2010), the elastic LTB moment for members with a slender web is calculated with $J = 0$, where J is St. Venant torsional constant. Conversely, in CEN (2005), the value of J is always counted in the calculation of the elastic LTB moment. In this study, the values of $(F_y/F_e)^{0.5}$ are calculated based on the elastic LTB moment obtained as specified in AISC (2010) or MBMA/AISC (2010). Therefore, for each beam with a different length, there is a different CEN (2005) curve. It should be noted that the plateau strength of CEN (2005) is essentially the same as the capacity of AISC (2010) and MBMB/AISC (2010). For the cross sections with compact flanges and a slender web considered in this study, the effective section modulus S_{eff} in CEN (2005) is practically the same as $R_{pg}S_{xc}$ in AISC (2010).

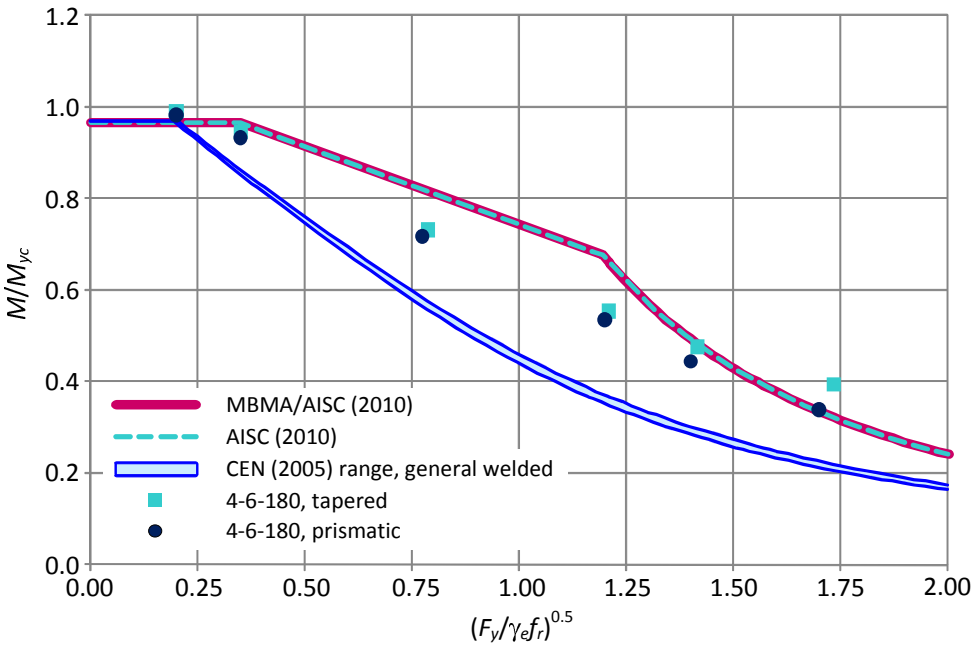

Figure 7.19. Analysis results for $h/b_{fc} = 4.0$, $b_{fc}/2t_{fc} = 6$, and $h/t_w = 180$

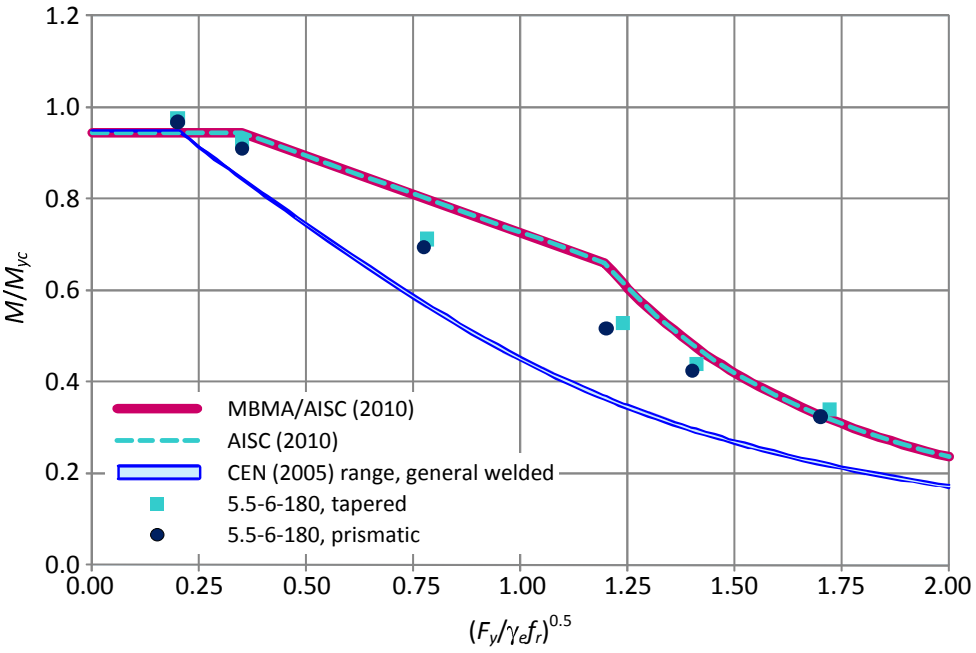

Figure 7.20. Analysis results for $h/b_{fc} = 5.5$, $b_{fc}/2t_{fc} = 6$, and $h/t_w = 180$

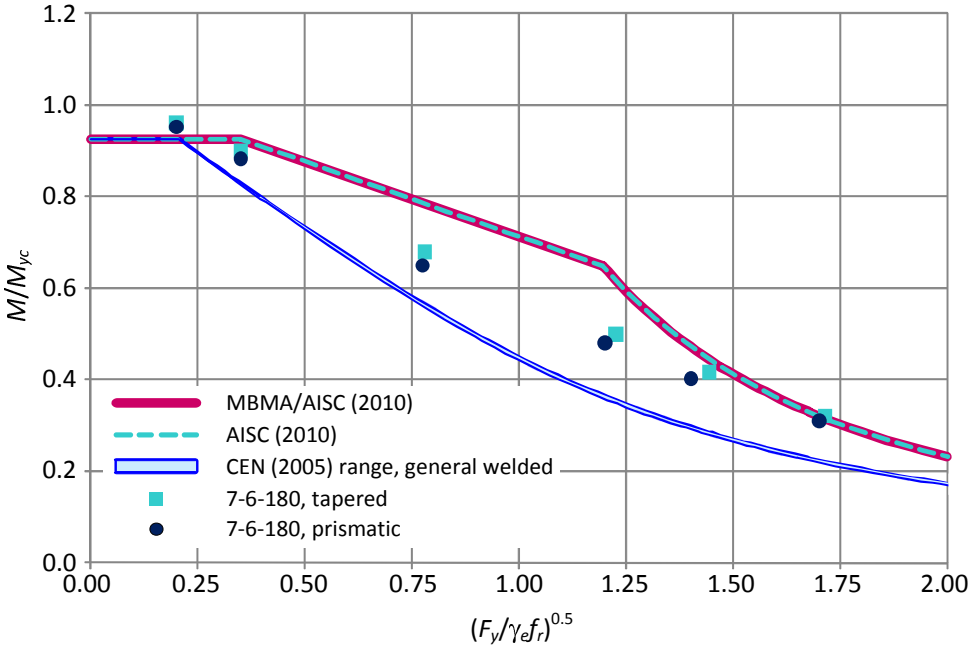

Figure 7.21. Analysis results for $h/b_{fc} = 7.0$, $b_{fc}/2t_{fc} = 6$, and $h/t_w = 180$

As seen in the previous cases, the LTB strengths of tapered beams are practically same as the LTB strengths of the equivalent prismatic beams. It can be concluded that this findings holds regardless of the flange and web slenderness and the ratio of h/b_{fc}. Figure 7.19 shows that the tapered beam with $(F_y/F_e)^{0.5} = 1.7$ develops 0.39 M_{yc} while the corresponding prismatic beam develops 0.34 M_{yc}. It should be noted that these beams are extremely long ($L_b/r_t = 123$ for the prismatic beam) such that the web at the shallow end of the tapered beam is very stocky ($h/t_w = 45.5$). Since the elastic LTB moment of tapered beams is calculated based on $J = 0$ because of the slender web at the deep end (MBMA/AISC 2010), this results in slightly conservative elastic LTB capacity based on MBMA/AISC (2010) for the extremely long tapered beam.

For the test beams with a slender web shown above, the virtual test simulation develops the plateau strengths quite well. As in the previous cases considered, the virtual test simulation strengths fall between the AISC (2010) and MBMB/AISC (2010) capacities and the CEN (2005) strengths. It is important to note that in the cases with a slender web, the nominal strengths based on AISC (2010) and MBMA/AISC (2010) are not as unconservative as the corresponding nominal strengths for the test cases with a noncompact web ($h/t_w = 100$) shown in the previous section. Table 7.7 summarizes the values of $M_{FEA}/M_{MBMA\text{-}AISC}$ for tapered members with $b_{fc}/2t_{fc} = 6$ and $h/t_w = 180$. The average value of $M_{FEA}/M_{MBMA\text{-}AISC}$ in Table 7.7 is 0.95 while average of $M_{FEA}/M_{MBMA\text{-}AISC}$ in Table 7.4 is 0.86. It should be noted that the case with $h/b_{fc}= 4$ and $(F_y/F_e)^{0.5} = 1.7$ in Table 7.7 is not included in the calculation of the average $M_{FEA}/M_{MBMA\text{-}AISC}$ since the corresponding case with $h/t_w = 100$ is not available in Table 7.4.

Table 7.7. Summary of $M_{FEA}/M_{MBMA\text{-}AISC}$ for tapered members with $b_{fc}/2t_{fc} = 6$, $h/t_w = 180$, and $h/b_{fc} = 4$, 5.5, and 7

$M_{FEA}/M_{MBMA\text{-}AISC}$	$(F_y/F_e)^{0.5}$					
Case	0.2	0.35	0.775	1.2	1.4	1.7
4-6-180	1.03	0.98	0.90	0.84	0.99	1.23
5.5-6-180	1.03	0.98	0.89	0.86	0.92	1.06
7-6-180	1.04	0.97	0.86	0.81	0.94	1.02

7.2.1.5 Members with compact flanges and large h/b_{fc} ($b_{fc}/2t_{fc} = 6$ and $h/b_{fc} = 5.5$ and 7)

From Sections 7.2.1.2 and 7.2.1.4, it is observed that the plateau strength calculated based on AISC (2010) is overly optimistic for the beams with large h/b_{fc} and a noncompact web. On the other hand, the maximum moment capacity in AISC (2010) matches well with the virtual test simulation results for the beams with a slender web. This means that the web plastification factor R_{pc} may be too optimistic for the members with large h/b_{fc} and a compact or noncompact web. To study the relationship between the web slenderness and the maximum moment capacity of the beams with large h/b_{fc}, additional study cases are selected. Table 7.8 shows the geometric parameters of the selected test members. These additional test cases combined with the test members shown in the previous sections (the cases with $h/t_w = 100$ and 180), can show how the plateau strength varies with a range of the web slenderness from compact ($h/t_w = 85$) to slender ($h/t_w = 180$).

Figures 7.22 through 7.24 show the analysis results of beams with $h/b_{fc} = 5.5$, $b_{fc}/2t_{fc} = 6$, and $h/t_w = 85$, 115, and 130. In addition, Table 7.9 shows a summary of $M_{FEA}/M_{MBMA\text{-}AISC}$ for all the tapered beams with $h/b_{fc} = 5.5$ considered in this chapter. Based on AISC (2010), the web slenderness $h/t_w = 85$ is within the compact limit so that the AISC plateau strength of the beams with $h/t_w = 85$ is $R_{pc}M_{yc} = M_p$. However, the

Table 7.8. Geometric parameters of selected members.

h/b_{fc}	$b_{fc}/2t_{fc}$	h/t_w	b_{fc}/b_{ft}	t_{fc}/t_{ft}	β degrees
5.5	6	85	1	1	0 to 10
		115			
		130			
7	6	85	1	1	0 to 10
		115			
		130			

virtual test simulation result of the test beam with $h/b_{fc} = 5.5$ and $h/t_w = 85$ is 8 % smaller than the plastic moment M_p at $(F_y/F_e)^{0.5} = 0.2$. Furthermore, based on AISC (2010), the plateau of the moment capacity curves extends up to $(F_y/F_e)^{0.5} \leq 0.35$. It can be seen in Figure 7.22 and Table 7.9 that at $(F_y/F_e)^{0.5} = 0.35$, the LTB capacity based on virtual test simulation decreases even further so that the virtual test simulation result is 17 % smaller than $R_{pc}M_{yc}$. The same observations can be made for the test beams with a more slender web. It should be noted, however, the differences between the AISC (2010) plateau strengths and the corresponding virtual test simulation results are smaller for the members with a more slender web. In other words, as the value of R_{pc} approaches 1.0, the virtual test simulation results are closer to the maximum moment capacity of AISC (2010). With $h/t_w = 180$, the bending strength reduction factor R_{pg} applies in the resistance calculations in AISC (2010) or MBMA-AISC (2010). One can observe that the bending strength reduction factor R_{pg} provides reasonable estimates compared to the virtual test simulation results (see Figure 7.20 and Table 7.9).

Table 7.10 shows a summary of M_{FEA}/M_{yc} for the tapered beams with $h/b_{fc} = 5.5$, $b_{fc}/2t_{fc} = 6$, and all the web slenderness ratios considered in this chapter. It can be noted that the decrease in the M_{FEA}/M_{yc} from $(F_y/F_e)^{0.5} = 0.2$ to 0.35 is smaller for the beams

with a more slender web. It is also important to note that the values of M_{FEA}/M_{yc} for all the doubly-symmetric beams with $h/b_{fc} = 5.5$ are essentially the same for $(F_y/F_e)^{0.5} > 0.35$. For $(F_y/F_e)^{0.5} \leq 0.35$, a clear decrease in the moment capacities as the web slenderness value increases is observed in Table 7.10. However the decrease in M_{FEA}/M_{yc} with a more slender web is not as much as the decrease in M_{max}/M_{yc} obtained from AISC (2010). As a result, the M_{FEA}/M_{AISC} or $M_{FEA}/M_{MBMA\text{-}AISC}$ values are significantly smaller for the beams with a stocker web as seen in Table 7.9. The same observations can be made for the test beams with $h/b_{fc} = 7$. Figures 7.25 through 7.27 show the analysis results for the doubly-symmetric test beams with $h/b_{fc} = 7$. In addition, Table 7.11 shows a summary of $M_{FEA}/M_{MBMA\text{-}AISC}$ for all the doubly-symmetric tapered members with $h/b_{fc} = 7$ considered in this study. As seen in Table 7.9, the values of $M_{FEA}/M_{MBMA\text{-}AISC}$ are significantly smaller for the beams with smaller web slenderness values.

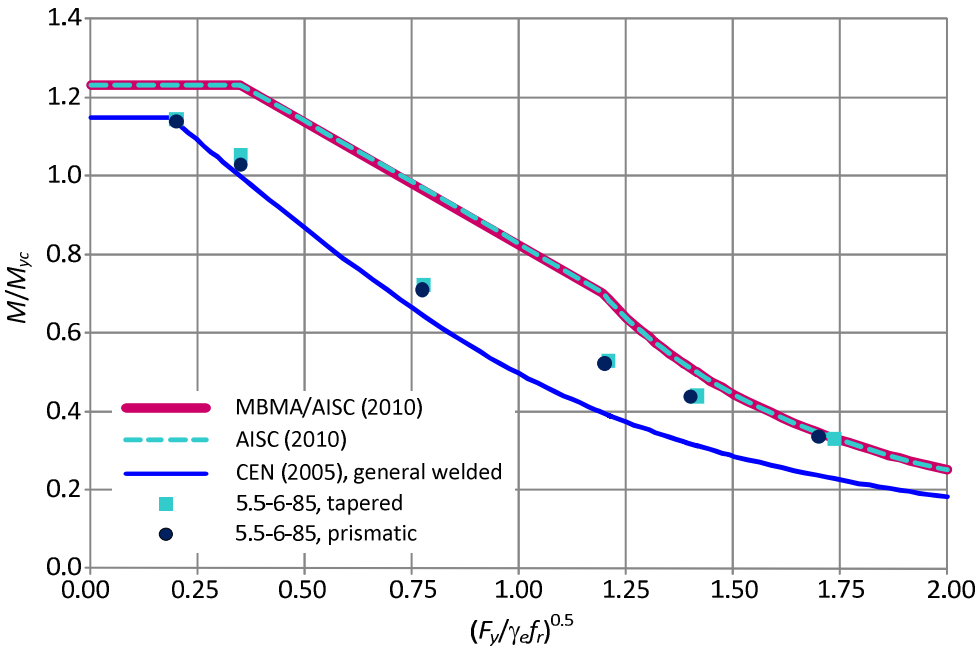

Figure 7.22. Analysis results for $h/b_{fc} = 5.5$, $b_{fc}/2t_{fc} = 6$, and $h/t_w = 85$.

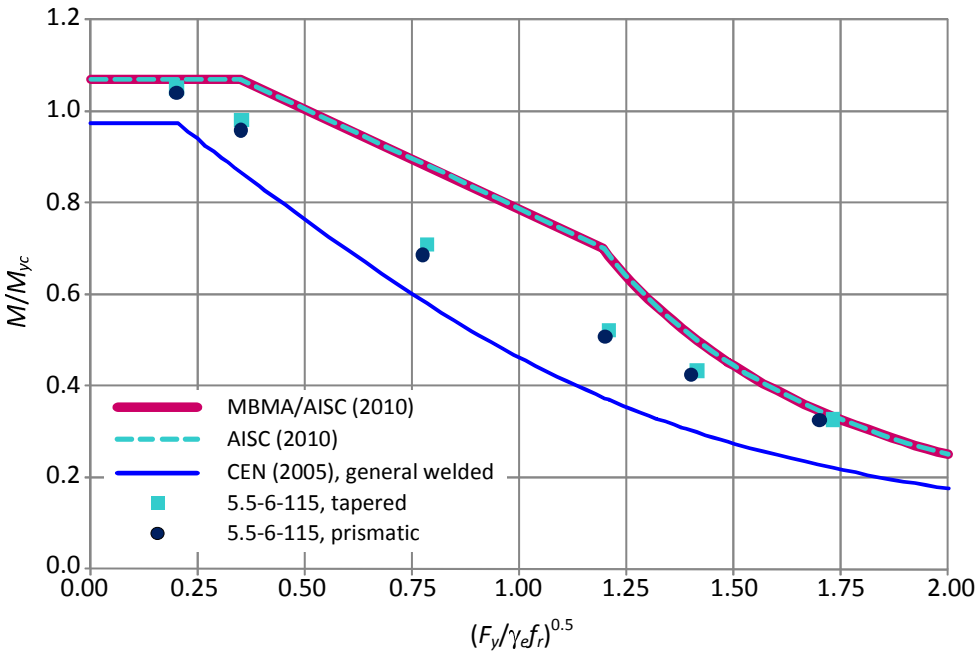

Figure 7.23. Analysis results for $h/b_{fc} = 5.5$, $b_{fc}/2t_{fc} = 6$, and $h/t_w = 115$.

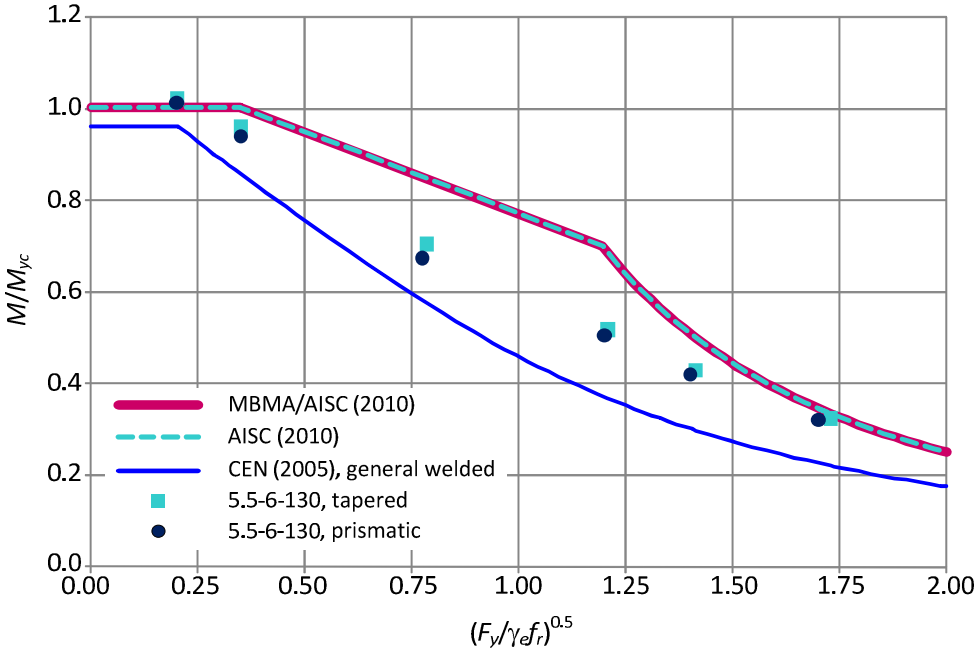

Figure 7.24. Analysis results for $h/b_{fc} = 5.5$, $b_{fc}/2t_{fc} = 6$, and $h/t_w = 130$.

Table 7.9. Summary of $M_{FEA}/M_{MBMA\text{-}AISC}$ for tapered members with $h/b_{fc} = 5.5$, $b_{fc}/2t_{fc} = 6$, and $h/t_w = 85$, 100, 115, 130, and 180.

$M_{FEA}/M_{MBMA\text{-}AISC}$	$(F_y/F_e)^{0.5}$					
Case	0.2	0.35	0.775	1.2	1.4	1.7
5.5-6-85	0.92	0.83	0.73	0.75	0.86	0.97
5.5-6-100	0.94	0.86	0.76	0.74	0.84	0.95
5.5-6-115	0.97	0.90	0.78	0.73	0.83	0.94
5.5-6-130	1.01	0.94	0.79	0.72	0.82	0.93
5.5-6-180	1.02	0.96	0.87	0.78	0.88	0.99

Table 7.10. Summary of M_{FEA}/M_{yc} for tapered members with $h/b_{fc} = 5.5$, $b_{fc}/2t_{fc} = 6$, and $h/t_w = 85$, 100, 115, 130, and 180.

M_{FEA}/M_{yc}	$(F_y/F_e)^{0.5}$					
Case	0.2	0.35	0.775	1.2	1.4	1.7
5.5-6-85	1.15	1.05	0.72	0.53	0.44	0.33
5.5-6-100	1.09	1.01	0.71	0.53	0.44	0.33
5.5-6-115	1.05	0.98	0.71	0.52	0.43	0.33
5.5-6-130	1.02	0.96	0.71	0.52	0.43	0.32
5.5-6-180	0.98	0.92	0.71	0.53	0.44	0.34

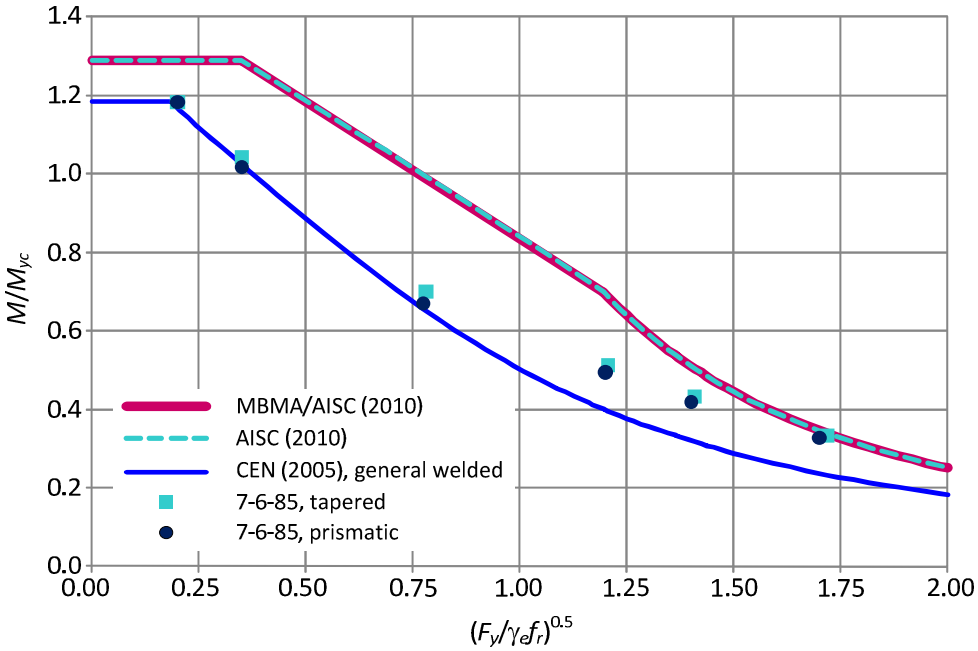

Figure 7.25. Analysis results for $h/b_{fc} = 7$, $b_{fc}/2t_{fc} = 6$, and $h/t_w = 85$.

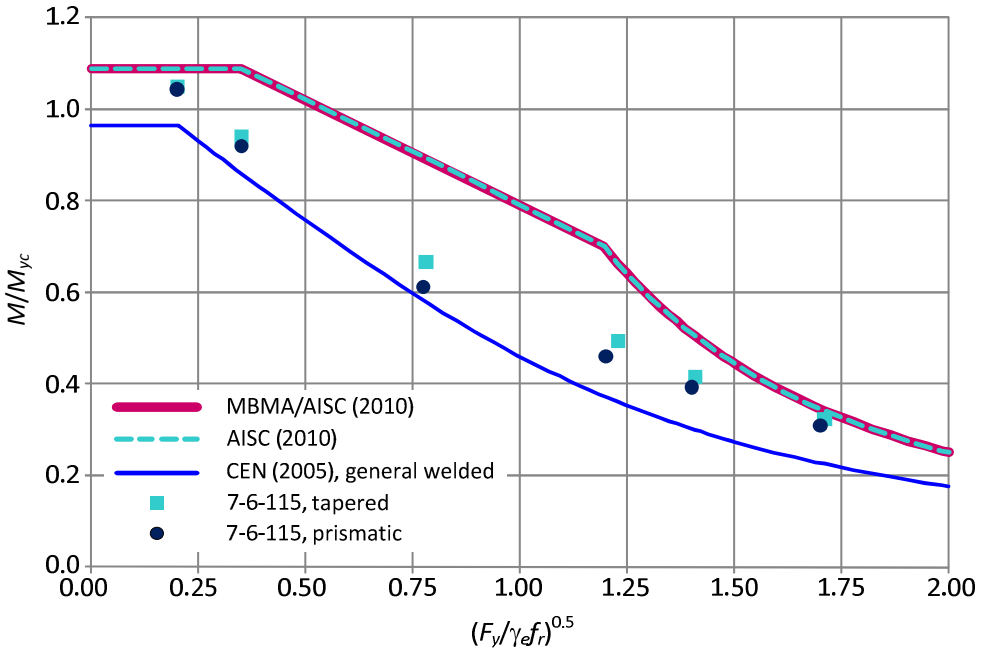

Figure 7.26. Analysis results for $h/b_{fc} = 7$, $b_{fc}/2t_{fc} = 6$, and $h/t_w = 115$.

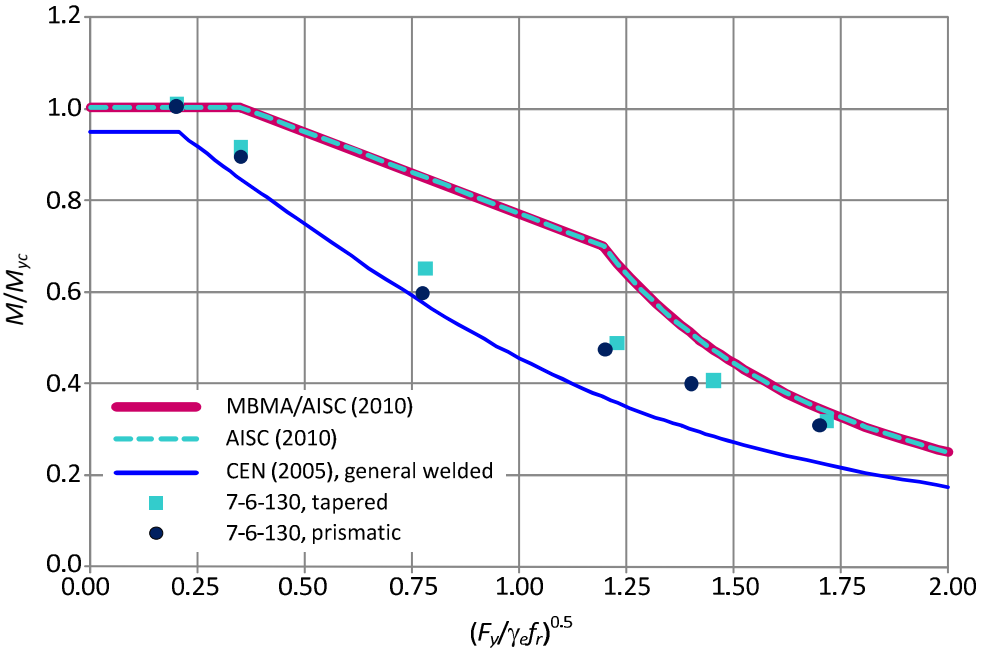

Figure 7.27. Analysis results for $h/b_{fc} = 7$, $b_{fc}/2t_{fc} = 6$, and $h/t_w = 130$.

Table 7.11. Summary of $M_{FEA}/M_{MBMA\text{-}AISC}$ for tapered members with $h/b_{fc} = 7$, $b_{fc}/2t_{fc} = 6$, and $h/t_w = 85$, 100, 115, 130, and 180.

$M_{FEA}/M_{MBMA\text{-}AISC}$	$(F_y/F_e)^{0.5}$					
Case	0.2	0.35	0.775	1.2	1.4	1.7
7-6-85	0.92	0.81	0.71	0.74	0.86	0.98
7-6-100	0.93	0.82	0.73	0.73	0.84	0.97
7-6-115	0.96	0.86	0.75	0.75	0.83	0.94
7-6-130	1.01	0.91	0.77	0.74	0.86	0.94
7-6-180	1.04	0.97	0.86	0.81	0.94	1.02

Conceptually, a beam that has a compact cross-section and a very short length should develop the full plastic moment of the cross-section. In Section 7.2.1.1, it is shown that the finite element simulations of beams with $b_{fc}/2t_{fc} = 6$, $h/t_w = 40$, and $h/b_{fc} =$ 1, 1.5, and 2 develop the plastic moment M_p at $(F_y/F_e)^{0.5} = 0.2$. At $(F_y/F_e)^{0.5} = 0.35$, the virtual test simulation results are slightly smaller than M_p but the differences in the virtual test simulation results and M_p are not significant. The maximum difference is 5 % for the test beams with $h/b_{fc} = 1.5$ and 2. On the other hand, it is found in the current section that if the beams have large h/b_{fc}, then even with a compact cross-section and a very short length ($b_{fc}/2t_{fc} = 6$, $h/t_w = 85$, and $(F_y/F_e)^{0.5} = 0.2$), the maximum capacities of these beams are smaller than M_p.

Figures 7.28 and 7.29 show the von Mises and the equivalent plastic strain contours of the beams with $h/b_{fc} = 1$ and $h/b_{fc} = 5.5$. It can be seen that the length of the beam with $h/b_{fc} = 5.5$ to achieve $(F_y/F_e)^{0.5} = 0.2$ is shorter than the web depth. With h/b_{fc} = 1.0, the ratio of unbraced length to the web depth is 4.3. Figure 7.28(a) shows that the region with von Mises stresses higher than 55 ksi expands throughout the unbraced length to a greater extent than in Figure 7.29(a). It can be seen that with $h/b_{fc} = 5.5$, the

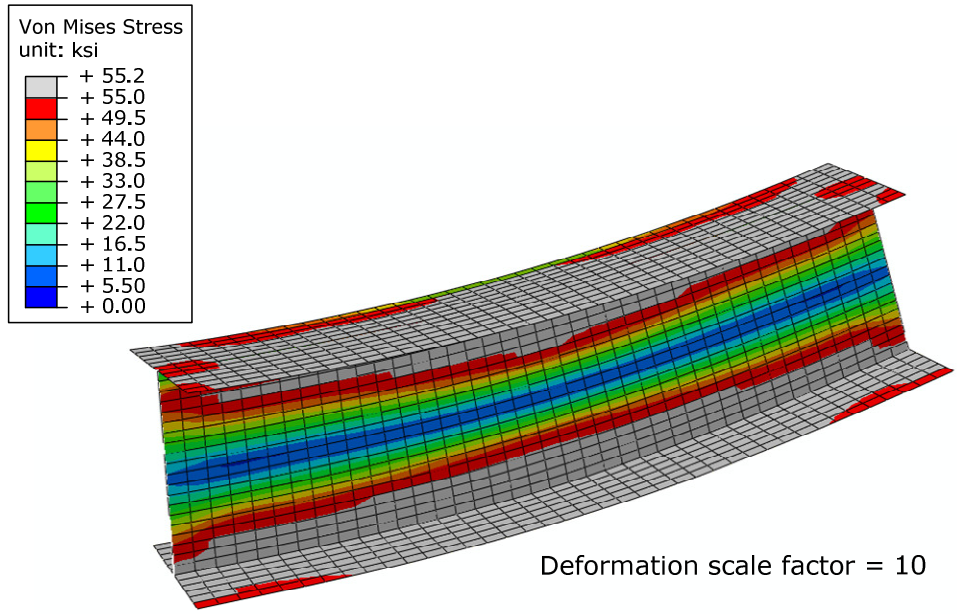

(a) von Mises stress contour

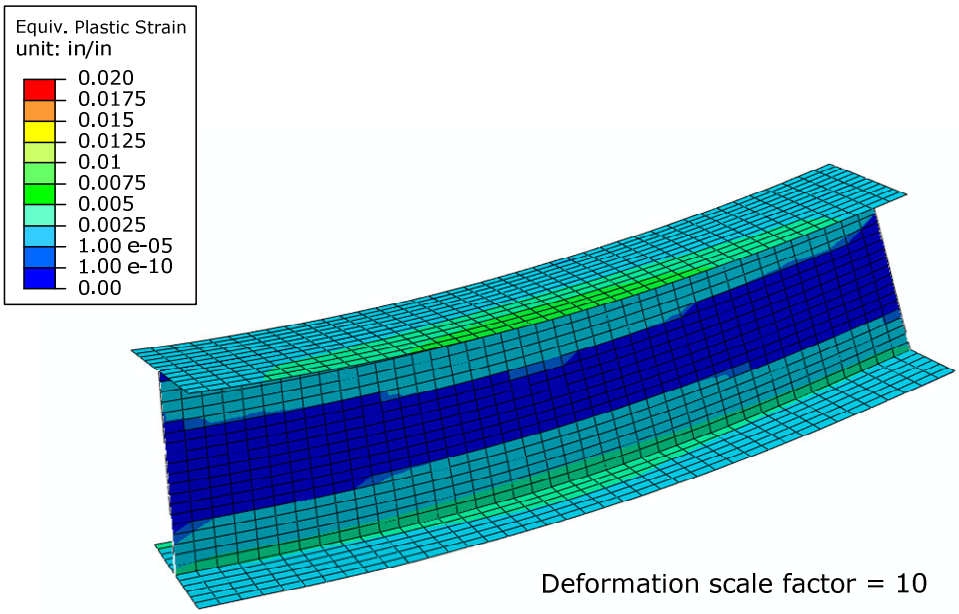

(b) Equivalent plastic strain contour

Figure 7.28. von Mises stress and equivalent plastic strain contour plots at peak load (prismatic beam with $h/b_{fc} = 1$, $b_{fc}/2t_{fc} = 6$, $h/t_w = 40$, and $(F_y/F_e)^{0.5} = 0.2$).

top region of the web and the compression flange are locally buckled before the member develops significant yielding in the top of the web. This behavior is even more evident in Figures 7.30 and 7.31 where the equivalent plastic strain contours are shown at the top and bottom surfaces of the web panels. Figure 7.30 shows equivalent plastic strain contours that are very similar on the front and back surfaces. This means that there is essentially no local buckling in the web panel of the test beam with h/b_{fc} = 1.0. Conversely, Figure 7.31 shows distinctively different equivalent plastic strain contours for the front and back surfaces of the web panel. It also can be seen that the compression flange is noticeably twisted due to the local buckling in the web panel in this case.

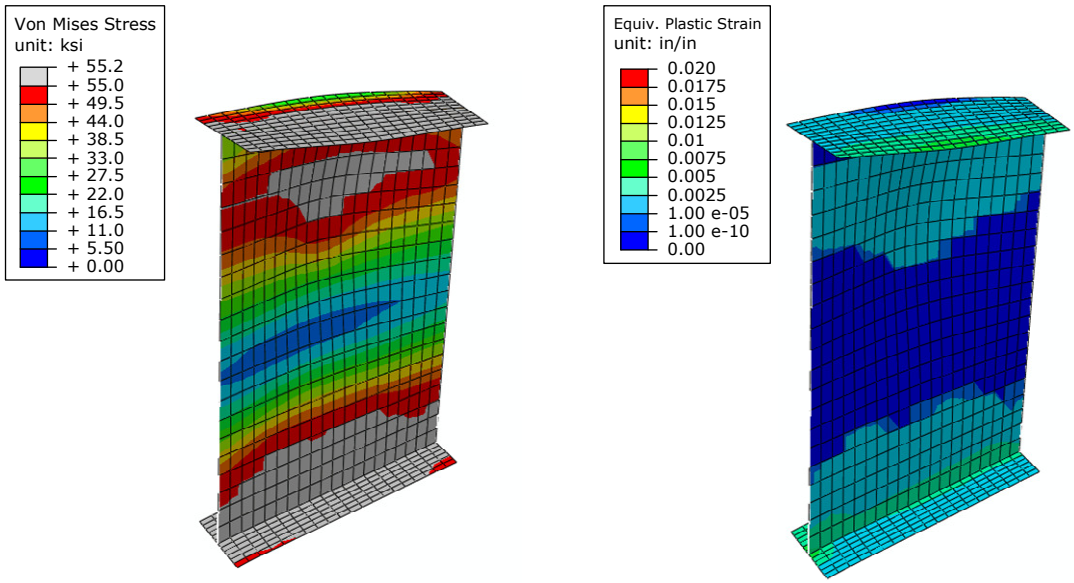

(a) von Mises stress contour

(b) Equivalent plastic strain contour

Figure 7.29. von Mises stress and equivalent plastic strain contour plots at peak load (tapered beam with h/b_{fc} = 5.5, $b_{fc}/2t_{fc}$ = 6, h/t_w = 85, and $(F_y/F_e)^{0.5}$ = 0.2).

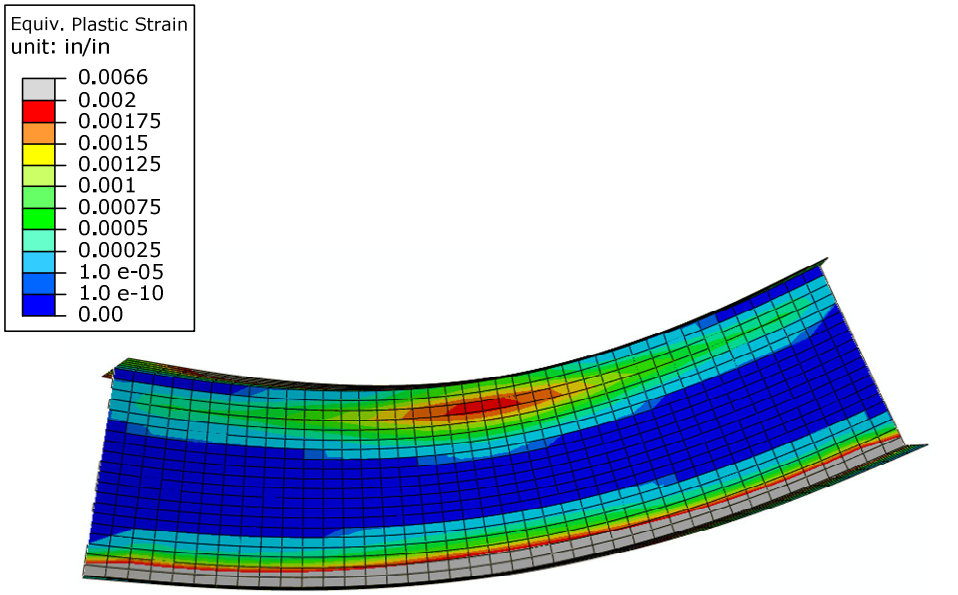

(a) Front surface

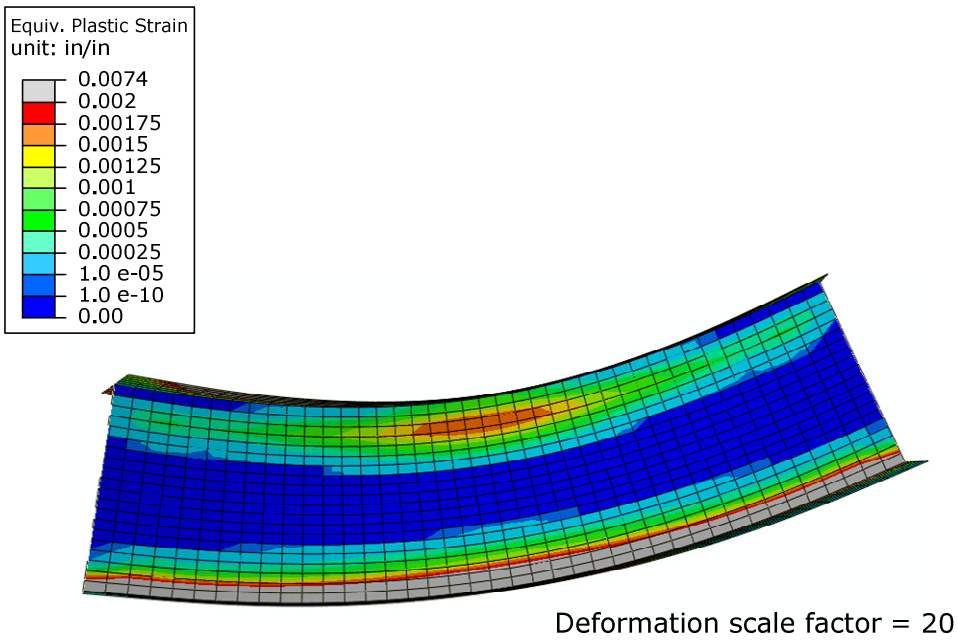

(b) Back surface

Figure 7.30. Equivalent plastic strain contour plots at peak load (prismatic beam with $h/b_{fc} = 1$, $b_{fc}/2t_{fc} = 6$, $h/t_w = 40$, and $(F_y/F_e)^{0.5} = 0.2$).

Based on the observations discussed above, the reason why the beams with large h/b_{fc} cannot reach M_p with a stocky web and the short unbraced length can be explained as follows. When the beams have narrow flanges relative to the web depth, the plastic moment of the cross-section becomes significantly larger than the yield moment. For the beams with $h/b_{fc} = 7$ and $h/t_w = 85$ shown in Figure 7.25, the ratio of the plastic moment to the yield moment, M_p/M_{yc} is 1.29. The majority of the plastic moment capacity for this type of beam, i.e., the beam with very narrow flanges, comes from the deep web panel. However, as discussed above it seems that the compression side of the deep web panel is locally buckled before it is fully yielded. As a result, the beams with narrow flanges cannot develop the full plastic moment capacity even with a very short unbraced length.

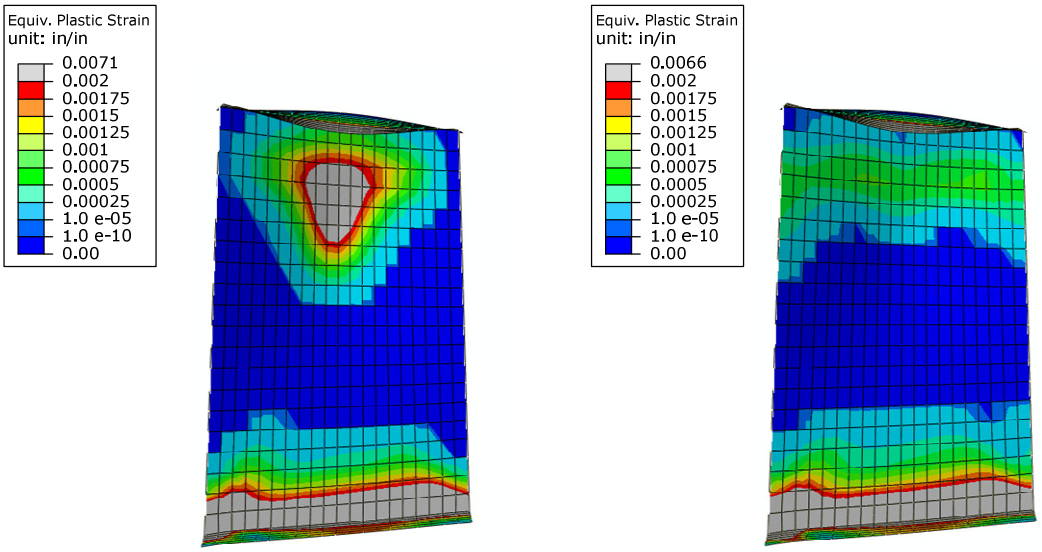

Figure 7.31. Equivalent plastic strain contour plots at peak load (tapered beam with $h/b_{fc} = 5.5$, $b_{fc}/2t_{fc} = 6$, $h/t_w = 85$, and $(F_y/F_e)^{0.5} = 0.2$).

7.2.2 Singly-Symmetric Tests with Uniform-Stress Conditions

7.2.2.1 Members with compact flanges and a noncompact web ($b_{fc}/2t_{fc} = 6$, $h/t_w = 100$)

It is observed in the previous section that the test cases with $b_{fc}/2t_{fc} = 6$ and $h/t_w = 100$ are the worst cases where the AISC (2010) and MBMA/AISC (2010) resistances are significantly unconservative compared to the virtual test simulation results and the CEN (2005) resistances. Therefore, it is decided to study the effect of singly-symmetric sections on the LTB strengths using the test cases with $b_{fc}/2t_{fc} = 6$, $h/t_w = 100$, and $h/b_{fc} = 4$ and 7.

Figures 7.32 and 7.33 illustrate the virtual test simulation results and the nominal resistances for members with $h/b_{fc} = 4$, $b_{fc}/2t_{fc} = 6$, $h/t_w = 100$, and $b_{fc}/b_{ft} = 1.5$ and $t_{fc}/t_{ft} = 1.5$ respectively. With $b_{fc}/b_{ft} = 1.5$, the ratio of clear web depth to tension flange width h/b_{ft} is 6 and the flange slenderness $b_{ft}/2t_{ft}$ is 4, and with $t_{fc}/t_{ft} = 1.5$, the h/b_{ft} value is 4 and the $b_{ft}/2t_{ft}$ value is 9. Since the tension flanges are smaller than the compression flanges for these cases, the maximum moment capacity is governed by tension flange yielding (TFY) in AISC (2010) and MBMA/AISC (2010). In Figures 7.32 and 7.33, the horizontal line represents the TFY limit for these members. With the singly-symmetric geometry and $(F_y/F_e)^{0.5} = 1.4$ and 1.7, the web slenderness h/t_w at the shallow end of tapered members becomes less than 40 even with a taper angle $\beta = 5°$. Therefore, these tapered cases are not considered in this study.

Based on CEN (2005), the test members with $h/b_{fc} = 4$, $b_{fc}/2t_{fc} = 6$, $h/t_w = 100$, and $b_{fc}/b_{ft} = 1.5$ and $t_{fc}/t_{ft} = 1.5$ are categorized as "effective Class 2" section. This is because the web is Class 3 but the flanges are Class 1. It should be noted that the doubly

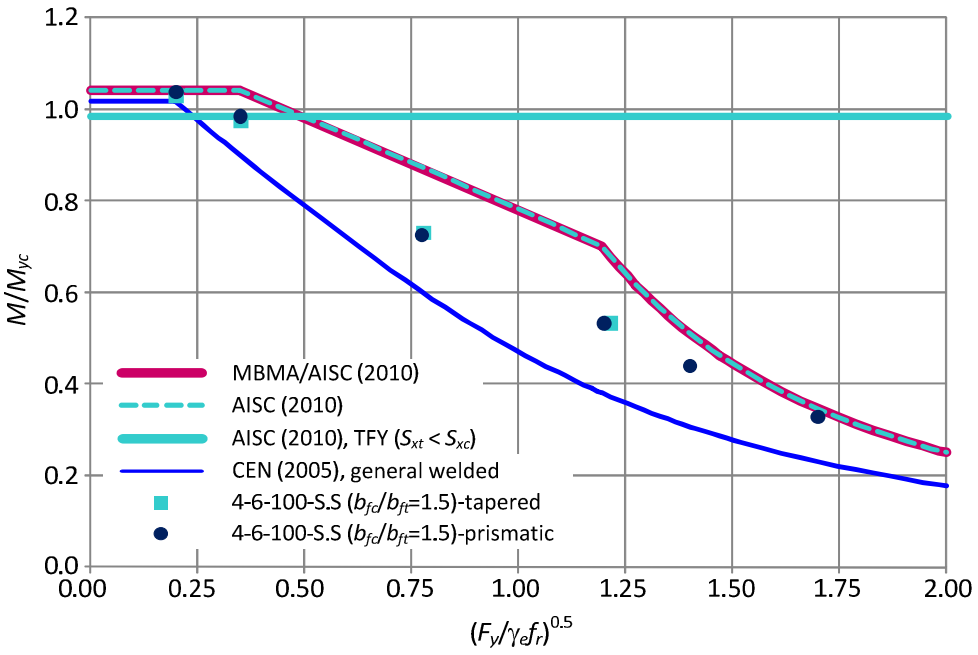

Figure 7.32. Analysis results for $h/b_{fc} = 4.0$, $b_{fc}/2t_{fc} = 6$, $h/t_w = 100$, and $b_{fc}/b_{ft} = 1.5$.

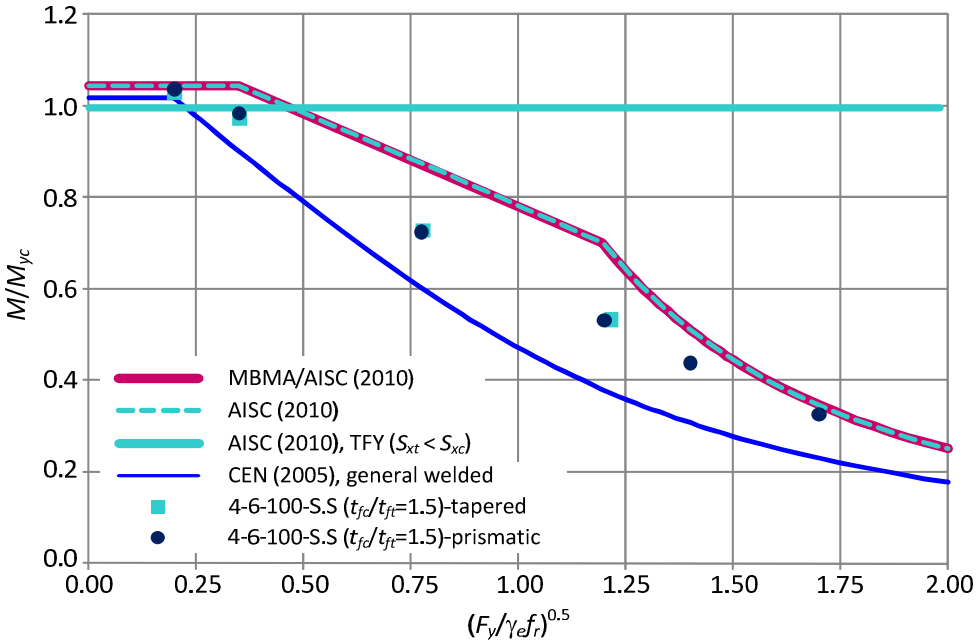

Figure 7.33. Analysis results for $h/b_{fc} = 4.0$, $b_{fc}/2t_{fc} = 6$, $h/t_w = 100$, and $t_{fc}/t_{ft} = 1.5$.

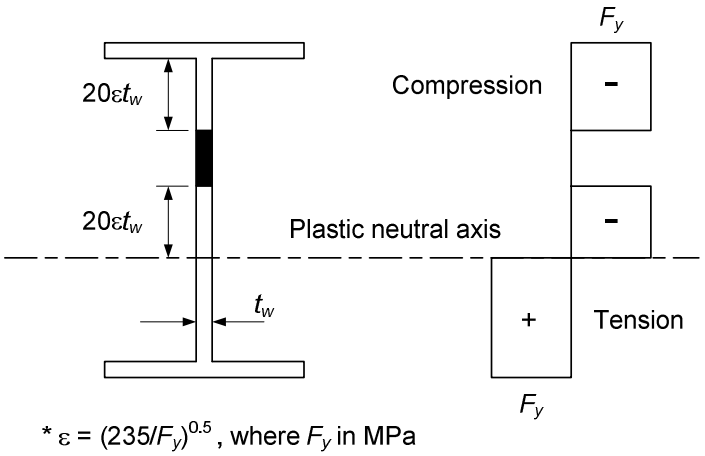

Figure 7.34. Effective web depth for effective Class 2 cross-section.

symmetric section with $h/b_{fc} = 4$, $b_{fc}/2t_{fc} = 6$, and $h/t_w = 100$ is Class 4 in the previous section. For effective Class 2 sections, the plastic section modulus is calculated based on an effective cross section that includes only an effective portion of the web plate. The effective portion of the web plate is obtained as shown in Figure 7.34. It should be noted that the plateau strength from CEN (2005) is very close to that of AISC (2010) for the cases shown in Figures 7.32 and 7.33.

It can be seen in Figures 7.32 and 7.33 that there is practically no difference between the LTB strengths (M_{FEA}/M_{yc}) whether the flange widths or the flange thicknesses are varied. This can be confirmed in Table 7.12, which shows a summary of M_{FEA}/M_{yc} values for tapered members with $h/b_{fc} = 4$, $b_{fc}/2t_{fc} = 6$, and $h/t_w = 100$. The smaller plateau strengths of the singly-symmetric beams in Table 7.12 are due to the reduction in the plastic moments of these beams. Figures 7.8, 7.32, and 7.33 show the virtual test simulation results are practically the same as the AISC (2010) resistances at $(F_y/F_e)^{0.5} = 0.2$. Table 7.12 also shows the values of M_{FEA}/M_{yc} of the doubly-symmetric beams with $(F_y/F_e)^{0.5} = 0.775$ and 1.2 are very close to the values of M_{FEA}/M_{yc} of the

corresponding singly-symmetric beams. It should be noted that the CEN (2005) curves shown in Figures 7.8, 7.32, and 7.33 are practically the same, while the AISC (2010) curve for doubly-symmetric beams is somewhat optimistic compared to the corresponding curves for singly-symmetric beams with $b_{fc}/b_{ft} = 1.5$ or $t_{fc}/t_{ft} = 1.5$.

Table 7.12. Summary of M_{FEA}/M_{yc} for tapered members with $h/b_{fc} = 4$, $b_{fc}/2t_{fc} = 6$, and $h/t_w = 100$.

M_{FEA}/M_{yc}	$(F_y/F_e)^{0.5}$			
Case	0.2	0.35	0.775	1.2
4-6-100	1.08	1.03	0.74	0.54
4-6-100-S.S (b_{fc}/b_{ft}=1.5)	1.03	0.97	0.73	0.53
4-6-100-S.S (t_{fc}/t_{ft}=1.5)	1.03	0.97	0.73	0.53

Figures 7.35 to 7.37 show the virtual test simulation results for singly-symmetric test beams with $h/b_{fc} = 7$, $b_{fc}/2t_{fc} = 6$, and $h/t_w = 100$. Figure 7.35 shows the test beams with larger compression flanges ($b_{fc}/b_{ft} = 1.5$), and Figures 7.36 and 7.37 show test beams with smaller compression flanges ($b_{fc}/b_{ft} = 0.67$ and $t_{fc}/t_{ft} = 0.67$). It should be noted that with b_{fc}/b_{ft} =1.5, the ratio of clear web depth to tension flange width h/b_{ft} becomes 10.5. MBMA/AISC (2010) limits the value of h/b_f to less than or equal to 7. This case is studied for the demonstration purpose. For $h/b_{fc} = 7$, $b_{fc}/2t_{fc} = 6$, and $h/t_w = 100$, the tension flange thickness t_{ft} is smaller than the web thickness t_w if $t_{fc}/t_{ft} = 1.5$. Therefore, the test beams with $h/b_{fc} = 7$, $b_{fc}/2t_{fc} = 6$, $h/t_w = 100$, and $t_{fc}/t_{ft} = 1.5$ are not considered.

The test beams with $h/b_{fc} = 7$, $b_{fc}/2t_{fc} = 6$, $h/t_w = 100$, and $b_{fc}/b_{ft} = 1.5$ have effective Class 2 sections based on CEN (2005). It can be seen in Figure 7.35 that the plateau of the CEN (2005) general welded-section curve is essentially the same as the one

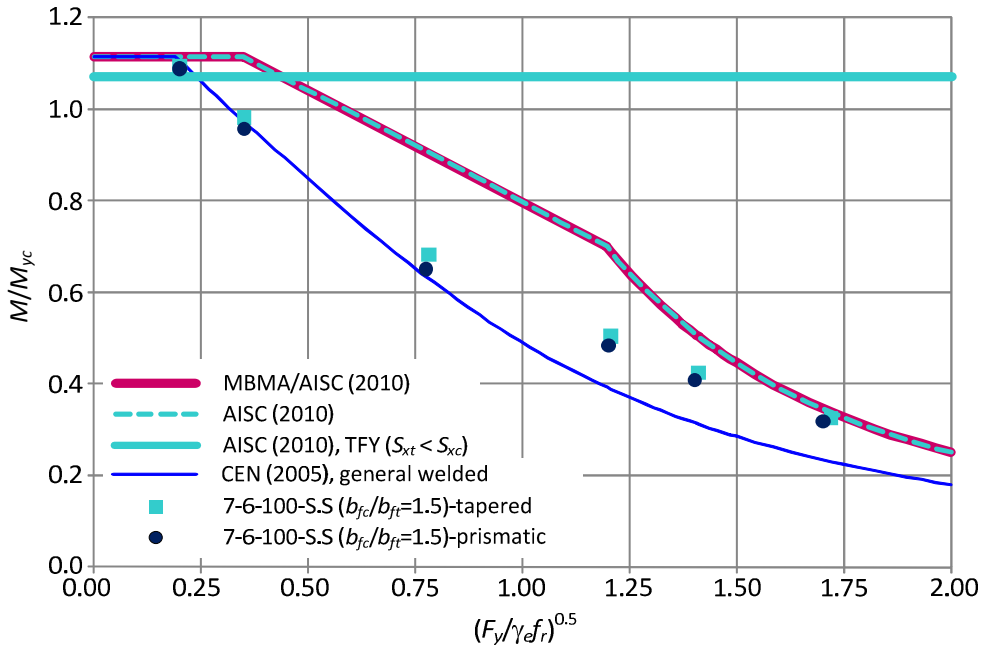

Figure 7.35. Analysis results for $h/b_{fc} = 7$, $b_{fc}/2t_{fc} = 6$, $h/t_w = 100$, and $b_{fc}/b_{ft} = 1.5$.

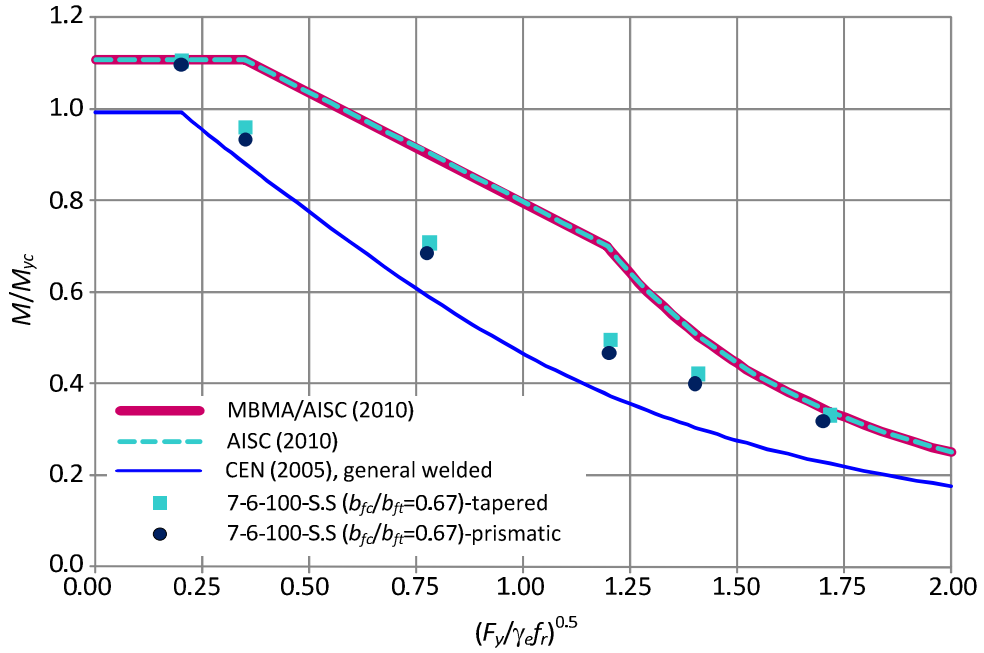

Figure 7.36. Analysis results for $h/b_{fc} = 7$, $b_{fc}/2t_{fc} = 6$, $h/t_w = 100$, and $b_{fc}/b_{ft} = 0.67$.

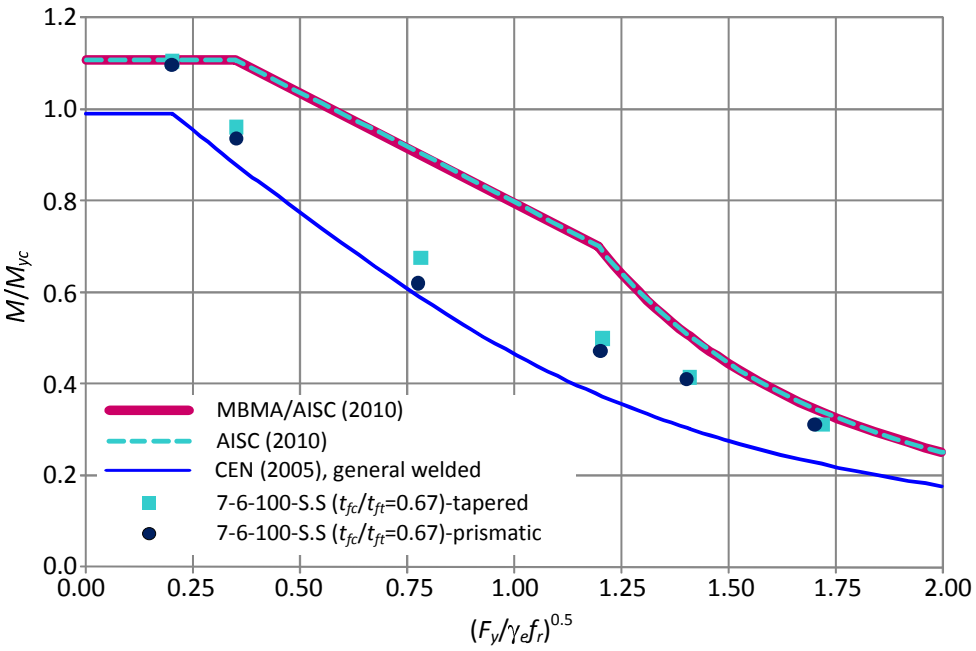

Figure 7.37. Analysis results for $h/b_{fc} = 7$, $b_{fc}/2t_{fc} = 6$, $h/t_w = 100$, and $t_{fc}/t_{ft} = 0.67$.

of the AISC (2010) curve, which is calculated by $R_{pc}M_{yc}$. In this case, the virtual test simulation results are essentially equal to the CEN (2005) strengths at shorter lengths with $(F_y/F_e)^{0.5} \leq 0.775$. The virtual test simulation results of the beams in elastic LTB region are somewhat larger than the CEN (2005) resistances.

The cross sections of the beams with the smaller compression flanges are Class 4 sections in CEN (2005). As a result, the maximum moment capacity of CEN (2005) shown in Figures 7.36 and 7.37 are smaller than AISC (2010). It can be seen in Figures 7.36 and 7.37 that the LTB strengths of test beams with smaller compression flanges are not much different whether the flange widths or the flange thicknesses are varied as seen in the results of the cases with larger compression flanges in Figures 7.32 and 7.33. Table 7.13 shows a summary of M_{FEA}/M_{yc} for the cases with $h/b_{fc} = 7$, $b_{fc}/2t_{fc} = 6$, and $h/t_w = 100$. It should be noted that for all the cases shown in Figures 7.35 to 7.37, the

compression flange dimensions are the same. Only the tension flange size is varied when the flange width or the flange thickness is varied. Therefore it can be concluded that if the beams have the same h/b_{fc}, $b_{fc}/2t_{fc}$, h/t_w and compression flange sizes then the values of M_{FEA}/M_{yc} are the same.

In Figure 7.37, it can be seen that the LTB strength of the prismatic beam with $(F_y/F_e)^{0.5} = 0.775$ is smaller than the one of tapered beam with the same $(F_y/F_e)^{0.5}$. The value of M_{FEA}/M_{yc} of this prismatic beam is 0.62, while the value of M_{FEA}/M_{yc} of the corresponding tapered beam is 0.68. Figures 7.38 and 7.39 show the equivalent plastic strain contours for these prismatic and tapered beams with $h/b_{fc} = 7$, $b_{fc}/2t_{fc} = 6$, $h/t_w = 100$, $t_{fc}/t_{ft} = 0.67$, and $(F_y/F_e)^{0.5} = 0.775$ at the peak load. For both beams, about half of the compression flange and the bottom web-flange juncture along the entire length are yielded at the peak load. Figure 7.40 illustrates the equivalent plastic strain contour for the same tapered beam shown in Figure 7.39, but at the applied load level $M_{applied}/M_{yc}$ of 0.625, which is close to the peak load level of the corresponding prismatic member. At this point, the tapered beam shows yielding just at the tip of the compression flange.

Table 7.13. Summary of M_{FEA}/M_{yc} for tapered members with $h/b_{fc} = 7$, $b_{fc}/2t_{fc} = 6$, and $h/t_w = 100$.

M_{FEA}/M_{yc}	$(F_y/F_e)^{0.5}$					
Case	0.2	0.35	0.775	1.2	1.4	1.7
7-6-100	1.11	0.98	0.68	0.50	0.42	0.33
7-6-100-S.S (b_{fc}/b_{ft}=1.5)	1.10	0.98	0.68	0.50	0.42	0.33
7-6-100-S.S (b_{fc}/b_{ft}=0.67)	1.11	0.96	0.71	0.50	0.42	0.31
7-6-100-S.S (t_{fc}/t_{ft}=0.67)	1.11	0.96	0.68	0.50	0.41	0.33

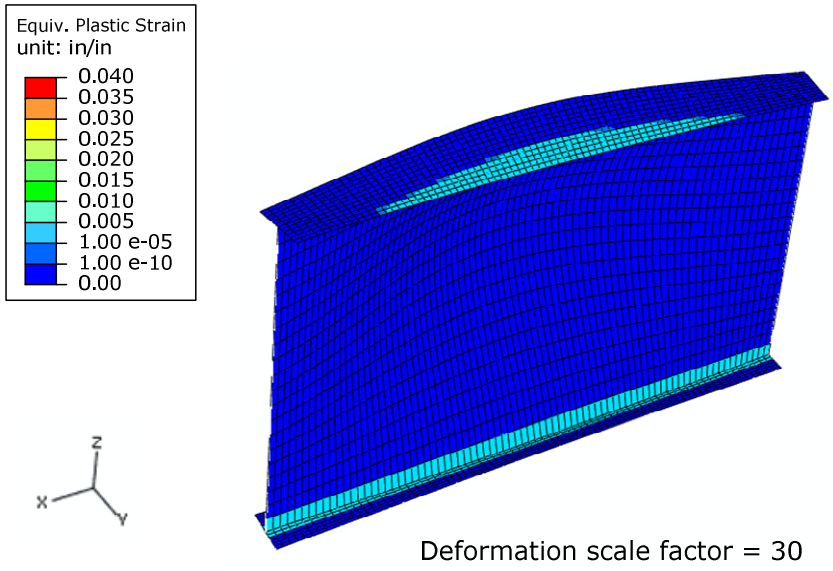

Figure 7.38. Equivalent plastic strain contour plot at peak load
(prismatic beam with $h/b_{fc} = 7$, $b_{fc}/2t_{fc} = 6$, $h/t_w = 100$, $t_{fc}/t_{ft} = 0.67$, and $(F_y/F_e)^{0.5} = 0.775$).

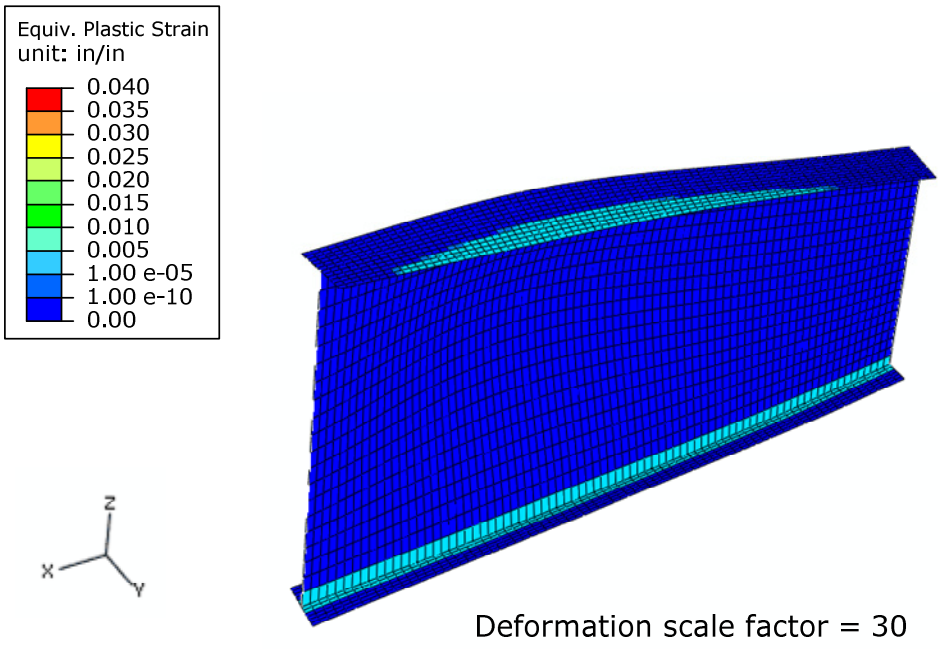

Figure 7.39. Equivalent plastic strain contour plot at peak load
(tapered beam with $h/b_{fc} = 7$, $b_{fc}/2t_{fc} = 6$, $h/t_w = 100$, $t_{fc}/t_{ft} = 0.67$, and $(F_y/F_e)^{0.5} = 0.775$).

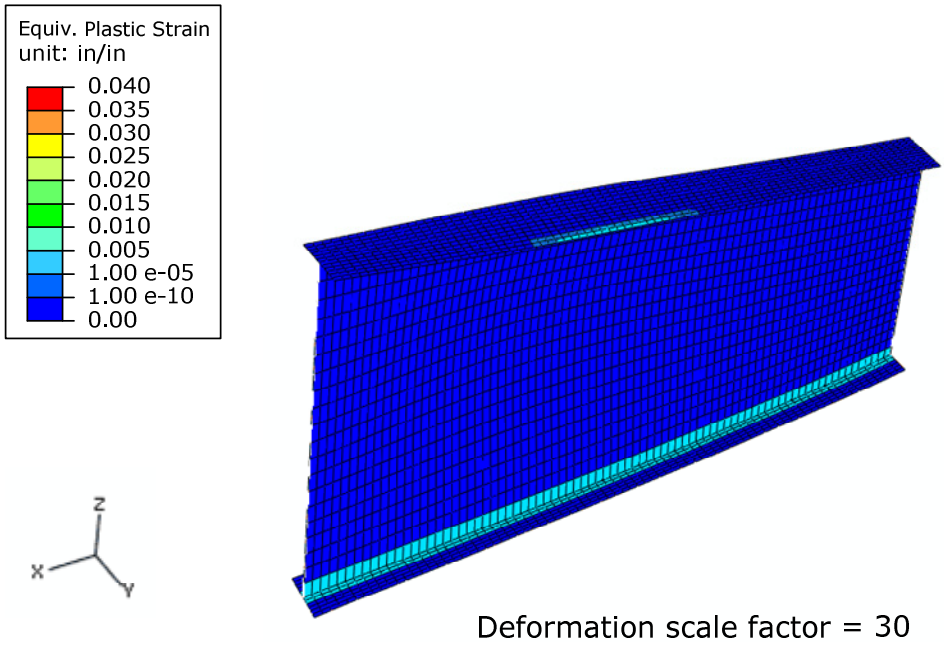

Figure 7.40. Equivalent plastic strain contour plot at $M_{applied}/M_{yc} = 0.625$ (tapered beam with $h/b_{fc} = 7$, $b_{fc}/2t_{fc} = 6$, $h/t_w = 100$, $t_{fc}/t_{ft} = 0.67$, and $(F_y/F_e)^{0.5} = 0.775$).

7.2.2.2 Members with compact flanges and a slender web ($b_{fc}/2t_{fc} = 6$ and $h/t_w = 180$)

Figures 7.41 and 7.42 illustrate the LTB strengths of prismatic and tapered members with $h/b_{fc} = 4$, $b_{fc}/2t_{fc} = 6$, $h/t_w = 180$, and $b_{fc}/b_{ft} = 1.5$ and $t_{fc}/t_{ft} = 1.5$ respectively. The TFY limits of AISC (2010) shown in Figures 7.41 and 7.42 are practically the same as the plateau strength of CEN (2005). The virtual test simulation results show both prismatic and tapered beam models with shorter lengths can develop the LTB strengths, which are larger than the TFY limit. Table 7.14 shows a summary of M_{FEA}/M_{yc} of tapered beams with $h/b_{fc} = 4$, $b_{fc}/2t_{fc} = 6$, and $h/t_w = 180$. As seen in the previous section, the single symmetry of cross sections has little effect on the values of M_{FEA}/M_{yc}.

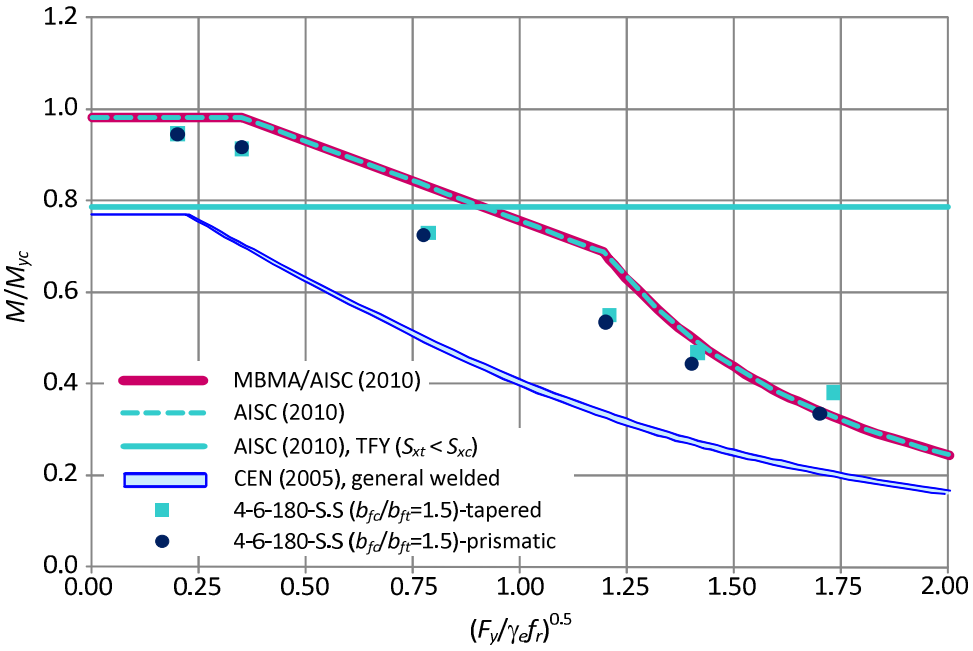

Figure 7.41. Analysis results for $h/b_{fc} = 4$, $b_{fc}/2t_{fc} = 6$, $h/t_w = 180$, and $b_{fc}/b_{ft} = 1.5$.

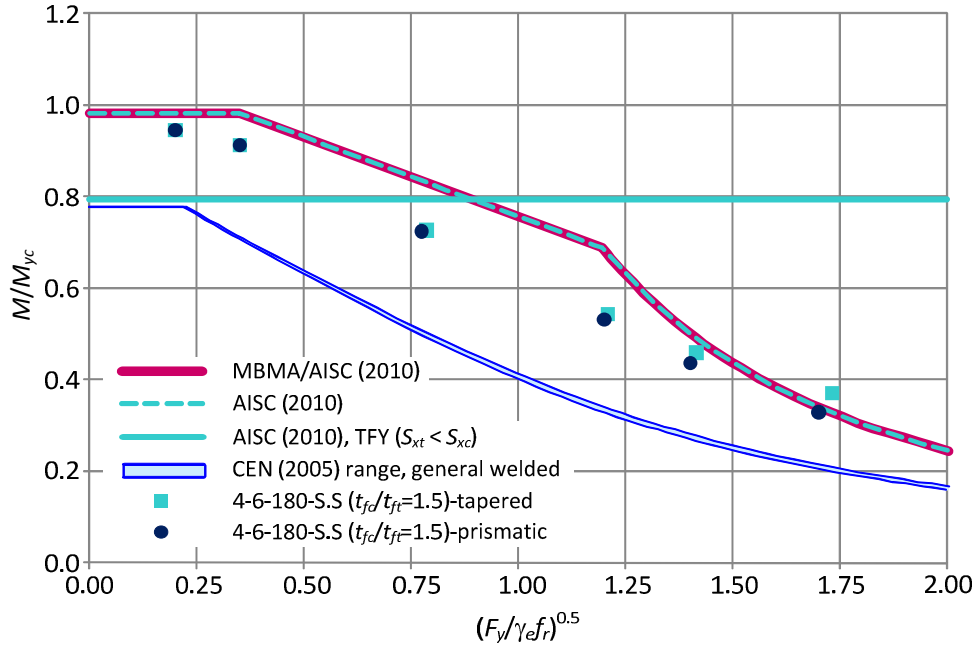

Figure 7.42. Analysis results for $h/b_{fc} = 4$, $b_{fc}/2t_{fc} = 6$, $h/t_w = 180$, and $t_{fc}/t_{ft} = 1.5$.

Table 7.14. Summary of M_{FEA}/M_{yc} for tapered members with $h/b_{fc} = 4$, $b_{fc}/2t_{fc} = 6$, and $h/t_w = 180$.

M_{FEA}/M_{yc}	$(F_y/F_e)^{0.5}$					
Case	0.2	0.35	0.775	1.2	1.4	1.7
4-6-180	0.99	0.94	0.73	0.55	0.48	n/a
4-6-180-S.S (b_{fc}/b_{ft}=1.5)	0.95	0.91	0.73	0.55	0.47	0.38
4-6-180-S.S (t_{fc}/t_{ft}=1.5)	0.95	0.91	0.73	0.54	0.46	0.37

Figures 7.43 to 7.46 show the virtual test simulation results of prismatic and tapered members with $h/b_{fc} = 7$, $b_{fc}/2t_{fc} = 6$, $h/t_w = 180$ and $b_{fc}/b_{ft} = 1.5$, $t_{fc}/t_{ft} = 1.5$, $b_{fc}/b_{ft} = 0.67$, and $t_{fc}/t_{ft} = 0.67$ respectively. In Figures 7.43 and 7.44, the TFY limits of AISC (2010) are shown as well. For these cases, the plateau strengths of CEN (2005) are smaller than the TFY limits of AISC (2010). It can be seen that the virtual test simulation results of the prismatic and tapered beam models with larger compression flanges are close to or somewhat smaller than the AISC (2010) resistances. For all the cases shown in Figures 7.43 and 7.44, the virtual test simulation results are larger than the CEN (2005) estimates.

For the members with smaller compression flanges shown in Figures 7.45 and 7.46, the plateau strengths of CEN (2005) are slightly larger than the ones of AISC (2010). As seen in the case with doubly-symmetric cross sections, the virtual test simulation results are close to or somewhat smaller than the AISC (2010) nominal strengths. It can be seen in Figures 7.45 and 7.46 the virtual test simulation results match the CEN (2005) nominal strengths for the beams with $(F_y/F_e)^{0.5} = 0.2$ and 0.35.

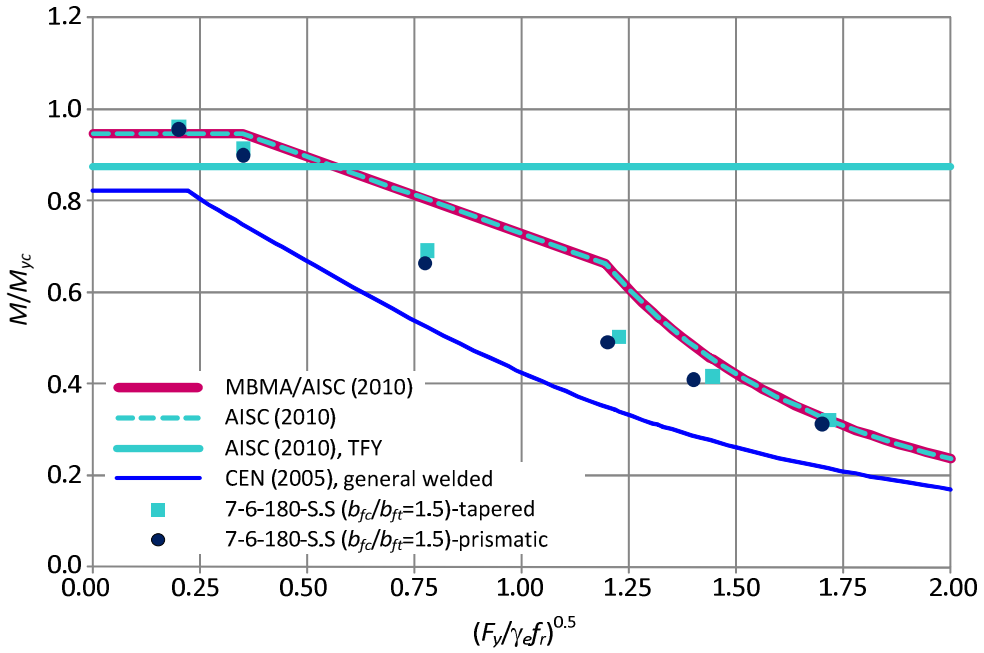

Figure 7.43. Analysis results for $h/b_{fc} = 7$, $b_{fc}/2t_{fc} = 6$, $h/t_w = 180$, and $b_{fc}/b_{ft} = 1.5$.

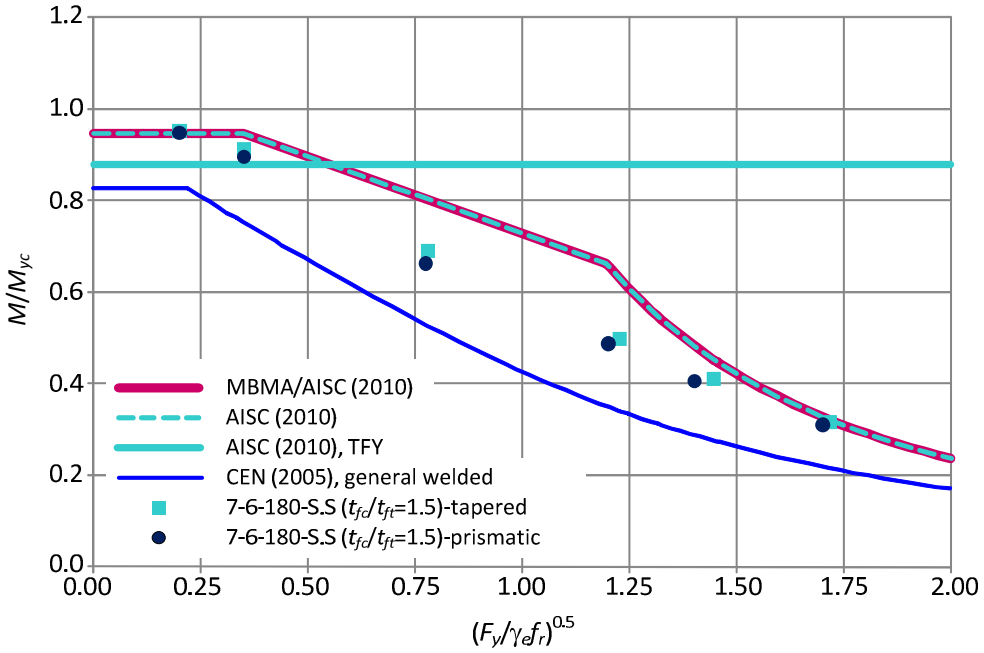

Figure 7.44. Analysis results for $h/b_{fc} = 7$, $b_{fc}/2t_{fc} = 6$, $h/t_w = 180$, and $t_{fc}/t_{ft} = 1.5$.

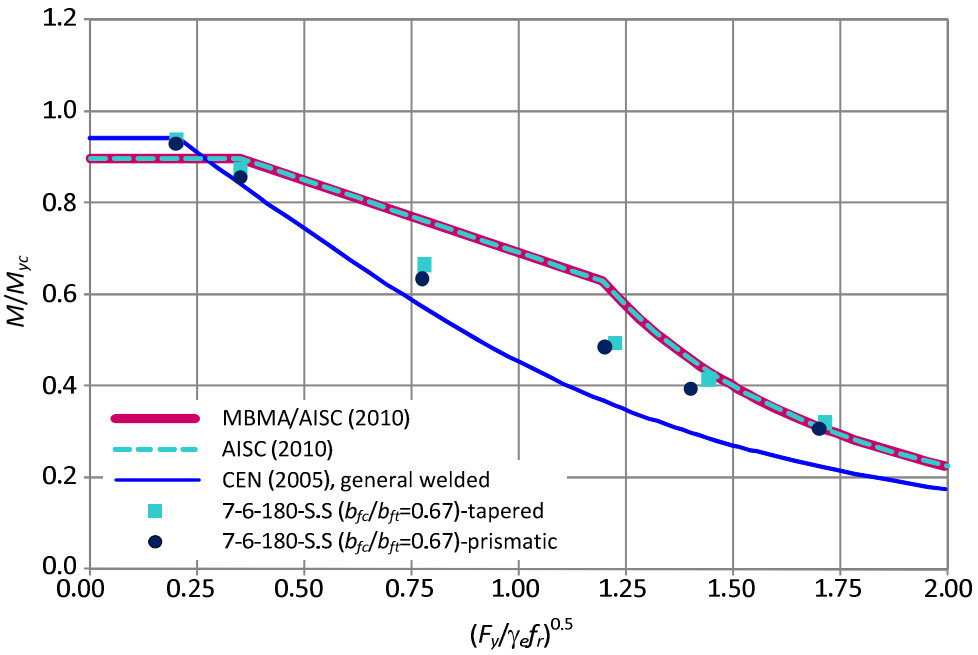

Figure 7.45. Analysis results for $h/b_{fc} = 7$, $b_{fc}/2t_{fc} = 6$, $h/t_w = 180$, and $b_{fc}/b_{ft} = 0.67$.

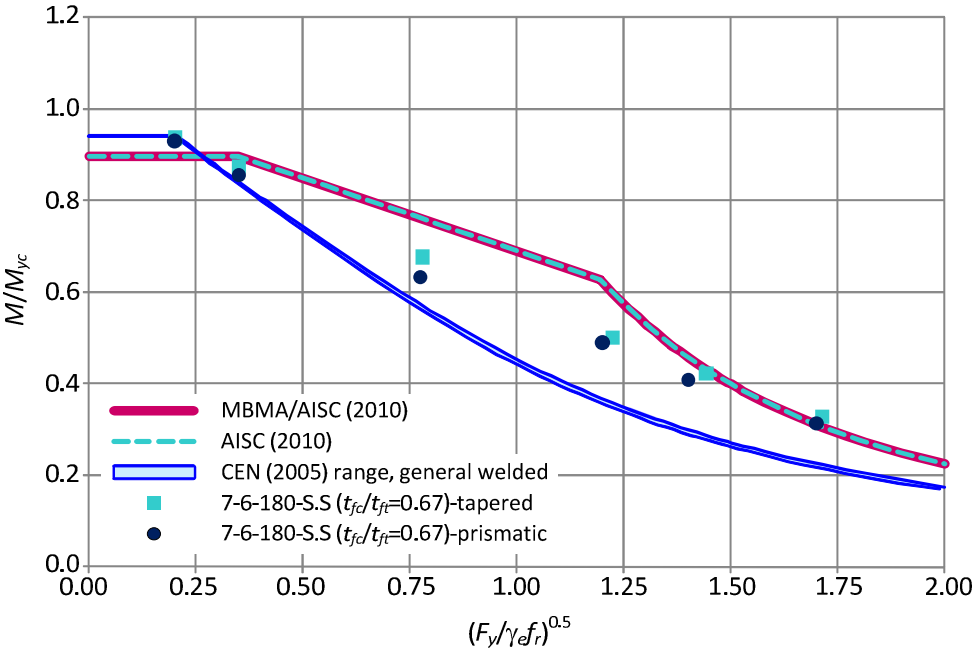

Figure 7.46. Analysis results for $h/b_{fc} = 7$, $b_{fc}/2t_{fc} = 6$, $h/t_w = 180$, and $t_{fc}/t_{ft} = 0.67$.

Table 7.15 summarizes M_{FEA}/M_{yc} values for tapered beams with $h/b_{fc} = 7.0$, $b_{fc}/2t_{fc} = 6$, and $h/t_w = 180$. Based on Tables 7.14 and 7.15, the same conclusion can be made as the previous section: For the beams with the same cross-section properties (h/b_{fc}, $b_{fc}/2t_{fc}$, and h/t_w), if the compression flange sizes are the same, the values of M_{FEA}/M_{yc} are also practically same especially at $(F_y/F_e)^{0.5} \geq 0.35$.

Table 7.15. Summary of M_{FEA}/M_{yc} for tapered members with $h/b_{fc} = 7$, $b_{fc}/2t_{fc} = 6$, and $h/t_w = 180$.

M_{FEA}/M_{yc}	$(F_y/F_e)^{0.5}$					
Case	0.2	0.35	0.775	1.2	1.4	1.7
7-6-180	0.96	0.90	0.68	0.50	0.42	0.32
7-6-180-S.S (b_{fc}/b_{ft}=1.5)	0.96	0.91	0.69	0.50	0.42	0.32
7-6-180-S.S (t_{fc}/t_{ft}=1.5)	0.95	0.91	0.69	0.50	0.41	0.32
7-6-180-S.S (b_{fc}/b_{ft}=0.67)	0.96	0.91	0.69	0.50	0.42	0.32
7-6-180-S.S (t_{fc}/t_{ft}=0.67)	0.94	0.87	0.68	0.50	0.42	0.33

7.2.2.3 Members with noncompact flanges and a noncompact web ($b_{fc}/2t_{fc} = 12$ and $h/t_w = 130$)

Figures 7.47 and 7.48 illustrate the LTB strengths of prismatic members with $h/b_{fc} = 1$, $b_{fc}/2t_{fc} = 12$, $h/t_w = 130$, and $b_{fc}/b_{ft} = 1.5$ and $t_{fc}/t_{ft} = 1.5$ respectively. These are extreme cases where the plastic neutral axis falls within the compression flange and the plastic moment M_p becomes smaller than the yield moment based on the compression flange M_{yc}. This results in the significant decrease in the maximum moment capacity of these test beams. However, the ratio of elastic section modulus referred to tension and

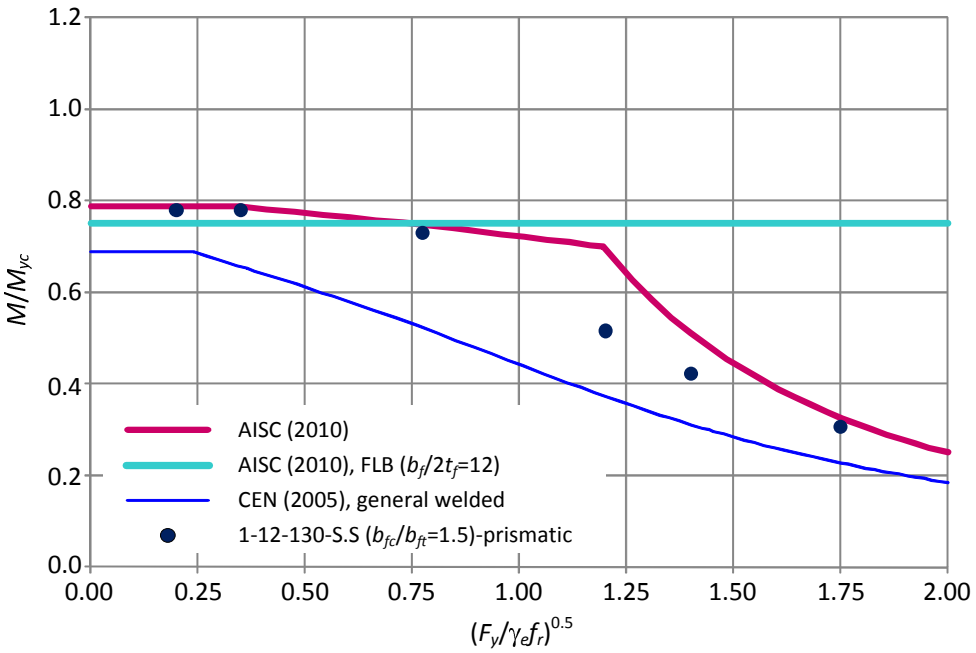

Figure 7.47. Analysis results for $h/b_{fc} = 1$, $b_{fc}/2t_{fc} = 12$, $h/t_w = 130$, and $b_{fc}/b_{ft} = 1.5$.

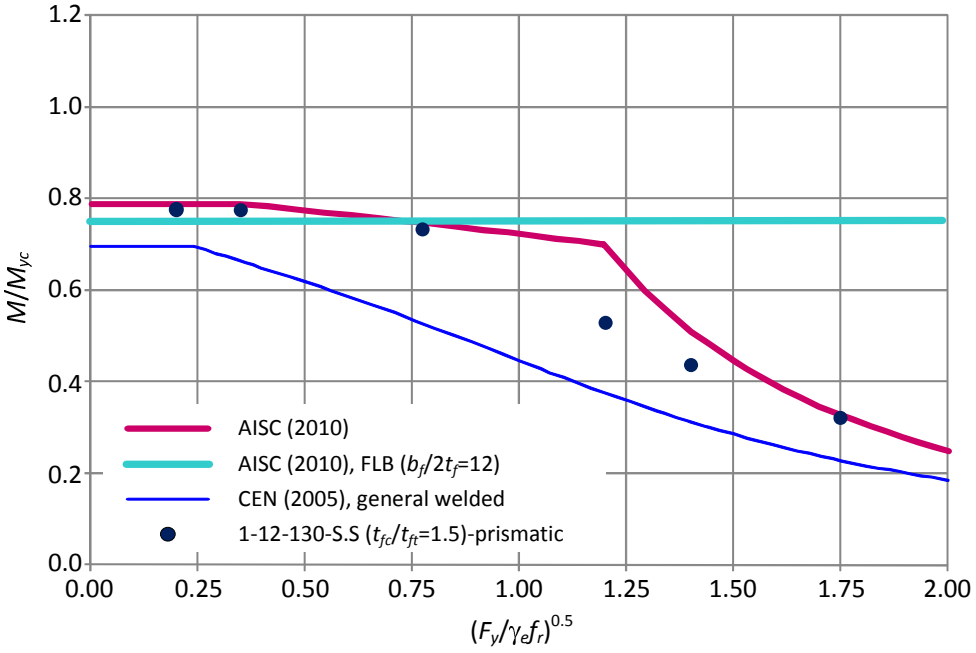

Figure 7.48. Analysis results for $h/b_{fc} = 1$, $b_{fc}/2t_{fc} = 12$, $h/t_w = 130$, and $t_{fc}/t_{ft} = 1.5$.

compression flanges S_{xt}/S_{xc} for this test case is 0.705, which makes the LTB capacity at the inelastic LTB limit, $(F_y/F_e)^{0.5} = 1.2$ to be $0.7M_{yc}$ in AISC (2010). As a result, the inelastic LTB regions in the AISC (2010) resistance curves are very flat as shown in Figures 7.47 and 7.48. The cross sections of these test members are Class 4 sections in CEN (2005) and the value of the moment capacity ratio M_{CEN}/M_{yc} at the plateau is 0.7, which is close to the value of M_{yt}/M_{yc}.

The virtual test simulation results in this case essentially match the AISC (2010) curve at $(F_y/F_e)^{0.5} = 0.2$, 0.35, 0.775, and 1.75. The virtual test simulation results are smaller than the AISC (2010) strengths at $(F_y/F_e)^{0.5} = 1.2$ and 1.4. For all the beam members, the virtual test simulation results are larger than the CEN (2005) strengths. A summary of M_{FEA}/M_{yc} values for test members with $h/b_{fc} = 1$, $b_{fc}/2t_{fc} = 12$, and $h/t_w = 130$ is shown in Table 7.16. It can be seen that the values of M_{FEA}/M_{yc} are reduced from 1.02 or 0.96 to 0.78 at the plateau when the cross sections are singly symmetric. This is the only case considered in this study where significant differences in the M_{FEA}/M_{yc} values for $(F_y/F_e)^{0.5} \leq 0.35$ exist between the doubly-symmetric and singly-symmetric members. This is because of the significantly smaller plastic moment of the selected singly-symmetric members. For the test beams with $(F_y/F_e)^{0.5} \geq 0.775$, the values of M_{FEA}/M_{yc} are essentially the same whether the cross sections are doubly symmetric or singly symmetric in Table 7.16.

7.2.3 Doubly-Symmetric Tests with Stress-Gradient Conditions

7.2.3.1 Members with compact flanges and a compact web ($b_{fc}/2t_{fc} = 6$ and $h/t_w = 40$)

Figures 7.49 through 7.51 show the analysis results of members of compact sections with h/b_{fc} values of 1.0, 1.5 and 2.0 under moment-gradient loadings.

Table 7.16. Summary of M_{FEA}/M_{yc} for prismatic members with $h/b_{fc} = 1.0$, $b_{fc}/2t_{fc} = 12$, and $h/t_w = 130$.

M_{FEA}/M_{yc}	$(F_y/F_e)^{0.5}$					
Case	0.2	0.35	0.775	1.2	1.4	1.75
1-12-130	1.02	0.96	0.74	0.53	0.43	0.33
1-12-130-S.S (b_{fc}/b_{ft}=1.5)	0.78	0.78	0.73	0.52	0.42	0.31
1-12-130-S.S (t_{fc}/t_{ft}=1.5)	0.78	0.78	0.73	0.53	0.44	0.32

For these members, a zero moment is applied at the shallow end and the maximum moment is applied at the deep end, which results in the maximum moment-gradient effect on beams in single curvature bending ($C_b = 1.75$ using the C_b equation in Commentary Chapter F in AISC 2010). To account for the moment gradient effects on LTB, the CEN (2005) provisions have the moment gradient factor C_1, which is used in the calculations of the elastic LTB moment. This factor is determined based on the ratio of two end moments applied to the beams. For the beams with zero moment at one end, the value of C_1 in CEN (2005) is 1.88. For the rolled-section beams, where the most optimistic resistance curve is permitted by CEN (2005), an additional factor f can be used in the calculation of nominal LTB strengths for further consideration of moment-gradient loadings. In Figures 7.49 to 7.51, the CEN (2005) rolled curve 1 is obtained using both the C_1 and f factors. Because of the moment gradient loadings, the test beams have significant internal shear forces. Therefore, without any additional stiffeners, the beams with shorter lengths fail due to shear not lateral torsional buckling. In this research, the cases governed by shear failure are excluded from the discussion. The webs are unstiffened in all of the test cases considered in this research.

It can be seen in Figures 7.49 to 7.51, the virtual test simulation results are larger than the plateau strengths of the AISC (2010) and CEN (2005) curves for the beams with $(F_y/F_e)^{0.5}$ = 0.2, 0.35, and 0.775. The virtual test simulation results of the beams with $(F_y/F_e)^{0.5}$ = 1.4 and 1.75 are close to the elastic LTB strengths of AISC (2010) curves. It is observed that the AISC (2010) estimates are significantly optimistic compared to the virtual test simulation results for the beams with $(F_y/F_e)^{0.5}$ = 1.2. In all the beams shown in Figures 7.49 to 7.51, the CEN (2005) rolled curves 1 and 2, provide reasonable lower bounds to the virtual test simulation results. The CEN (2005) general welded section curve is significantly conservative compared to the virtual test simulation results and other resistance curves.

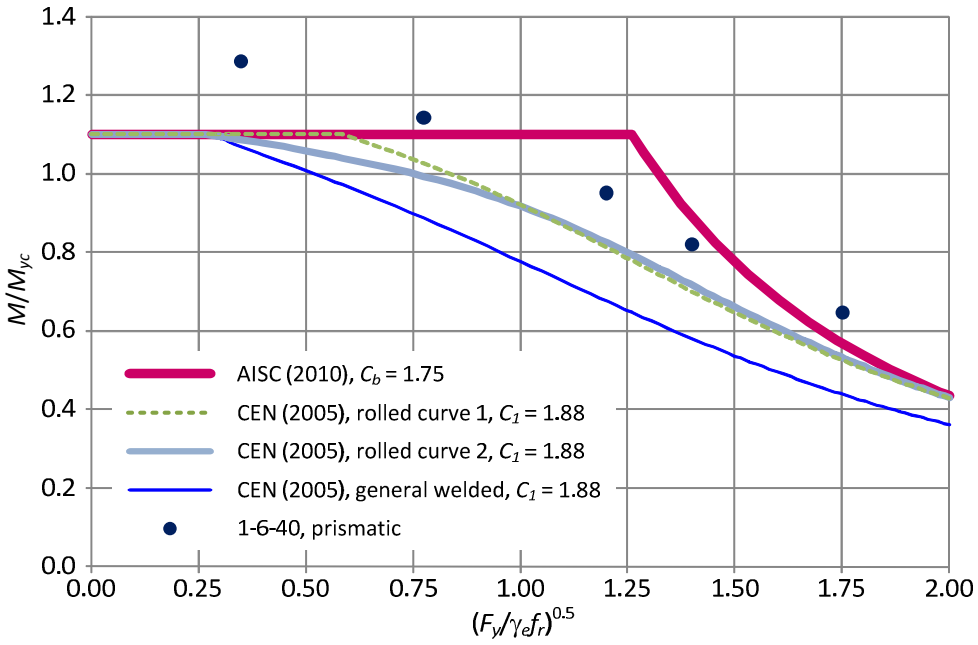

Figure 7.49. Analysis results for h/b_{fc} = 1.0, $b_{fc}/2t_{fc}$ = 6, h/t_w = 40, and C_b = 1.75.

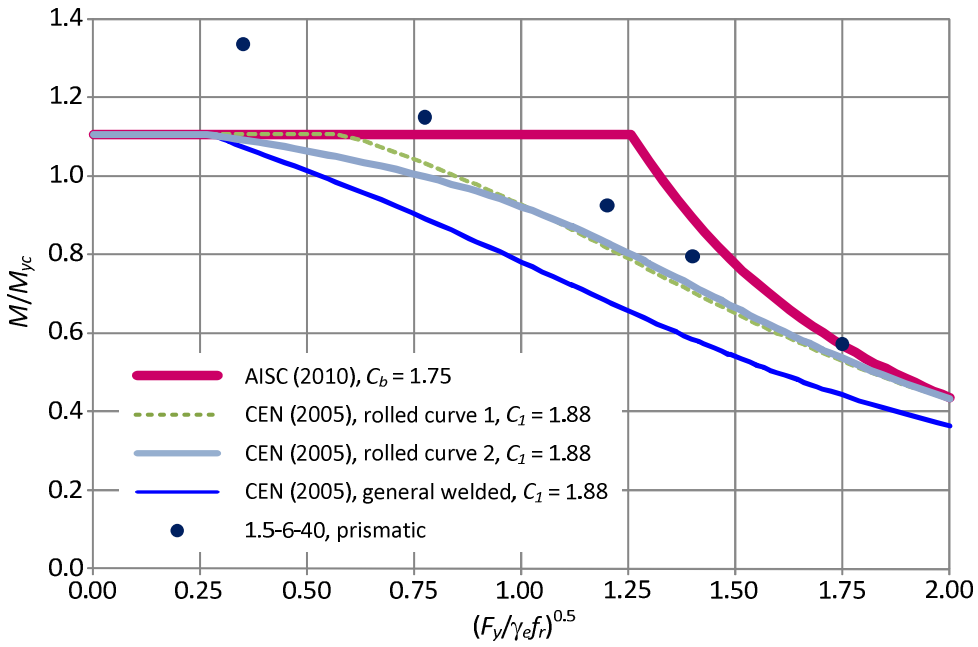

Figure 7.50. Analysis results for $h/b_{fc} = 1.5$, $b_{fc}/2t_{fc} = 6$, $h/t_w = 40$, and $C_b = 1.75$.

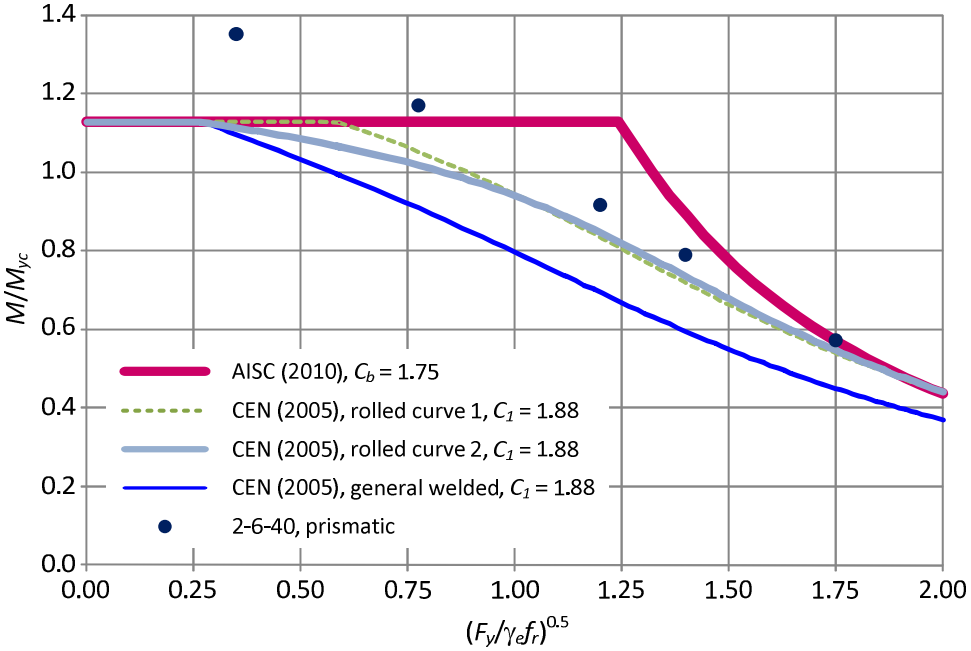

Figure 7.51. Analysis results for $h/b_{fc} = 2.0$, $b_{fc}/2t_{fc} = 6$, $h/t_w = 40$, and $C_b = 1.75$.

7.2.3.2 Members with compact flanges and a noncompact web ($b_{fc}/2t_{fc}$ = 6 and h/t_w = 100)

Figures 7.52 through 7.54 show the analysis results of members with compact flanges and a noncompact web and h/b_{fc} values of 4.0, 5.5, and 7.0. For tapered beams, MBMA/AISC (2010) suggests using the AASHTO (2007) equations to calculate the stress gradient factor as shown in Chapters 3 and 4. All the C_b factors shown for tapered beams in this study are obtained using the AASHTO (2007) equations as explained in Section 4.4.1. As for prismatic beams, for a given tapered beam, the maximum C_b for single curvature bending is obtained with a zero moment at one end. However, if the same loading scheme is applied to five tapered beams with different lengths, each tapered beam has a different C_b due to the tapered geometry. Because it is desirable to have one C_b value for five tapered beams in order to complete one LTB resistance curve, a target constant value of C_b is determined for each case. The procedure to achieve this is described subsequently.

First, the C_b value of each tapered beam is calculated applying a zero moment at one end. If all the tapered beams considered have the same taper angle, the longest beam has the smallest C_b value for the case with a zero moment at one end. Since only single curvature bending is considered in this study, the smallest C_b with the given loading becomes the target C_b for all other test beams. Finally, the appropriate loadings are determined for other tapered beams and equivalent prismatic beams such that the same C_b value can be obtained. For the cases shown in Figures 7.52 to 7.54, the values of the stress gradient factor C_b are 1.21, 1.38, and 1.48 respectively. The corresponding values of the moment gradient factors C_1 in CEN (2005) are 1.21, 1.41, and 1.53.

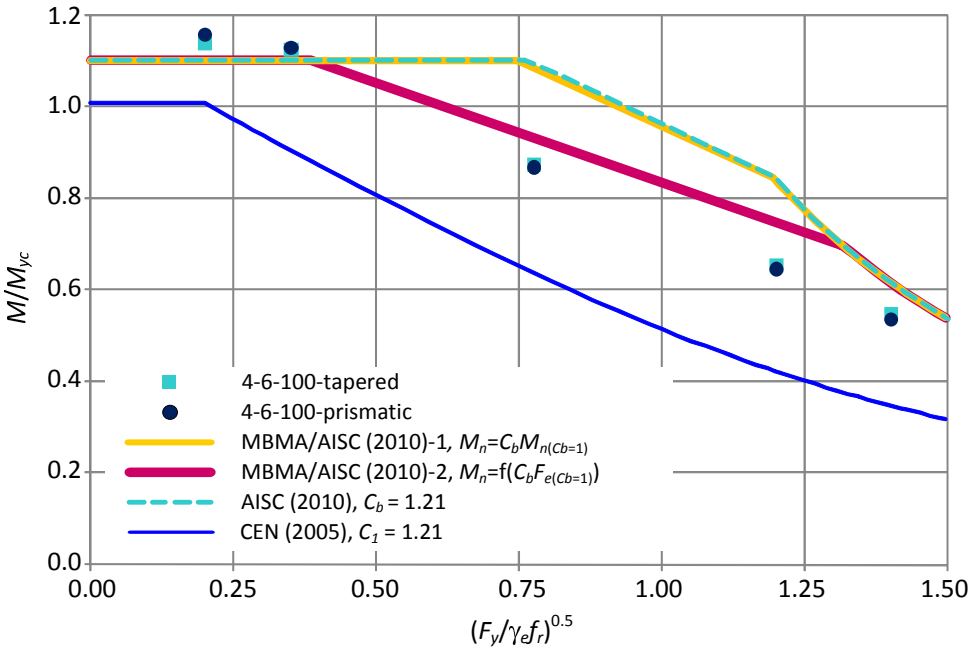

Figure 7.52. Analysis results for h/b_{fc} =4.0, $b_{fc}/2t_{fc}$ = 6, h/t_w = 100, and C_b = 1.21.

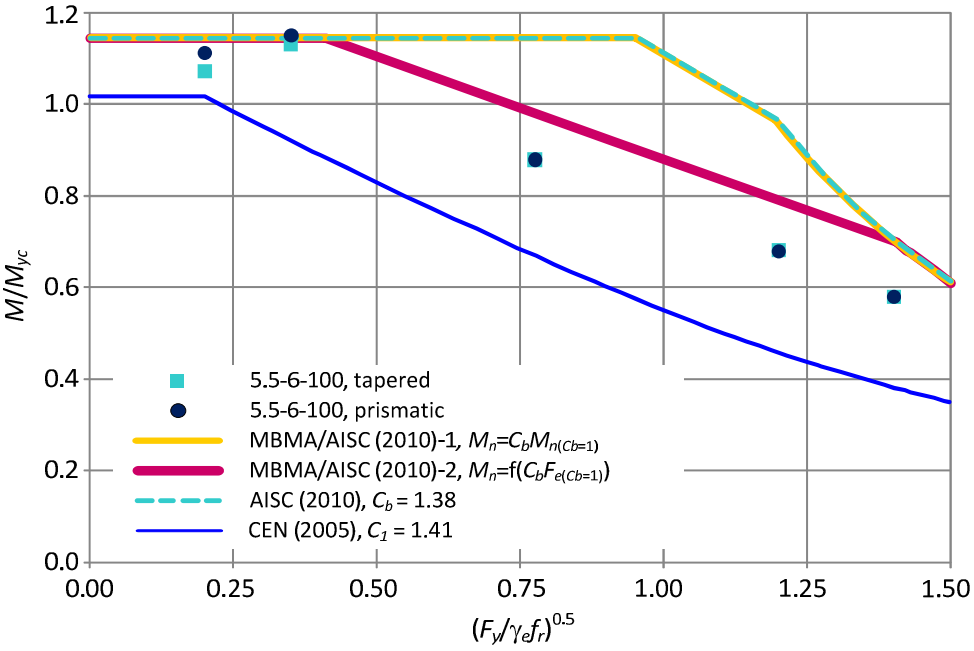

Figure 7.53. Analysis results for h/b_{fc} =5.5, $b_{fc}/2t_{fc}$ = 6, h/t_w = 100, and C_b = 1.38.

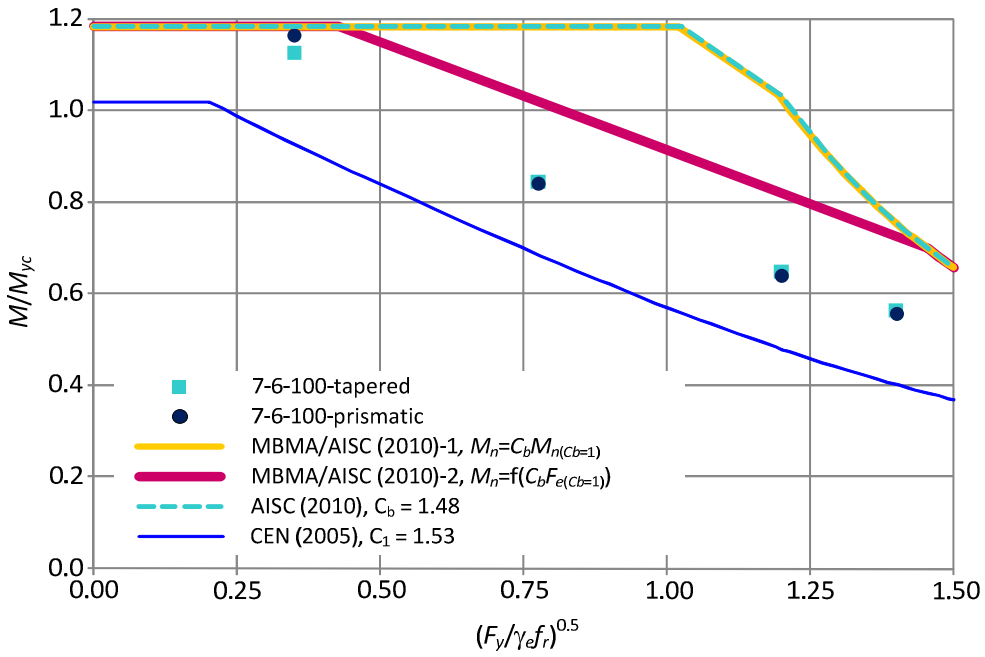

Figure 7.54. Analysis results for h/b_{fc} =7.0, $b_{fc}/2t_{fc}$ = 6, h/t_w = 100, and C_b = 1.48.

For the stress gradient cases, MBMA/AISC (2010) provides two procedures to calculate the LTB strengths of tapered beams. The first procedure is similar to that for the LTB strength calculations of prismatic beams in AISC (2010). First, the LTB strength based on the uniform-bending condition is obtained. Then the stress gradient factor C_b is applied as a multiplier to the uniform-bending LTB strength. The result of this is the LTB strength of a given tapered beam under the stress gradient condition. The second procedure is as follows. The stress gradient factor C_b is applied when the elastic LTB stress F_e is calculated. The new elastic LTB stress C_bF_e is then used in the LTB equations instead of F_e. The final result is the stress-gradient LTB strength. The first procedure gives larger LTB strengths, especially for the cases with large C_b values. The benefit of the second procedure is that once a designer determines F_e based on the given

boundary conditions and the applied loadings, the stress-gradient LTB strength can be obtained directly from the LTB equations without the complication of determining the uniform stress LTB strength and the correct stress-gradient factor for the complex loadings and boundary conditions. In Figures 7.52 to 7.54, the first procedure is denoted by "MBMA/AISC (2010)-1, $M_n=C_bM_{n(Cb=1)}$" and the second procedure is denoted by "MBMA/AISC (2010)-1, M_n=f($C_bF_{e(Cb=1)}$)." For prismatic members, the AISC (2010) and CEN (2005) resistance curves are plotted directly. The values of moment gradient factor used with design provisions are shown in these figures as well. It should be noted that the same C_b values are used with AISC (2010) and MBMA/AISC (2010).

The cases shown in Figures 7.52 to 7.54 are the worst cases where the AISC LTB strengths are significantly optimistic compared to the virtual test simulation results in uniform-stress or uniform-bending conditions. For the stress-gradient (or moment-gradient) conditions, the AISC (2010) and MBMA/AISC (2010)-1 procedures are significantly unconservative compared to the virtual test simulation results, especially within the inelastic LTB region. The MBMA/AISC (2010)-2 procedure provides reasonable estimates of the LTB strengths for test beams with h/b_{fc} = 4 and 5.5. For test beams with h/b_{fc} = 7, the LTB strengths based on the MBMA/AISC (2010)-2 procedure as well as the AISC (2010) and the MBMA/AISC (2010)-1 procedures are unconservative compared to the virtual test simulation results. For all the cases, the CEN (2005) LTB strengths are smaller than all the LTB resistances based on other design provisions and the virtual test simulation results.

It is important to note in Figures 7.52 to 7.54 that the MBMA/AISC (2010)-2 procedure provides a reasonable fit to the virtual test simulation results for both prismatic

and tapered beams. Even though the LTB resistances based on the MBMA/AISC (2010)-2 procedure are significantly larger than the virtual test simulation results for test beams with $h/b_{fc} = 7$, the continuous decrease of the LTB strengths from $(F_y/F_e)^{0.5} = 0.35$ to 1.4 can be seen in the virtual test simulation results as well as the MBMA/AISC (2010)-2 curve.

7.2.3.3 Members with noncompact flanges and a noncompact web ($b_{fc}/2t_{fc} = 12$ and $h/t_w = 130$)

In this section, test beams with noncompact flanges and a noncompact web with $h/b_{fc} = 1$, 2, and 4 are studied. The virtual test simulation results of these beams are shown in Figures 7.55 through 7.57. For the beams with shorter lengths with $h/b_{fc} = 1$ and 2, shear failure governs under the given moment-gradient loadings. Therefore, only three and four data points are shown in Figures 7.55 and 7.56. For all the cases, the CEN (2005) general welded-section curves provide significantly conservative strengths compared to the AISC (2010) curve and the virtual test simulation results. The AISC (2010) curves provide reasonable estimates for prismatic beams shown in Figures 7.58 to 7.60 in general except for the prismatic beam with $h/b_{fc} = 4$ and $(F_y/F_e)^{0.5} = 1.2$. For the tapered beams with $h/b_{fc} = 4$ and $(F_y/F_e)^{0.5} = 1.2$, the MBMA/AISC (2010)-2 curve provides better estimate compared to the MBMA/AISC (2010)-1 curve. For other tapered beams, the two MBMA/AISC (2010) curves provide the same estimates.

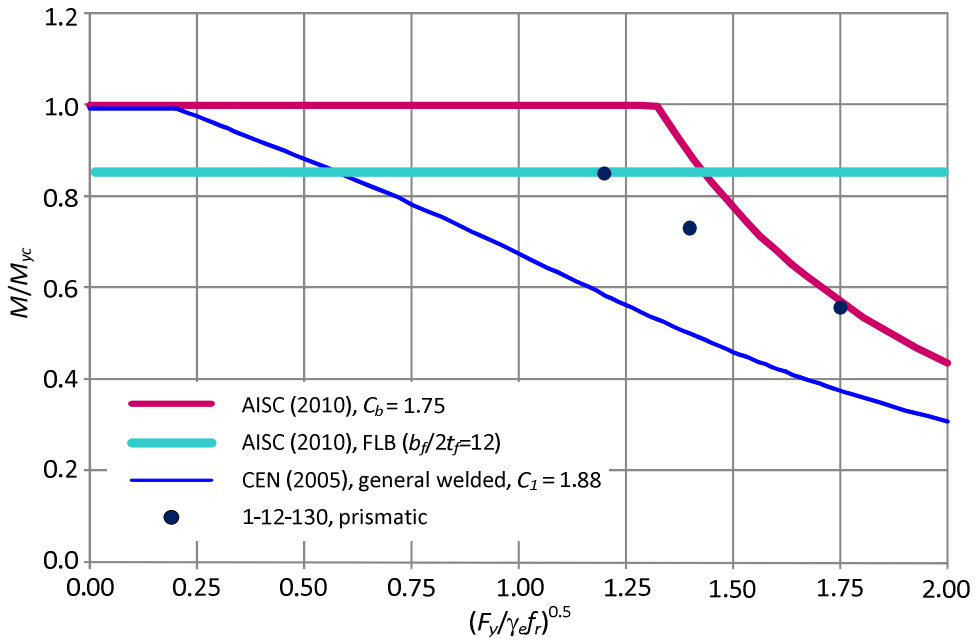

Figure 7.55. Analysis results for $h/b_{fc} = 1.0$, $b_{fc}/2t_{fc} = 12$, $h/t_w = 130$, and $C_b = 1.75$.

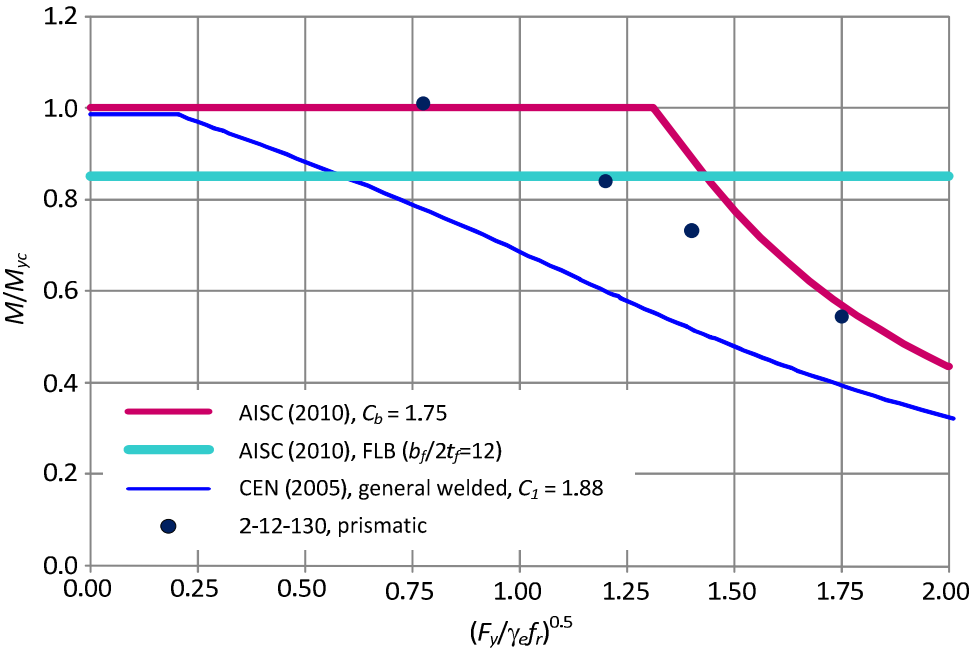

Figure 7.56. Analysis results for $h/b_{fc} = 2.0$, $b_{fc}/2t_{fc} = 12$, $h/t_w = 130$, and $C_b = 1.75$.

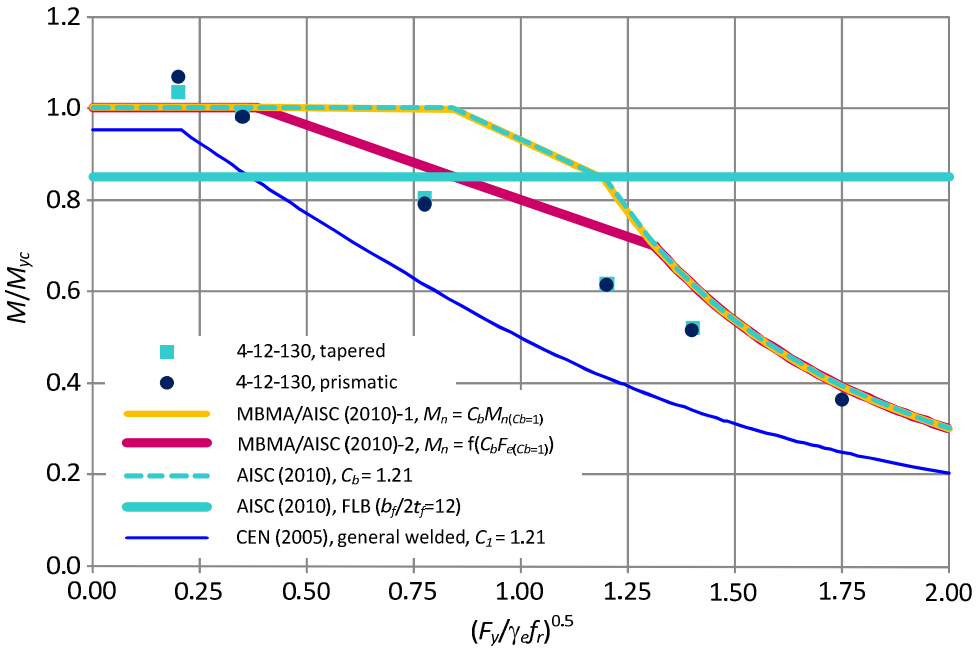

Figure 7.57. Analysis results for $h/b_{fc} = 4.0$, $b_{fc}/2t_{fc} = 12$, $h/t_w = 130$, and $C_b = 1.21$.

7.2.3.4 Members with compact flanges and a slender web ($b_{fc}/2t_{fc} = 6$ and $h/t_w = 180$)

Figures 7.58 through 7.60 show the analysis results of members with compact flanges and a slender web and $h/b_{fc} = 4$, 5.5, and 7. The values of the moment gradient factor C_b are 1.17, 1.14, and 1.20 for cases with $h/b_{fc} = 4$, 5.5, and 7 respectively. The corresponding C_1 values are 1.16, 1.29, and 1.20. For all the prismatic beams, the virtual test simulation results are close to the AISC (2010) curves within the plateau and the elastic LTB ranges. Within the inelastic LTB range ($(F_y/F_e)^{0.5} = 0.775$ and 1.2), the virtual test simulation results are 17 % smaller than the AISC (2010) estimates in average. The same observation can be made with respect to the MBMA/AISC (2010)-1 estimates for all the tapered beams. As seen in the previous section, the MBMA/AISC (2010)-2 curve provides reasonable estimates of the virtual test simulation results for all the tapered beams considered in this section.

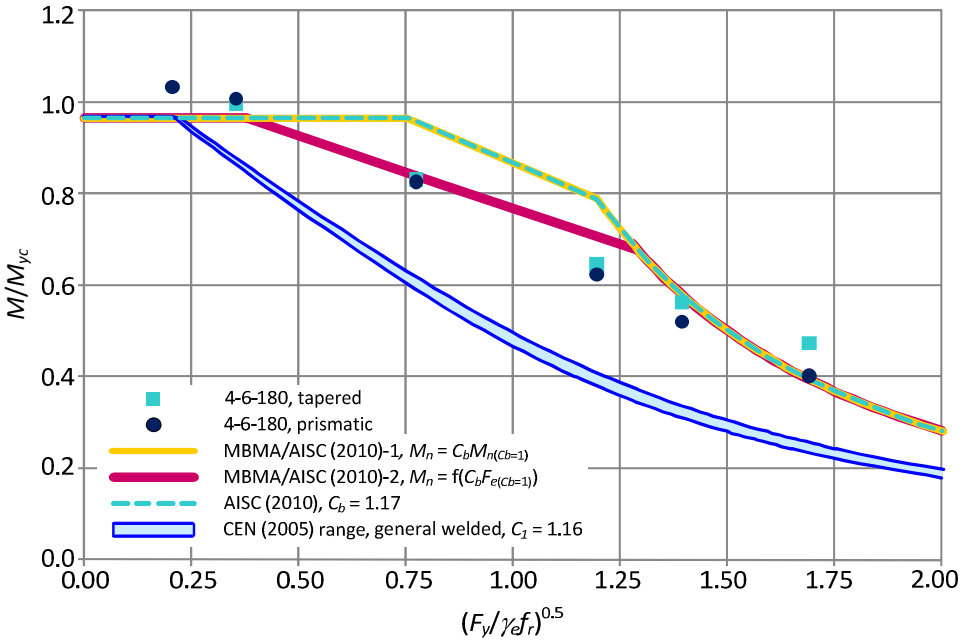

Figure 7.58. Analysis results for $h/b_{fc} = 4.0$, $b_{fc}/2t_{fc} = 6$, $h/t_w = 180$, and $C_b = 1.17$.

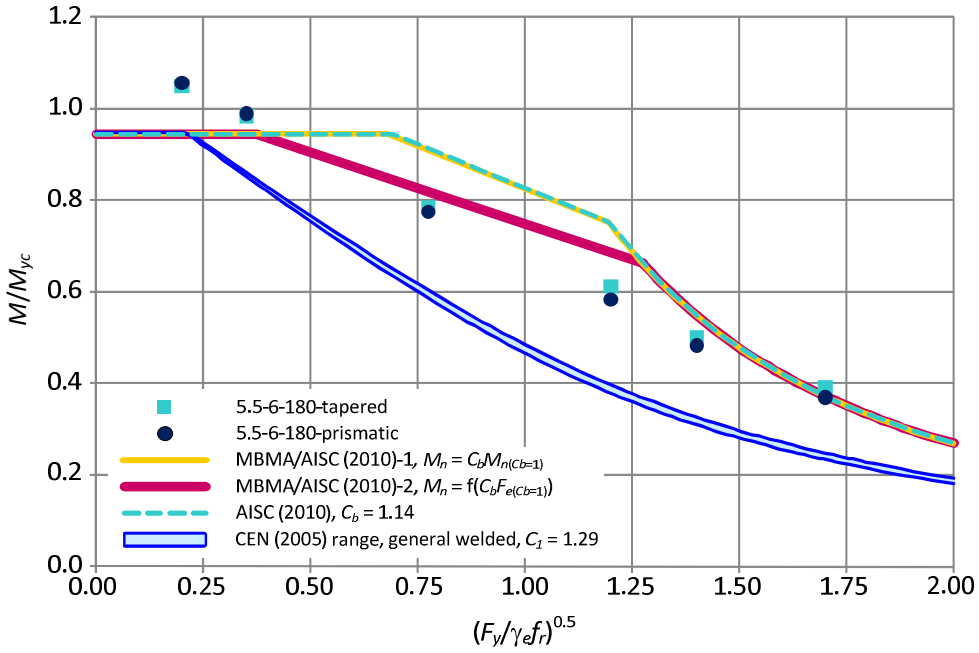

Figure 7.59. Analysis results for $h/b_{fc} = 5.5$, $b_{fc}/2t_{fc} = 6$, $h/t_w = 180$, and $C_b = 1.14$.

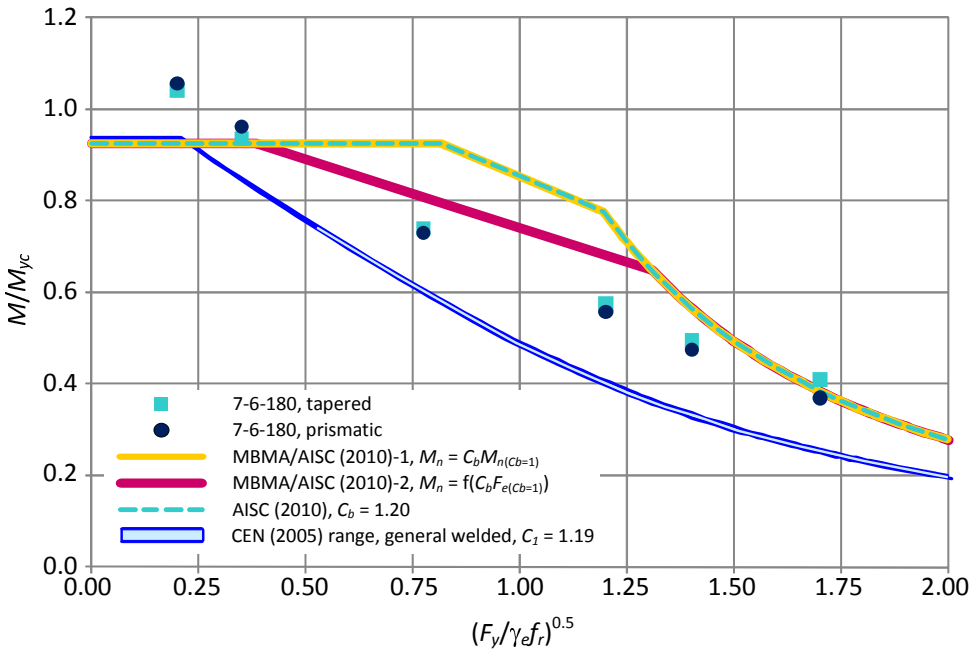

Figure 7.60. Analysis results for $h/b_{fc} = 7.0$, $b_{fc}/2t_{fc} = 6$, $h/t_w = 180$, and $C_b = 1.20$.

7.2.4 Singly-Symmetric Tests with Stress-Gradient Conditions

7.2.4.1 Members with compact flanges and a compact web ($b_{fc}/2t_{fc} = 6$ and $h/t_w = 100$)

Figures 7.61 and 7.62 show the analysis results of singly-symmetric members with $h/b_{fc} = 4$, $b_{fc}/2t_{fc} = 6$, $h/t_w = 100$, and $C_b = 1.33$ and 1.34. The same members with uniform-stress or uniform-bending conditions are shown in Figures 7.32 and 7.33. In Figures 7.61 and 7.62, the tension flange yielding (TFY) limit states are shown as a horizontal line. The TFY limit is slightly smaller than a yield moment M_{yc}. For all the cases, the AISC (2010) and the MBMA/AISC (2010)-1 curves provide the largest design strengths. The virtual test simulation results for the prismatic and the tapered beams with $(F_y/F_e)^{0.5} = 1.2$ are 26 % smaller than the design strengths of the AISC (2010) and the MBMA/AISC (2010)-1 curves. The MBMA/AISC (2010)-2 strengths are close to the virtual test simulation results of all the tapered beams shown in Figures 7.61 and 7.62.

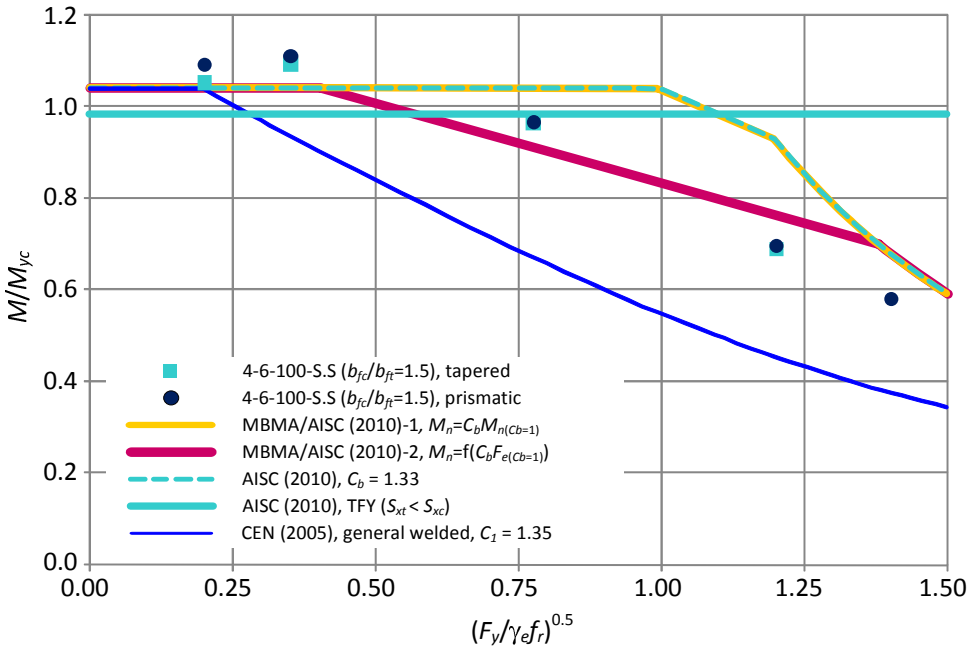

Figure 7.61. Analysis results for $h/b_{fc} = 4.0$, $b_{fc}/2t_{fc} = 6$, $h/t_w = 100$, and $b_{fc}/b_{ft} = 1.5$.

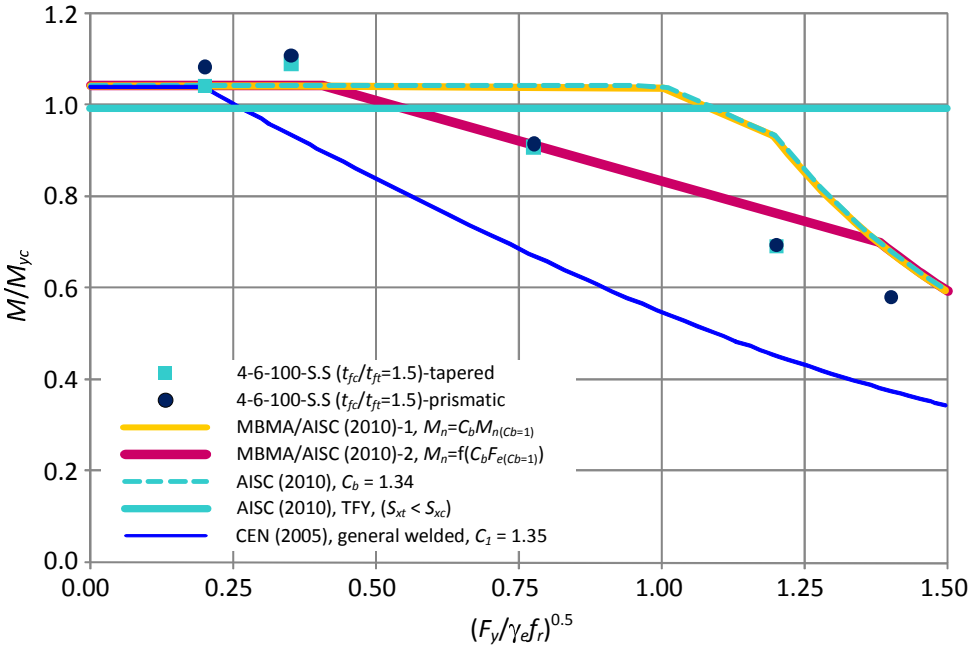

Figure 7.62. Analysis results for $h/b_{fc} = 4.0$, $b_{fc}/2t_{fc} = 6$, $h/t_w = 100$, and $t_{fc}/t_{ft} = 1.5$.

The CEN (2005) strengths are significantly conservative for all the prismatic beams especially for the cases with $(F_y/F_e)^{0.5} > 0.35$.

Figures 7.63 through 7.65 show the analysis results for singly-symmetric members with $h/b_{fc} = 7.0$, $b_{fc}/2t_{fc} = 6$, and $h/t_w = 100$. The test beams shown in Figure 7.63 have a larger compression flange with $b_{fc}/b_{ft} = 1.5$ while the test beams shown in Figures 7.64 and 7.65 have smaller compression flanges with $b_{fc}/b_{ft} = 0.67$ and $t_{fc}/t_{ft} = 0.67$ respectively. The virtual test simulation results and nominal strengths of the corresponding doubly-symmetric members are shown in Figure 7.54. In Figures 7.64 and 7.65, the virtual test simulation results for the beams with $(F_y/F_e)^{0.5} = 0.2$ are not shown. This is because the virtual test simulation results for these beams cannot be obtained due to numerical problems.

By comparing the virtual test simulation results of test beams with doubly-symmetric cross sections and with singly-symmetric cross sections, it can be observed that the single symmetry of cross sections does not affect the M_{FEA}/M_{yc} values for the beams with $(F_y/F_e)^{0.5} = 0.775$, 1.2, and 1.4. In addition, it can be seen in Figures 7.63 to 7.65 that the M_{FEA}/M_{yc} values of test beams with same $(F_y/F_e)^{0.5}$ are not affected whether the compression flanges are smaller or larger. As discussed above, if the beams have the same h/b_{fc}, $b_{fc}/2t_{fc}$, h/t_w, and compression flanges, the change in the geometry of tension flanges has little effect on the LTB strengths.

In Figures 7.63 to 7.65, the virtual test simulation results of beams with $(F_y/F_e)^{0.5} = 0.2$ and 0.35 are very close to the maximum moment capacities of AISC (2010) and MBMA/AISC (2010). However, for the beams with $(F_y/F_e)^{0.5} = 0.775$, 1.2, and 1.4, the AISC (2010) and the MBMA/AISC (2010)-1 strengths are significantly larger than the

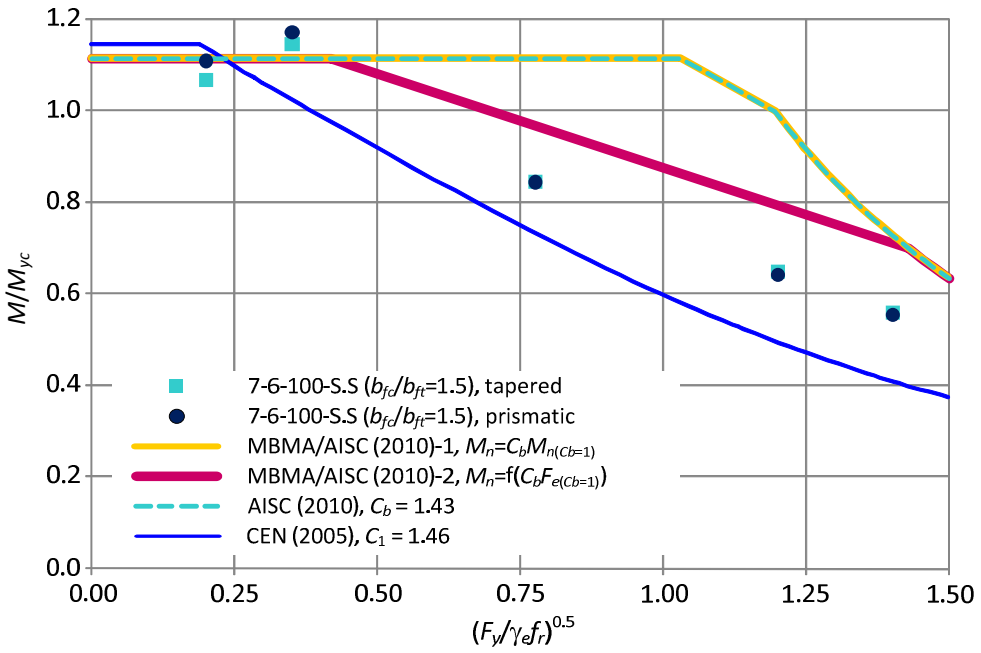

Figure 7.63. Analysis results for $h/b_{fc} = 7.0$, $b_{fc}/2t_{fc} = 6$, $h/t_w = 100$, and $b_{fc}/b_{ft} = 1.5$.

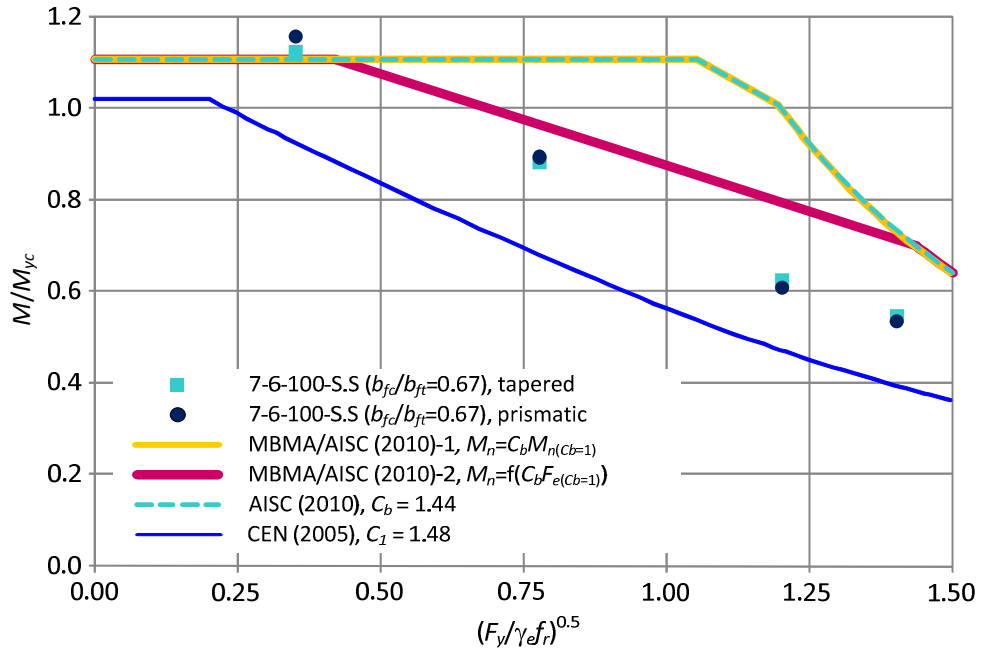

Figure 7.64. Analysis results for $h/b_{fc} = 7.0$, $b_{fc}/2t_{fc} = 6$, $h/t_w = 100$, and $b_{fc}/b_{ft} = 0.67$.

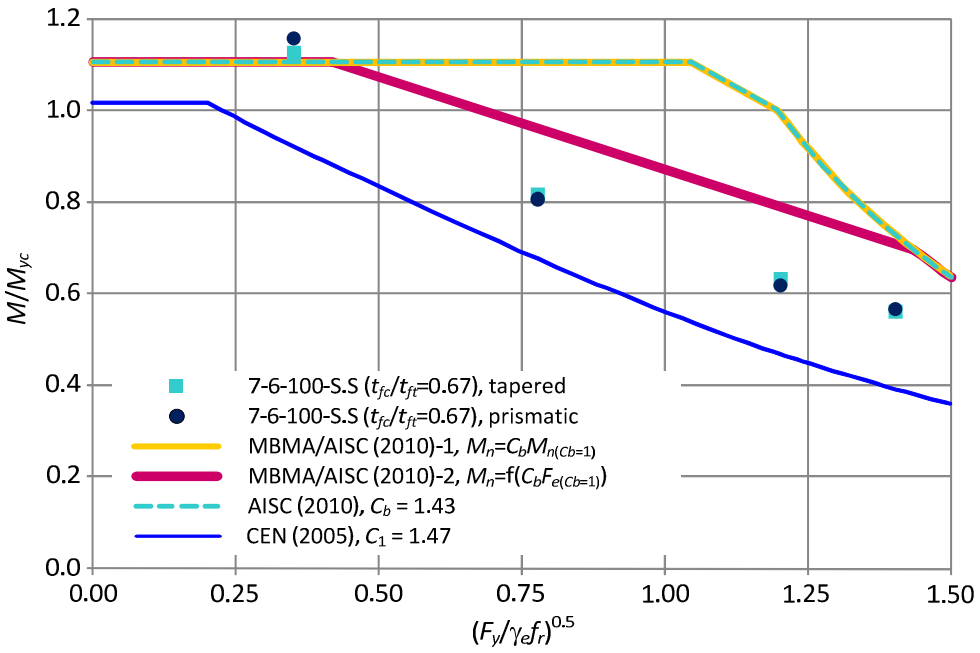

Figure 7.65. Analysis results for $h/b_{fc} = 7.0$, $b_{fc}/2t_{fc} = 6$, $h/t_w = 100$, and $t_{fc}/t_{ft} = 0.67$.

virtual test simulation results. For these beams, the MBMA/AISC (2010)-2 strengths are 22 % larger than the virtual test simulation results in average. For all the test beams except the ones with $h/b_{fc} = 7.0$, $b_{fc}/2t_{fc} = 6$, $h/t_w = 100$, and $b_{fc}/b_{ft} = 1.5$, the CEN (2005) nominal strengths are significantly smaller than the virtual test simulation results.

7.2.4.2 Members with compact flanges and a slender web ($b_{fc}/2t_{fc} = 6$, $h/t_w = 180$)

In Figures 7.66 through 7.69, the virtual test simulation results of singly symmetric members with compact flanges, a slender web and $h/b_{fc} = 7$ are shown. As seen in previous sections, the single symmetry of the cross sections does not change the values of M_{FEA}/M_{yc} significantly. In addition, test beams with the same $(F_y/F_e)^{0.5}$ show practically the same M_{FEA}/M_{yc} values whether the beams have larger compression flanges or smaller compression flanges.

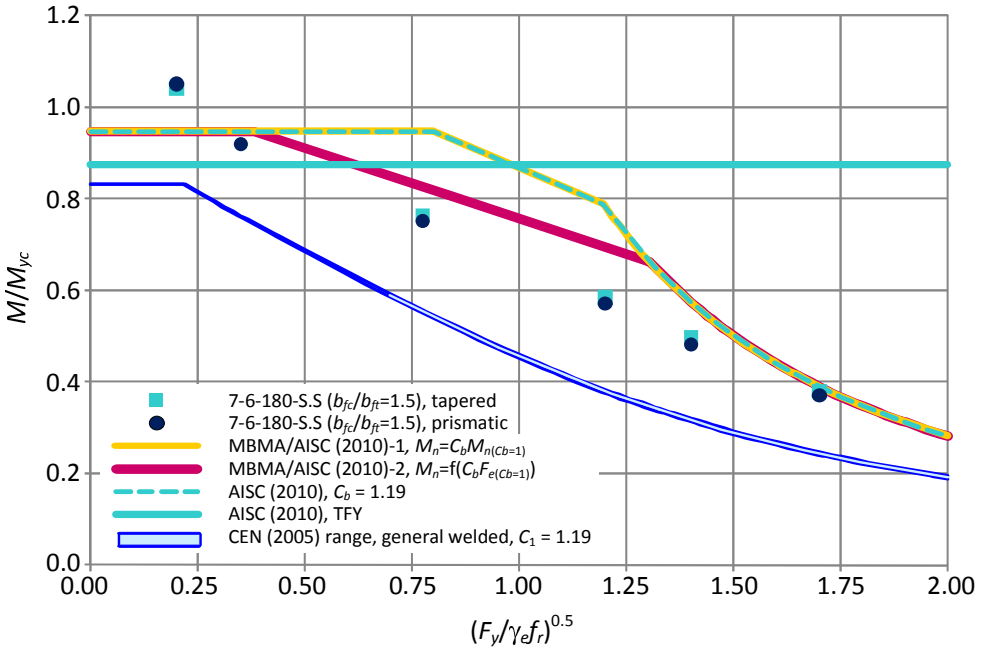

Figure 7.66. Analysis results for $h/b_{fc} = 7.0$, $b_{fc}/2t_{fc} = 6$, $h/t_w = 180$, and $b_{fc}/b_{ft} = 1.5$.

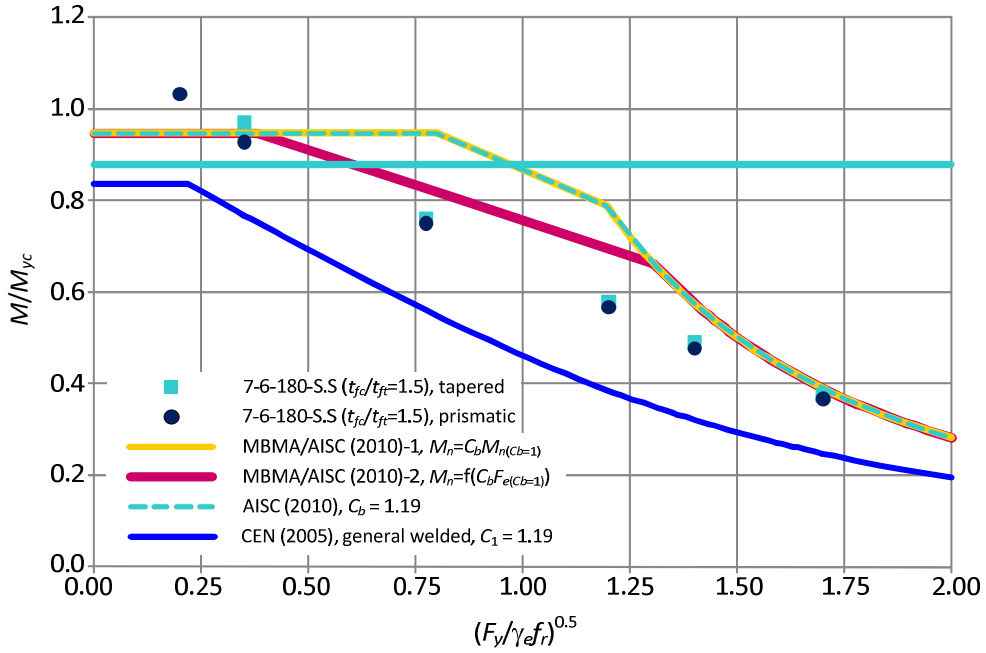

Figure 7.67 Analysis results for $h/b_{fc} = 7.0$, $b_{fc}/2t_{fc} = 6$, $h/t_w = 180$, and $t_{fc}/t_{ft} = 1.5$.

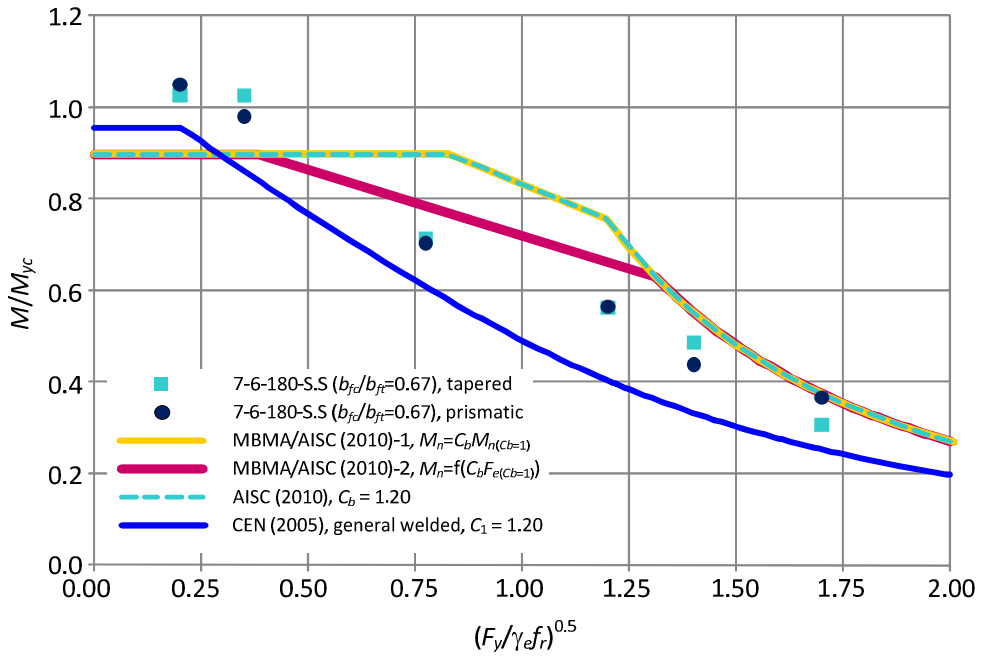

Figure 7.68. Analysis results for $h/b_{fc} = 7.0$, $b_{fc}/2t_{fc} = 6$, $h/t_w = 180$, and $b_{fc}/b_{ft} = 0.67$.

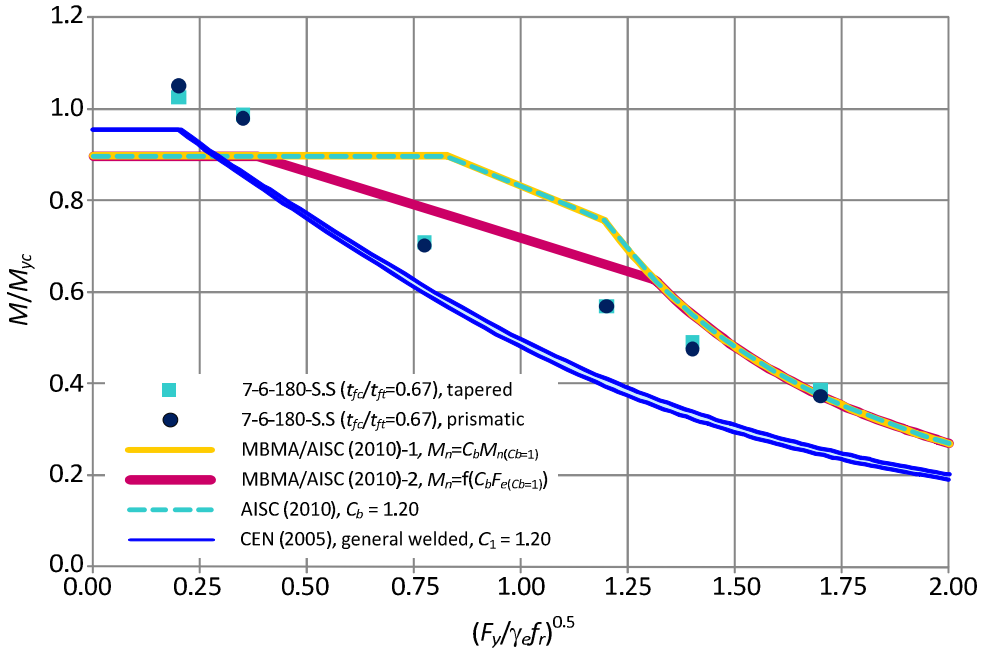

Figure 7.69. Analysis results for $h/b_{fc} = 7.0$, $b_{fc}/2t_{fc} = 6$, $h/t_w = 180$, and $t_{fc}/t_{ft} = 0.67$.

7.3 Recommendations

In this section, the reliability index β for beam lateral torsional buckling is estimated based on the virtual test results shown above and the experimental test data obtained from White and Jung (2008), White and Kim (2008), and Righman (2005). It should be noted that the data from the tests conducted by Righman (2005) were not available at the time of previous study by White and Kim (2008). The AISC (2010) and MBMA/AISC (2010) provisions are used for prismatic and tapered members respectively. For all the cases, the load model statistics for ASCE 7 (ASCE 2006) are used for the reliability index estimation. It is found that the reliability assessment obtained from the experimental test data is significantly different from that obtained from the virtual tests conducted in this research. As a result, different sets of modifications can be recommended for the design of beam lateral torsional buckling based on the experimental test data and the virtual test results. The differences in the reliability assessment of the experimental and virtual tests and the corresponding recommendations are discussed below.

7.3.1 Reliability Assessment

7.3.1.1 Cases under uniform-stress (or uniform-bending) conditions

White and Jung (2008) show the estimation of the reliability index for a total of 277 tests including rolled- and welded-section tests under uniform-bending conditions. The procedures for calculating β used in White and Jung (2008) are as follows. Assuming the resistance R and the load effect Q are lognormally distributed in LFRD, then

$$\beta = \frac{\ln\left(\frac{\overline{R}}{\overline{Q}}\right)}{\sqrt{V_R^{\,2} + V_Q^{\,2}}} \qquad \text{(Eq. 7.3)}$$

where $\overline{R}$ and $\overline{Q}$ = mean values of R and Q and V_R and V_Q = corresponding coefficient of variation. The mean resistance and its coefficient of variation are obtained by

$$\overline{R} = R_n \overline{\rho}_M \overline{\rho}_G \overline{\rho}_P = R_n \overline{\rho}_R \quad \text{and} \quad V_R = \sqrt{V_M^{\,2} + V_G^{\,2} + V_P^{\,2}} \qquad \text{(Eq. 7.4a and b)}$$

For flexural members, $\overline{\rho}_P$ = mean M_{test}/M_n and V_P = coefficient of variation of M_{test}/M_n. To calculate $\overline{\rho}_R$, the following values for the material and geometry bias factors and the corresponding coefficients of variation are used. For inelastic LTB resistances, $\overline{\rho}_M = 1.06$ and $V_M = 0.06$ are used. These values are estimated based on the yield strength of steel obtained by Bartlett et al. (2003) (Galambos 2004). For the test cases with $1.25 \leq f < 1.5$ collected in White and Jung (2008), the authors suggest using $\overline{\rho}_M = 1.00$ and $V_M = 0.00$ as $E = 29000$ ksi is used in all of the calculations. For the geometry bias factor and the coefficient of variation, $\overline{\rho}_G = 1.00$ and $V_G = 0.05$ are selected as reasonable values as in Yura et al. (1978), Cooper et al. (1978), and Galambos (2004).

Using a similar first-order reliability approach, the mean and the coefficient of variation of the load effect are

$$\overline{Q} = \sum \overline{\rho}_{Q_i} Q_i \quad \text{and} \quad V_Q = \frac{\sqrt{\sum \left(\overline{\rho}_{Q_i} V_{Q_i} Q_i\right)^2}}{\overline{Q}} \qquad \text{(Eq. 7.5a and b)}$$

where Q_i = nominal load effects, $\overline{\rho}_{Q_i}$ = ratios of the respective mean values to the nominal values, and V_{Q_i} = corresponding coefficient of variation.

Based on a load combination of $1.2D + 1.6L$ in ASCE 7 (ASCE 2006), Eq. 7.3 can be rearranged into the form

$$\beta = \frac{1}{\sqrt{V_R^{\,2} + V_Q^{\,2}}} \ln\left[\frac{\overline{\rho}_R}{\phi}\left(\frac{1.2 + 1.6(L/D)}{\overline{\rho}_D + \overline{\rho}_L(L/D)}\right)\right] \quad \text{(Eq. 7.6)}$$

where

$$V_Q = \frac{\sqrt{(\overline{\rho}_D V_D)^2 + (\overline{\rho}_L V_L (L/D))^2}}{\overline{\rho}_D + \overline{\rho}_L (L/D)} \quad \text{(Eq. 7.7)}$$

In this study, $\phi = 0.9$ and $L/D = 3.0$ is used for all cases. For the effects of dead and live load due to use and occupancy, White and Jung (2008) used the following statistical parameters obtained from Ellingwood et al. (1980): $\overline{\rho}_D = 1.05$, $V_D = 0.10$, $\overline{\rho}_L = 1.00$, and $V_L = 0.25$.

Figure 7.70 shows the reliability indices obtained from the experimental test data collected by White and Jung (2008) for various ranges of $f = (F_y/\gamma_e f_r)^{0.5}$. Figure 7.70(a) appears in White and Jung (2008) with an abscissa of $c = KL_b(E/F_y)^{0.5}/r_t$, which is a normalized parameter for unbraced lengths. Figures 7.70(b) and (c) are produced in this dissertation to investigate the characteristics of β in terms of different cross-section parameters. It can be seen in Figure 7.70(a) that the reliability indices are approximately constant for all the ranges of f for the rolled member tests. For the welded member tests, β decreases within $0.65 \leq f < 1.25$ and then increases for the tests with $1.25 \leq f < 1.5$. In Sections 7.1 and 7.2, the virtual test simulation also shows significantly smaller M_{test}/M_n for test beams with $0.65 < f < 1.25$. Figure 7.70(b) illustrates that the variation of β is larger for the welded members with compact webs than for the welded members with slender webs. In both cases, the smallest β are estimated for $0.65 \leq f < 0.95$ ($\beta = 2.19$ for

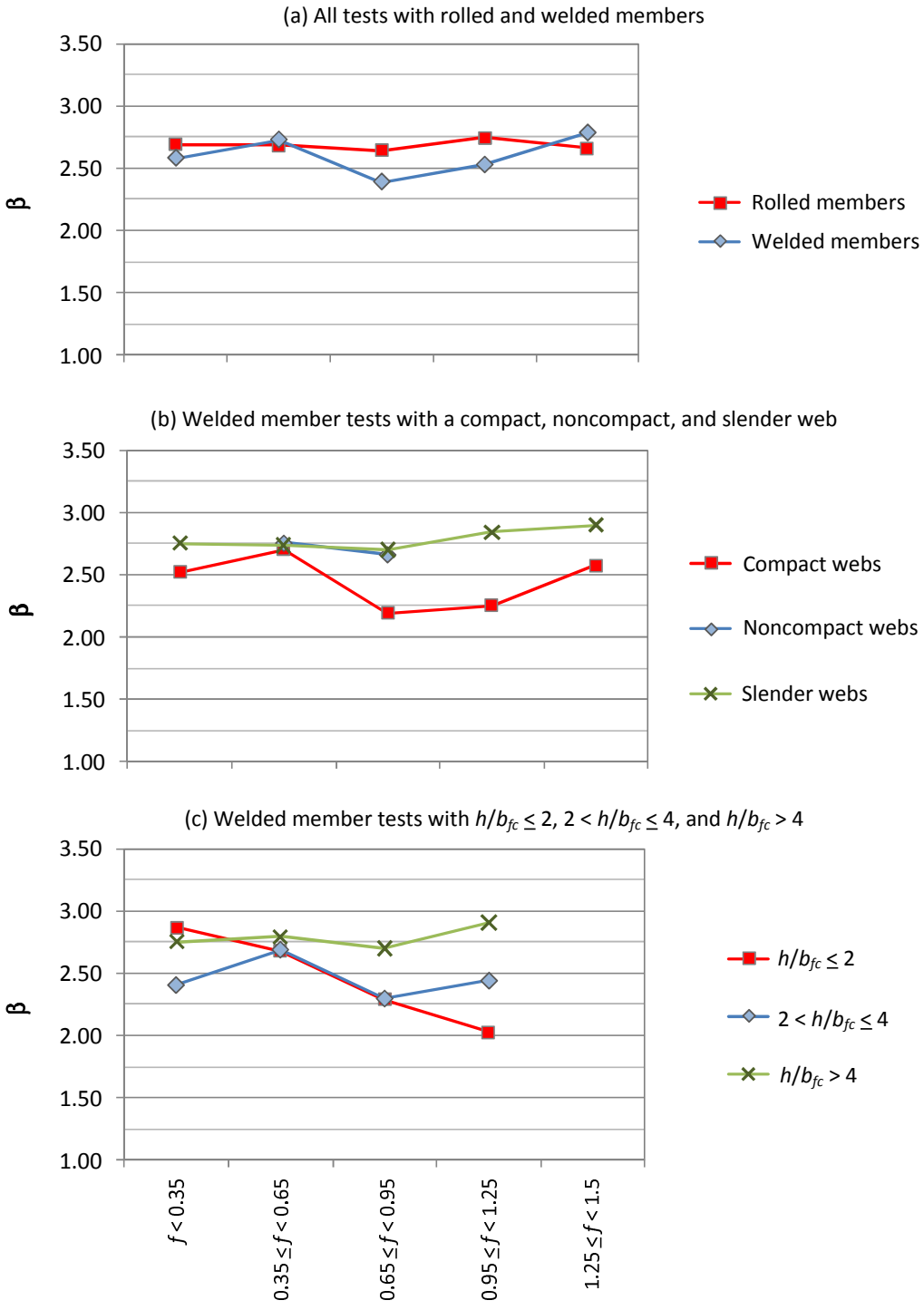

Figure 7.70. Reliability indices for various ranges of $f = (F_y/\gamma_e f_r)^{0.5}$, uniform-bending test data (White and Jung 2008).

the compact-web members and $\beta = 2.70$ for the slender-web members). Figure 7.70(c) shows the estimated β for the welded members with $h/b_{fc} \leq 2$, $2 < h/b_{fc} \leq 4$, and $h/b_{fc} > 4$. For all the groups of h/b_{fc}, the test data of members with $1.25 \leq (F_y/\gamma_e f_r)^{0.5} \leq 1.5$ is too limited to estimate the reliability indices. Therefore these points are not shown in Figure 7.70(c). The β values for the members with $2 < h/b_{fc} \leq 4$ are less than or approximately equal to the β values for the members with $h/b_{fc} \leq 2$ or $h/b_{fc} > 4$ for $(F_y/\gamma_e f_r)^{0.5} < 0.95$. As indicated in Figure 7.70(c), the experimental test data collected by White and Jung (2008) shows no reduction in M_{test}/M_n as h/b_{fc} increases. However, it should be noted that there are a very limited number of tests conducted with a noncompact web, and zero tests are available with a compact or noncompact web with $h/b_{fc} > 4$. In Sections 7.1 and 7.2, it is discussed that the combination of a compact or noncompact web and $h/b_{fc} = 5.5$ and 7 produces the smallest values of M_{FEA}/M_n.

In this study, the reliability indices for the virtual tests are estimated using the same procedures suggested by White and Jung (2008). As in White and Jung (2008), the reliability indices of the slender-web sections are calculated based on the R_{pg} factor calculated using the compression flange stress $M_{AISC(Rpg=1)}/S_{xc}$. It should be noted that in the previous sections, all the virtual test simulation results and resistance curves are shown based on R_{pg} obtained using F_{yc} as indicated in AISC (2010). However, the use of R_{pg} based on the compression flange stress $M_{AISC(Rpg=1)}/S_{xc}$ provides better predictions of the LTB resistances especially for the elastic LTB region. Because the R_{pg} factor based on $M_{AISC(Rpg=1)}/S_{xc}$ is slightly larger than the R_{pg} factor based on F_{yc}, the resulting M_{AISC} value is more liberal.

Table 7.17 shows the summary of M_{test}/M_n calculated for the virtual tests conducted in this research where M_n is the nominal strengths calculated by AISC (2010) for the prismatic members and by MBMA/AISC (2010) for the tapered members and f is the normalized flange stress term $(F_y/\gamma_e f_r)^{0.5}$. Appendix H shows the values of M_{test}/M_n for all the virtual test cases considered in this research, where M_n is calculated using the AISC (2010) and MBMA/AISC (2010) provisions.

Table 7.17. Summary of M_{test}/M_n statistics for virtual tests under uniform-bending or uniform-stress conditions (prismatic and tapered members)

	all	$f < 0.35$	$0.35 \leq f < 0.65$	$0.65 \leq f < 0.95$	$0.95 \leq f < 1.25$	$1.25 \leq f < 1.5$	$f > 1.5$
(a) Prismatic members							
N	168	20	21	32	32	32	31
Maximum	1.04	1.04	0.97	0.98	0.87	1.02	1.04
Median	0.86	0.99	0.90	0.81	0.74	0.84	0.94
Minimum	0.66	0.92	0.79	0.67	0.66	0.77	0.89
Mean	0.86	0.98	0.90	0.81	0.74	0.84	0.94
V (%)	11.32	3.75	6.39	9.99	6.23	5.80	3.90
(b) Tapered members							
N	124	17	18	25	25	22	17
Maximum	1.04	1.04	0.98	0.89	0.83	0.95	1.00
Median	0.87	1.00	0.91	0.82	0.77	0.87	0.96
Minimum	0.71	0.92	0.81	0.71	0.72	0.82	0.92
Mean	0.87	0.99	0.91	0.81	0.77	0.87	0.96
V (%)	10.02	4.22	6.12	6.42	3.99	3.94	2.62

In Tables 7.17(a) and 7.17(b), the mean value of M_{test}/M_n varies from 0.74 to 0.99 for the prismatic member tests while the mean M_{test}/M_n varies from 0.77 to 0.99 for the tapered member tests. The mean M_{test}/M_n values for both prismatic and tapered members continuously decrease from the range of $f < 0.35$ to $0.95 < f < 1.25$ then increase for $1.25 \leq f < 1.5$ and $f \geq 1.5$. The largest coefficient of variation occurs for $0.65 \leq f < 0.95$ for both prismatic and tapered members. It is important to note that the means and coefficients of variation of $M_{test}/M_{n(AISC)}$ for prismatic members are similar to the corresponding values of $M_{test}/M_{n(MBMA\text{-}AISC)}$ in most cases except for $0.65 \leq (F_y/\gamma_e f_r)^{0.5} <$

0.95. In addition, $M_{n(AISC)}$ is essentially same as $M_{n(MBMA\text{-}AISC)}$ for the uniform-stress or uniform-bending conditions as seen in Section 7.1. Therefore, Tables 7.18 and 7.19 show the M_{test}/M_n statistics for the combined sets of the prismatic and tapered members.

Table 7.18 shows a summary of M_{test}/M_n statistics for members with different categories of the web slenderness. It should be noted that only the test cases with h/b_{fc} = 5.5 and 7 are considered for the statistics of members with a compact web. This is because that the test cases with h/b_{fc} = 1, 1.5, and 2 and a compact web are rolled-section type members and these cases show significantly distinct results compared to the test cases with h/b_{fc} = 5.5 and 7 and a compact web (see Section 7.1). Therefore, it is decided to conduct the separate reliability assessment for the test cases with h/b_{fc} = 1, 1.5, and 2 and h/t_w = 40.

Table 7.18. Summary of M_{tset}/M_n statistics for virtual tests under uniform-bending or uniform-stress conditions (members with a compact, noncompact, and slender web).

	all	$f < 0.35$	$0.35 \le f < 0.65$	$0.65 \le f < 0.95$	$0.95 \le f < 1.25$	$1.25 \le f < 1.5$	$f > 1.5$
(a) Members with a compact web							
N	34	6	6	6	6	5	5
Maximum	1.00	0.96	0.90	0.80	0.80	0.88	1.00
Median	0.86	0.93	0.84	0.74	0.76	0.86	0.97
Minimum	0.67	0.92	0.79	0.67	0.71	0.82	0.95
Mean	0.85	0.93	0.85	0.74	0.76	0.86	0.97
V (%)	10.73	1.88	5.15	6.58	4.21	2.67	1.89
(b) Members with a noncompact web							
N	151	18	20	30	30	28	25
Maximum	1.02	1.02	0.96	0.98	0.81	0.91	1.00
Median	0.84	0.98	0.87	0.79	0.74	0.84	0.94
Minimum	0.66	0.93	0.81	0.68	0.66	0.77	0.89
Mean	0.85	0.98	0.88	0.79	0.74	0.84	0.94
V (%)	11.04	2.75	4.54	9.24	5.19	3.82	2.98
(c) Members with a slender web							
N	89	10	10	18	18	18	15
Maximum	1.04	1.04	0.98	0.89	0.83	0.95	1.00
Median	0.87	1.03	0.97	0.86	0.77	0.87	0.94
Minimum	0.71	1.02	0.95	0.81	0.71	0.79	0.89
Mean	0.88	1.03	0.97	0.85	0.77	0.86	0.94
V (%)	10.01	0.82	1.07	3.04	4.33	5.65	3.63

It can be seen from Tables 7.18(a) through (c) that the means of M_{tset}/M_n for the test members with a compact web are smaller than that for the test members with a noncompact or slender web and $f < 0.95$. For test members with $f \geq 0.95$, the means of M_{tset}/M_n for the compact-web members are close to or slightly smaller than that for the members with a noncompact or slender web. Table 7.18(b) shows that the coefficient of variation of M_{tset}/M_n for the noncompact-web members with $0.65 \leq f < 0.95$ is significant (9.24 %). This is due to the significantly smaller M_{tset}/M_n values for the test members with $h/b_{fc} = 5.5$ and 7 and $h/t_w \leq 100$.

Tables 7.19(a) to 7.19(c) show a summary of M_{tset}/M_n statistics for three different groups of h/b_{fc}. For each range of f, the means of M_{tset}/M_n for members with $h/b_{fc} = 5.5$ and 7 are smaller than that for members with $h/b_{fc} = 4$ in general. For the elastic LTB resistance $f > 1.5$, the means of M_{tset}/M_n for different groups of h/b_{fc} are very similar. For all the groups of h/b_{fc}, the smallest mean of M_{tset}/M_n is for the test members with $0.95 \leq f < 1.25$, which is the vicinity of the inelastic LTB limit, $L_b = L_r$ or $(F_y/F_L)^{0.5} = (1/0.7)^{0.5} = 1.20$. Table 7.20 shows a summary of M_{tset}/M_n for virtual tests with $h/b_{fc} = 1$, 1.5, and 2 and $h/t_w = 40$. As mentioned above, these cases show larger mean values of M_{tset}/M_n for all ranges of $f = (F_y/\gamma_e f_r)^{0.5}$ than those seen in Table 7.18.

Figure 7.71 illustrates the reliability indices for various ranges of $f = (F_y/\gamma_e f_r)^{0.5}$ for the virtual test simulations. Figures 7.71(a) through (c) are the same types of plots shown in Figures 7.70(a) to (c) for the test cases considered in White and Jung (2008). It can be seen that the values of β illustrated in Figure 7.71(a) are significantly smaller than the β values seen in Figure 7.70(a) for $f \geq 0.35$. Based on the experimental test data considered in White and Jung (2008), the minimum β is 2.37 (estimated for the rolled members with

$0.65 \leq f < 0.95$) while the minimum β is 1.20 based on the virtual test simulation results conducted in this study (β of 1.20 is estimated for the prismatic members with $0.95 < f < 1.25$). In addition, for $f < 0.95$, the β values for the compact-web members are the smallest (see Figure 7.71b). On the other hand, for $f > 0.95$, the β values are similar for all categories of web slenderness. The minimum β is 1.06 for the compact-web members

Table 7.19. Summary of M_{tset}/M_n statistics for virtual tests under uniform-bending or uniform-stress conditions (members with i) h/b_{fc}= 1 and 2, ii) h/b_{fc}= 4, and iii) h/b_{fc}= 5.5 and 7)

	all	$f < 0.35$	$0.35 \leq f < 0.65$	$0.65 \leq f < 0.95$	$0.95 \leq f < 1.25$	$1.25 \leq f < 1.5$	$f > 1.5$
				(a) Members with h/b_{fc} = 1 and 2			
N	15	0	0	4	4	4	3
Maximum	1.00			0.98	0.77	0.86	1.00
Median	0.86			0.92	0.75	0.85	0.95
Minimum	0.74			0.85	0.74	0.83	0.94
Mean	0.86			0.92	0.75	0.85	0.96
V (%)	10.29			8.04	1.60	1.53	3.41
				(b) Members with h/bfc = 4			
N	65	6	6	16	16	13	8
Maximum	1.03	1.03	0.98	0.89	0.82	0.95	0.98
Median	0.87	0.98	0.93	0.84	0.78	0.87	0.96
Minimum	0.73	0.95	0.89	0.79	0.73	0.84	0.94
Mean	0.87	0.99	0.93	0.84	0.78	0.88	0.96
V (%)	8.67	3.10	3.90	3.72	2.97	3.85	1.27
				(c) Members with h/bfc = 5.5 and 7			
N	194	28	30	34	34	34	34
Maximum	1.04	1.04	0.98	0.88	0.83	0.89	1.00
Median	0.86	0.99	0.88	0.78	0.74	0.83	0.94
Minimum	0.66	0.92	0.79	0.67	0.66	0.77	0.89
Mean	0.86	0.99	0.89	0.78	0.73	0.83	0.94
V (%)	11.49	4.32	6.46	7.70	5.18	3.94	3.47

Table 7.20. Summary of M_{tset}/M_n statistics for virtual tests under uniform-bending or uniform-stress conditions (members with h/b_{fc}= 1, 1.5, and 2 and with h/t_w = 40).

	all	$f < 0.35$	$0.35 \leq f < 0.65$	$0.65 \leq f < 0.95$	$0.95 \leq f < 1.25$	$1.25 \leq f < 1.5$	$f > 1.5$
				Members with h/b_{fc} = 1, 1.5, and 2 and h/t_w = 40			
N	17	3	3	3	3	3	2
Maximum	1.04	1.00	0.96	0.93	0.87	1.02	1.04
Median	0.95	1.00	0.95	0.89	0.82	0.92	1.02
Minimum	0.81	1.00	0.95	0.86	0.81	0.90	0.99
Mean	0.94	1.00	0.95	0.89	0.83	0.95	1.02
V (%)	7.34	0.11	0.27	4.00	3.78	6.55	3.64

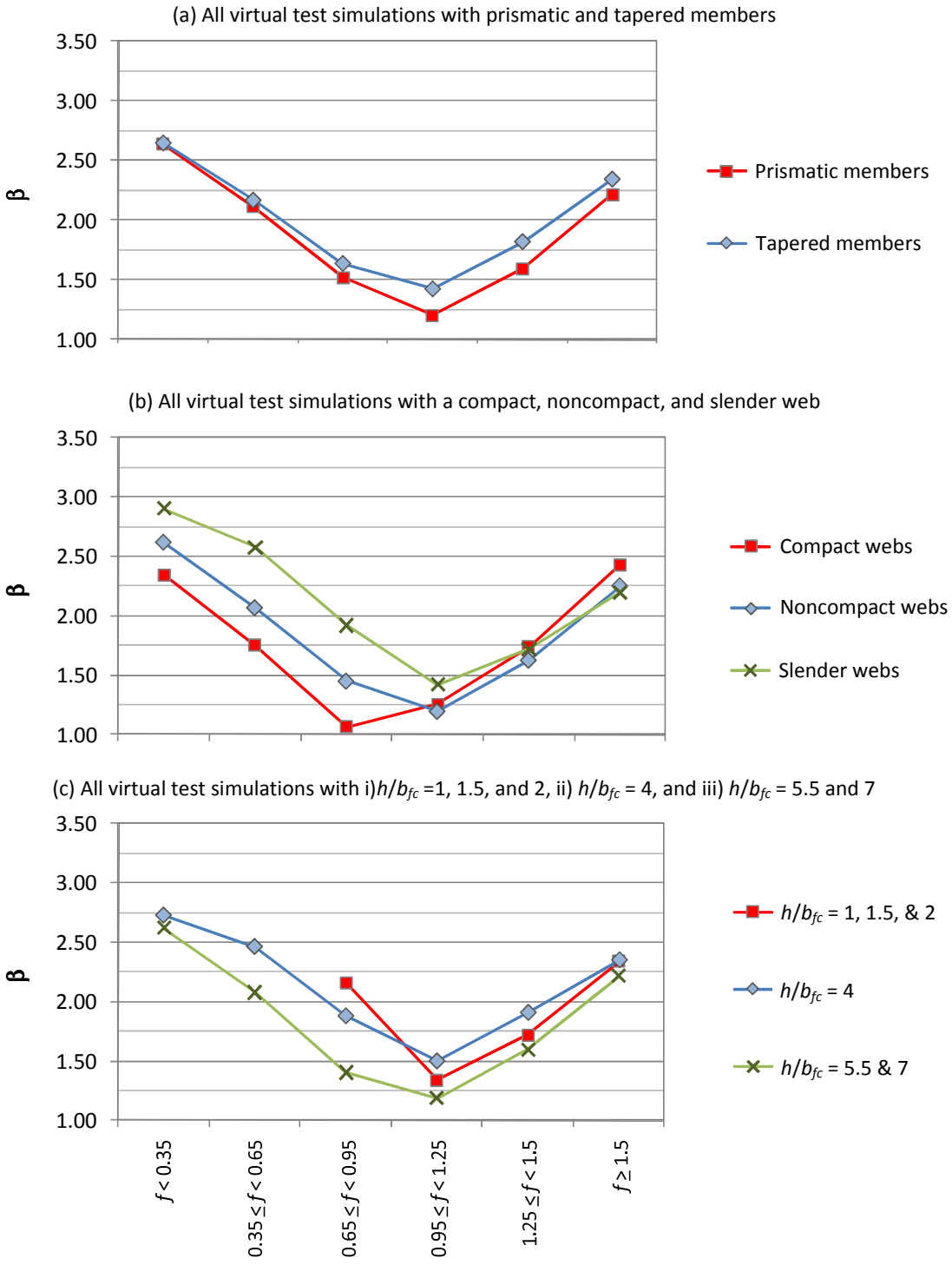

Figure 7.71. Reliability indices for various ranges of $f = (F_y/\gamma_e f_r)^{0.5}$, uniform-stress test simulations, prismatic and tapered members.

with $0.65 < f < 0.95$ in Figure 7.71(b). As discussed above, this low β comes from the test case with $h/b_{fc} = 7$ and $h/t_w = 85$, which shows the smallest M_{test}/M_n values within the inelastic LTB range ($0.65 < f < 1.25$). In Figure 7.70(c), the β values for three different h/b_{fc} groups are shown. As seen in the M_{test}/M_n statistics in Table 7.19, the test members with $h/b_{fc} = 5.5$ and 7 shows the smallest β for all the ranges of $f = (F_y/\gamma_e f_r)^{0.5}$. The minimum β is 1.19 for the test members with $h/b_{fc} = 5.5$ and 7 and $0.95 < f < 1.25$. It can be seen that all the plots shown in Figures 7.71(a) to (c) have a "v" shape with the minimum β at $0.95 < f < 1.25$ except the test members with a compact web shown in Figures 7.71(b). As mentioned above, the range of $0.95 < f < 1.25$ is the vicinity of the inelastic LTB limit, $L_b = L_r$ or $(F_y/F_e)^{0.5} = (F_y/F_L)^{0.5}$. For the elastic LTB region $f > 1.5$, the values of β are 2.2 and 2.4 for prismatic and tapered members respectively. These values are slightly smaller than the targeted reliability index of 2.6 for statically determinate beams under uniform bending (Galambos 2004, Galamos and Ravindra 1976).

Figure 7.72 shows the reliability indices for prismatic members with $h/b_{fc} = 1$, 1.5, and 2 and $h/t_w = 40$. The data point for $f \geq 1.5$ is not shown because there are only two virtual tests for this range. As indicated above, the values of β for these members are significantly larger than those for the members with $h/b_{fc} = 4$, 5.5, and 7 and a compact web. It should be noted, however, that these cases also show the same type of "v" shape with the minimum β at $0.95 < f < 1.25$, which is shown in Figure 7.71.

7.3.1.2 Cases under stress-gradient (or moment-gradient) conditions

White and Kim (2008) collected a total of 164 test cases to estimate the reliability indices for both rolled- and welded-section tests under moment-gradient loadings. In

addition, Righman (2005) conducted three-point bending tests with twelve welded-section girders. The tests conducted by Righman (2005) provided additional data for the LTB strengths of members with a noncompact or slender web and a singly-symmetric cross section ($I_{yc}/I_{yt} < 0.4$). In this study the reliability indices for tests under moment-gradient conditions are estimated based on the test data in White and Kim (2008) and the tests performed by Righman (2005). The reliability indices for moment-gradient tests are also calculated as described in the beginning of Section 7.3.1.1.

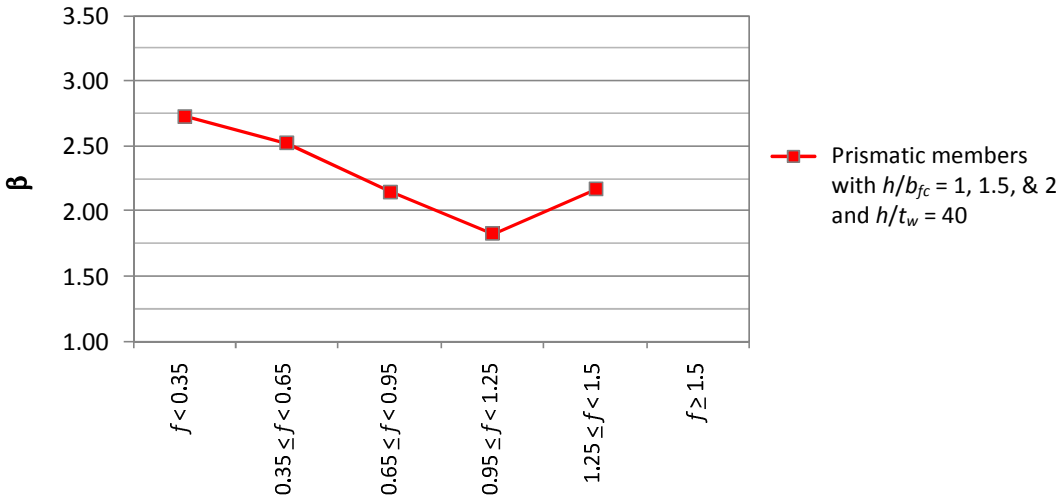

Figure 7.72. Reliability indices for various ranges of $f = (F_y/\gamma_e f_r)^{0.5}$, uniform-stress test simulations, prismatic members with h/b_{fc} = 1, 1.5, & 2 and h/t_w = 40.

Figure 7.73 shows the reliability indices of tests under moment-gradient conditions. It can be seen that the values of β for the moment-gradient tests with rolled members are larger than those for the uniform-bending tests. Conversely, for the moment-gradient tests with welded members, β decreases from 3.2 for $f < 0.35$ to 2.1 for $0.95 \leq f < 1.25$. The minimum β for the uniform-bending tests with welded members is 2.39 in Figure 7.70(a). The relatively low β value for $0.95 \leq f < 1.25$ is due to two test

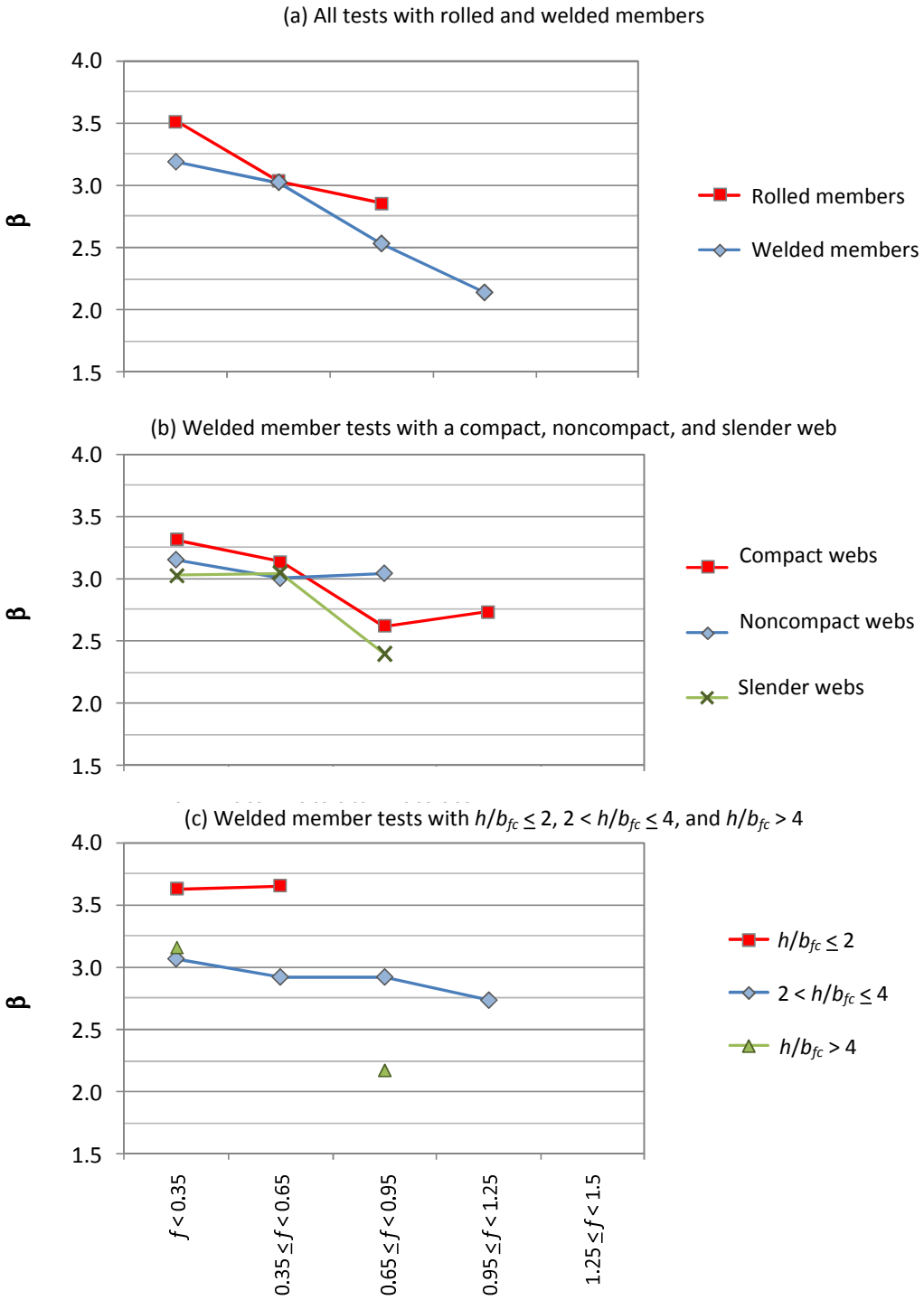

Figure 7.73. Reliability indices for various ranges of $f = (F_y/\gamma_e f_r)^{0.5}$, moment-gradient test data (White and Kim 2008 and Righman 2005).

cases from Righman (2005). These test members are extremely singly symmetric with compact flanges and a slender web. The ratio of weak-axis moment of inertia of each flange I_{yc}/I_{yt} is less than 0.30 for these two tests.

Figure 7.74 shows the reliability indices of the moment-gradient tests for different ranges of I_{yc}/I_{yt}. It can be seen that the reliability index decreases for the tests with $I_{yc}/I_{yt} < 0.3$. However, the decrease in the values of M_{test}/M_n for the tests with $I_{yc}/I_{yt} < 0.3$ has not been observed with the virtual test simulations conducted in this study. In this research, eight cases, which have $b_{fc}/b_{ft} = 0.67$ resulting in $I_{yc}/I_{yt} = 0.29$ have been analyzed. As seen in the previous sections, the test members with $b_{fc}/b_{ft} = 0.67$ show essentially the same results as the test members with $b_{fc}/b_{ft} = 1.5$, which have $I_{yc}/I_{yt} = 3.45$.

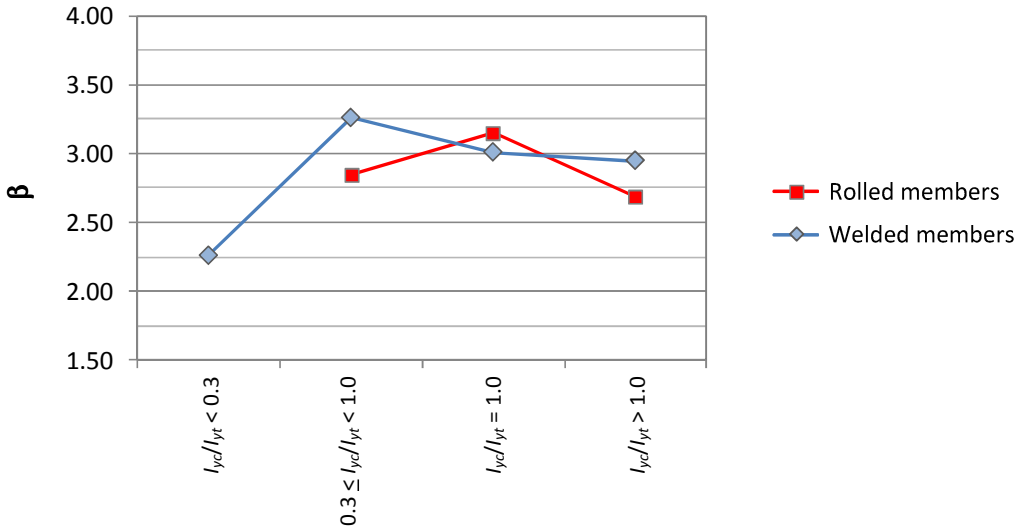

Figure 7.74. Reliability indices for various ranges of I_{yc}/I_{yt}, moment-gradient test data (White and Kim 2008 and Righman 2005).

In Figure 7.73(b), it is observed that the reliability indices of tests with different web slenderness are very similar for $f \leq 0.65$. The reliability index values for the

noncompact-web tests are close to constant for all the ranges of f. On the other hand, β decreases for the welded tests with a compact or slender web with $f > 0.65$. The tests with $h/b_{fc} \leq 2$ and $h/b_{fc} > 4$ are limited so that there are only two data points in Figure 7.73(c) for each group. It can be seen that the tests with $h/b_{fc} > 4$ and $0.65 \leq f < 0.95$ show significantly lower β compared to tests members with smaller h/b_{fc}. On the other hand, the tests with $h/b_{fc} < 2$ and $f \leq 0.65$ show β larger than 3.5. It is most likely that these cases have the effect of strain hardening as well as the large moment gradient effect, which provide the test strengths much larger than the plateau strength of LTB. For the tests with $2< h/b_{fc} \leq 4$, the reliability index values are approximately constant for $f < 0.95$. For $0.95 \leq f < 1.25$, β decreases slightly.

Tables 7.21 to 7.24 show a summary of M_{test}/M_n statistics for virtual tests under moment-gradient or stress-gradient conditions. It should be noted that for all the values of M_{test}/M_n shown in Tables 7.21 to 7.24, M_n are obtained using the AISC (2010) provisions for prismatic members and the MBMA/AISC (2010)-1 procedure for tapered members.

Table 7.21 shows the minimum means of M_{test}/M_n for test members at $0.95 \leq f < 1.25$ as seen in Table 7.17. Table 7.22 demonstrates that the values of M_{test}/M_n are smaller for members with a noncompact web than for members with a slender web for all the ranges of f. Since no test member with a compact web analyzed with moment-gradient or stress-gradient conditions (except the members with $h/b_{fc} = 1$, 1.5, and 2 and $h/t_w = 40$), no data is shown for members with a compact web in Table 7.22. It is shown in Table 7.23 that the members with larger h/b_{fc} have smaller values of M_{test}/M_n as seen in Table 7.19. The members with $h/b_{fc} = 1$ and 2 and shorter unbraced lengths are governed

by shear failure (members with $f < 0.65$) and flange local buckling (members with $0.65 \leq f < 0.95$). Therefore, no data is shown for these cases in Table 7.23.

Lastly, Table 7.24 shows the summary of M_{tset}/M_n statistics for virtual tests with $h/b_{fc} = 1$, 1.5, and 2 and $h/t_w = 40$. It can be seen that the means of M_{tset}/M_n are larger compared to other tests shown in Tables 7.21 to 7.23. However, these cases also show the minimum M_{tset}/M_n for members with $0.95 \leq f < 1.25$.

Table 7.21. Summary of M_{tset}/M_n statistics for virtual tests under moment-gradient or stress-gradient conditions (prismatic and tapered members)

	all	$f < 0.35$	$0.35 \leq f < 0.65$	$0.65 \leq f < 0.95$	$0.95 \leq f < 1.25$	$1.25 \leq f < 1.5$	$f > 1.5$
(a) Prismatic members							
N	90	6	11	19	21	20	13
Maximum	1.17	1.17	1.09	1.04	0.86	0.92	1.14
Median	0.85	1.10	1.05	0.79	0.74	0.82	0.94
Minimum	0.61	0.97	0.98	0.71	0.61	0.73	0.88
Mean	0.87	1.09	1.04	0.84	0.74	0.82	0.95
V (%)	15.32	7.02	3.09	12.22	10.32	6.24	7.44
(b) Tapered members							
N	70	5	11	16	16	14	8
Maximum	1.14	1.14	1.14	0.93	0.81	0.95	1.00
Median	0.83	1.12	1.02	0.80	0.73	0.83	0.92
Minimum	0.62	1.03	0.95	0.71	0.62	0.71	0.88
Mean	0.86	1.11	1.03	0.81	0.72	0.82	0.93
V (%)	15.74	4.11	4.99	6.65	8.22	7.97	4.65

Table 7.22. Summary of M_{tset}/M_n statistics for virtual tests under moment-gradient or stress-gradient conditions (members with a noncompact and slender web).

	all	$f < 0.35$	$0.35 \leq f < 0.65$	$0.65 \leq f < 0.95$	$0.95 \leq f < 1.25$	$1.25 \leq f < 1.5$	$f > 1.5$
(a) Members with a noncompact web							
N	77	3	12	18	20	18	6
Maximum	1.05	1.05	1.05	0.93	0.85	0.89	0.97
Median	0.81	1.03	1.02	0.79	0.72	0.82	0.91
Minimum	0.61	0.97	0.95	0.71	0.61	0.71	0.88
Mean	0.83	1.02	1.01	0.80	0.70	0.80	0.92
V (%)	15.03	4.02	2.91	8.29	10.55	7.01	4.07
(b) Members with a slender web							
N	71	8	10	14	14	13	12
Maximum	1.17	1.17	1.14	0.87	0.81	0.95	1.00
Median	0.86	1.13	1.05	0.80	0.73	0.82	0.92
Minimum	0.71	1.07	1.01	0.78	0.71	0.79	0.88
Mean	0.89	1.13	1.06	0.81	0.75	0.83	0.93
V (%)	15.19	2.87	3.76	3.92	4.48	5.21	4.46

Table 7.23. Summary of M_{tset}/M_n statistics for virtual tests under moment-gradient or stress-gradient conditions (members with i. h/b_{fc} = 1 and 2, ii. h/b_{fc} = 4, and iii. h/b_{fc} = 5.5 and 7).

	all	$f < 0.35$	$0.35 \le f < 0.65$	$0.65 \le f < 0.95$	$0.95 \le f < 1.25$	$1.25 \le f < 1.5$	$f > 1.5$
				(a) Members with h/b_{fc} = 1 and 2			
N	6	0	0	0	2	2	2
Maximum	0.97				0.85	0.82	0.97
Median	0.84				0.84	0.82	0.96
Minimum	0.82				0.84	0.82	0.95
Mean	0.88				0.84	0.82	0.96
V (%)	7.91				0.85	0.25	1.38
				(b) Members with h/bfc = 4			
N	37	3	4	10	10	8	2
Maximum	1.07	1.07	1.05	0.93	0.81	0.95	0.98
Median	0.86	1.05	1.03	0.87	0.75	0.86	0.95
Minimum	0.73	1.03	1.02	0.79	0.73	0.84	0.92
Mean	0.87	1.05	1.03	0.85	0.76	0.87	0.95
V (%)	11.95	1.91	1.15	6.20	3.56	3.87	4.42
				(c) Members with h/bfc = 5.5 and 7			
N	105	8	18	22	22	21	14
Maximum	1.17	1.17	1.14	0.86	0.80	0.87	1.00
Median	0.81	1.13	1.04	0.79	0.71	0.79	0.90
Minimum	0.61	0.97	0.95	0.71	0.61	0.71	0.88
Mean	0.85	1.12	1.04	0.78	0.69	0.79	0.92
V (%)	17.09	5.66	4.49	4.72	8.24	5.57	4.05

Table 7.24. Summary of M_{tset}/M_n statistics for virtual tests under moment-gradient or stress-gradient conditions (members with h/b_{fc} = 1, 1.5, and 2 and h/t_w = 40).

	all	$f < 0.35$	$0.35 \le f < 0.65$	$0.65 \le f < 0.95$	$0.95 \le f < 1.25$	$1.25 \le f < 1.5$	$f > 1.5$
				Members with h/b_{fc} = 1, 1.5, and 2 and h/t_w = 40			
N	12	0	0	3	3	3	3
Maximum	1.14			1.04	0.86	0.92	1.14
Median	0.96			1.04	0.84	0.89	1.01
Minimum	0.81			1.04	0.81	0.89	1.00
Mean	0.96			1.04	0.84	0.90	1.05
V (%)	10.48			0.04	3.10	2.00	7.23

Figure 7.75 shows the estimations of reliability index for the virtual test simulations under stress-gradient or moment-gradient loadings. In Figure 7.75(a), it can be seen that the reliability index values for the stress-gradient virtual simulations are larger than those for the uniform-stress virtual tests shown in Figure 7.71(a) for $f < 0.65$. In Figure 7.75(a), the β values are 3.20 and 2.82 for the first two data points of the

tapered members. In Figure 7.71(a), the corresponding β values are 2.64 and 2.17. However, for $0.65 \leq f < 0.95$, β drastically decreases to 1.60 and for $0.95 \leq f < 1.25$, β becomes 1.04, which is the smallest value. For the elastic LTB region ($f \geq 1.5$), β is 2.12. As mentioned above, no test case is studied with a compact web except test cases with h/b_{fc} = 1, 1.5, and 2 and h/t_w = 40. Also, the virtual test simulation results with h/b_{fc} = 1 and 2 are too limited to obtain the reliability indices. Therefore in Figures 7.75(b) and (c), the reliability indices are shown only for members with a noncompact or slender web and with h/b_{fc} = 4 and h/b_{fc} = 5.5 and 7. It is shown in Figures 7.75(b) and (c) that the β values are smaller for the tests with a noncompact web or h/b_{fc} = 5.5 and 7. Only exception is test members with h/b_{fc} = 5.5 and 7 and $f < 0.35$. This is the only case where the reliability index for members with h/b_{fc} = 5.5 and 7 is larger than that for members with h/b_{fc} = 4.

The reliability indices shown in Figure 7.75 are based on M_{test}/M_n where M_n is calculated using the AISC (2010) and MBMA/AISC (2010)-1 procedures for moment-gradient and stress-gradient LTB resistances. The MBMA/AISC (2010)-1 procedure ($M_n = C_b M_{n(Cb=1)}$) is recommended for linearly tapered members with no step transition in the flanges. In MBMA/AISC (2010), the MBMA/AISC (2010)-2 procedure (M_n = f($C_b F_{e(Cb=1)}$)) is suggested for general tapered members. It is shown in Section 7.2 that the MBMA/AISC (2010)-2 procedure provides better estimations of the LTB resistances for the virtual test simulation results compared to other procedures, the AISC (2010) and MBMA/AISC (2010)-1 procedures. Figure 7.76 shows the reliability indices estimated using the MBMA/AISC (2010) -2 procedure for the tapered members. In Figure 7.76(a), the reliability indices obtained using the MBMA/AISC (2010)-2 procedure are compared

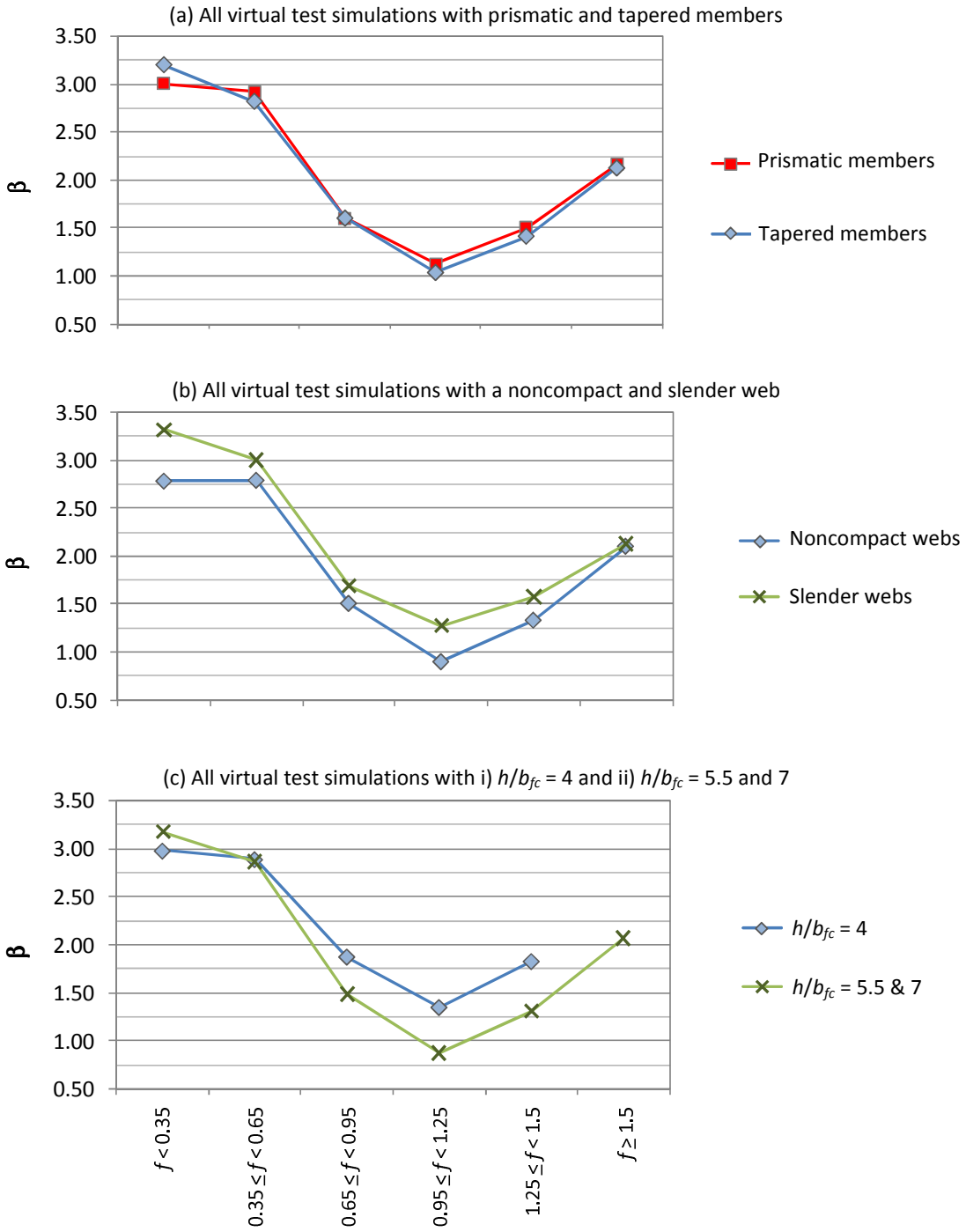

Figure 7.75. Reliability indices for various ranges of $f = (F_y/\gamma_e f_r)^{0.5}$, stress-gradient test simulations, prismatic and tapered members.

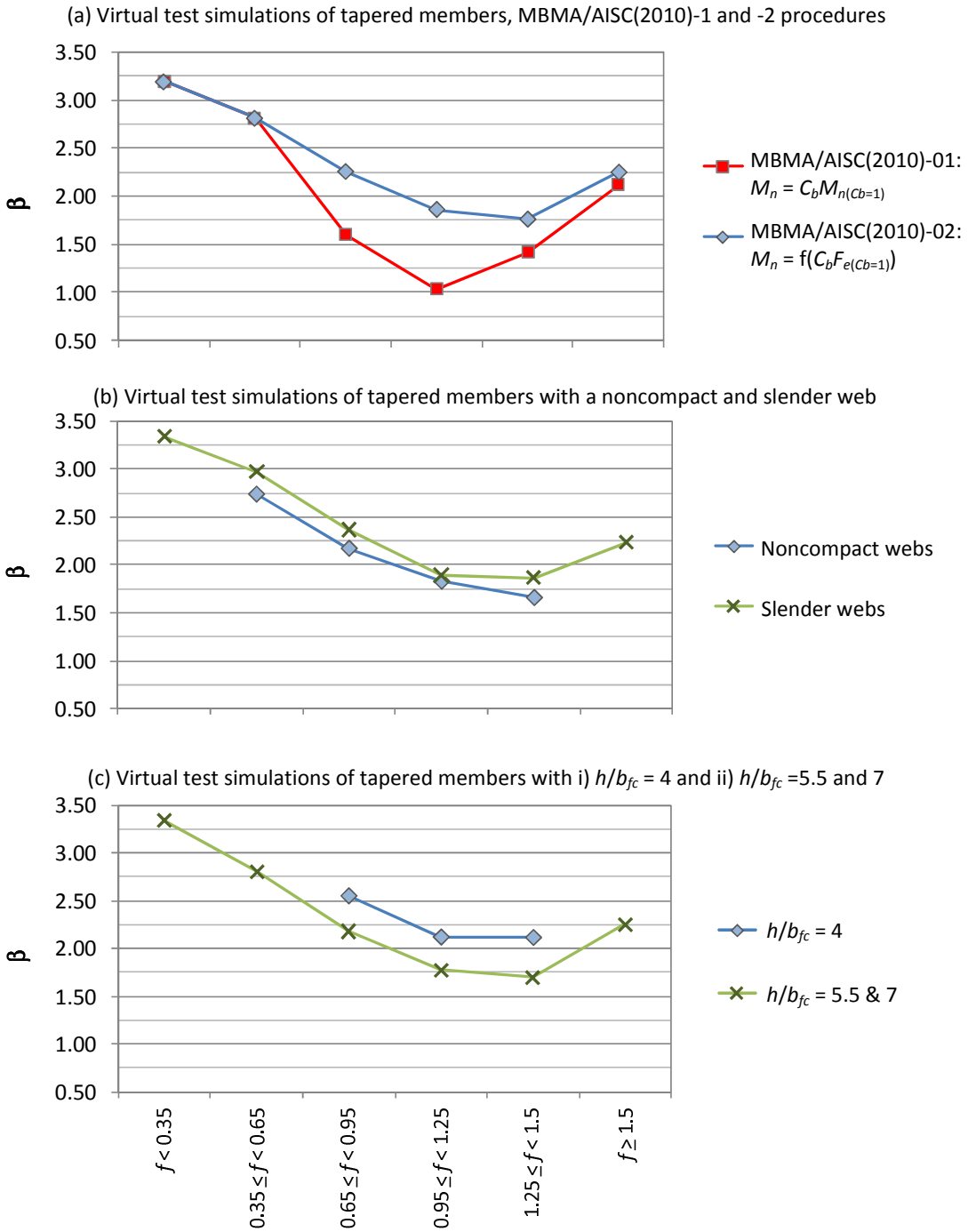

Figure 7.76. Reliability indices for various ranges of $f = (F_y/\gamma_e f_r)^{0.5}$, stress-gradient test simulations, tapered members, MBMA/AISC-2 procedure

with those obtained using the MBMA/AISC (2010)-1 procedure. it can be seen that using the MBMA/AISC (2010)-2 procedure, there is no drastic change in β as seen in Figure 7.75 (a). The smallest β value based on the MBMA/AISC (2010)-2 procedure is 1.55, which is larger than the smallest β based on the MBMA/AISC (2010)-1 procedure (β = 1.04). Figure 7.76 illustrates that the MBMA/AISC (2010)-1 procedure also shows the smallest β values for the test members with a noncompact web or h/b_{fc} = 5.5 and 7 show as seen in Figure 7.75. It should be noted that with the MBMA/AISC (2010)-2 procedure, the transition of the inelastic and elastic LTB resistances is within $1.25 \leq f <$ 1.5. This is because the normalized flange stress term $f = (F_y/\gamma_e f_r)^{0.5}$ is based on $C_b = 1$.

It is important to recognize that the smaller β values (in Figures 7.71, 7.75, and 7.76) are estimated based on the results from virtual test simulations using the single residual stress pattern and the single geometric imperfection described in Chapter 5. If the beams have different residual stresses and/or geometric imperfections, the M_{test}/M_n values and the corresponding β estimates will be different. In the reliability assessment of the experimental test data, it is implicitly assumed that the mean and the dispersion of residual stresses and geometric imperfections in practice are represented within the statistics for M_{test}/M_n from the tests. However, information about actual residual stress patterns and the geometric imperfections in the field (and in many of the tests) is somewhat unknown. In a few significant studies, careful measurements show more optimistic residual stresses and geometric imperfections (Dux and Kitipornchai 1983 and Wong-Chaung and Kitipornchai 1985). In other research (Richter 1998), the test beams are single-side welded (determined by private communication). The residual stresses of the single-side welded members are expected to be smaller than those of the double-side

welded members. Furthermore, it is important to recognize that there are a limited number of experimental tests, which have large h/b_{fc} and a compact or noncompact web. Virtual test simulation results show that the AISC (2010) and MBMA/AISC (2010) LTB calculations give overly optimistic LTB resistances for beams with these characteristics.

Rebelo et al. (2009) also use virtual test simulations based on deterministic residual stress patterns and geometric imperfections for the reliability assessment of the CEN (2005) design procedures in their research. They also recognize that the experimental tests tend to show higher strengths than virtual simulations. However, they explain that they use virtual test simulations for the reliability assessment of the CEN (2005) design provisions because the range of member geometries utilized in experimental tests is limited. Rebelo et al. (2009) select the deterministic residual stress patterns (one for rolled I-section and another for welded I-sections) and geometric imperfection involving a flange sweep and a cross-section twist. It should be recognized that the selected residual stress pattern for welded I-sections in Rebelo et al. (2009) has a constant compressive residual stress at the flange tips, which is pessimistic compared to physical tests. The LTB resistance curves in CEN (2005) generally provide lower bounds for the virtual test simulation results conducted in Rebelo et al. (2009).

It is clearly shown in the above that the results of the reliability assessment are significantly different depending on which set of data is used: the experimental test data or the virtual test simulation results. Both data sets have their limitations. The experimental test data is rather sparse in many of the ranges of the design space while the virtual test simulation results are based on a single residual stress pattern and a single geometric imperfection. These patterns and imperfections are typically less optimistic

than the values measured in physical tests (in the limited cases where detailed measurements have been taken). Therefore they may not provide the best representation of actual residual stresses and geometric imperfections. Therefore, in this research, separate sets of recommendations are proposed for potential improvements of the LTB resistance calculations based on 1) the experimental test data and 2) the virtual test simulation results.

7.3.2 Recommended Resistance Calculations for Lateral Torsional Buckling

Based on the virtual test results and the experimental test data and the corresponding estimates of reliability indices, a number of important issues are observed. Based on these key observations, the recommendations on the resistance calculations of lateral torsional buckling are developed in this research. The key observations from the virtual test results and the experimental test data are as follows:

- Sections 7.1 and 7.2 show that the plateau length of the LTB design curve, L_p or $(F_y/\gamma_e f_r)^{0.5} = 0.35$ is too optimistic for all the virtual test cases considered in this research. The difference in the LTB strength at $(F_y/\gamma_e f_r)^{0.5} = 0.35$ and at $(F_y/\gamma_e f_r)^{0.5} = 0.2$ is larger for members with larger h/b_{fc} and/or a thicker web. Based on the experimental test data, however, it appears that the plateau strength is well developed at $L_b = L_p\,(= 1.1 r_t (E/F_y)^{0.5})$.
- The virtual test simulations illustrate that the combined effect of residual stresses and geometric imperfections is significant at $L_b = L_r$ or $(F_y/F_e)^{0.5} = (F_y/F_L)^{0.5}$ (=1.2 for $F_L = 0.7F_y$). In Section 7.1, the virtual test simulation results at $(F_y/F_e)^{0.5} = 1.2$ and 1.5 are smaller than the elastic LTB resistances based on AISC (2010) and MBMA/AISC (2010). For test members with longer unbraced lengths, $(F_y/F_e)^{0.5} = 1.7$ or 1.75, the

virtual test simulation results are close to the elastic LTB resistances in AISC (2010) and MBMA/AISC (2010). The β of the experimental test data also decreases slightly for welded members with $0.95 \leq f < 1.25$ in Figure 7.70. Figure 7.74 also shows significant reduction in β for both rolled and welded members with $0.95 \leq f < 1.25$. This shows that the value of F_L should be reduced such that the inelastic LTB region in the LTB design curves is extended to account for the combined effect of residual stresses and geometric imperfection for longer beams.

- The AISC (2010) and MBMA/AISC (2010) provisions suggest a linear representation of LTB resistances between the plateau and the inelastic LTB limit ($L_b = L_r$ or $(F_y/F_e)^{0.5} = (F_y/F_L)^{0.5}$). However, in Sections 7.2 and 7.3, the virtual test simulations demonstrate that this linear representation of the inelastic LTB strength is not appropriate for beams with large h/b_{fc} and a compact or noncompact web. It is discussed in Sections 7.2 and 7.3 that the data points from the virtual test simulations show a concave shape within the inelastic LTB region. Based on the experimental test data, however, the linear inelastic LTB design curve seems work well.
- It is found from the virtual test simulations that a cross section with large h/b_{fc} and thicker webs cannot develop its plastic strength even with a very short unbraced length. As shown in Section 7.1, if a cross section has large h/b_{fc} and a thicker web, it has a large shape factor, which mostly comes from the large web area. However, the narrow flanges of this type of cross sections cannot provide enough restraint to the web. As a result, the web is buckled and the compression flange is twisted before the cross section fully develops its plastic strength (see Figure 7.31). Therefore, it is necessary to use a web compactness limit in which the effect of M_p/M_y and the ratio

of a compression web area to a compression flange area is accounted for.

Based on the important observations discussed above, the following recommendations are proposed:

1. Based on the experimental test data:
   a. A new F_L value of 0.6 F_{yc} is recommended to account for the combined effects of residual stresses and geometric imperfections within the longer inelastic LTB region.
   b. It is recommended that the web compactness limit λ_{pw} be calculated as follows:

$$\lambda_{pw} = \frac{h_c / h_p \sqrt{E / F_y}}{\left[0.54\left(M_p / M_y\right) - 0.136\left(b_{fc}t_{fc} / h_p t_w\right)\right]^2} \le \min\left(3.76\sqrt{E / F_y}, \lambda_{rw}\right) \quad \text{(Eq. 7.8)}$$

where $M_y = \min(M_{yc}, M_{yt})$. If $h_p t_w / b_{fc} t_{fc} = 1.5$, this equation becomes the current AISC (2010) equation for λ_{pw} for singly-symmetric cross sections. Equation 7.8 is originally developed by Barth and White (1997), as a web compactness limit to develop M_p. This equation is adopted in AISC (2010) for singly-symmetric cross sections with a simplification where 0.09 is used instead of $0.136(b_{fc}t_{fc}/h_p t_w)$. In this research, the use of Eq. 7.8 is recommended for both doubly and singly-symmetric cross sections.

It is found that by using Eq. 7.8, a thicker web is required to develop M_p for members with large h/b_{fc}. For example, the members with $h/b_{fc} = 7$ and $b_{fc}/2t_{fc} = 6$ need $h/t_w = 50$ to develop M_p. Based on the current AISC (2010), a web with $h/t_w = 85$ is categorized as a compact web (using $F_y = 55$ ksi) regardless of h/b_{fc}. It should be noted that for all the W shapes in AISC Manual, Eq. 7.8 gives λ_{pw} =

$3.76(E/F_y)^{0.5}$ as the current AISC (2010) provisions. Also for most of the welded-member tests collected by White and Jung (2008) and White and Kim (2008), there is no change in the calculated LTB strength due to the use of Eq. 7.8 since most of these tests have a small h/b_{fc} such that $\lambda_{pw} = 3.76(E/F_y)^{0.5}$.

2. Based on virtual test simulations

   a. A shorter plateau length $L_p = 0.63 r_t(E/F_y)^{0.5}$, or $(F_y/F_e)^{0.5} = 0.2$ is recommended. It is clearly demonstrated in Sections 7.1 and 7.2 that the current AISC (2010) plateau length is optimistic based on the virtual test simulation results. This proposed plateau length is the same as the one that CEN (2005) suggests for general types of cross sections.

   b. A new F_L value of $0.4\ F_{yc}$ is recommended to account for the combined effect of residual stresses and geometric imperfections within a longer inelastic LTB region. Based on the experimental test data, $F_L = 0.6\ F_{yc}$ works well. However, the virtual test simulations indicate that the inelastic LTB curve should be extended further. That is, they indicate greater combined residual stress and geometric imperfection effects. Therefore, $F_L = 0.4\ F_{yc}$ is proposed based on the virtual test simulations.

   c. A bi-linear inelastic LTB curve is created by introducing a new intermediate LTB strength point M_m between the plateau strength $R_{pg}R_{pc}M_{yc}$ and $R_{pg}F_LS_{xc}$. The use of a bi-linear inelastic LTB curve accounts for the concave shape of the virtual test simulation results within the inelastic LTB region. The intermediate LTB strength M_m is obtained by

$$M_m = \frac{1}{2} R_{pg}\left(R_{pc}M_{yc} + F_L S_{xc}\right) \times (1 - \alpha)$$

at $L_m = \frac{1}{2}\left(L_p + L_r\right)$ *or* $f_m = \frac{1}{2}\left[0.63/\pi + \sqrt{F_y/F_L}\right]$ (Eq. 7.9a and b)

where

$$\alpha = -0.001\left(\frac{h_c}{t_w}\right) + 0.03\left(\frac{h}{b_{fc}}\right) + 0.08 \geq 0.0 \quad \text{(Eq. 7.10)}$$

For all the virtual tests considered in this research, $F_L = 0.4F_{yc}$ and corresponding $f_m = 0.89$. Therefore, LTB design resistances can be calculated as follows:

$$M_n = R_{pg}R_{pc}M_{yc} \qquad \text{for} \quad \left(F_y/F_e\right)^{0.5} \leq \frac{0.63}{\pi} \quad \text{(Eq. 7.11a)}$$

$$M_n = R_{pg}R_{pc}M_{yc}\left[1 - \left(1 - \frac{M_m}{R_{pg}R_{pc}M_{yc}}\right)\frac{\left(\pi\sqrt{F_y/F_e} - 0.63\right)}{\left(\pi f_m - 0.63\right)}\right]$$

$$\text{for} \quad \frac{0.63}{\pi} < \left(F_y/F_e\right)^{0.5} \leq f_m \quad \text{(Eq. 7.11b)}$$

$$M_n = M_m\left[1 - \left(1 - \frac{R_{pg}F_L S_{xc}}{M_m}\right)\frac{\left(\sqrt{F_y/F_e} - f_m\right)}{\left(\sqrt{F_y/F_L} - f_m\right)}\right]$$

$$\text{for} \quad f_m < \left(F_y/F_e\right)^{0.5} \leq \left(F_y/F_L\right)^{0.5} \quad \text{(Eq. 7.11c)}$$

$$M_n = R_{pg}F_e S_{xc} \qquad \text{for} \quad \left(F_y/F_e\right)^{0.5} > \left(F_y/F_L\right)^{0.5} \quad \text{(Eq. 7.11d)}$$

d. It is recommended to calculate a web compactness limit λ_{pw} using Eq. 7.8. As mentioned above, Eq. 7.8 provides significant improvements in the resulting plateau strengths especially for beams with a large h/b_{fc} and a thicker web. The improved plateau strengths correlate well with the virtual test simulation results.

Figure 7.77 shows the virtual test simulation results and the suggested resistance curve for the test case with $h/b_{fc} = 2$, $b_{fc}/2t_{fc} = 6$, and $h/t_w = 40$. For this case, α is 0.1 from Eq. 7.10 and $\lambda_{pw} = 3.76(E/F_y)^{0.5} = 86.34$ using $E = 29000$ ksi and $F_y = 55$ ksi. The recommended resistance curve provides essentially the same LTB strengths compared to the virtual test simulation results obtained using the best-fit Prawel residual stress pattern shown in Chapter 5. The LTB strengths obtained from the virtual test simulations using the Lehigh residual stress pattern are slightly smaller than the recommended design curve for $(F_y/\gamma_\epsilon f_r)^{0.5} \geq 1.2$.

Figure 7.78 shows the suggested resistance curve for the test case with $h/b_{fc} = 7$, $b_{fc}/2t_{fc} = 6$, and $h/t_w = 85$ as well as the virtual test simulation results and the current resistance curves of AISC (2010), MBMA/AISC (2010), and CEN (2005). It should be noted that the plateau strength of the recommended design curve is 1.16, which is close to the virtual test simulation strength at $(F_y/\gamma_\epsilon f_r)^{0.5} = 0.2$. Based on Eq. 7.8, the web slenderness of these beams are noncompact so that R_{pc} is less than M_p/M_{yc}. Furthermore, this case has $\alpha = 0.21$, which is the largest α obtained from all the cases considered in this research for virtual test simulation. Figure 7.78 illustrates that the recommended design curve provide close to or slightly larger LTB strengths than the virtual test simulations of both prismatic and tapered members.

Figure 7.79 illustrates the recommended resistance curve for the test case with noncompact flanges and a noncompact web ($h/b_{fc} = 2$, $b_{fc}/2t_{fc} = 12$, and $h/t_w = 130$). For this case, α is 0.01, which results in approximately a linear elastic LTB curve between $(F_y/\gamma_\epsilon f_r)^{0.5} = 0.2$ to $(F_y/\gamma_\epsilon f_r)^{0.5} = (F_y/F_L)^{0.5} = 1.58$. It can be seen in Figure 7.79 that the recommended resistance curve matches the analysis results of virtual test simulations very well.

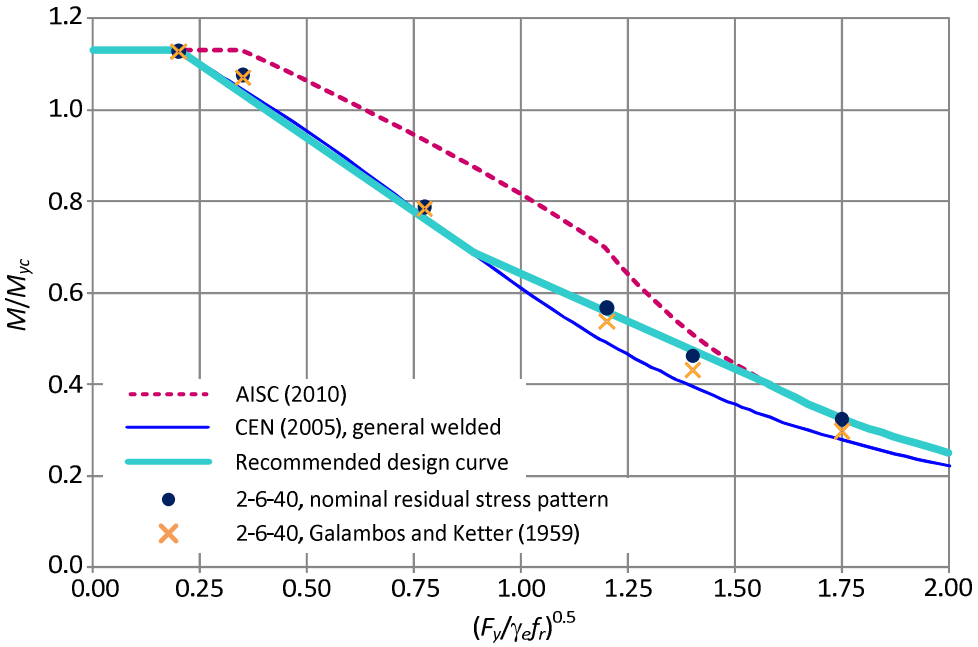

Figure 7.77. Recommended resistance curve for $h/b_{fc} = 2$, $b_{fc}/2t_{fc} = 6$, and $h/t_w = 40$.

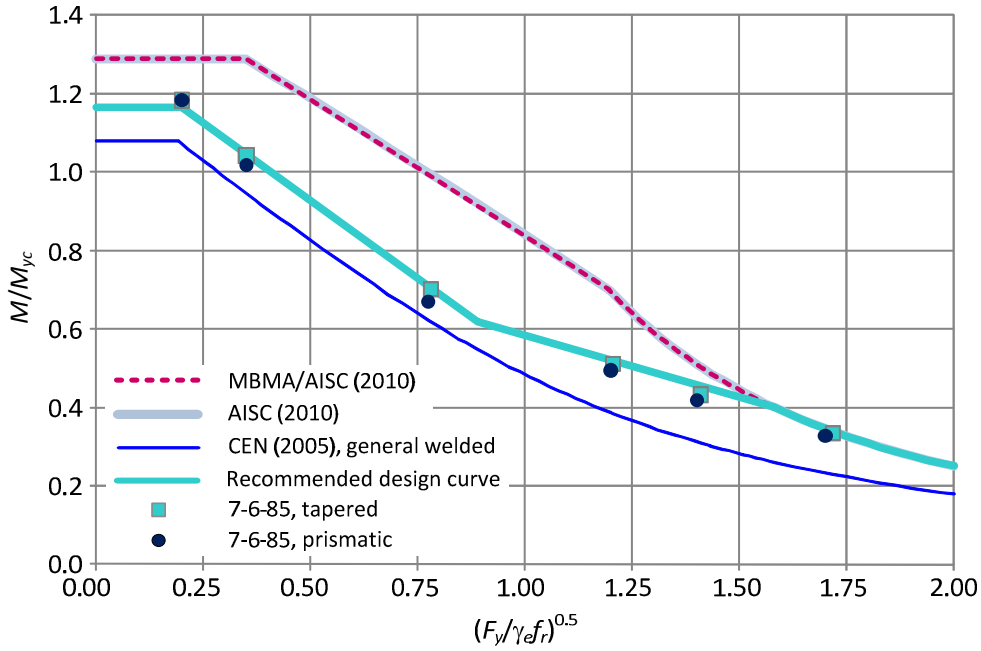

Figure 7.78. Recommended resistance curve for $h/b_{fc} = 7$, $b_{fc}/2t_{fc} = 6$, and $h/t_w = 85$.

Figure 7.80 shows the recommended resistance curve for the test beams with h/b_{fc} = 7, $b_{fc}/2t_{fc}$ = 6, and h/t_w = 180. From Eq. 7.10, α is 0.11 for this case. The recommended resistance curve provide slightly smaller LTB strengths compared to the virtual test simulation results for the test members with h/t_w = 180 in general.

It should be noted that Figures 7.77 to 7.80 show the bi-linear representation of the inelastic LTB strengths provides good estimations of the virtual test simulation results. For test beams with large h/b_{fc} and small h/t_w, the bi-linear LTB curve for $0.2 \leq (F_y/\gamma_e f_r)^{0.5} \leq 1.58$ shows a deep "v" shape. Also the theoretical elastic LTB curve works well for beams with longer lengths, $(F_y/\gamma_e f_r)^{0.5} \geq 1.7$.

Figure 7.81 shows the reliability indices for the experimental test data obtained by White and Jung (2008) using the recommendations discussed above: 1) the use of F_L = $0.6F_y$ and 2) the calculation of λ_{pw} using Eq. 7.8. It can be seen that the reliability indices are improved especially for $0.65 \leq f \leq 1.25$.

Figure 7.82 shows the reliability index estimations of the virtual test simulations under the uniform-stress loadings based on the recommended resistance calculations. It should be noted that the web slenderness groups shown in Figure 7.82 (b) are based on the current AISC (2010) provisions ($\lambda_{pw} = 3.76\ (E/F_y)^{0.5}$). Compared to Figure 7.71, the recommended resistance calculations provide more constant reliability indices for all the ranges of $f = (F_y/\gamma_e f_r)^{0.5}$. Furthermore, the reliability index values are significantly improved especially for $0.65 \leq f \leq 1.25$.

Figure 7.82 illustrates that the reliability index values decreases for larger f = $(F_y/\gamma_e f_r)^{0.5}$. This can be explained as follows. The virtual test simulations are conducted using a single geometric imperfection, which is a compression flange sweep of $L_b/1000$.

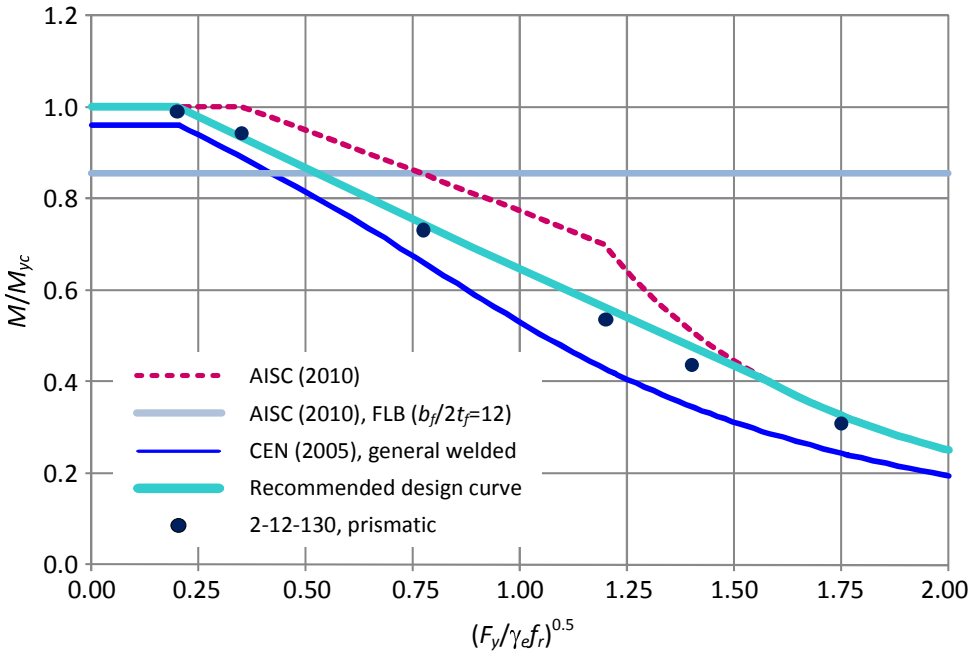

Figure 7.79. Recommended resistance curve for $h/b_{fc} = 2.0$, $b_{fc}/2t_{fc} = 12$, and $h/t_w = 130$.

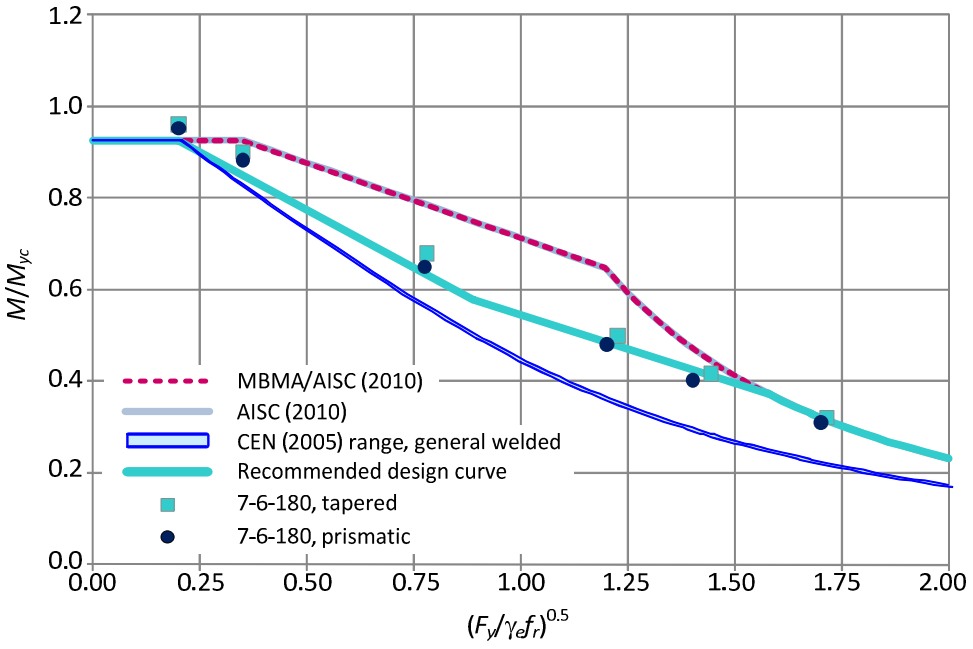

Figure 7.80. Recommended resistance curve for $h/b_{fc} = 7.0$, $b_{fc}/2t_{fc} = 6$, and $h/t_w = 180$.

Therefore, the magnitude of imperfection is proportional to the unbraced length of a given beam, i.e., longer beams have a larger geometric imperfection in the compression flange. This causes smaller β as unbraced lengths increases, i.e., the value of $f = (F_y/\gamma_e f_r)^{0.5}$ increases. It should be noted in Figures 7.82(b) and (c) that the proposed recommendations significantly reduce the differences in the reliability indices for different web slenderness groups or different h/b_{fc} groups.

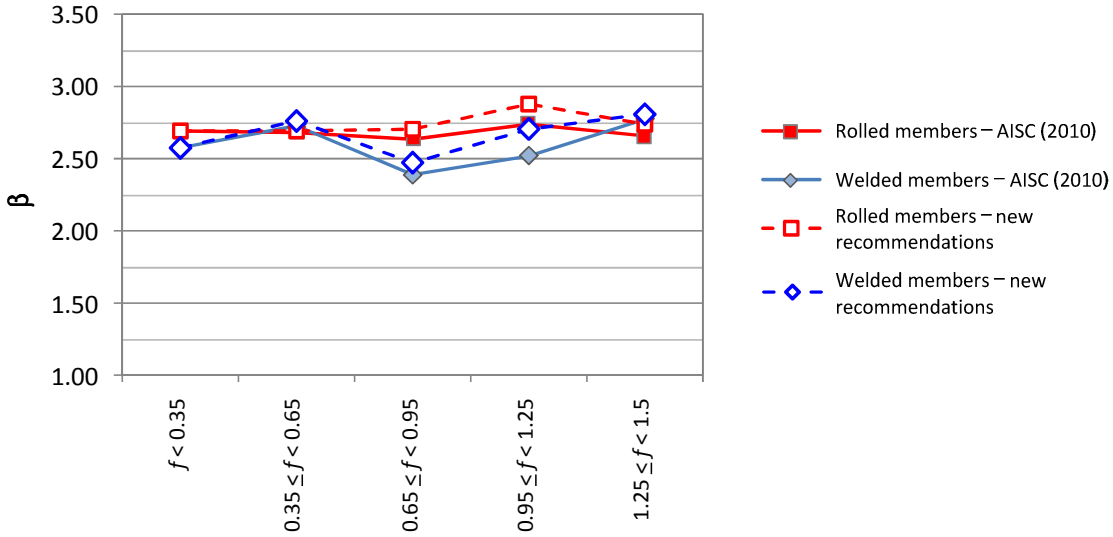

Figure 7.81. Reliability indices for various ranges of $f = (F_y/\gamma_e f_r)^{0.5}$, based on recommended resistance calculations, uniform-bending test data collected by White and Jung (2008).

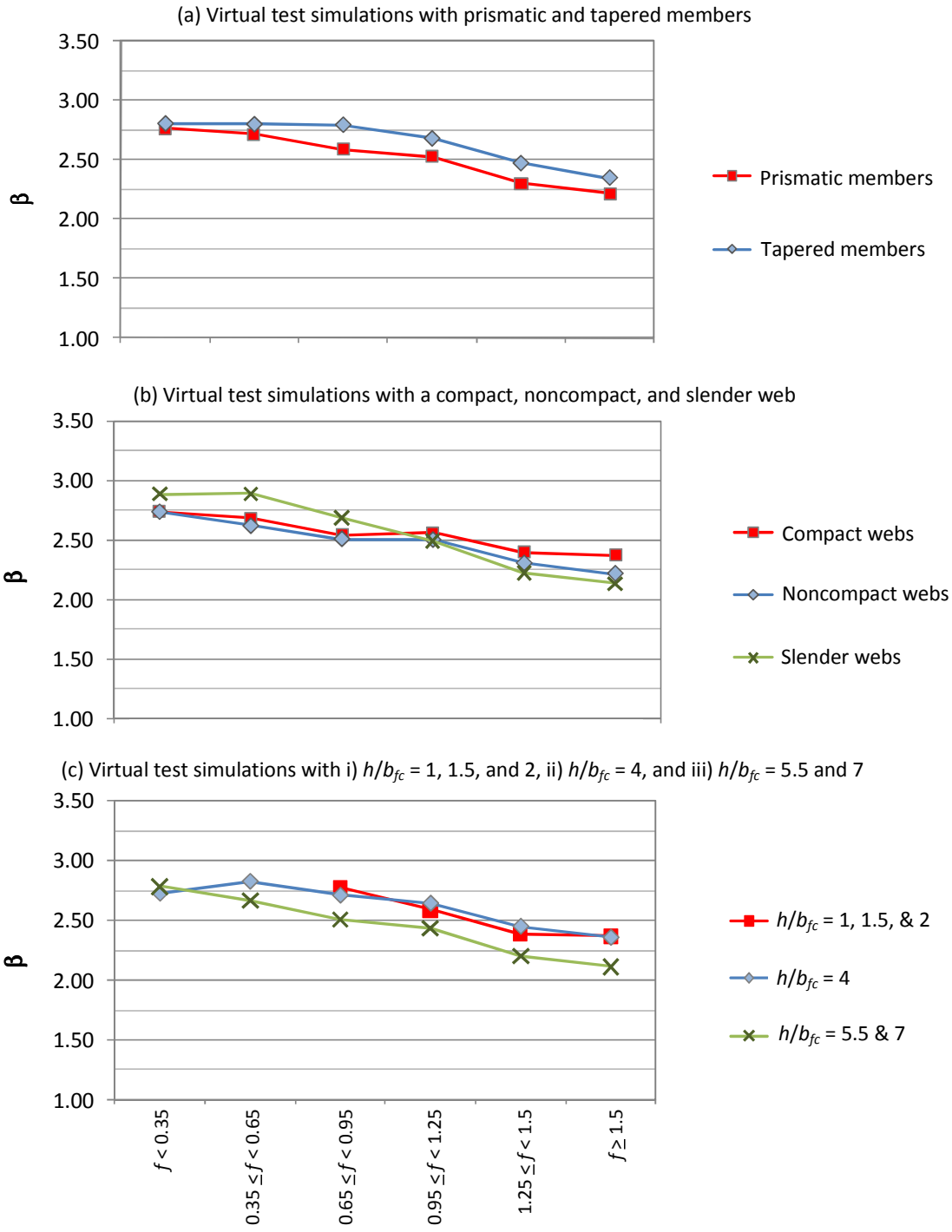

Figure 7.82. Reliability indices for various ranges of $f = (F_y/\gamma_e f_r)^{0.5}$, based on recommended resistance calculations and uniform-stress test simulations.

Figures 7.83 to 7.86 illustrate the recommended LTB resistance curves for moment-gradient or stress-gradient cases. In each figure, two recommended design curves are shown. The recommended design curve 1 is obtained using the AISC (2010) procedure (or the MBMA/AISC(2010)-1 procedure), $M_n = C_b M_{n(Cb=1)}$ with new recommendations discussed above. The recommended design curve 2 is obtained using the MBMA/AISC(2010)-2 procedure, $M_n = f(C_b F_{e(Cb=1)})$. It should be noted that it is proposed to use the MBMA/AISC (2010)-2 procedure not only for tapered members but also for prismatic members.

Figure 7.83 shows that the recommended design curve 1 provides better estimates for the virtual test simulations results than the recommended design curve 1 for beams with $h/b_{fc} = 2$, $b_{fc}/2t_{fc} = 6$, and $h/t_w = 40$. It is found that the LTB design strengths calculated using the proposed recommendations on LTB resistance calculations combined with $M_n = C_b M_{n(Cb=1)}$ correlate well with the virtual test simulation results for beams with $h/b_{fc} = 1$, 1.5, and 2 and $h/t_w = 40$. Interestingly, the recommended design curve 2 shown in Figure 7.82 is really close to the CEN (2005) design curve.

Converse to what is shown in Figure 7.83, Figure 7.84 shows that the recommended design curve 2 provides accurate to slightly conservative estimates of LTB strengths compared to the virtual test simulations for beams with large $h/b_{fc} = 7$ and $h/t_w = 100$. The same conclusion can be made for beams with $h/b_{fc} = 5.5$ and $h/t_w = 100$. For these beams, the recommended design curve 1 gives overly optimistic resistances as shown in Figure 7.84.

Figure 7.85 shows that the virtual test simulation results for beams with $h/b_{fc} = 2$, $b_{fc}/2t_{fc} = 12$, and $h/t_w = 130$ are in between the two recommended curves. The recommended design curve 1 is overly optimistic, while the recommended curve 2 is

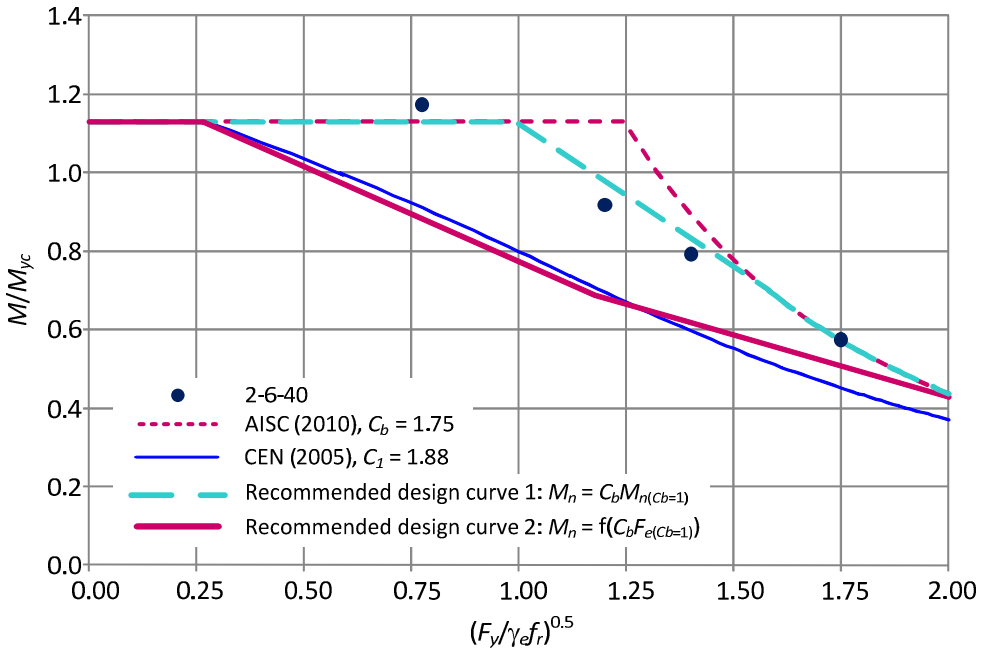

Figure 7.83. Recommended resistance curves for $h/b_{fc} = 2$, $b_{fc}/2t_{fc} = 6$, and $h/t_w = 40$ under moment gradient ($C_b = 1.75$).

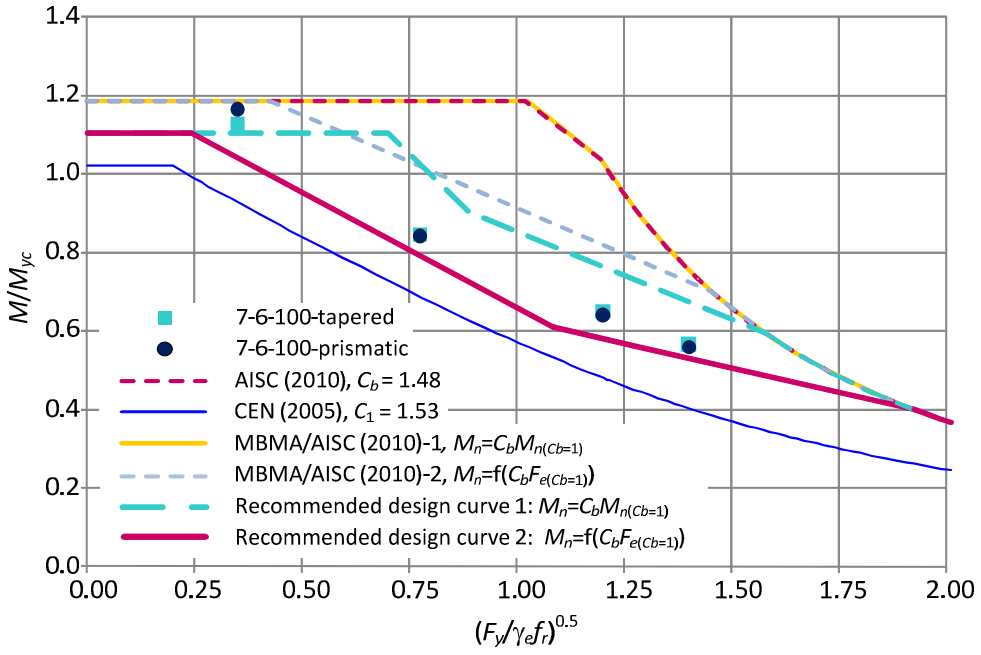

Figure 7.84. Recommended resistance curves for $h/b_{fc} = 7.0$, $b_{fc}/2t_{fc} = 6$, and $h/t_w = 100$ under stress-gradient or moment-gradient conditions ($C_b = 1.48$).

significantly conservative compared to the virtual test simulations. The two recommended curves give the same estimates for longer beams with $(F_y/\gamma_e f_r)^{0.5} \geq 2.0$. Figure 7.86 also demonstrates that the virtual test simulation results for beams with h/b_{fc} = 7, $b_{fc}/2t_{fc}$ = 6, and h/t_w = 180 are in between the two recommended curves. The differences in the LTB resistances suggested by the two recommended curves are smaller in Figure 7.86 than those are shown in Figures 7.83 to 7.85. It should be noted that the moment gradient factor C_b for the case shown in Figure 7.86 (C_b = 1.20) is smaller than C_b for other cases shown in Figures 7.83 to 7.85 (C_b = 1.75 and 1.48). In Figure 7.86, the recommended design curve 1 provides slightly unconservative resistances compared to the virtual test simulations. The LTB resistances based on the recommended design curve 2 are slightly conservative for test beams with $(F_y/F_e)^{0.5} < 1.2$.

Based on the limited test cases with h/b_{fc} = 1, 1.5, and 2 considered in this study, it appears that the recommended design curve 1 works well for the test beams with rolled-section type cross-sections. For these cases, the recommended design curve 2 is significantly conservative. This explains the good correlations of the design checks based on the MBMA/AISC (2010)-1 procedure with the experimental tests conducted by Salter et al. (1980) and Shiomi and Kurata (1984) (see Chapter 6). All the tapered beam-columns tested by Salter et al. (1980) and Shiomi and Kurata (1984) are rolled sections.

However, even with h/b_{fc} = 2, if the web is noncompact, the predictions based on the recommended design curve 1 are overly unconservative especially for beams with $(F_y/F_e)^{0.5}$ = 0.775 (see Figure 7.85). One should recognize that if the moment-gradient effect is smaller, i.e., $C_b < 1.75$, the predictions based on the two recommended design curves would be closer to the virtual test simulation results than those shown in Figure 7.85.

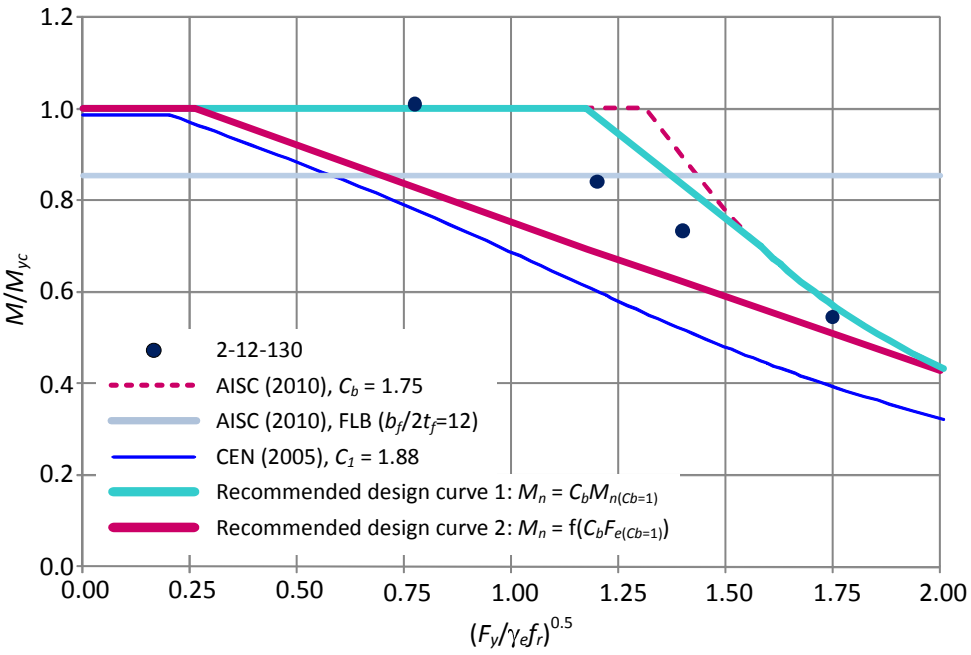

Figure 7.85. Recommended resistance curve for $h/b_{fc} = 2$, $b_{fc}/2t_{fc} = 12$, and $h/t_w = 130$ under moment gradient ($C_b = 1.75$).

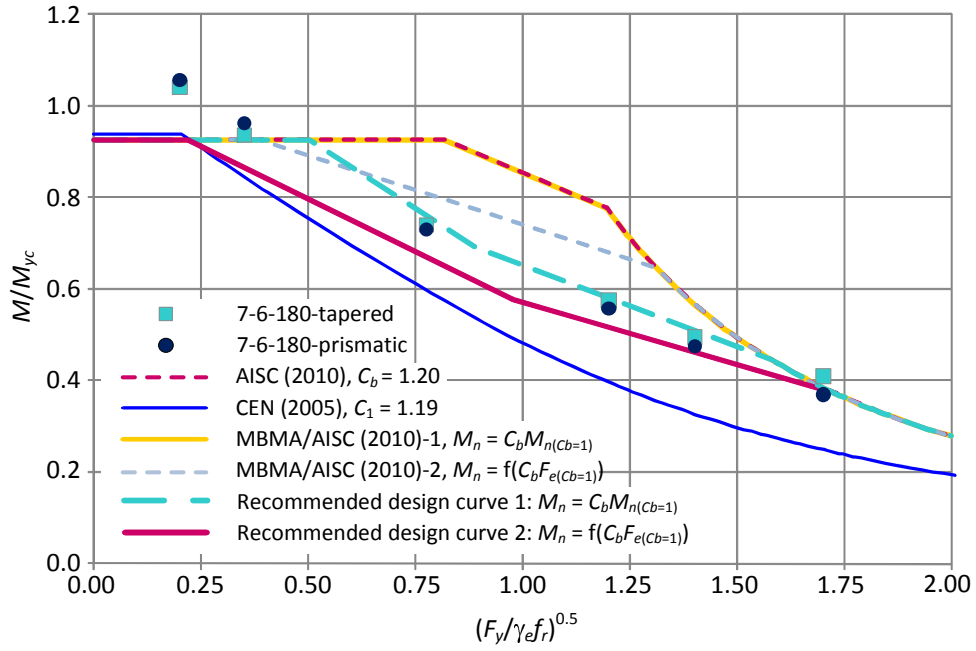

Figure 7.86. Recommended resistance curve for $h/b_{fc} = 7$, $b_{fc}/2t_{fc} = 6$, and $h/t_w = 180$ under stress-gradient or moment-gradient conditions ($C_b = 1.20$).

For beams with large h/b_{fc} and a thicker web, the recommended design curve 2 seems provide better predictions compared to the virtual test simulations (see Figure 7.84). The recommended design curve 2 correlates with the virtual test simulation results better for beams with larger h/b_{fc} and large α, where α is calculated based on Eq. 7.10. For these cases, the recommended design curve 1 is significantly unconservative as seen in Figure 7.84. For beams with larger h/b_{fc} and small α (e.g., test beams shown in Figure 7.86), the two recommended design curves give similar predictions.

Figure 7.87 shows reliability indices for moment-gradient test data obtained from White and Kim (2008) and Righman (2005) using the MBMA/AISC-2 procedure as well as the recommendations on the LTB strength calculations discussed above ($F_L = 0.6F_y$ and λ_{pw} calculated by Eq. 7.8). In Figure 7.87, the reliability indices estimated using the current AISC procedure are also shown. It can be seen that by using the MBMA/AISC-2 procedure the reliability indices for $0.65 \leq f \leq 1.25$ are improved significantly for both rolled and welded members. As a result, overall consistency of the reliability indices is improved for welded members.

Figure 7.88 shows the reliability index estimations of the stress-gradient virtual tests based on the recommended resistance calculations and the MBMA/AISC (2010)-1 procedure. It can be seen that the MBMA/AISC (2010)-1 procedure provides consistent but smaller β for $f \geq 0.65$. The range of β for these cases is from 2.08 to 2.30. However, for $f < 0.65$, β ranges from 3.02 to 3.23. Figures 7.88 (b) and (c) show that beams with a noncompact web and $h/b_{fc} = 5.5$ and 7 provide smaller β. As in Figure 7.81, the web slenderness groups in Figure 7.88 (b) are based on the current AISC (2010) provisions ($\lambda_{pw} = 3.76\ (E/F_y)^{0.5}$).

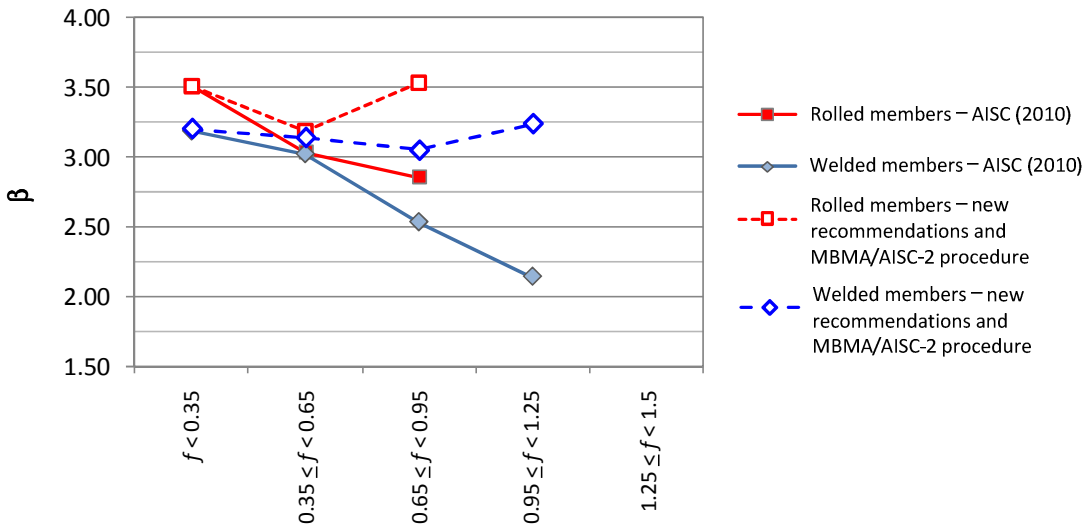

Figure 7.87. Reliability indices for various ranges of $f = (F_y/\gamma_e f_r)^{0.5}$, based on recommended resistance calculations and MBMA/AISC-2 procedure, moment-gradient test data obtained from White and Kim (2008) and Righman (2005).

Figure 7.89 shows the reliability index estimations of the virtual tests under stress-gradient conditions using the recommended LTB resistance calculations and the MBMA/AISC (2010)-2 procedure. By using the MBMA/AISC (2010)-2 procedure, the reliability index values gradually decrease from $f < 0.35$ to $1.25 \leq f < 1.5$. For these cases, the range of β is from 2.81 to 3.32. The reliability index values for beams with $f \geq 1.5$ are 2.26 for prismatic members and 2.32 for tapered members. Figures 7.89 (b) and (c) illustrates that the MBMA/AISC (2010)-2 procedure provides smaller differences in the reliability indices for beams with different h/t_w or different h/b_{fc} groups.

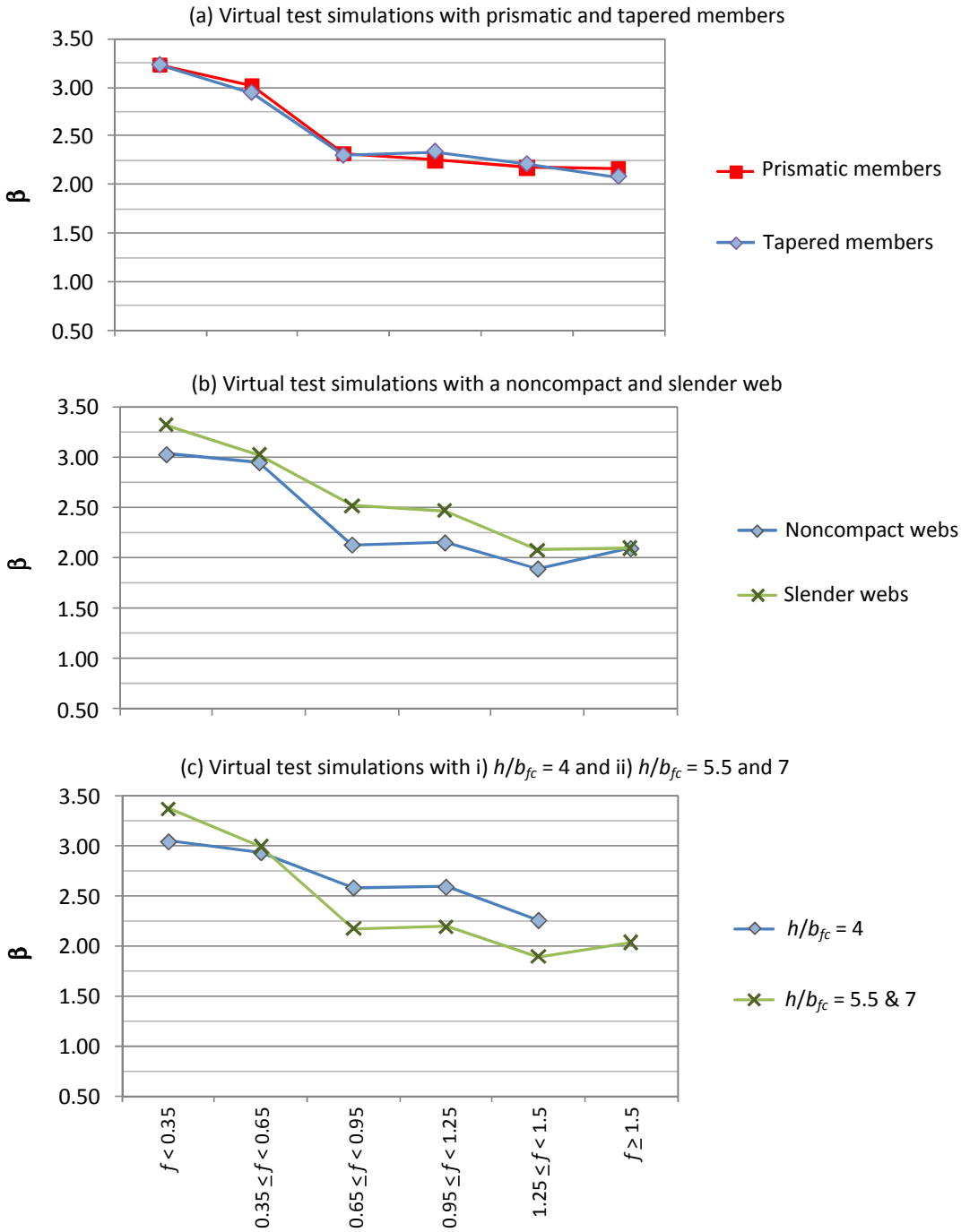

Figure 7.88. Reliability indices for various ranges of $f = (F_y/\gamma_e f_r)^{0.5}$, based on the recommended resistance calculations and the MBMA/AISC (2010)-1 procedure, virtual test simulation under stress-gradient conditions.

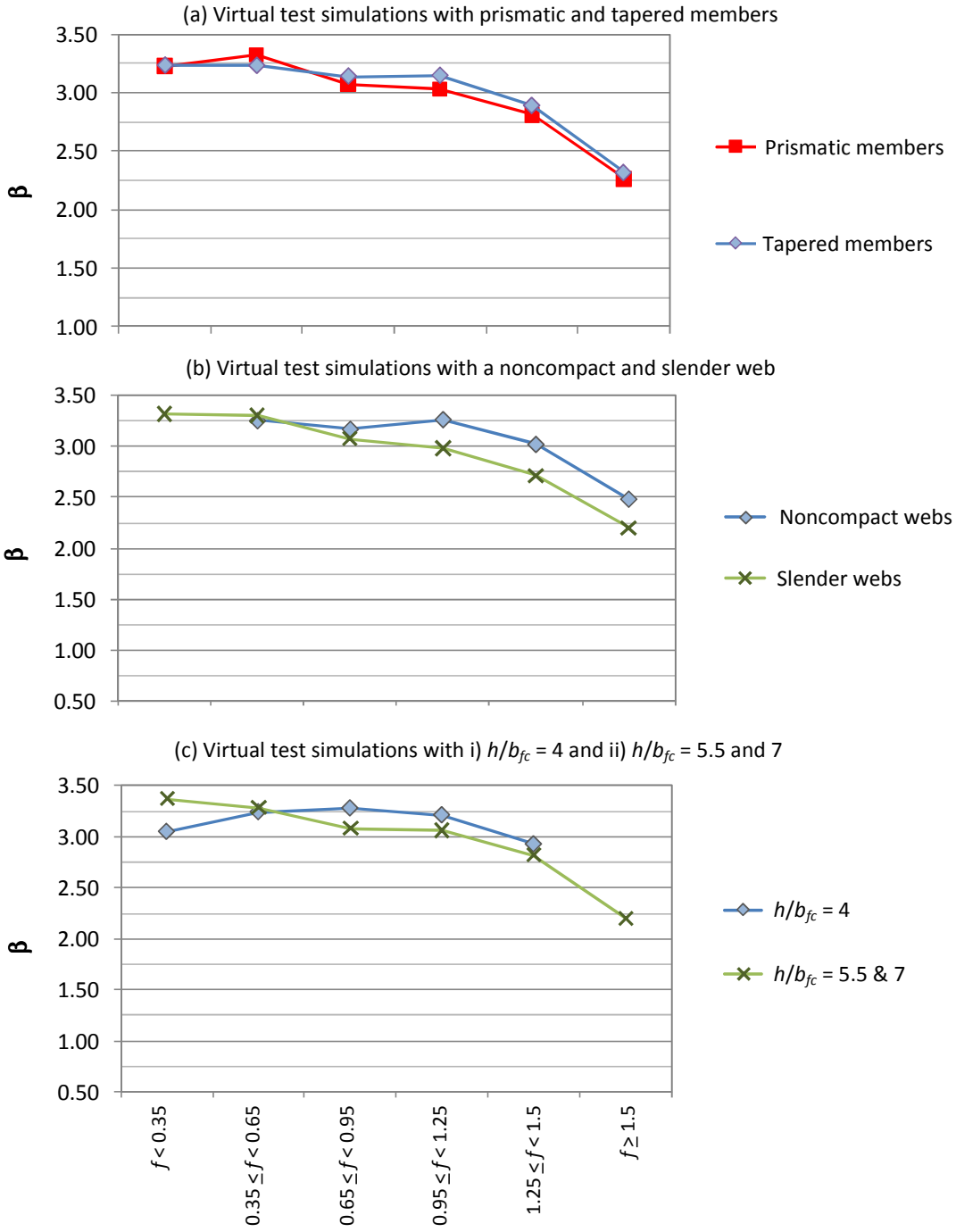

Figure 7.89. Reliability indices for various ranges of $f = (F_y/\gamma_e f_r)^{0.5}$, based on the recommended resistance calculations and the MBMA/AISC (2010)-2 procedure, virtual test simulation under stress-gradient conditions.

CHAPTER VIII

EVALUATION OF FRAMING SYSTEMS BY FINITE ELEMENT VIRTUAL TEST SIMULATION

In this chapter, two representative example metal building frames (one single- or clear-span frame and one modular frame) are evaluated by 1) the stability analysis and design approaches discussed above and adopted in MBMA/AISC (2010) and 2) the 3D full nonlinear virtual test simulations using the four-node shell elements in ABAQUS. The selected frames have the following general characteristics:

1. Single-span frame
    - 90 ft span
    - 19 ft eave height
    - ½:12 roof slope
    - 25 ft frame spacing
    - 300 ft building length
2. Modular frame
    - 6 interior bays, each with a 50 ft span
    - 19 ft eave height
    - ½:12 roof slope
    - 25 ft frame spacing
    - 300 ft building length
    - All the interior columns are simply-connected gravity (leaner) columns

Both frames are symmetric about their ridge line and have simple base conditions. The steel minimum yield strength is taken as F_y = 55 ksi and the elastic modulus is taken as E = 29,000 ksi throughout all the studies (with the exception of the interior pipe columns in the modular frame, for which F_y = 36 ksi). The span-to-eave height of the single-span frame is selected as a relatively large value (4.74). This in turn generates a relatively large axial thrust in the rafters. Also, the ½:12 roof slope is a practical minimum below which many designers would consider the two rafters in the single-span frame as a single member spanning between the exterior columns. In this study, the rafters in the single-span frame are considered as two separate members with a length equal to the distance from the knee to the ridge. The reader should note that this is a relatively minor consideration when the direct analysis method is employed, since the in-plane column resistance term is calculated simply as $P_{ni} = QP_y$. The modular frame has a vertical column located at its ridge as well as several other intermediate columns, and thus each span of the rafters is considered as a separate member.

The single-span frame is representative of typical clear-span designs in that the overall second-order effects under 1.6 of the ASD load combinations are rather small. This is consistent with the findings by Guo and Roddis (1999) for various clear-span frame geometries and loadings. AISC (2010) requires that the ASD loads must be increased by α = 1.6, to capture the proper second-order effects, followed by dividing the resulting internal forces and moments by α = 1.6 prior to making the resistance checks[1]. However, due to the influence of axial compression in the rafters, the appropriate calculation of K factors (or the elastic buckling load ratio γ_{ex}) for the columns and the

[1] Guo and Roddis (1999) conducted their second-order analysis studies at the working load level, i.e., at α = 1. However, their conclusions are also applicable at α = 1.6.

rafters requires special attention in applying the effective length method to the single-span frame.

The above modular frame characteristics are representative of metal building designs in which significant overall sidesway *P*-Δ effects are expected. However, due to the vertical support provided to the rafters by the interior gravity (leaner) columns, the gravity load moments in the exterior columns, and the corresponding thrusts generated in the rafters, are substantially reduced in this type of structure.

The above example frames were designed for conditions in Reading, California using ASCE 7-05 (ASCE 2005). The detailed design of the frames was conducted by Mr. Duane Becker of Chief Buildings, using first-order elastic analysis with the ASD load combinations in ASCE 7-05 and an extension of the AISC (1989) ASD provisions. The following subsections present the specific frame geometries followed by summaries of the first-order and second-order analysis results conducted using GT-Sabre and the analysis-design checks obtained using the second-order elastic analysis results and the prototype AISC (2010) based procedures. The design check results for the lateral load resisting columns and the results at several key locations or segments along the rafters are presented for each of the frames. In addition, the results from the 3D full nonlinear virtual test simulations are discussed.

The ASD load combinations considered in the analyses are as follows:

- Load Case 1 (LC1): Dead + Collateral + Uniform Snow
- Load Case 2 (LC2): Dead + Collateral + 0.75(Snow + Wind)
- Load Case 3 (LC3): Dead + Collateral + Unbalanced Snow

Also, several cases of the load combination

- Load Case 4 (LC4): Dead + Collateral + Patterned Snow

are addressed for the modular frame at locations where these cases give the largest unity checks. In the 3D full nonlinear analysis, only the Load Case 1 is considered. The following are the basic loading parameters and magnitudes for both of the frames:

- Dead load: 1.96 psf (single-span frame) and 1.95 psf (modular frame) plus the self weight of the frame members
- Collateral: 3.0 psf
- Live load: 12.0 psf
- Wind load:
  - Basic wind speed: 85 mph
  - Exposure category: C (q = 14.15 psf)
- Snow load:
  - Ground snow load: 30 psf
  - Exposure factor C_e: 1.0
  - Thermal factor C_t: 1.0
  - Importance factor I: 1.0
  - $p_f = p_s$ = 21 psf

As mentioned above, the first-order and second-order elastic analysis solutions in this chapter are conducted for the above design loadings using GT-Sabre (Chang 2006) . The second-order elastic analysis solutions are conducted using three different models:

1) Nominal perfectly straight and plumb geometry, nominal elastic stiffness.
2) AISC (2010) effective length procedure (same as (1) but with a minimum lateral load of $N_i = 0.002Y_i$ at each "level" of the frame under gravity-only load combinations). Since the example frames are non-rectangular, a separate notional load, equal to 0.002 of the column axial force, is applied at the top of each of the column members.

3) AISC (2010) direct analysis procedure (using 0.8 of the nominal elastic stiffness and a nominal out-of-plumb geometry of 0.002*H*, where *H* is the height above the base of the frame). Neither of the example frames have member axial forces large enough to require the modeling of member out-of-straightness or the use of τ_b less than one.

The planar frame elements in GT-Sabre are capable of representing general nonprismatic member geometries. However, the GT-Sabre capabilities for representing member distributed loading are limited. The design loadings are applied as distributed loads in the original linear elastic analysis and design by Chief Buildings. In GT-Sabre, nodes of the analysis model are placed at the purlin and girt locations, at cross-section transitions and at the mid-length between the girts. Concentrated loads are applied at each node based on the corresponding tributary lengths. The member lengths and the girt and purlin spacings are generally such that the difference between these two representations is quite small.

The 3D full nonlinear virtual test simulations for the example frames are conducted using ABAQUS. The basic procedures of these virtual test simulations are essentially same as described in Chapter 5 except the geometric imperfections. All the segments in the framing systems are modeled with a four-node shell element except the interior leaner columns in the modular frame. The idealized pinned base conditions are applied to the columns. All the purlin and girt locations and the diagonal bracing locations are modeled as an idealized rigid bracing by restraining the out-of-plane displacements. The best-fit Prawel residual stress pattern shown in Section 5.3 is applied in the example frame models. To generate geometric imperfection shapes, the following steps are employed.

(1) An eigenvalue buckling analysis is conducted with the given loadings.

(2) From the analysis results from (1), the eigenvalue buckling modes, which show the deformations in the critical segments identified in the design check calculations, are selected.

(3) The geometric imperfection is obtained by combining the eigenvalue buckling modes selected in Step (2) with a maximum imperfection magnitude of $L_b/1000$.

8.1 Clear Span Frame

8.1.1 Overview

Figure 8.1 shows an elevation view of the single-span frame. Table 8.1 summarizes the specific web and flange geometries for the five member lengths in this structure, including the panel at the knee of the frame. This frame uses a singly-symmetric tapered section for its columns. The column web is nominally 7/32 in thick and the total column depth tapers from d = 10 in. at the base to d = 40.75 in at the bottom of the knee joint. This gives a web slenderness ranging from h/t_w = 42 at the column base to 182 at the knee. The outside flange of the columns is 6 x 3/8 in ($b_f/2t_f$ = 8) while the inside flange is 6 x 1/2 in ($b_f/2t_f$ = 6). Both of these slenderness values satisfy the AISC (2010) compactness criteria for flange local buckling. The rafters have doubly-symmetric cross-sections with 6 in x 3/8 in top and bottom flanges ($b_f/2t_f$ = 8) along their entire length. Also, these members have two linear tapers between the knee and the ridge, with the first taper ranging from d = 40.75 in at the knee to d = 23 in at 20 ft inside of the knee, and the second taper ranging from d = 23 in to 24.75 in at the ridge. The web of the rafter is 1/4 in thick in the 10 ft length next to the knee (length C in Figure 8.1), 3/16 in thick in the next 10 ft length (length D), and 5/32 in thick in the remainder of the rafter

span (length E). These dimensions result in a range of h/t_w from 119 to 166 in the rafters. Based on the above proportions, the member webs are classified as slender both under flexure and under compression in every unbraced segment of the single-span frame, with the exception of the unbraced length (c1-c2) at the bottom of the column, which is classified as noncompact under flexure.

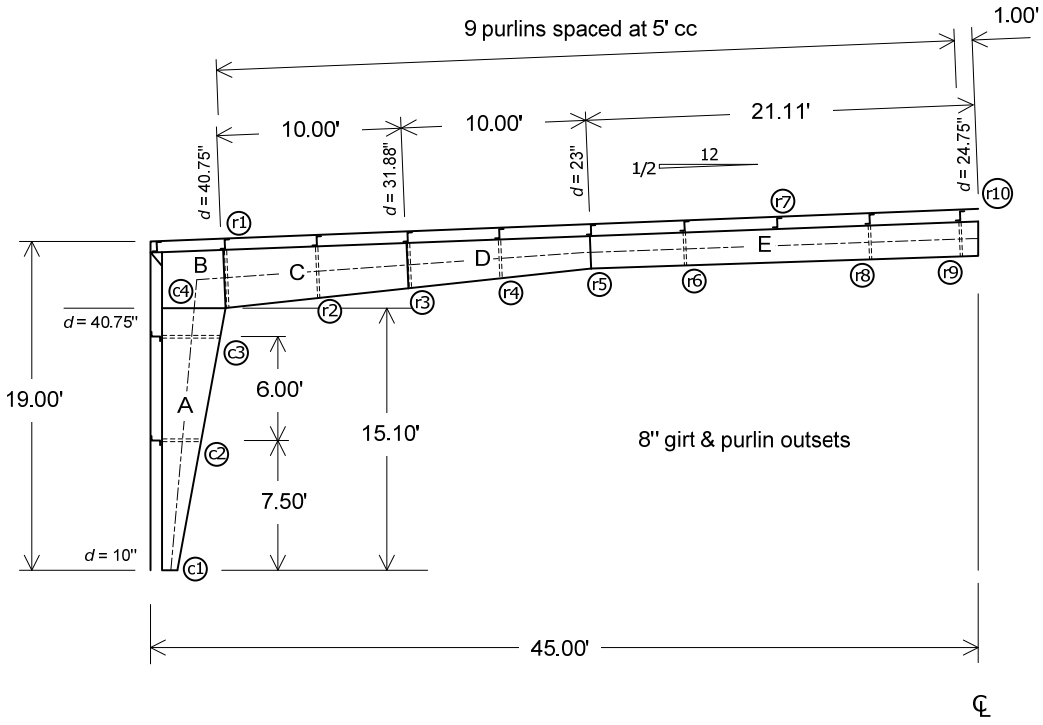

Figure 8.1. Elevation view of single-span frame.

The outside flanges of the columns and rafters are supported laterally by the girts or purlins. Diagonal braces to the inside flanges are indicated by double dashed lines in Figure 8.1. The purlins are spaced at 5 ft on center except at the knee of the frame, and the girts are located at 7.5 and 6 ft spacings starting from the base of the frame. Both of the column flanges are braced laterally at the above girt locations. The bottom flange of

the rafters is unsupported at the purlin locations 20 ft and 30 ft from the inside of the knee, but otherwise both flanges are braced at each purlin location. The bottom of the knee panels is taken as a brace point for the columns. The brace points and the section transitions in Figure 8.1 are sufficiently close to one another such that the section transitions are assumed to be located at the brace points without any loss in accuracy.

The finite element model of the single-span frame is created based on the straight reference axes for the columns and the rafters. The reference axis for the columns is determined by connecting the centroid of the cross-section at c1 and c4. The reference axis for the rater is determined by a straight line with a 0.5/12 slope, which connects from the centroid of the cross section at r1 to a reference point at r10. It is confirmed that the analysis results using this reference axis are essentially same as the analysis results using the centroidal axis for the example frames.

Results from each of the load combinations for the maximum bending moment and axial force in the leeward column, and for the maximum positive and negative bending moments and the corresponding axial force in the rafters, are presented in the following section. This is followed by a presentation of the analysis and design assessments by the effective length and direct analysis methods for the columns, for the critical rafter segment in negative bending (segment r1-r2), and for the critical rafter segment in positive bending (segment r8-r9). These member lengths have the following attributes:

- The columns have a singly-symmetric cross-section with a larger inside flange, a relatively large web taper and equal unbraced lengths for both flanges.

- Segment r1-r2 has a doubly-symmetric cross-section, a relatively large web taper, and equal unbraced lengths for both flanges.
- Segment r8-r9 has a doubly-symmetric cross-section, a relatively small web taper, and equal unbraced lengths for both flanges.

Table 8.1. Summary of web and flange geometry, single-span frame.

Length	Location	Web				Inside Flange			Outside Flange		
		d (in)	t_w (in)	h/t_w	h_c/t_w	b_f (in)	t_f (in)	$b_f/2t_f$	b_f (in)	t_f (in)	$b_f/2t_f$
A	c1	10.00	7/32	42	36	6.0	1/2	6.0	6.0	3/8	8.0
	c2	25.27		112	103						
	c3	37.49		167	157						
	c4	40.75		182	172						
B			7/32								
C	r1	40.75	1/4	160		6.0	3/8	8.0	6.0	3/8	8.0
	r2	36.31		142							
	r3	31.88		125							
D	r3	31.88	3/16	166		6.0	3/8	8.0	6.0	3/8	8.0
	r4	27.44		142							
	r5	23.00		119							
E	r5	23.00	5/32	142		6.0	3/8	8.0	6.0	3/8	8.0
	r6	23.42		145							
	r7	23.84		148							
	r8	24.25		150							
	r9	24.67		153							
	r10	24.75		154							

8.1.2 First-Order and Second-Order Elastic Analysis Results

Table 8.2 gives a summary of the linear elastic analysis reactions and member internal axial forces and moments generated in the original design of the single-span frame by Chief Buildings and in the solutions conducted in this study using GT-Sabre. These forces and moments are at 1.6 of the ASD load levels, where $\alpha = 1.6$ is the required factor for the subsequent consideration of second-order effects. Where the axial forces and moments differ in the left or right column or rafter, the larger values are reported. The axial force and moment in both columns are reported for LC3. Column 1 and rafter 1 are the members on the left-hand side of the ridge in the elevation view of the frame whereas column 2 and rafter 2 are on the right-hand side. Figures 8.2 and 8.3 show the distributions of the applied wind and unbalanced snow loadings on the single-span

Table 8.2. Linear elastic analysis forces and moments, single-span frame, $\alpha = 1.6^{*}$.

Load Case 1		Chief	GT-Sabre	Difference
Reactions	R_y (kips)	50.1	50.0	-0.1%
	R_x (kips)	43.7	43.1	-1.3%
Columns	P_{max} (kips)	53.6	53.5	-0.3%
	M_{max} (ft-kips)	593	585	-1.4%
Rafters	P_{max} (kips)	47.0	44.8	-4.7%
	M_{max}^{-} (ft-kips)	-600	-593	-1.2%
	M_{max}^{+} (ft-kips)	217	227	4.5%

Load Case 2		Chief	GT-Sabre	Difference
Vertical Reactions	R_{y1} (kips)	25.1	24.9	-0.9%
	R_{y2} (kips)	29.0	29.1	0.6%
	ΣR_y (kips)	54.1	54.0	-0.1%
Horizontal Reactions	R_{x1} (kips)	20.5	20.8	1.6%
	R_{x2} (kips)	-25.8	-26.1	1.4%
	ΣR_x (kips)	-5.3	-5.3	0.3%
Columns	P_{max} (kips)	31.1	31.2	0.2%
	M_{max} (ft-kips)	325	333	2.7%
Rafters	P_{max} (kips)	23.8	23.3	-2.0%
	M_{max}^{-} (ft-kips)	-325	-335	2.9%
	M_{max}^{+} (ft-kips)	115	122	6.8%

Load Case 3		Chief	GT-Sabre	Difference
Reactions	R_{y1} (kips)	33.4	33.5	0.1%
	R_{y2} (kips)	49.4	49.4	-0.1%
	ΣR_y (kips)	82.9	82.8	0.0%
	R_x (kips)	38.1	37.6	-1.2%
Column 1	P_{max} (kips)	36.6	36.5	-0.3%
	M_{max} (ft-kips)	530	524	-1.2%
Column 2	P_{max} (kips)	52.6	52.4	-0.4%
	M_{max} (ft-kips)	509	503	-1.2%
Rafters	P_{max} (kips)	41.5	39.4	-5.1%
	M_{max}^{-} (ft-kips)	-548	-542	-1.0%
	M_{max}^{+} (ft-kips)	236	243	3.1%

* The cells for the maximum moments and the corresponding axial forces are shaded.

frame. The other loadings are uniformly distributed and are summarized at the beginning of Chapter 8. For purposes of discussion, the unbalanced snow load is placed on the right-hand side of the ridge. As a result, the single-span frame tends to drift to the left under the unbalanced snow load combination. Therefore, the notional lateral loads for the effective length method analysis solution, and the nominal frame out-of-plumbness for calculation of the required internal forces in the direct analysis method, are applied to the left for this load case.

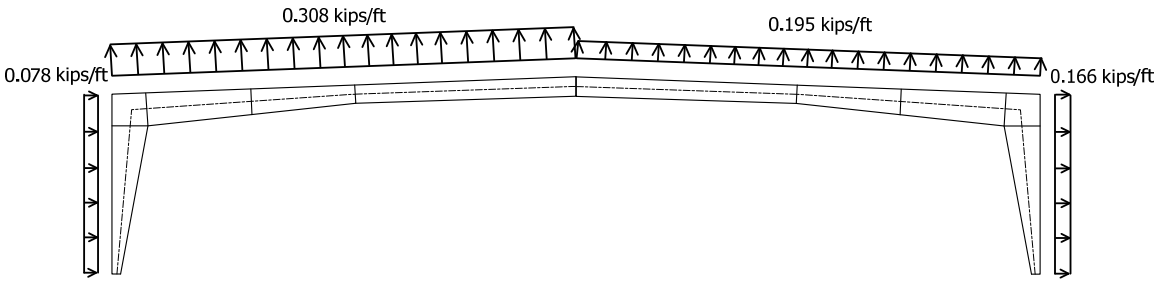

Figure 8.2. Wind load distribution (wind from left), single-span frame.

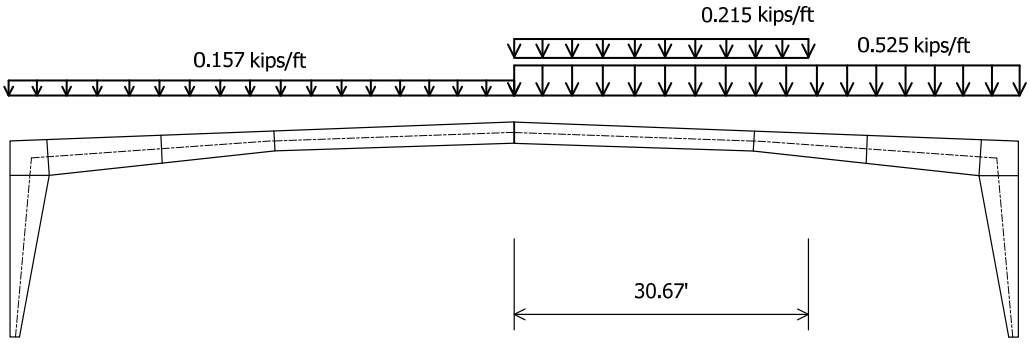

Figure 8.3. Unbalanced snow load distribution, single-span frame.

The differences between the Chief and GT-Sabre results shown in Table 8.2 are minor and are mainly due to two factors: (1) modeling of the applied forces as distributed loadings in the solutions by Chief versus the use of closely-spaced concentrated loads in

the solutions by GT-Sabre, and (2) minor differences in the modeling of the nonprismatic member geometries (e.g., representation of the member geometry at the knee of the frame, calculation of the stiffnesses associated with the tapered member geometries, etc.). All of the forces from the Chief and GT-Sabre solutions that must be the same based on equilibrium (i.e., the total vertical and horizontal reactions) are well within one percent of one another. The horizontal thrust reactions, the rafter axial forces, and the member internal moments from the different linear elastic analyses are generally within a few percent of one another. The cells for the governing maximum linear elastic moments and the corresponding axial forces are shaded in the table. The largest difference between the Chief and GT-Sabre results in these cells is 6.8 % (M_{max}^{+} for LC2, rafters).

Table 8.3 compares the internal axial forces and bending moments obtained from the different GT-Sabre analyses (at $\alpha = 1.6$) for the single-span frame. One can observe that the differences between the various analysis solutions are quite small for this structure. These small differences are expected, since as discussed at the beginning of Chapter 8, the second-order effects tend to be small at the design load levels in clear-span frames.

Figures 8.4 through 8.6 show the direct analysis method internal axial force and moment distributions for the three load combinations considered in this study for the single-span frame. Load case 1 (Dead + Collateral + Snow) governs the design of the columns and the critical rafter segment in negative bending (segment r1-r2) whereas load case 3 (Dead + Collateral + Unbal-anced Snow) governs the design of the rafters for positive bending moment (segment r8-r9).

Table 8.3. Axial forces and moments from different types of analysis, single-span frame, $\alpha = 1.6$.

Load Case 1	Analysis Type	P_{max} (kips)	M_{max}^{+} (ft-kips)	M_{max}^{-} (ft-kips)
Column 2	1st-order elastic, $Y_i = 0.0$	53.5	585	
	2nd-order elastic, $Y_i = 0.0$	53.2	599	
	Effective Length	53.2	601	
	Direct Analysis	53.1	605	
Rafter 2	1st-order elastic, $Y_i = 0.0$	44.8		-593
Segment	2nd-order elastic, $Y_i = 0.0$	45.2		-607
r1-r2	Effective Length	45.2		-609
	Direct Analysis	45.3		-613
Rafter 1	1st-order elastic, $Y_i = 0.0$	43.2	227	
Segment	2nd-order elastic, $Y_i = 0.0$	44.0	238	
r8-r9	Effective Length	44.0	238	
	Direct Analysis	44.3	241	

Load Case 2	Analysis Type	P_{max} (kips)	M_{max}^{+} (ft-kips)	M_{max}^{-} (ft-kips)
Column 2	1st-order elastic, $Y_i = 0.0$	31.2	333	
	Effective Length	31.0	337	
	Direct Analysis	31.0	339	
Rafter 2	1st-order elastic, $Y_i = 0.0$	23.2		-335
Segment	Effective Length	23.3		-339
r1-r2	Direct Analysis	23.3		-341
Rafter 2	1st-order elastic, $Y_i = 0.0$	22.0	122	
Segment	Effective Length	22.2	126	
r8-r9	Direct Analysis	22.2	126	

Load Case 3	Analysis Type	P_{max} (kips)	M_{max}^{+} (ft-kips)	M_{max}^{-} (ft-kips)
Column 2	1st-order elastic, $Y_i = 0.0$	52.4	503	
	2nd-order elastic, $Y_i = 0.0$	52.3	509	
	Effective Length	52.2	508	
	Direct Analysis	52.3	509	
Rafter 1	1st-order elastic, $Y_i = 0.0$	38.8		-542
Segment	2nd-order elastic, $Y_i = 0.0$	39.4		-559
r1-r2	Effective Length	39.4		-560
	Direct Analysis	39.6		-564
Rafter 2	1st-order elastic, $Y_i = 0.0$	37.4	243	
Segment	2nd-order elastic, $Y_i = 0.0$	38.0	254	
r8-r9	Effective Length	38.0	254	
	Direct Analysis	38.2	257	

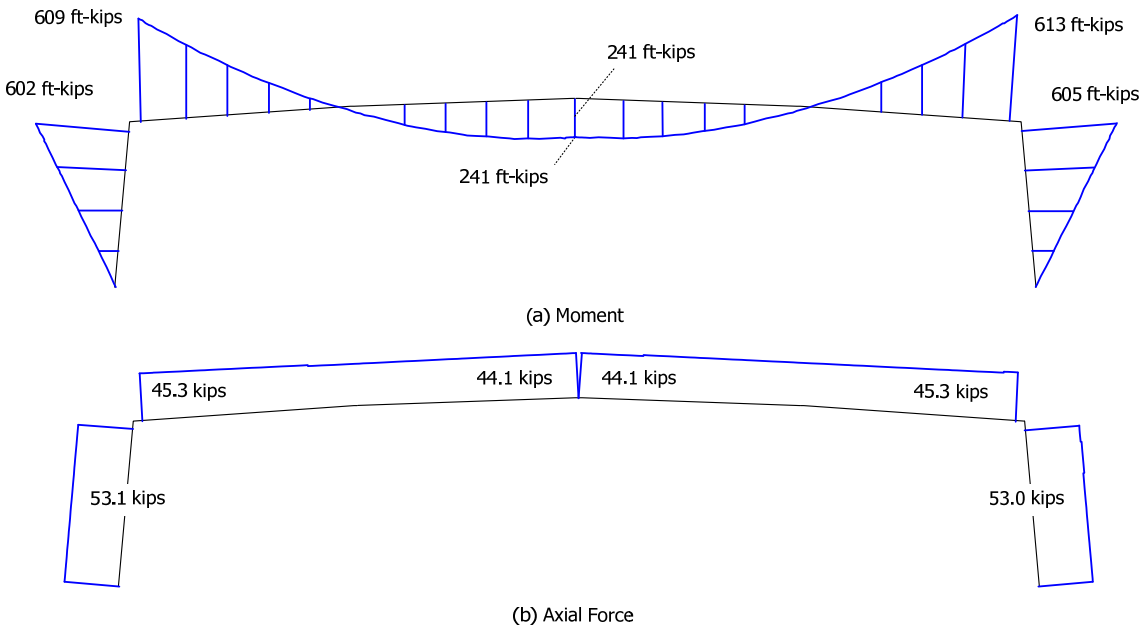

Figure 8.4. Moment and axial force distributions, single-span frame, direct analysis method, LC1 (Dead + Collateral + Uniform Snow, $\alpha = 1.6$).

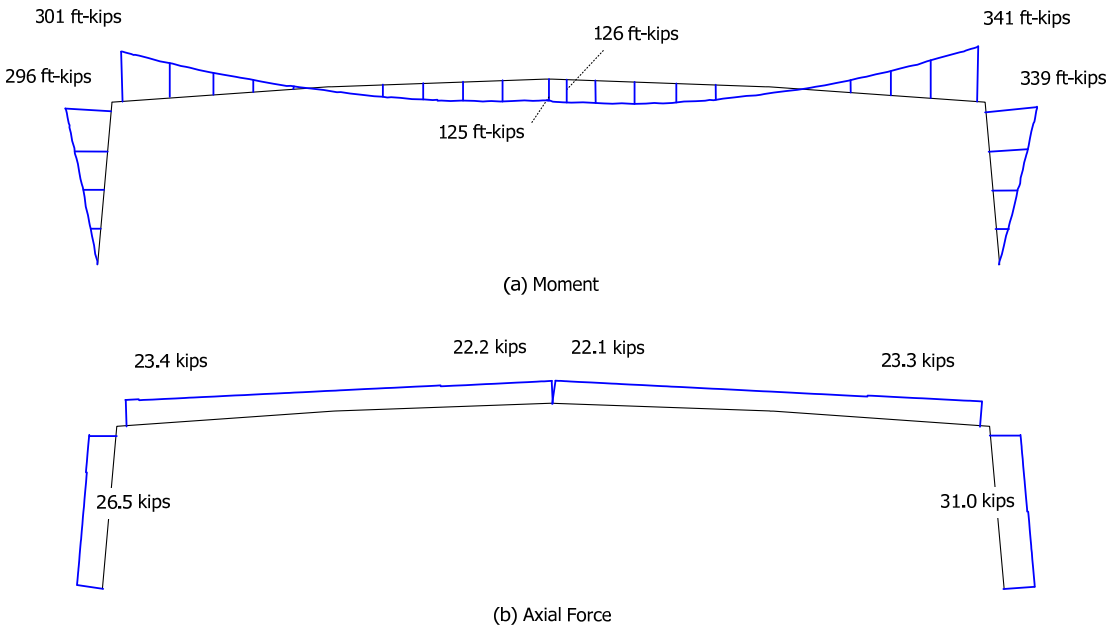

Figure 8.5. Moment and axial force distributions, single-span frame, direct analysis method, LC2 (Dead + Collateral + 0.75(Snow + Wind), $\alpha = 1.6$).

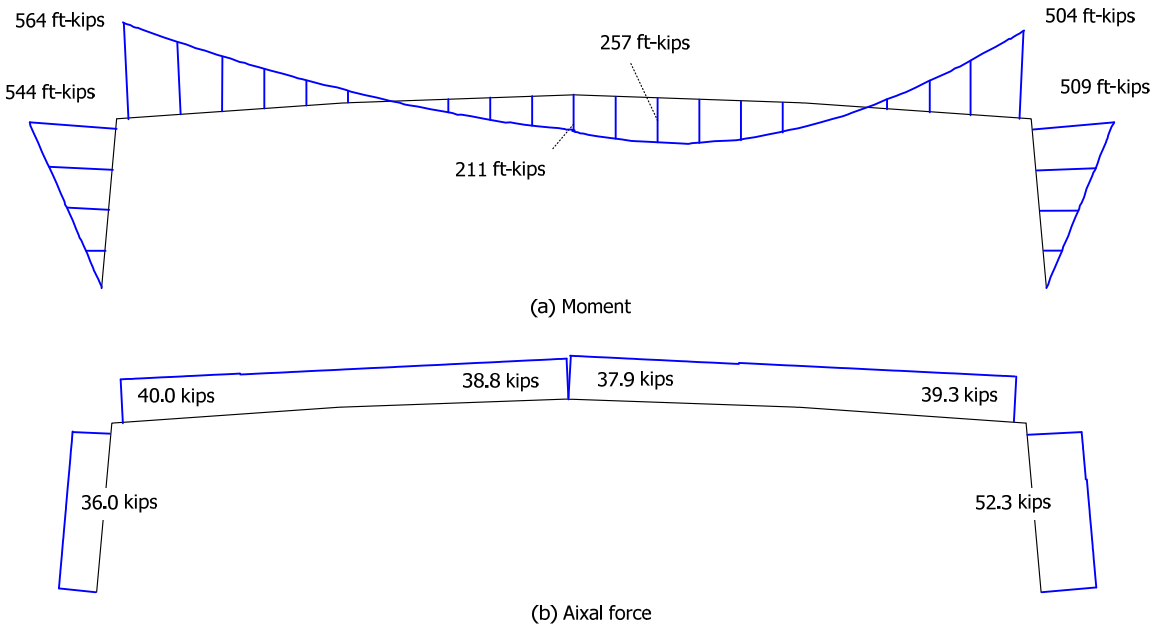

Figure 8.6. Moment and axial force distributions, single-span frame, direct analysis method, LC3 (Dead + Collateral + Unbalanced Snow, $\alpha = 1.6$).

8.1.3 Axial Capacity Ratios P_r/P_c

Tables 8.4 to 8.5 summarize the intermediate and final results pertaining to the calculation of the axial capacity ratios for the single-span frame. These tables parallel the procedure summarized in Section 3.2.2. The axial capacity ratios are determined separately for the in-plane and out-of-plane column buckling limit states. The in-plane results for the columns (c1-c4) are shown first, followed by the out-of-plane calculations for each of the column segments (c1-c2, c2-c3 and c3-c4), then the in-plane results for the rafters (r1-r10), and finally the out-of-plane calculations for the critical rafter segments (r1-r2 and r8-r9). The results are shown for the effective length and the direct analysis methods in each of these cases. In the cases where the cell values are identical for the direct analysis and the effective length methods, the direct analysis values are

indicated by the " symbol. Appendices D and E provide a detailed illustration of the calculations corresponding to each of the steps of Section 3.2.2 for the single-span frame.

The most complex part of the determination of the axial capacity ratio is generally the calculation of the elastic buckling load ratios γ_e. This process is outlined for the single-span frame in the next two subsections, followed by a discussion of the remainder of the calculations.

8.1.3.1 Calculation of the Elastic Buckling Load Ratio γ_e (in-plane buckling)

For the application of the effective length method, the *in-plane* elastic buckling load ratio γ_e can be determined for the columns using a rigorous elastic buckling analysis of the complete frame. For LC 1, this gives $\gamma_e = 19.3$ (note that this load ratio is relative to the ASD load combination level, i.e., relative to the loadings for $\alpha = 1.0$). It is important to note that a buckling analysis using the AISC (2010) commentary story-stiffness based procedure (discussed subsequently in Section 8.2.3.1 below) gives $\gamma_e = 26.2$. The smaller value of 19.3 is due to the influence of axial compression in the rafters. None of various procedures described in the AISC (2010) Commentary include the influence of axial compression in the rafters of gable frames. Also, generally they do not account for the influence of axial compression in horizontal beams of rectangular frames, such as the axial thrust in the girder of a rectangular portal frame.

Lee et al. (1981) provide a chart-based method for determining the elastic buckling loads in frames with tapered-web members. The Lee et al. (1981) procedure also generally neglects the influence of axial compression in the rafters on the frame elastic sidesway buckling resistance. As discussed by Watwood (1985), “this does not appear to the writer to be a sound approach due to the fact that in computing the

restraining stiffness values at each end of a single rafter, use is made of the column and the other rafter, which are subject to simultaneous buckling. In such a case neither member can provide rotational restraint for the other at the joint…. the alinement chart procedure is not applicable when both the column and the rafter are under significant compression."

Cary and Murray (1997) recommend a simplified effective length factor equation that is very close in its fundamental basis and development to the story-stiffness based procedure in the AISC (2010) Commentary. The Cary and Murray equation and a generalized form of the AISC (2010) story-stiffness based procedure, applicable for frames with unequal height columns (and in which the *P*-δ effect on the bending stiffness of the rafters is small), are discussed in Section 8.2.3.1 below. These methods are not applicable to the example single-span frame because they do not include the influence of axial compression in the rafters. The Cary and Murray (1997) equation predicts $\gamma_e = 26.1$ for load case 1 on the single-span frame. If a rigorous elastic buckling analysis of the complete frame is conducted in which one-half of the total vertical load is lumped at the top of each of the exterior columns, one obtains $\gamma_e = 32.0$. One can observe that the AISC (2010) story-stiffness based calculation of $\gamma_e = 26.2$ is 82 percent of the rigorous elastic buckling analysis solution obtained by lumping the vertical loads at the column tops. This is due to implicit conservative assumptions regarding the influence of *P*-δ effects in the AISC (2010) equation. The *P*-δ effects on the elastic buckling solution are essentially nil for load case 1 of the single-span frame, when the loads are lumped at the column tops. The Cary and Murray solution of $\gamma_e = 26.1$ is essentially the same as the AISC (2010) story-stiffness based solution for this problem. Nevertheless, all of these

values are overly-optimistic estimates for the load ratio at incipient sidesway buckling of the single-span frame under the physical LC1 loadings. The majority of the gravity load in LC1 is applied to the rafters. In as such, significant bending is induced within the structure, leading to substantial horizontal thrusts at the base of the frame. These thrusts in turn induce substantial axial compression in the rafters, reducing the stiffness of the rafters in this case primarily due to *P*-δ effects (in the rafters). As a result of this reduced stiffness, the single-span frame exhibits elastic sidesway buckling at γ_e = 19.3 rather than 32.0 by a rigorous analysis or 26.2 or 26.1 by the above approximate methods.

One should not lose sight of the fact that, although the above story-stiffness based procedures significantly over-predict the elastic buckling load of the single-span frame, all of the above γ_e values are quite large. This indicates that the actual stability effects (i.e., the amplification of the frame displacements and internal moments at α = 1.6 of the ASD load combination levels) should be quite small, which is indeed the case. Therefore, to a certain extent, all of the above discussions about accuracy of the different elastic buckling solutions are a bit pointless for the example single-span frame. Nevertheless, the traditional effective length method requires the calculation of the frame sidesway buckling capacity, such that the anchor points $P_{n(KLi)}$ can be determined for the various members in the structure (see Figures 2.6, 2.7, 2.10 and 2.11 from the previous discussions in Chapter 2). In cases like the example single-span frame, where the structure's actual internal actions are actually dominated by slightly amplified internal bending moments, not by column flexural buckling, the traditional effective length method over-emphasizes the behavior associated with the theoretical column flexural buckling limit state. In contrast, the direct analysis method focuses on an estimate of the

physical response of the structure under the loadings it is being designed for, and it compares the corresponding estimated internal moments and axial forces against a more realistic estimate of the physical member capacities.

In recognition of the fact that when γ_e is large, the design checks are generally insensitive to the column elastic buckling loads or effective lengths, the AISC (2010) effective length method provisions allow the simple use of $K = 1$ when $\Delta_{2nd}/\Delta_{1st}$, the ratio of the second-order to the first-order sidesway displacements (at $\alpha = 1.6$ in ASD), is less than or equal to 1.1 (see Table 2.1). The example single-span frame satisfies this restriction, and therefore, all the column in-plane buckling results summarized in Tables 8.4 to 8.6 are based effectively on $K = 1$. For general non-prismatic, nonuniformly loaded members, one may interpret that these provisions permit the calculation of the column γ_e values (for in-plane buckling) assuming braced simply-supported end conditions at the ends of the member lengths. Based on this idealization, the method of successive approximations (Timoshenko and Gere 1961) is a convenient way of performing the γ_e calculation, giving $\gamma_e = 210$ and 361 for column c1-c4 under load cases 1 and 2 respectively. The column in-plane axial capacity ratios for the effective length method in Tables 8.4 and 8.5 are all based on these values of γ_e.

It is emphasized that the AISC (2010) effective length method provisions still require the calculation of (or an estimate of) the second-order internal moments and forces, even when $\Delta_{2nd}/\Delta_{1st} \leq 1.1$. This is necessary in general to maintain the accuracy of the beam-column unity checks (White and Hajjar 1997).

In the effective length method, engineering judgment is required when considering the calculation of γ_e for the rafters. If one uses the above results from the

Table 8.4. Calculation of axial capacity ratios, single-span frame, load case 1.

Location	Method	γ_e	x_1 (ft)	P_r (kips)	$(f_r/F_y)_{max}$	F_{n1} (ksi)	γ_{n1}	x_{max} (ft)	f (ksi)	Q_s	Q_a	Q	$(f_r/QF_y)_{max}$	F_n (ksi)	P_r/P_c	Governing P_r/P_c
Seg. c1-c4	Effective Length	210	0.0	33.3	0.0834	53.7	11.7	0.0	53.7	1.00	0.964	0.964	0.087	51.8	0.148	
(in-plane)	Direct Analysis			33.1				"	55.0	1.00	0.961	0.961	0.087	52.9	0.144	
Seg. c1-c2	Effective Length	16.6	0.0	33.3	0.0834	40.7	8.9	0.0	40.7	1.00	0.990	0.990	0.084	40.4	0.190	0.190
(out-of-plane)	Direct Analysis	16.7	"	33.1	0.0831	40.6	8.9	"	40.6	1.00	0.990	0.990	0.084	40.4	0.189	0.189
Seg. c2-c3	Effective Length	26.0	7.5	33.3	0.0571	41.5	13.2	7.5	41.5	1.00	0.707	0.707	0.081	31.9	0.165	0.165
(out-of-plane)	Direct Analysis	26.0	"	33.2	0.0570	41.5	13.2	"	41.5	1.00	0.707	0.707	0.081	31.8	0.164	0.164
Seg. c3-c4	Effective Length	366	13.5	33.2	0.0455	53.6	21.4	13.5	53.6	1.00	0.549	0.549	0.083	29.8	0.140	0.148
(out-of-plane)	Direct Analysis	366	"	33.2	0.0455	53.6	21.4	"	53.6	1.00	0.549	0.549	0.083	29.8	0.140	0.144
Seg. r1-r10	Effective Length	37.7	20.0	27.7	0.0632	46.1	13.3	20.0	46.1	1.00	0.703	0.703	0.090	34.2	0.170	
(in-plane)	Direct Analysis			27.8				"	55.0	1.00	0.692	0.692	0.092	38.0	0.153	
Seg. r1-r2	Effective Length	38.1	5.0	28.2	0.0383	41.3	19.6	5.0	41.3	1.00	0.558	0.558	0.069	26.2	0.135	0.170
(out-of-plane)	Direct Analysis	38.1	"	28.3	0.0384	41.3	19.6	"	41.3	1.00	0.558	0.558	0.069	26.2	0.135	0.153
Seg. r8-r9	Effective Length	39.0	35.0	27.5	0.0613	46.2	13.7	35.0	46.2	1.00	0.686	0.686	0.089	33.5	0.168	0.170
(out-of-plane)	Direct Analysis	38.8	"	27.7	0.0616	46.2	13.6	"	46.2	1.00	0.686	0.686	0.090	33.5	0.169	0.169

Table 8.5. Calculation of axial capacity ratios, single-span frame, load case 2.

Location	Method	γ_e	x_1 (ft)	P_r (kips)	$(f_r/F_y)_{max}$	F_{n1} (ksi)	γ_{n1}	x_{max} (ft)	f (ksi)	Q_s	Q_a	Q	$(f_r/QF_y)_{max}$	F_n (ksi)	P_r/P_c	Governing P_r/P_c
Seg. c1-c4	Effective Length	361	0.0	19.4	0.0487	53.7	20.1	0.0	53.7	1.00	0.964	0.964	0.051	51.8	0.086	
(in-plane)	Direct Analysis			19.4				"	55.0	1.00	0.961	0.961	0.051	52.9	0.084	
Seg. c1-c2	Effective Length	28.5	0.0	19.4	0.0487	40.7	15.2	0.0	40.7	1.00	0.990	0.990	0.049	40.4	0.111	0.111
(out-of-plane)	Direct Analysis	28.5	"	19.4	0.0486	40.7	15.2	"	40.7	1.00	0.990	0.990	0.049	40.4	0.111	0.111
Seg. c2-c3	Effective Length	45.1	7.5	19.1	0.0329	41.5	23.0	7.5	41.5	1.00	0.707	0.707	0.047	31.9	0.095	0.095
(out-of-plane)	Direct Analysis	45.2	"	19.1	0.0328	41.5	23.0	"	41.5	1.00	0.707	0.707	0.047	31.9	0.095	0.095
Seg. c3-c4	Effective Length	642	13.5	18.9	0.0259	53.6	37.6	13.5	53.6	1.00	0.549	0.549	0.047	29.8	0.080	0.086
(out-of-plane)	Direct Analysis	642	"	18.9	0.0259	53.6	37.6	"	53.6	1.00	0.549	0.549	0.047	29.8	0.080	0.084
Seg. r1-r10	Effective Length	74.3	20.0	14.1	0.0322	46.2	26.1	20.0	46.2	1.00	0.703	0.703	0.046	34.2	0.087	
(in-plane)	Direct Analysis			14.1				"	55.0	1.00	0.692	0.692	0.047	38.0	0.078	
Seg. r1-r2	Effective Length	73.9	5.0	14.6	0.0198	41.3	38.0	5.0	41.3	1.00	0.558	0.558	0.035	26.2	0.069	0.087
(out-of-plane)	Direct Analysis	73.9	"	14.6	0.0198	41.3	38.0	"	41.3	1.00	0.558	0.558	0.035	26.2	0.069	0.078
Seg. r8-r9	Effective Length	77.5	35.0	13.9	0.0308	46.2	27.2	35.0	46.2	1.00	0.686	0.686	0.045	33.5	0.085	0.087
(out-of-plane)	Direct Analysis	77.3	"	13.9	0.0309	46.2	27.1	"	46.2	1.00	0.686	0.686	0.045	33.5	0.085	0.085

Table 8.6. Calculation of axial capacity ratios, single-span frame, load case 3.

Location	Method	γ_e	x_1 (ft)	P_r (kips)	$(f_r/F_y)_{max}$	F_{n1} (ksi)	γ_{n1}	x_{max} (ft)	f (ksi)	Q_s	Q_a	Q	$(f_r/QF_y)_{max}$	F_n (ksi)	P_r/P_c	Governing P_r/P_c
Seg. r1-r10	Effective Length	43.5	20.0	24.2	0.0552	46.2	15.2	20.0	46.2	1.00	0.703	0.703	0.079	34.2	0.148	
(in-plane)	Direct Analysis			24.2				"	55.0	1.00	0.692	0.692	0.080	38.0	0.134	
Seg. r8-r9	Effective Length	45.2	35.0	23.8	0.0529	46.2	15.9	35.0	46.2	1.00	0.686	0.686	0.077	33.5	0.145	0.148
(out-of-plane)	Direct Analysis	45.0	"	23.9	0.0532	46.2	15.8	"	46.2	1.00	0.686	0.686	0.078	33.5	0.146	0.146

rigorous elastic sidesway buckling analysis, γ_e is equal to 19.3 also for the rafters in LC1. However, at the elastic buckling of the single-span frame under 19.3 times the Dead + Collateral + Snow load combination, the predominant action of the rafters is in providing rotational restraint to the tops of the columns. This is evidenced by the critical buckling mode shape for this load case, shown in Figure 8.7. Because of this behavior, a common practice is to base the calculation of γ_e for the rafters on an alternate buckling model. In many cases in past practice, e.g. (Lee et al. 1981), an alternate buckling model is used in which the influence of axial compression in the column is neglected and the column is assumed to restrain the buckling of the rafter. However, since the columns of the frame buckle in sidesway (or the entire frame buckles in sidesway, depending on one's perspective) at a load level significantly smaller than the γ_e for buckling of the rafters with an assumed end restraint from the columns, one should be suspicious about such a model. Because any rigorous justification of this type of approach is not available, the rafter γ_e values in Tables 8.4 to 8.6 are obtained from an isolated buckling analysis of these members assuming braced simply-supported end conditions. That is, the γ_e of the rafters is determined using the actual rafter unsupported lengths in the plane of bending, assuming the rafter ends are simply supported and braced against sidesway. As noted previously, the ridge is taken as a brace point in defining the member lengths. This approach gives $\gamma_e = 37.7$ for LC1 on the single-span frame. Watwood (1985) discusses this approach, but chooses to use the γ_e for buckling of the complete framing system in determining the rafter axial load capacity ratios in his gable frame.

In the direct analysis method, the in-plane member length effects are all incorporated into the second-order analysis of the structure and the in-plane nominal axial

Figure 8.7. Critical elastic buckling mode, single-span frame, LC1, $\gamma_e = 19.3$.

resistance is handled on a cross-section by cross-section basis. That is, $P_{ni} = QP_y$.

8.1.3.2 Calculation of the Elastic Buckling Load Ratio γ_e (out-of-plane buckling)

For the calculation of out-of-plane γ_e values in both the effective length and the direct analysis methods, the Euler load based on the actual unsupported length of each of the member segments (McGuire 1968) is used. Specifically, the authors use Eqs. 4.1 and 4.2 with $K = 1$ for evaluation of the out-of-plane γ_e in all the example calculations. It should be noted that both flanges are braced at the ends of each of the segments considered in Tables 8.4 to 8.6. Cases where the inside flange has a larger unbraced length than the outside flange are addressed in the subsequent modular frame example.

It is possible to account for the end restraint provided to the most critical segments from adjacent less critical segments in determining the out-of-plane buckling loads. This increases the calculated buckling load for the critical segment while decreasing the calculated buckling loads for the adjacent unbraced lengths. One obtains a single buckling load at which the multiple unbraced lengths considered in the buckling model fail together as a subassembly. This buckling load is larger than the smallest buckling load obtained by considering each of the unbraced lengths as separate simply-supported segments. However, in highly optimized designs using tapered-web members,

the restraint from the adjacent segments tends to be smaller than typically encountered in designs using prismatic members. Also, it should be noted that the physical out-of-plane buckling behavior of the members in typical metal building frames is far removed from the problem of out-of-plane buckling under concentric axial compression. The physical out-of-plane buckling behavior typically involves combined axial compression and major-axis bending, with the member stresses being dominated by the bending actions, not by the axial compression. Member out-of-plane buckling (or in-plane buckling) under the unrealistic loading of pure axial compression actually has very little to do with the true stability response. The *K* factor for lateral-torsional buckling of the member as a beam typically represents the stability behavior better than the *K* factor based on out-of-plane flexural buckling under pure axial compression when the axial load is small.

Generally, one should limit the number of unbraced segments included in the above subassembly buckling model. Otherwise, benefits are obtained for the most critical unbraced length, but other "stronger" unbraced lengths that do not participate significantly in the buckling of the critical segment will be inappropriately penalized. The rafter r1-r9 of the single-span frame can be considered as an example of this issue. The Engineer could construct an out-of-plane buckling model involving the entire length of the rafter, r1-r9. However, in this case, the *K* factors for some of the unbraced segments will be inappropriately large. Typically, a good practice is to limit the subassembly buckling model to three adjacent segments. This is the approach taken by Nethercot and Trahair (1976) for calculation of LTB effective length factors for prismatic beams.

If a subassembly model is constructed for concurrent out-of-plane buckling of the three column segments (c1-c4) in the single-span frame, one obtains $\gamma_e = 22.8$ for LC1. Based on the simplified assumption of ideally-pinned base conditions at location c1, segment c1-c2 is the most critical of the column segments ($\gamma_e = 16.6$ and 16.7 for the effective length method and the direct analysis method respectively in Table 8.4). Therefore, the calculated buckling strength of this segment is increased while the calculated buckling strength of the adjacent segment c2-c3 is decreased from $\gamma_e = 26.0$ to 22.8 by the use of the subassembly buckling model. However, in the subsequent flexure and beam-column checks for column c1-c4, segment c2-c3 is more critical. Hence, if the above subassembly model is used for determining the segment axial capacity ratios P_r/P_c, the result is that the unity check for the governing segment c2-c3 is slightly increased. The problem here is that c2-c3 is indeed the critical unbraced length for column c1-c4 for the actual internal loading, which is dominated by bending actions. A more representative design check (representative of the actual behavior of the member under predominant bending plus a small amount of axial compression) is obtained by using the actual segment unbraced lengths in determining P_r/P_c, and by considering the effect of end restraint in checking the LTB resistance of segment c2-c3.

8.1.3.3 Completion of the Calculations of P_r/P_c

The remainder of the results shown in Tables 8.4 to 8.6 follows the general procedure of Section 3.3.3 closely, and for the most part, should be readily apparent. However, a few additional terms are introduced in the tables. The term x_1 is the location from the base of the column or the knee of the rafter, measured along the length of the outside flanges, at which f_r/F_y is maximum and F_{n1} is determined (see step 4 of the

general procedure). The term x_{max} is the corresponding location at which f_r/QF_y is a maximum. The tables show the calculation of the in-plane and out-of-plane values for the axial capacity ratio P_r/P_c. Also, in the last column of the tables, the governing (largest) value of P_r/P_c from the in-plane and out-of-plane checks is listed. The reader should note that the in-plane value for P_r/P_c can come from a location along the in-plane unbraced length that is completely different from the location for the out-of-plane value of P_r/P_c, which always comes from the out-of-plane segment under consideration. For instance, considering the rafter and LC1, the in-plane P_r/P_c of 0.170 from the effective length method or 0.153 from the direct analysis method comes from the smaller cross-section at 20 ft from the knee of the frame. These P_r/P_c values are larger than the governing out-of-plane P_r/P_c values for segment r1-r2, which are located at x = 5 ft from the knee of the frame (i.e., P_r/P_c = 0.135 for both the effective length and for the direct analysis methods).

8.1.4 Flexural Capacity Ratios M_r/M_c

Tables 8.7 to 8.9 summarize the calculation of the flexural capacity ratios for the single-span frame. As discussed in the previous sections, the determination of the flexural capacity ratio for LTB has many similarities to the axial capacity ratio calculations. However, the LTB flexural capacity ratios are somewhat simpler since the interaction between flange local buckling and lateral torsional buckling is insignificant for practical I-section members. The second through the ninth columns of the above tables show the key intermediate and final LTB results. These columns parallel the general procedure of Section 3.3.3. Appendices D and E provide a detailed illustration of

the calculations corresponding to each of the steps of the Section 3.3.3) procedure, plus example FLB calculations.

The elastic LTB load ratios γ_{eLTB} in Tables 8.7 to 8.9 are calculated using the recommended procedure detailed in Section 4.4.1. It should be noted that for all the tapered segments, the stress-gradient effect is embedded in the elastic LTB load ratios γ_{eLTB} in Tables 8.7 to 8.9. Also, the rigorous elastic LTB analyses on each of the unbraced segments are conducted using idealized simply-supported end conditions at the ends of the segments, with the segments subjected solely to the bending moment distribution obtained from second-order elastic analysis (zero axial compression). The differences between the γ_{eLTB} values determined by the procedure shown in Section 4.4.1 and the values determined by a rigorous 3D LTB analysis of the idealized segments are small for the linearly tapered segments considered in the example single-span frame. It is emphasized that the influence of end restraint from adjacent less critically loaded segments is not considered in these calculations. The potential consideration of these effects is addressed subsequently.

The fourth column of Tables 8.7 to 8.9 gives the position $x_{max(LTB)}$ relative to the column base or the rafter knee, measured along the length of the outside flanges, at which M_r/M_{yc} is maximum in each of the members while the fifth column gives the maximum M_r/M_{yc} values. The sixth column reports the bend buckling strength reduction factor for LTB, $R_{pg(LTB)}$, which is obtained from the cross-section where the M_r/M_c value is the largest. This is followed by the web plastification factor R_{pc} for each of the segments, which is evaluated at the same cross-section as $R_{pg(LTB)}$. When the segment has a slender web, the value of R_{pc} equals 1.0. The single-span frame is representative of many metal

building frame designs in that only one of the segments, segment c1-c2 with the smallest web depth at the bottom of the columns, has a noncompact web. The elastic LTB resistances are calculated using $J = 0$ for all of the segments with the exception of segment c1-c2. The use of a finite value for J tends to increase the LTB resistance by only a minor amount for the types of cross-sections considered in this study. Furthermore, the elastic LTB resistances based on the cross-section theoretical J value (Eq. 4.4c) are generally unrealizable for slender-web members due to the influence of web distortion (Bradford 1992; White and Jung 2008).

The $R_{pg(LTB)}$ values in Tables 8.7 to 8.9 are calculated in a slightly different manner than specified in AISC (2010). The AISC technical and specification committees opted to simplify the bend-buckling strength reduction factor in AISC (2010) (Eq. F5-6) by using the yield strength F_y rather than an estimate of the compression flange stress at the member strength limit in the equation for this term. AASHTO (2004) also invokes this simplification, which is based on the fact that its effect on the value of R_{pg} is typically quite small. However, AASHTO (2004) also suggests a more refined calculation for R_{pg} that provides some additional benefit in cases where the flexural resistance is governed by stability considerations. The refined calculation is essentially the same as in the R_{pg} formula of AISC (1989) ASD and AISC (1999) LRFD, but with the compression flange stress at the member strength limit ($M_{n(Rpg=1)}/S_{xc}$):

$$R_{pg} = 1 - \frac{a_{wc}}{1200 + 300a_{wc}}\left(\frac{h_c}{t_w} - 5.7\sqrt{\frac{E}{M_{n(R_{pg}=1)}/S_{xc}}}\right) \geq 1.0 \qquad \text{(Eq. 8.1)}$$

where

Table 8.7. Calculation of flexural capacity ratios, single-span frame, load case 1.

Location	Method	γ_{eLTB}	$x_{max(LTB)}$ (ft)	$(M_r/M_{yc})_{max}$	$R_{pg(LTB)}$	R_{pc}	$M_{n(LTB)}$ (ft-kips)	$M_r/M_{c(LTB)}$	$x_{max(FLB)}$ (ft)	$R_{pg(FLB)}$	$M_{n(FLB)}$ (ft-kips)	$M_r/M_{c(FLB)}$	$x_{max(TFY)}$ (ft)	$M_{n(TFY)}$ (ft-kips)	$M_r/M_{c(TFY)}$	Gov. M_r (ft-kips)	Governing M_r/M_c
Seg. c1-c2	Effective Length	4.8	7.5	0.453	1.000	1.038	376	0.833	7.5	1.000	430	0.729	7.5	404	0.775	187	0.833
	Direct Analysis	4.8	"	0.456	1.000	1.038	376	0.840	"	1.000	430	0.734	"	404	0.781	189	0.840
Seg. c2-c3	Effective Length	4.7	13.5	0.485	0.976	1.000	602	0.933	13.5	0.966	669	0.839	12.0	553	0.903	336	0.933
	Direct Analysis	4.7	"	0.488	0.976	1.000	602	0.939	"	0.966	669	0.844	"	553	0.909	338	0.939
Seg. c3-c4	Effective Length	61.4	13.7	0.485	0.944	1.000	661	0.858	15.1	0.944	732	0.856	13.5	623	0.901	336	0.901
	Direct Analysis	61.0	"	0.488	0.944	1.000	661	0.864	"	0.944	732	0.862	"	623	0.907	338	0.907
Seg. r1-r2	Effective Length	5.3	0.0	0.534	0.960	1.000	624	1.019	0.0	0.949	676	0.940				380	1.019
	Direct Analysis	5.2	"	0.537	0.960	1.000	624	1.025	"	0.949	676	0.946				383	1.025
Seg. r8-r9	Effective Length	7.4	40.0	0.475	0.983	1.000	287	0.864	40.0	0.978	306	0.812				149	0.864
	Direct Analysis	7.3	"	0.481	0.982	1.000	287	0.875	"	0.978	306	0.822				151	0.875

Table 8.8. Calculation of flexural capacity ratios, single-span frame, load case 2.

Location	Method	γ_{eLTB}	$x_{max(LTB)}$ (ft)	$(M_r/M_{yc})_{max}$	$R_{pg(LTB)}$	R_{pc}	$M_{n(LTB)}$ (ft-kips)	$M_r/M_{c(LTB)}$	$x_{max(FLB)}$ (ft)	$R_{pg(FLB)}$	$M_{n(FLB)}$ (ft-kips)	$M_r/M_{c(FLB)}$	$x_{max(TFY)}$ (ft)	$M_{n(TFY)}$ (ft-kips)	$M_r/M_{c(TFY)}$	Gov. M_r (ft-kips)	Governing M_r/M_c
Seg. c1-c2	Effective Length	8.3	7.5	0.262	1.000	1.038	375	0.483	7.5	1.000	430	0.422	7.5	404	0.448	108	0.483
	Direct Analysis	8.2	"	0.264	1.000	1.038	375	0.486	"	1.000	430	0.424	"	404	0.451	109	0.486
Seg. c2-c3	Effective Length	8.3	12.0	0.275	0.976	1.000	537	0.528	13.5	0.966	669	0.474	10.7	498	0.514	170	0.528
	Direct Analysis	8.3	"	0.276	0.976	1.000	537	0.531	"	0.966	669	0.477	"	498	0.517	171	0.531
Seg. c3-c4	Effective Length	109	13.5	0.274	0.944	1.000	654	0.485	15.1	0.944	732	0.481	13.5	623	0.509	190	0.509
	Direct Analysis	108	"	0.276	0.944	1.000	654	0.488	"	0.944	732	0.483	"	623	0.512	191	0.512
Seg. r1-r2	Effective Length	9.5	0.0	0.297	0.960	1.000	624	0.567	0.0	0.949	676	0.524				212	0.567
	Direct Analysis	9.4	"	0.299	0.960	1.000	624	0.570	"	0.949	676	0.526				213	0.570
Seg. r8-r9	Effective Length	13.9	40.0	0.251	0.983	1.000	287	0.456	40.0	0.978	306	0.428				78	0.456
	Direct Analysis	13.8	"	0.252	0.983	1.000	287	0.459	"	0.978	306	0.431				79	0.459

Table 8.9. Calculation of flexural capacity ratios, single-span frame, load case 3.

Location	Method	γ_{eLTB}	$x_{max(LTB)}$ (ft)	$(M_r/M_{yc})_{max}$	$R_{pg(LTB)}$	R_{pc}	$M_{n(LTB)}$ (ft-kips)	$M_r/M_{c(LTB)}$	$x_{max(FLB)}$ (ft)	$R_{pg(FLB)}$	$M_{n(FLB)}$ (ft-kips)	$M_r/M_{c(FLB)}$	$x_{max(TFY)}$ (ft)	$M_{n(TFY)}$ (ft-kips)	$M_r/M_{c(TFY)}$	Gov. M_r (ft-kips)	Governing M_r/M_c
Seg. r8-r9	Effective Length	7.1	35.0	0.518	0.982	1.000	283	0.938	35.0	0.981	300	0.882				159	0.938
	Direct Analysis	7.1	"	0.524	0.982	1.000	283	0.948	"	0.981	300	0.892				160	0.948

$a_{wc} = h_c t_w / b_{fc} t_{fc}$ = ratio of two times the web area in compression (due to flexure only) to the compression flange area,

h_c/t_w = web slenderness based on the depth of the web in compression due to flexure, h_c.

$M_{n(Rpg = 1)}$ = AISC (2010) based flexural resistance with $R_{pg} = 1.0$, taken at the cross-section under consideration.

$M_{n(Rpg = 1)} / S_{xc}$ = compression flange stress at $M_{n(Rpg = 1)}$, where S_{xc} is calculated at the cross-section corresponding to $M_{n(Rpg = 1)}$.

Obviously, when $M_{n(Rpg = 1)}$ is less than M_{yc}, $M_{n(Rpg = 1)} /S_{xc}$ is less than F_{yc} and the resulting value of R_{pg} is larger. The term $R_{pg(LTB)}$ in Tables 8.7 to 8.9 is calculated using $M_{n(Rpg = 1)}$ based on the LTB limit state.

The eighth column of Tables 8.7 to 8.9 gives the calculated LTB flexural resistance $M_{n(LTB)}$ using Eqs. 3.16, 3.19 and 3.20 as applicable. This is followed by the corresponding flexural capacity ratio $M_r/M_{c(LTB)} = M_r/(M_{n(LTB)}/\Omega)$. The $M_r/M_{c(LTB)}$ cells are shaded in the cases where the flexural resistance is governed by the LTB check. The LTB flexural resistance is smaller than $R_{pg(LTB)}M_{yc}$ and the LTB check governs relative to the flange local buckling (FLB) and tension flange yielding (TFY) checks in all of the segments except the short segments c3-c4 at the tops of the columns.

The next several columns of Tables 8.7 to 8.9 summarize the FLB and TFY flexural resistance checks. As noted previously, these checks are entirely cross-section based. The locations of the critical cross-sections are denoted by the symbols $x_{max(FLB)}$ and $x_{max(TFY)}$. The TFY checks are not shown for the rafter segments in the single-span frame, since the rafters are doubly-symmetric and therefore the TFY limit state does not apply. Also, the $R_{pg(FLB)}$ term is evaluated using $M_{n(Rpg = 1)}$ based solely on the FLB limit state.

The last two columns of Tables 8.7 to 8.9 give the governing value of M_r, i.e., the one corresponding to the governing flexural limit state check, and the corresponding governing $M_r/M_c = M_r/(M_n/\Omega)$.

8.1.5 Member Unity Checks

Table 8.10 summarizes the governing M_r/M_c and P_r/P_c values and the corresponding unity checks for the single-span frame segments and load combinations considered in this study. The unity checks for load case 3 are conducted only for the rafter segment r8-r9, since LC3 governs the check for this segment but LC1 governs for all of the other segments. The unity check values from both the original design by Chief Buildings and from the prototype procedures are listed in the table. The prototype unity checks are all based on Eqs. 2.5. As a simplification, the largest M_r/M_c and P_r/P_c values are combined in all cases to obtain the values shown in the table. This is slightly different from the procedure outlined in the previous sections, i.e., separate in-plane and out-of-plane unity checks. However, when Eqs. 2.5 are used for both the in-plane and out-of-plane beam-column strength checks, the differences between the simplified single curve and separate in-plane and out-of-plane curves is typically very small. If separate in-plane and out-of-plane unity checks are conducted, the in-plane equations are based on the in-plane P_r/P_c and the governing M_r/M_c values from FLB and TFY, while the out-of-plane equations are based on the out-of-plane P_r/P_c plus the governing M_r/M_c from all three flexural limit states.

The governing unity check values are shaded in Table 8.10. One can observe that the unity checks from the prototype effective length and direct analysis procedures are very close in all cases. However, the direct analysis values are approximately one percent

higher for segment r8-r9. This is due to the fact that the major-axis bending moments calculated by direct analysis are in general slightly higher, while the out-of-plane beam-column resistance equations are the same for both the effective length and the direct analysis methods.

The prototype unity check values are four to twelve percent larger than the Chief Buildings values. The governing unity check for the columns is 1.02 for segment c2-c3 for both of the prototype methods. The corresponding unity check in the original Chief design is 0.92 for segment c2-c3, 10 percent smaller. Also, the governing unity check for the rafter segment in negative bending is 1.10 for both the prototype effective length method and the direct analysis method. The Chief design gives 1.00 for the same segment. The primary reasons for these larger unity check values are:

(1) The differences between the column moments and rafter end moments determined using GT-Sabre and the values determined in the original Chief Buildings design.

(2) The differences between the AISC (2010) checks and the representative AISC (1989) ASD LTB checks implemented by Chief. The Chief unity check calculations are based on a cross-section by cross-section evaluation of Eq. 2.1, using $C_m = 0.85$, $K_i = 1.5$ for the columns and 1.0 for the rafters in determining F_e', and the AISC (1989) prismatic member equations for the flexural resistance using the properties at each cross-section to determine F_b.

For LC1, the first-order GT-Sabre moments are 8 and 7 ft-kips smaller than in the Chief solution (585 versus 593 ft-kips for the columns and 593 versus 600 ft-kips for the rafters), decreases of 1.4 and 1.2 %. However the second-order effects in the direct analysis solution increase the column and rafter end moments from 585 to 605 ft-kips and 593 to

Table 8.10. Unity checks, single-span frame.

		Load Case 1				Load Case 2				Load Case 3			
Location	Method	Governing *Mr*/*Mc*	Governing *Pr*/*Pc*	U.C. AISC(10)	U.C. Chief	Governing *Mr*/*Mc*	Governing *Pr*/*Pc*	U.C. AISC(10)	U.C. Chief	Governing *Mr*/*Mc*	Governing *Pr*/*Pc*	U.C. AISC(10)	U.C. Chief
Seg. c1-c2	Effective Length	0.833	0.190	0.93	0.89	0.483	0.111	0.54	0.51				
	Direct Analysis	0.840	0.189	0.93		0.486	0.111	0.54					
Seg. c2-c3	Effective Length	0.933	0.165	1.02[1]	0.92	0.528	0.095	0.58	0.51				
	Direct Analysis	0.939	0.164	1.02[1]		0.531	0.095	0.58					
Seg. c3-c4	Effective Length	0.901	0.148	0.98	0.93	0.509	0.086	0.55	0.51				
	Direct Analysis	0.907	0.144	0.98		0.512	0.084	0.55					
Seg. r1-r2	Effective Length	1.019	0.170	1.10[2]	1.00	0.567	0.087	0.61	0.54				
	Direct Analysis	1.025	0.153	1.10[3]		0.570	0.078	0.61					
Seg. r8-r9	Effective Length	0.864	0.170	0.95	0.84	0.456	0.087	0.50	0.44	0.938	0.148	1.01	0.90
	Direct Analysis	0.875	0.169	0.96		0.459	0.085	0.50		0.948	0.146	1.02	

[1] 0.99 if LTB end restraint of segment c2-c3 is considered

[2] 1.03 if LTB end restraint of segment r1-r2 is considered

[3] 1.02 if LTB end restraint of segment r1-r2 is considered

613 ft-kips respectively, increases of 3.4 % in both cases. These results are 2.0 and 2.2 % larger than the Chief solution.

Figure 8.8 shows an example comparison of the flexural resistances from AISC (2010) and AISC (1989) versus the unbraced length L_b (K = 1) for a prismatic member composed of the cross-section at location r1 in the rafter. This figure is similar to plots for prismatic members with various cross-section geometries presented by White and Chang (2004). White and Chang illustrate the AISC (2010) flexural resistances for a wide range of member geometries, and show that in most cases, the AISC (2010) resistances are larger than the base AISC (1989) values. In some cases, the AISC (2010) strengths are dramatically larger. However, for prismatic slender-web members with C_b ≅ 1 (near uniform bending), the AISC (2010) curve tends to "chop off" a corner of the base AISC (1989) curve within the inelastic LTB range. The unbraced lengths of many of the segments in the example frames are close to this corner. The AISC (1989) flexural resistance is generally too optimistic in the vicinity of this point. Extensive comparisons to experimental data indicate that the AISC (2010) curves provide a highly accurate characterization of the physical strengths for prismatic members (White and Jung 2004). The AISC (1989) resistance is 7.1 % larger than the AISC (2010) resistance at L_b = 5 ft for the prismatic member example in Figure 8.8. For rafter segment r1-r2 in the single-span frame, C_b = 1.08 based on the compression flange stresses under LC1, and the final resulting M_n is 624 ft-kips. For the hypothetical prismatic members considered in Figure 8.8, M_n = 617 ft-kips for L_b = 5 ft and C_b = 1.0 using the AISC (2010) provisions. As discussed in Chapter 7, the AISC (2010) LTB resistance equations are optimistic based on the virtual test simulations. The cross-section considered in Figure 8.8 has compact

flanges and a slender web with h/b_{fc} = 6.7 ($b_{fc}/2t_{fc}$ = 8 and h/t_w = 160). For this cross-section, the M_n value based on the recommended procedure for L_b = 5ft and C_b = 1.0 is 557 ft-kips, which is 10 % smaller than M_n = 617 ft-kips.

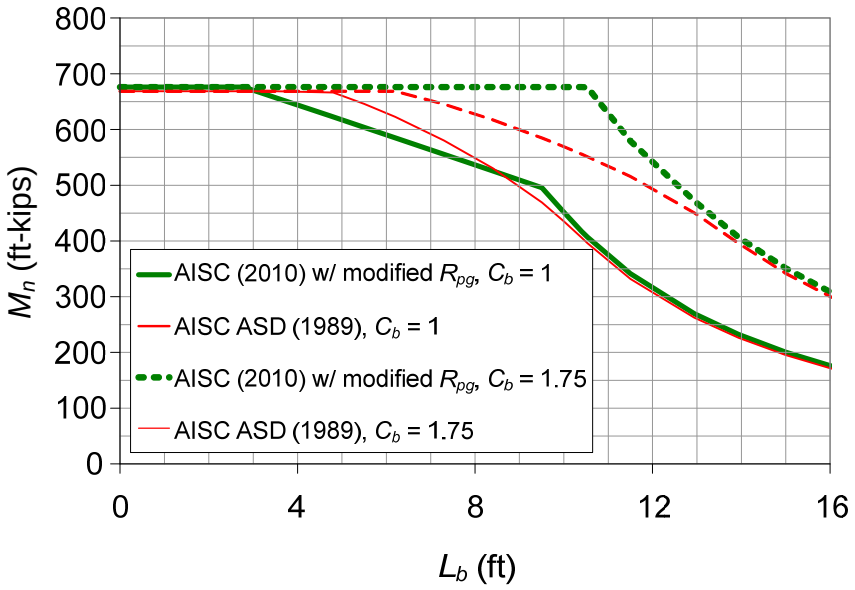

Figure 8.8. Comparison of the AISC (2010) and AISC ASD (1989) flexural resistances for a prismatic member composed of the cross-section at rafter location r1 in the single-span frame (h x t_w = 40 x 1/4 in, b_f x t_f = 6 x 3/8 in).

If one considers the development of the AISC (1989) resistance equations, the reason for their above overprediction of the physical strengths is readily apparent. Figure 8.9 shows the three base equations from AISC (1989) for the example cross-section considered in Figure 8.8. The inelastic LTB resistance in AISC (1989) is quantified by AISC-ASD Eq. (F1-6). This equation is the same, and extends up to an anchor point value (at L_b = 0.0) equal to $1.1R_{PG}M_{yc}$, regardless of the web slenderness. However, the experimental results clearly indicate that the shape and amplitude of the inelastic LTB resistance curve is influenced significantly by the web slenderness (White and Jung 2004).

The virtual test simulation results in Chapter 7 also confirm this effect. The AISC (2010) flexural resistance equations capture the effect of the web slenderness on the inelastic LTB resistance curve.

In addition to the above behavior, the tapered-web member resistance equations in AISC (1989) ASD assume a base elastic LTB resistance accounting fully for both the contributions from warping and St. Venant torsion. That is, the AISC (1989) ASD tapered-web member resistance equations reduce the member flexural resistance due to slender web effects only via the web bend buckling strength reduction factor R_{PG}.

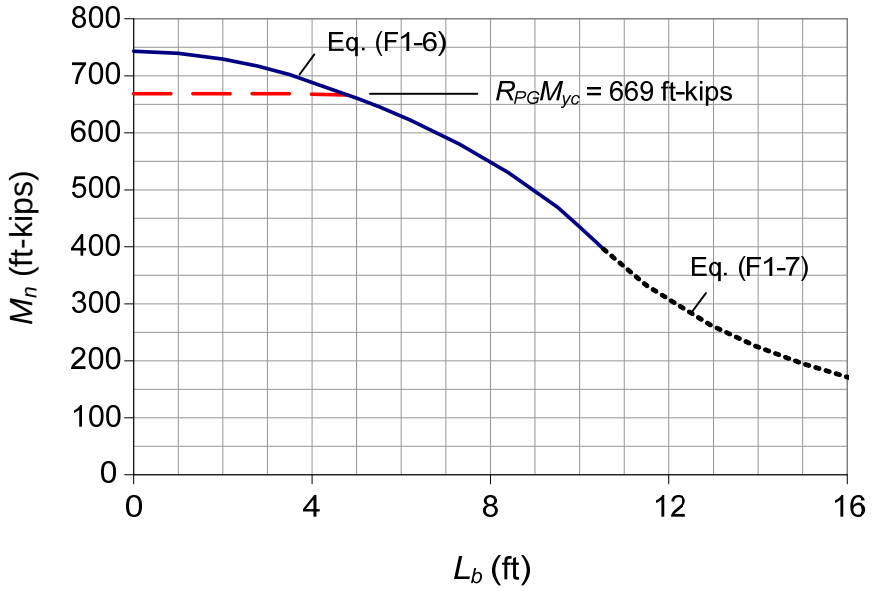

Figure 8.9. AISC (1989) flexural resistance equations, prismatic member composed of the cross-section at rafter location r1 in the single-span frame (h x t_w = 40 x 1/4 in, b_f x t_f = 6 x 3/8 in).

However, for members with slender webs, AISC (2010) effectively uses $J = 0$ in determining the LTB resistance, in addition to the use of a similar strength reduction

factor R_{pg} (Eq. 8.1). White and Jung (2004) and White and Kim (2004) show that this gives an accurate representation of the resistances of slender-web prismatic members.

Figure 8.10 illustrates the AISC (2010) and AISC (1989) flexural resistances versus the unbraced length L_b ($K = 1$) for a representative singly-symmetric prismatic I-section member that has a noncompact web. In this case, one can observe that the AISC (2010) provisions give a more liberal estimate of the flexural resistance for most of the unbraced lengths and uniform bending. For small L_b less than about 6 ft, the resistance of these members is larger in AISC (2010) because the governing maximum moment resistance is larger than the yield moment to the tension flange M_{yt} (due to the noncompact web). AISC (1989) implicitly limits the maximum potential nominal resistance of these members to M_{yt}. For L_b larger than about 10 ft, AISC (2010) gives a larger LTB resistance than the base AISC (1989) prismatic member equations because AISC (1989) does not include the contribution from the St. Venant torsional stiffness for these members. However, for L_b approximately between 7 and 10 ft, AISC (2010) still gives slightly smaller strengths than AISC (1989). This is due to the previously discussed problem that the AISC (1989) Eq. (F1-6) does not include any consideration of the web slenderness effects. If the recommended LTB resistance equations (see Chapter 7) are used for this cross section ($h/b_{fc} = 4$, $h/t_w = 128$, and $b_{fc}/2t_{fc} = 6$), the values of M_n would be 10 % smaller at $L_b = 6$ ft (324 ft-kips) and 16 % smaller at $L_b = 12$ ft (218 ft-kips) than the AISC (2010) resistances for $C_b = 1.0$. As seen in Figure 8.8, for moment gradient and $C_b = 1.75$, AISC (2010) gives a more liberal estimate of the cross-section flexural resistances for all unbraced lengths than AISC (1989).

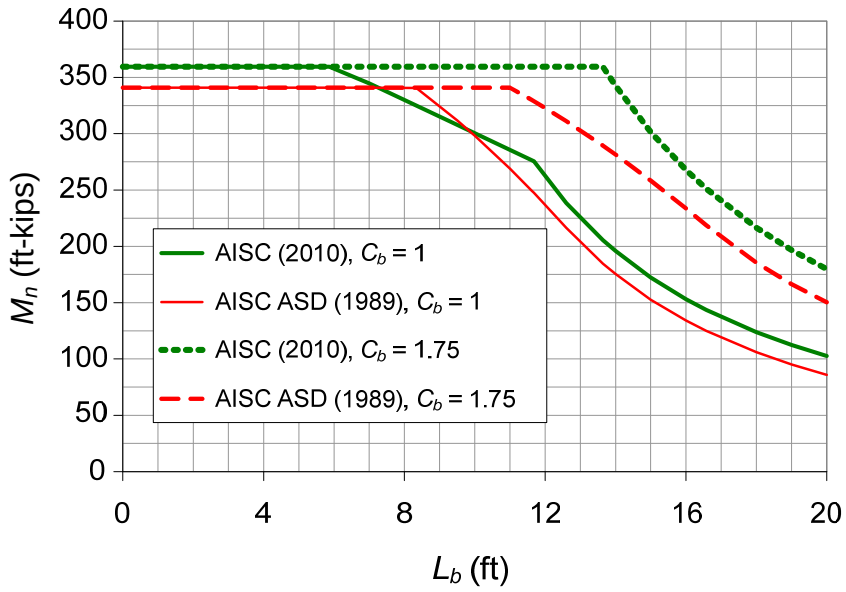

Figure 8.10. Comparison of the AISC (2010) and AISC ASD (1989) flexural resistances for a prismatic member with h x t_w = 24 x 3/16 in, b_{fc} x t_{fc} = 6 x 1/2 in, b_{ft} x t_{ft} = 6 x 3/8 in and F_y = 55 ksi.

As noted previously, more liberal and more representative unity checks are obtained generally if the LTB restraint from adjacent less critical segments is considered in the evaluation of the γ_{eLTB} values. Based on inspection of Tables 8.7 and 8.8, one can observe that the short column segment c3-c4 should provide substantial restraint to the middle segment c2-c3. In fact, this restraint should be enough to easily increase the LTB resistance for c2-c3 such that the TFY limit state governs. Under this scenario, the unity checks for this segment under LC1 become

0.165/2 + 0.903 = 0.99 by the effective length method and

0.164/2 + 0.909 = 0.99 by the direct analysis method

(versus 0.92 in the original Chief design). The differences in these unity checks with the Chief value are due largely to the slightly greater moment calculated at the knee of the frame in GT-Sabre (see Tables 8.2 and 8.3).

Similarly, some additional benefit can be expected by accounting for the restraint at the end of the rafter segment r1-r2 from the adjacent segment r2-r3. In this case, $M_{n(FLB)} = R_{pg(FLB)}M_{yc}$ since the flanges are compact. Assuming sufficient end restraint to develop the FLB moment capacity, the unity checks for segment r1-r2 under LC1 become

0.170/2 + 0.940 = 1.03 by the effective length method and

0.153/2 + 0.946 = 1.02 by the direct analysis method

versus 1.00 in the original Chief design.

8.1.6 Virtual Test Simulation Results

The virtual test simulation of the example frame systems are conducted using ABAQUS. Since the entire framing system is analyzed, the application of the appropriate imperfection shapes is crucial in order to capture the real physical behavior of the frame. As discussed in the beginning of this chapter, the geometric imperfections are applied at the location where the design-checks are relatively large for LC1. For the single-span frame, the eigenvalue buckling mode shapes that involve with the web buckling of the segments c3-c4 and r1-r2, the region near the ridge and the panel zone are selected. Since all the eigenvalue buckling modes show mainly the web local buckling, the flange sweep imperfection is also generated. The flange sweep with the amplitude of $L_b/1000$ is applied on the compression flanges of the segments c3-c4, r1-r3, and r9-r10.

Figure 8.11 shows the von Mises and equivalent plastic strain contours with the deformed shape of the single-span frame at the peak load. At the peak load, the members in the frame have not been yielded significantly. The web panels of the segments c2-c3 and c3-c4 are yielded close to the outside flanges mainly due to the large residual stresses along the web-flange juncture areas. The failure of the single-span frame is dominated

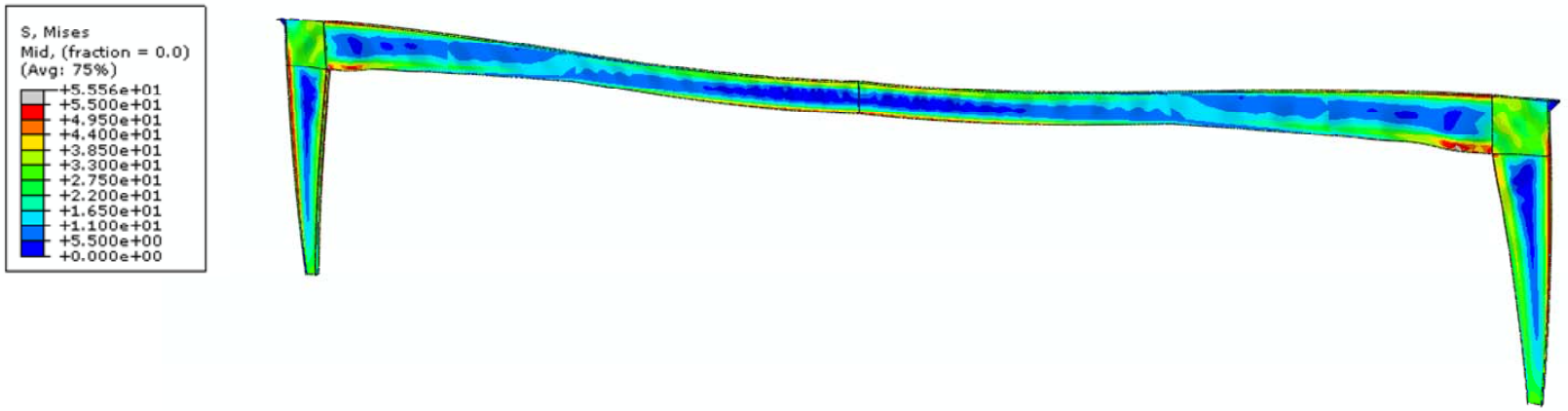

(a) von Mises stress contour at peak load

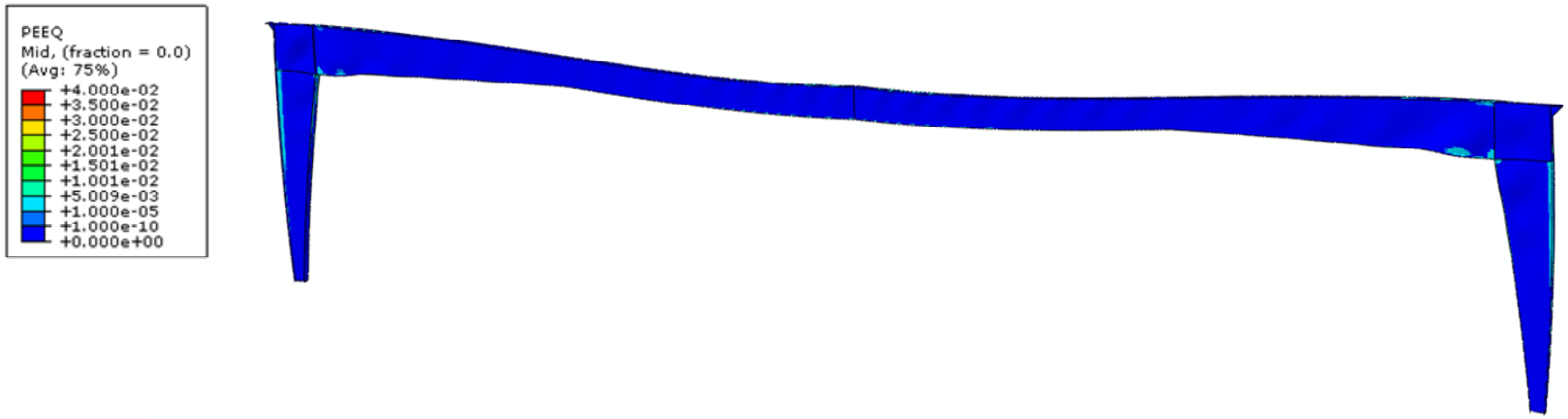

(b) Equivalent plastic strain contour at peak load

Figure 8.11. von Mises stress and equivalent plastic strain contours at peak load (deformation scale factor = 5).

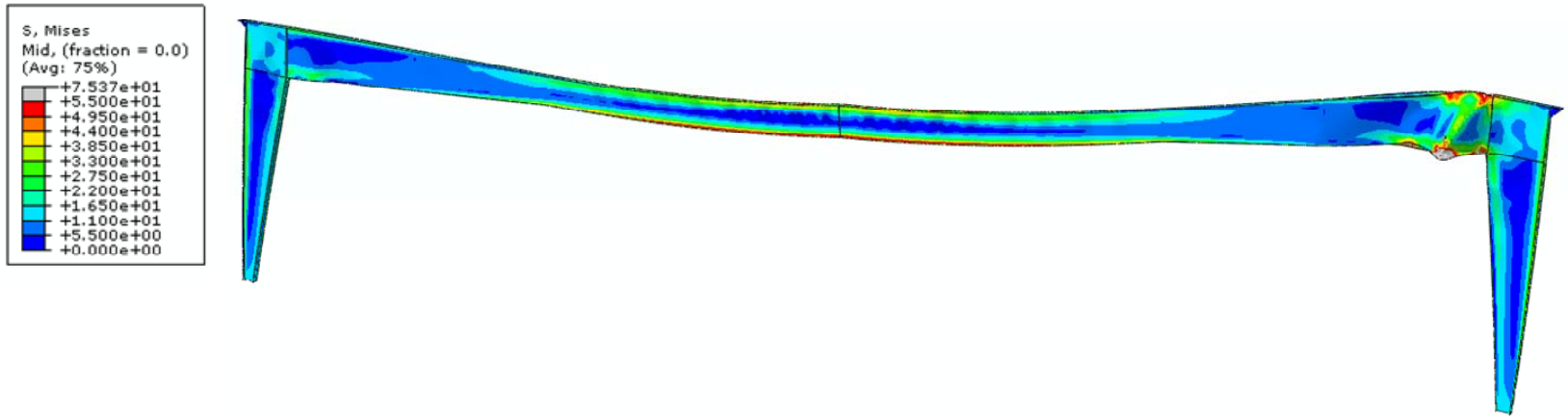

(a) von Mises stress contour at the end of analysis

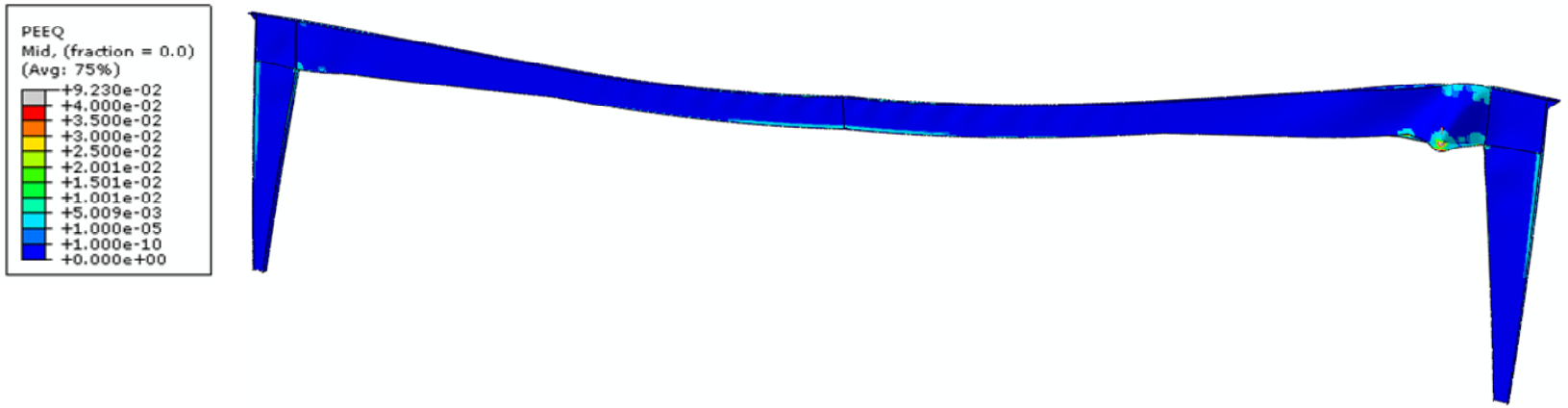

(b) Equivalent plastic strain contour at the end of analysis

Figure 8.12. von Mises stress and equivalent plastic strain contours at the end of the analysis (deformation scale factor = 5).

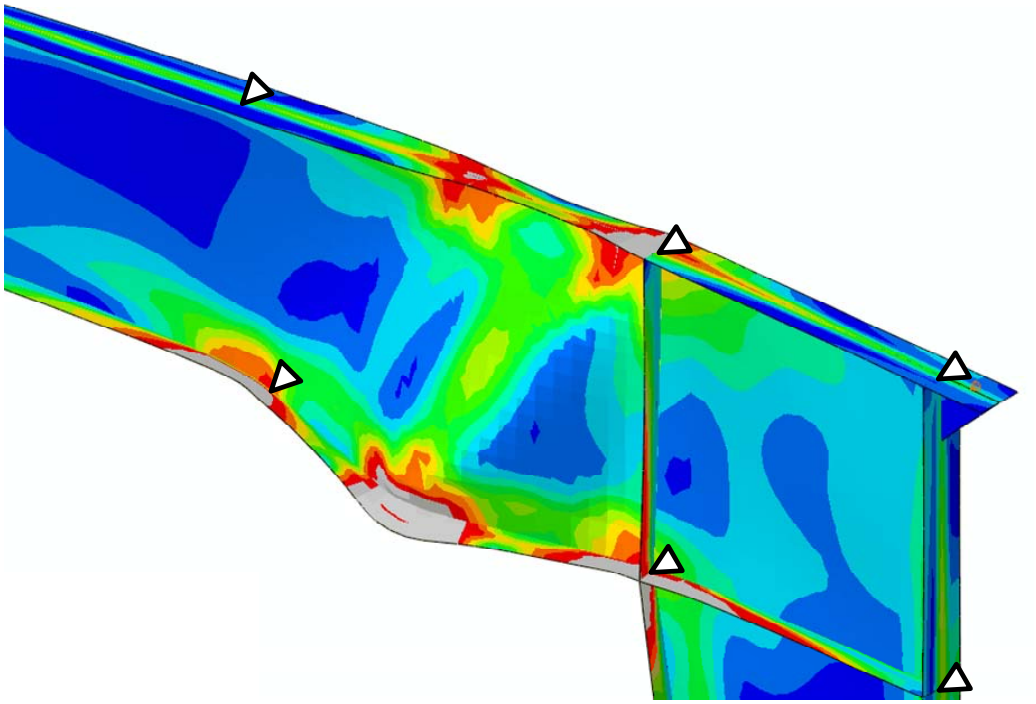

Figure 8.13. von Mises contour and deformed shape of the segment r1-r2 on the leeward side at the end of analysis (deformed scale factor = 2).

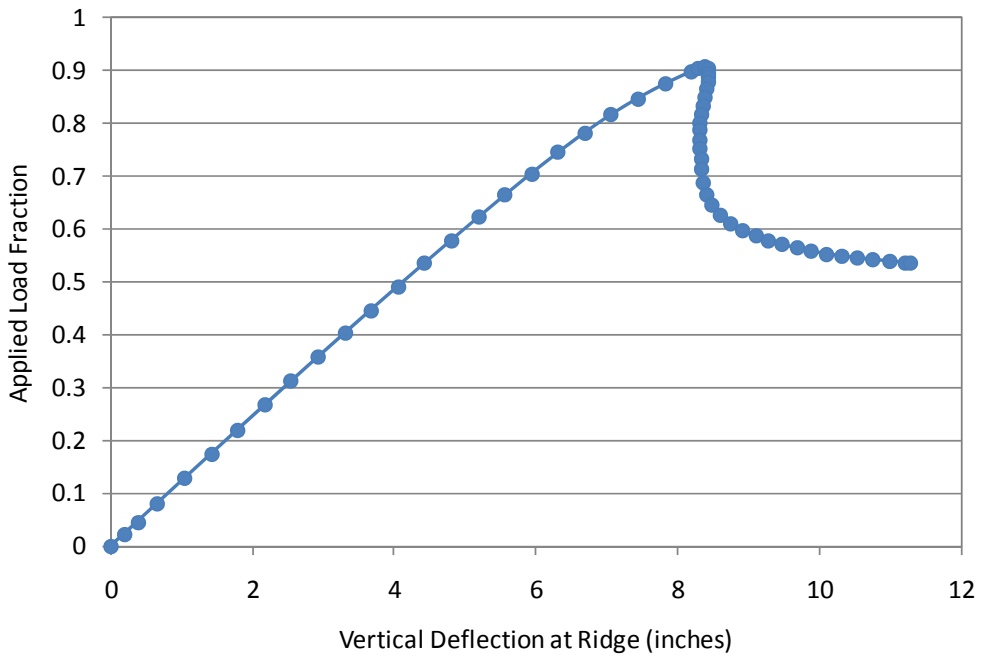

Figure 8.14. Load vs. deflection plot of the virtual test of the single-span frame

by the member local buckling of the segment r1-r2 on the leeward side. This can be seen clearly in Figure 8.12, which shows the same response contours at the end of the analysis. One can see the segment r1-r2 has a lateral torsional buckling failure on the compression flange. It should be noted that the segment r1-r2 is the most critical segment based on the design checks for LC1 (see Table 8.10). Furthermore, the LTB limit state governs the flexural load ratio of the segment r1-r2 in Table 8.7. The load-deflection plot using the vertical deflection at the ridge is shown in Figure 8.14.

One can calculate that the LRFD load combination of LC1 ($1.2D + 1.2C + 1.6S$) is the same as 1.52 ($D + C + S$) for the clear span frame based on the load ratio $S/(D+C)$ = 21/4.96 = 4.23. Based on Appendix 1 in AISC (2010), the inelastic analysis should be conducted using $0.9F_y$ and $0.9E$. One can show that comparing the nominal design resistances to inelastic analysis results with $0.9F_y$ and $0.9E$ is the same as comparing (1/0.9) times nominal design resistances to inelastic analysis results with nominal F_y and E. In Figure 8.14, the ordinate is the normalized applied load fraction of the LRFD load combination of LC1 divided by $\phi_b = 0.9$, i.e., $1/0.9 \times (1.2D + 1.2C + 1.6S)) = 1/0.9 \times 1.52(D + C + S) = 1.69(D + C + S)$. It can be seen that the ABAQUS results show that the single-span frame develops 91% of the LRFD strength limit load.

It should be noted that AISC (2010) requires to use LRFD for a rigorous analysis (Appendix 1 in AISC 2010). For this reason, the results shown in this section are not directly comparable to the unity checks shown in Table 8.10. However, one can observe that approximately the governing unity check value of 1.10 for r1-r2 in Table 8.10 indicates the clear span frame reaches its limit state at 1/U.C. = 1/1.10 = 0.91 of the design load. It should be noted that in general, the calculation of 1/U.C to approximate

the limit load of a given structure is not valid because of the 2nd-order effects. However, since the clear span frame has small 2nd-order effects, the limit load can be estimated approximately by 1/U.C. If the recommended calculations for lateral torsional buckling are applied, the governing unity check value is larger than 1.10.

8.2 Modular Frame

8.2.1 Overview

Figure 8.15 shows an elevation view of the modular frame design. Table 8.11 summarizes the specific web and flange geometries for the 14 different lengths (A-N) in this frame. The modular frame uses a doubly-symmetric tapered section for its exterior columns. The exterior column web is nominally 1/8 in thick and the total column depth tapers from d = 10 in at the base to d = 25 in at the bottom of the knee joint. This gives a web slenderness ranging from h/t_w = 76 at the column base to 196 at the top of the column. The column flanges are 6 x 1/4 in ($b_f/2t_f$ = 12), which makes them noncompact in flexure and slender in uniform axial compression by the AISC (2010) flange local buckling criteria. The rafters are composed mostly of doubly-symmetric cross-sections, but lengths F, G, L and M are singly-symmetric. All the rafter flanges are 6 in wide.

Lengths C, D and E in the exterior span of the rafters are all doubly-symmetric and prismatic with 1/4 in thick flanges and 25 in total depth. Length F is singly-symmetric and has a 5/16 in top flange ($b_f/2t_f$ = 9.6, noncompact in flexure and slender in uniform axial compression) and a 3/8 in compact bottom flange ($b_f/2t_f$ = 8). Also, this length has a mild linear taper from d = 25 to 26 in at the first interior column. The webs for lengths C and E are 5/32 in thick, such that their h/t_w is 157, whereas length D has a thinner 1/8 in thick web (h/t_w = 196) and length F has a thicker 3/16 in web (h/t_w = 130 to 135).

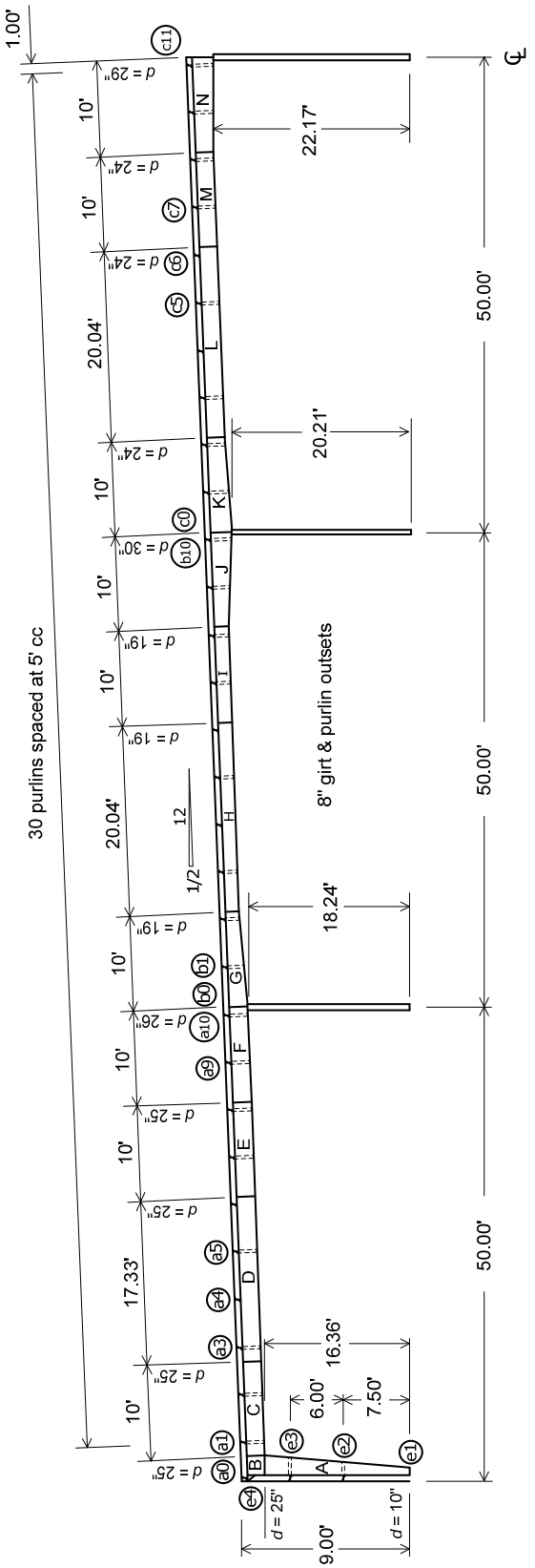

Figure 8.15. Elevation view of modular frame

Table 8.11. Summary of web and flange geometry, modular frame[1].

Length	Location	Web				Inside Flange			Outside Flange		
		d (in)	t_w (in)	h/t_w	h_c/t_w	b_f (in)	t_f (in)	$b_f/2t_f$	b_f (in)	t_f (in)	$b_f/2t_f$
A	e1	10.00	1/8	76		6.0	1/4	12.0	6.0	1/4	12.0
	e2	16.88		131							
	e3	22.38		175							
	e4	25.00		196							
B			5/32								
C	a0-a2'	25.00	5/32	157		6.0	1/4	12.0	6.0	1/4	12.0
D	a2'-a6'	25.00	1/8	196		6.0	1/4	12.0	6.0	1/4	12.0
E	a6'-a8'	25.00	5/32	157		6.0	1/4	12.0	6.0	1/4	12.0
F	a8'	25.00	3/16	130	124	6.0	3/8	8.0	6.0	5/16	9.6
	a9	25.41		132	126						
	a10	25.91		135	129						
	b0	26.00		135	129						
G	b0	26.00	3/16	135	129	6.0	3/8	8.0	6.0	5/16	9.6
	b1	23.13		120	114						
	b2	19.64		101	96						
	b2'	19.00		98	92						
H	b2'-b6'	19.00	5/32	118		6.0	1/4	12.0	6.0	1/4	12.0
I	b6'-b8'	19.00	1/8	148		6.0	1/4	12.0	6.0	1/4	12.0
J	b8'	19.00	3/16	98		6.0	5/16	9.6	6.0	5/16	9.6
	b9	23.46		122							
	b10	28.96		151							
	c0	30.00		157							
K	c0	30.00	3/16	157		6.0	5/16	9.6	6.0	5/16	9.6
	c1	27.57		144							
	c2	24.57		128							
	c2'	24.00		125							
L	c2'-c6'	24.00	3/16	123	133	6.0	1/2	6.0	6.0	3/8	8.0
M	c6'-c8'	24.00	3/16	123	133	6.0	1/2	6.0	6.0	3/8	8.0
N	c8'	24.00	7/32	107		6.0	1/4	12.0	6.0	1/4	12.0
	c9	26.00		117							
	c10	28.50		128							
	c11	29.00		130							

[1] The prime marks on the location symbols indicate positions corresponding to a cross-section transition. The symbols without prime marks represent purlin locations as shown in Figure 8.11.

The first interior span starts with length G. This length has a substantial taper from the 26 in depth at the first interior column to d = 19 in at 10 ft inside of this column. It has a larger compact bottom (compression) flange (t_f = 3/8 in, $b_f/2t_f$ = 8), a 5/16 in thick top flange, and a 3/16 in thick web. Lengths H and I are prismatic and each has 1/4 in thick flanges and 19 in total section depth. Length H uses a 5/32 in thick web (h/t_w =

118) whereas length I has a 1/8 in thick web (h/t_w = 148). Length J completes the first interior span by tapering the depth from d = 19 in at 10 ft outside the second interior column to d = 30 in at this column. It has a 3/16 in web, giving h/t_w from 98 to 157. It has equal-size 5/16 in thick flanges ($b_f/2t_f$ = 9.6).

The inner-most span starts with a taper within length K from d = 30 in at the second interior column to d = 24 in at 10 ft inside of this column. Its web is 3/16 in thick, giving h/t_w = 157 to 125, and its flanges are the same thickness as those of length J (5/16 in). Lengths L and M are prismatic singly-symmetric sections with d = 24 in, t_w = 3/16 (h/t_w = 123), and t_f = 3/8 and 1/2 in for their top and bottom flanges. Lastly, length N has a taper from d = 24 in at 10 ft inside the center column up to d = 29 in at the center column. It has a 7/32 in web, giving a range for its web slenderness of h/t_w = 107 to 152. Its flanges are the same size with t_f =1/4 in.

Based on the above proportions, the member webs are classified as slender both under flexure and under compression within a large number of the unbraced segments in the modular frame; however, the webs within lengths F, G, H and N, and segments b8'-b9 in length J and c2 to c2' in length K are classified as noncompact under flexure.

The outside flanges of the columns and rafters of the modular frame are supported laterally by the girts or purlins. Diagonal braces to the inside flanges are indicated by double dashed lines in Figure 8.15. The purlins are spaced at 5 ft on center except at the knee of the frame, and girts are located at 7.5 and 6 ft spacing starting from the base of the exterior columns. Both of the column flanges are braced laterally at the two girt locations. The bottom flange of the rafters is unsupported at two of the purlin locations within the positive moment region of each of their spans (at locations a4, a6, b4, b6, c4

and c6), but otherwise both flanges are laterally restrained at each purlin. The exterior spans of the rafters and the tops of the exterior columns are assumed to be braced laterally at the panel zone edges at the knee of the frame (locations a0 and e4).

Similar to the procedure for the single-span frame, the straight reference axes are used to create the finite element model in GT-Sabre. For the modular frame, a straight line connecting the cross-section centroids of e1 and e4 is used for the exterior columns. For the rafters, a straight line is determined based on the 0.5/12 roof slope and the cross-section centroid of a1. As mentioned above, the changes in the GT-Sabre analysis due to the use of the reference axes rather than the centroidal axes is negligible.

Results from each of the considered load combinations for the bending moment at the top of the exterior columns, the axial force in the exterior columns, and the maximum positive and negative bending moments and the corresponding axial forces in each of the rafter spans, are provided in the following section. This is followed by a presentation of the analysis and design assessments by the effective length and direct analysis methods for the exterior columns and for the following rafter segments:

- Length D, segment a3-a5: This segment is prismatic and has a doubly-symmetric slender-web cross-section subjected to positive bending moment. The unbraced length for its bottom flange is two times that for its top flange. Its flanges are noncompact in flexure and slender under uniform axial compression.
- Length F, segment a9-a10: This segment has a relatively mild taper and a singly-symmetric slender-web cross-section with a larger bottom flange. It is subjected to negative bending moment and its flanges have equal unbraced lengths. This segment

has a compact bottom flange in flexure, but its top flange is slender under uniform axial compression.

- Length G, segment a10-b1: This segment has a relatively large taper and a singly-symmetric slender-web cross-section with a larger bottom flange. Also, this segment is subjected to negative bending moment. Its flanges are the same as in F and have equal unbraced lengths.
- Length L, segment c5-c7: This segment is prismatic, but has a singly-symmetric slender-web cross-section with a larger bottom (tension) flange. It is subjected to positive bending moment and has an unbraced length for its bottom flange of two times that for its top flange. Both of its flanges are compact.

The exterior columns for the modular frame are doubly-symmetric slender-web sections with a relatively mild web taper and equal unbraced lengths for both flanges. Both of their flanges are noncompact under flexure and slender under uniform axial compression.

8.2.2 First-Order and Second-Order Elastic Analysis Results

Table 8.12 presents the linear elastic analysis reactions and member internal axial forces and moments generated in the original design of the modular frame by Chief Buildings and in the solutions conducted in this study using GT-Sabre. These forces and moments are at 1.6 of the ASD load levels, where $\alpha = 1.6$ is the required factor for the subsequent consideration of second-order effects. Where the axial forces and moments differ in the left or right column or rafter, the larger values are reported. The axial force and moment in both columns are reported for load cases 3, 4a and 4b. Column 1 and rafter 1 are the members on the left-hand side of the ridge in the elevation view of the frame whereas column 2 and rafter 2 are on the right-hand side. The maximum first-order elastic moment values are highlighted in the table.

Table 8.12. Linear elastic analysis forces and moments, modular frame, $\alpha = 1.6^{*}$.

Load Case 1		Chief	GT-Sabre	Difference
Reactions	R_y (kips)	25.6	25.7	0.6%
	R_x (kips)	7.8	7.9	0.4%
Columns	P_{max} (kips)	25.9	26.0	0.3%
	M_{max} (ft-kips)	111	113	1.3%
Rafter Spans a	P_{max} (kips)	8.7	8.8	0.8%
	M_{max}^{-} (ft-kips)	-263	-259	-1.6%
	M_{max}^{+} (ft-kips)	126	126	0.5%
Rafter Spans b	P_{max} (kips)	9.8	8.9	-8.6%
	M_{max}^{-} (ft-kips)	-263	-259	-1.6%
	M_{max}^{+} (ft-kips)	77.1	80.8	4.7%
Rafter Spans c	P_{max} (kips)	9.5	8.9	-6.2%
	M_{max}^{-} (ft-kips)	-248	-244	-1.5%
	M_{max}^{+} (ft-kips)	108	109	1.6%

Load Case 2		Chief	GT-Sabre	Difference
Vertical Reactions	R_{y1} (kips)	12.2	11.8	-2.6%
	R_{y2} (kips)	15.5	15.5	0.0%
	ΣR_y (kips)	27.7	27.4	-1.2%
Horizontal Reactions	R_{x1} (kips)	2.1	2.2	6.6%
	R_{x2} (kips)	-6.7	-6.9	2.6%
	ΣR_x (kips)	-4.6	-4.7	0.8%
Columns	P_{max} (kips)	15.8	15.7	-0.7%
	M_{max} (ft-kips)	72.3	76.4	5.7%
Rafter Spans a	P_{max} (kips)	4.2	4.3	2.3%
	M_{max}^{-} (ft-kips)	-151	-149	-1.1%
	M_{max}^{+} (ft-kips)	69.9	70.8	1.2%
Rafter Spans b	P_{max} (kips)	4.0	3.7	-8.3%
	M_{max}^{-} (ft-kips)	-151	-149	-1.1%
	M_{max}^{+} (ft-kips)	45.9	47.6	3.6%
Rafter Spans c	P_{max} (kips)	3.1	2.9	-7.6%
	M_{max}^{-} (ft-kips)	-150	-148	-1.0%
	M_{max}^{+} (ft-kips)	69.4	69.2	-0.3%

* The cells corresponding to the maximum moments are shaded.

Table 8.12 (continued). Linear elastic analysis forces and moments, modular frame, $\alpha = 1.6^{*}$.

Load Case 3		Chief	GT-Sabre	Difference
Reactions	R_{y1} (kips)	12.8	12.8	0.2%
	R_{y2} (kips)	25.1	25.3	0.8%
	ΣR_y (kips)	37.9	38.1	0.6%
	R_x (kips)	5.8	5.9	2.1%
Column 1	P_{max} (kips)	13.0	13.0	0.2%
	M_{max} (ft-kips)	87.4	88.2	1.0%
Column 2	P_{max} (kips)	25.4	25.5	0.3%
	M_{max} (ft-kips)	79.5	80.4	1.1%
Rafter 2	P_{max} (kips)	6.7	6.8	0.5%
Span a	M_{max}^{-} (ft-kips)	-246	-242	-1.8%
	M_{max}^{+} (ft-kips)	152	153	0.4%
Rafter 2	P_{max} (kips)	7.7	6.9	-10.8%
Span b	M_{max}^{-} (ft-kips)	-323	-315	-2.3%
	M_{max}^{+} (ft-kips)	54.4	57.8	6.3%
Rafter 2	P_{max} (kips)	8.6	7.6	-12.0%
Span c	M_{max}^{-} (ft-kips)	-323	-315	-2.3%
	M_{max}^{+} (ft-kips)	252	254	0.5%

Load Case 4a		Chief	GT-Sabre	Difference
Reactions	R_{y1} (kips)	26.2	26.0	-0.9%
	R_{y2} (kips)	16.8	16.9	0.4%
	ΣR_y (kips)	43.0	42.9	-0.4%
	R_x (kips)	6.9	6.8	-0.5%
Column 1	P_{max} (kips)	26.5	26.2	-1.2%
	M_{max} (ft-kips)	95.2	95.8	0.7%
Column 2	P_{max} (kips)	17.0	17.1	0.3%
	M_{max} (ft-kips)	101.1	101.6	0.4%
Rafter 1	P_{max} (kips)	7.8	7.8	0.1%
Span a	M_{max}^{-} (ft-kips)	-213	-209	-1.6%
	M_{max}^{+} (ft-kips)	157	159	1.0%
Rafter	P_{max} (kips)	8.1	7.6	-7.1%
Spans b	M_{max}^{-} (ft-kips)	-213	-209	-1.6%
	M_{max}^{+} (ft-kips)	48.8	52.1	6.7%
Rafter	P_{max} (kips)	7.9	7.5	-4.8%
Spans c	M_{max}^{-} (ft-kips)	-154	-151	-2.0%
	M_{max}^{+} (ft-kips)	74.2	76.6	3.1%

* The cells corresponding to the maximum moments are shaded.

Table 8.12 (continued). Linear elastic analysis forces and moments, modular frame, $\alpha = 1.6^{*}$.

Load Case 4b		Chief	GT-Sabre	Difference
Reactions	R_{y1} (kips)	24.6	24.3	-1.2%
	R_{y2} (kips)	16.5	16.6	0.7%
	ΣR_y (kips)	41.1	40.9	-0.4%
	R_x (kips)	6.1	6.2	2.4%
Column 1	P_{max} (kips)	24.8	24.5	-1.1%
	M_{max} (ft-kips)	85.3	86.7	1.6%
Column 2	P_{max} (kips)	16.7	16.8	0.4%
	M_{max} (ft-kips)	90.4	91.6	1.3%
Rafter 1	P_{max} (kips)	7.0	7.1	0.7%
Span a	M_{max}^{-} (ft-kips)	-283	-279	-1.4%
	M_{max}^{+} (ft-kips)	132.6	132.0	-0.5%
Rafter 1	P_{max} (kips)	8.2	7.3	-10.9%
Span b	M_{max}^{-} (ft-kips)	-283	-279	-1.4%
	M_{max}^{+} (ft-kips)	86.7	88.0	1.5%
Rafter	P_{max} (kips)	7.3	6.9	-5.0%
Spans c	M_{max}^{-} (ft-kips)	-212	-209	-1.4%
	M_{max}^{+} (ft-kips)	71.4	70.9	-0.6%

* The cells corresponding to the maximum moments are shaded.

Figures 8.16 through 8.19 show the distributions of the applied wind, unbalanced snow and patterned snow loadings on the modular frame. The other loadings are uniformly distributed and are summarized at the beginning of this chapter. Load case 4a involves 100 % of the snow load on one of the exterior spans (spans a) combined with 50 % of the snow load on all the other spans, whereas load case 4b involves 100 % of the snow load on one exterior span and the adjacent interior span (span b) along with 50 % of the snow load on all the other spans. For purposes of discussion, the unbalanced snow load is placed on the right-hand side of the ridge for LC3 whereas the maximum snow load is applied on the left-hand side of the ridge in LC4a and LC4b. Therefore, the notional lateral loads for the effective length method analysis, and the notional frame

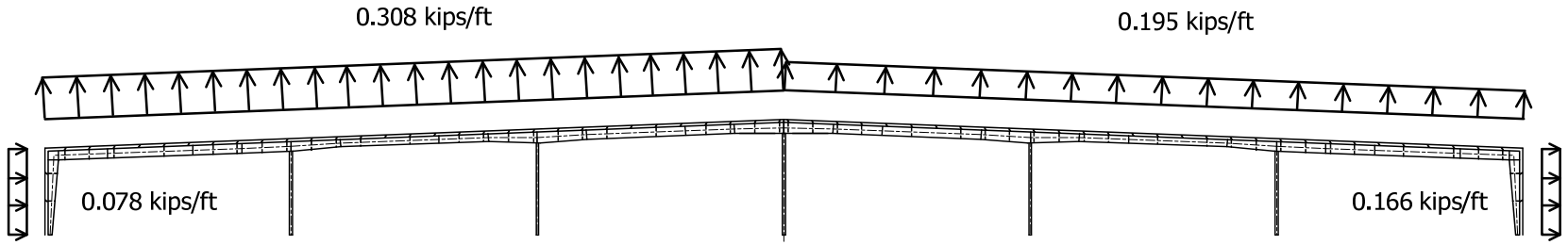

Figure 8.16. Wind load distribution (wind from left), modular frame.

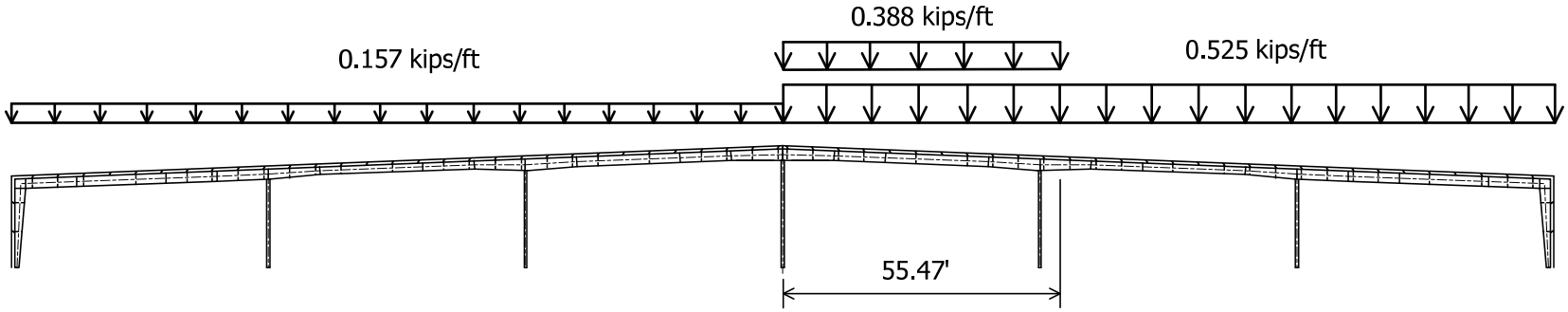

Figure 8.17. Unbalanced snow load distribution, modular frame.

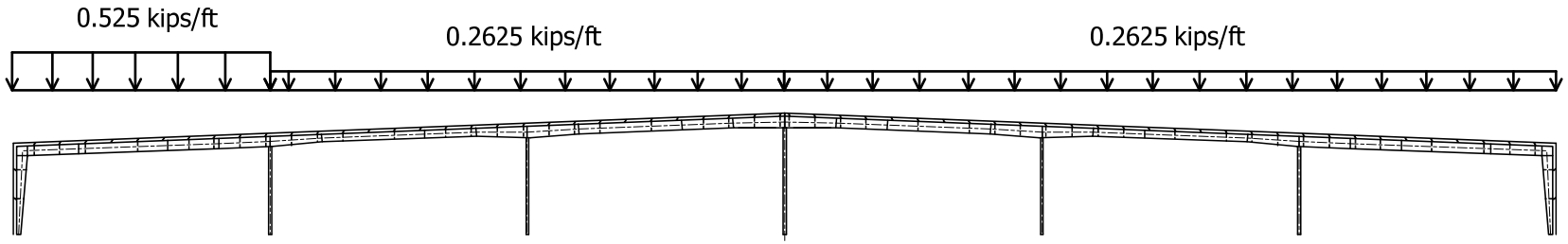

Figure 8.18. Patterned snow load distribution in load case 4a (100 % of snow load on one exterior span combined with 50 % of the snow load on all the other spans).

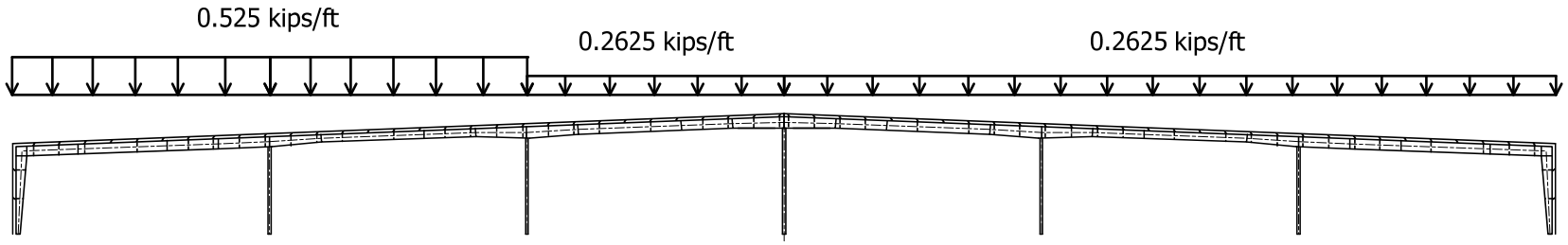

Figure 8.19. Patterned snow load distribution in load case 4b (100 % of snow load on one exterior span and the adjacent span combined with 50 % of the snow load on all other spans).

out-of-plumbness for calculation of the required internal forces in the direct analysis solution, are applied to the left for LC3 whereas they are applied to the right for load cases 4a and 4b. These are the directions that the frame tends to drift under the applied loadings.

Similar to the comparisons for the single-span frame, the results from the analyses conducted by Chief Buildings and by GT-Sabre are very close to one another. The largest difference in the calculated moments is 6.7 % (for the LC4a maximum positive moment in the first interior span, spans b). However, this M_{max}^{+} value is not the maximum governing positive moment for this span. The cells for the governing maximum linear elastic moments are shaded in the table. The largest difference between the Chief and GT-Sabre results for these moments is 2.3 % (M_{max}^{-} for LC3, rafter 2, span c). The percentage differences are somewhat larger for some of the axial loads in the rafters. However, the rafter axial compression is generally quite small, and therefore these differences are inconsequential.

The amplification of the sidesway deflections and moments is relatively large in the modular frame. Since the axial compression in the rafters is rather minor and the incline of the exterior columns is small, the AISC (2010) story-stiffness based method can be used to obtain a reasonable estimate of the sidesway amplifier for this structure.

However, the equations presented in the AISC (2010) commentary are based on the assumption of rectangular frame geometry. They need to be generalized for unequal column heights before they can be applied to the example modular frame. The recommended general equations are as follows:

$$\Delta_{2nd} = B_2 \Delta_{1st} \quad \text{and} \quad M_{lt.2nd} = B_2 M_{lt} \qquad \text{(Eq. 8.2a)}$$

where:

Δ_{2nd} = second-order sidesway displacement

Δ_{1st} = first-order sidesway displacement

$M_{lt.2nd}$ = second-order sidesway moment

M_{lt} = first-order moment due to sidesway (lateral translation)

$$B_2 = \frac{1}{1 - \frac{\alpha}{\gamma_{e.story}}} \qquad \text{(Eq. 8.2b)}$$

$$\gamma_{e.story} = \frac{(0.85 + 0.15R_L)\Sigma(H_i / \Delta_H)}{\Sigma_{all}(P_i / L_i)} \qquad \text{(Eq. 8.2c)}$$

= story elastic buckling load ratio

P_i = axial load in column i

L_i = length of column i

H_i = horizontal force in column i due to the applied load H (note that due to the inclination of the columns, H_i differs somewhat from the column shear force)

$$R_L = \frac{\Sigma_{leaner}(P_i / L_i)}{\Sigma_{all}(P_i / L_i)} \qquad \text{(Eq. 8.2d)}$$

The summation symbol Σ_{leaner} indicates summation over all of the leaning columns whereas the symbol Σ_{all} indicates summation over all the columns of the story.

For load case 1, the required column axial forces (with the columns numbered from 1 to 7 from left to right, calculated using linear elastic analysis at $\alpha = 1.0$) are $P_1 = P_7 = 16.2$ kips, $P_2 = P_6 = 35.1$ kips, $P_3 = P_5 = 34.2$ kips and $P_4 = 33.0$ kips. The column lengths are taken as $L_1 = L_7 = 17.36$ ft, $L_2 = L_6 = 19.37$ ft, $L_3 = L_5 = 21.46$ ft and $L_4 = 23.54$ ft (the lengths from the column bases to the rafter reference axis in GT-Sabre). For

a total unit horizontal load H = 1 kip, one-half applied at the top of each of the exterior lateral load resisting columns, the first-order side-sway displacement Δ_H is 0.314 in. By substituting the above values into Eqs. 8.2, one obtains

$\gamma_{e.story}$ = 3.69

B_2 = 1.37 at the ASD working load level (α = 1.0), and

B_2 = 1.77 at the strength load level (α = 1.6).

The elastic buckling load ratio is γ_{ex} = 3.87 based on a rigorous eigenvalue buckling analysis of the complete structure.

Since the amplification of the sidesway displacements $B_2 = \Delta_{2nd}/\Delta_{1st}$ is larger than 1.5 at the strength load level (α = 1.6), AISC (2010) disallows the use of the effective length method for LC1 in this frame. This is due to the fact that in some cases, the internal forces and moments are significantly underestimated in frames having a sidesway amplification this large. The cantilever beam-column previously discussed in Section 2.6.1 is a simple example that illustrates this issue. Nevertheless, a large fraction of the LC1 moments in the modular frame are due to gravity loadings and are thus not affected by B_2. Although AISC (2010) provides a user note that suggests the application of B_2 to the total moments as a simple conservative procedure, this practice would lead to substantially conservative results for the modular frame. For this type of frames, the methods to conduct a simple approximate second-order analysis suggested by Kuchenbecker et al. (2004) and White et al. (2007a & b) would provide better results.

Another reason for disallowing the AISC (2010) effective length method for structures with $B_2 > 1.5$ is that the rigorous application of this approach can lead to significantly conservative results for frames with large sidesway amplification but in

which the internal moments are dominated by non-sway bending. This is the case for the modified DP-13 example summarized in Section 2.6.2 and it is the case for the example modular frame.

As noted previously in Section 1.1, Cary and Murray (1997) recommend a simplified K factor equation for the columns in frames composed of general non-prismatic members. The method is very similar to the effective length factor associated with the AISC (2010) story-stiffness based approach. The Cary and Murray equation can be expressed for frames with unequal height columns as

$$K_i = \sqrt{\frac{\pi^2 EI_{oi}}{P_i L_i^2}\left[\frac{\Sigma\left(P_i / L_i\right)}{60\Sigma\left(EI_{oi} / L_i^3\right)} + \frac{\Sigma\left(P_i / L_i\right)}{\Sigma\left(H_i / \Delta_H\right)}\right]} \qquad \text{(Eq. 8.3a)}$$

where I_{oi} is the smallest moment of inertia along the length of column "*i*", i.e., the moment of inertia at the base of a linearly-tapered column, K_i is the effective length factor referenced to the Euler load $\pi^2 EI_{io}/L_i^2$ for a prismatic column having a moment of inertia of I_{oi}, and the other terms are as defined above. The Cary and Murray equation is an extension of Lui's (1992) developments for prismatic frame members to members with linear web tapers. Equation 8.3a can be substituted into the expression

$$P_{ei} = \frac{\pi^2 EI_{oi}}{(K_i L_i)^2} \qquad \text{(Eq. 8.3b)}$$

to determine the contribution of column "*i*" to the total sidesway buckling resistance. For a symmetric frame with only two (exterior) lateral load resisting columns, each of the same height (but with the interior leaner columns having a different height), an additional simplification suggested by Cary and Murray can be invoked such that Eq. 8.3a can be written as

$$K_{ext} = \sqrt{\frac{\pi^2 EI_{oext}}{P_{ext}L_{ext}^2}\left[\frac{P_{ext}L_{ext}^2}{60EI_{oext}} + \frac{\Sigma(P_i / L_i)}{\Sigma(H_i / \Delta_H)}\right]} \qquad \text{(Eq. 8.3c)}$$

where P_{ext} is the axial load in the exterior columns at the ASD load combination level, L_{ext} is the length of the exterior columns, and I_{oext} is the moment of inertia at the bottom of these columns. For the example modular frame, if the exterior column axial forces are taken equal to one another for load case 1 (neglecting the minor influence of the notional horizontal loads), if Eq. 8.3c is substituted into Eq. 8.3b for either of the exterior columns, and finally if this result is divided by the column axial force at the ASD load combination level (P_i), one obtains

$$\gamma_{e.story} = \frac{1}{\left[\frac{P_{ext}L_{ext}^2}{60EI_{oext}} + \frac{\Sigma(P_i / L_i)}{\Sigma(H_i / \Delta_H)}\right]} \qquad \text{(Eq. 8.3d)}$$

Upon substituting the numerical values for the modular frame into Eq. (37d), one obtains $\gamma_{e.story} = 3.73$.

In many cases, the result from Eq. 8.2c will be slightly conservative compared to the result from Eq. 8.3d. However, the term $P_{ext}L_{ext}^2/60EI_{oext}$ in Eq. 8.3d and the comparable more general term in Eq. 8.3a involve a number of approximations that tend to limit their accuracy relative to rigorous solutions: (1) the assumption of reverse-curvature bending in the columns, (2) the assumption that $\Sigma(P_i/L_i) / \Sigma(EI_{oi}/L_i^3) = (P_{ext}/L_{ext}) / (EI_{oext}/L_{ext}^3)$, and (3) the use of the coefficient "60" for nonprismatic columns, whereas this coefficient is derived based on the *P*-δ stiffness reduction in a prismatic member. The AISC technical and specification committees opted for the simpler forms in Eqs. 8.2, which tend to account for the *P*-δ effects on the sidesway in a slightly to moderately conservative fashion for most frames.

It is preferable to work directly with calculated values of $\gamma_{e.story}$ when considering the in-plane stability general sway frames, rather than working with member effective length factors. This is because in-plane sidesway stability truly is a *story buckling* problem rather than a member buckling problem. However, if one wishes to determine column effective length factors, these values can be determined using the equation

$$K = \sqrt{\frac{\gamma_{e.DAM}}{\gamma_{e.story}}} \qquad \text{(Eq. 8.4)}$$

where $\gamma_{e.DAM}$ is the in-plane column buckling load ratio used in the Direct Analysis Method (i.e., based on the actual column unsupported length in the plane of bending and simply-supported end conditions). Equation 8.4 highlights the fact that even for general nonprismatic column members, the effective length is defined based on the ratio of the member buckling load using simply supported end conditions (corresponding to $K = 1$) to the member load at sidesway buckling of the structure (corresponding to $K \neq 1$). This convention was employed by Lee et al. (1981) in their original work. The value $\gamma_{e.DAM}$ can be obtained easily using the method of successive approximations (Timoshenko and Gere 1961) as discussed previously. For the modular frame example, $\gamma_{e.DAM} = 109.2$ and thus $K = 5.44$ based on $\gamma_{e.story} = 3.69$. If the eigenvalue buckling analysis value of $\gamma_e = 3.87$ is used, one obtains $K = 5.31$.

Table 8.13 compares the internal axial forces and bending moments obtained from the different GT-Sabre analyses (at $\alpha = 1.6$) for the modular frame. Although B_2 is equal to 1.77 for LC1, the maximum second-order moment in the exterior columns from the direct analysis method is only 1.09 times larger than the corresponding first-order moment (123 vs 113 ft-kips). For the wind load combination, LC2, the amplification of

the column moment is only 1.11 (84.5 vs 76.4 ft-kips). These smaller amplification values are due to the fact that a large fraction of the exterior column moments are non-sway gravity moments. However, one should note that the maximum exterior column moment is amplified 1.42 times (125 vs 88.2 ft-kips) for the unbalanced snow load case (LC3) and by 1.23 (125 vs 102 ft-kips) and 1.22 (112 vs 91.6 ft-kips) for the patterned snow load cases LC4a and LC4b. These larger amplifications are due to the nonsymmetric gravity loading, and thus the existence of significant non-sway moments from the gravity loads alone under these load combinations. The B_2 values for load combinations LC2, LC3, LC4a and LC4b are 1.30, 1.55, 1.43 and 1.48 respectively.

The second-order amplification of the maximum rafter moments is generally smaller than the amplification of the column moments. The largest amplification of these moments predicted by the direct analysis approach is 1.12 (172 vs 153 ft-kips for the maximum positive bending moment in spans a under load case 3). Obviously, if one were to use $B_2 = 1.55$ (for LC3) as a flat single amplification factor to the above first-order moments, the resulting estimate of the amplified second-order moments would be quite conservative. The procedure proposed by White et al. (2007a & b) is a more rational approach for amplifying first-order elastic analysis results. This method avoids the cumbersome subdivision of the analysis into separate no-translation (*nt*) and lateral translation (*lt*) parts, which is necessary in general for good accuracy of the AISC (2010) B_1-B_2 amplification factor procedure.

Figures 8.20 through 8.24 show the direct analysis method internal axial force and moment distributions for the five load combinations considered in this study for the modular frame. Load case 3 governs the design of the inner-most spans for both positive

Table 8.13. Axial forces and moments from different types of analysis, modular frame, $\alpha = 1.6$.

Load Case 1	Analysis Type	P_{max} (kips)	M_{max}^{+} (ft-kips)	M_{max}^{-} (ft-kips)
Column 2	1st-order elastic, Yi = 0.0	26.0	113	
	2nd-order elastic, Yi = 0.0	25.9	112	
	Effective Length	26.2	121	
	Direct Analysis	26.2	123	
Rafters	1st-order elastic, Yi = 0.0	8.8	126	-259
Span a	2nd-order elastic, Yi = 0.0	8.5	128	-260
	Effective Length	9.0	132	-263
	Direct Analysis	9.0	133	-263
Rafters	1st-order elastic, Yi = 0.0	8.9	80.8	-259
Span b	2nd-order elastic, Yi = 0.0	8.8	81.1	-260
	Effective Length	9.1	81.9	-263
	Direct Analysis	9.1	82.1	-263
Rafters	1st-order elastic, Yi = 0.0	8.9	109	-244
Span c	2nd-order elastic, Yi = 0.0	8.9	110	-245
	Effective Length	9.0	110	-246
	Direct Analysis	9.0	110	-246
Rafter 1	1st-order elastic, Yi = 0.0	8.2	126	
Segments	2nd-order elastic, Yi = 0.0	8.1	128	
a3-a5	Effective Length	7.6	132	
	Direct Analysis	7.5	133	
Rafter 1	1st-order elastic, Yi = 0.0	6.8		-233
Segment	2nd-order elastic, Yi = 0.0	6.6		-235
a9-a10	Effective Length	6.1		-237
	Direct Analysis	6.0		-238
Rafter 1	1st-order elastic, Yi = 0.0	8.9		-259
Segment	2nd-order elastic, Yi = 0.0	8.8		-260
a10-b1	Effective Length	8.6		-263
	Direct Analysis	8.5		-263
Rafter 1	1st-order elastic, Yi = 0.0	7.8	109	
Segments	2nd-order elastic, Yi = 0.0	7.8	110	
c5-c7	Effective Length	7.7	110	
	Direct Analysis	7.7	110	

Table 8.13 (continued). Axial forces and moments from different types of analysis, modular frame, $\alpha = 1.6$.

Load Case 2	Analysis Type	P_{max} (kips)	M_{max}^{+} (ft-kips)	M_{max}^{-} (ft-kips)
Column 2	1st-order elastic, *Yi* = 0.0	15.7	76.4	
	Effective Length	15.7	79.6	
	Direct Analysis	15.9	84.5	
Rafters	1st-order elastic, *Yi* = 0.0	4.3	70.8	-149
Span a	Effective Length	4.1	69.6	-148
	Direct Analysis	3.9	67.5	-147
Rafters	1st-order elastic, *Yi* = 0.0	3.7	47.6	-149
Span b	Effective Length	3.5	47.9	-149
	Direct Analysis	3.4	48.3	-149
Rafters	1st-order elastic, *Yi* = 0.0	2.9	69.2	-148
Span c	Critical Load	2.8	69.1	-149
	Direct Analysis	2.7	68.8	-149
Rafter 2	1st-order elastic, *Yi* = 0.0	3.1	70.8	
Segments	Effective Length	3.3	69.6	
a3-a5	Direct Analysis	3.5	67.5	
Rafter 2	1st-order elastic, *Yi* = 0.0	2.0		-134
Segment	Effective Length	2.2		-134
a9-a10	Direct Analysis	2.4		-132
Rafter 2	1st-order elastic, *Yi* = 0.0	3.2		-149
Segment	Effective Length	3.2		-148
a10-b1	Direct Analysis	3.4		-147
Rafter 2	1st-order elastic, *Yi* = 0.0	1.9	69.2	
Segments	Effective Length	1.9	69.1	
c5-c7	Direct Analysis	1.9	68.8	

Table 8.13 (continued). Axial forces and moments from different types of analysis, modular frame, $\alpha = 1.6^{*}$.

Load Case 3	Analysis Type	P_{max} (kips)	M_{max}^{+} (ft-kips)	M_{max}^{-} (ft-kips)
Column 2	1st-order elastic, *Yi* = 0.0	25.5	80.4	
	2nd-order elastic, *Yi* = 0.0	24.8	57.6	
	Effective Length	24.5	50.8	
	Direct Analysis	24.2	39.7	
Column 1	1st-order elastic, *Yi* = 0.0	13.0	88.2	
	2nd-order elastic, *Yi* = 0.0	13.5	109	
	Effective Length	13.7	115	
	Direct Analysis	13.9	125	
Rafters Span a	1st-order elastic, *Yi* = 0.0	6.8	153	-242
	2nd-order elastic, *Yi* = 0.0	7.5	164	-249
	Effective Length	7.9	167	-250
	Direct Analysis	8.4	172	-254
Rafters Span b	1st-order elastic, *Yi* = 0.0	6.9	57.8	-315
	2nd-order elastic, *Yi* = 0.0	7.2	55.7	-313
	Effective Length	7.5	55.1	-312
	Direct Analysis	7.9	54.1	-311
Rafters Span c	1st-order elastic, *Yi* = 0.0	7.6	254	-315
	2nd-order elastic, *Yi* = 0.0	7.3	256	-313
	Effective Length	7.3	257	-312
	Direct Analysis	7.5	258	-311
Rafter 2 Segments a3-a5	1st-order elastic, *Yi* = 0.0	6.2	153	
	2nd-order elastic, *Yi* = 0.0	5.0	164	
	Effective Length	4.6	167	
	Direct Analysis	4.0	172	
Rafter 2 Segment a9-a10	1st-order elastic, *Yi* = 0.0	4.8		-216
	2nd-order elastic, *Yi* = 0.0	3.4		-222
	Effective Length	3.0		-224
	Direct Analysis	2.4		-227
Rafter 2 Segment a10-b1	1st-order elastic, *Yi* = 0.0	6.9		-242
	2nd-order elastic, *Yi* = 0.0	6.4		-249
	Effective Length	6.3		-250
	Direct Analysis	6.0		-254
Rafter 2 Segments c5-c7	1st-order elastic, *Yi* = 0.0	5.8	254	
	2nd-order elastic, *Yi* = 0.0	6.0	256	
	Effective Length	6.1	257	
	Direct Analysis	6.2	258	

* The maximum moments and the corresponding axial forces are shaded.

Table 8.13 (continued). Axial forces and moments from different types of analysis, modular frame, $\alpha = 1.6^{*}$.

Load Case 4a	Analysis Type	P_{max} (kips)	M_{max}^{+} (ft-kips)	M_{max}^{-} (ft-kips)
Column 2	1st-order elastic, *Yi* = 0.0	17.1	102	
	2nd-order elastic, *Yi* = 0.0	17.4	115	
	Effective Length	17.5	120	
	Direct Analysis	17.6	125	
Column 1	1st-order elastic, *Yi* = 0.0	26.2	95.8	
	2nd-order elastic, *Yi* = 0.0	25.8	81.9	
	Effective Length	25.6	76.8	
	Direct Analysis	25.4	70.8	
Rafters Span a	1st-order elastic, *Yi* = 0.0	7.8	159	-209
	2nd-order elastic, *Yi* = 0.0	8.1	166	-214
	Effective Length	8.4	169	-215
	Direct Analysis	8.6	172	-217
Rafters Span b	1st-order elastic, *Yi* = 0.0	7.6	52.1	-209
	2nd-order elastic, *Yi* = 0.0	7.8	53.5	-214
	Effective Length	8.0	53.9	-215
	Direct Analysis	8.2	54.5	-217
Rafters Span c	1st-order elastic, *Yi* = 0.0	7.5	76.6	-151
	2nd-order elastic, *Yi* = 0.0	7.7	77.7	-153
	Effective Length	7.7	78.0	-153
	Direct Analysis	7.8	78.5	-154
Rafter 1 Segments a3-a5	1st-order elastic, *Yi* = 0.0	7.2	159	
	2nd-order elastic, *Yi* = 0.0	6.4	166	
	Effective Length	6.2	169	
	Direct Analysis	5.9	172	
Rafter 1 Segment a9-a10	1st-order elastic, *Yi* = 0.0	5.8		-184
	2nd-order elastic, *Yi* = 0.0	4.9		-189
	Effective Length	4.6		-190
	Direct Analysis	4.2		-191
Rafter 1 Segment a10-b1	1st-order elastic, *Yi* = 0.0	7.6		-209
	2nd-order elastic, *Yi* = 0.0	7.4		-214
	Effective Length	7.3		-215
	Direct Analysis	7.2		-217
Rafter 1 Segments c5-c7	1st-order elastic, *Yi* = 0.0	6.8	76.6	
	2nd-order elastic, *Yi* = 0.0	6.8	77.7	
	Effective Length	6.7	78.0	
	Direct Analysis	6.7	78.5	

* The maximum moments and the corresponding axial forces are shaded.

Table 8.13 (continued). Axial forces and moments from different types of analysis, modular frame, $\alpha = 1.6^{*}$.

Load Case 4b	Analysis Type	P_{max} (kips)	M_{max}^{+} (ft-kips)	M_{max}^{-} (ft-kips)
Column 2	1st-order elastic, Yi = 0.0	16.8	91.6	
	2nd-order elastic, Yi = 0.0	17.0	101.2	
	Effective Length	17.2	107	
	Direct Analysis	17.3	112	
Column 1	1st-order elastic, Yi = 0.0	24.5	86.7	
	2nd-order elastic, Yi = 0.0	24.1	75.9	
	Effective Length	24.0	70.2	
	Direct Analysis	23.8	65.1	
Rafters Span a	1st-order elastic, Yi = 0.0	7.1	132	-279
	2nd-order elastic, Yi = 0.0	7.3	137	-283
	Effective Length	7.6	140	-284
	Direct Analysis	7.8	142	-286
Rafters Span b	1st-order elastic, Yi = 0.0	7.3	88.0	-279
	2nd-order elastic, Yi = 0.0	7.1	87.5	-283
	Effective Length	7.3	87.0	-284
	Direct Analysis	7.5	86.6	-286
Rafters Span c	1st-order elastic, Yi = 0.0	6.9	72.0	-209
	2nd-order elastic, Yi = 0.0	7.0	71.7	-209
	Effective Length	7.1	71.4	-208
	Direct Analysis	7.2	71.2	-208
Rafter 1 Segments a3-a5	1st-order elastic, Yi = 0.0	6.5	132	
	2nd-order elastic, Yi = 0.0	5.9	137	
	Effective Length	5.6	140	
	Direct Analysis	5.3	142	
Rafter 1 Segment a9-a10	1st-order elastic, Yi = 0.0	5.1		-252
	2nd-order elastic, Yi = 0.0	4.4		-256
	Effective Length	4.1		-257
	Direct Analysis	3.8		-259
Rafter 1 Segment a10-b1	1st-order elastic, Yi = 0.0	7.3		-279
	2nd-order elastic, Yi = 0.0	7.1		-283
	Effective Length	7.0		-284
	Direct Analysis	6.9		-286
Rafter 2 Segments c5-c7	1st-order elastic, Yi = 0.0	6.2	72.0	
	2nd-order elastic, Yi = 0.0	6.4	71.7	
	Effective Length	6.5	71.4	
	Direct Analysis	6.6	71.2	

* The maximum moments and the corresponding axial forces are shaded.

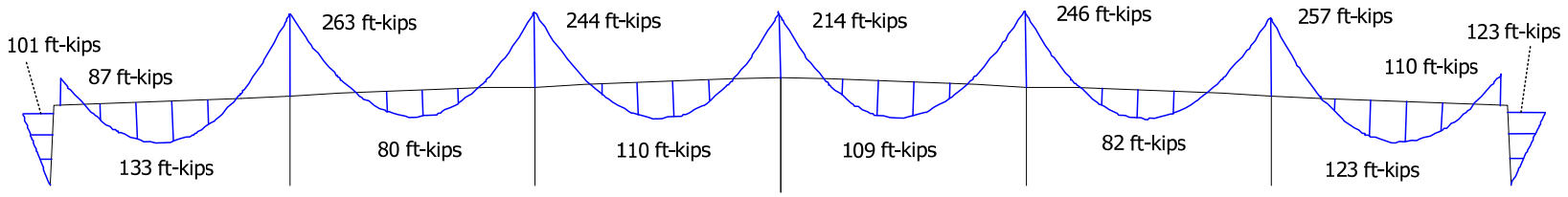

(a) Moment

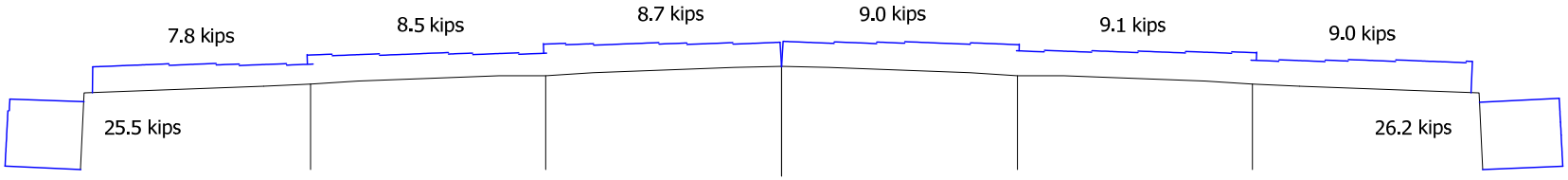

(b) Axial force

Figure 8.20. Moment and axial force distributions, modular frame, direct analysis method, LC1 (Dead + Collateral + Uniform Snow, $\alpha = 1.6$).

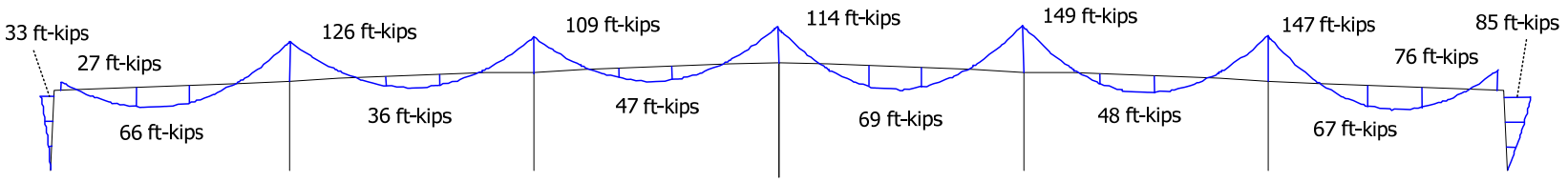

(a) Moment

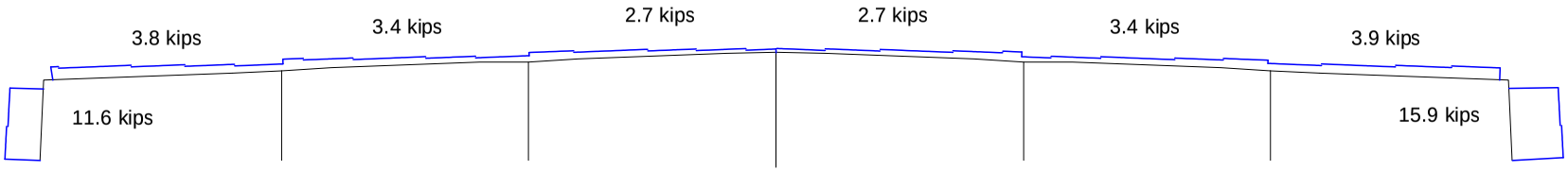

(b) Axial force

Figure 8.21. Moment and axial force distributions, modular frame, direct analysis method, LC2 (Dead + Collateral + 0.75(Snow + Wind), $\alpha = 1.6$).

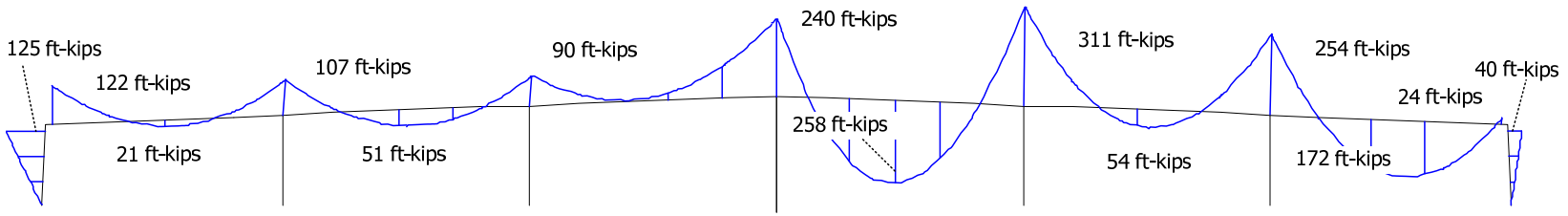

(a) Moment

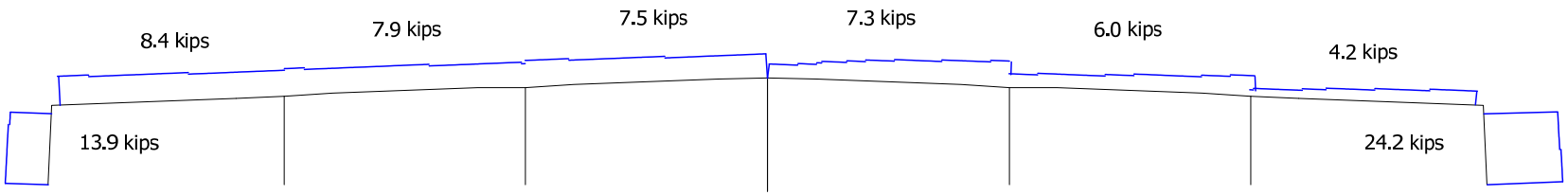

(b) Axial force

Figure 8.22. Moment and axial force distributions, modular frame, direct analysis method, LC3 (Dead + Collateral + Unbalanced Snow, $\alpha = 1.6$).

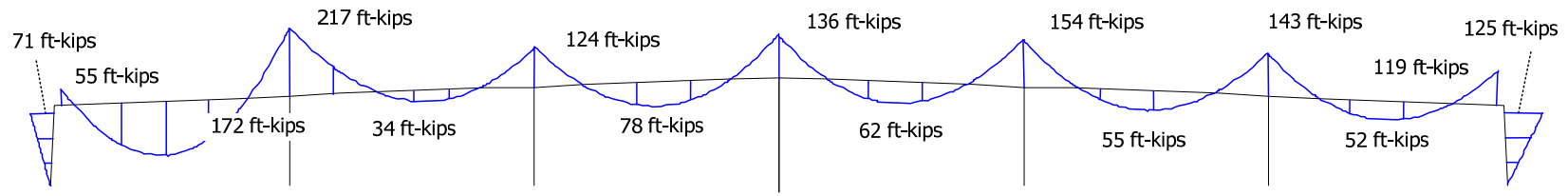

(a) Moment

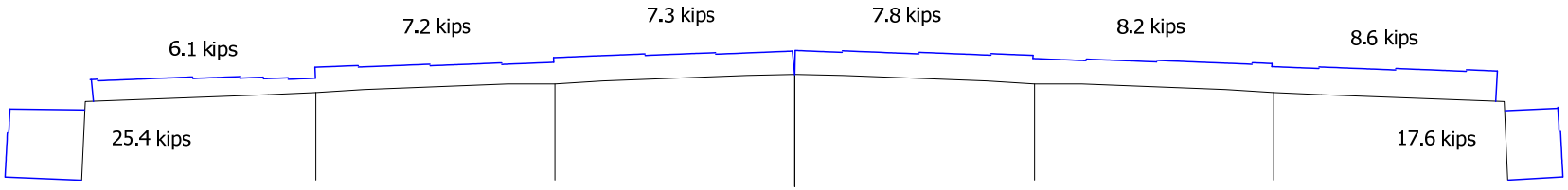

(b) Axial force

Figure 8.23. Moment and axial force distributions, modular frame, direct analysis method, LC4a (Dead + Collateral + Patterned Snow, 100 % of snow load on one exterior span, $\alpha = 1.6$).

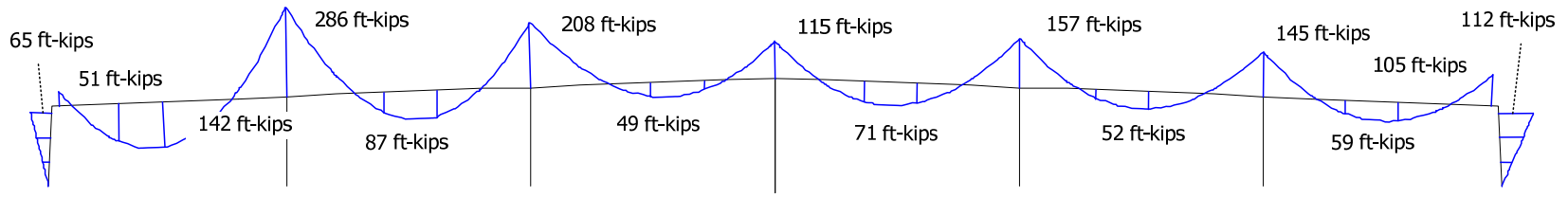

(a) Moment

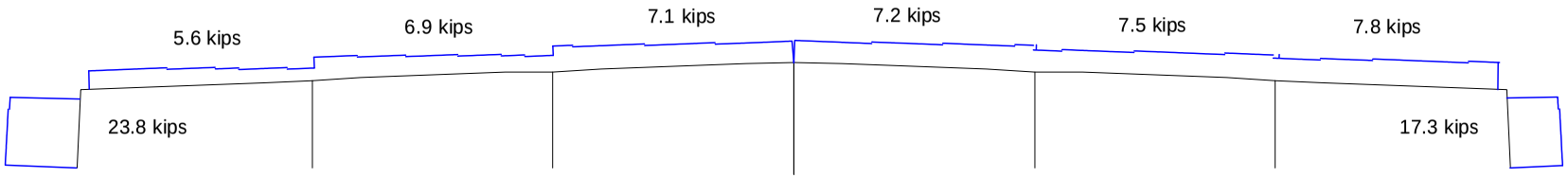

(b) Axial force

Figure 8.24. Moment and axial force distributions, modular frame, direct analysis method, LC4b (Dead + Collateral + Patterned Snow, 100 % of snow load on one exterior span plus adjacent interior span, $\alpha = 1.6$).

and negative bending moment, load case 4a governs the design of the exterior spans (spans a) for positive moment, load cases 1 and 4a are approximately equally critical for the columns and the rafters at the knee of the frame, and load case 4b governs the design of the exterior spans (spans a) and the first interior spans (spans b) for negative bending over the first interior column as well as the positive bending in the first interior spans. The corresponding effective length and direct analysis method maximum moments and the corresponding axial forces are highlighted in Table 8.13.

8.2.3 Axial Capacity Ratios P_r/P_c

Tables 8.14 through 8.19 summarize the intermediate and final results pertaining to the calculation of the axial capacity ratios for the modular frame. Similar to Tables 8.4 to 8.6 for the single-span frame, these tables parallel the general procedure summarized in Section 3.2.1. The axial capacity ratios are determined separately for the in-plane and out-of-plane column buckling limit states. The in-plane results for the exterior columns (e1-e4) are shown first, followed by the out-of-plane calculations for each of the column segments (e1-e2, e2-e3 and e3-e4), then the in-plane results for the rafter spans a (a1-a10), the out-of-plane calculations for the critical span a segments a3-a5 and a9-a10, the in-plane results for the rafter spans b (b1-b10), the out-of-plane calculations for the critical span b segment in negative bending (a10-b1), the in-plane results for the rafter spans c (c1-c10), and finally the out-of-plane calculations for the critical span c segments in positive bending (c5-c7). The results are shown for the effective length and the direct analysis methods in each of these cases. In the cases where the cell values are identical for the direct analysis and the effective length methods, the direct analysis values are indicated by the " symbol. Appendices F and G provide a detailed illustration of the

calculations corresponding to each of the steps of the procedure discussed in Section 3.2.1.

Two of the segments considered in Tables 8.14 to 8.19 have a larger unbraced length for the inside flange, segments a3-a5 and c5-c7. The results shown in the tables for these segments are based on the constrained-axis torsional buckling as described in Section 4.3.1. Also, only flexural buckling is considered for the out-of-plane column limit states in the modular frame. All the members in the modular frame satisfy the potential restrictions on t_{f1}/t_{f2} suggested in Sections 4.2.1 and 4.2.3 for which the reduction in the column out-of-plane buckling resistance due to coupled torsional and flexural buckling might be considered negligible.

The evaluation of the elastic buckling load ratios γ_e shown in Tables 8.14 to 8.19 is slightly different from that discussed for the single-span frame in Section 8.1.3 above. The AISC (2010) story-stiffness based values for the γ_e corresponding to in-plane sidesway buckling, e.g., $\gamma_e = 3.69$ for LC1 (see Section 8.2.2), are used for the modular frame (with the effective length method) rather than using rigorous elastic sidesway buckling analysis values for each of the load combinations. Due to the substantial P-Δ effects from the five interior leaner columns in this frame, the γ_e values for in-plane sidesway buckling are quite small relative to the out-of-plane γ_e values for the exterior columns and the in-plane and out-of-plane γ_e values for the rafters. This leads to a substantial increase in the P_r/P_c of the exterior columns for this frame, when the effective length method is employed ($P_r/P_c = 0.516$ for LC1 in Table 8.14). However, one can observe that the corresponding exterior column in-plane P_r/P_c values based on the direct analysis method are much smaller (i.e., $P_r/P_c = 0.161$ for LC1). This is similar to the

behavior demonstrated previously by the modified DP-13 frame example of Section 2.6.2. The direct analysis method does a better job of tracking the physical internal forces in the structure, and thus uses a cross-section based calculation for the axial capacity ratio. Conversely, the effective length method conservatively (and somewhat artificially, for problems in which the member stresses are dominated by non-sway flexure) reduces the column axial resistance to compensate for its underprediction of the internal bending moments. The P_r/P_c values for all the column segments are in all cases governed by the out-of-plane resistance in the direct analysis method whereas they are in all cases governed by the in-plane resistance in the effective length method.

The γ_e values for all the out-of-plane column limit state checks, and for the in-plane rafter flexural buckling checks using the effective length method, are based on elastic flexural buckling using the actual unbraced lengths and assuming simply-supported end conditions at the segment ends. If a subassembly model is constructed to estimate the concurrent out-of-plane buckling of the three segments of the columns e1-e4, one obtains $\gamma_e = 26.4$ for LC1 (versus $\gamma_e = 19.4$, 30.5 and 135 for segments e1-e2, e2-e3 and e3-e4 respectively in Table 8.14). Therefore, the bottom unbraced length of the column is the most critical with respect to out-of-plane buckling using the widely established simple approach of neglecting the braced buckling interaction between the adjacent member segments. As noted subsequently, the top segment of the columns (e3-e4) is the most critical for flexure though. As noted in Section 8.1.3 above, a more representative design check is obtained by using the actual segment unbraced lengths in determining P_r/P_c, and by considering the effect of end restraint in checking the LTB resistance.

Table 8.14. Calculation of axial capacity ratios, modular frame, load case 1.

Location	Method	γ_e	x_1 (ft)	P_r (kips)	$(f_r/F_y)_{max}$	F_{n1} (ksi)	γ_{n1}	x_{max} (ft)	f (ksi)	Q_s	Q_a	Q	$(f_r/QF_y)_{max}$	F_n (ksi)	P_r/P_c	Governing P_r/P_c
Column Segments																
Seg. e1-e4	Effective Length	3.69	0.0	16.3	0.071	12.6	3.24	7.5	10.4	0.841	0.864	0.727	0.0807	10.4	0.516	
(in-plane)	Direct Analysis			16.4				"	55.0	0.841	0.722	0.607	0.0967	33.4	0.161	
Seg. e1-e2	Effective Length	19.4	0.0	16.3	0.0710	40.6	10.4	7.5	33.6	0.841	0.755	0.635	0.0924	27.7	0.195	0.516
(out-of-plane)	Direct Analysis	19.4	"	16.4	0.0710	40.6	10.4	"	33.6	0.841	0.755	0.635	0.0924	27.7	0.195	0.195
Seg. e2-e3	Effective Length	30.5	7.5	16.2	0.0585	43.5	13.5	7.5	43.5	0.841	0.737	0.620	0.0944	29.5	0.182	0.516
(out-of-plane)	Direct Analysis	30.5	"	16.3	0.0586	43.5	13.5	"	43.5	0.841	0.737	0.620	0.0945	29.5	0.182	0.182
Seg. e3-e4	Effective Length	135	13.5	16.2	0.0512	51.8	18.4	13.5	51.8	0.841	0.641	0.539	0.0951	28.7	0.164	0.516
(out-of-plane)	Direct Analysis	135	"	16.2	0.0513	51.8	18.3	"	51.8	0.841	0.641	0.539	0.0953	28.7	0.164	0.164
Rafter Segments																
Seg. a0-b0	Effective Length	127	10.0	4.8	0.0144	43.7	55.2	10.0	43.7	0.841	0.617	0.518	0.0278	25.3	0.052	
(in-plane)	Direct Analysis			4.7				"	55.0	0.841	0.604	0.508	0.0278	27.9	0.046	
Seg. a3-a5	Effective Length	37.7	11.4	4.7	0.0142	25.2	32.2	11.4	25.2	0.841	0.653	0.549	0.0259	19.7	0.066	0.066
(out-of-plane)	Direct Analysis	38.4	"	4.7	0.0140	25.2	32.8	"	25.2	0.841	0.653	0.549	0.0255	19.7	0.065	0.065
Seg. a9-a10	Effective Length	257	41.4	3.8	0.0080	44.8	102.3	41.4	44.8	0.956	0.654	0.626	0.0127	30.3	0.024	0.052
(out-of-plane)	Direct Analysis	263	"	3.7	0.0078	44.8	105.1	"	44.8	0.956	0.654	0.626	0.0124	30.3	0.024	0.046
Seg. b0-c0	Effective Length	60.0	57.3	5.0	0.0155	35.1	41.1	77.4	34.9	0.841	0.717	0.603	0.0256	25.2	0.056	
(in-plane)	Direct Analysis			5.0				"	55.0	0.841	0.688	0.578	0.0264	31.8	0.044	
Seg. a10-b1	Effective Length	184	51.4	5.4	0.0117	45.3	70.4	48.4	43.2	0.956	0.660	0.631	0.0177	30.5	0.034	0.056
(out-of-plane)	Direct Analysis	185	"	5.3	0.0116	45.3	70.9	"	43.2	0.956	0.660	0.631	0.0176	30.5	0.033	0.044
Seg. c0-c11	Effective Length	148	106.4	5.3	0.0117	43.2	67.0	101.4	41.7	0.956	0.616	0.589	0.0192	28.0	0.037	
(in-plane)	Direct Analysis			5.3				"	55.0	0.956	0.593	0.567	0.0199	31.2	0.033	
Seg. c5-c7	Effective Length	65.1	121.4	4.8	0.0091	27.2	54.2	121.4	27.2	1.000	0.757	0.757	0.0120	24.4	0.034	0.037
(out-of-plane)	Direct Analysis	65.3	"	4.8	0.0091	27.2	54.4	"	27.2	1.000	0.757	0.757	0.0120	24.4	0.034	0.034

Table 8.15. Calculation of axial capacity ratios, modular frame, load case 2.

Location	Method	γ_e	x_1 (ft)	P_r (kips)	$(f_r/F_y)_{max}$	F_{n1} (ksi)	γ_{n1}	x_{max} (ft)	f (ksi)	Q_s	Q_a	Q	$(f_r/QF_y)_{max}$	F_n (ksi)	P_r/P_c	Governing P_r/P_c
Column Segments																
Seg. e1-e4	Effective Length	6.98	0.0	9.8	0.0427	14.4	6.12	7.5	11.8	0.841	0.85	0.715	0.0492	11.8	0.273	
(in-plane)	Direct Analysis			9.9				"	55.0	0.841	0.722	0.607	0.0584	33.4	0.097	
Seg. e1-e2	Effective Length	32.3	0.0	9.8	0.0427	40.6	17.3	7.5	33.4	0.841	0.756	0.635	0.0553	27.6	0.117	0.273
(out-of-plane)	Direct Analysis	32.1	"	9.9	0.0430	40.6	17.2	"	33.4	0.841	0.756	0.635	0.0558	27.7	0.118	0.118
Seg. e2-e3	Effective Length	51.2	7.5	9.7	0.0349	43.5	22.7	7.5	43.5	0.841	0.737	0.620	0.0563	29.5	0.109	0.273
(out-of-plane)	Direct Analysis	50.7	"	9.8	0.0352	43.5	22.5	"	43.5	0.841	0.737	0.620	0.0568	29.5	0.110	0.110
Seg. e3-e4	Effective Length	228	13.5	9.6	0.0303	51.8	31.0	13.5	51.8	0.841	0.641	0.539	0.0563	28.7	0.097	0.273
(out-of-plane)	Direct Analysis	226	"	9.7	0.0306	51.8	30.7	"	51.8	0.841	0.641	0.539	0.0568	28.7	0.098	0.098
Rafter Segments																
Seg. a0-b0	Effective Length	309	11.4	2.1	0.0063	44.3	128.2	11.4	44.3	0.841	0.616	0.518	0.0121	25.5	0.023	
(in-plane)	Direct Analysis			2.2				"	55.0	0.841	0.604	0.508	0.0133	27.9	0.022	
Seg. a3-a5	Effective Length	87.9	16.4	2.0	0.0061	25.2	75.1	16.4	25.2	0.841	0.653	0.549	0.0111	19.7	0.028	0.028
(out-of-plane)	Direct Analysis	81.7	"	2.2	0.0066	25.2	69.8	"	25.2	0.841	0.653	0.549	0.0120	19.7	0.031	0.031
Seg. a9-a10	Effective Length	733	41.4	1.3	0.0028	44.8	292.4	41.4	44.8	0.956	0.654	0.626	0.0045	30.3	0.008	0.022
(out-of-plane)	Direct Analysis	658	"	1.5	0.0031	44.8	262.5	"	44.8	0.956	0.654	0.626	0.0050	30.3	0.009	0.022
Seg. b0-c0	Effective Length	186	61.4	1.8	0.0055	36.6	120.6	61.4	36.6	0.855	0.715	0.611	0.0090	26.2	0.019	
(in-plane)	Direct Analysis			1.9				"	55.0	0.855	0.680	0.581	0.0099	32.0	0.016	
Seg. a10-b1	Effective Length	485	51.4	2.0	0.0044	45.3	186.0	48.4	43.2	0.956	0.660	0.631	0.0067	30.5	0.013	0.019
(out-of-plane)	Direct Analysis	468	"	2.1	0.0046	45.3	179.5	"	43.2	0.956	0.660	0.631	0.0069	30.5	0.013	0.016
Seg. c0-c11	Effective Length	597	101.4	1.7	0.0035	45.1	233.0	101.4	45.1	0.956	0.609	0.583	0.0060	28.5	0.011	
(in-plane)	Direct Analysis			1.7				"	55.0	0.956	0.593	0.567	0.0062	31.2	0.010	
Seg. c5-c7	Effective Length	270	126.4	1.2	0.0022	27.2	225.0	126.4	27.2	1.000	0.757	0.757	0.0029	24.4	0.008	0.011
(out-of-plane)	Direct Analysis	269	"	1.2	0.0022	27.2	223.7	"	27.2	1.000	0.757	0.757	0.0029	24.4	0.008	0.010

Table 8.16. Calculation of axial capacity ratios, modular frame, load case 3.

Location	Method	γ_e	x_1 (ft)	P_r (kips)	$(f_r/F_y)_{max}$	F_{n1} (ksi)	γ_{n1}	x_{max} (ft)	f (ksi)	Q_s	Q_a	Q	$(f_r/QF_y)_{max}$	F_n (ksi)	P_r/P_c	Governing P_r/P_c
Seg. c0-c11	Effective Length	197	106.4	4.4	0.0096	44.1	83.3	101.4	43.2	0.956	0.613	0.586	0.0161	28.2	0.031	
(in-plane)	Direct Analysis			4.4				"	55.0	0.956	0.593	0.567	0.0166	31.2	0.028	
Seg. c5-c7	Effective Length	82.6	126.4	3.8	0.0072	27.2	68.7	126.4	27.2	1.000	0.757	0.757	0.0095	24.4	0.027	0.031
(out-of-plane)	Direct Analysis	81.3	"	3.9	0.0073	27.2	67.6	"	27.2	1.000	0.757	0.757	0.0096	24.4	0.027	0.028

Table 8.17. Calculation of axial capacity ratios, modular frame, load case 4a.

Location	Method	γ_e	x_1 (ft)	P_r (kips)	$(f_r/F_y)_{max}$	F_{n1} (ksi)	γ_{n1}	x_{max} (ft)	f (ksi)	Q_s	Q_a	Q	$(f_r/QF_y)_{max}$	F_n (ksi)	P_r/P_c	Governing P_r/P_c
Seg. a0-b0	Effective Length	160	10.0	3.9	0.0118	44.0	68.1	10.0	44.0	0.841	0.616	0.518	0.0227	25.4	0.043	
(in-plane)	Direct Analysis			3.7				"	55.0	0.841	0.604	0.508	0.0220	27.9	0.037	
Seg. a3-a5	Effective Length	46.2	11.4	3.9	0.0116	25.2	39.4	11.4	25.2	0.841	0.653	0.549	0.0212	19.7	0.054	0.054
(out-of-plane)	Direct Analysis	48.6	"	3.7	0.0111	25.2	41.5	"	25.2	0.841	0.653	0.549	0.0201	19.7	0.052	0.052

Table 8.18. Calculation of axial capacity ratios, modular frame, load case 4b.

Location	Method	γ_e	x_1 (ft)	P_r (kips)	$(f_r/F_y)_{max}$	F_{n1} (ksi)	γ_{n1}	x_{max} (ft)	f (ksi)	Q_s	Q_a	Q	$(f_r/QF_y)_{max}$	F_n (ksi)	P_r/P_c	Governing P_r/P_c
Seg. a0-b0	Effective Length	177	10.0	3.6	0.0107	44.1	74.9	10.0	44.1	0.841	0.616	0.518	0.0206	25.4	0.039	
(in-plane)	Direct Analysis			3.4				"	55.0	0.841	0.604	0.508	0.0200	27.9	0.033	
Seg. a9-a10	Effective Length	380	41.4	2.6	0.0054	44.8	151.8	41.4	44.8	0.956	0.654	0.626	0.0086	30.3	0.016	0.039
(out-of-plane)	Direct Analysis	411	"	2.4	0.0050	44.8	163.9	"	44.8	0.956	0.654	0.626	0.0079	30.3	0.015	0.033
Seg. b0-c0	Effective Length	76.7	57.3	4.0	0.0123	35.3	52.1	57.3	35.3	0.855	0.718	0.614	0.0201	25.7	0.044	
(in-plane)	Direct Analysis			3.9				"	55.0	0.855	0.680	0.581	0.0208	32.0	0.035	
Seg. a10-b1	Effective Length	226	51.4	4.4	0.0095	45.3	86.6	48.4	43.2	0.956	0.660	0.631	0.0144	30.5	0.027	0.044
(out-of-plane)	Direct Analysis	229	"	4.3	0.0094	45.3	87.8	"	43.2	0.956	0.660	0.631	0.0142	30.5	0.027	0.035

One should note that although the γ_e values for some of the segments in Tables 8.14 to 8.19 are quite large, the values of F_{n1} and F_n are relatively small compared to F_y = 55 ksi. This is particularly true for the rafters of the modular frame, and it is due to the fact that the axial loads P_r and the corresponding axial stresses f_r are small. The column resistance at the theoretical anchor point P_c needed for the beam-column interaction equations is reduced somewhat relative to QP_y in the flexural buckling resistance calculations. The column strengths of the unbraced segments are governed effectively by inelastic flexural buckling in the out-of-plane direction. Again, for the in-plane check in the direct analysis method, the column stability effects are accounted for within the analysis side of the design equations.

8.2.4 Flexural Capacity Ratios M_r/M_c

Tables 8.19 to 8.23 summarize the calculation of the flexural capacity ratios for the modular frame. These calculations are essentially the same as the calculations already described for the single-span frame in Section 8.1.4 above. The reader is referred to Section 8.1.4 for a discussion of the information provided in these tables. Appendices F and G provide a detailed illustration of the calculation of the flexural capacity ratios. For the LTB checks in the modular frame, the unbraced length of the top flange is used for the segments in positive bending while the unbraced length of the bottom flange is used for the segments in negative bending. The exterior column flexural resistances are governed entirely by the flange local buckling (FLB) checks in the modular frame. This is due to the relatively slender column flanges (see Table 8.11). Also, the rafter segment a4-a5 are governed by FLB (see Tables 8.19, 8.20 and 8.22). However, the segment c5-c6, which has compact compression flanges, are governed by LTB (see Tables 8.19 to

Table 8.19. Calculation of flexural capacity ratios, modular frame, load case 1.

Location	Method	γ_{eLTB}	$x_{max(LTB)}$ (ft)	$(M_r/M_{yc})_{max}$	$R_{pg(LTB)}$	R_{pc}	$M_{n(LTB)}$ (ft-kips)	$M_r/M_{c(LTB)}$	$x_{max(FLB)}$ (ft)	$R_{pg(FLB)}$	$M_{n(FLB)}$ (ft-kips)	$M_r/M_{c(FLB)}$	$x_{max(TFY)}$ (ft)	$M_{n(TFY)}$ (ft-kips)	$M_r/M_{c(TFY)}$	Gov. M_r (ft-kips)	Governing M_r/M_c
Column Segments																	
Seg. e1-e2	Effective Length	9.4	7.5	0.256	1.000	1.000	123	0.477	7.5	1.000	118	0.501				35	0.501
	Direct Analysis	9.2	"	0.261	1.000	1.000	123	0.487	"	1.000	118	0.510				36	0.510
Seg. e2-e3	Effective Length	8.1	13.5	0.321	0.961	1.000	170	0.618	13.5	0.965	161	0.652				63	0.652
	Direct Analysis	8.0	"	0.327	0.961	1.000	170	0.628	"	0.965	161	0.663				64	0.663
Seg. e3-e4	Effective Length	30.8	16.4	0.337	0.927	1.000	208	0.607	16.4	0.939	180	0.702				76	0.702
	Direct Analysis	30.3	"	0.342	0.927	1.000	208	0.617	"	0.939	180	0.713				77	0.713
Rafter Segments																	
Seg. a4-a5	Effective Length	9.2	21.4	0.366	0.932	1.000	199	0.689	21.4	0.939	180	0.763				82	0.763
PRISMATIC	Direct Analysis	9.1	"	0.369	0.932	1.000	199	0.696	"	0.939	180	0.770				83	0.770
Seg. a9-a10	Effective Length	10.1	46.4	0.435	1.000	1.005	326	0.757	46.4	1.000	342	0.723	46.4	317	0.779	148	0.779
	Direct Analysis	10.1	"	0.437	1.000	1.005	326	0.760	"	1.000	342	0.725	"	317	0.782	149	0.782
Seg. a10-b1	Effective Length	7.3	47.3	0.480	1.000	1.004	320	0.855	47.3	1.000	343	0.799	47.3	318	0.861	164	0.861
	Direct Analysis	7.2	"	0.482	1.000	1.004	320	0.858	"	1.000	343	0.801	"	318	0.864	165	0.864
Seg. c5-c6	Effective Length	16.0	121.4	0.211	1.000	1.000	309	0.371	121.4	0.998	325	0.354				69	0.371
PRISMATIC	Direct Analysis	16.0	"	0.212	1.000	1.000	309	0.372		0.998	325	0.354				69	0.372

Table 8.20. Calculation of flexural capacity ratios, modular frame, load case 2.

Location	Method	γ_{eLTB}	$x_{max(LTB)}$ (ft)	$(M_r/M_{yc})_{max}$	$R_{pg(LTB)}$	R_{pc}	$M_{n(LTB)}$ (ft-kips)	$M_r/M_{c(LTB)}$	$x_{max(FLB)}$ (ft)	$R_{pg(FLB)}$	$M_{n(FLB)}$ (ft-kips)	$M_r/M_{c(FLB)}$	$x_{max(TFY)}$ (ft)	$M_{n(TFY)}$ (ft-kips)	$M_r/M_{c(TFY)}$	Gov. M_r (ft-kips)	Governing M_r/M_c
Column Segments																	
Seg. e1-e2	Effective Length	11.5	7.5	0.197	1.000	1.000	122	0.371	7.5	1.000	118	0.386				27.0	0.386
	Direct Analysis	10.9	"	0.208	1.000	1.000	122	0.391	"	1.000	118	0.407				29.0	0.407
Seg. e2-e3	Effective Length	11.1	13.5	0.223	0.961	1.000	169	0.431	13.5	0.965	161	0.452				44.0	0.452
	Direct Analysis	10.5	"	0.236	0.961	1.000	169	0.457	"	0.965	161	0.479				46.0	0.479
Seg. e3-e4	Effective Length	45.8	16.4	0.223	0.927	1.000	181	0.402	16.4	0.939	180	0.462				50.0	0.462
	Direct Analysis	43.1	"	0.236	0.927	1.000	181	0.426	"	0.939	180	0.490				53.0	0.490
Rafter Segments																	
Seg. a4-a5	Effective Length	17.7	21.4	0.194	0.932	1.000	202	0.359	21.4	0.939	180	0.404				44.0	0.404
	Direct Analysis	18.3	"	0.188	0.932	1.000	203	0.346	"	0.939	180	0.391				42.0	0.391
Seg. a9-a10	Effective Length	17.2	46.4	0.245	1.000	1.005	325	0.429	46.4	1.000	342	0.408	46.4	317	0.440	84.0	0.440
	Direct Analysis	17.4	"	0.243	1.000	1.005	325	0.425	"	1.000	342	0.404	"	317	0.436	83.0	0.436
Seg. a10-b1	Effective Length	13.4	47.3	0.271	1.000	1.004	322	0.481	47.3	1.000	343	0.451	47.3	318	0.487	93.0	0.487
	Direct Analysis	13.6	"	0.269	1.000	1.004	322	0.477	"	1.000	343	0.447	"	318	0.482	92.0	0.482
Seg. c5-c6	Effective Length	25.1	121.4	0.133	1.000	1.000	305	0.236	121.4	0.998	325	0.222				43.0	0.236
	Direct Analysis	25.2	"	0.132	1.000	1.000	305	0.236	"	0.998	325	0.221				43.0	0.236

Table 8.21. Calculation of flexural capacity ratios, modular frame, load case 3

Location	Method	γ_{eLTB}	$x_{max(LTB)}$ (ft)	$(M_r/M_{yc})_{max}$	$R_{pg(LTB)}$	R_{pc}	$M_{n(LTB)}$ (ft-kips)	$M_r/M_{c(LTB)}$	$x_{max(FLB)}$ (ft)	$R_{pg(FLB)}$	$M_{n(FLB)}$ (ft-kips)	$M_r/M_{c(FLB)}$	$x_{max(TFY)}$ (ft)	$M_{n(TFY)}$ (ft-kips)	$M_r/M_{c(TFY)}$	Gov. M_r (ft-kips)	Governing M_r/M_c
Seg. c5-c6	Effective Length	6.8	121.4	0.493	1.000	1.000	305	0.878	121.4	0.998	325	0.825				160	0.878
	Direct Analysis	6.8	"	0.495	1.000	1.000	305	0.881	"	0.998	325	0.828				161	0.881

Table 8.22. Calculation of flexural capacity ratios, modular frame, load case 4a.

Location	Method	γ_{eLTB}	$x_{max(LTB)}$ (ft)	$(M_r/M_{yc})_{max}$	$R_{pg(LTB)}$	R_{pc}	$M_{n(LTB)}$ (ft-kips)	$M_r/M_{c(LTB)}$	$x_{max(FLB)}$ (ft)	$R_{pg(FLB)}$	$M_{n(FLB)}$ (ft-kips)	$M_r/M_{c(FLB)}$	$x_{max(TFY)}$ (ft)	$M_{n(TFY)}$ (ft-kips)	$M_r/M_{c(TFY)}$	Gov. M_r (ft-kips)	Governing M_r/M_c
Seg. a4-a5	Effective Length	7.2	21.4	0.469	0.932	1.000	199	0.885	21.4	0.939	180	0.978				105	0.978
	Direct Analysis	7.0	"	0.477	0.932	1.000	198	0.903	"	0.939	180	0.995				107	0.995

Table 8.23. Calculation of flexural capacity ratios, modular frame, load case 4b.

Location	Method	γ_{eLTB}	$x_{max(LTB)}$ (ft)	$(M_r/M_{yc})_{max}$	$R_{pg(LTB)}$	R_{pc}	$M_{n(LTB)}$ (ft-kips)	$M_r/M_{c(LTB)}$	$x_{max(FLB)}$ (ft)	$R_{pg(FLB)}$	$M_{n(FLB)}$ (ft-kips)	$M_r/M_{c(FLB)}$	$x_{max(TFY)}$ (ft)	$M_{n(TFY)}$ (ft-kips)	$M_r/M_{c(TFY)}$	Gov. M_r (ft-kips)	Governing M_r/M_c
Seg. a9-a10	Effective Length	8.8	46.4	0.473	1.000	1.005	325	0.827	46.4	1.000	342	0.785	46.4	317	0.847	161	0.847
	Direct Analysis	8.8	"	0.475	1.000	1.005	325	0.831	"	1.000	342	0.790	"	317	0.851	162	0.851
Seg. a10-b1	Effective Length	6.9	47.3	0.520	1.000	1.004	321	0.923	47.3	1.000	343	0.864	47.3	318	0.932	178	0.932
	Direct Analysis	6.9	"	0.523	1.000	1.004	321	0.928	"	1.000	343	0.869	"	318	0.938	179	0.938

8.21). For the singly-symmetric sections in segments a9-a10 and a10-b1, the flexural resistance is governed by tension-flange yielding (TFY) (see Tables 8.19, 8.20 and 8.23). As noted previously, segments a4-a5 and c5-c6 are prismatic. Therefore, the AISC (2010) equations are applied directly to determine the flexural resistances for these segments. The γ_e values are reported for these segments in Tables 8.19 to 8.22 only for informational purposes. They are not utilized in calculating the $M_{n(LTB)}$ of segments a4-a5 and c5-c6. When γ_e is calculated for segment a10-b1 using the recommended procedure shown in Section 4.4.1, it is assumed that the segment is linearly tapered with d = 30 in at a10 and d = 19 in at b1. This is necessary due to the fact that the recommended approach is applicable only for linearly tapered members. Also, load height effects associated with the concentrated column reaction being located within the unbraced length are not considered. Further study is needed to determine the limit beyond which one can ignore the effect of steps in the cross-section geometry, multiple tapered-web geometries, etc. in applying the proposed equations for calculating γ_{eLTB}. Since the cross-section transition and the column reaction are located quite close to section a10, these approximations are believed to be accurate.

8.2.5 Member Unity Checks

Table 8.24 shows the governing M_r/M_c and P_r/P_c values and the corresponding unity checks for the segments and load combinations considered in this study for the modular frame. Only the governing unity checks on the rafter segments are shown for load cases 3, 4a and 4b. Both the unity check values from the original design by Chief Buildings and from the prototype procedures are listed in the table. The prototype unity check calculations are all based on Eqs. 2.5. As a simplification, the largest M_r/M_c and

P_r/P_c values are combined in all cases to obtain the unity check values provided in the table. As noted in Section 8.1.5, if Eqs. 2.5 are used for separate in-plane and out-of-plane beam-column strength checks, the differences relative to the simplified single strength interaction curve calculated with the maximum M_r/M_c and P_r/P_c values are very small. If separate in-plane and out-of-plane unity checks are conducted, the in-plane checks are based on the in-plane P_r/P_c and the governing M_r/M_c values for FLB and TFY, while the out-of-plane checks are based on the out-of-plane P_r/P_c plus the governing M_r/M_c from all three of the flexural limit states

The governing unity check values are shaded in Table 8.24. Due to the large second-order effects in the modular frame, and the conservative nature of the effective length method for sway frames in which the applied stresses are dominated by non-sway flexure, the unity check values determined by the prototype effective length and direct analysis methods are dramatically different for the exterior columns. The governing unity check for the exterior columns using the AISC (2010) effective length method is 1.13 versus 0.78 by the direct analysis method under load case 1, a 45 % increase. This difference is mainly due to the large leaner column effects in the modular frame and their influence on the elastic sidesway buckling resistance of the structure, combined with the conservatism of the effective length approach in problems where the member stresses are dominated by non-sway flexure. As illustrated previously in Section 2.6.2, the direct analysis method provides a better representation of the true stability behavior for structures with light member axial loads and large second-order effects. The direct analysis method gives a more accurate estimate of the actual internal moments within the structure at the strength limit, and it compares these internal moments versus a reasonable

estimate of the actual member internal resistances. Conversely, the effective length method reduces the axial resistance anchor point of the beam-column interaction equations, P_c, to account for its underestimation of the true internal second-order moments. As illustrated previously by Figure 2.10, the effective length method tends to give a conservative estimate of the beam-column and frame resistance for these types of structures, due to its over-emphasis on the behavior of the frame under the unrealistic loading case of pure axial compression in the beam-column members.

Interestingly, the governing column direct analysis method unity check value of 0.80 is very close to the Chief Buildings value of 0.73 determined in the original design using an extension of the AISC (1989) ASD provisions and a linear elastic analysis. One should note that the second-order column moments determined in the GT-Sabre direct analysis calculations for LC1 (123 ft-kips in Table 8.13) are not all that different from the Chief and GT-Sabre column first-order elastic moments for this frame (111 and 113 ft-kips respectively in Table 8.12). Also, since the flexural resistance of the exterior columns is governed by flange local buckling, the AISC (2010) and AISC (1989) ASD based resistance checks are very similar for these columns. Therefore, it appears that the primary difference between the large unity check value of 1.14 obtained using the AISC (2010) effective length procedure versus the Chief value of 0.73 lies in the in-plane elastic sidesway buckling analysis used in determining the column axial capacity ratios. As illustrated previously in Figure 2.10, the effective length method appears to significantly overcompensate for the leaner column effects in frames where the second-order effects are large, but the columns are subjected to relatively small axial stresses and relatively small flexural stresses due to sidesway. Conversely, in frames where the

columns are subjected to larger axial stresses and relatively large sidesway moments, the direct analysis method and the effective length method give very comparable results (e.g., see the cantilever beam-column example in Section 2.6.1).

In contrast to the column unity checks, the unity check values for the rafter segments in the modular frame are nearly the same by both the effective length and direct analysis procedures. The unity check values by the prototype AISC (2010) procedures are larger than the Chief Buildings results for all the segments (1.01 and 1.02 versus 0.94 for segment a4-a5 under LC4a, 0.87 and 0.87 vs 0.81 for segment a9-a10 under LC4b, 0.95 and 0.96 versus 0.92 for segment a10-b1 under LC4b, and 0.89 and 0.89 versus 0.82 for segment c5-c6 under LC3). The increases relative to the Chief Buildings results are believed to be due in part to minor differences between the second-order elastic rafter bending moments determined in GT-Sabre versus the first-order elastic moments determined by Chief in a number of these cases (see Tables 8.12 and 8.13). Furthermore, the AISC (2010) LTB resistance for segment c5-c6 is slightly smaller than the corresponding base AISC (1989) flexural resistance. For this segment, some reduction in the prototype unity check value may be possible by accounting for end restraint effects from the adjacent less critical unbraced lengths. However, these benefits are believed to be rather small in this case. All of the other rafter segments considered in Table 8.24 are governed either by flange local buckling (FLB) or tension flange yielding (TFY). The base nominal FLB and TFY resistances in AISC (1989) and AISC (2010) are very similar for the slender-web type members considered in the modular frame example of this study. Therefore, the differences between the prototype AISC (2010) checks and the Chief values are not expected to be due to any significant differences in the underlying flexural

Table 8.24. Unity checks, modular frame.

		Load Case 1				Load Case 2				Load Case 3			
Location	Method	Governing *Mr / Mc*	Governing *Pr / Pc*	U.C. AISC(10)	U.C. Chief	Governing *Mr / Mc*	Governing *Pr / Pc*	U.C. AISC(10)	U.C. Chief	Governing *Mr / Mc*	Governing *Pr / Pc*	U.C. AISC(10)	U.C. Chief
Column Segments													
Seg. e1-e2	Effective Length	0.501	0.516	0.96	0.56	0.386	0.273	0.62	0.42				
	Direct Analysis	0.510	0.195	0.61		0.407	0.118	0.47					
Seg. e2-e3	Effective Length	0.652	0.516	1.10	0.68	0.452	0.273	0.67	0.47				
	Direct Analysis	0.663	0.182	0.75		0.479	0.110	0.53					
Seg. e3-e4	Effective Length	0.702	0.516	1.14	0.73	0.462	0.273	0.68	0.47				
	Direct Analysis	0.713	0.164	0.80		0.490	0.098	0.54					
Rafter Segments													
Seg. a4-a5	Effective Length	0.763	0.066	0.80	0.76	0.404	0.028	0.42	0.42				
	Direct Analysis	0.770	0.065	0.80		0.391	0.031	0.41					
Seg. a9-a10	Effective Length	0.779	0.052	0.81	0.74	0.440	0.022	0.45	0.43				
	Direct Analysis	0.782	0.046	0.81		0.436	0.022	0.45					
Seg. a10-b1	Effective Length	0.861	0.056	0.89	0.85	0.487	0.019	0.50	0.49				
	Direct Analysis	0.864	0.044	0.89		0.482	0.016	0.49					
Seg. c5-c6	Effective Length	0.372	0.037	0.39	0.36	0.236	0.011	0.24	0.23	0.878	0.031	0.89	0.82
	Direct Analysis	0.373	0.034	0.39		0.236	0.010	0.24		0.881	0.028	0.90	

		Load Case 4a				Load Case 4b			
Location	Method	Governing *Mr / Mc*	Governing *Pr / Pc*	U.C. AISC(10)	U.C. Chief	Governing *Mr / Mc*	Governing *Pr / Pc*	U.C. AISC(10)	U.C. Chief
Rafter Segments									
Seg. a4-a5	Effective Length	0.978	0.054	1.01	0.82				
	Direct Analysis	0.995	0.052	1.02					
Seg. a9-a10	Effective Length					0.847	0.039	0.87	0.81(1)
	Direct Analysis					0.851	0.033	0.87	
Seg. a10-b1	Effective Length					0.932	0.044	0.95	0.92
	Direct Analysis					0.938	0.035	0.96	

(1) Chief Buildings unity check for a9-a10 is reported at a nodal location at x = 46.1 ft from a0, measured parallel to the roof line. This location is slightly inside of the maximum moment location in segment a9-a10, at a10 (x=46.4 ft from a0).

resistances in the modular frame example. The increases for segment a9-a10 appear to be due to a difference in the critical location assumed in these separate design evaluations. The unity checks in the Chief solution are determined from a nodal location at x = 46.1 ft from location a0 in Figure 8.24, measured parallel to the roof line. This location is slightly inside the maximum moment location in segment a9-a10 determined in the GT-Sabre analyses, which is at a10 (i.e, at x = 46.4 ft from a0).

8.2.6 Virtual Test Simulation Results

The general procedures for the virtual test modeling of the modular frame are the same as the single-span frame. Similar to the single-span frame, the geometric imperfections are applied at the location where the design-checks are relatively large for LC1, in the vicinity of the nodes a1, a4, a5, and a6, and the top of the exterior columns (see Table 8.24). Figure 8.25 shows the load-deflection plot using the sidesway displacement at e4. It is clear that the modular frame fails due to a sidesway stability failure. As explained in Section 8.1.6, the ordinate of this plot is the normalized applied load fraction of the LRFD strength limit divided by the factor of 0.9, $1/0.9 \times (1.2D + 1.2C + 1.6S) = 1/0.9 \times 1.52(D + C + S) = 1.69(D + C + S)$. Figure 8.25 shows the modular frame has 20 % more capacity than the strength limit load. Figure 8.26 shows the von Mises and equivalent plastic strain contours with the deformed shape of the modular frame at the peak load. The modular frame has not been significantly yielded at the peak load.

In Figure 8.27, the buckling in the out-of-plane direction of the compression flange can be seen in the segment a10-b1. The flexural capacity ratio for this segment is governed by TFY in Table 8.19. However, if the recommended LTB provisions described in Chapter 7 are used, the strength check is governed by LTB and the LTB

ratio of M_r/M_c for the segment a10-b1 becomes 0.87. As mentioned in Section 8.16, the result shown in Figure 8.25 is not directly comparable to the unity check shown in Table 8.24. Furthermore, the modular frame has large 2nd-order effects so the limit load cannot be approximated by 1/U.C. In Table 8.24, the governing unity check based on the direct analysis method is 0.89 for the segment a10-b1 at the design load of $1.6(D + C + S)$. Assuming conservatively that the modular frame reaches its limit state without significant additional load, then the limit load of the modular frame based on ASD is $1.6\ (D + C + S)$, which is 79 % of $[1.2 \times 1.69(D + C + S)]$. In Figure 8.25, one can observe that the lateral deflection of the modular frame is increased drastically once the applied load fraction reaches 1.08 × LRFD limit load. The assumed ASD limit load based on the unity check, $1.6(D + C + S)$ is 88 % of $[1.08 \times 1.69(D + C + S)]$.

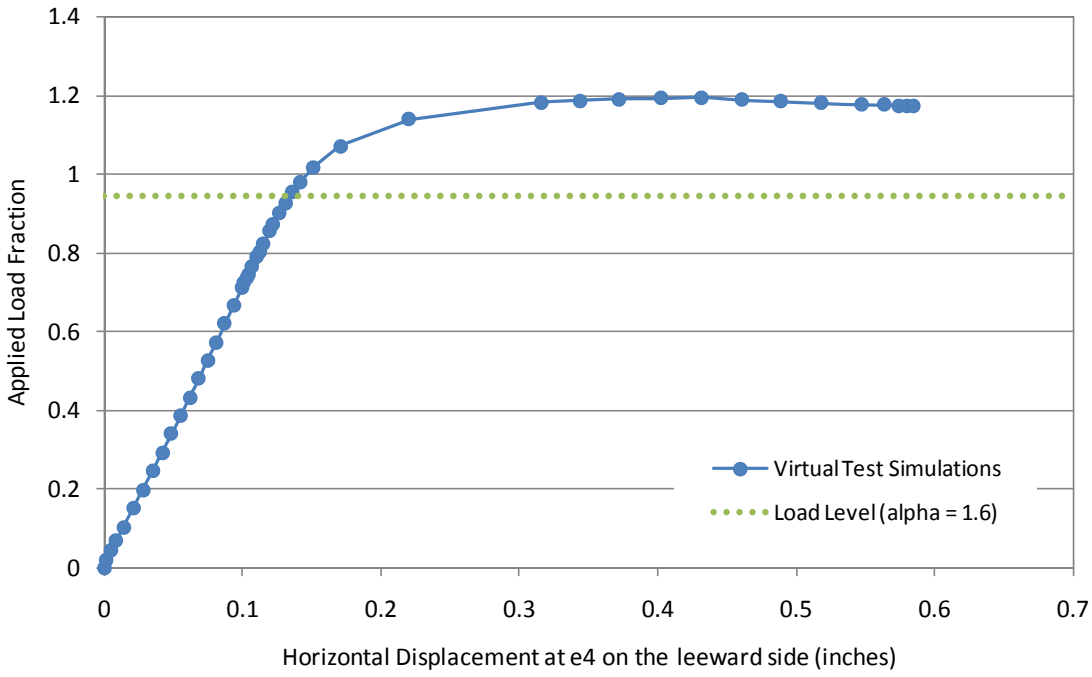

Figure 8.25. Load vs. deflection plot of modular frame.

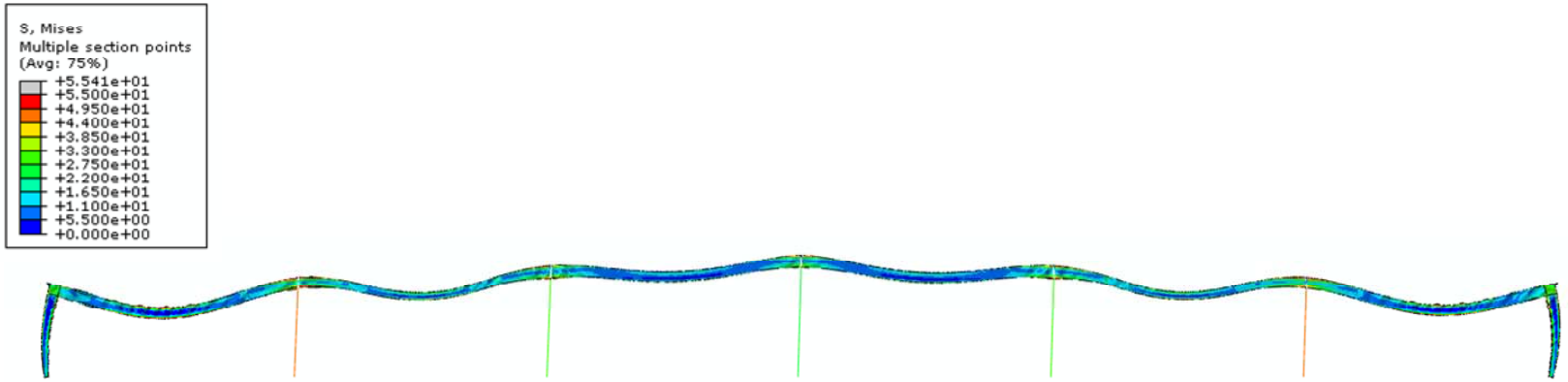

(a) von Mises stress contour at peak load

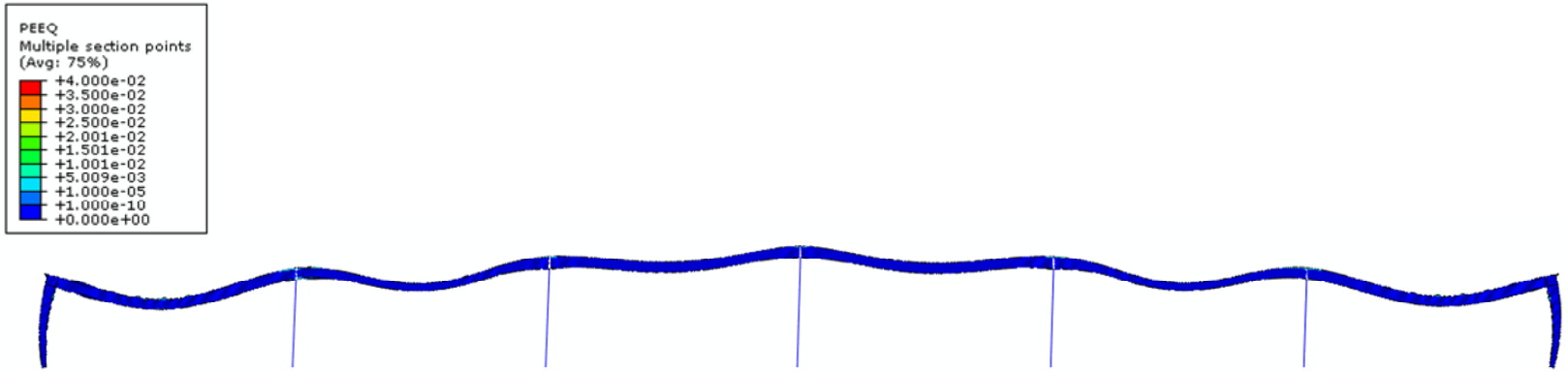

(b) Equivalent plastic strain contour at peak load

Figure 8.26. von Mises and equivalent plastic strain contour at peak load (deformation scale factor = 20).

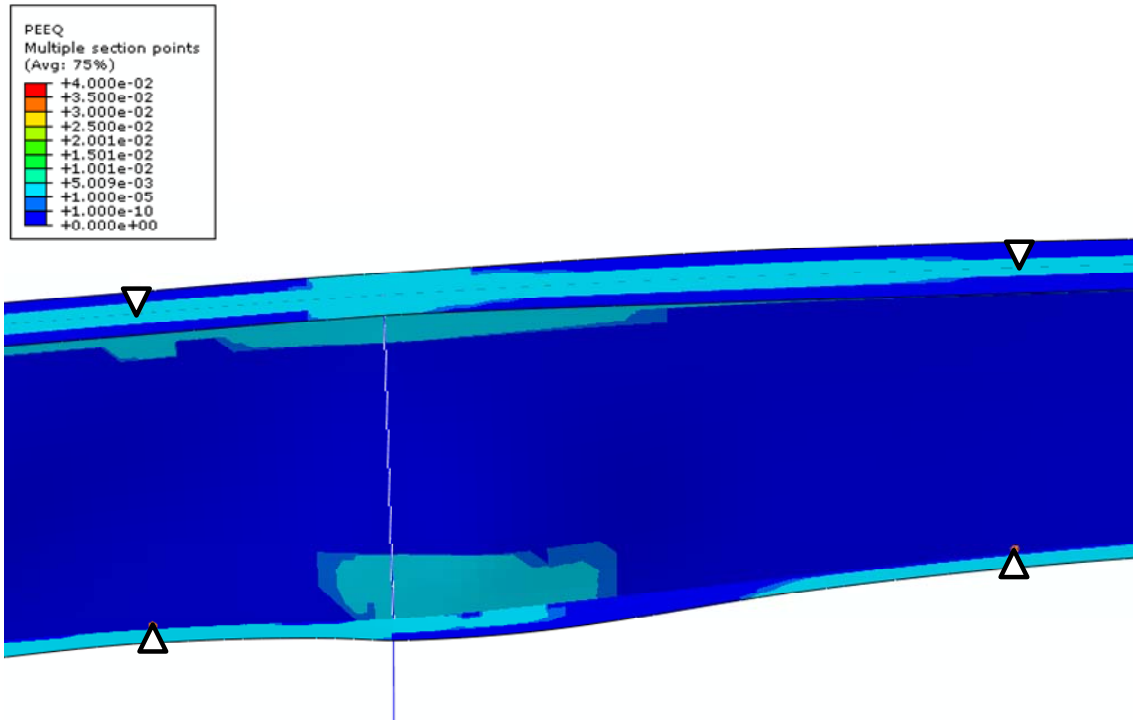

Figure 8.27. Equivalent plastic strain contour of segment a10-b1 (deformation scale factor = 5).

CHAPTER IX

CONCLUSIONS

9.1. Summary and Conclusions of the Research

This research focuses on the development of extensions to the AISC (2010) Specification for the design of frames using web-tapered and other non-prismatic members. The fundamental approach employed in these extensions is a mapping of the theoretical elastic buckling strength of a non-prismatic member to the corresponding nominal design strength using the concept of an equivalent prismatic member. The terms γ_e and $(f_r/F_{y.eq})_{\max}$ are introduced to both generalize and simplify the application of the mapping concept. The symbol γ_e denotes the elastic buckling load ratio, that is, the ratio of the load at theoretical elastic buckling to the required design load. The term $(f_r/F_{y.eq})_{\max}$ is the maximum ratio of the stress caused by the required design load, f_r, to the equivalent yield stress, $F_{y.eq}$. The equivalent yield stress $F_{y.eq}$ is taken equal to QF_y for calculation of the column axial resistance in members having sections with slender cross-section elements under uniform axial compression, and it is otherwise taken equal to F_y. The terms γ_e and $(f_r/F_{y.eq})_{\max}$ and the base AISC mappings from the theoretical elastic buckling resistance to the nominal design resistance provide a basic framework for application of the AISC (2010) Specification to web-tapered members and other general nonprismatic members. In addition, this approach can be used as an accurate to slightly conservative generalization of prismatic member provisions in other steel design standards to accommodate the design of general nonprismatic members.

The calculation of γ_e for a broad range of geometries and configurations is key to the usefulness of the proposed approach. Therefore, a number of practical simplified methods for estimating various elastic buckling strengths are investigated in this research. Simplified elastic buckling calculations are developed for in-plane and out-of-plane flexural buckling, torsional or flexural-torsional buckling, constrained-axis torsional buckling and lateral torsional buckling of unbraced lengths with linearly-tapered web depths. The proposed calculations are based largely on the use of the cross-section at the middle of the governing unbraced length along with prismatic member elastic buckling equations. To evaluate these proposed design-oriented methods, parametric studies are conducted using open-section thin-walled beam theory and elastic eigenvalue buckling analysis. It is concluded that the proposed simplified methods can estimate the elastic buckling solutions for web-tapered members with good accuracy. The largest differences between the simplified estimates and the elastic eigenvalue buckling solutions for web-tapered members occur for the case of lateral torsional buckling of beams under double curvature bending. However, the errors are conservative, and it is recognized that individual unbraced lengths in members with linearly-tapered webs are rarely subjected to double curvature bending. These simplified elastic buckling calculations as well as the recommendations for applying the AISC (2010) provisions to the design of frames using nonprismatic members have been adopted in the AISC Design Guide 25, *Frame Design using Web-Tapered Members* (MBMA/AISC 2010).

In this research, an extensive parametric study is conducted using virtual test simulation to investigate the beam lateral torsional buckling (LTB) resistances of prismatic and web-tapered members. As a first step, it is crucial to establish and validate

the virtual test simulation procedures. For this purpose, a number of physical experimental tests are selected involving both prismatic and web-tapered members. These tests are used to verify 1) the ability of the virtual test simulation procedures to predict the experimental test results, 2) the effect of selected nominal residual stress patterns, and 3) the effect of selected nominal geometric imperfection shapes and magnitude.

Based on a limited number of available cases, it is demonstrated that if the virtual test simulations are performed using the measured data for the residual stresses and the geometric imperfections, the virtual test simulation results are essentially the same as the experimental test results. This is observed for the virtual test simulations of the tests conducted by Dux and Kitipornchai (1983) and Wong-Chung and Kitipornchai (1987). For all the other test cases considered in this research, unfortunately complete information about the physical residual stresses and geometric imperfections is not available. Furthermore, the tests conducted by Dux and Kitipornchai (1983) and Wong-Chung and Kitipornchai (1987) are rolled I-section members whereas the primary emphasis of this research is on welded built-up section members. Therefore a residual stress pattern for welded I-section members is selected for virtual test simulation in this research. The effect of the selected residual stress pattern as well as different representative residual stress patterns is studied by comparing virtual test simulation results with experimental test results for the physical tests considered in this research.

A residual stress pattern is selected for the detailed studies conducted in this research that is a fit to residual stress data obtained by sectioning from a representative tapered I-section member by Prawel et al. (1974). The selected pattern can be said to be

a rather optimistic one in that it has a smaller magnitude of the residual stresses than observed in other studies for welded specimens. It is also relatively optimistic compared to other patterns typically used in analytical studies of welded I-section members, such as those utilized in the development of the Eurocode 3 (CEN 2005) member resistance equations (Rebelo et al. 2009). Furthermore, a compression flange sweep of L_b/1000 is selected for the detailed member studies. This geometric imperfection is the maximum permitted for column members in the AISC Code of Standard Practice (AISC 2005). In addition, this geometric imperfection is the same basic pattern and magnitude assumed in virtual test simulation studies used as a primary basis for the Eurocode 3 (CEN 2005) member resistance equations (Rebelo et al. 2009).

It is shown that the nominal residual stress pattern selected for the detailed studies in this research, combined with a compression flange sweep imperfection of L_b/1000, gives a reasonable lower bound to experimental test strengths for all uniform bending tests. For moment-gradient tests, the above residual stresses and geometric imperfections give moderately smaller to accurate solutions compared to experimental test strengths except one test in Schilling (1985), where FLB governs. For beam-column tests, the above initial conditions in virtual test simulation give moderately smaller to accurate solutions compared to experimental test strengths except two beam-column tests in Prawel et al. (1974). These tests are LB-C-3 and LB-C-7, where the virtual test simulations give 15 and 12 % larger strengths than the experimental test strengths. It should be noted that these beam-columns are flexural dominated members, where FLB governs. It appears that the compression flange sweep imperfection of L_b/1000 gives moderately unconservative solutions for members where FLB governs. However, the

typical welded members in metal building frames are braced such that LTB governs their flexural resistances in general. Therefore, all the virtual test simulation studies in this work are conducted using the selected nominal residual stress pattern and flange sweep imperfection unless noted otherwise.

Using the available experimental test data for web-tapered members obtained from the literature, the web-tapered member resistance calculations developed in this research are evaluated. It should be noted that there is a very limited number of experimental tests using web-tapered members. Furthermore, in the most of these tests, the members have compact sections. Conversely, in metal building frames, the members generally have compact or noncompact flanges and a noncompact or slender web. The results from the design procedures are compared with member strengths measured from the experimental tests as well as with the results from virtual simulations of these tests.

In general, the member resistances based on the proposed design procedures are conservative compared to the experimental test data except for two test cases in Prawel et al. (1974), LB-5 and LB-C-8. For these cases, the maximum strengths measured from the experimental tests are slightly smaller than the member resistances calculated by the recommended design procedures. The unity checks of LB-5 and LB-C-8 based on the maximum strengths measured in the experiments are 0.93 and 0.98 respectively. The LB-5 beam has three unbraced lengths with the critical middle segment governed by LTB. It is observed in the virtual test simulation of LB-5 that the shear tension field action is dominant in the end segment at the deep end. It appears that due to this shear failure, the restraint effect from the deep-end segment is smaller than that of fully braced condition as assumed in the design procedures. The LB-C-8 test is a beam-column cantilever

subjected to small axial and large flexural loads. One should note that the plates of this beam-column are prepared by oxygen cut. Prawel et al. (1974) tested an identical beam-column which has cross-section plates prepared by shear cut (LB-C-7). The measured maximum strength of LB-C-7 is 5 % larger than that of LB-C-8. The corresponding unity check for LB-C-7 is 1.03. Both tests LB-C-7 and LB-C-8 failed by local buckling in the compression flange near the deep end. The authors provided no conclusion about the effect of the different cutting methods on the FLB strengths. However, they concluded that the oxygen cut members show larger LTB strengths.

As mentioned above, the design checks based on the procedures developed in Chapter 3 are also compared to the virtual test simulation results for web-tapered members. For tests in Prawel et al. (1974), the member resistances based on the design procedures are slightly unconservative for the beam tests and are conservative for the beam-column tests. For the two beam-column tests in Shiomi and Kurata (1984), the design checks are accurate to conservative compared to the virtual test simulation results. For the two beam-column tests selected from Salter et al. (1980), the design checks are unconservative for one test (C1) and are conservative for the other test (C8) compared to the virtual test simulations. The beam-column check of C1 is dominated by flexural resistance ($P_r/P_c = 0.31$ and $M_r/M_c = 0.84$) and the nominal flexural resistance of C1 is the plateau strength M_p due to a large C_b factor, 1.27. The virtual simulation study conducted in this research demonstrates that the design checks tend to be unconservative compared to the virtual test simulation results for beams with a large moment-gradient factor. It should be noted that for the tests conducted by Salter et al. (1980), the virtual test simulation is conducted using a residual stress pattern recommended by Salter et al.

(1980) as being representative for their test members. This is a nominal residual stress pattern proposed originally by Young and Robinson (1975).

After the above virtual test simulation procedures are evaluated, a parametric study is conducted for the assessment of beam lateral torsional buckling (LTB) resistances for prismatic and web-tapered members. A total of 351 uniform-stress (or uniform-bending) cases and 191 stress-gradient (or moment-gradient) cases are considered. For each tapered member, an equivalent prismatic member is created. The results of the virtual test simulations are compared with the AISC (2010) and CEN (2005) resistances for the prismatic members, and with the procedures developed in Chapter 3, for the web-tapered members. The web-tapered member resistances determined based on the above procedures are referred to as the MBMA/AISC (2010) resistances in the discussion below. The key findings from this parametric study are as follows:

- The LTB resistances of the web-tapered members are essentially the same or slightly larger than the equivalent prismatic members. In other words, the parametric study demonstrates that the strength behavior of web-tapered members compares closely with the corresponding strength of the equivalent prismatic members. This confirms the fundamental concept developed in this research for the framework of the design of frames using web-tapered members.
- The ratio of the clear web depth to the compression flange width h/b_{fc} has a significant effect on the LTB resistances of both the web-tapered members and the prismatic members. This aspect is recognized in the development of the LTB calculations of CEN (2005), but is generally not recognized in the AISC equations other than via its impact on the member elastic LTB resistance. CEN (2005) suggests

different buckling strength curves for beams with $h/b_f \leq 2$ and with $h/b_f > 2$. The AISC (2010) provisions suggest one buckling curve for all the cases. The results of the virtual test simulations demonstrate that if $h/b_{fc} \geq 4$, the LTB resistances of the web-tapered and prismatic members are significantly smaller than the nominal strengths of MBMA/AISC (2010) and AISC (2010), especially within the inelastic LTB region. The differences in the LTB strengths between the virtual test simulations and the nominal resistances of MBMA/AISC (2010) and AISC (2010) become larger for beams with larger h/b_{fc}.

(For doubly-symmetric beams with $h/b_{fc} = 4$, $b_{fc}/2t_{fc} = 6$, and $h/t_w = 100$ under uniform bending, the LTB strengths obtained from virtual test simulation M_{FEA} are 20.5 % smaller than the nominal MBMA/AISC(2010) and AISC (2010) resistances M_n in average for $0.775 \leq (F_y/\gamma_e f_r)^{0.5} \leq 1.2$. For corresponding beams with $h/b_{fc} = 5.5$ and 7, M_{FEA} is 24.1 and 29.8 % smaller than M_n in average. For doubly-symmetric beams with $b_{fc}/2t_{fc} = 6$, $h/t_w = 180$ under uniform bending, the average values of M_{FEA}/M_n are 0.84, 0.83, and 0.79 for $h/b_{fc} = 4$, 5.5, and 7 respectively for $0.775 \leq (F_y/\gamma_e f_r)^{0.5} \leq 1.2$.)

- The virtual test simulation results also demonstrate that if beams with $h/b_{fc} < 4$ have noncompact flanges and a noncompact web, the LTB resistances of these beams are significantly smaller than the nominal strengths of AISC (2010), especially within the inelastic LTB range. One should note that for these beams, the FLB governs for $(F_y/\gamma_e f_r)^{0.5} \leq 0.775$.

(Doubly-symmetric prismatic beams with $b_{fc}/2t_{fc} = 12$ and $h/t_w = 130$ under uniform bending, the average M_{FEA}/M_n values are 0.80 and 0.81 for $h/b_{fc} = 1$ and 2 for $0.775 \leq (F_y/\gamma_e f_r)^{0.5} \leq 1.2$).

- It should be recognized that the 267 ASTM A6 wide-flange sections listed in the AISC 13th Edition Manual have a maximum h/b_{fc} of 3.05. Furthermore, 176 of these sections have $h/b_{fc} \leq 2$. For the test beams with the cross sections comparable to the rolled I-sections, the virtual test simulation results are close to or moderately smaller than the AISC (2010) resistances. One should recognize that for these test beams, the use of the Lehigh residual stress pattern (Galambos and Ketter 1959) for rolled I-sections gives essentially the same results as those obtained using the selected nominal residual stress pattern for welded I-sections.

  (For doubly-symmetric beams with $b_{fc}/2t_{fc} = 12$ and $h/t_w = 40$ under uniform bending conditions, the average M_{FEA}/M_n values are 0.90, 0.85, and 0.84 for $h/b_{fc} = 1$, 1.5, and 2 respectively for $0.775 \leq (F_y/\gamma_e f_r)^{0.5} \leq 1.2$.)

- The virtual test simulations demonstrate that the plateau strengths of the AISC (2010) and MBMA/AISC (2010) resistance curves are overly optimistic for the beams with $h/b_{fc} \geq 4$ and a compact or noncompact web. The worst case considered in this research is a beam with $h/b_{fc} = 7$, $b_{fc}/2t_{fc} = 6$, and $h/t_w = 85$. This beam cannot develop the plateau strength, M_p.

  (The plateau of the AISC (2010) and MBMA/AISC (2010) curves extends to $(F_y/\gamma_e f_r)^{0.5} = 0.35$. Doubly-symmetric beams with $h/b_{fc} = 4$, $b_{fc}/2t_{fc} = 6$, and $h/t_w = 85$ under uniform bending, $M_{FEA}/(M_n=M_p) = 0.90$ in average for $(F_y/\gamma_e f_r)^{0.5} \leq 0.35$. The corresponding beams with $h/b_{fc} = 5.5$ and 7 give $M_{FEA}/(M_n=M_p) = 0.89$ and 0.86 in

average for $(F_y/\gamma_e f_r)^{0.5} \leq 0.35$. Conversely, doubly-symmetric prismatic beams with $h/b_{fc} \leq 2$, $b_{fc}/2t_{fc} = 6$ and $h/t_w = 40$ under uniform bending give the average $M_{FEA}/(M_n=M_p) = 0.98$ for $(F_y/\gamma_e f_r)^{0.5} \leq 0.35$.)

- In addition, it is found that the plateau length of the AISC (2010) and MBMA/AISC (2010) resistance curve is too optimistic for the beams with welded-section type cross sections. The virtual test simulation results support the plateau length of the general welded-section curve in CEN (2005). For the beams with larger h/b_{fc} and smaller h/t_w, the need of the shorter plateau length becomes more obvious.

  (Based on the AISC (2010) and MBMA/AISC (2010) flexural equations, the plateau extends to $(F_y/\gamma_e f_r)^{0.5} = 0.35$. However, virtual test simulation gives smaller flexural strength at $(F_y/\gamma_e f_r)^{0.5} = 0.35$ than at $(F_y/\gamma_e f_r)^{0.5} = 0.2$. Double-symmetric beams with $h/b_{fc} = 4$, $b_{fc}/2t_{fc} = 6$, and $h/t_w = 180$ under uniform bending give the average $M_{FEA}/M_n = 1.0$ and 0.98 at $(F_y/\gamma_e f_r)^{0.5} = 0.2$ and 0.35 respectively. Doubly-symmetric beams with $h/b_{fc} = 7$, $b_{fc}/2t_{fc} = 6$ and $h/t_w = 85$ under uniform bending give the average $M_{FEA}/M_n = 0.92$ and 0.80 at $(F_y/\gamma_e f_r)^{0.5} = 0.2$ and 0.35 respectively. That is, M_{FEA} at $(F_y/\gamma_e f_r)^{0.5} = 0.35$ is 13 % smaller than that at $(F_y/\gamma_e f_r)^{0.5} = 0.2$. The CEN (2005) resistance curve for general welded sections, the plateau extends to $(F_y/\gamma_e f_r)^{0.5} = 0.2$.)

- It is found that the LTB strength at the inelastic LTB limit (corresponding to $L_b = L_r$, and thus $F_{eLTB} = 0.7F_y$ and $M_n = F_{eLTB} S_{xc} = 0.7 M_{yc}$ for most cases) is too optimistic for all the parametric study beams considered in this research. The virtual test simulations demonstrate that the strengths of all beams with $F_{e.LTB}$ in the vicinity of $0.7F_y$ are influenced substantially by combined residual stress and geometric imperfection effects. As a result, the LTB strengths of beams with the unbraced

lengths close to the inelastic LTB limit are smaller than the nominal elastic LTB strengths of AISC (2010) and MBMA/AISC (2010). The combined residual stress and geometric imperfection effects are more significant for beams with larger h/b_{fc}. Conversely, the elastic LTB strengths of beams with significantly longer unbraced lengths are close to the nominal elastic LTB strengths of AISC (2010) and MBMA/AISC (2010).

(For beams with $b_{fc}/2t_{fc} = 6$ and $h/t_w = 40$ under uniform bending, the values of $M_{FEA}/M_n = M_{FEA}/(0.7M_{yc})$ are 0.87, 0.82, and 0.81 for h/b_{fc}= 1, 1.5, and 2 respectively at $(F_y/\gamma_e f_r)^{0.5} = (1/0.7)^{0.5} = 1.2$. For beams with $b_{fc}/2t_{fc} = 6$ and $h/t_w = 100$ under uniform bending, M_{FEA}/M_n = 0.78, 0.76, and 0.71 for h/b_{fc} = 4, 5.5, and 7 respectively at $(F_y/\gamma_e f_r)^{0.5} = 1.2$. Conversely, M_{FEA} for these beams are close to M_n at $(F_y/\gamma_e f_r)^{0.5}$ = 1.7. The values of M_{FEA}/M_n are 0.96, 0.97, and 0.95 for h/b_{fc}= 4, 5.5, and 7 respectively.)

- Due to the aspects explained above (the optimistic nominal LTB strengths at the plateau and at the inelastic LTB limit and the optimistic plateau lengths), the nominal LTB resistances obtained from AISC (2010) and MBMA/AISC (2010) are optimistic compared to the virtual test simulations, especially for the beams with $h/b_{fc} \geq 4$, $b_{fc}/2t_{fc} = 6$, and a compact or noncompact web. In addition, the AISC (2010) and MBMA/AISC (2010) nominal LTB resistances are unconservative for the beams with $h/b_{fc} \geq 4$ and a slender web and for beams with $h/b_{fc} < 4$ and noncompact flanges and a noncompact web. However, the errors are not as large for these beams.

  (For doubly-symmetric beams with $h/b_{fc} \geq 4$, $b_{fc}/2t_{fc} = 6$, and $h/t_w = 85$ under uniform bending, the range of M_{FEA}/M_n values is 0.76 at $(F_y/\gamma_e f_r)^{0.5} = 1.2$ to 0.93 at $(F_y/\gamma_e f_r)^{0.5}$

= 0.2. For corresponding beams with $h/t_w = 100$, the range of M_{FEA}/M_n values is 0.68 at $(F_y/\gamma_e f_r)^{0.5} = 1.2$ to 0.98 at $(F_y/\gamma_e f_r)^{0.5} = 0.2$. However, for doubly-symmetric beams with $h/b_{fc} \geq 4$, $b_{fc}/2t_{fc} = 6$, and $h/t_w = 180$ under uniform bending, the range of M_{FEA}/M_n is 0.72 at $(F_y/\gamma_e f_r)^{0.5} = 1.2$ to 1.04 at $(F_y/\gamma_e f_r)^{0.5} = 0.2$. Similarly for doubly-symmetric beams with $h/b_{fc} < 4$, $b_{fc}/2t_{fc} = 12$, and $h/t_w = 130$ under uniform bending, the M_{FEA}/M_n range is 0.75 at $(F_y/\gamma_e f_r)^{0.5} = 1.2$ to 1.0 at $(F_y/\gamma_e f_r)^{0.5} = 1.75$.)

- It is found that the virtual test simulation strengths indicate a definite concave shape within the inelastic LTB region for the beams with $h/b_{fc} \geq 4$. This finding supports the concave LTB resistance curve of CEN (2005) for general welded I-sections. For the beams with the cross-sections comparable to the rolled I-sections ($h/b_{fc} \leq 2$, $b_{fc}/2t_{fc} = 6$, and $h/t_w = 40$), the virtual test simulation results are close to the shape of the LTB resistance curve of CEN (2005), which is only slightly convex within the inelastic LTB region.
- The effect of single symmetry on the LTB resistances is also studied in this research. Cases with larger compression flanges as well as with larger tension flanges are considered. It is found that the single symmetry has a negligible effect on the accuracy of the predictions by the nominal strength equations of AISC (2010) and MBMA/AISC (2010). Conversely, the single symmetry affects the accuracy of the CEN (2005) resistances especially for relatively short beams with $(F_y/F_e) \leq 0.775$. For some cases, the CEN (2005) predictions for singly-symmetric beams are more accurate than that for doubly-symmetric beams. This occurs when the singly-symmetric members have "*effective Class 2*" sections so the plateau strength of CEN (2005) is increased. As a result, the differences between the CEN (2005) resistances

and the virtual test simulation results become smaller. For other cases, the CEN (2005) plateau strength is decreased due to the combination of smaller tension flanges and Class 4 cross-sections. The decreased plateau strengths are often close to the TFY limit of AISC (2010) and MBMA/AISC (2010). When the CEN (2005) plateau strength is decreased for singly-symmetric beams, the resulting M_{FEA}/M_n values for CEN (2005) are smaller than those for doubly-symmetric beams.

- In AISC (2010), the moment-gradient LTB resistances are obtained in one way: by scaling the uniform-bending LTB resistances with the moment gradient factor C_b. In this research, two procedures are suggested to calculate the stress-gradient LTB resistances of the web-tapered members. The first procedure (referred to as the *MBMA/AISC-1 procedure*) is essentially the same as the above AISC (2010) method. The uniform-stress LTB resistances are scaled by the stress gradient factor C_b. In the second procedure (referred to as the *MBMA/AISC-2 procedure* in this dissertation), the stress-gradient factor C_b is applied to the elastic LTB load ratio γ_{eLTB}. That is, one multiplies γ_{eLTB} (based on the uniform stress conditions) by the stress-gradient factor C_b: $\gamma_{eLTB(Cb)} = C_b\gamma_{eLTB}$. Alternately, in general, the elastic LTB load ratio γ_{eLTB} can be obtained by a rigorous buckling analysis based on the given load and boundary conditions and using open-section thin-walled beam theory. In this approach, the stress gradient effect is already imbedded in this γ_{eLTB}, i.e., $\gamma_{eLTB\ (Cb)} = \gamma_{eLTB}$. Therefore, the stress-gradient LTB resistances are calculated by using the LTB resistance equation with $\gamma_{eLTB\ (Cb)}$. CEN (2005) calculates the moment-gradient LTB resistances in this fashion for general I-section members. Also, the former AISC Allowable Stress Design Specification (AISC 1989) accounts for moment gradient

effects in this way.

The virtual test simulations indicate that the MBMA/AISC-2 procedure provides better estimates of the stress-gradient LTB resistances within the inelastic LTB region. For the plateau strength and the elastic LTB resistances of relatively long beams, the LTB resistances from the MBMA/AISC-2 procedure are identical to the ones from the MBMA/AISC-1 procedure.

It is important to estimate the implications of the above virtual test simulation results on the underlying structural reliability for statically determinate beam members. In this regard, it is also useful to consider an estimate of the structural reliability based on prior experimental test data as provided by White and Jung (2008), White and Kim (2008) and Righman (2005). All the experimental tests used for the reliability assessment are prismatic member tests. This is because the experimental tests using web-tapered beams are too limited to perform a reliability assessment.

It is found that the reliability indices β obtained from the virtual test simulations for the uniform-stress and uniform-bending cases are generally approximately equal to or smaller than those obtained from experimental test data within the plateau strength and the elastic LTB regions. However, they are significantly smaller within the inelastic LTB region compared to the reliability indices estimated from experimental test data. In addition, the β values based on the stress-gradient (and moment-gradient) virtual test simulations are significantly smaller than that of the moment-gradient tests within the inelastic LTB region. The β values based on the physical moment-gradient tests within the elastic LTB range are not available. However, it should be recognized that the reliability for elastic LTB under moment gradient should be comparable to the reliability

for elastic LTB under uniform bending. The reliability indices for physical uniform-bending tests are 2.6 and 2.75 for rolled and welded members respectively. These are larger than the reliability index for moment-gradient tests considered in virtual test simulation, which is 2.16.

It is shown in Chapter 7 that the observations and the reliability assessment obtained from the experimental test data and the virtual test simulations are significantly different. Furthermore, both data sets have their limitations. Therefore, in this research, separate sets of recommendations are developed for potential improvement of the LTB resistance calculations based on 1) the experimental test data and 2) the virtual test simulations. The recommended resistance calculations are as follows:

1. Based on the experimental test data:

- Calculate the nominal LTB resistance at the inelastic LTB limit as $M_n = R_{pg}F_LS_{xc}$ where $F_L = 0.6F_{yc}$.
- Calculate the web compactness limit λ_{pw} using Eq. 7.8, which is originally developed by Barth and White (1997).
- Use the MBMA/AISC (2010)-2 procedure for both prismatic and tapered members to calculate the LTB resistances under moment-gradient or stress-gradient conditions.

2. Based on the virtual test simulations:

- Use shorter plateau length $L_p = 0.63r_t(E/F_y)^{0.5}$ or $(F_y/F_e)^{0.5} = 0.2$.
- Calculate the nominal LTB resistance at the inelastic LTB limit as $M_n = R_{pg}F_LS_{xc}$ where $F_L = 0.4F_{yc}$.
- Use a multi-linear representation of inelastic LTB resistances using Eqs. 7. 9 to 7. 11.

- Calculate the web compactness limit λ_{pw} using Eq. 7.8, which is originally developed by Barth and White (1997).
- Use the MBMA/AISC (2010)-2 procedure for both prismatic and tapered members to calculate the LTB resistances under moment-gradient or stress-gradient conditions.

Based on these recommended changes, the reliability indices for the virtual test simulation cases are re-calculated. It is demonstrated that the recommended LTB resistance calculations provide better and more consistent reliability indices for all the LTB ranges.

Lastly this dissertation presents the example design calculations and the virtual test simulation results of two example metal building frames. The selected example frames are a clear span frame and a modular frame. Both the direct analysis method and the effective length method are used for the stability design of the example frames. The design checks based on the proposed procedures are compared with the design checks obtained in the common design practice. It is shown that both the direct analysis method and the effective length method provide essentially the same design checks in general. However, when the frame has large second-order effect (the modular frame under the gravity load case), the effective length method provides significantly conservative unity checks for the lateral-load resisting columns. For the selected example frames, the virtual test simulations are performed considering the residual stresses and the geometric imperfections. The virtual test simulation of the clear span frame shows the failure in one of the rafter segments as indicated in the unity check results. The virtual test simulation of the modular frame shows that the frame has approximately 20 % more capacity than the nominal LRFD design strength.

9.2. Impact of the Research

There are a number of important contributions that this research provides. The impact of this research is discussed subsequently.

- The most important contribution of this research is the development of the general framework for design of frames using nonprismatic members. A mapping of the elastic buckling strength of nonprismatic members to the nominal resistance of equivalent prismatic members is applied in the basic framework. By introducing the terms γ_e and $(f_r/F_{y.eq})_{\max}$, this fundamental concept is more generalized and simplified. In this research, the basic framework is used to apply the AISC (2010) provisions for design of frames using web-tapered and other nonprismatic members. The same approach can be used as an accurate to slightly conservative generalization of prismatic member provisions in other steel design standards to accommodate the design of general nonprismatic members.
- In this research, the practical design-oriented procedures are developed to calculate the elastic buckling solutions for the prismatic and web-tapered members. The suggested procedures are straightforward so that these procedures can be easily incorporated in the software that Engineers want to use for their design calculations.
- Virtual test simulation conducted in this research is a 3D nonlinear finite element analysis including the residual stresses and geometric imperfections, which is a substantially refined simulation. The general procedures of virtual test simulation are validated in details by comparing the results with the experimental tests. These procedures can serve as the guidelines for virtual test simulation in other analytical studies.

- The lateral torsional buckling resistances of prismatic and web-tapered members are investigated comprehensively using virtual test simulation. It is found that the resistances of web-tapered members are fundamentally comparable to that of prismatic members. This indicates that if new updates or developments are introduced in the design of prismatic members, the same updates or developments potentially apply to the design of web-tapered members. Similarly, if the design procedures for web-tapered members are updated, the design procedures for prismatic members can be updated in a same fashion.
- This research provides a large number of parametric study data for the lateral torsional buckling resistances of prismatic and web-tapered members. One should note that this parametric study data includes beams with cross-section properties that are considered in a limited number of experimental studies. .The virtual test simulation data obtained in this research can serve as additional data points in the future developments or updates of the beam LTB resistance calculations.
- For the two example frames shown in Chapter 8, detailed descriptions are provided for the design check calculations based on the procedures developed in Chapter 3. In addition, the values of all the key parameters required in the resistance calculations are provided. The calculation of the in-plane flexural buckling load ratio of the lateral-load resisting columns is described in details as well. The information provided in Chapter 8 is very useful for better understanding of the frame design using web-tapered members.

9.3. Future Study

There are a number of issues should be investigated to refine the design procedures of the frames using web-tapered members. The suggested future works are as follows:

- In the direct analysis method, the stiffness reduction factor 0.8 is applied to the frames with web-tapered members in this research. The stiffness reduction factor 0.8 is developed focusing on rectangular frames with prismatic members. The virtual test simulation result of the modular frame indicates that the use of $0.8E$ can be conservative for frames with web-tapered members. A parametric study should be conducted to determine if a smaller amount of stiffness reduction can be justified in the direct analysis method for frames with web-tapered members.
- In this research, the bracing demands in the frames are not investigated. It is assumed that the flanges are braced appropriately where the purlins or girts and the diagonal bracings are located. However, there exist large variations in the design of the purlins or girts and the diagonal bracings. It is desirable to provide the design requirements for the bracing systems in the metal building frames. When the bracing system requirements are determined, then the guidelines for consideration of the end restraint effects from the adjacent segments in the member resistance calculations can be established.
- It is clearly indicated that there is a significant distinction in the reliability assessment based on the experimental test data and the virtual test simulations. As indicated above, both data sets have their limitations. The experimental test data is rather sparse in many of the ranges of the design space while the virtual test simulations

results are based on a single residual stress pattern and a single geometric imperfection. The only way to resolve the differences in these two data sets is to conduct a Monte Carlo simulation with appropriate distributions of residual stress patterns and geometric imperfections. .

- The shear capacity of web-tapered beams is not studied in this research. In the parametric study of beams under stress gradient (and moment gradient), the beams that collapse due to the shear failure are not considered. It is desirable to study the shear resistances of web-tapered beams using virtual test simulation so that the procedures for the shear resistance calculations and the transverse stiffener requirements can be developed.

APPENDIX A

AXIAL CAPACITY RATIO CALCULATIONS USING THE AISI (2001) PROVISIONS

The AISI (2001) nominal column strength P_n is determined as

$$P_n = A_{eff} F_n \qquad \text{(Eq. A.1)}$$

where F_n is the nominal axial stress, which may be calculated by

$$F_n = \left(0.658^{\frac{1}{\gamma_e (f_r / F_y)}} \right) F_{y.} \qquad \text{for } \gamma_e \left(\frac{f_r}{F_y} \right) \geq 0.44 \qquad \text{(Eq. A.2a)}$$

$$F_n = 0.877 \gamma_e f_r \qquad \text{for } \gamma_e \left(\frac{f_r}{F_{y.}} \right) < 0.44 \qquad \text{(Eq. A.2b)}$$

f_r is member axial stress calculated by

$$f_r = P_r / A_{eff} \qquad \text{(Eq. A.3)}$$

and A_{eff} is the effective area of cross-section calculated by

$$A_{eff} = A_g - \Sigma \left(A_{gi} - A_{effi} \right) \qquad \text{(Eq. A.4)}$$

where A_{gi} is the gross area of a cross-section element and A_{effi} is the effective area of a cross-section element. For members with no slender cross-section elements, $A_{eff} = A_g$. The effective area of a cross-section element is calculated by $A_{effi} = (b_{eff}\, t)_i$ where t is the thickness of an element and b_{eff} is the effective width of a slender rectangular plate element which is determined by

$$b_{eff} = 0.959 t \sqrt{\frac{E k_c}{F_n}} \left[1 - \frac{0.211}{(b/t)} \sqrt{\frac{E k_c}{F_n}} \right] \leq b \qquad \text{(Eq. A.5)}$$

using an appropriate value of a local buckling coefficient k_c for different cross-section elements in different sections. One should recognize that the ratios f_r/F_y in Eqs. A.2 are equivalent to the ratios $f_r/F_{y.eq}$ in Eqs. 3.6. For members with slender elements, $f_r/F_y = P_r/A_{eff}F_y$ in Eqs. A.2, which is equivalent to f_r/QF_y in Eqs. 3.6.

This section outlines a procedure for application of the AISI (2001) axial resistance equations to the calculation of the axial capacity for web-tapered and nonprismatic members. Each step of this procedure is explained below. Representative results are shown in Figure A.1:

1) Calculate $f_r = P_r/A_{eff}$ at various sections along the member length using $F_n = F_y$ in Eq. A.5 (see Figures A.1a and b). One should recognize that A_{eff} increases even though A_{eff}/A_g decreases from the shallow end to the deep end of a web-tapered member (see Figure A.1c).
2) For checking the in-plane resistance by the direct analysis method, the corresponding member axial resistance ratio is simply $P_r/A_{eff}F_y$ assuming that the caveats discussed below are satisfied. Then, $f_r/F_c = P_r/P_c = P_r/(A_{eff}F_y/\Omega_c)$ in ASD or $P_r/(\phi_c A_{eff}F_y)$ in LRFD and the calculations are complete at this step. The governing P_r/P_c is the largest value obtained for all the cross-sections along the member unsupported length in the plane of bending. As explained in Section 3.2.2, this simplified calculation is valid only when $\alpha P_r \leq 0.10P_{eL}$. For $\alpha P_r > 0.10P_{eL}$, one must include a nominal member out-of-straightness within the analysis as explained in Section 3.1, or alternately, P_{ni} may be calculated as detailed in the subsequent steps using the member γ_{ex} based on idealized simply-supported end conditions. In many metal building frames, $\alpha P_r \leq 0.10P_{eL}$. For checking the member out-of-plane strength in

the direct analysis method, or for checking the in-plane or out-of-plane strength using the effective length approach, continue to the next step.

3) Determine the minimum load ratio for elastic buckling of the member $\gamma_{e,min} = \min(\gamma_{ex}, \gamma_{ey}, \gamma_{eTF})$ as appropriate, where γ_{ex} is the critical load ratio for elastic flexural buckling about the major axis, γ_{ey} is the critical load ratio for elastic flexural buckling about the minor axis, and γ_{eTF} is the critical load ratio for elastic torsional or flexural-torsional buckling. The term $\gamma_{e,min}$ is simply the multiple of f_r (and P_r) required to reach incipient elastic buckling of the member as a column subjected to concentric axial load (see Figure A.1d). As noted in Section 3.2.2, it is important to recognize that only one $\gamma_{e,min}$ exists for a given member unbraced length under consideration.

4) Calculate the member axial capacity at the cross-section corresponding to $f_r/F_{y.eq.max} = (P_r/A_{eff}F_y)_{\max}$, accounting for local buckling effects, by substituting $\gamma_{e,min}$ and $(P_r/A_{eff}F_y)_{\max}$ in Eqs. A.2. The axial capacity ratio is $f_r/F_c = f_r/(F_n/\Omega)$ in ASD, or $f_r/F_c = f_r/\phi_c F_n$ in LRFD (see Figure A.1e). The axial capacity ratio is always the largest at the cross-section with the largest $f_r/F_{y.eq} = P_r/A_{eff}F_y$. This is a simplified approach to calculate the axial capacity ratio using the AISI (2001) resistance equations. If a more accurate calculation is desired, continue to the next step.

5) Calculate new A_{eff} at various sections along the member length using F_n obtained in Step (4) and in Figure A.1d. Using this revised A_{eff}, repeat Steps (1) through (4) (Figures A.1a to e) until the solution converges.

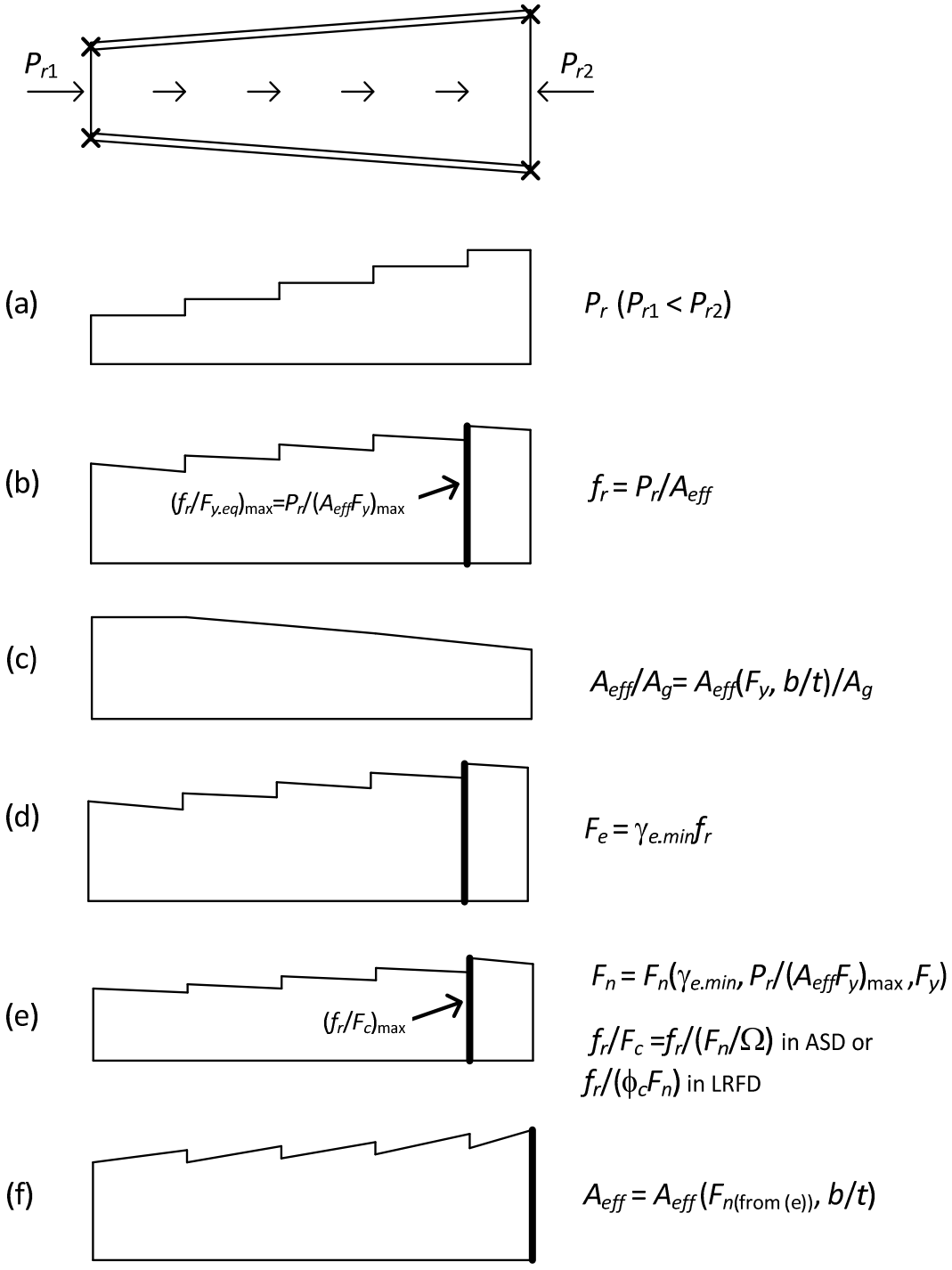

Figure A.1. Axial capacity calculations using AISC (2010) resistance equations.

APPENDIX B

NOMINAL FLEXURAL RESISTANCES AND UNITY CHECKS USING THE MBMA/AISC-2 PROCEDURE

Table B.1. Flexural resistance calculations (Prawel et al. 1974)

Group	Member	γ_{eLTB}	$x_{max(LTB)}$ (in)	$(M_r/M_{yc})_{max}$	$R_{pg(LTB)}$	R_{pc}	$M_{n(LTB)}$ (ft-kips)	$M_r/M_{c(LTB)}$	$x_{max(FLB)}$ (in)	$R_{pg(FLB)}$	$M_{n(FLB)}$ (ft-kips)	$M_r/M_{c(FLB)}$	Gov. M_r (ft-kips)	Governing M_r/M_c
(1)	LB-3	2.54	62	1.094	1.000	1.027	53	1.176	36	1.000	71	1.062	63	1.176
	LB-5	6.60	42	0.935	1.000	1.027	58	0.929	24	1.000	71	0.907	54	0.929
	LB-6	3.94	24	1.005	1.000	1.028	67	1.037	24	1.000	71	0.977	69	1.037
(2)	LB-C-5	4.28	0.0	0.906	0.982	1.000	122	0.977	0.0	0.987	113	1.057	119	1.057
	LB-C-6	3.91	0.0	0.991	0.982	1.000	122	1.069	0.0	0.987	113	1.157	131	1.157
	LB-C-10	3.91	0.0	0.955	0.982	1.000	122	1.033	0.0	0.987	113	1.115	126	1.115
	LB-C-11	3.95	0.0	0.935	0.982	1.000	122	1.013	0.0	0.987	113	1.091	123	1.091
(3)	LB-C-1	3.91	0.0	1.051	1.000	1.059	83	1.053	0.0	1.000	76	1.146	87	1.146
	LB-C-12	4.64	0.0	0.952	1.000	1.059	83	0.947	0.0	1.000	76	1.038	79	1.038
	LB-C-9	4.36	0.0	1.032	1.000	1.059	83	1.024	0.0	1.000	76	1.125	85	1.125
	LB-C-4	4.66	0.0	0.996	1.000	1.059	84	0.986	0.0	1.000	76	1.086	82	1.086
(4)	LB-C-2	6.34	0.0	1.103	1.000	1.076	40	1.037	0.0	1.000	37	1.135	42	1.135
	LB-C-3	7.20	0.0	0.966	1.000	1.076	40	0.909	0.0	1.000	37	0.994	37	0.994
	LB-C-7	6.96	0.0	0.995	1.000	1.076	40	0.936	0.0	1.000	37	1.023	38	1.023
	LB-C-8	7.38	0.0	0.946	1.000	1.076	40	0.889	0.0	1.000	37	0.973	36	0.973

Table B.2. Unity check calculations (Prawel et al. 1974)

Group	Member	Governing P_r/P_c	Governing M_r/M_c	U.C.
(1)	LB-3	0.002	1.176	1.18
	LB-5	0.004	0.929	0.93
	LB-6	0.006	1.037	1.04
(2)	LB-C-5	0.070	1.057	1.09
	LB-C-6	0.077	1.157	1.20
	LB-C-10	0.048	1.115	1.14
	LB-C-11	0.047	1.091	1.11
(3)	LB-C-1	0.001	1.146	1.15
	LB-C-12	0.014	1.038	1.05
	LB-C-9	0.027	1.125	1.14
	LB-C-4	0.045	1.086	1.11
(4)	LB-C-2	0.020	1.135	1.15
	LB-C-3	0.018	0.994	1.00
	LB-C-7	0.011	1.023	1.03
	LB-C-8	0.011	0.973	0.98

Table B.3. Flexural resistance calculations (Salter et al. 1980)

Group	Member	γ_{eLTB}	$x_{max(LTB)}$ (in)	$(M_r/M_{yc})_{max}$	$R_{pg(LTB)}$	R_{pc}	$M_{n(LTB)}$ (ft-kips)	$M_r/M_{c(LTB)}$	$x_{max(FLB)}$ (in)	$R_{pg(FLB)}$	$M_{n(FLB)}$ (ft-kips)	$M_r/M_{c(FLB)}$	Gov. M_r (ft-kips)	Governing M_r/M_c
(1)	C1	2.32	5.5	0.975	1.000	1.160	59	0.986	5.5	1.000	69	0.840	58	0.986
	C2	3.46	5.5	0.691	1.000	1.154	54	0.695	5.5	1.000	62	0.599	37	0.695
	C3	3.74	5.5	0.685	1.000	1.142	47	0.687	5.5	1.000	53	0.600	32	0.687
(2)	C4	3.68	5.5	0.881	1.000	1.184	37	0.826	5.5	1.000	41	0.744	31	0.826
	C5	6.01	5.5	0.612	1.000	1.170	27	0.570	5.5	1.000	29	0.526	15	0.570
(3)	C6	3.46	5.5	0.685	1.000	1.148	55	0.692	5.5	1.000	63	0.596	38	0.692
	C7	3.64	5.5	0.684	1.000	1.146	49	0.686	5.5	1.000	56	0.597	33	0.686
	C8L	8.09	5.5	0.817	1.000	1.161	70	0.717	5.5	1.000	71	0.704	50	0.717

Table B.4. Unity check calculations (Salter et al. 1980)

Group	Member	Governing P_r/P_c	Governing M_r/M_c	U.C.
(1)	C1	0.312	0.986	1.19
	C2	0.619	0.695	1.24
	C3	0.623	0.687	1.23
(2)	C4	0.365	0.826	1.10
	C5	0.760	0.570	1.27
(3)	C6	0.608	0.692	1.22
	C7	0.606	0.686	1.22
	C8L	0.595	0.717	1.23

Table B.5. Flexural resistance calculations (Shiomi and Kurata 1984)

Group	Member	γ_{eLTB}	$x_{max(LTB)}$ (in)	$(M_r/M_{yc})_{max}$	$R_{pg(LTB)}$	R_{pc}	$M_{n(LTB)}$ (ft-kips)	$M_r/M_{c(LTB)}$	$x_{max(FLB)}$ (in)	$R_{pg(FLB)}$	$M_{n(FLB)}$ (ft-kips)	$M_r/M_{c(FLB)}$	Gov. M_r (ft-kips)	Governing M_r/M_c
(1)	OT1.4-2	10.9	79	0.688	1.000	1.140	45	0.608	79	1.000	45	0.603	27	0.608
	OT1.4-4	8.77	98	0.708	1.000	1.160	44	0.625	98	1.000	45	0.610	28	0.625
	OT1.6-1	1.84	118	0.785	1.000	1.187	40	0.863	118	1.000	52	0.661	35	0.863
	OT1.6-2	14.4	79	0.41	1.000	1.142	48	0.37	79	1.000	50	0.359	18	0.370
	OT1.6-4	9.51	98	0.539	1.000	1.134	55	0.496	98	1.000	58	0.475	27	0.496
	OT1.6-5	5.81	118	0.602	1.000	1.146	52	0.574	118	1.000	57	0.526	30	0.574
	OT1.8-1	12.6	79	0.466	1.000	1.149	50	0.417	79	1.000	52	0.405	21	0.417
	OT1.8-3	8.13	98	0.532	1.000	1.134	58	0.499	98	1.000	61	0.469	29	0.499
	OT1.8-4	6.22	98	0.657	1.000	1.145	64	0.614	98	1.000	68	0.573	39	0.614
	OT1.8-5	5.73	118	0.586	1.000	1.144	61	0.563	118	1.000	67	0.513	34	0.563
	OT2.0-1	12.0	79	0.372	1.000	1.141	46	0.345	79	1.000	49	0.326	16	0.345
	OT2.0-3	4.62	98	0.567	1.000	1.142	59	0.566	98	1.000	67	0.497	33	0.566
	OT2.0-4	5.17	118	0.629	1.000	1.143	75	0.607	118	1.000	83	0.550	46	0.607
	OT2.0-5	6.12	118	0.53	1.000	1.149	75	0.509	118	1.000	83	0.461	38	0.509
	OT2.2-3	7.76	98	0.497	1.000	1.128	73	0.474	98	1.000	79	0.440	35	0.474
	OT2.2-5	4.54	118	0.634	1.000	1.135	77	0.626	118	1.000	86	0.558	48	0.626
	OT2.4-1	9.80	79	0.400	1.000	1.135	56	0.379	79	1.000	61	0.352	21	0.379
	OT2.4-3	6.23	98	0.422	1.000	1.137	53	0.422	98	1.000	60	0.371	22	0.422
	OT2.4-4	4.65	118	0.619	1.000	1.132	92	0.613	118	1.000	104	0.547	57	0.613
(2)	IT1.4-1	52.1	79	0.645	1.000	1.133	42	0.569	79	1.000	42	0.569	24	0.569
	IT1.6-2	47.1	79	0.670	1.000	1.112	49	0.602	79	1.000	49	0.602	29	0.602
	IT1.8-3	30.5	79	0.957	1.000	1.122	50	0.853	79	1.000	50	0.853	43	0.853
	IT2.2-5	23.1	79	0.964	1.000	1.122	53	0.859	79	1.000	53	0.859	46	0.859
	IT2.4-6	20.7	79	1.091	1.000	1.177	60	0.927	79	1.000	60	0.927	56	0.927

Table B.6. Unity check calculations (Shiomi and Kurata 1984)

Group	Member	Governing P_r/P_c	Governing M_r/M_c	U.C.
(1)	OT1.4-2	0.644	0.608	1.18
	OT1.4-4	0.480	0.625	1.04
	OT1.6-1	0.569	0.863	1.34
	OT1.6-2	0.691	0.370	1.02
	OT1.6-4	0.654	0.496	1.09
	OT1.6-5	0.559	0.574	1.07
	OT1.8-1	0.809	0.417	1.18
	OT1.8-3	0.709	0.499	1.15
	OT1.8-4	0.526	0.614	1.07
	OT1.8-5	0.569	0.563	1.07
	OT2.0-1	0.834	0.345	1.14
	OT2.0-3	0.657	0.566	1.16
	OT2.0-4	0.584	0.607	1.12
	OT2.0-5	0.805	0.509	1.26
	OT2.2-3	0.709	0.474	1.13
	OT2.2-5	0.617	0.626	1.17
	OT2.4-1	0.983	0.379	1.32
	OT2.4-3	0.857	0.422	1.23
	OT2.4-4	0.618	0.613	1.16
(2)	IT1.4-1	0.554	0.569	1.06
	IT1.6-2	0.604	0.602	1.14
	IT1.8-3	0.407	0.853	1.17
	IT2.2-5	0.306	0.859	1.07
	IT2.4-6	0.177	0.927	1.02

APPENDIX C

NOMINAL FLEXURAL RESISTANCES AND UNITY CHECKS USING THE MBMA/AISC-1 PROCEDURE WITH γ_{eLTB} CALCULATED BY THE CHAPTER 4 PROCEDURE.

Table C.1. Flexural resistance calculations (Prawel et al. 1974)

Group	Member	γ_{eLTB}	C_b	$x_{max(LTB)}$ (in)	$(M_r/M_{yc})_{max}$	$R_{pg(LTB)}$	R_{pc}	$M_{n(LTB)}$ (ft-kips)	$M_r/M_{c(LTB)}$	$x_{max(FLB)}$ (in)	$R_{pg(FLB)}$	$M_{n(FLB)}$ (ft-kips)	$M_r/M_{c(FLB)}$	Gov. M_r (ft-kips)	Governing M_r/M_c
(1)	LB-3	1.19	1.00	62	1.094	1.000	1.027	47	1.329	36.0	1.000	71	1.062	63	1.329
	LB-5	3.04	1.00	42	0.935	1.000	1.027	54	1.002	24.0	1.000	71	0.907	54	1.002
	LB-6	2.82	1.16	24	1.005	1.000	1.028	71	0.977	24.0	1.000	71	0.977	69	0.977
(2)	LB-C-5	1.30	1.24	0.0	0.906	0.991	1.000	129	0.924	0.0	0.987	113	1.057	119	1.057
	LB-C-6	1.19	1.24	0.0	0.991	0.991	1.000	129	1.012	0.0	0.987	113	1.157	131	1.157
	LB-C-10	1.21	1.23	0.0	0.955	0.992	1.000	128	0.986	0.0	0.987	113	1.115	126	1.115
	LB-C-11	1.23	1.23	0.0	0.935	0.992	1.000	128	0.965	0.0	0.987	113	1.091	123	1.091
(3)	LB-C-1	1.13	1.39	0.0	1.051	1.000	1.059	88	0.993	0.0	1.000	76	1.146	87	1.146
	LB-C-12	1.33	1.39	0.0	0.952	1.000	1.059	88	0.900	0.0	1.000	76	1.038	79	1.038
	LB-C-9	1.21	1.40	0.0	1.032	1.000	1.059	88	0.975	0.0	1.000	76	1.125	85	1.125
	LB-C-4	1.29	1.40	0.0	0.996	1.000	1.059	88	0.941	0.0	1.000	76	1.086	82	1.086
(4)	LB-C-2	2.17	1.74	0.0	1.103	1.000	1.076	41	1.025	0.0	1.000	37	1.135	42	1.135
	LB-C-3	1.49	1.74	0.0	0.966	1.000	1.076	41	0.898	0.0	1.000	37	0.994	37	0.994
	LB-C-7	1.45	1.75	0.0	0.995	1.000	1.076	41	0.925	0.0	1.000	37	1.023	38	1.023
	LB-C-8	1.53	1.75	0.0	0.946	1.000	1.076	41	0.879	0.0	1.000	37	0.973	36	0.973

Table C.2. Unity check calculations (Prawel et al. 1974)

Group	Member	Governing P_r/P_c	Governing M_r/M_c	U.C.
(1)	LB-3	0.002	1.329	1.33
	LB-5	0.004	1.002	1.00
	LB-6	0.006	0.977	0.98
(2)	LB-C-5	0.070	1.057	1.09
	LB-C-6	0.077	1.157	1.20
	LB-C-10	0.048	1.115	1.14
	LB-C-11	0.047	1.091	1.11
(3)	LB-C-1	0.001	1.146	1.15
	LB-C-12	0.014	1.038	1.05
	LB-C-9	0.027	1.125	1.14
	LB-C-4	0.045	1.086	1.11
(4)	LB-C-2	0.020	1.135	1.15
	LB-C-3	0.018	0.994	1.00
	LB-C-7	0.011	1.023	1.03
	LB-C-8	0.011	0.973	0.98

Table C.3. Flexural resistance calculations (Salter et al. 1980)

Group	Member	γ_{eLTB}	C_b	$x_{max(LTB)}$ (in)	$(M_r/M_{yc})_{max}$	$R_{pg(LTB)}$	R_{pc}	$M_{n(LTB)}$ (ft-kips)	$M_r/M_{c(LTB)}$	$x_{max(FLB)}$ (in)	$R_{pg(FLB)}$	$M_{n(FLB)}$ (ft-kips)	$M_r/M_{c(FLB)}$	Gov. M_r (ft-kips)	Governing M_r/M_c
(1)	C1	0.98	1.18	5.5	0.975	1.000	1.160	56	1.043	5.5	1.000	69	0.840	58	1.043
	C2	1.43	1.18	5.5	0.691	1.000	1.154	51	0.732	5.5	1.000	62	0.599	37	0.732
	C3	1.50	1.21	5.5	0.685	1.000	1.142	46	0.698	5.5	1.000	53	0.600	32	0.698
(2)	C4	1.61	1.12	5.5	0.881	1.000	1.184	35	0.872	5.5	1.000	41	0.744	31	0.872
	C5	2.44	1.17	5.5	0.612	1.000	1.170	27	0.576	5.5	1.000	29	0.526	15	0.576
(3)	C6	1.42	1.18	5.5	0.685	1.000	1.148	52	0.730	5.5	1.000	63	0.596	38	0.730
	C7	1.48	1.21	5.5	0.684	1.000	1.146	47	0.702	5.5	1.000	56	0.597	33	0.702
	C8L	3.75	1.04	5.5	0.817	1.000	1.161	66	0.758	5.5	1.000	71	0.704	50	0.758

Table C.4. Unity check calculations (Salter et al. 1980)

Group	Member	Governing P_r/P_c	Governing M_r/M_c	U.C.
(1)	C1	0.312	1.043	1.24
	C2	0.619	0.732	1.27
	C3	0.623	0.698	1.24
(2)	C4	0.365	0.872	1.14
	C5	0.760	0.576	1.27
(3)	C6	0.608	0.730	1.26
	C7	0.606	0.702	1.23
	C8L	0.595	0.758	1.27

Table C.5. Flexural resistance calculations (Shiomi and Kurata 1984)

Group	Member	γ_{eLTB}	C_b	$x_{max(LTB)}$ (in)	$(M_r/M_{yc})_{max}$	$R_{pg(LTB)}$	R_{pc}	$M_{n(LTB)}$ (ft-kips)	$M_r/M_{c(LTB)}$	$x_{max(FLB)}$ (in)	$R_{pg(FLB)}$	$M_{n(FLB)}$ (ft-kips)	$M_r/M_{c(FLB)}$	Gov. M_r (ft-kips)	Governing M_r/M_c
(1)	OT1.4-2	3.49	1.48	79	0.688	1.000	1.140	45	0.603	79	1.000	45	0.603	27	0.603
	OT1.4-4	2.91	1.47	98	0.708	1.000	1.160	45	0.610	98	1.000	45	0.610	28	0.610
	OT1.6-1	0.77	1.43	118	0.785	1.000	1.187	38	0.904	118	1.000	52	0.661	35	0.904
	OT1.6-2	4.93	1.41	79	0.41	1.000	1.142	50	0.359	79	1.000	50	0.359	18	0.359
	OT1.6-4	3.28	1.39	98	0.539	1.000	1.134	58	0.475	98	1.000	58	0.475	27	0.475
	OT1.6-5	2.11	1.39	118	0.602	1.000	1.146	57	0.526	118	1.000	57	0.526	30	0.526
	OT1.8-1	4.53	1.34	79	0.466	1.000	1.149	52	0.405	79	1.000	52	0.405	21	0.405
	OT1.8-3	2.95	1.34	98	0.532	1.000	1.134	61	0.469	98	1.000	61	0.469	29	0.469
	OT1.8-4	2.23	1.36	98	0.657	1.000	1.145	68	0.573	98	1.000	68	0.573	39	0.573
	OT1.8-5	2.15	1.34	118	0.586	1.000	1.144	67	0.513	118	1.000	67	0.513	34	0.513
	OT2.0-1	4.65	1.29	79	0.372	1.000	1.141	49	0.326	79	1.000	49	0.326	16	0.326
	OT2.0-3	1.80	1.32	98	0.567	1.000	1.142	62	0.533	98	1.000	67	0.497	33	0.533
	OT2.0-4	2.02	1.31	118	0.629	1.000	1.143	82	0.558	118	1.000	83	0.550	46	0.558
	OT2.0-5	2.39	1.28	118	0.53	1.000	1.149	80	0.48	118	1.000	83	0.461	38	0.480
	OT2.2-3	2.93	1.28	98	0.497	1.000	1.128	79	0.440	98	1.000	79	0.440	35	0.440
	OT2.2-5	1.78	1.26	118	0.634	1.000	1.135	79	0.604	118	1.000	86	0.558	48	0.604
	OT2.4-1	3.93	1.21	79	0.400	1.000	1.135	59	0.365	79	1.000	61	0.352	21	0.365
	OT2.4-3	2.67	1.20	98	0.422	1.000	1.137	53	0.422	98	1.000	60	0.371	22	0.422
	OT2.4-4	1.87	1.25	118	0.619	1.000	1.132	95	0.594	118	1.000	104	0.547	57	0.594
(2)	IT1.4-1	22.6	1.09	79	0.645	1.000	1.133	42	0.569	79	1.000	42	0.569	24	0.569
	IT1.6-2	21.0	1.08	79	0.670	1.000	1.112	49	0.602	79	1.000	49	0.602	29	0.602
	IT1.8-3	14.2	1.07	79	0.957	1.000	1.122	50	0.853	79	1.000	50	0.853	43	0.853
	IT2.2-5	11.3	1.05	79	0.964	1.000	1.122	53	0.859	79	1.000	53	0.859	46	0.859
	IT2.4-6	10.3	1.05	79	1.091	1.000	1.177	60	0.927	79	1.000	60	0.927	56	0.927

Table C.6. Unity check calculations (Shiomi and Kurata 1984)

Group	Member	Governing P_r/P_c	Governing M_r/M_c	U.C.
(1)	OT1.4-2	0.644	0.603	1.18
	OT1.4-4	0.480	0.610	1.02
	OT1.6-1	0.569	0.904	1.37
	OT1.6-2	0.691	0.359	1.01
	OT1.6-4	0.654	0.475	1.08
	OT1.6-5	0.559	0.526	1.03
	OT1.8-1	0.809	0.405	1.17
	OT1.8-3	0.709	0.469	1.13
	OT1.8-4	0.526	0.573	1.04
	OT1.8-5	0.569	0.513	1.03
	OT2.0-1	0.834	0.326	1.12
	OT2.0-3	0.657	0.533	1.13
	OT2.0-4	0.584	0.558	1.08
	OT2.0-5	0.805	0.480	1.23
	OT2.2-3	0.709	0.440	1.10
	OT2.2-5	0.617	0.604	1.15
	OT2.4-1	0.983	0.365	1.31
	OT2.4-3	0.857	0.422	1.23
	OT2.4-4	0.618	0.594	1.15
(2)	IT1.4-1	0.554	0.569	1.06
	IT1.6-2	0.604	0.602	1.14
	IT1.8-3	0.407	0.853	1.17
	IT2.2-5	0.306	0.859	1.07
	IT2.4-6	0.177	0.927	1.02

APPENDIX D

EXAMPLE CALCULATIONS FOR SEGMENT c2-c3 IN CLEAR SPAN FRAME USING DIRECT ANALYSIS METHOD

Example Calculations, Direct Analysis Method, Segment c2-c3, Clear-Span Frame

This example provides detailed MathCAD worksheet calculations pertaining to the direct analysis method. These calculations correspond to the columns in the clear-span frame example and load case 1 (Dead + Collateral + Uniform Snow). The in-plane axial capacity ratio for the column c1-c4 is addressed first. This is followed by the calculation of the out-of-plane axial capacity ratio, then calculation of the flexural capacity ratio, for column segment c2-c3. Finally, the calculation of the unity check value is shown for segment c2-c3.

Material Properties :

$E := 29000ksi$ $F_y := 55ksi$

In-Plane Axial Capacity Ratio (Seg. c1-c4)

The following calculations correspond to the cross-section located at the maximum f_r/QF_y, at x = 0.0 ft (c1). The geometry of the cross-section at x = 0.0 ft is as follows :

FLANGE: $b_{fi} := 6in$ $b_{fo} := 6in$

$t_{fi} := 0.5in$ $t_{fo} := 0.375in$

WEB: $h := 9.125in$

$t_w := 0.21875in$

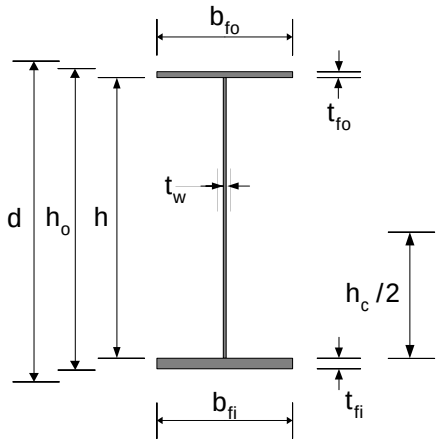

$d := h + t_{fi} + t_{fo}$ $d = 10.0 \cdot in$

$h_o := h + \frac{t_{fi}}{2} + \frac{t_{fo}}{2}$ $h_o = 9.6 \cdot in$

Cross-Section Properties:

Flange area : $A_{fi} := b_{fi} \cdot t_{fi}$ $A_{fi} = 3.00 \cdot in^2$ $A_{fo} := b_{fo} \cdot t_{fo}$ $A_{fo} = 2.25 \cdot in^2$

Web area: $A_w := h \cdot t_w$ $A_w = 2.00 \cdot in^2$

Total section area : $A := A_{fi} + A_{fo} + A_w$ $A = 7.25 \cdot in^2$

Location of Centroid:

$$h_c := 2 \cdot \left[\frac{A_{fi} \cdot \left(\frac{t_{fi}}{2} \right) + A_w \cdot \left(t_{fi} + \frac{h}{2} \right) + A_{fo} \cdot \left(t_{fi} + h + \frac{t_{fo}}{2} \right)}{A} - t_{fi} \right] \qquad h_c = 8.1 \cdot in$$

Moment of inertia:

$$I_x := \left[\frac{b_{fi} \cdot t_{fi}^3}{12} + A_{fi} \cdot \left(\frac{h_c}{2} + \frac{t_{fi}}{2} \right)^2 \right] + \left[\frac{t_w \cdot h^3}{12} + A_w \cdot \left(\frac{h_c}{2} - \frac{h}{2} \right)^2 \right] + \left[\frac{b_{fo} \cdot t_{fo}^3}{12} + A_{fo} \cdot \left(d - \frac{h_c}{2} - t_{fi} - \frac{t_{fo}}{2} \right)^2 \right]$$

$I_x = 132.2 \cdot in^4$

(1) Calculate f_r:

$P_r := 33.1 kips$ at x = 0.0 ft

$f_r := \frac{P_r}{A}$ $f_r = 4.6 \cdot ksi$

Check web slenderness:

$\lambda_w := \frac{h}{t_w}$ $\lambda_w = 41.7$ $\lambda_{rw} := 1.49 \cdot \left(\frac{E}{F_y}\right)^{0.5}$ $\lambda_{rw} = 34.2$

Since $\lambda_w > \lambda_{rw}$, the web is slender and $Q_a < 1$.

Calculate kc:

$$k_c := \begin{cases} 0.35 & \text{if } \frac{4}{\sqrt{\frac{h}{t_w}}} \le 0.35 \\ 0.76 & \text{if } 0.76 < \frac{4}{\sqrt{\frac{h}{t_w}}} \\ \frac{4}{\sqrt{\frac{h}{t_w}}} & \text{otherwise} \end{cases}$$

$k_c = 0.619$

** Note : The limits on kc are 0.35 <= kc =< 0.76*

Calculate Qs:

$$Q_S := \begin{cases} 1.0 & \text{if } \frac{b_{fi}}{2 \cdot t_{fi}} \le 0.64 \cdot \sqrt{\frac{E \cdot k_c}{F_y}} \\ \frac{0.90 \cdot E \cdot k_c}{F_y \cdot \left(\frac{b_{fi}}{2 \cdot t_{fi}}\right)^2} & \text{if } \frac{b_{fi}}{2 \cdot t_{fi}} > 1.17 \cdot \sqrt{\frac{E \cdot k_c}{F_y}} \\ 1.415 - 0.65 \cdot \left(\frac{b_{fi}}{2 \cdot t_{fi}}\right) \cdot \sqrt{\frac{F_y}{E \cdot k_c}} & \text{otherwise} \end{cases}$$

** NOTE : Since the outside flange is in net tension due to the combination of axial compression and flexure, Qs is calculated based on the inside flange.*

$Q_S = 1$

Calculate Qa:

$f := F_y$

$$b_e := \begin{cases} \min\left[1.92 \cdot t_w \cdot \sqrt{\frac{E}{f}} \cdot \left(1 - \frac{0.34}{\frac{h}{t_w}} \cdot \sqrt{\frac{E}{f}}\right), h\right] & \text{if } \frac{h}{t_w} \geq 1.49 \cdot \sqrt{\frac{E}{f}} \\ h & \text{otherwise} \end{cases} \qquad b_e = 7.84 \cdot in$$

$A_{eff} := b_e \cdot t_w + b_{fi} \cdot t_{fi} + b_{fo} \cdot t_{fo}$ $\qquad A_{eff} = 6.96 \cdot in^2$

$Q_a := \frac{A_{eff}}{A}$ $\qquad Q_a = 0.961$

Calculate Q:

$$Q := \begin{cases} 1 & \text{if } \lambda_w < \lambda_{rw} \\ Q_a \cdot Q_s & \text{otherwise} \end{cases} \qquad Q = 0.961$$

Calculate f_r/QF_y:

$$\frac{f_r}{Q \cdot F_y} = 0.08641$$

(2) Calculate $F_n = QF_y$ and $P_r/P_c = f_r/F_c$:

$F_n := Q \cdot F_y$ $\qquad F_n = 52.9 \cdot ksi$

$\Omega := 1.67$

$F_c := \frac{F_n}{\Omega}$ $\qquad F_c = 31.7 \cdot ksi$

$$\frac{f_r}{F_c} = 0.144$$

Out-of-Plane Axial Capacity Ratio (Seg. c2-c3)

Geometry of Cross-Section at x = 7.5 (c2):

Note : f_r/F_y is maximum in segment c2-c3 at x = 7.5 (c2).

FLANGE: $b_{fi} := 6in$ $b_{fo} := 6in$

$t_{fi} := 0.5in$ $t_{fo} := 0.375in$

WEB: $h := 24.395in$

$t_w := 0.21875in$

Cross-section Area:

$A := h \cdot t_w + b_{fi} \cdot t_{fi} + b_{fo} \cdot t_{fo}$ $A = 10.59 \cdot in^2$

Moment of Inertia about y axis:

$$I_y := \frac{1}{12} \cdot t_{fi} \cdot b_{fi}^3 + \frac{1}{12} \cdot t_{fo} \cdot b_{fo}^3 + \frac{1}{12} \cdot h \cdot t_w^3 \qquad I_y = 15.77 \cdot in^4$$

(1) Calculate f_r:

$P_r := 33.2kips$

$$f_r := \frac{P_r}{A} \qquad f_r = 3.14 \cdot ksi$$

Calculate minor axis buckling load:

$L_b := 6.023ft$

$$P_{cry} := \frac{\pi^2 \cdot E \cdot I_y}{L_b^2} \qquad P_{cry} = 864.1 \cdot kips$$

(2-3) Calculate γ_{ey}:

$$\gamma_{ey} := \frac{P_{cry}}{P_r} \qquad \gamma_{ey} = 26$$

$$\frac{f_r}{F_y} = 0.0570$$

***Note: since both flanges are equally braced and the cross-section satisfies the suggested limits on Iy1/Iy2, torsional-flexural buckling does not need to be considered**

$\gamma_e := \gamma_{ey}$

Calculate F_e:

$$F_e := \gamma_e \cdot f_r \qquad F_e = 81.6 \cdot ksi$$

(4) Calculate F_{n1}:

$$Q := 1$$

$$F_{n1} := \begin{cases} \left(0.658^{\frac{1}{\gamma_e \cdot \frac{f_r}{Q \cdot F_y}}}\right) \cdot Q \cdot F_y & \text{if } \gamma_e \cdot \frac{f_r}{Q \cdot F_y} \geq 0.44 \\ 0.877 \cdot F_e & \text{otherwise} \end{cases} \qquad F_{n1} = 41.5 \cdot ksi$$

(5) Calculate γ_{n1}:

$$\gamma_{n1} := \frac{F_{n1}}{f_r} \qquad \gamma_{n1} = 13.2$$

The following calculations correspond to the cross-section located at the maximum f_r/QF_y. In segment c2-c3, the location where f_r/QF_y is maximum is also at x = 7.5 ft (c2).

(6) Calculate f at x = 7.5 ft as f_r at x = 7.5 times γ_{n1}:

$$f := 41.5ksi$$

**Note : In this case, the location where f_l/QF_y is maximum is the same location where f_l/F_y is maximum. Therefore, $f = F_{n1}$.*

Calculate k_c:

$$k_c := \begin{cases} 0.35 & \text{if } \frac{4}{\sqrt{\frac{h}{t_w}}} \leq 0.35 \\ 0.76 & \text{if } 0.76 < \frac{4}{\sqrt{\frac{h}{t_w}}} \\ \frac{4}{\sqrt{\frac{h}{t_w}}} & \text{otherwise} \end{cases} \qquad k_c = 0.38$$

Calculate Qs:

$$Q_s := \begin{cases} 1.0 & \text{if } \frac{b_{fi}}{2 \cdot t_{fi}} \le 0.64 \cdot \sqrt{\frac{E \cdot k_c}{F_y}} \\ \frac{0.90 \cdot E \cdot k_c}{F_y \cdot \left(\frac{b_{fi}}{2 \cdot t_{fi}}\right)^2} & \text{if } \frac{b_{fi}}{2 \cdot t_{fi}} > 1.17 \cdot \sqrt{\frac{E \cdot k_c}{F_y}} \\ 1.415 - 0.65 \cdot \left(\frac{b_{fi}}{2 \cdot t_{fi}}\right) \cdot \sqrt{\frac{F_y}{E \cdot k_c}} & \text{otherwise} \end{cases} \qquad Q_s = 1$$

Calculate Qa:

$$b_e := \begin{cases} \min\left[1.92 \cdot t_w \cdot \sqrt{\frac{E}{f}} \cdot \left(1 - \frac{0.34}{\frac{h}{t_w}} \cdot \sqrt{\frac{E}{f}}\right), h\right] & \text{if } \frac{h}{t_w} \ge 1.49 \cdot \sqrt{\frac{E}{f}} \\ h & \text{otherwise} \end{cases} \qquad b_e = 10.2 \cdot in$$

$$A_{eff} := b_e \cdot t_w + b_{fi} \cdot t_{fi} + b_{fo} \cdot t_{fo} \qquad A_{eff} = 7.5 \cdot in^2$$

$$Q_a := \frac{A_{eff}}{A} \qquad Q_a = 0.707$$

(7) Calculate Q:

$$Q := \begin{cases} 1 & \text{if } \lambda_w < \lambda_{rw} \\ Q_a \cdot Q_s & \text{otherwise} \end{cases}$$

$$Q = 0.707$$

Calculate f_r/QF_y:

$$\frac{f_r}{Q \cdot F_y} = 0.0807$$

Calculate F_e:

$$F_e := \gamma_e \cdot f_r \qquad F_e = 81.6 \cdot ksi$$

(8) Calculate F_n:

$$F_n := \begin{cases} \left(0.658^{\frac{1}{\gamma_e \cdot \frac{f_r}{Q \cdot F_y}}}\right) \cdot Q \cdot F_y & \text{if } \gamma_e \cdot \frac{f_r}{Q \cdot F_y} \geq 0.44 \\ 0.877 \cdot F_e & \text{otherwise} \end{cases} \qquad F_n = 31.9 \cdot ksi$$

(9) Calculate f_r/F_c:

$\Omega := 1.67$

$F_c := \frac{F_n}{\Omega}$ $\qquad F_c = 19.1 \cdot ksi$

$\frac{f_r}{F_c} = 0.164$

The larger of the in-plane and out-of-plane axial capacity ratios is the governing one for the segment under considerarion. For segment c2-c3 (load case #1), the out-of-plane value governs.

$P_r := 33.2 kips$

$P_c := 202.3 kips$ $\qquad \frac{P_r}{P_c} = 0.164$

Flexural Capacity Ratio (Seg. c2-c3)

Lateral Torsional Buckling (LTB) Resistance

Within the segment c2-c3, M_r/M_y is maximum at x = 13.5 ft. The geometry and properties of the cross-section at x = 13.5 ft are as follows:

FLANGE:

$b_{fi} := 6in$ $\qquad b_{fo} := 6in$

$t_{fi} := 0.5in$ $\qquad t_{fo} := 0.375in$

WEB:

$h := 36.615in$

$t_w := 0.21875in$

$d := h + t_{fi} + t_{fo}$ $\qquad d = 37.5 \cdot in$

$h_o := h + \frac{t_{fi}}{2} + \frac{t_{fo}}{2}$ $\qquad h_o = 37.1 \cdot in$

Cross-Section Properties:

Flange area : $A_{fi} := b_{fi} \cdot t_{fi}$ $A_{fi} = 3.00 \cdot in^2$ $A_{fo} := b_{fo} \cdot t_{fo}$ $A_{fo} = 2.25 \cdot in^2$

Web area: $A_w := h \cdot t_w$ $A_w = 8.01 \cdot in^2$

Total section area : $A := A_{fi} + A_{fo} + A_w$ $A = 13.26 \cdot in^2$

Location of Centroid:

$$h_c := 2 \cdot \left[\frac{A_{fi} \cdot \left(\frac{t_{fi}}{2} \right) + A_w \cdot \left(t_{fi} + \frac{h}{2} \right) + A_{fo} \cdot \left(t_{fi} + h + \frac{t_{fo}}{2} \right)}{A} - t_{fi} \right] \qquad h_c = 34.5 \cdot in$$

Moment of inertia:

$$I_x := \left[\frac{b_{fi} \cdot t_{fi}^3}{12} + A_{fi} \cdot \left(\frac{h_c}{2} + \frac{t_{fi}}{2} \right)^2 \right] + \left[\frac{t_w \cdot h^3}{12} + A_w \cdot \left(\frac{h_c}{2} - \frac{h}{2} \right)^2 \right] + \left[\frac{b_{fo} \cdot t_{fo}^3}{12} + A_{fo} \cdot \left(d - \frac{h_c}{2} - t_{fi} - \frac{t_{fo}}{2} \right)^2 \right]$$

$I_x = 2682.8 \cdot in^4$

Section Modulus to the Compression Flange (Inside Flange):

$y_c := \frac{h_c}{2} + t_{fi}$ $y_c = 17.7 \cdot in$

$S_{xc} := \frac{I_x}{y_c}$ $S_{xc} = 151.2 \cdot in^3$

Section Modulus to the Tension Flange (Outside Flange):

$y_t := h - \frac{h_c}{2} + t_{fo}$ $y_t = 19.7 \cdot in$

$S_{xt} := \frac{I_x}{y_t}$ $S_{xt} = 135.9 \cdot in^3$

St. Venant Torsion Constant:

Since the web is slender, J = 0.

M_y:

$M_{yc} := S_{xc} \cdot F_y$ $M_{yc} = 692.85 \cdot ft \cdot kips$

$M_{yt} := S_{xt} \cdot F_y$ $M_{yt} = 622.82 \cdot ft \cdot kips$

$M_y := min(M_{yc}, M_{yt})$ $M_y = 622.82 \cdot ft \cdot kips$

F_L:

$$F_L := \begin{cases} 0.7 \cdot F_y & \text{if } \frac{S_{xt}}{S_{xc}} \geq 0.7 \\ \max\left(F_y \cdot \frac{S_{xt}}{S_{xc}}, 0.5F_y\right) & \text{otherwise} \end{cases} \qquad F_L = 38.5 \cdot ksi$$

The location of plastic neutral axis:

$$h_p := 2 \cdot \frac{\left(h \cdot t_w\right) + \left(b_{fo} \cdot t_{fo}\right) - \left(b_{fi} \cdot t_{fi}\right)}{2 \cdot t_w} \qquad h_p = 33.2 \cdot in$$

Plastic Moment, M_p:

$$M_p := A_{fi} \cdot F_y \cdot \left(\frac{h_p}{2} + \frac{t_{fi}}{2}\right) + \left(\frac{h_p}{2}\right)^2 \cdot t_w \cdot F_y \cdot \frac{1}{2} \ldots \qquad M_p = 778.99 \cdot ft \cdot kips$$
$$+ \left(h - \frac{h_p}{2}\right)^2 \cdot t_w \cdot F_y \cdot \frac{1}{2} \ldots$$
$$+ A_{fo} \cdot F_y \cdot \left(h - \frac{h_p}{2} + \frac{t_{fo}}{2}\right)$$

Check web slenderness:

$$\lambda_w := \frac{h_c}{t_w} \qquad \lambda_w = 157.69 \qquad \lambda_{rw} := 5.7 \cdot \sqrt{\frac{E}{F_y}} \qquad \lambda_{rw} = 130.89$$

$$m := \frac{1}{\left(0.54 \cdot \frac{M_p}{M_y} - 0.09\right)^2} \qquad m = 2.9$$

**Note : m is calculated using the equation from AASHTO, which is the same as the AISC equation for singly symmetric sections; AISC uses λ_{pw} = 3.76 x sqrt(E/Fy) for doubly symmetric sections.*

$$\lambda_{pw} := \min\left(m \cdot \sqrt{\frac{E}{F_y}}, \lambda_{rw}\right) \qquad \lambda_{pw} = 67.01$$

R_{pc}:

Since the web is slender,

$R_{pc} := 1$

**Note : m & λ_{pw} are not needed, since the web is slender; they are shown simply to illustrate the requirements for the web to be compact*

(1) Determine M_r. As stated above, M_r/M_{yc} is maximum at x = 13.5 ft:

$M_r := 338.32 ft \cdot kips$ $\qquad \frac{M_r}{M_{yc}} = 0.488$

(2) Determine F_{eLTB}. To obtain F_{eLTB} (or γ_e) for lateral torsional buckling (LTB), the approximate procedure proposed by Yura and Helwig (1996) is used.

Calculate the compression flange stresses along the unbraced length of the segment.
The compression flange stresses at the quarter span, mid-span & max stress points (at α = 1.6) are:

$f_{q1} := 41.58ksi$ $\quad f_{mid} := 42.41ksi$

$f_{q2} := 42.84ksi$ $\quad f_{max} := 42.97ksi$

**Note : Subscripts q1 and q2 are used for the quarter points of the unbraced length. Subscript mid is used for the mid-span of the segment and max is used for the point where the applied flange stress is maximum.*

Calculate Cb using the base AISC (2005) equation (neglecting the Rm term) but with the compression flange stresses instead of the member moments.

$$C_b := \frac{12.5 \cdot f_{max}}{2.5 \cdot f_{max} + 3 \cdot f_{q1} + 4 \cdot f_{mid} + 3 \cdot f_{q2}} \qquad C_b = 1.013$$

The geometry and properties of the cross-section at mid-span of the segment are as follows:

FLANGE: $b_{fi} := 6in$ $\quad b_{fo} := 6in$ **WEB:** $h := 30.505in$

$t_{fi} := 0.5in$ $\quad t_{fo} := 0.375in$ $\quad t_w := 0.21875in$

Calculate M_{emid} with J = 0:

$S_{xmid} := 119.46in^3$

$L_b := 6.023ft$ $\quad r_t := 1.508in$

$$M_{emid} := \frac{\pi^2 \cdot E \cdot S_{xmid}}{\left(\frac{L_b}{r_t}\right)^2} \qquad M_{emid} = 1240.4 \cdot ft \cdot kips$$

**Note : Even though the height of the c2-c3 segment is 6 ft, the centroidal axis is inclined such that Lb = 6.023 ft. In this calculation, the exact unbraced length is used.*

Calculate F_{eLTB} corresponding to the cross-section having the largest applied flange stress (at x = 13.5 ft in this case):

$$F_{eLTB} := C_b \cdot \frac{M_{emid}}{S_{xmid}} \qquad F_{eLTB} = 126.2 \cdot ksi$$

Calculate F_{eLTB}/F_y:

$$\frac{F_{eLTB}}{F_y} = 2.294$$

Calculate γ_e:

γ_e is calculated as the ratio of F_{eLTB} to the applied flange stress f_r where M_r/M_{yc} is maximum (at x = 13.5 ft in this case). The geometry and properties of the cross-section at x = 13.5 ft are as follows:

FLANGE: $b_{fi} := 6in$ $b_{fo} := 6in$ **WEB:** $h := 36.615in$

$t_{fi} := 0.5in$ $t_{fo} := 0.375in$ $t_w := 0.21875in$

$S_{xmax} := 151.22in^3$

$M_r := 338.32ft \cdot kips$

$f_r := \frac{M_r}{S_{xmax}}$ $f_r = 26.8 \cdot ksi$

$\gamma_e := \frac{F_{eLTB}}{f_r}$ $\gamma_e = 4.70$

Calculate M_{nLTB} based on $R_{pg} = 1.0$:

$$M_{nLTB1} := \begin{cases} R_{pc} \cdot M_{yc} & \text{if } \frac{F_{eLTB}}{F_y} \geq \frac{\pi^2}{1.1^2} \\ R_{pc} \cdot M_{yc} \cdot \left[1 - \left(1 - \frac{F_L \cdot S_{xc}}{R_{pc} \cdot M_{yc}}\right) \cdot \left(\frac{\pi \cdot \sqrt{\frac{F_y}{F_{eLTB}}} - 1.1}{\pi \cdot \sqrt{\frac{F_y}{F_L}} - 1.1}\right)\right] & \text{if } \frac{F_L}{F_y} \leq \frac{F_{eLTB}}{F_y} < \frac{\pi^2}{1.1^2} \\ F_{eLTB} \cdot S_{xc} & \text{if } \frac{F_{eLTB}}{F_y} < \frac{F_L}{F_y} \end{cases}$$

$M_{nLTB1} = 617 \cdot ft \cdot kips$

Calculate $R_{pg(LTB)}$ based on the largest web slenderness. In this case, M_r/M_{yc} is maximum at the same location where h/t_w is maximum (x = 13.5 ft):

$a_{wc} := \frac{h_c \cdot t_w}{b_{fi} \cdot t_{fi}}$ $a_{wc} = 2.5$

$$R_{pgLTB} := min\left[1, 1 - \frac{a_{wc}}{1200 + 300 \cdot a_{wc}} \cdot \left(\frac{h_c}{t_w} - 5.7 \cdot \sqrt{\frac{E}{\frac{M_{nLTB1}}{S_{xc}}}}\right)\right] \qquad R_{pgLTB} = 0.976$$

(3) Calculate M_{nLTB}:

$$M_{nLTB} := \begin{cases} R_{pgLTB} \cdot R_{pc} \cdot M_{yc} & \text{if } \frac{F_{eLTB}}{F_y} \geq \frac{\pi^2}{1.1^2} \\ R_{pgLTB} \cdot R_{pc} \cdot M_{yc} \cdot \left[1 - \left(1 - \frac{F_L \cdot S_{xc}}{R_{pc} \cdot M_{yc}}\right) \cdot \left(\frac{\pi \cdot \sqrt{\frac{F_y}{F_{eLTB}}} - 1.1}{\pi \cdot \sqrt{\frac{F_y}{F_L}} - 1.1}\right)\right] & \text{if } \frac{F_L}{F_y} \leq \frac{F_{eLTB}}{F_y} < \frac{\pi^2}{1.1^2} \\ R_{pgLTB} \cdot F_{eLTB} \cdot S_{xc} & \text{if } \frac{F_{eLTB}}{F_y} < \frac{F_L}{F_y} \end{cases}$$

$M_{nLTB} = 602 \cdot ft \cdot kips$

(4) Calculate M_r/M_{cLTB}:

$\Omega := 1.67$

$M_{cLTB} := \frac{M_{nLTB}}{\Omega}$ $\qquad M_{cLTB} := 360.5 ft \cdot kips$

$\frac{M_r}{M_{cLTB}} = 0.938$

Flange Local Buckling (FLB) Resistance

Flange local buckling is checked for each cross-section throughout the member. The following calculations correspond to the cross-section located at the maximum M_r/M_{nFLB}, at x = 13.5 ft (c3). For the geometry of the cross-section at x = 13.5 ft, see the lateral torsional buckling calculations.

Flange slenderness check:

$\lambda_{fc} := \frac{b_{fi}}{2 \cdot t_{fi}}$ $\qquad \lambda_{fc} = 6.0$ $\qquad \lambda_{pf} := 0.38 \cdot \sqrt{\frac{E}{F_y}}$ $\qquad \lambda_{pf} = 8.7$

$k_c := 0.35$ $\lambda_{rf} := 0.95 \cdot \sqrt{\frac{k_c \cdot E}{F_L}}$ $\lambda_{rf} = 15.4$

Flange is compact.

Calculate R_{pgFLB}:

$M_{nFLB\_R1} := R_{pc} \cdot M_{yc}$ $M_{nFLB\_R1} = 692.9 \cdot ft \cdot kips$

$$R_{pgFLB} := min\left[1, 1 - \frac{a_{wc}}{1200 + 300 \cdot a_{wc}} \cdot \left(\frac{h_c}{t_w} - 5.7 \cdot \sqrt{\frac{E}{\frac{M_{nFLB\_R1}}{S_{xc}}}}\right)\right] \qquad R_{pgFLB} = 0.966$$

Calculate M_{nFLB}:

$M_{nFLB} := R_{pgFLB} \cdot R_{pc} \cdot M_{yc}$

$M_{nFLB} = 669 \cdot ft \cdot kips$

Calculate M_l/M_{cFLB}:

$\Omega := 1.67$

$M_{cFLB} := \frac{M_{nFLB}}{\Omega}$ $M_{cFLB} = 400.6 \cdot ft \cdot kips$

$\frac{M_l}{M_{cFLB}} = 0.845$

Tension Flange Yielding (TFY) Resistance

Tension flange yielding is checked for each cross-section throughout the member. The following calculations correspond to the cross-section located at the maximum M_l/M_{nTFY}, at x = 13.5 ft. The geometry and properties of the cross-section at x = 13.5 ft as follows:

FLANGE: $b_{fi} := 6in$ $b_{fo} := 6in$ **WEB:** $h := 36.560in$

$t_{fi} := 0.5in$ $t_{fo} := 0.375in$ $t_w := 0.21875in$

$M_l := 301.12ft \cdot kips$

$M_{yt} := 553.3ft \cdot kips$

R_{pt}:

Since the web is slender,

$R_{pt} := 1$

Calculate M_{nTFY}:

$M_{nTFY} := R_{pt} \cdot M_{yt}$ $\quad M_{nTFY} = 553.3 \cdot ft \cdot kips$

Calculate M_r/M_{cTFY}:

$\Omega := 1.67$

$M_{cTFY} := \frac{M_{nTFY}}{\Omega}$ $\quad M_{cTFY} = 331.3 \cdot ft \cdot kips$

$\frac{M_r}{M_{cTFY}} = 0.909$

Governing Flexural Resistance

The maximum of the three flexural capacity ratios governs. For segment c2-c3 and load case 1, the lateral-torsional buckling check governs.

$M_r := 338.32 ft \cdot kips$

$M_c := 360.5 ft \cdot kips$ $\quad \frac{M_r}{M_c} = 0.938$

Unity Check (Seg. c2-c3)

$$UC := \begin{cases} \frac{1}{2} \cdot \left(\frac{P_r}{P_c} \right) + \frac{M_r}{M_c} & \text{if } \frac{P_r}{P_c} < 0.2 \\ \frac{P_r}{P_c} + \frac{8}{9} \cdot \frac{M_r}{M_c} & \text{otherwise} \end{cases}$$

$UC = 1.02$

APPENDIX E

EXAMPLE CALCULATIONS FOR SEGMENT c2-c3 IN CLEAR SPAN FRAME USING EFFECTIVE LENGTH METHOD

Example Calculations, Effective Length Method, Segment c2-c3, Clear-Span Frame

This example provides detailed MathCAD worksheet calculations pertaining to the effective length method. These calculations correspond to the columns in the clear-span frame example and load case 1 (Dead + Collateral + Uniform Snow). The in-plane axial capacity ratio for column c1-c4 is addressed first. This is followed by a brief summary of the out-of-plane axial capacity and the flexural capacity ratios for column segment c2-c3. These calculations are essentially the same as illustrated for the Direct Analysis Method. Finally, the calculation of the unity check value is shown for segment c2-c3.

Material Properties :

$E := 29000ksi$ $F_y := 55ksi$

In-Plane Axial Capacity Ratio (Seg. c1-c4)

The following calculations correspond to the cross-section located at the maximum f_r/F_y, at x = 0.0 ft (c1). The geometry of the cross-section at x = 0.0 ft is as follows :

FLANGE: $b_{fi} := 6in$ $b_{fo} := 6in$

$t_{fi} := 0.5in$ $t_{fo} := 0.375in$

WEB: $h := 9.125in$

$t_w := 0.21875in$

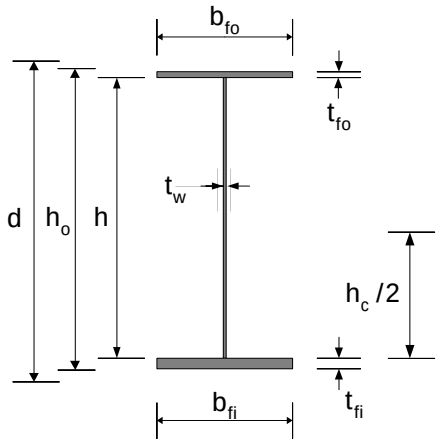

$d := h + t_{fi} + t_{fo}$ $d = 10.000 \cdot in$

$h_o := h + \frac{t_{fi}}{2} + \frac{t_{fo}}{2}$ $h_o = 9.563 \cdot in$

Cross-Section Properties:

Flange area : $A_{fi} := b_{fi} \cdot t_{fi}$ $A_{fi} = 3.00 \cdot in^2$ $A_{fo} := b_{fo} \cdot t_{fo}$ $A_{fo} = 2.25 \cdot in^2$

Web area: $A_w := h \cdot t_w$ $A_w = 2.00 \cdot in^2$

Total section area : $A := A_{fi} + A_{fo} + A_w$ $A = 7.25 \cdot in^2$

Location of Centroid:

$$h_c := 2 \cdot \left[\frac{A_{fi} \cdot \left(\frac{t_{fi}}{2} \right) + A_w \cdot \left(t_{fi} + \frac{h}{2} \right) + A_{fo} \cdot \left(t_{fi} + h + \frac{t_{fo}}{2} \right)}{A} - t_{fi} \right] \qquad h_c = 8.090 \cdot in$$

Moment of inertia:

$$I_x := \left[\frac{b_{fi} \cdot t_{fi}^3}{12} + A_{fi} \cdot \left(\frac{h_c}{2} + \frac{t_{fi}}{2} \right)^2 \right] + \left[\frac{t_w \cdot h^3}{12} + A_w \cdot \left(\frac{h_c}{2} - \frac{h}{2} \right)^2 \right] + \left[\frac{b_{fo} \cdot t_{fo}^3}{12} + A_{fo} \cdot \left(d - \frac{h_c}{2} - t_{fi} - \frac{t_{fo}}{2} \right)^2 \right]$$

$I_x = 132.2 \cdot in^4$

(1) Calculate f_r:

$P_r := 33.3 kips$ at x = 0.0 ft

$f_r := \frac{P_r}{A}$ $f_r = 4.6 \cdot ksi$

(2-3) Calculate γ_{ex}:

In this case, $\Delta_{2nd}/\Delta_{1st} = B_2 < 1.1$. Therefore, γ_e may be calculated based on K = 1.
Using the method of successive approximations per Thomas (2005) and K = 1, γ_e is:

$\gamma_e := 210_*$

Calcuate F_e:

$F_e := \gamma_e \cdot f_r$ $F_e = 965 \cdot ksi$

(4) Calculate F_{n1}:

$Q := 1$

$$F_{n1} := \begin{cases} \left(0.658^{\frac{1}{\gamma_e \cdot \frac{f_r}{Q \cdot F_y}}}\right) \cdot Q \cdot F_y & \text{if } \gamma_e \cdot \frac{f_r}{Q \cdot F_y} \geq 0.44 \\ 0.877 \cdot F_e & \text{otherwise} \end{cases} \qquad F_{n1} = 53.7 \cdot ksi$$

(5) Calculate γ_{n1}:

$\gamma_{n1} := \frac{F_{n1}}{f_r}$ $\gamma_{n1} = 11.7$

The following calculations correspond to the cross-section located at the maximum f_r/QF_y.
In the segment c1-c4, the location where f_r/QF_y is maximum is also at x = 0.0 ft (c1).

(6) Calculate f at x = 0.0 ft as f_r at x = 0.0 times γ_{n1}:

$f := 53.7 ksi$

**Note : In this case, the location where f_r/QF_y is maximum is the same location where f_r/F_y is maximum. Therefore, $f = F_{n1}$.*

Check web slenderness:

$$\lambda_w := \frac{h}{t_w} \qquad \lambda_w = 41.7 \qquad \lambda_{rw} := 1.49 \cdot \left(\frac{E}{F_y}\right)^{0.5} \qquad \lambda_{rw} = 34.2$$

Since $\lambda_w > \lambda_{rw}$, the web is slender and $Q_a < 1$.

Calculate kc:

$$k_c := \begin{cases} 0.35 & \text{if } \frac{4}{\sqrt{\frac{h}{t_w}}} \le 0.35 \\ 0.76 & \text{if } 0.76 < \frac{4}{\sqrt{\frac{h}{t_w}}} \\ \frac{4}{\sqrt{\frac{h}{t_w}}} & \text{otherwise} \end{cases} \qquad k_c = 0.619$$

** Note : The limit of kc is 0.35 <= kc =< 0.76*

Calculate Qs:

$$Q_S := \begin{cases} 1.0 & \text{if } \frac{b_{fi}}{2 \cdot t_{fi}} \le 0.64 \cdot \sqrt{\frac{E \cdot k_c}{F_y}} \\ \frac{0.90 \cdot E \cdot k_c}{F_y \cdot \left(\frac{b_{fi}}{2 \cdot t_{fi}}\right)^2} & \text{if } \frac{b_{fi}}{2 \cdot t_{fi}} > 1.17 \cdot \sqrt{\frac{E \cdot k_c}{F_y}} \\ 1.415 - 0.65 \cdot \left(\frac{b_{fi}}{2 \cdot t_{fi}}\right) \cdot \sqrt{\frac{F_y}{E \cdot k_c}} & \text{otherwise} \end{cases}$$

** NOTE : Since the outside flange is in net tension due to the combination of axial compression and flexure, Qs is calculated based on the inside flange.*

$$Q_S = 1$$

Calculate Qa:

$$b_e := \begin{cases} \min\left[1.92 \cdot t_w \cdot \sqrt{\frac{E}{f}} \cdot \left(1 - \frac{0.34}{\frac{h}{t_w}} \cdot \sqrt{\frac{E}{f}}\right), h\right] & \text{if } \frac{h}{t_w} \ge 1.49 \cdot \sqrt{\frac{E}{f}} \\ h & \text{otherwise} \end{cases} \qquad b_e = 7.91 \cdot in$$

$$A_{eff} := b_e \cdot t_w + b_{fi} \cdot t_{fi} + b_{fo} \cdot t_{fo} \qquad A_{eff} = 6.98 \cdot in^2$$

$$Q_a := \frac{A_{eff}}{A} \qquad Q_a = 0.963$$

(7) Calculate Q:

$$Q := \begin{cases} 1 & \text{if } \lambda_w < \lambda_{rw} \\ Q_a \cdot Q_s & \text{otherwise} \end{cases} \qquad Q = 0.963$$

Calculate f_r/QF_y:

$$\frac{f_r}{Q \cdot F_y} = 0.0867$$

(8-9) Calculate F_n and $P_r/P_c = f_r/F_c$:

$$F_e := \gamma_e \cdot f_r \qquad F_e = 965 \cdot ksi$$

$$F_n := \begin{cases} \left(0.658^{\frac{1}{\gamma_e \cdot \frac{f_r}{Q \cdot F_y}}}\right) \cdot Q \cdot F_y & \text{if } \gamma_e \cdot \frac{f_r}{Q \cdot F_y} \geq 0.44 \\ 0.877 \cdot F_e & \text{otherwise} \end{cases} \qquad F_n = 51.8 \cdot ksi$$

$$\Omega := 1.67$$

$$F_c := \frac{F_n}{\Omega} \qquad F_c = 31.007 \cdot ksi$$

$$\frac{f_r}{F_c} = 0.148$$

Out-of-Plane Axial Capacity Ratio (Seg. c2-c3)

Same as the procedure for direct analysis method.

For segment c2-c3 (load case 1), out-of-plane buckling governs the axial capacity ratio

$$P_r := 33.3 kips \qquad P_c := 202.0 kips$$

$$\frac{P_r}{P_c} = 0.165$$

Flexural Capacity Ratio (Seg. c2-c3)

Same as the procedure for direct analysis method.

For segment c2-c3 (load case 1), lateral-torsional buckling governs the flexural resistance.

$M_r := 336.1 ft \cdot kips$ $M_c := 360.4 ft \cdot kips$

$$\frac{M_r}{M_c} = 0.933$$

Unity Check (Seg. c2-c3)

$$UC := \begin{cases} \frac{1}{2} \cdot \left(\frac{P_r}{P_c} \right) + \frac{M_r}{M_c} & \text{if } \frac{P_r}{P_c} < 0.2 \\ \frac{P_r}{P_c} + \frac{8}{9} \cdot \frac{M_r}{M_c} & \text{otherwise} \end{cases}$$

$UC = 1.02$

APPENDIX F

EXAMPLE CALCULATIONS FOR SEGMENT e1-e2 IN MODULAR FRAME USING DIRECT ANALYSIS METHOD

Example Calculations, Direct Analysis Method, Segment e1-e2, Modular Frame

This example provides detailed MathCAD worksheet calculations pertaining to the direct analysis method. These calculations correspond to the exterior columns in the modular frame and load case 1 (Dead + Collateral + Uniform Snow). The in-plane axial capacity ratio for the column segments e1-e4 is addressed first. This is followed by the calculation of the out-of-plane axial capacity ratio, then the calculation of the flexural capacity ratio, for column segment e1-e2. Finally, the calculation of the unity check value is shown for segment e1-e2.

Material Properties :

$E := 29000ksi$ $F_y := 55ksi$

In-Plane Axial Capacity Ratio (Seg. e1-e4)

The following calculations correspond to the cross-section located at the maximum f_r/QF_y, at x = 7.5 ft (e2). The geometry of the cross-section at x = 7.5 ft is as follows :

FLANGE:

$b_f := 6in$

$t_f := 0.25in$

WEB:

$h := 16.4in$

$t_w := 0.125in$

$d := h + 2 \cdot t_f$ $d = 16.90 \cdot in$

$h_o := h + t_f$ $h = 16.40 \cdot in$

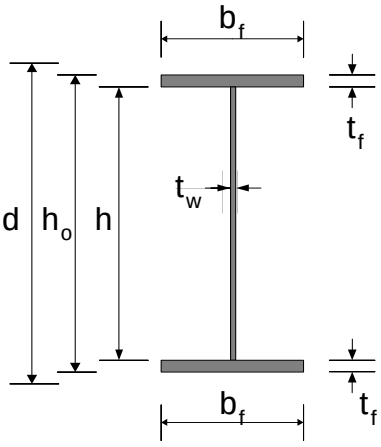

Cross-Section Properties:

Flange area : $A_f := b_f \cdot t_f$ $A_f = 1.50 \cdot in^2$

Web area: $A_w := h \cdot t_w$ $A_w = 2.05 \cdot in^2$

Total section area : $A := 2 \cdot A_f + A_w$ $A = 5.05 \cdot in^2$

Moment of inertia:

$$I_x := 2 \cdot \left[\frac{b_f \cdot t_f^{\,3}}{12} + A_f \cdot \left(\frac{h}{2} + \frac{t_f}{2} \right)^2 \right] + \frac{t_w \cdot h^3}{12} \qquad I_x = 253.9 \cdot in^4$$

(1) Calculate f_r:

$P_r := 16.355kips$ at x = 7.5 ft

$f_r := \frac{P_r}{A}$ $f_r = 3.24 \cdot ksi$

Check web slenderness:

$$\lambda_w := \frac{h}{t_w} \qquad \lambda_w = 131.2 \qquad \lambda_{rw} := 1.49 \cdot \left(\frac{E}{F_y}\right)^{0.5} \qquad \lambda_{rw} = 34.2$$

Since $\lambda_w > \lambda_{rw}$, the web is slender and $Q_a < 1$.

Calculate kc:

$$k_c := \begin{cases} 0.35 & \text{if } \frac{4}{\sqrt{\frac{h}{t_w}}} \le 0.35 \\ 0.76 & \text{if } 0.76 < \frac{4}{\sqrt{\frac{h}{t_w}}} \\ \frac{4}{\sqrt{\frac{h}{t_w}}} & \text{otherwise} \end{cases} \qquad k_c = 0.350$$

** Note : The limits of kc are 0.35 <= kc =< 0.76*

Calculate Qs:

$$Q_s := \begin{cases} 1.0 & \text{if } \frac{b_f}{2 \cdot t_f} \le 0.64 \cdot \sqrt{\frac{E \cdot k_c}{F_y}} \\ \frac{0.90 \cdot E \cdot k_c}{F_y \cdot \left(\frac{b_f}{2 \cdot t_f}\right)^2} & \text{if } \frac{b_f}{2 \cdot t_f} > 1.17 \cdot \sqrt{\frac{E \cdot k_c}{F_y}} \\ 1.415 - 0.65 \cdot \left(\frac{b_f}{2 \cdot t_f}\right) \cdot \sqrt{\frac{F_y}{E \cdot k_c}} & \text{otherwise} \end{cases}$$

$$Q_s = 0.841$$

Calculate Qa:

$$f := F_y$$

$$b_e := \begin{cases} \min\left[1.92 \cdot t_w \cdot \sqrt{\frac{E}{f}} \cdot \left(1 - \frac{0.34}{\frac{h}{t_w}} \cdot \sqrt{\frac{E}{f}}\right), h\right] & \text{if } \frac{h}{t_w} \ge 1.49 \cdot \sqrt{\frac{E}{f}} \\ h & \text{otherwise} \end{cases} \qquad b_e = 5.18 \cdot in$$

$A_{eff} := b_e \cdot t_w + 2b_f \cdot t_f$ $A_{eff} = 3.65 \cdot in^2$

$Q_a := \frac{A_{eff}}{A}$ $Q_a = 0.722$

Calculate Q:

$Q := \begin{cases} 1 & if \quad \lambda_w < \lambda_{rw} \\ Q_a \cdot Q_s & otherwise \end{cases}$ $Q = 0.607$

Calculate f_r/QF_y:

$\frac{f_r}{Q \cdot F_y} = 0.09695$

(2) Calculate $F_n = QF_y$ and $P_r/P_c = f_r/F_c$:

$F_n := Q \cdot F_y$ $F_n = 33.4 \cdot ksi$

$\Omega := 1.67$

$F_c := \frac{F_n}{\Omega}$ $F_c = 20.0 \cdot ksi$

$\frac{f_r}{F_c} = 0.162$

Out-of-Plane Axial Capacity Ratio (Seg. e1-e2)

Geometry of Cross-Section at x = 0.0 (e1):

Note : f_r/F_y is maximum in segment e1-e2 at x = 0.0.

FLANGE:

$b_f := 6in$

$t_f := 0.25in$

WEB:

$h := 9.5in$

$t_w := 0.125in$

Cross-section Area:

$A := h \cdot t_w + 2 \cdot b_f \cdot t_f$ $A = 4.19 \cdot in^2$

Moment of Inertia about y axis:

$$I_y := 2\cdot\left(\frac{1}{12}\cdot t_f\cdot b_f^{\,3}\right) + \frac{1}{12}\cdot h\cdot t_w^{\,3} \qquad I_y = 9.00\cdot in^4$$

(1) Calculate f_r at x = 0:

$P_r := 16.36 kips$

$$f_r := \frac{P_r}{A} \qquad f_r = 3.91\cdot ksi$$

Calculate minor axis buckling load:

$L_b := 7.5 ft$

$$P_{cry} := \frac{\pi^2\cdot E\cdot I_y}{L_b^{\,2}} \qquad P_{cry} = 318.1\cdot kips$$

(2-3) Calculate γ_{ey}:

$$\gamma_{ey} := \frac{P_{cry}}{P_r} \qquad \gamma_{ey} = 19.4$$

$$\frac{f_r}{F_y} = 0.0710$$

***Note: since both flanges are equally braced and the cross-section is doubly-symmetric, torsional and torsional-flexural buckling do not need to be considered**

$\gamma_e := \gamma_{ey}$

Calculate F_e corresponding to the cross-section at x = 0, where fr/Fy is maximum:

$$F_e := \gamma_e\cdot f_r \qquad F_e = 76.0\cdot ksi$$

(4) Calculate F_{n1}:

$Q := 1$

$$F_{n1} := \begin{cases} \left(0.658^{\frac{1}{\gamma_e\cdot\frac{f_r}{Q\cdot F_y}}}\right)\cdot Q\cdot F_y & \text{if } \gamma_e\cdot\frac{f_r}{Q\cdot F_y} \geq 0.44 \\ 0.877\cdot F_e & \text{otherwise} \end{cases} \qquad F_{n1} = 40.6\cdot ksi$$

(5) Calculate γ_{n1}:

$$\gamma_{n1} := \frac{F_{n1}}{f_r} \qquad \gamma_{n1} = 10.4$$

The following calculations correspond to the cross-section located at the maximum f_r/QF_y, at x = 7.5 ft (e2). The geometry of the cross-section at x = 7.5 ft is as follows :

FLANGE:

$b_f := 6in$

$t_f := 0.25in$

WEB:

$h := 16.38in$

$t_w := 0.125in$

Cross-section Area:

$$A := h \cdot t_w + 2 \cdot b_f \cdot t_f \qquad A = 5.0 \cdot in^2$$

Calculate f_r at x = 7.5 ft:

$P_r := 16.36kips$ at x = 7.5 ft

$$f_r := \frac{P_r}{A} \qquad f_r = 3.24 \cdot ksi$$

(6) Calculate f at x = 7.5 ft as f_r at x = 7.5 times γ_{n1}:

$$f := f_r \cdot \gamma_{n1} \qquad f = 33.7 \cdot ksi$$

Calculate Qs:

$k_c := 0.35$ (See previous calculations)

$$Q_s := 1.415 - 0.65 \cdot \left(\frac{b_f}{2 \cdot t_f} \right) \cdot \sqrt{\frac{F_y}{E \cdot k_c}} \qquad Q_s = 0.841$$

Calculate Qa:

$$b_e := \begin{cases} \min\left[1.92 \cdot t_w \cdot \sqrt{\frac{E}{f}} \cdot \left(1 - \frac{0.34}{\frac{h}{t_w}} \cdot \sqrt{\frac{E}{f}} \right), h \right] & \text{if } \frac{h}{t_w} \geq 1.49 \cdot \sqrt{\frac{E}{f}} \\ h & \text{otherwise} \end{cases} \qquad b_e = 6.5 \cdot in$$

$A_{eff} := b_e \cdot t_w + 2 \cdot b_f \cdot t_f$ $\quad A_{eff} = 3.8 \cdot in^2$

$Q_a := \frac{A_{eff}}{A}$ $\quad Q_a = 0.755$

(7) Calculate Q:

$$Q := \begin{cases} 1 & \text{if } \lambda_w < \lambda_{rw} \\ Q_a \cdot Q_s & \text{otherwise} \end{cases}$$

$Q = 0.635$

Calculate f_r/QF_y:

$$\frac{f_r}{Q \cdot F_y} = 0.0928$$

(8) Calculate F_n:

$$F_n := \begin{cases} \left(0.658^{\frac{1}{\gamma_e \cdot \frac{f_r}{Q \cdot F_y}}}\right) \cdot Q \cdot F_y & \text{if } \gamma_e \cdot \frac{f_r}{Q \cdot F_y} \geq 0.44 \\ 0.877 \cdot F_e & \text{otherwise} \end{cases} \qquad F_n = 27.7 \cdot ksi$$

(9) Calculate f_r/F_c:

$\Omega := 1.67$

$F_c := \frac{F_n}{\Omega}$ $\quad F_c = 16.6 \cdot ksi$ $\qquad \frac{f_r}{F_c} = 0.195$

<u>The larger of in-plane and out-of-plane capacity ratios is the governing one for the segment under considerarion. For segment e1-e2 (load case #1), the out-of-plane value governs.</u>

$P_r := 16.36 kips$

$P_c := F_c \cdot A$ $\quad P_c = 83.7 \cdot kips$ $\qquad \frac{P_r}{P_c} = 0.195$

Flexural Capacity Ratio (Seg. e1-e2)

Lateral Torsional Buckling (LTB) Resistance

Within the segment e1-e2, M_r/M_y is maximum at x = 7.5 ft. The geometry and properties of the cross-section at x = 7.5 ft are as follows:

FLANGE:

$b_f := 6in$

$t_f := 0.25in$

WEB:

$h := 16.38in$

$t_w := 0.125in$

$d := h + 2 \cdot t_f$ $\quad d = 16.9 \cdot in$

$h_o := h + t_f$ $\quad h_o = 16.6 \cdot in$

Cross-Section Area:

Flange area : $A_f := b_f \cdot t_f$ $\quad A_f = 1.5 \cdot in^2$

Web area: $A_w := h \cdot t_w$ $\quad A_w = 2.0 \cdot in^2$

Total section area : $A := 2 \cdot A_f + A_w$ $\quad A = 5.0 \cdot in^2$

Moment of inertia:

$$I_x := 2 \cdot \left[\frac{b_f \cdot t_f^3}{12} + A_f \cdot \left(\frac{h}{2} + \frac{t_f}{2} \right)^2 \right] + \frac{t_w \cdot h^3}{12} \qquad I_x = 253.21 \cdot in^4$$

Section Modulus to the Compression Flange:

$$y_c := \frac{h}{2} + t_f \qquad y_c = 8.4 \cdot in$$

$$S_{xc} := \frac{I_x}{y_c} \qquad S_{xc} = 30.0 \cdot in^3$$

St. Venant Torsion Constant:

Since web is slender, J = 0.

M_y:

$M_{yc} := S_{xc} \cdot F_y$ $\quad M_{yc} = 137.51 \cdot ft \cdot kips$

$M_y := M_{yc}$ $\quad M_y = 137.51 \cdot ft \cdot kips$

F_L:

Since the cross-section is doubly symmetric,

$F_L := 0.7 \cdot F_y$ $\quad F_L = 38.5 \cdot ksi$

Plastic Moment, M_p:

$$M_p := A_f \cdot F_y \cdot \left(\frac{h}{2} + \frac{t_f}{2}\right) + \left(\frac{h}{2}\right)^2 \cdot t_w \cdot F_y \cdot \frac{1}{2} \ldots + \left(\frac{h}{2}\right)^2 \cdot t_w \cdot F_y \cdot \frac{1}{2} \ldots + A_f \cdot F_y \cdot \left(\frac{h}{2} + \frac{t_f}{2}\right)$$

$M_p = 152.76 \cdot ft \cdot kips$

**Note : Since the cross-section is doubly symmetric, the location of plastic neutral axis is same as the location of the elastic neutral axis.*

Check web slenderness:

$\lambda_w := \frac{h}{t_w}$ $\quad \lambda_w = 131.04$ $\quad \lambda_{rw} := 5.7 \cdot \sqrt{\frac{E}{F_y}}$ $\quad \lambda_{rw} = 130.89$

$$m := \frac{1}{\left(0.54 \cdot \frac{M_p}{M_y} - 0.09\right)^2}$$

$m = 3.85$

**Note : m is calculated using the equation from AASHTO, which is the same as the AISC equation for singly symmetric sections; AISC uses λ_{pw} = 3.76 x sqrt(E/Fy) for doubly symmetric sections.*

$\lambda_{pw} := min\left(m \cdot \sqrt{\frac{E}{F_y}}, \lambda_{rw}\right)$ $\quad \lambda_{pw} = 88.32$

R_{pc}:

Since the web is slender,

$R_{pc} := 1$

**Note : m & λ_{pw} are not needed, since the web is slender; they are shown simply to illustrate the requirements for the web to be compact*

(1) Determine M_r. As stated above, M_r/M_y is maximum at x = 7.5 ft:

$M_r := 35.92 ft \cdot kips$ $\quad \frac{M_r}{M_y} = 0.261$

(2) Determine F_{eLTB}. To obtain F_{eLTB} (or γ_e) for lateral torsional buckling (LTB), the approximate procedure proposed by Yura and Helwig (1996) is used.

Calculate the compression flange stresses along the unbraced length of the segment.
The compression flange stresses at quarter span, mid-span & max stress points (at α = 1.6) are:

$f_{q1} := 8.99ksi$ $\quad f_{mid} := 15.25ksi$

$f_{q2} := 19.72ksi$ $\quad f_{max} := 22.99ksi$

**Note : Subscripts q1 and q2 are used for the quarter points of the unbraced length. Subscript mid is used for the mid-span of the segment and max is used for the point where the applied flange stress is maximum.*

Calculate Cb using the base AISC (2005) equation (neglecting the Rm term) but with the compression flange stresses instead of the member moments.

$$C_b := \frac{12.5 \cdot f_{max}}{2.5 \cdot f_{max} + 3 \cdot f_{q1} + 4 \cdot f_{mid} + 3 \cdot f_{q2}} \qquad C_b = 1.405$$

The geometry and properties of the cross-section at mid-span of the segment are as follows:

FLANGE: $b_f := 6in$ $\quad t_f := 0.25in$

WEB: $h := 12.94in$ $\quad t_w := 0.125in$

Calculate M_{emid} with J = 0:

$S_{xmid} := 22.697in^3$

$L_b := 7.5ft$ $\quad r_t := 1.615in$

$$M_{emid} := \frac{\pi^2 \cdot E \cdot S_{xmid}}{\left(\frac{L_b}{r_t}\right)^2} \qquad M_{emid} = 174.32 \cdot ft \cdot kips$$

Calculate F_{eLTB}, corresponding to the cross-section having the largest applied flange stress (at x = 7.5 ft in this case), as follows:

$$F_{eLTB} := C_b \cdot \frac{M_{emid}}{S_{xmid}} \qquad F_{eLTB} = 129.4 \cdot ksi$$

Calculate F_{eLTB}/F_y:

$$\frac{F_{eLTB}}{F_y} = 2.354$$

Calculate γ_e:

γ_e is calculated as the ratio of F_{eLTB} to the applied flange stress f_r where M_r/M_{yc} is maximum (at x = 7.5 ft in this case). The geometry and properties of the cross-section at x = 7.5 ft are as follows:

FLANGE: $b_f := 6in$ $t_f := 0.25in$

WEB: $h := 16.38in$ $t_w := 0.125in$

$S_{xmax} := 30.045in^3$

$M_r := 35.92ft \cdot kips$

$f_r := \frac{M_r}{S_{xmax}}$ $f_r = 14.3 \cdot ksi$

$\gamma_e := \frac{F_{eLTB}}{f_r}$ $\gamma_e = 9.0$

Calculate M_{nLTB} based on $R_{pg} = 1.0$:

$$M_{nLTB1} := \begin{cases} R_{pc} \cdot M_{yc} & \text{if } \frac{F_{eLTB}}{F_y} \geq \frac{\pi^2}{1.1^2} \\ R_{pc} \cdot M_{yc} \cdot \left[1 - \left(1 - \frac{F_L \cdot S_{xc}}{R_{pc} \cdot M_{yc}} \right) \cdot \left(\frac{\pi \cdot \sqrt{\frac{F_y}{F_{eLTB}}} - 1.1}{\pi \sqrt{\frac{F_y}{F_L}} - 1.1} \right) \right] & \text{if } \frac{F_L}{F_y} \leq \frac{F_{eLTB}}{F_y} < \frac{\pi^2}{1.1^2} \\ F_{eLTB} \cdot S_{xc} & \text{if } \frac{F_{eLTB}}{F_y} < \frac{F_L}{F_y} \end{cases}$$

$M_{nLTB1} = 123 \cdot ft \cdot kips$

Calculate $R_{pg(LTB)}$ based on the largest web slenderness. In this case, M_r/M_{yc} is maximum at the same location where h/t_w is maximum (x = 7.5 ft):

$h_c := \frac{h}{2}$

$a_{wc} := \frac{2 \cdot h_c \cdot t_w}{b_f \cdot t_f}$ $a_{wc} = 1.4$

$$R_{pgLTB} := min\left[1, 1 - \frac{a_{wc}}{1200 + 300 \cdot a_{wc}} \cdot \left(\frac{2 \cdot h_c}{t_w} - 5.7 \cdot \sqrt{\frac{E}{\frac{M_{nLTB1}}{S_{xc}}}}\right)\right] \qquad R_{pgLTB} = 1.00$$

(3) Calculate M_{nLTB}:

$$M_{nLTB} := \begin{cases} R_{pgLTB} \cdot R_{pc} \cdot M_{yc} & \text{if } \frac{F_{eLTB}}{F_y} \geq \frac{\pi^2}{1.1^2} \\ R_{pgLTB} \cdot R_{pc} \cdot M_{yc} \cdot \left[1 - \left(1 - \frac{F_L \cdot S_{xc}}{R_{pc} \cdot M_{yc}}\right) \cdot \left(\frac{\pi \cdot \sqrt{\frac{F_y}{F_{eLTB}}} - 1.1}{\pi \sqrt{\frac{F_y}{F_L}} - 1.1}\right)\right] & \text{if } \frac{F_L}{F_y} \leq \frac{F_{eLTB}}{F_y} < \frac{\pi^2}{1.1^2} \\ R_{pgLTB} \cdot F_{eLTB} \cdot S_{xc} & \text{if } \frac{F_{eLTB}}{F_y} < \frac{F_L}{F_y} \end{cases}$$

$$M_{nLTB} = 123 \cdot ft \cdot kips$$

(4) Calculate M_r/M_{cLTB}:

$$\Omega := 1.67$$

$$M_{cLTB} := \frac{M_{nLTB}}{\Omega}$$

$$\frac{M_r}{M_{cLTB}} = 0.489$$

Flange Local Buckling (FLB) Resistance

Flange local buckling is checked for each cross-section throughout the segment. The following calculations correspond to the cross-section located at the maximum M_r/M_{nFLB}, at x = 7.5 ft (e2). For the geometry of the cross-section at x = 7.5 ft, see the lateral torsional buckling checks.

Flange slenderness check:

$$\lambda_{fc} := \frac{b_f}{2 \cdot t_f} \qquad \lambda_{fc} = 12.0 \qquad \lambda_{pf} := 0.38 \cdot \sqrt{\frac{E}{F_y}} \qquad \lambda_{pf} = 8.7$$

$k_c := 0.35$ $\lambda_{rf} := 0.95 \cdot \sqrt{\frac{k_c \cdot E}{F_L}}$ $\lambda_{rf} = 15.4$

Flange is noncompact.

Calculate R_{pgFLB}:

$$M_{nFLB\_R1} := R_{pc} \cdot M_{yc} - \left(R_{pc} \cdot M_{yc} - F_L \cdot S_{xc}\right) \cdot \left(\frac{\lambda_{fc} - \lambda_{pf}}{\lambda_{rf} - \lambda_{pf}}\right)$$

$$R_{pgFLB} := min\left[1, 1 - \frac{a_{wc}}{1200 + 300 \cdot a_{wc}} \cdot \left(\frac{h}{t_w} - 5.7 \cdot \sqrt{\frac{E}{\frac{M_{nFLB\_R1}}{S_{xc}}}}\right)\right] \qquad R_{pgFLB} = 1.00$$

Calculate M_{nFLB}:

$$M_{nFLB} := R_{pgFLB} \cdot \left[R_{pc} \cdot M_{yc} - \left(R_{pc} \cdot M_{yc} - F_L \cdot S_{xc}\right) \cdot \left(\frac{\lambda_{fc} - \lambda_{pf}}{\lambda_{rf} - \lambda_{pf}}\right)\right]$$

$M_{nFLB} = 117 \cdot ft \cdot kips$

Calculate M_r/M_{cFLB}:

$\Omega := 1.67$

$M_{cFLB} := \frac{M_{nFLB}}{\Omega}$ $M_{cFLB} = 70.3 \cdot ft \cdot kips$

$\frac{M_r}{M_{cFLB}} = 0.511$

Tension Flange Yielding (TFY) Resistance

Since the cross-section of the segment under consideration is doubly symmetric, the tension flange yielding limit state does not apply.

Governing Flexural Resistance

The maximum of three flexural capacity ratios governs. For segment e1-e2 and load case 1, flange local buckling governs.

$M_r := 35.92 ft \cdot kips$

$M_c := 70.3 ft \cdot kips$

$$\frac{M_r}{M_c} = 0.511$$

Unity Check (Seg. e1-e2)

$$UC := \begin{cases} \frac{1}{2} \cdot \left(\frac{P_r}{P_c} \right) + \frac{M_r}{M_c} & \text{if } \frac{P_r}{P_c} < 0.2 \\ \frac{P_r}{P_c} + \frac{8}{9} \cdot \frac{M_r}{M_c} & \text{otherwise} \end{cases}$$

$UC = 0.61$

APPENDIX G

EXAMPLE CALCULATIONS FOR SEGMENT e1-e2 IN MODULAR FRAME USING EFFECTIVE LENGTH METHOD

Example Calculations, Effective Length Method, Segment e1-e2, Modular Frame

This example provides detailed MathCAD worksheet calculations pertaining to the effective length method. These calculations correspond to the exterior columns in the modular frame and load case 1 (Dead + Collateral + Uniform Snow). The in-plane axial capacity ratio for the column segments e1-e4 is addressed first. This is followed by a brief summary of the required strengths and resistances corresponding to the out-of-plane axial capacity and flexural capacity ratios. The resistance calculations for these ratios are the same as those presented for the direct analysis method. Finally, the calculation of the unity check value is shown for segment e1-e2.

Material Properties

$E := 29000ksi$ $F_y := 55ksi$

In-Plane Axial Capacity Ratio (Seg. e1-e4)

(1) Calculate f_r:

The geometry of the cross-section **at x = 0 ft (e1) where fr/Fy is maximum** is as follows:

FLANGE: $b_f := 6in$

$t_f := 0.25in$

WEB: $h := 9.5in$

$t_w := 0.125in$

Cross-section Area; $A := h \cdot t_w + 2 \cdot b_f \cdot t_f$ $A = 4.188 \cdot in^2$

And P_r at x = 0 ft is ;

$P_r := 16.3kips$ $f_r := \frac{P_r}{A}$ $\frac{f_r}{F_y} = 0.0708$

(2-3) Calculate γ_e. First determine γ_{ex}.

For this calculation, apply a lateral load at the top of each of the columns equal to Pi/Li. The total lateral load is H = ΣPi/Li = 1.344 kips.

First-order sidesway displacement due to H

$\Delta_H := 0.421933in$

Column axial load, P_i $(\alpha = 1.6)$ from second-order elastic analysis per the AISC (2005) Effective Length Method:

1. The exterior columns ;

$P_1 := 25.98kips$ $P_7 := 25.98kips$

***Note :** Subscripts 1 to 7 denote the columns numbered from 1 to 7 from left to right.*

2. The interior columns ;

$P_2 := 56.2kips$ $P_3 := 54.65kips$ $P_4 := 52.79kips$

$P_5 := 54.65kips$ $P_6 := 56.2kips$

The height of the columns are ;

1. The exterior columns ;

$L_1 := 208.29in$ $L_7 := L_1$

2. The interior columns ;

$L_2 := 232.43in$ $L_3 := 257.46in$ $L_4 := 282.48in$

$L_5 := L_3$ $L_6 := L_2$

Horizontal force in exterior columns, H_i (H_i = 0 in interior leaner columns):

$H_1 := 0.673kips$ $H_7 := 0.673kips$

Calculate R_L:

Summation of P_i / L_i of the leaner columns:

$$\frac{P_2}{L_2} + \frac{P_3}{L_3} + \frac{P_4}{L_4} + \frac{P_5}{L_5} + \frac{P_6}{L_6} = 1.095 \cdot \frac{kips}{in}$$

Summation of P_i / L_i of all the columns:

$$\frac{P_1}{L_1} + \frac{P_7}{L_7} + \left(\frac{P_2}{L_2} + \frac{P_3}{L_3} + \frac{P_4}{L_4} + \frac{P_5}{L_5} + \frac{P_6}{L_6}\right) = 1.344 \cdot \frac{kips}{in}$$

$$R_L := \frac{\frac{P_2}{L_2} + \frac{P_3}{L_3} + \frac{P_4}{L_4} + \frac{P_5}{L_5} + \frac{P_6}{L_6}}{\frac{P_1}{L_1} + \frac{P_7}{L_7} + \left(\frac{P_2}{L_2} + \frac{P_3}{L_3} + \frac{P_4}{L_4} + \frac{P_5}{L_5} + \frac{P_6}{L_6}\right)} \qquad R_L = 0.814$$

Calculate $\Sigma H/\Delta_H$:

$$\frac{H_1}{\Delta_H} + \frac{H_7}{\Delta_H} = 3.19 \cdot \frac{kips}{in}$$

Calculate γ_e:

$$\gamma_{e\_1.6} := \frac{\left(0.85 + 0.15 \cdot R_L\right) \cdot \left(\frac{H_1}{\Delta_H} + \frac{H_7}{\Delta_H}\right)}{\frac{P_1}{L_1} + \frac{P_7}{L_7} + \left(\frac{P_2}{L_2} + \frac{P_3}{L_3} + \frac{P_4}{L_4} + \frac{P_5}{L_5} + \frac{P_6}{L_6}\right)} \qquad \gamma_{e\_1.6} = 2.307$$

The γ_e value obtained above is based on the design load level with α = 1.6. Therefore, the γ_e based on the service load is ;

$$\gamma_e := \gamma_{e\_1.6} \cdot 1.6 \qquad \gamma_e = 3.69$$

Calculate F_e :

$$F_e := \gamma_e \cdot f_r \qquad F_e = 14.366 \cdot ksi$$

(4) Calculate F_{n1}:

$$Q := 1$$

$$F_{n1} := \begin{cases} \left(0.658^{\frac{1}{\gamma_e \cdot \frac{f_r}{Q \cdot F_y}}}\right) \cdot Q \cdot F_y & \text{if } \gamma_e \cdot \frac{f_r}{Q \cdot F_y} \geq 0.44 \\ 0.877 \cdot F_e & \text{otherwise} \end{cases} \qquad F_{n1} = 12.6 \cdot ksi$$

(5) Calculate γ_{n1}:

$$\gamma_{n1} := \frac{F_{n1}}{f_r} \qquad \gamma_{n1} = 3.2$$

The following calculations correspond to the cross-section located at the maximum f_r/QF_y, at x = 7.5 ft. The geometry of the cross-section at x =7.5 ft is as follows :

FLANGE:

$b_f := 6in$

$t_f := 0.25in$

WEB:

$h := 16.38in$

$t_w := 0.125in$

Cross-section Area; $A := h \cdot t_w + 2 \cdot b_f \cdot t_f$ $A = 5.047 \cdot in^2$

Calculate f_r:

$P_r := 16.3 kips$

$f_r := \frac{P_r}{A}$ $f_r = 3.229 \cdot ksi$

(6) Calculate f as γ_{n1} times f_r at x = 7.5 ft:

$f := 10.4 ksi$ $k_c := 0.35$

**Note : For detailed calculations, see the corresponding Direct Analysis Method example*

(7) Calculate Q

$Q_s := 0.841$ $Q_a := 0.864$

$Q := Q_s \cdot Q_a$ $Q = 0.727$

$\frac{f_r}{Q \cdot F_y} = 0.0808$

Calculate F_e:

$F_e := \gamma_e \cdot f_r$ $F_e = 11.919 \cdot ksi$

(8) Calculate F_n:

$$F_n := \begin{cases} \left(0.658^{\frac{1}{\gamma_e \cdot \frac{f_r}{Q \cdot F_y}}}\right) \cdot Q \cdot F_y & \text{if } \gamma_e \cdot \frac{f_r}{Q \cdot F_y} \geq 0.44 \\ 0.877 \cdot F_e & \text{otherwise} \end{cases}$$ $F_n = 10.5 \cdot ksi$

(9) Calculate f_r/F_c:

$\Omega := 1.67$

$F_c := \frac{F_n}{\Omega}$ $F_c = 6.259 \cdot ksi$

$\frac{f_r}{F_c} = 0.516$

Out-of-Plane Axial Capacity Ratio (Seg. e1-e2)

Same as the procedure for direct analysis method.

For segment e1-e2 (load case 1), the in-plane axial capacity ratio governs

$P_r := 16.3kips$ $P_c := 31.59kips$

$$\frac{P_r}{P_c} = 0.516$$

Flexural Capacity Ratio (Seg. e1-e2)

Same as the procedure for direct analysis method.

For segment e1-e2 (load case 1), flange local buckling governs the flexural resistance.

$M_r := 35.2ft \cdot kips$ $M_c := 70.4ft \cdot kips$

$$\frac{M_r}{M_c} = 0.500$$

Unity Check (Seg. e1-e2)

$$UC := \begin{cases} \frac{1}{2} \cdot \left(\frac{P_r}{P_c} \right) + \frac{M_r}{M_c} & \text{if } \frac{P_r}{P_c} < 0.2 \\ \frac{P_r}{P_c} + \frac{8}{9} \cdot \left(\frac{M_r}{M_c} \right) & \text{otherwise} \end{cases}$$

$UC = 0.96$

APPENDIX H

SUMMARY OF M_{test}/M_n FOR ALL THE VIRTUAL TEST CASES CONSIDERED IN THIS RESEARCH USING AISC (2010) AND MBMA/AISC (2010)

In this Appendix, the values of M_{test}/M_n based on the current AISC (2010) and MBMA/AISC (2010) provisions are tabulated for all the virtual tests considered in this research. These M_{test}/M_n values are used for the estimation of reliability indices shown in Figures 7.71, 7.75, and 7.76 in Section 7.3. Test cases governed by flange local buckling or tension flange yielding are not included in the calculations of reliability indices. These cases are noted by FLB and TFY in the following tables. In addition, test cases which show shear failure modes are also excluded in the calculations of reliability indices. These cases are noted by SF. Lastly, test members which show larger capacity due to the strain hardening effects are noted by SH. These tests are not considered in the reliability assessment of the design provisions.

Table H.1. M_{test}/M_n values for all the virtual tests using prismatic members under uniform bending (M_n is calculated based on AISC 2010).

case	D/b_{fc}	$b_{fc}/2t_{fc}$	D/t_w	Symmetry of Cross Sections	M_{test}/M_n					
					$f < 0.35$	$0.35 \le f < 0.65$	$0.65 \le f < 0.95$	$0.95 \le f < 1.25$	$1.25 \le f < 1.5$	$f > 1.5$
p1	1	6	40	DS	1.00	0.96	0.93	0.87	1.02	n/a
p2	1	12	130	DS	FLB	FLB	0.85	0.75	0.85	1.00
p3				SSb	FLB	FLB	0.98	0.74	0.83	0.94
p4				SSt	FLB	FLB	0.98	0.76	0.86	0.98
p5	1.5	6	40	DS	1.00	0.95	0.89	0.82	0.92	1.04
p6	2	6	40	DS	1.00	0.95	0.86	0.81	0.90	0.99
p7	2	12	130	DS	FLB	FLB	0.86	0.77	0.86	0.95
p8	4	6	85	DS	0.95	0.89	0.79	0.77	0.87	0.97
p9			100	DS	0.97	0.92	0.81	0.76	0.86	0.96
p10				SSb	TFY	TFY	0.83	0.76	0.88	0.95
p11				SSt	TFY	TFY	0.83	0.76	0.86	0.94
p12			180	DS	1.02	0.97	0.87	0.78	0.87	0.98
p13				SSb	TFY	TFY	0.86	0.77	0.87	0.97
p14				SSt	TFY	TFY	0.86	0.76	0.86	0.95
p15	4	12	130	DS	FLB	FLB	0.79	0.73	0.84	0.96
p16	5.5	6	85	DS	0.92	0.83	0.73	0.75	0.86	0.97
p17			100	DS	0.94	0.86	0.76	0.74	0.84	0.95
p18			115	DS	0.97	0.90	0.78	0.73	0.83	0.94
p19			130	DS	1.01	0.94	0.79	0.72	0.82	0.93
p20			180	DS	1.02	0.96	0.86	0.76	0.83	0.94
p21	7	6	85	DS	0.92	0.79	0.67	0.71	0.82	0.95
p22			100	DS	0.93	0.81	0.68	0.68	0.79	0.92
p23				SSb	TFY	0.86	0.72	0.69	0.80	0.92
p24				SSbT	0.99	0.84	0.76	0.67	0.78	0.92
p25				SStT	0.99	0.84	0.69	0.67	0.81	0.90
p26			115	DS	0.96	0.84	0.68	0.66	0.77	0.89
p27			130	DS	1.00	0.89	0.70	0.68	0.78	0.89
p28			180	DS	1.03	0.95	0.81	0.72	0.79	0.90
p29				SSb	TFY	TFY	0.81	0.72	0.80	0.90
p30				SSt	TFY	TFY	0.81	0.71	0.80	0.90
p31				SSbT	1.03	0.95	0.82	0.74	0.79	0.89
p32				SStT	1.04	0.95	0.81	0.75	0.82	0.91

Table H.2. M_{test}/M_n values for all the virtual tests using tapered members under uniform flexural stress conditions (M_n is calculated based on MBMA/AISC 2010).

case	D/b_{fc}	$b_{fc}/2t_{fc}$	D/t_w	Symmetry of Cross Sections	M_{test}/M_n					
					f < 0.35	0.35 ≤ f < 0.65	0.65 ≤ f < 0.95	0.95 ≤ f < 1.25	1.25 ≤ f < 1.5	f > 1.5
t1	4	6	85	DS	0.96	0.90	0.80	0.80	n/a	n/a
t2			100	DS	0.98	0.93	0.82	0.79	0.91	n/a
t3				SSb	TFY	TFY	0.84	0.81	n/a	n/a
t4				SSt	TFY	TFY	0.84	0.79	n/a	n/a
t5			180	DS	1.03	0.98	0.89	0.82	0.95	n/a
t6				SSb	TFY	TFY	0.87	0.80	0.94	n/a
t7				SSt	TFY	TFY	0.87	0.79	0.92	n/a
t8	4	12	130	DS	FLB	FLB	0.82	0.77	0.87	n/a
t9	5.5	6	85	DS	0.93	0.86	0.75	0.77	0.88	1.00
t10			100	DS	0.95	0.88	0.78	0.77	0.87	0.99
t11			115	DS	0.98	0.92	0.81	0.76	0.84	0.98
t12			130	DS	1.02	0.96	0.83	0.76	0.86	0.97
t13			180	DS	1.03	0.98	0.88	0.83	0.87	1.00
t14	7	6	85	DS	0.92	0.81	0.71	0.74	0.86	0.98
t15			100	DS	0.93	0.82	0.73	0.73	0.84	0.97
t16				SSb	TFY	0.88	0.76	0.73	0.84	0.96
t17				SSbT	1.00	0.87	0.79	0.72	0.84	0.98
t18				SStT	1.00	0.87	0.75	0.73	0.82	0.92
t19			115	DS	0.96	0.86	0.75	0.75	0.83	0.94
t20			130	DS	1.01	0.91	0.77	0.74	0.86	0.94
t21			180	DS	1.04	0.97	0.85	0.77	0.87	0.94
t22				SSb	TFY	TFY	0.85	0.76	0.87	0.94
t23				SSt	TFY	TFY	0.85	0.76	0.86	0.93
t24				SSbT	1.04	0.97	0.86	0.78	0.87	0.94
t25				SStT	1.04	0.97	0.87	0.79	0.89	0.96

Table H.3. M_{test}/M_n values for all the virtual tests using prismatic members under moment gradient (M_n is calculated based on AISC 2010).

case	D/b_{fc}	$b_{fc}/2t_{fc}$	D/t_w	C_b	Symmetry of Cross Sections	M_{test}/M_n					
						f < 0.35	0.35 ≤ f < 0.65	0.65 ≤ f < 0.95	0.95 ≤ f < 1.25	1.25 ≤ f < 1.5	f > 1.5
pg1	1	6	40	1.75	DS	SF	SH	1.04	0.86	0.92	1.14
pg2	1	12	130	1.75	DS	SF	SF	FLB	0.85	0.82	0.97
pg3	1.5	6	40	1.75	DS	SF	SH	1.04	0.84	0.89	1.00
pg4	2	6	40	1.75	DS	SH	SH	1.04	0.81	0.89	1.01
pg5	2	12	130	1.75	DS	SF	SF	FLB	0.84	0.82	0.95
pg6	4	6	100	1.21	DS	1.05	1.02	0.79	0.76	0.87	n/a
pg7				1.33	SSb	TFY	TFY	0.93	0.75	0.86	n/a
pg8				1.34	SSt	TFY	TFY	0.88	0.74	0.85	n/a
pg9			180	1.17	DS	1.07	1.05	0.86	0.78	0.88	0.98
pg10	4	12	130	1.21	DS	FLB	FLB	0.79	0.73	0.84	0.92
pg11	5.5	6	100	1.38	DS	n/a	1.00	0.77	0.70	0.82	n/a
pg12			180	1.14	DS	1.12	1.05	0.85	0.77	0.84	0.94
pg13	7	6	100	1.48	DS	n/a	0.98	0.71	0.62	0.74	n/a
pg14				1.43	SSb	TFY	1.05	0.76	0.64	0.76	n/a
pg15				1.44	SSbT	SF	1.04	0.81	0.61	0.73	n/a
pg16				1.43	SStT	SF	1.05	0.73	0.62	0.78	n/a
pg17			180	1.20	DS	SH	1.04	0.79	0.71	0.79	0.89
pg18				1.19	SSb	TFY	TFY	0.79	0.72	0.79	0.90
pg19				1.19	SSt	TFY	TFY	0.79	0.71	0.79	0.89
pg20				1.20	SSbT	1.17	1.09	0.78	0.74	n/a	0.88
pg21				1.20	SStT	1.17	1.09	0.78	0.74	0.81	0.89

Table H.4. M_{test}/M_n values for all the virtual tests using tapered members under stress gradient conditions (M_n is calculated based on the MBMA/AISC 2010-1 procedure).

case	D/b_{fc}	$b_{fc}/2t_{fc}$	D/t_w	C_b	Symmetry of Cross Sections	M_{test}/M_n					
						$f < 0.35$	$0.35 \le f < 0.65$	$0.65 \le f < 0.95$	$0.95 \le f < 1.25$	$1.25 \le f < 1.5$	$f > 1.5$
tg1	4	6	100	1.21	DS	1.03	1.02	0.80	0.77	0.89	n/a
tg2				1.33	SSb	TFY	TFY	0.93	0.74	n/a	n/a
tg3				1.34	SSt	TFY	TFY	0.87	0.74	n/a	n/a
tg4			180	1.17	DS	n/a	1.03	0.87	0.81	0.95	1.16
tg5	4	12	130	1.21	DS	FLB	FLB	0.81	0.73	0.85	n/a
tg6	5.5	6	100	1.38	DS	0.94	0.99	0.77	0.70	0.83	n/a
tg7			180	1.14	DS	1.11	1.04	0.86	0.80	0.87	1.00
tg8	7	6	100	1.48	DS	n/a	0.95	0.71	0.63	0.75	n/a
tg9				1.43	SSb	TFY	1.03	0.76	0.65	0.72	0.90
tg10				1.44	SSbT	SF	1.02	0.80	0.62	0.75	0.89
tg11				1.43	SStT	SF	1.02	0.74	0.63	0.71	0.88
tg12			180	1.20	DS	1.12	1.01	0.80	0.73	0.82	0.99
tg13				1.19	SSb	TFY	TFY	0.81	0.73	0.82	0.92
tg14				1.19	SSt	TFY	TFY	0.80	0.73	0.81	0.91
tg15				1.20	SSbT	1.14	1.14	0.79	0.73	0.83	n/a
tg16				1.20	SStT	1.14	1.10	0.79	0.74	0.84	0.93

Table H.5. M_{test}/M_n values for all the virtual tests using tapered members under stress gradient conditions (M_n is calculated based on the MBMA/AISC 2010-2 procedure).

case	D/b_{fc}	$b_{fc}/2t_{fc}$	D/t_w	C_b	Symmetry of Cross Sections	M_{test}/M_n					
						$f < 0.35$	$0.35 \le f < 0.65$	$0.65 \le f < 0.95$	$0.95 \le f < 1.25$	$1.25 \le f < 1.5$	$f > 1.5$
tg1	4	6	100	1.21	DS	1.03	1.02	0.93	0.87	0.89	n/a
tg2				1.33	SSb	TFY	TFY	1.06	0.91	n/a	n/a
tg3				1.34	SSt	TFY	TFY	1.00	0.91	n/a	n/a
tg4			180	1.17	DS	n/a	1.03	0.99	0.90	0.95	n/a
tg5	4	12	130	1.21	DS	FLB	FLB	0.92	0.84	0.85	n/a
tg6	5.5	6	100	1.38	DS	0.94	0.99	0.89	0.86	0.83	n/a
tg7			180	1.14	DS	1.11	1.04	0.96	0.88	0.87	1.00
tg8	7	6	100	1.48	DS	n/a	0.95	0.83	0.79	0.78	n/a
tg9				1.43	SSb	TFY	1.03	0.87	0.82	0.79	n/a
tg10				1.44	SSbT	SF	1.02	0.92	0.79	0.77	n/a
tg11				1.43	SStT	SF	1.02	0.85	0.80	0.79	n/a
tg12			180	1.20	DS	1.12	1.01	0.91	0.83	0.82	0.99
tg13				1.19	SSb	TFY	TFY	0.92	0.82	0.82	0.92
tg14				1.19	SSt	TFY	TFY	0.92	0.82	0.81	0.91
tg15				1.20	SSbT	1.14	1.14	0.91	0.83	0.83	n/a
tg16				1.20	SStT	1.14	1.10	0.90	0.84	0.84	0.93

* Note: The M_{test}/M_n values that are updated due to the use of the MBMA/AISC 2010-2 procedure are highlighted in this table.

APPENDIX I

SUMMARY OF M_{test}/M_n FOR ALL THE VIRTUAL TEST CASES CONSIDERED IN THIS RESEARCH USING NEW RECOMMENDATIONS SUGGESTED IN SECTION 7.3

In this Appendix, the values of M_{test}/M_n based on the new recommendations suggested in Section 7.3 are tabulated for all the virtual tests considered in this research. These M_{test}/M_n values are used for the estimation of reliability indices shown in Figures 7.82, 7.84, and 7.85 in Section 7.3.

Table I.1. M_{test}/M_n values for all the virtual tests using prismatic members under uniform bending (M_n is calculated based on the recommendations in Section 7.3).

case	D/b_{fc}	$b_{fc}/2t_{fc}$	D/t_w	Symmetry of Cross Sections	M_{test}/M_n					
					$f < 0.35$	$0.35 \le f < 0.65$	$0.65 \le f < 0.95$	$0.95 \le f < 1.25$	$1.25 \le f < 1.5$	$f > 1.5$
p1	1	6	40	DS	1.00	1.04	1.09	1.08	1.08	n/a
p2	1	12	130	DS	FLB	FLB	0.98	0.93	0.91	1.00
p3				SSb	FLB	FLB	1.17	1.02	0.94	0.94
p4				SSt	FLB	FLB	1.17	1.05	0.97	0.98
p5	1.5	6	40	DS	1.00	1.03	1.03	1.02	0.98	1.03
p6	2	6	40	DS	1.00	1.04	1.03	1.01	0.97	0.99
p7	2	12	130	DS	FLB	FLB	0.98	0.95	0.92	0.95
p8	4	6	85	DS	0.99	1.00	0.98	0.97	0.94	0.97
p9			100	DS	0.99	1.02	0.99	0.98	0.94	0.96
p10				SSb	TFY	TFY	1.02	1.00	0.95	0.95
p11				SSt	TFY	TFY	1.02	1.00	0.94	0.94
p12			180	DS	1.02	1.03	0.99	0.96	0.93	0.98
p13				SSb	TFY	TFY	1.00	0.97	0.94	0.97
p14				SSt	TFY	TFY	1.00	0.97	0.93	0.95
p15	4	12	130	DS	FLB	FLB	0.96	1.00	0.97	0.96
p16	5.5	6	85	DS	0.99	0.99	0.97	0.97	0.94	0.97
p17			100	DS	0.99	0.99	0.98	0.97	0.93	0.95
p18			115	DS	1.00	1.00	0.98	0.97	0.92	0.94
p19			130	DS	1.01	1.02	0.98	0.97	0.92	0.93
p20			180	DS	1.02	1.03	1.00	0.96	0.91	0.94
p21	7	6	85	DS	1.02	0.97	0.94	0.95	0.91	0.95
p22			100	DS	1.00	0.96	0.92	0.92	0.89	0.92
p23				SSb	TFY	0.97	0.95	0.94	0.90	0.92
p24				SSbT	1.00	0.95	0.99	0.91	0.88	0.92
p25				SStT	1.00	0.95	0.90	0.92	0.90	0.90
p26			115	DS	0.99	0.96	0.91	0.90	0.87	0.89
p27			130	DS	1.00	0.98	0.91	0.94	0.89	0.89
p28			180	DS	1.03	1.03	0.98	0.92	0.88	0.90
p29				SSb	TFY	TFY	0.99	0.95	0.90	0.90
p30				SSt	TFY	TFY	0.99	0.94	0.89	0.90
p31				SSbT	1.04	1.03	0.97	0.94	0.86	0.89
p32				SStT	1.04	1.03	0.97	0.95	0.89	0.91

Table I.2. M_{test}/M_n values for all the virtual tests using tapered members under uniform flexural stress conditions (M_n is calculated based on the recommendations in Section 7.3).

case	D/b_{fc}	$b_{fc}/2t_{fc}$	D/t_w	Symmetry of Cross Sections	M_{test}/M_n					
					f < 0.35	0.35 ≤ f < 0.65	0.65 ≤ f < 0.95	0.95 ≤ f < 1.25	1.25 ≤ f < 1.5	f > 1.5
t1	4	6	85	DS	0.99	1.02	0.99	0.99	n/a	n/a
t2			100	DS	1.00	1.03	1.00	0.99	0.97	n/a
t3				SSb	TFY	TFY	1.03	1.01	n/a	n/a
t4				SSt	TFY	TFY	1.03	1.01	n/a	n/a
t5			180	DS	1.03	1.05	1.02	1.00	1.02	n/a
t6				SSb	TFY	TFY	1.02	1.01	1.01	n/a
t7				SSt	TFY	TFY	1.01	1.00	0.99	n/a
t8	4	12	130	DS	FLB	FLB	0.99	0.97	0.94	n/a
t9	5.5	6	85	DS	1.00	1.02	0.99	0.99	0.96	1.00
t10			100	DS	1.00	1.02	1.01	0.99	0.95	0.99
t11			115	DS	1.01	1.03	1.02	1.00	0.95	0.98
t12			130	DS	1.02	1.05	1.04	1.00	0.95	0.97
t13			180	DS	1.03	1.05	1.03	1.01	0.95	1.00
t14	7	6	85	DS	1.02	1.00	0.99	0.98	0.95	0.98
t15			100	DS	1.00	0.98	0.99	0.97	0.94	0.97
t16				SSb	TFY	0.99	1.00	0.99	0.94	0.96
t17				SSbT	1.01	0.97	1.03	0.96	0.93	0.92
t18				SStT	1.01	0.97	0.99	0.97	0.92	0.98
t19			115	DS	1.00	0.99	0.99	0.99	0.92	0.94
t20			130	DS	1.01	1.00	1.00	0.98	0.93	0.94
t21			180	DS	1.04	1.05	1.03	0.97	0.94	0.94
t22				SSb	TFY	TFY	1.03	0.99	0.94	0.94
t23				SSt	TFY	TFY	1.03	0.98	0.93	0.93
t24				SSbT	1.04	1.05	1.02	0.97	0.93	0.94
t25				SStT	1.04	1.05	1.04	0.98	0.95	0.96

Table I.3. M_{test}/M_n values for all the virtual tests using prismatic members under moment gradient (M_n is calculated based on the recommendations in Section 7.3 and the MBMA/AISC 2010-1 procedure).

case	D/b_{fc}	$b_{fc}/2t_{fc}$	D/t_w	C_b	Symmetry of Cross Sections	M_{test}/M_n					
						$f < 0.35$	$0.35 \le f < 0.65$	$0.65 \le f < 0.95$	$0.95 \le f < 1.25$	$1.25 \le f < 1.5$	$f > 1.5$
pg1	1	6	40	1.75	DS	SF	SH	1.04	0.96	0.98	1.13
pg2	1	12	130	1.75	DS	SF	SF	FLB	0.86	0.87	0.97
pg3	1.5	6	40	1.75	DS	SF	SH	1.04	0.95	0.96	1.00
pg4	2	6	40	1.75	DS	SH	SH	1.04	0.94	0.95	1.01
pg5	2	12	130	1.75	DS	SF	SF	FLB	0.85	0.88	0.95
pg6	4	6	100	1.21	DS	1.07	1.04	0.97	0.97	0.94	n/a
pg7				1.33	SSb	TFY	TFY	1.03	0.98	0.94	n/a
pg8				1.34	SSt	TFY	TFY	0.97	0.98	0.94	n/a
pg9			180	1.17	DS	1.07	1.05	0.98	0.97	0.94	0.98
pg10	4	12	130	1.21	DS	FLB	FLB	0.92	0.94	0.91	0.92
pg11	5.5	6	100	1.38	DS	n/a	1.05	0.89	0.93	0.91	n/a
pg12			180	1.14	DS	1.12	1.05	1.00	0.96	0.91	0.94
pg13	7	6	100	1.48	DS	n/a	1.05	0.82	0.84	0.83	n/a
pg14				1.43	SSb	TFY	1.07	0.86	0.88	0.86	n/a
pg15				1.44	SSbT	SF	1.06	0.90	0.82	0.82	n/a
pg16				1.43	SStT	SF	1.06	0.82	0.84	0.87	n/a
pg17			180	1.20	DS	SH	1.04	0.94	0.91	0.87	0.89
pg18				1.19	SSb	TFY	TFY	0.96	0.93	0.89	0.90
pg19				1.19	SSt	TFY	TFY	0.96	0.92	0.88	0.89
pg20				1.20	SSbT	1.17	1.09	0.91	0.93	n/a	0.88
pg21				1.20	SStT	1.17	1.09	0.91	0.94	0.88	0.89

Table I.4. M_{test}/M_n values for all the virtual tests using tapered members under stress gradient conditions (M_n is calculated based on the recommendations in Section 7.3 and the MBMA/AISC 2010-1 procedure).

case	D/b_{fc}	$b_{fc}/2t_{fc}$	D/t_w	C_b	Symmetry of Cross Sections	M_{test}/M_n					
						$f < 0.35$	$0.35 \le f < 0.65$	$0.65 \le f < 0.95$	$0.95 \le f < 1.25$	$1.25 \le f < 1.5$	$f > 1.5$
tg1	4	6	100	1.21	DS	1.05	1.04	0.98	0.98	0.96	n/a
tg2				1.33	SSb	TFY	TFY	1.03	0.97	n/a	n/a
tg3				1.34	SSt	TFY	TFY	0.96	0.97	n/a	n/a
tg4			180	1.17	DS	n/a	1.03	0.99	1.00	1.01	n/a
tg5	4	12	130	1.21	DS	FLB	FLB	0.93	0.95	0.92	n/a
tg6	5.5	6	100	1.38	DS	n/a	1.04	0.89	0.93	0.91	n/a
tg7			180	1.14	DS	1.11	1.04	1.01	1.01	0.94	1.00
tg8	7	6	100	1.48	DS	n/a	1.02	0.83	0.85	0.84	n/a
tg9				1.43	SSb	TFY	1.04	0.86	0.89	0.87	0.90
tg10				1.44	SSbT	SF	1.03	0.89	0.84	0.84	0.89
tg11				1.43	SStT	SF	1.03	0.83	0.86	0.86	0.88
tg12			180	1.20	DS	1.12	1.04	1.07	1.05	1.03	1.13
tg13				1.19	SSb	TFY	TFY	0.98	0.95	0.92	0.92
tg14				1.19	SSt	TFY	TFY	0.97	0.94	0.91	0.91
tg15				1.20	SSbT	1.14	1.14	0.93	0.93	0.90	n/a
tg16				1.20	SStT	1.14	1.10	0.92	0.94	0.91	0.93

Table I.5. M_{test}/M_n values for all the virtual tests using prismatic members under moment gradient (M_n is calculated based on the recommendations in Section 7.3 and the MBMA/AISC 2010-2 procedure).

case	D/b_{fc}	$b_{fc}/2t_{fc}$	D/t_w	C_b	Symmetry of Cross Sections	M_{test}/M_n					
						$f < 0.35$	$0.35 \le f < 0.65$	$0.65 \le f < 0.95$	$0.95 \le f < 1.25$	$1.25 \le f < 1.5$	$f > 1.5$
pg1	1	6	40	1.75	DS	SF	SH	1.31	1.38	1.31	1.27
pg2	1	12	130	1.75	DS	SF	SF	FLB	1.23	1.17	1.09
pg3	1.5	6	40	1.75	DS	SF	SH	1.32	1.36	1.29	1.13
pg4	2	6	40	1.75	DS	SH	SH	1.33	1.35	1.28	1.13
pg5	2	12	130	1.75	DS	SF	SF	FLB	1.22	1.18	1.07
pg6	4	6	100	1.21	DS	1.07	1.12	1.11	1.09	1.03	n/a
pg7				1.33	SSb	TFY	TFY	1.26	1.18	1.10	n/a
pg8				1.34	SSt	TFY	TFY	1.19	1.18	1.10	n/a
pg9			180	1.17	DS	1.07	1.11	1.10	1.05	1.00	0.99
pg10	4	12	130	1.21	DS	FLB	FLB	1.06	1.06	1.01	0.92
pg11	5.5	6	100	1.38	DS	n/a	1.12	1.11	1.15	1.09	n/a
pg12			180	1.14	DS	1.12	1.11	1.09	1.03	0.97	0.94
pg13	7	6	100	1.48	DS	n/a	1.12	1.06	1.10	1.05	n/a
pg14				1.43	SSb	TFY	1.14	1.09	1.13	1.07	n/a
pg15				1.44	SSbT	SF	1.12	1.14	1.06	1.02	n/a
pg16				1.43	SStT	SF	1.13	1.04	1.08	1.08	n/a
pg17			180	1.20	DS	SH	1.12	1.09	1.05	1.01	1.02
pg18				1.19	SSb	TFY	TFY	1.07	1.04	0.98	0.91
pg19				1.19	SSt	TFY	TFY	1.07	1.03	0.97	0.90
pg20				1.20	SSbT	1.17	1.16	1.03	1.03	n/a	0.89
pg21				1.20	SStT	1.17	1.16	1.03	1.04	0.96	0.91

Table I.6. M_{test}/M_n values for all the virtual tests using tapered members under stress gradient conditions (M_n is calculated based on the recommendations in Section 7.3 and the MBMA/AISC 2010-2 procedure).

case	D/b_{fc}	$b_{fc}/2t_{fc}$	D/t_w	C_b	Symmetry of Cross Sections	M_{test}/M_n					
						$f < 0.35$	$0.35 \le f < 0.65$	$0.65 \le f < 0.95$	$0.95 \le f < 1.25$	$1.25 \le f < 1.5$	$f > 1.5$
tg1	4	6	100	1.21	DS	1.05	1.11	1.12	1.11	1.05	n/a
tg2				1.33	SSb	TFY	TFY	1.26	1.17	n/a	n/a
tg3				1.34	SSt	TFY	TFY	1.18	1.17	n/a	n/a
tg4			180	1.17	DS	n/a	1.09	1.11	1.09	1.08	n/a
tg5	4	12	130	1.21	DS	FLB	FLB	1.08	1.07	1.02	n/a
tg6	5.5	6	100	1.38	DS	n/a	1.10	1.11	1.15	1.09	n/a
tg7			180	1.14	DS	1.11	1.11	1.10	1.09	1.00	1.00
tg8	7	6	100	1.48	DS	n/a	1.08	1.07	1.12	1.07	n/a
tg9				1.43	SSb	TFY	1.11	1.09	1.14	1.07	1.00
tg10				1.44	SSbT	SF	1.09	1.13	1.09	1.04	0.99
tg11				1.43	SStT	SF	1.10	1.05	1.10	1.07	0.97
tg12			180	1.20	DS	1.12	1.09	1.10	1.08	1.05	1.13
tg13				1.19	SSb	TFY	TFY	1.09	1.06	1.01	0.93
tg14				1.19	SSt	TFY	TFY	1.08	1.05	1.00	0.92
tg15				1.20	SSbT	1.14	1.21	1.04	1.03	0.98	n/a
tg16				1.20	SStT	1.14	1.17	1.04	1.04	0.99	0.94

REFERENCES

AASHTO (2004), *AASHTO LRFD Bridge Design Specifications*, 3rd Edition, American Association of State Highway and Transportation Officials, Washington, DC.

AASHTO (2007), *AASHTO LRFD Bridge Design Specifications*, 4th Edition, American Association of State Highway and Transportation Officials, Washington, DC.

AISC (1978), *Specification for the Design, Fabrication and Erection of Structural Steel for Building*, November 1, American Institute of Steel Construction, Chicago, IL.

AISC (1986), *Load and Resistance Factor Design Specification for Structural Steel Buildings*, September 1,American Institute of Steel Construction, Chicago, IL.

AISC (1989), *Specification for Structural Steel Buildings - Allowable Stress and Plastic Design*, June 1, American Institute of Steel Construction, Chicago, IL.

AISC (1993), *Load and Resistance Factor Design Specification for Structural Steel Buildings*, December 1, American Institute of Steel Construction, Chicago, IL.

AISC (1999), *Load and Resistance Factor Design Specification for Structural Steel Buildings*, December 27, American Institute of Steel Construction, Chicago, IL.

AISC (2005), *Specification for Structural Steel Buildings*, ANSI/AISC 360-05, American Institute of Steel Construction, Chicago, IL, March 9.

AISC (2010), *Specification for Structural Steel Buildings*, ANSI/AISC 360-10, American Institute of Steel Construction, Chicago, IL, (to appear).

AISI (2001), *North American Specification for the Design of Cold-Formed Structural Steel Members*, American Institute of Steel Construction, Washington, DC.

ASCE (1997), Effective Length and Notional Load Approaches for Assessing Frame Stability: Implications for American Steel Design, Task Committee on Effective Length, Technical Committee on Load and Resistance Factor Design, Structural Engineering Institute, American Society of Civil Engineers, 442 pp.

ASCE (2006), "Minimum Design Loads for Buildings and Other Structures," *ASCE/SEI 7-05*, Reson, Va.

Andrade, A. Camotim, D. and e Costa, P.P. (2005), "Elastic Lateral-Torsional Buckling Behavior of Doubly symmetric Tapered Beam-Columns," *Proceedings*, Annual Technical Session, Structural Stability Research Council, University of Missouri, Rolla, MO, 445-468.

Bairstow, L. and Stedman, E.W. (1914), "Critical Loads of Long Struts of Varying Sections," *Engineering*, 98, p. 403.

Barth, K.E. and White, D.W. (1997), "Finite Element Evaluation of Pier Moment-Rotation Characteristics in Continuous-Span Steel I-Girders," *Engineering Structures*, Vol. 20, No. 8, pp. 761-778.

Bazant, Z.P. and Cedolin, L. (1991), *Stability of Structures – Elastic, Inelastic, Fracture and Damage Theories*, Oxford University Press, New York, 984 pp.

Bleich, F. (1952), *Buckling strength of Metal Structures*, McGraw-Hill, New York, NY.

Boissonnade, N. and Maquoi, R. (2005), "A Geometrically and Materially Non-linear 3-D Beam Finite Element for the Analysis of Tapered Steel Members," *Steel Structures*, 5, 413-419.

Bradford, M.A. (1992), "Lateral-Distortional Buckling of Steel I-Section Members," *Journal of Constructional Steel Research*, 23, 97-116.

Bradford, M.A. and Hancock, G.J. (1984), "Elastic Interaction of Local and Lateral Buckling in Beams," *Thin Walled Structures*, 2, 1-25.

Butler, D.J. and Anderson, G.C. (1963), "The Elastic Buckling of Tapered Beam-Columns," *Welding Journal Research Supplement*, Vol. 42, No. 1.

Butler, D.J. (1966), "Elastic Buckling Tests on Laterally and Torsionally Braced Tapered I-Beams," *Welding Journal Research Supplement*, Vol. 45, No. 1.

Cary, W.C. III and Muray, T.M. (1997), "Effective Lengths of Web-Tapered Columns in Rigid Metal Building Frames," Report No. CE/VPI-ST 97/06, May, 59 pp.

CEN (2005), Eurocode 3: *Design of Steel Structures, Part 1.1-General Rules and Rules for Buildings*, EN 1993-1-1:2005: E, Incorporating Corrigendum February 2006, European Committee for Standardization, Brussels, Belgium, 91 pp.

Chang, C.J. (2006), *GT-Sabre User Manual*, School of Civil and Environmental Engineering, Georgia Institute of Technology, Atlanta, GA.

Chen, W.F. and Lui, E.M. (1987), *Structural Stability, Theory and Implementation*, Elsevier, New York, NY.

Cherry, S. (1960), "The Stability of Beams with Buckled Compression Flanges," *The Structural Engineer*, 38(9), 277-85.

Davies, J.M. (1990), "In plane Stability in Portal Frames," *Structural Engineer*, 68(8),

Davies, J.M. and Brown, B.A. (1996), *Plastic Design to BS 5950*, Steel Construction Institute, Blackwell Science, 326 pp.

Davis, B.D. (1996), "LRFD Evaluation of Full-Scale Metal Building Frame Tests," M.S. Thesis, Charles Via Department of Civil Engineering, Virginia Polytechnic Institute and State University, Blacksburg, VA, 255 pp.

Deierlein, G. (2003), "Background and Illustrative Examples on Proposed Direct Analysis Method for Stablity Design of Moment Frames," Report on behalf of AISC TC10, July 13 2003, 17 pp.

Deierlein, G. (2004), "Stable Improvements: Direct Analysis Method for Stability Design of Steel-Framed Buildings," *Structural Engineer*, November, 24-28.

Dinnik, A.N. (1914), *I svest. Gornogo Inst.*, Ekaterinoslav.

Dinnik, A.N. (1916), *Vestnik Ingenerov*, Moscow.

Dinnik, A.N. (1929), "Design of Columns of Varying Cross Sections," ASME Transactions, AMP-51-11, Vol. 51, McGraw-Hill, New York, NY, 165-171.

Dinnik, A.N. (1932), "Design of Columns of Varying Cross Sections," ASME Transactions, AMP-54-16, Vol. 54, McGraw-Hill, New York, NY, 105-109.

Dux and Kitipornchai (1983), "Inelastic Beam Buckling Experiments," *Journal of Constructional Steel Research*, Vol. 3, No. 1, 3-9.

ECCS (1983), "Ultimate Limit State Calculation of Sway Frames with Rigid Joints," Technical Working Group 8.2, Systems, Publication No. 33, European Commission for Constructional Steelwork, November, 20 pp.

Essa, H.S. and Kennedy, D.J.L. (2000), "Proposed Provisions for the Design of Steel Beam-Columns in S16-2001," *Canadian Journal of Civil Engineering*, 27, 610-619.

Forest, R. and Murray, T.M. (1982), "Rigid Frame Studies, Full Scale Frame Tests," Research Report No. FSEL/STAR 82-01, School of Civil Engineering and Environmental Science, University of Oklahoma, Norman, OK, 109 pp.

Galambos, T.V. (1988), *Guide to Stability Design Criteria for Metal Structures*, 4th Ed., Wiley, New York, NY.

Galambos, T.V. (2001a), "Strength of Singly Symmetric I-Shaped Beam-Columns," *Engineering Journal*, AISC, 38(2), 65-77.

Galambos, T.V. (2001b), Personal communication.

Galambos, T.V. (2004), "Reliability of the Member Stability Criteria in the 2005 AISC Specification," *International Journal of Steel Structures*, 4(4), 233-230.

Galambos, T.V. and Ketter, R.L. (1959), "Columns Under Combined Bending and Thrust," *Journal of the Engineering Mechanics Division*, ASCE, 85(EM2), 135-152.

Galambos, T.V. and Ravindra, M.K. (1976), "Load and Resistance Factor Design Criteria for Steel Beams," *Research Report No. 27*, Structural Division, Civil and Environmental Engineering Department, Washington University, St. Louis.

Gaiotti, R. and Smith, B.S. (1989), "P-Delta Analysis of Building Structures," *Journal of Structural Engineering*, 115(1), 755-770.

Guo, C.Q. and Roddis, W.M.K. (1999), "The Significance of P-D Effects in Single-Story Metal Building Design," Structural Engineering and Engineering Materials, SL Report 99-2, University of Kansas Center for Research, Lawrence, KS.

Jenner, R.K., Densford, T.A., Astaneh-Asl, A. and Murray, T.M. (1985b), "Experimental Investigation of Rigid Frames Including Knee Connection Studies, Frame FR1 Tests, Report No. FSEL//MESCO 85-02, Fears Structural Engineering Laboratory, School of Civil Engineering and Environmental Science, University of Oklahoma, Norman, OK, July, 210 pp.

Jenner, R.K., Densford, T.A., Astaneh-Asl, A. and Murray, T.M. (1985c), "Experimental Investigation of Rigid Frames Including Knee Connection Studies, Frame FR2 Tests, Report No. FSEL//MESCO 85-03, Fears Structural Engineering Laboratory, School of Civil Engineering and Environmental Science, University of Oklahoma, Norman, OK, August, 263 pp.

Jimenez Lopez, G.A. (1998), "Inelastic Stability of Tapered Structural Members," Doctoral dissertation, University of Minnesota, Minneapolis-St. Paul, MN, 201 pp.

Jimenez, G.A. (2005), "Restrained Web-Tapered Columns," A Practical Design Approach," *Proceedings*, Annual Technical Session, Structural Stability Research Council, University of Missouri, Rolla, MO, 225-240.

Jimenez, G.A. (2006), "Further Studies on the Lateral-Torsional of Steel Web-Tapered Beam-Columns," *Proceedings*, Annual Technical Session, Structural Stability Research Council, University of Missouri, Rolla, MO, 267-280.

Jimenez, G. and Galambos, T.V. (2001), "Inelastic Stability of Pinned Tapered Columns," *Proceedings*, Annual Technical Session, Structural Stability Research Council, University of Missouri, Rolla, MO, 143-158.

Kaehler, R.C., White, D.W. and Kim, Y.-D. (2010), "Frame Design Using Web-Tapered Members," AISC Design Guide 25, MBMA/AISC, (to appear)

Kaehler, R.C.,(2005), "Proposed Design Guide Research Parameter Limits," Notes, Metal Building Manufacturers Association.

King, C. (2001a), *In-Plane Stability of Portal Frames to BS 5950-1:2000*, SCI Publication P292, Steel Construction Institute, Ascot, Berkshire, 213 pp.

King, C. (2001b), *Design of Single Span Steel Portal Frames to BS 5950-1:2000*, SCI Publication P252, Steel Construction Institute, Ascot, Berkshire.

Kim, Y.D. and White, D.W. (2008), "Lateral Torsional Buckling Strength of Prismatic and Web-Tapered Beams," *Proceedings*, Annual Technical Session, Structural Stability Research Council, Missouri University of Science and Technology, Rolla, MO, April.

Kuchenbecker, G.H., White, D.W. and Surovek-Maleck, A.E. (2004), "Simplified Design of Building Frames using First-Order Analysis and K = 1.0," *Proceedings*, SSRC Annual Technical Sessions, April, 20 pp.

Lagrange (1770-1773), "Sur la figure des colonnes," *Misc. Taurinensia*, Vol. 5. (Reprinted in "Oeuvres de Lagrange," Vol. 2, Gauthier-Villars, Paris, 1868, pp. 125-170.)

Lee, G.C., Morrell, M.L. and Ketter, R.L. (1972), "Design of Tapered Members," *Welding Research Council Bulletin*, No. 173, 1-32.

Lee, G.C. and Morrell, M.L. (1975), "Application of AISC design provisions for tapered members," *Engineering Journal*, AISC, 12(1), 1-13.

Lee, G.C., Chen, Y.C. and Hsu, T.L. (1979), "Allowable Axial Stress of Restrained Multi-Segment, Tapered Roof Girders," *Welding Research Council Bulletin*, No. 248, May, 1-28.

Lee, G.C. and Hsu, T.L. (1981), "Tapered Columns with Unequal Flanges," *Welding Research Council Bulletin*, No. 272, November, 15-23.

Lee, G.C., Ketter, R.L. and Hsu, T.L. (1981), *The Design of Single Story Rigid Frames*, Metal Building Manufacturers Association, Cleveland, OH, 267 pp.

LeMessurier, W. J. (1977), "A Practical Method of Second Order Analysis. Part 2: Rigid Frames," Engineering Journal, AISC, 13(4), 89-96.

Lu, L.W. (1965), "Effective Length of Columns in Gable Frames," *Engineering Journal*, AISC, January, 6-7.

Lui, E.M. (1992), "A Novel Approach for K Factor Determination," *Engineering Journal*, AISC 29(4), 150-159.

Maleck, A.E. and White, D.W. (2003), "Direct Analysis Approach for the Assessment of Frame Stability: Verification Studies," *Proceedings*, SSRC Annual Technical Sessions, 18 pp.

Maleck, Andrea E. (2001), "Second-Order Inelastic and Modified Elastic Analysis and Design Evaluation of Planar Steel Frames," Ph.D. Dissertation, Georgia Institute of Technology, 579 pp.

Martinez-Garcia, J.M. (2002), "Benchmark Studies to Evaluate New Provisions for Frame Stability Using Second-Order Analysis," M.S. Thesis, School of Civil Engineering, Bucknell Univ., 241 pp.

MBMA (2006), *Metal Building Systems Manual*, 2006 Ed., Matal Building Manufacturers Association, Cleveland, OH.

McGuire, W. (1968), *Steel Structures*, Prentice Hall, Englewood Cliffs, NJ.

Morrell, M.L. and Lee, G.C. (1974), "Allowable Stresses for Web-Tapered Beams with Lateral Restraints," *Welding Research Council Bulletin*, No. 192. 1-12.

Naranayan (1983), *Beams and Beam Columns: Stability and Strength*, Applied Science, London, UK, 242 pp.

Nethercot (1974), "Residual Stresses and Their Influence upon the Lateral Buckling of Rolled Steel Beams," *The Structural Engineer*, 52(3), 89-96.

Nethercot, D.A. and Trahair, N.S. (1976), "Lateral Buckling Approximations for Elastic Beams," *The Structural Engineer*, 54(6), 197-204.

Newmark, N.M. (1943), "A Numerical Procedure for Computing Deflections, Moments and Buckling Loads," *Transactions ASCE*, 108, 1161-88Ostwald (1910), "Klassiker der exakten Wissenschaften" No. 175, Leipzig.

Ozgur, C., Kim, Y.D., and White, D.W. (2007), "Consideration of End Restraint Effects in Web-Tapered Members," Structural Engineering Mechanics and Materials Report No. 32, School of Civil and Environmental Engineering, Georgia Institute of Technology, Atlanta, GA, June.

Polyzois, D. and Raftoyiannis, I.G. (1998), "Lateral-Torsional Stability of Steel Web-Tapered I-Beams," *Journal of Structural Engineering*, ASCE, 124(10), 1208-1216.

Prawel, S.P., Morrell, M.L. and Lee, G.C. (1974), "Bending and Buckling Strength of Tapered Structural Members," Welding Research Supplement, Vol. 53, February, 75-84.

Rebelo, C., Lopes, N., Simoes da Silva, L., Nethercot, D., and Vila Real, P.M.M. (2009), "Statistical Evaluatio of the Lateral-Torsional Buckling Resistance of Steel I-Beams, Part 1: Variability of the Eurocode 3 Resistance Model," *Journal of Constructional Steel Research*, 65, 818-831.

Richter, J.F. (1998), "Flexural Capacity of Slender Web Plate Girders," M.S. Thesis, The University of Texas at Austin, Austin, TX, 133 pp.

SAA (1998), Steel Structures, AS4100-1998, Standards Association of Australia, Australian Institute of Steel Construction, Sydney, Australia.

Salmon, C.G. and Johnson, J.E. (1996), *Steel Structures, Design and Behavior*, 4th Ed., Prentice Hall, NJ, 1024 pp.

Salter, J.B., Anderson, D., and May, I.M. (1980), "Tests on Tapered Steel Columns," *The Structural Engineer*, 58A(6), 189-193.

Salvadori, M. G. (1951), "Numerical Computation of Buckling Loads by Finite Differences," ASCE, *Transactions*, 116, 590-625.

Shiomi, H., Nishikawa, S. and Kurata, M. (1983), "Tests on Tapered Steel Beam-Columns," *Transactions of JSCE*, 15, 99-101.

Shiomi, H. and Kurata, M. (1984), "Strength Formula for Tapered Beam-Column," *Journal of Structural Engineering*, 110(7), 1630-1643.

Silvestre, N. and Camotim, D. (2002), "Post-Buckling Behavior, Imperfection Sensitivity and Mode Interaction in Pitched-Roof Steel Frames," *Proceedings*, Annual Technical Session, Structural Stability Research Council, University of Missouri, Rolla, MO, 139-162.

Simulia (2009), *ABAQUS/Standard Version 6.9-1*, Simulia, Inc. Providence, RI.

Surovek-Maleck A.E. and White, D.W. (2004a), "Alternative Approaches for Elastic Analysis and Design of Steel Frames. I: Overview," *Journal of Structural Engineering*, ASCE, 130(8), 1186-1196.

Surovek-Maleck A.E. and White, D.W. (2004b), "Alternative Approaches for Elastic Analysis and Design of Steel Frames. II: Verification Studies," *Journal of Structural Engineering*, ASCE, 130(8), 1197-1205.

Timoshenko, S.P. (1936), *Theory of Elastic Stability*, McGraw-Hill, New York, NY, 518 pp.

Timoshenko, S.P. and Gere, J.M. (1961), *Theory of Elastic Stability*, McGraw-Hill Book Company, New York, NY, 541 pp.

Vandepitte, D. (1982), "Non-iterative Analysis of Frames Including the P-Δ Effect," *Journal of Constructional Steel Research*, 2(2), 3-10.

Watwood, V.B. (1985), "Gable Frame Design Considerations," *Journal of Structural Engineering*, ASCE, 111(7), 1543-1558.

White, D.W. (2006), "Structural Behavior of Steel," *Steel Bridge Design Handbook,* National Steel Bridge Alliance, Chapter 6.

White, D.W. (2008), "Unified Flexural Resistance Equations for Stability Design of Steel I-Section Members: Overview," *Journal of Structural Engineering*, ASCE, 134(9), 1405-1424.

White, D.W. and Barth, K.E. (1998), "Strength and Ductility of Compact-Flange I-Girders in Negative Bending," *Journal of Constructional Steel Research*, 45(3), 241-279.

White, D.W. and Chang, C.J. (2007), "Improved Flexural Stability Design of I-Section Members in AISC (2005) – A Case Study Comparison to AISC (1989) ASD," *Engineering Journal,* AISC, 3rd quarter.

White, D.W. and Hajjar, J.F. (1991), "Application of Second-Order Elastic Analysis in LRFD: Research to Practice," *Engineering Journal*, AISC, 4th quarter, 133-148.

White, D.W. and Jung, S.-K. (2008), "Unified Resistance Equations for Stability Design of Steel I-Section Members: Uniform Bending Tests," *Journal of Structural Engineering*, ASCE, 134(9), 1450-1470.

White, D.W. and Kim, S.-C. (2003), "Simplified Strength Calculations for Noncompact and Slender Web I-Section Beam-Column," Structural Engineering, Mechanics and Materials, Report No. 28, School of Civil and Environmental Engineering, Georgia Institute of Technology, Atlanta, GA 41pp.

White, D.W. and Kim, Y.D. (2008), "Unified Resistance Equations for Stability Design of Steel I-Section Members: Moment Gradient Tests," *Journal of Structural Engineering*, ASCE, 134(9), 1471-1486.

White, D.W., Surovek-Maleck, A.E. and Kim, S.-C. (2007a), "Direct Analysis and Design Using Amplified First-Order Analysis, Part 1 – Combined Braced and Gravity Framing Systems," *Engineering Journal*, AISC, 4th quarter, 305-322.

White, D.W., Surovek-Maleck, A.E. and Chang, C.-J. (2007b), "Direct Analysis and Design Using Amplified First-Order Analysis, Part 2 – Moment Frames and General Rectangular Framing Systems," *Engineering Journal*, AISC, 4th quarter, 323-340.

White, D.W., Surovek, A.E., Alemdar, B.N., Chang, C.-J., Kim, Y.D., and Kuchenbecker, G.H. (2006), "Stability Analysis and Design of Steel Building Frames: The AISC (2005) Specification and Beyond," *International Journal of Steel Structures*, 6(2), 71-92 pp.

Wong-Chung, A.D. and Kitipornchai, S. (1987), "Partially Braced Inelastic Beam Buckling Experiments," *Journal of Constructional Steel Research*, 7, 189-211.

Young, B.W. and Robinson, K.W. (1975), "Buckling of Axially Loaded Welded Steel Columns," *The Structural Engineer*, 53(5), 203-207.

Yura, J. and Helwig, T. (1996), "Bracing for Stability," Short Course Notes, Structural Stability Research Council.

VITA

Yoon Duk Kim was born in Seoul, South Korea on 23 August 1978, the daughter of Yong Jin Kim and Young Hee Hahm. She attended Hanyang University where she studied architectural engineering and received her Bachelor of Science in February 2001. In August 2002, she moved to United States to attend the Graduate School of Civil and Environmental Engineering at Georgia Institute of Tech. Upon receiving her Master's degree in 2004, Yoon Duk continued her graduate study pursuing a Doctoral Degree in Civil Engineering at Georgia Institute of Technology.